The Study and Application of Membrane Binding Supramolecular Self-associating Amphiphiles

Jessica Emily Boles

Thesis for the degree of Doctor of Philosophy

University of Kent

School of Natural Sciences

2022

Abstract

With the looming threat of antimicrobial resistance (AMR) and the distinct absence of new antimicrobial agents on the market, the development of novel therapeutic treatments against AMR bacteria is vital. The work detailed herein demonstrates the potential for supramolecular self-associating amphiphiles (SSAs) to act as the first anionic antimicrobial potentiator of **novobiocin (52)** and **rifampicin (53)** against ESKAPE pathogen P*seudomonas aeruginosa*. The most effective combination offered a dramatic 8-fold decrease of the MIC of **novobiocin (52)**, from 3.2 mM to 0.4 mM in the presence of a non-inhibitory SSA concentration. Extensive physicochemical characterisation of SSA/antimicrobial interactions offer explanations for the observed synergistic behaviour.

This thesis validates the hypothesis that SSAs are bacterial membrane disruptors through the employment of fluorescence spectroscopy. The urea benzothiazole SSAs were found to exhibit the highest level of broad range vesicle lysis, however a lack of correlation was observed between vesicle lysis and selective SSA: phospholipid interaction. The ability for SSAs to induce membrane fluidity was explored, revealing the carboxylate moiety over a sulfonate can selectively increase the membrane fluidity of bacterial model membranes over eukaryotic. Finally, a patch clamp method was optimised, providing insight into the potential transport mechanism of SSAs in the presence of an anionophore.

Publications generated from data presented within this thesis

1. **Supramolecular self-associating amphiphiles (SSAs) as enhancers of antimicrobial agents towards *Escherichia coli* (*E. coli*),** J. E. Boles, R. J. Ellaby, H. J. Shepherd and J. R. Hiscock, *RSC Adv.*, 2021, **11**, 9550-9556.[1]

2. **Anionic self-assembling supramolecular potentiators of antimicrobial activity against Gram-negative bacteria,** J. E. Boles, G. T. Williams, N. Allen, L. J. White, K. L. F. Hilton, P. I. A. Popoola, D. P. Mulvihill and J. R. Hiscock, *Adv. Therap,* 2022, DOI: 10.1002/adtp.2200024.[2]

3. **Establishing the selective phospholipid membrane coordination, permeation and lysis properties for a series of 'druggable' supramolecular self-associating antimicrobial amphiphiles,** J. E. Boles, C. Bennett, J. Baker, H. A. Kotak, E. R. Clark, Y. Long, L. J. White, H. Y. Lai, C. K. Hind, J. M. Sutton, M. D. Garrett, A. Cheasty, J. L. Ortega-Roldan, M. Charles, C. J. E. Haynes and J. R. Hiscock, *Chem. Sci,* 2022, DOI:10.1039/D2SC02630A.[3]

4. **Towards the Prediction of Antimicrobial Efficacy for Hydrogen Bonded, Self-Associating Amphiphiles,** N. Allen, J. E. Boles, L. J. White, G. T. Williams, D. F. Chu, R. J. Ellaby, H. J. Shepherd, K. K. L. Ng, L. R. Blackholly, B. Wilson, D. P. Mulvihill and J. R. Hiscock, *ChemMedChem*, 2020, **15**, 2193–2205.[4]

Acknowledgements

Thank you to my supervisor Dr Jennifer Hiscock for being an incredible mentor, your ingenuity, knowledge, and drive is something I will continue to aspire to. I am incredibly grateful to Professor Dan Mulvihill, Dr Charlotte Hind and Dr Mark Sutton for their guidance and support throughout.

Many thanks to the Hiscock group members, both past and present, particularly George, Kira, Rebecca, Kendrick, Jack and Nyasha. My special thanks are extended to Lisa for your direction and encouragement but most importantly your friendship.

I also express endless gratitude to my family for their unfailing support and for being my ultimate cheer team.

Table of contents

Declaration of authorship

I, Jessica Emily Boles, declare that this thesis titled, 'The Study and Application of Membrane Binding Supramolecular Self-associating Amphiphiles' and the work presented, unless stated, are my own.

Signed: 

Date: 03.05.22

Abbreviations

AMP	Antimicrobial peptide
AMS	Aminomethane sulfonic acid
AMR	Antimicrobial resistance
CB7	Cucurbit[7]uril
CD	Cyclodextrin
CDI	1,1'-Carbonyldiimidazole
CL	Cardiolipin
CMC	Critical Micelle Concentration
CoEK	Cooperative equal *K*
D	Doublet (NMR)
D	Translational diffusion coefficient
$\mathbf{D_H}$	Hydrodynamic diameter
DCM	Dichloromethane
DLS	Dynamic Light Scattering
DMPK	Drug metabolism and pharmacokinetics
DMSO	Dimethylsulfoxide
DOFL	Danofloxacin
DNA	Deoxyribonucleic acid
EK	Equal *K*
$\boldsymbol{E_{max}}$	Energy maximum
$\boldsymbol{E_{min}}$	Energy minimum
HBA	Hydrogen bond acceptor
HBD	Hydrogen bond donator
J	Coupling constant (NMR)
***K*a**	Association constant
$\boldsymbol{K_B}$	Boltzmann constant
$\boldsymbol{K_{dim}}$	Dimerisation equal *K*
LB	Lysogeny broth
m	Multiplet (NMR)
MIC	Minimum inhibitory concentration

MRSA	Methicillin-resistant *Staphylococcus aureus*
MSSA	Methicillin-sensitive *Staphylococcus aureus*
MW	Molecular weight
NMR	Nuclear magnetic resonance spectroscopy
OD	Optical density
PBP	Penicillin-binding protein
PC	Phosphatidylcholine
PE	Phosphatidylethanolamine
PG	Phosphatidylglycerol
PPG	Poly(propylene glycol)
q	Quartet (NMR)
SEM	Scanning electron microscopy
SSA	Supramolecular Self-associating Amphiphile
t	Triplet (NMR)
TBA	Tetrabutylammonium
TEM	Transmission electron microscopy
VT	Variable temperature
WHO	World Health Organisation
XRD	X-ray diffraction
ZP	Zeta potential

1. Chapter 1

1.1. Supramolecular chemistry

The field of supramolecular chemistry was first acknowledged by the award of the Nobel Prize in 1987 to three of its pioneers; Jean-Marie Lehn, Charles Pederson and Donald Cram.[5] This branch of chemistry was defined by Lehn as 'chemistry beyond the molecule', based upon the association of two or more species by non-covalent intermolecular forces.[6]

Covalent interactions can range between 150 kJ mol^{-1} to 450 kJ mol^{-1}, non-covalent bonds in comparison are considerably weaker.[7] However, when such interactions are used cooperatively, stable supramolecular complexes are created. The weakest of the non-covalent interaction is Van de Waals, with strengths < 5 kJ mol^{-1}. Such interactions occur when electron distributions of adjacent atoms come into close contact, charge fluctuations align the partial positive charge of one atom with the partial negative charge of another (Figure 1).[8] A weak, non-directional attraction is established, highly dependent upon distance and polarisability of the molecule.

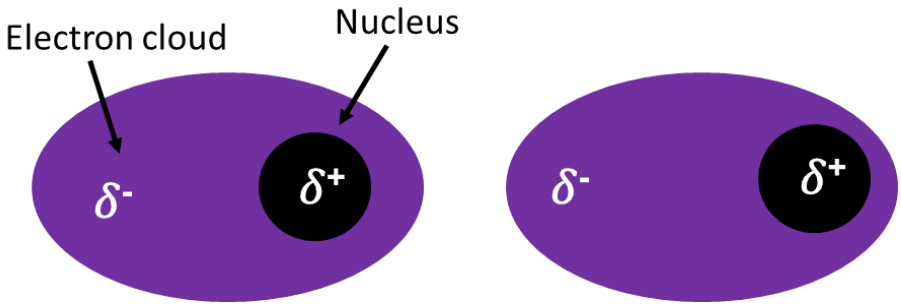

Figure 1 – A Van De Waals interaction between two atoms.

Prominent in π-conjugated systems, π-π stacking interactions arise through the intermolecular overlapping of p-orbitals. With energies of 5–50 kJ mol^{-1},[7] these interactions can be broadly classified into three types: face-to-face (centred), face-to-face (displaced) and edge-to-face (Figure 2).[9,10] Despite the maximal overlap offered by centred face-to-face, large, substituted aromatic rings favour displaced face-to-face π-π interactions. Here the interaction

occurs between the centre of one aromatic ring and the corner of another offset ring system. Edge-to-face interactions are instead favoured by small, unsubstituted aromatic rings, whereby the negative electron cloud of one conjugated system is attracted to the positive framework of an alternate system.[10,11]

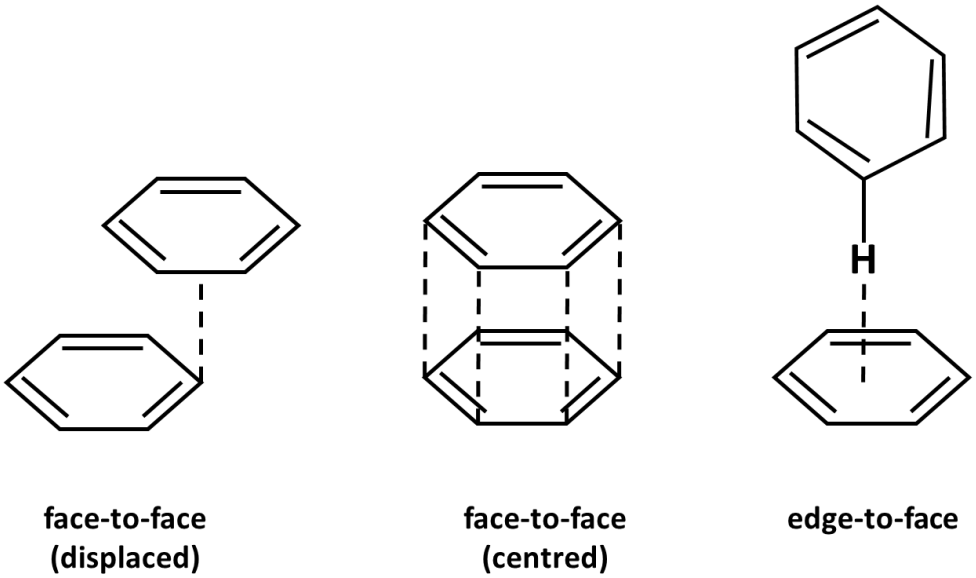

Figure 2 – The three types of π-π interactions; face-to-face (displaced), face-to-face (centred) and edge-to-face.[7]

Electrostatic interactions can be subdivided into three classes: ion-ion interactions (200-300 kJ mol^{-1}), ion-dipole interactions (50-200 kJ mol^{-1}) and dipole-dipole interactions (5-50 kJ mol^{-1}).[7] The strongest interaction, ion-ion, exhibits strength close to a covalent bond and such interaction is non-directional, it can occur in any orientation. In contrast, ion-dipole and dipole-dipole require the two species to be aligned in the optimal direction and therefore aggregates can only be formed from complementary pairs.[12]

Owing to the strength and high degree of directionality, the hydrogen bond offers a crucial non-covalent interaction in the design of supramolecular systems. Such an interaction occurs between a proton acceptor (electron withdrawing group) and a proton donor (hydrogen bond attached to an electronegative atom).[13] These interactions are classified primarily on strength.[14] Interactions are considered 'strong' with bond energies between 60-120 kJ mol^{-1}, typically these are formed between two strong bases, such as the HF^{2-} which forms a linear

hydrogen bond. Moderate interactions exhibit 'bent' geometries, with bond energies between 16-60 kJ mol^{-1}, such interactions are observed with carboxylic acids where the bond forms via electron lone pairs between a neutral donor and acceptor group.[7] As directionality of hydrogen bonds increase with strength,[13] the weakest hydrogen bond interactions, such as C-H---O, display little linearity, with bond angles ranging from 90-120°.[7]

Supramolecular chemistry has primarily found inspiration from biological events, one such example is the enzyme-substrate interaction, termed the 'lock and key' model. Emil Fischer proposed the model, first recognising that binding must be selective with the guest exhibiting a shape/size complementary to the host molecule. This is a natural example of the host-guest concept, whereby the 'host' molecule possesses a molecular cavity which accommodates the 'guest' molecule.[15]

Supramolecular chemistry not only encompasses host-guest chemistry but also self-assembly.[15] Deoxyribonucleic acid (DNA) is a widely recognised example of a naturally evolved self-assembled system. A single strand of DNA is highly selective towards complementary base pairs, adenine (A) forms two hydrogen bonds with thymine (T) and guanine (G) forms three hydrogen bonds with cytosine (C) (Figure 3).[16] A double helix is stabilised through a combination of hydrogen bonding and π- π stacking interactions.[17] DNA is a rare self-assembling molecule as the specific assembly code can precisely define which strands will pair.[18] This provides researchers with the ability to predictably control their products, exploited in the world of DNA nanotechnology.[19,20]

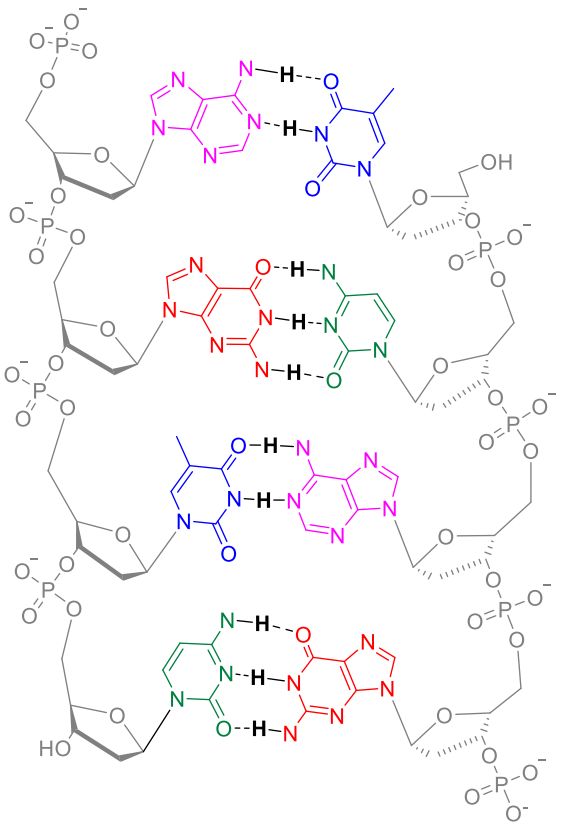

Figure 3 – A DNA double helix showing the Watson-crick base pairing of adenine (pink) and thymine (blue) via two hydrogen bonds and cytosine (green) and guanine (red) via three hydrogen bonds. The phosphate backbone is constructed of two antiparallel phosphate sugar chains (grey).

1.1.1. Amphiphiles

Amphiphiles are molecules possessing both hydrophilic (water-loving) and hydrophobic (water-hating) parts, linked together by covalent bonding. Conventionally, the hydrophobic component consists of a long hydrocarbon chain, either saturated or unsaturated and the hydrophilic head can be ionic or non-ionic. Amphiphiles can be classified into nonionic (**1**); anionic (**2**), cationic (**3**) and zwitterionic (**4**) (Figure 4).

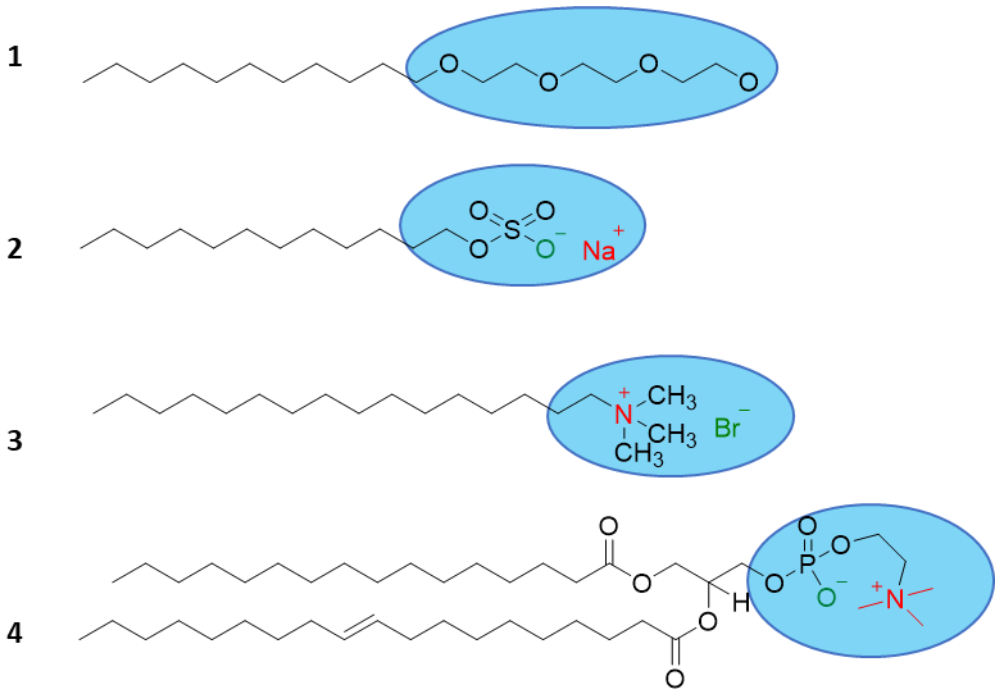

Figure 4 – Examples of **1**) nonionic (polyoxyethylene alkyl ether), **2**) anionic (sodium dodecyl sulfate, **3**) cationic (cetyltrimethylammonium bromide) and **4**) zwitterionic amphiphilic molecule (phosphatidylcholine).[21]

Surfactants are a special class of amphiphile and are defined as substances which adhere to the interface between a solution and an alternate phase (gas/solid).[22] Anionic surfactants are commonly employed in the cosmetic and toiletry industry.[23] An example is sodium dodecyl sulfate (**1**, Figure 4), used in laundry detergents,[24] medicated shampoos and facial cleansers.[25] Owing to the inherent negatively charged bacterial membrane surfaces,[26] cationic surfactants have gained significant attention as bacterial membrane disruptors.[27] Such amphiphiles have been strategically designed to mimic naturally occurring antimicrobial peptides, traditionally hindered by high manufacturing costs and poor pharmacokinetic properties.[28,29]

Molecular geometry of the surfactant molecules and solution conditions (temperature, pH, concentration)[30,31] dictate the shape and size of micellar aggregates.[21] This control provides the opportunity to develop and manipulate molecular architecture. Under aqueous conditions, the most recognised aggregation is the spherical micelle (Figure 5a), spontaneously forming in milliseconds and containing approx. 50-100 surfactant molecules.[23] At surfactant concentrations above the critical micelle concentration (CMC), molecules associate into sphere-shaped aggregates, whereby the polar hydrophilic heads are in contact with the water and alkyl tails are

shielded within the micelle core.[32] Spherical micelles are utilised in a range of applications including drug delivery,[33] diagnostics and nanomaterials.[34,35]

Cylindrical micelles, illustrated in Figure 5b, are predominantly formed by the addition of a strongly bound counter ion, this reduces the effective head group area allowing them to come closer.[36] Unlike spherical micelles, controlling the dimensions of cylindrical micelles provides a barrier to optimisation for various applications.[37] Additionally, uptake into cells can be substantially lower for elongated micelles vs spherical. Discher and co-workers investigated the cellular uptake of two polymeric micelles in rodents; one cylindrical in shape and the other spherical.[38] The cylindrical micelles were found to persist in the circulation for ten times longer than their spherical counterpart. Another common self-assembled structure is a bilayer, consisting of two stacked layers of amphiphilic molecules (Figure 5c), creating exterior polar surfaces and a non-polar interior. These structures can range in size from 10 μM – 10 nm and consist of one (unilamellar) or multiple (multilamellar) concentric bilayer surfaces.[21] The lipid bilayer is the universal basis for cell-membrane structure, as explored in Section 1.2.

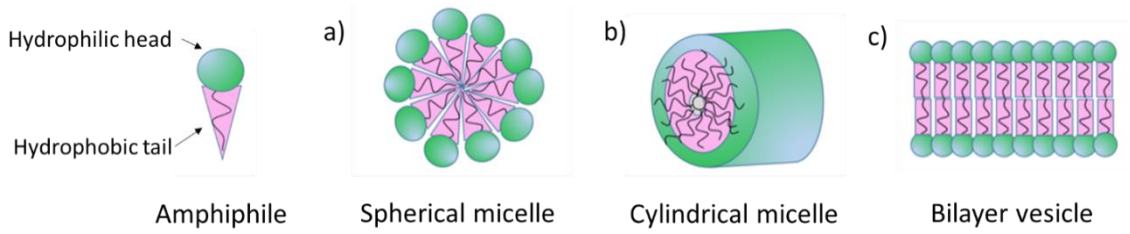

Figure 5 - Shapes of possible self-assembled structures formed by amphiphiles in water.[21]

1.1.2. Supra-amphiphiles

Supra-amphiphiles encompass those amphiphiles which also utilise non-covalent interactions such as hydrogen bonds,[39] electrostatic interactions and/or host-guest interactions to stabilise the self-associated structures.[40,41] Supra-amphiphiles have the advantage of controllability and stimuli-responsiveness, owing to the reversible nature of the non-covalent interactions.[42]

Such examples include the work conducted by Zhang *et al.* who designed two supra-amphiphiles; a wedge-shaped (**5**-**7**) and a dumbbell-shaped (**8**), shown in Figure 6.[43] Under aqueous conditions, assembled through π-π stacking interactions, **5**-**7** alone self-assemble into micelles and in a co-assembled system with **8**, self-assemble to form hollow vesicles. The addition of the dumbbell-shaped **8** causes the interface between the hydrophilic and hydrophobic regions to change from a curved interface to a flatter one. The reduction in curvature, releases strain, causing the transition from micelle to vesicle.

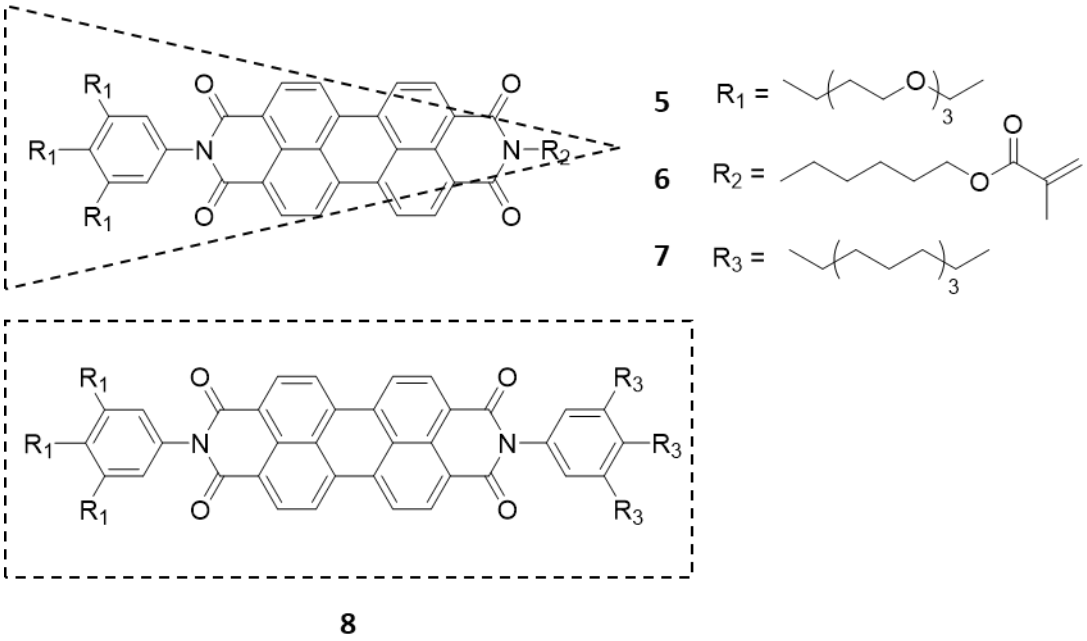

Figure 6 – Chemical structure of supra-amphiphiles synthesised by Zhang *et al.*; wedge-shaped (**5**-**7**) and dumbbell-shaped, **8**.[43]

Mediated by cooperative hydrogen bonding and host-guest chemistry, Dong and co-workers have developed supramolecular micellar and reverse micellar hydrogels from the same polypeptide based copolymer.[44] The resultant hydrogels are dual responsive to both pH and temperature, offering the potential for controlled drug-release. The loading capacity for the anti-cancer drug, doxorubicin was investigated, with the reverse micellar hydrogel accommodating a 10 % higher loading content, with a controlled release sustained over > 45 days.

Kim *et al.* synthesised an amide dendron-pyrene conjugate amphiphile (**9**) (Figure 7a) which self-assemble into vesicles under aqueous conditions.[45] Upon addition of a cyclodextrin (CD), host-guest complexation induces a helical transformation from vesicles to CD-coated nanotubes, as illustrated in Figure 7b. Additionally, the authors found this to be a reversible supramolecular transformation, using poly(propylene glycol) (PPG) to remove CD from the surface of the nanotubes, forming a pseudorotaxane as a by-product.

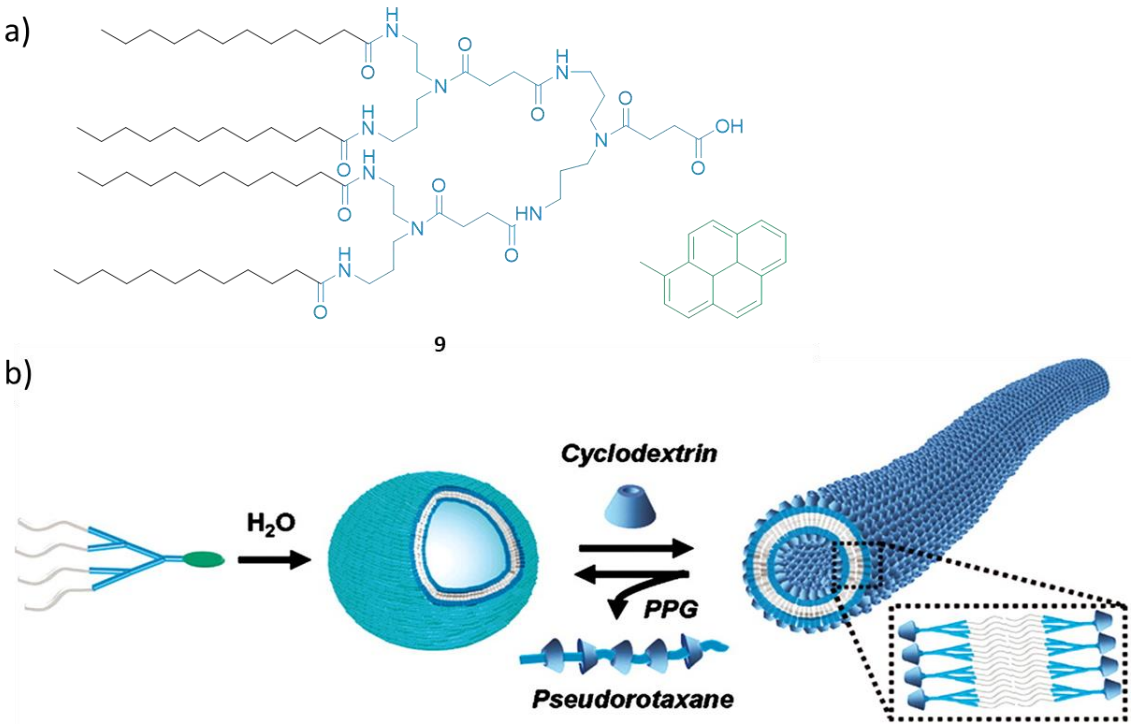

Figure 7 – a) Chemical structure of an amide dendron-pyrene conjugate amphiphile (**9**); b) schematic reversible route from amphiphile to vesicle to CD coated nanotube.[45]

1.2. The Bacterial membrane

The multi-layered bacterial cell envelope serves as a protection from the unpredictable and hostile external environment.[46] Bacteria can be grouped into two distinct groups based on fundamental structural differences in the cell envelope, and are classed as either Gram-positive or Gram-negative. In 1884, Christian Gram developed a staining procedure; one group retains the crystal violet dye (Gram-positive), and the other does not (Gram-negative).[47] Gram-negative bacteria is formed of three primary layers; the outer membrane, the peptidoglycan cell wall and

the inner membrane (Figure 8).[48] Gram-positive bacteria however lacks a protective outer membrane but consists of a much thicker peptidoglycan cell wall (Figure 8).[49] Long anionic polymers named teichoic acids, are embedded into the peptidoglycan layers, playing a crucial role in fundamental aspects of physiology, such as, the regulation of cell division and cell shape determination.[50]

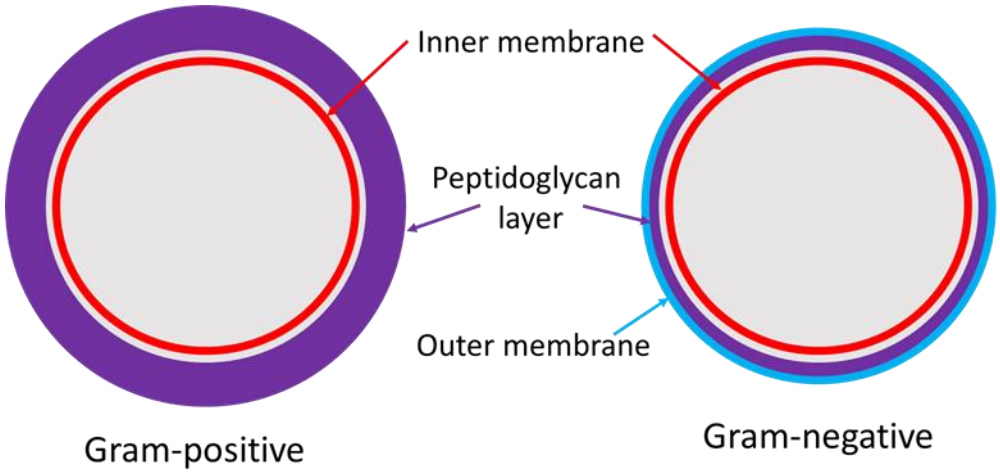

Figure 8 – The cell envelope of Gram-positive and Gram-negative bacteria.[51]

Bacterial membranes are composed of amphiphilic lipids, these can be categorised into glycerophospholipids (phospholipids), sphingolipids and sterols.[52] The most prevalent is the phospholipid, consisting of two fatty acids, a glycerol linking group, a phosphate moiety and a variable head group (Figure 9).[53] As discussed in Section 1.1.1, the amphiphilic nature of these lipids result in a self-assembled, semi-permeable bilayer, whereby the polar hydrophilic head group interacts with the aqueous environment and the hydrophobic lipid tails are concealed. The length and saturation of the fatty acids can determine the ability of the phospholipid molecules to stack against one another, Figure 9 illustrates how the presence of a double bond can create a small kink in the phospholipid tail.[54]

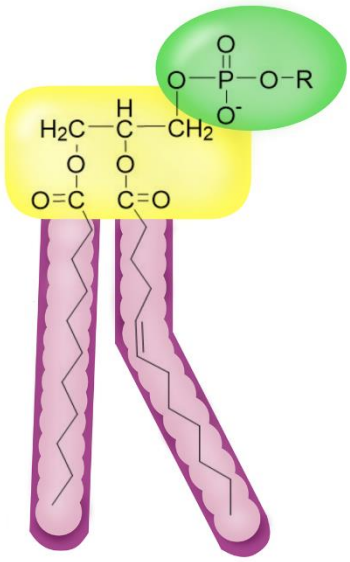

Figure 9 – The general structure of a glycerophospholipid (phospholipid). The hydrocarbon chain length and level of saturation can vary. Purple = hydrophobic tail, yellow = glycerol linking group, green = phosphate group.[52]

The phospholipid bilayer offers a functional barrier to the subcellar compartments, maintaining cell permeability of small neutral molecules (O_2, CO_2) and solvents (H_2O) but preventing diffusion of larger molecules (e.g., glucose) and ionic species (Cl^-, Na^+).[52] The addition of regulatory proteins and carbohydrates within the bilayer facilities closely-regulated membrane transport events, creating a fully-functioning membrane, capable of controlling the composition of the intracellular environment.[55]

1.2.1. Bacterial Phospholipid Membrane Composition

The chemical diversity of phospholipids is achieved through the variety and combination of building blocks. The hydrophobic fatty acid chains can vary in length, saturation and hydroxylation.[56] Alteration to the structure of the head group can further extend the diversity, a summary of some common structural modifications is presented in Table 1, along with the resultant change and nomenclature.[57]

Table 1- A summary of phospholipid structures; PE, PG, PC and CL, the position of the R group is illustrated in Figure 9.[57]

Lipid	R-group	Overall phospholipid charge
Phosphatidylethanolamine (PE)	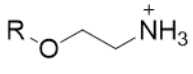	0
Phosphatidylcholine (PC)	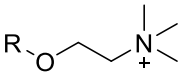	0
Phosphatidylglycerol (PG)	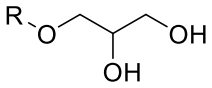	-1
Cardiolipin (CL)	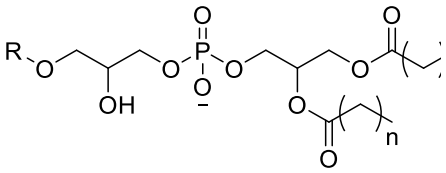	-2

The bacterial cell membrane predominantly contains mixtures of the polar phospholipids, PE and PG (Table 1).[58] Consequently, these membranes have been modelled synthetically using PE:PG 3:1,[58,59] however as detailed in recent review papers, this is not representative of many natural derived bacterial cells.[52,53] For example; Gram-positive methicillin-sensitive *Staphylococcus aureus* (MSSA) is composed of PG: L-PG : CL, 80: 12: 5.[60] Additionally, bacterial culture conditions,[61] life cycle and growth phase can impact phospholipid composition.[62–64] This is highlighted in the growth cycle of MSSA, where the composition changes from PG: L-PG: CL 79: 14: 4 in log phase growth to PG: L-PG: CL 66: 10: 14 during stationary growth phase.[65]

1.3. Membrane targeting antimicrobials

In 1928, Alexander Fleming kickstarted the beginning of the modern 'antibiotic era', discovering penicillin by chance after uncovering a mould contaminated agar plate.[66] Since then, antibiotics have revolutionized the treatment of infectious diseases worldwide and saved millions of lives.[67] Antimicrobial agents can be categorised based on mode of action, these include cell wall synthesis inhibitors,[68] protein synthesis inhibitors and nucleic acid synthesis inhibitors.[69–71] However, it is those antimicrobial agents which inhibit membrane function which form the focus of this section.

The bacterial lipid membrane is an attractive target in the design of antimicrobial agents, owing to the distinction from a mammalian membrane. On the surface of bacterial membranes, anionic lipids are exposed, whilst in eukaryotic membranes, anionic lipids face the interior of the cell.[72] Traditionally, such antimicrobials are cationic, allowing for greater selectivity towards anionic bacterial cell membranes. Such examples include polymyxins which are cationic cyclic peptides with long hydrophobic tails (**10**, **Error! Reference source not found.**).[73] Polymyxins are selectively toxic towards Gram-negative bacteria, interacting with lipopolysaccharide molecules present on the outer membrane.[74] The interaction between polymyxin and lipopolysaccharides causes the membrane permeability to increase, discharging molecules and increasing water uptake, disrupting the osmotic balance of the cell, leading to cell death.[75]

The first membrane-targeting antibiotic to become FDA-approved were antimicrobial peptides (AMPs).[76] Preferential binding of these agents to negatively charged and zwitterionic lipids provide AMPs with the necessary selectivity. AMPs are typically composed of 12-50 amino acids and defined by the inclusion of two or more positively charged residues (e.g lysine or arginine) and an abundance (> 50 %) of hydrophobic residues.[77,78] Most AMPs to date can be classified by their secondary structure; β-sheet, α-helix, extended, and loop.[78] Establishing

structure-activity relationship is difficult owing to the ability of AMPs to undergo confirmational changes upon adsorption into the bacterial cell membrane.[79]

One such example is daptomycin, which is one the most recent antibiotics to be launched for clinical use, the struture is shown in Figure 10.[80] First discovered in 1983, daptomycin is now considered an antibiotic of last resort, reserved for infections where first and second line treatments have failed. Unlike polymyxin, daptomycin is an anionic molecule by nature, the presence of calcium ions assist in overcoming the charge-charge repulsion with the anionic phospholipid heads.[81] Whilst polymyxin shows selectivity towards Gram-negative bacteria, daptomycin illicits higher activity against Gram-positive bacteria. The lipopeptide antibiotic is known to selectivity bind to PG, a phospholipid predominantly found in the outer membrane of Gram-positive bacterial species.[52,80]

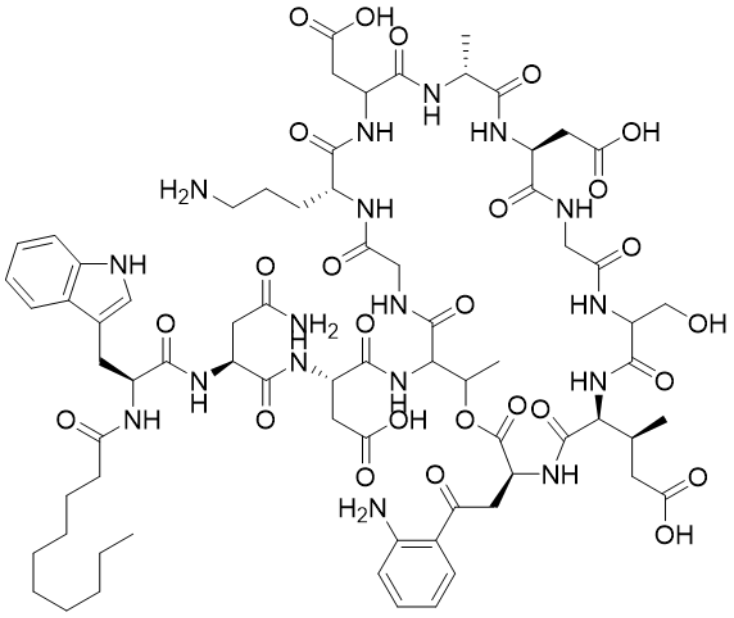

10

Figure 10 – Chemical structure of daptomycin, **10**.[82]

Legault *et al* have developed a new membrane targeting antibiotic, balsacone C, found to be active against > 30 clinical isolates of MRSA.[83] Following treatment, the authors observed no resistant isolates of MRSA against balsacone C, showing the potential of these agents to inhibit bacterial without inducing resistance. Fluorescence microscopy verified mechanism of action,

indicating a loss of cell membrane integrity following exposure to even low concentrations of balsacone C. Scanning electron microscopy (SEM) observations provided further evidence for this, exposing invaginations and structural alterations to the bacterial cell surface.[83]

1.4. Antimicrobial resistance

Following the acceptance of his Nobel Prize in 1945, Alexander Fleming cautioned that the misuse of antibiotics would lead to resistant bacteria.[84] True to his prediction, over 70 years later, antimicrobial resistance (AMR) is now manifesting on a global scale with particular bacterial strains now identified to be completely resistant to all currently marketed antimicrobial agents.[85] Causes for this crisis have been attributed to overuse,[86] inappropriate prescribing,[87] extensive agriculture use and unavailability of new antibiotics.[67,88]

A recent UK Government commissioned report emphasised the threat of AMR by predicting possible consequences if the widespread and excessive misuse of antibiotics were to continue at the same rate.[89] It has been predicted by the year 2050, 10 million global deaths a year will be attributable to AMR; in perspective this overtakes the number of deaths attributed to cancer in 2014 (Figure 11). The economic burden by 2050 is forecast to be $100 trillion worldwide. In 2019, it was estimated a total of 4.95 million deaths worldwide were associated with bacterial AMR, a value higher than those deaths attributed to major diseases malaria and HIV.[90]

To aid research focus, the World Health Organisation (WHO) published a list of antibiotic-resistant priority pathogens in urgent need for new antibiotics.[91] The 'CRITICAL' list included; Gram-negative carbapenem-resistant *Pseudomonas aeruginosa* and *Acinetobacter baumannii.* Efforts to supress the rise of AMR include; removing antibiotics from animal feed[92,93] and implementing evidence-based prescribing for both clinicians and veterinarians.[94] However, high drug discovery costs and poor market returns have resulted in no novel antimicrobial treatment brought to market since 1987.[95,96]

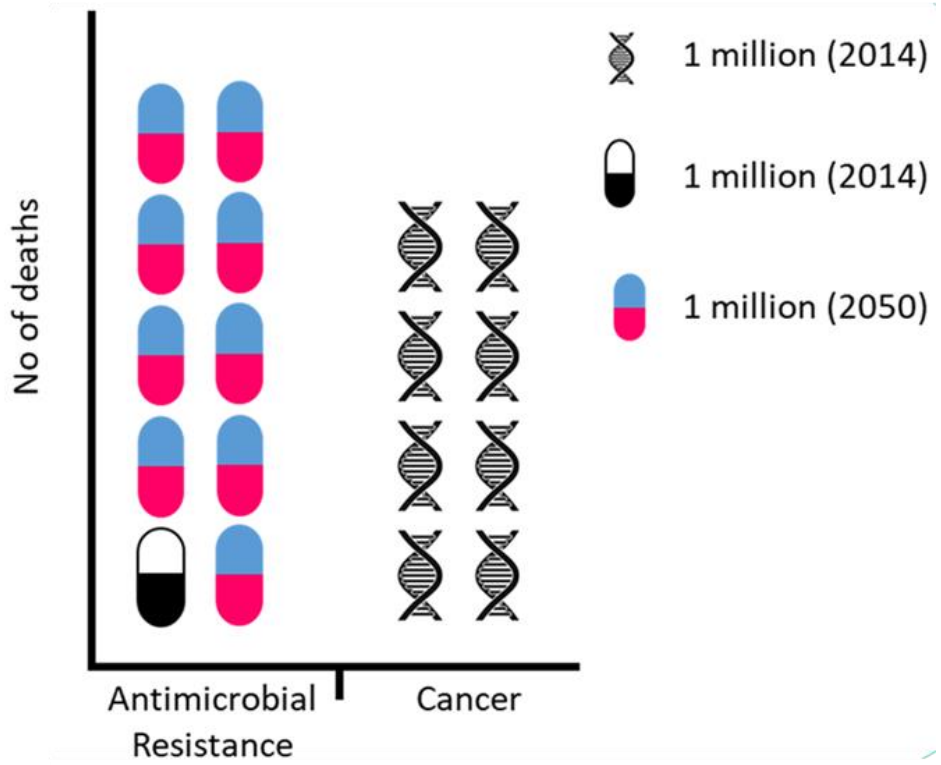

Figure 11 - Illustration showing the number of deaths caused by AMR and cancer in 2014 and the predicted number of deaths in 2050 attributable to AMR if current antibiotic practice persists.[89]

1.4.1. Mechanisms of resistance

Over many years, bacteria have evolved sophisticated mechanisms of resistance to evade the effects of antimicrobial agents and ultimately thrive in their presence.[97] The major mechanisms of resistance include:

a) Limiting uptake of a drug

Owing to the lipopolysaccharide outer membrane present in Gram-negative cells, bacteria already have an innate resistance to a great number of intracellular antimicrobial agents.[97] Porin (water-filled) channels traditionally allow hydrophilic molecules, such as β-lactams and fluoroquinolones access to the inner cell, however, resistance mechanism have developed which control the number and specific selectivity of porin channels present.[98] The formation of biofilms can further limit drug uptake. A self-produced polymer matrix provides a physical

barrier between bacteria and antimicrobial agent, showing up to 1000 times more antimicrobial resistance than the comparable planktonic cell.[99]

b) Modification of a drug target

Bacteria can interfere with antimicrobial target sites through protection, modification or offering an alternative low affinity target.[97] For example; alteration of the structure and number of penicillin-binding proteins (PBPs) directly impacts the amount of β-lactam drug that can bind and illicit an antimicrobial effect.[98] Low affinity targets include; an alternate b subunit of DNA gyrase or alternate RNA polymerase for novobiocin and rifampicin resistance, respectively.[100]

c) Inactivation of a drug

A successful mechanism of resistance is via the transfer of a chemical moiety to the active component of a drug, the most common being phosphoryl, acetyl or adenyl.[98] Irrespective of biochemical reaction, it is typically steric hinderance which decreases the avidity of the drug for the desired target.[97] Inactivation can also occur through destruction of the antibiotic molecule itself, for example; the production of enzymes which can destroy the amide bond in a β-lactam ring, rendering such a class ineffective.[97]

d) Active efflux of a drug

The role of an efflux pump is to extrude toxic substances from a cell but bacteria can exploit this function.[98] The expression of efflux pumps is tightly controlled, however mutation events can lead to overexpression.[101] The four major mechanism of resistance are illustrated in Figure 12.

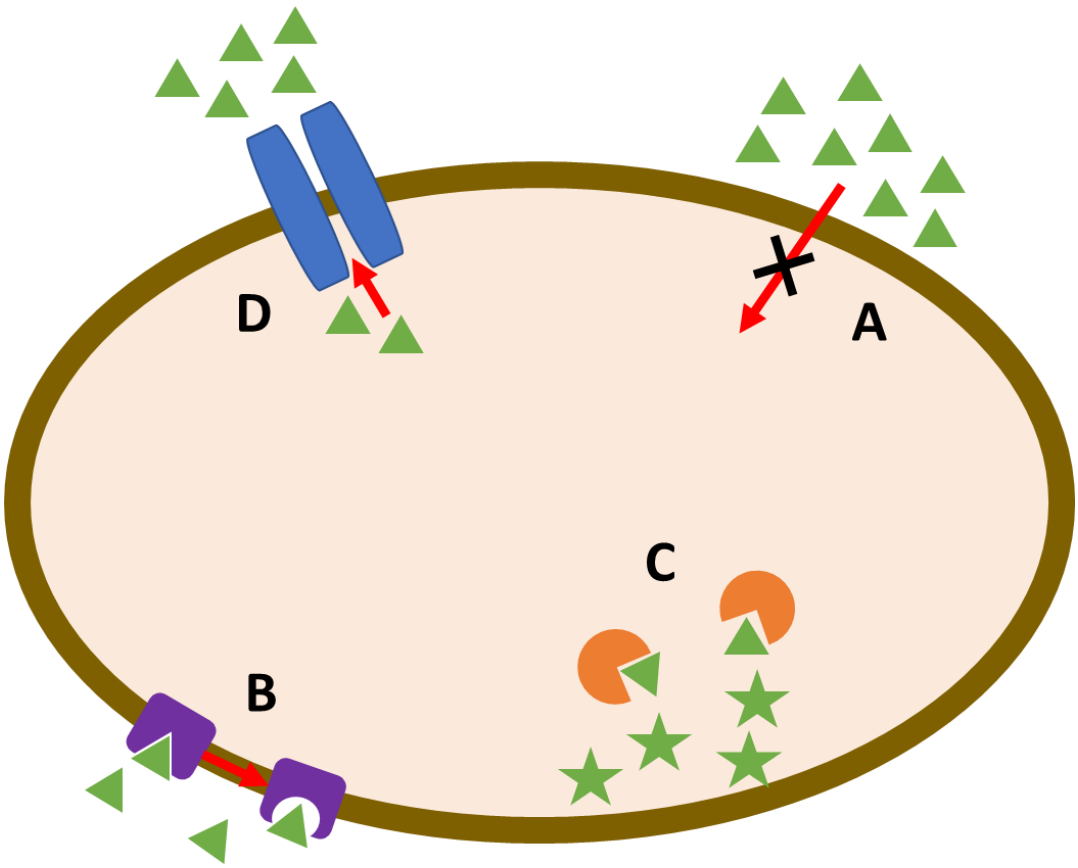

Figure 12 – An image of a cell illustrating the four main mechanisms of resistance a) limiting uptake of drug, b) modification of drug target, c) inactivation of drug and d) active efflux of a drug.[98]

1.5. Supramolecular Chemistry in AMR

Despite the lack of economic incentive, the development of novel next-generation antimicrobials to mitigate the spread of AMR has become vital. Many of these research efforts have been inspired by supramolecular chemistry.

Zhang *et al.* have synthesised a class of tubular molecules; attaching short antimicrobial peptides to the pillar[5]arene backbone.[102] These materials can insert in the bacterial lipid bilayer, forming unimolecular transmembrane channels. A high level of selectivity towards Gram-positive bacteria over mammalian erythrocytes has been observed, even at high tubular concentrations of 100 μM. A minimum inhibitory concentration (MIC) required to inhibit bacterial growth by 50 % (MIC_{50}) were determined, three synthetic tubular molecules exhibited MIC_{50} values < 0.8 μM against methicillin-resistant *Staphylococcus aureus* (MRSA). The

antimicrobial activity exhibited by these supramolecular constructs was found to be higher than the activity of Gramicidin, a marketed antimicrobial agent.

Mohanty and co-workers established a supramolecular approach to improving both the activity and shelf life of Danofloxacin (DOFL), a broad range fluoroquinolone antimicrobial drug.[103] As illustrated in Figure 13, DOFL was encapsulated within the macrocyclic host cucurbit[7]uril (CB7) (**11**) to produce **12**. Testing against four types of pathogenic bacteria, the MIC of DOFL was found to decrease by in the presence of CB7. The highest antimicrobial activity was observed against Gram-negative *Escherichia coli* and *Bacillus cereus*, resulting in a 3-5 fold reduction in MIC. In the presence of CB7, DOFL demonstrated enhanced thermal and photochemical stability and thus exhibited a longer shelf life as a combination.

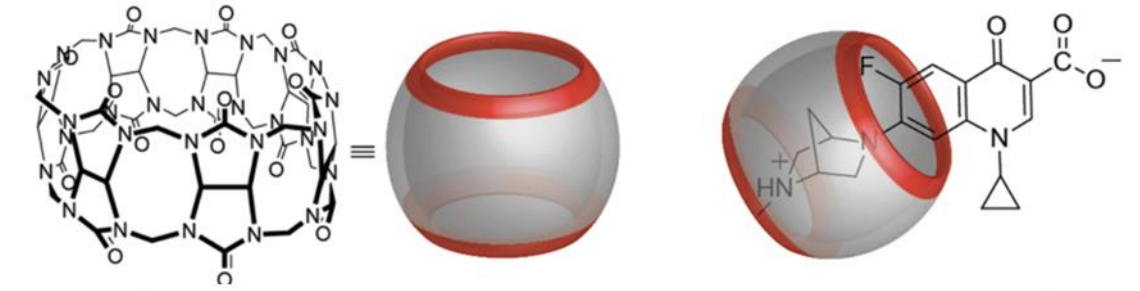

11 **12**

Figure 13 – Chemical structures of cucurbit[7]uril (CB7) (**11**) and DOFL.CB7 (**12**).[103]

It has been well documented that (thio) urea-based hydrogen bonding structures can possess antimicrobial activity against both gram-positive and gram-negative bacterial strains and as such can be incorporated into molecular weapons in the fight against AMR.[104–106] In 2001, Supuran and co-workers designed a class of urea-substituted derivatives whereby a selection were found to exhibit appreciable antimycobacterial activity against *Mycobacterium tuberculosis* (Figure 14).[107] In a primary screening assay, when supplied to the bacteria at 6.25 µg/mL, compounds **13**-**22** inhibited growth of *M. tuberculosis* by 78 – 89 %. This inhibition is comparable to two clinically relevant drugs, **isoniazid (43)** and **rifampicin (53)**. With such

bacteria termed 'the orphan disease' due to a void in the development of new antimycobacterial agents, these derivatives offer a promising advancement.[107]

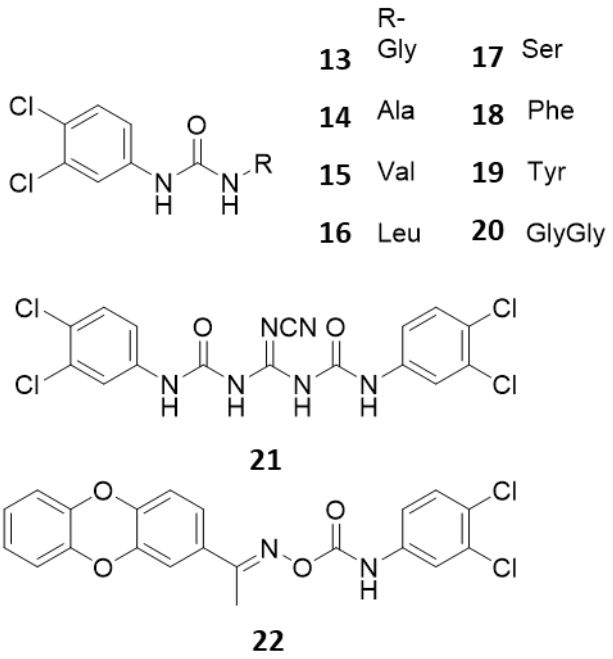

Figure 14 – Supuran *et al.* urea substituted antimycobacterial agents.[107]

The urea-spacer-sulfonate/carboxylate was incorporated into a novel class of dimeric and monomeric urea surfactants by Faustino and co-workers (Figure 15).[108] The physicochemical properties of these surfactants, including CMC was found to be easily controlled through the stepwise modification of the general molecular structure. For example, the substitution of the carboxylate for other polar head groups resulted in a reduction in the CMC, notably CO_2^- (**24**) > OPO_3^{2-} (**30**) > SO_3^- (**28**) > OSO_3^- (**29**). It was hypothesised the carboxylate surfactants were less prone to micellization due to the higher polarizability of those surfactants containing sulphur or phosphorus functionalities.

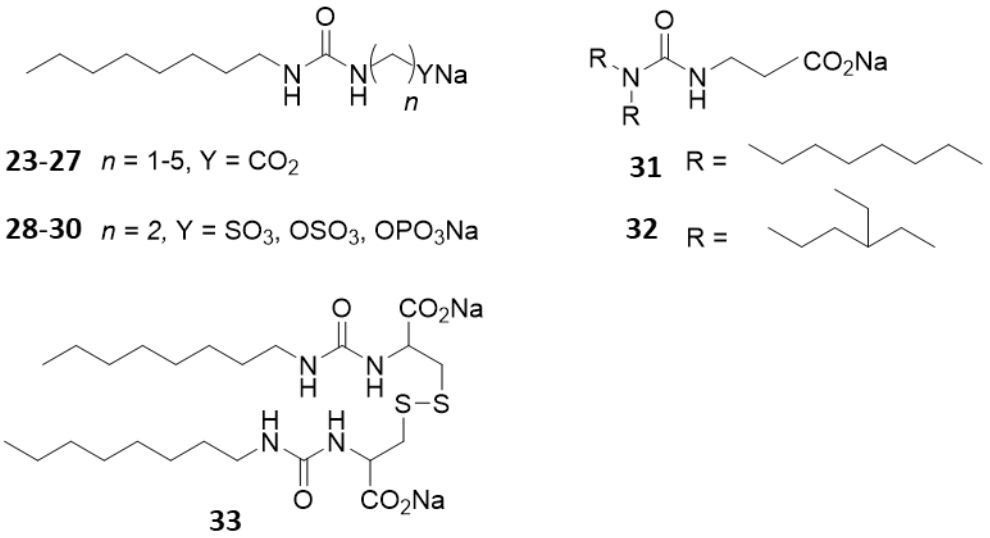

Figure 15 – Urea-spacer-anion surfactants designed by Faustino and co-workers [108,109]

The authors have more recently expanded their class of surfactants to include **33** (Figure 15), the dimeric species formed by linking two hydrophobic alkyl chains and two polar head groups which offers a low CMC of 0.6 moldm^{-3}.[109] This structure has been explored as a drug carrier for the poorly water-soluble drug, Amphotericin B. The reasonable molar solubilization capacity and low CMC has resulted in increased solubility of the drug in its monomeric, less toxic form, thus providing a promising alternative for the solubilisation of other amphiphilic, sparingly water-soluble drug molecules.

Building upon work from Faustino, Hiscock and co-workers have developed their own class of thio(urea) anion structure, known as supramolecular self-associating amphiphiles (SSAs).[110] The general structure of SSAs can be found in Figure 16.[110,111] The thio(urea) oxygen and the sulfonate/carboxylate functionalities provide two potential HBA sites, whilst the thio(urea) NHs provide the only HBD site. In addition to the substitution of the counter cation, the 'R' groups have been extensively altered through a series of stepwise modifications to change the acidity of the central HBD region.[4,110–115]

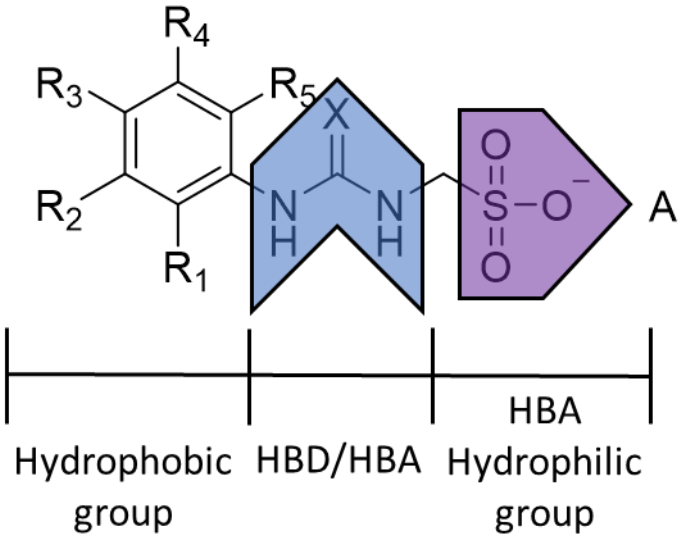

Figure 16 – General structure of SSAs synthesised by Hiscock *et al.*[110,111] X = O/S, A = counter cation. The hydrophilic group can also be a carboxylate.

These supramolecular systems can adopt several possible hydrogen bonding modes: *syn*- or *an*ti-urea–urea, urea–anion stacking and urea–anion dimerisation, as shown in Figure 17.[111] The uneven number of HBD vs HBA groups results in a 'frustrated system', where these 4 binding modes cannot occur at the same time.[110] The authors have shown, through single crystal X-ray analysis, these binding modes can be manipulated through modification of the amphiphiles functionalities. Specifically, the formation of urea-anion dimers is achieved through the selection of a weakly coordinating counter cation, such as tetrabutylammonium (TBA). Conversely, the substitution for a competitive HBD or a strongly coordinating counter cation, would give rise to the formation of urea-anion tapes or urea-urea binding modes respectively. Additional modulation of the HBD acidity, controlled through replacement of the 'R' and 'X' groups (Figure 16), can further optimise the formation of urea-anion hydrogen bonds.[111]

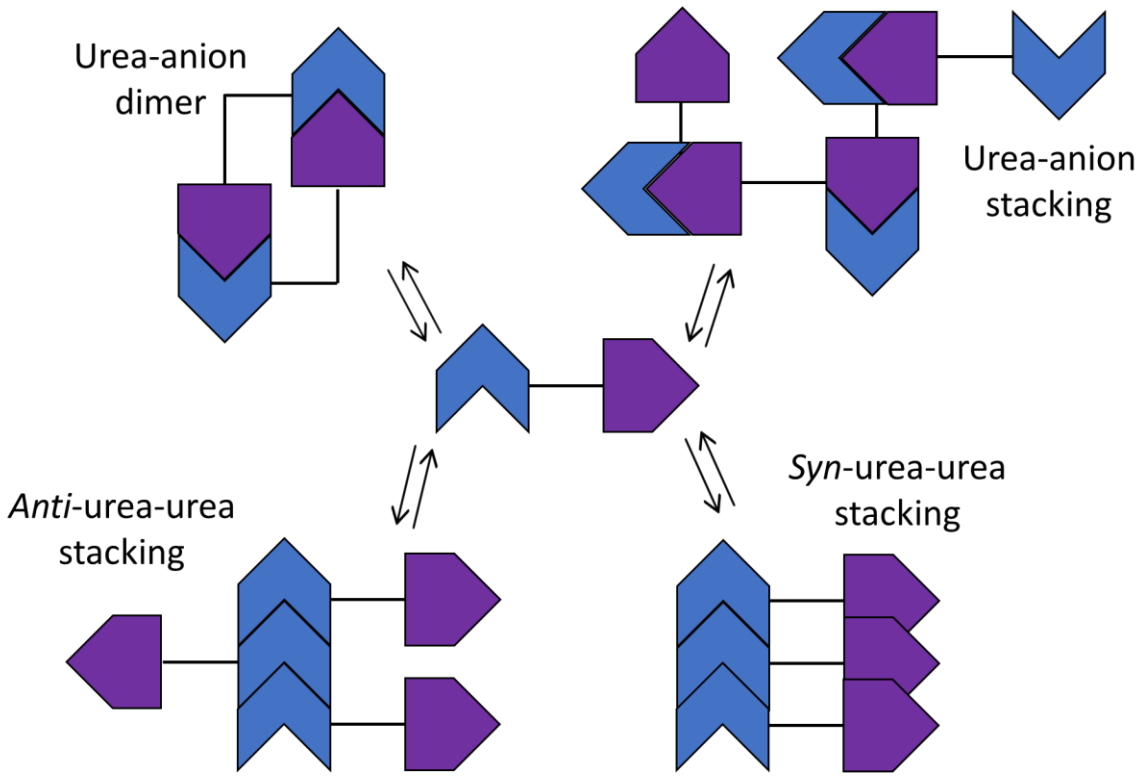

Figure 17 – Graphical representation of the four possible hydrogen bonding modes adopted by SSAs.

The authors next concentrated on synthesising a class of intrinsically fluorescent SSAs, enabling the direct visualisation of aggregates formed in the solution state.[112] Fluorescence and transmission microscopy was employed in combination with dynamic light scattering (DLS) and ^{1}H NMR studies to investigate the impact of solvent environment on self-associated structure formation. In solutions of 100 % dimethyl sulfoxide (DMSO), smaller dimeric species sized < 10 nm were primarily observed, whereas larger spherical aggregates > 100 nm were identified in pure aqueous conditions.[112]

The surface energy maximum (E_{max}) and minimum (E_{min}) values were calculated for this class of SSA using semi-empirical, low level PM6 modelling methods.[116] These predicted values were found to show good correlation with dimerisation constants derived from ^{1}H NMR dilution studies and were found to be inversely proportional with CMC.[112] This research has highlighted the potential use of simple computational modelling to predict the physical properties of this class of hydrogen bonded complex, allowing the construction of pre-designed supramolecular functional materials.

Hiscock *et al.* have identified SSAs to exhibit antimicrobial properties and have since focused efforts on the design of effective antibacterial agents. An initial focus was placed on investigating anthraquinone and anthracene SSA derivatives (Figure 18) as treatments against clinically relevant MRSA.[117]

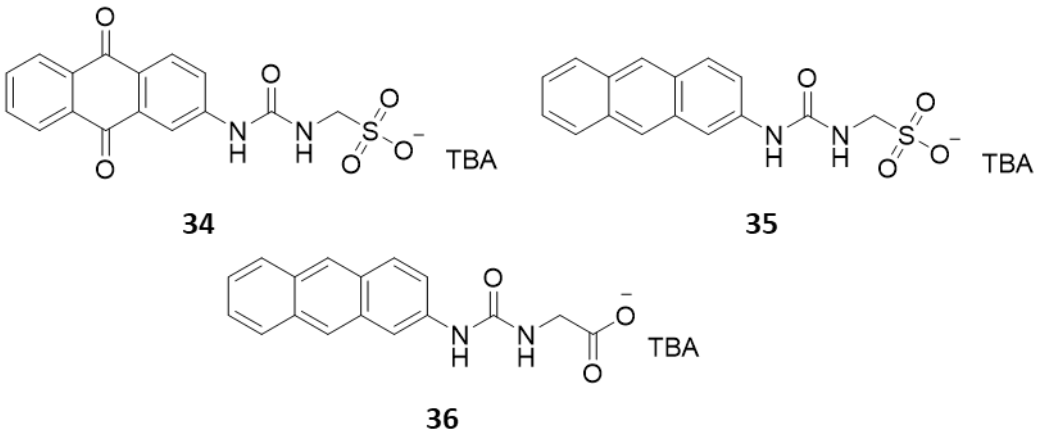

Figure 18 – Chemical structures of anthraquinone (**34**) and anthracene (**35**-**36**) SSA derivatives.[117]

SSA compounds **34**-**36** were all shown to illicit an antimicrobial response against clinically relevant MRSA, with the electron-rich anthracene SSA derivative (**35**) as the most effective agent, with a MIC_{50} value of 0.46 mM. The exchange for an anthraquinone group (**34**) was found to decrease antimicrobial efficacy, as was the substitution of the sulfonate functionality for the carboxylate (**36**), generating MIC_{50} values of 0.71 mM and 0.61 mM respectively. Interestingly, when **35** was supplied to MRSA bacteria in a 1 : 1 mixture with **34** or **36**, antibacterial activity was enhanced, lowering MIC_{50} values by half. In both cases, the CMC was also found to decrease in the presence of **35**, highlighting the significance of those self-associated structures for effective SSA delivery to the bacterial cell membrane.[117]

As aforementioned, the void in the discovery of new antibiotics since 1987,[95] and increasing number of naturally evolved resistant bacteria **highlight** the necessity for a new generation of antimicrobial agents. SSAs offer a viable and promising potential addition to the market, with broad spectrum activity expanding across both Gram-positive and Gram-negative bacterial strains and the opportunity to specifically targeting bacterial cells over eukaryotic. Additionally,

explored for the first time in this thesis is the potential for SSAs to work synergistically with currently marketed antimicrobials, both increasing efficacy and negating AMR mechanisms.

1.6. Aim and Objectives

1.6.1. Aim

To characterise and develop the first anionic self-assembling supramolecular enhancer of antimicrobial efficacy to aid in the fight against antimicrobial resistance.

1.6.2. Key objectives

- To co-formulate SSAs with a selection of antibiotics, antiseptics and antimicrobial/cytotoxic agents and perform extensive physiochemical analysis to elucidate any potential complex association events. (Chapter 1)
- To conduct antimicrobial testing of antibiotics in the presence of SSAs to establish potentiation against Gram-negative *Pseudomonas aeruginosa* and *Escherichia coli.* (Chapter 2)
- To utilise a variety of spectroscopic techniques and patch clamp technology to further explore SSA: phospholipid interactions. (Chapter 3)

2. Physicochemical characterisation of SSAs in combination with antimicrobial agents

2.1. Introduction

Antimicrobial resistance is now manifesting on a global scale, with cases of AMR reported for all currently marketed antimicrobials, including colistin, termed the 'antibiotic of last resort'.[118,119] As levels of resistance continue to rise alongside the absence of new antimicrobial agents to market, the effective therapeutic options become limited.[95] Using combination therapies is becoming a useful strategy against multi-drug resistance infections, with decreased developmental costs and a shorter route to clinical use. Pairs of antimicrobials can act synergistically, whereby the combined inhibitory effect is greater than the sum of the effect of the individual therapeutic agents.[120]

Supramolecular platforms such as the one designed by Zink and co-workers are a useful tool for the delivery of multiple drug agents. Here, a stimuli responsive supramolecular nanoplatform has shown to successfully co-deliver two antimicrobial drugs; melittin and ofloxacin.[121] The system was constructed of mesoporous silica nanoparticles and owing to the presence of oppositely charged pores of varying sizes, antimicrobial agents with diverse molecular weights and electrostatic charges could be incorporated. The nanoplatform efficiently released melittin and ofloxacin, synergistically eradicating *P. aeruginosa* biofilms. Supplying the drugs separately killed 20-30 % of the bacterial cells compared to the combination therapy which killed 100 %.

A supramolecular hydrogel developed by Wu *et al.* via coordination of PEGylated bisimidazolylbenzyl alcohol derivatives (**37**-**39**, Figure 19), enhanced the antimicrobial efficacy of silver nitrate ions.[122] Due to the broad spectrum antimicrobial activity, the element, silver has

been utilised as an antimicrobial agent for years, however it can be unstable when supplied to bacteria alone.[123] Upon combination with **37**-**39**, application of these supramolecular hydrogels to multidrug resistant strains of Gram-negative MRSA and Gram-positive bacteria *E .coli* resulted in an enhanced antimicrobial effect when compared to silver nitrate ions alone. The most effective combination being with **39** which exhibited an MIC of 2.44 μg/mL, approx. five times lower than silver nitrate alone.

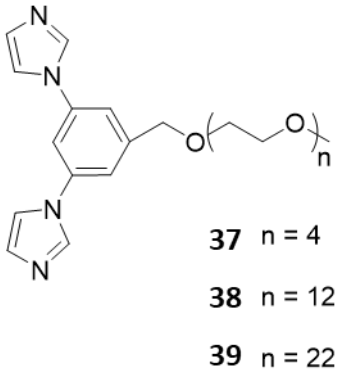

Figure 19 – Chemical structures of three PEGylated bisimidazolylbenzyl alcohols (**37**-**39**) synthesised by Wu *et al.* and combined with silver nitrate for the enhanced treatment of multidrug resistance bacterial strains. [122]

Bechinger and co-workers investigated the combination of two membrane-active, amphiphilic antimicrobials peptides: Magainin 2 and PGLa.[124] Fluorescence cross-correlation spectroscopy revealed the formation of a supramolecular construct formed of the two peptides at the membrane interface of a synthetic bacterial vesicle. When supplied in an equimolar mixture, the membrane affinity of both Magainin 2 and PGLa is significantly increased, providing evidence for the order of magnitude reduction in the MIC against clinically relevant *E. coli* ATCC 8739 when supplied in combination.[125]

As previously mentioned, (Section 1.5) Hiscock and co-workers have developed a class of thio (urea) anion structures, known as supramolecular self-associating amphiphiles (SSAs). This series have previously been shown to possess antimicrobial properties against a clinically relevant strain of Gram-positive MRSA.[117] Preliminary studies also revealed an enhanced

antimicrobial activity when two SSAs were supplied to the bacteria in a 1:1 ratio, this effect was synergistic.

The scope of these studies has since been extended to include testing SSAs against model Gram-negative *E. coli* bacteria of clinical interest, with a further > 50 structurally distinct SSA derivatives.[4] Supplementing the antimicrobial testing with extensive physicochemical analysis has allowed for the building of structure-activity relationship models derived from distinct parameters, including; zeta potential, dimerisation constants and CMC. Specifically, a decreasing MIC_{50} value for *E. coli* was found to correlate with a decreasing CMC, defining the critical SSA CMC value for the greatest antimicrobial effect to be < 11 mM.[4] This further highlights the importance of larger self-assembled structures for optimal antimicrobial activity and providing a vital tool for the design of ever-more effective next-generation SSA treatments.

More recently, Hiscock and co-workers have investigated the potential for these molecular constructs to act as solution-state molecular delivery vehicles.[126] The authors have designed an experimental framework to support fellow researchers in the investigation of complex multi-component, self-association events, such as those exhibited by co-formulated SSAs displayed in Figure 20. The molecular design of the SSAs chosen in this study allowed for the protonation of the terminal amines to incorporate anionic drug-like molecules such as coumarin (**40**) and salicylic acid (**41**) (Figure 20).

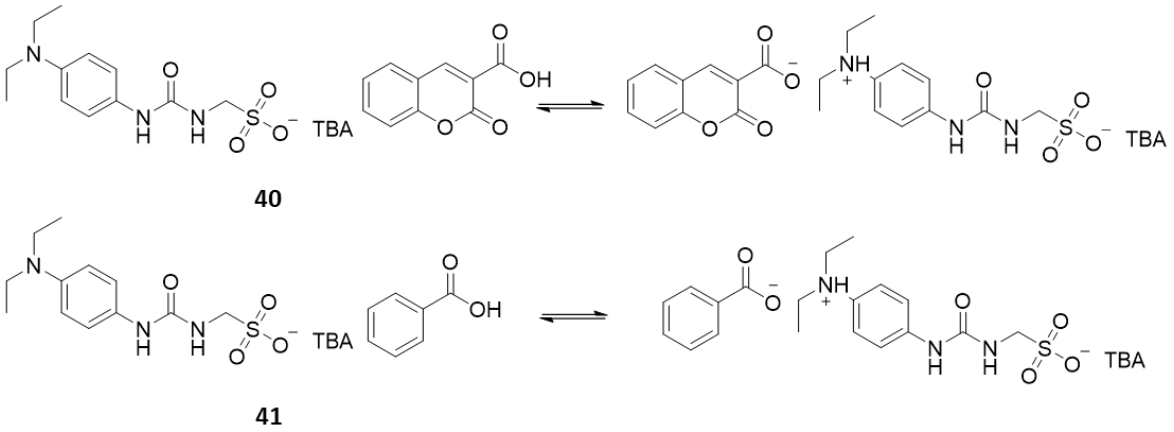

Figure 20 - Chemical structures of coformulation **40** and co-formulation **41**, showing the ability of the SSA to form a zwitterion.[126]

Quantitative ^{1}H NMR revealed the potential for the SSA constructs **40** and **41** to act as delivery vehicles, providing evidence for the incorporation of 81 % and 34 % of co-formulant agents respectively in a D_2O/ 5.0 % EtOH solution.[126] It is hypothesised that the 'drug like' species (coumarin and salicylic acid) are becoming encapsulated within spherical aggregates, previously visualised within the scope of previous studies via fluorescence microscopy.[113] The authors were also able to show that when the SSAs are co-formulated with coumarin and salicylic acid, aggregate stability is retained with zeta potential measurements of -43 mV and -36 mV respectively.[126]

2.1.1. Aims

The inherent antimicrobial nature of SSAs,[4,117] the synergistic SSA:SSA antimicrobial enhancement and the ability for the incorporation of small molecules has led to the work detailed within this chapter.[117,126] The summation of this evidence has prompted the hypothesis that this class of compound has the potential to act as efficacy enhancers for therapeutic agents.

Herein, SSA **42** is co-formulated with a selection of antibiotics, antiseptics and antimicrobial/cytotoxic agents (**43 – 47**), the chemical structures are provided in Figure 21. As antimicrobial activity is thought to be linked to the ability of SSAs to arrive at the surface of the

bacterial cell membrane as self-associated structures, understanding the effect of adding competitive co-formulant species into these systems is vital. Therefore, prior to antimicrobial testing, the SSA aggregates formed in the presence of secondary species (**43 – 47,** Figure 21) were extensively characterised to elucidate any potential complex association events. Subsequently, inhibition assays were performed with co-formulations **a**-**e** to assess the potential for SSAs to enhance the efficacy of the selected therapeutic agents against Gram-negative *E. coli* DH10B.

.

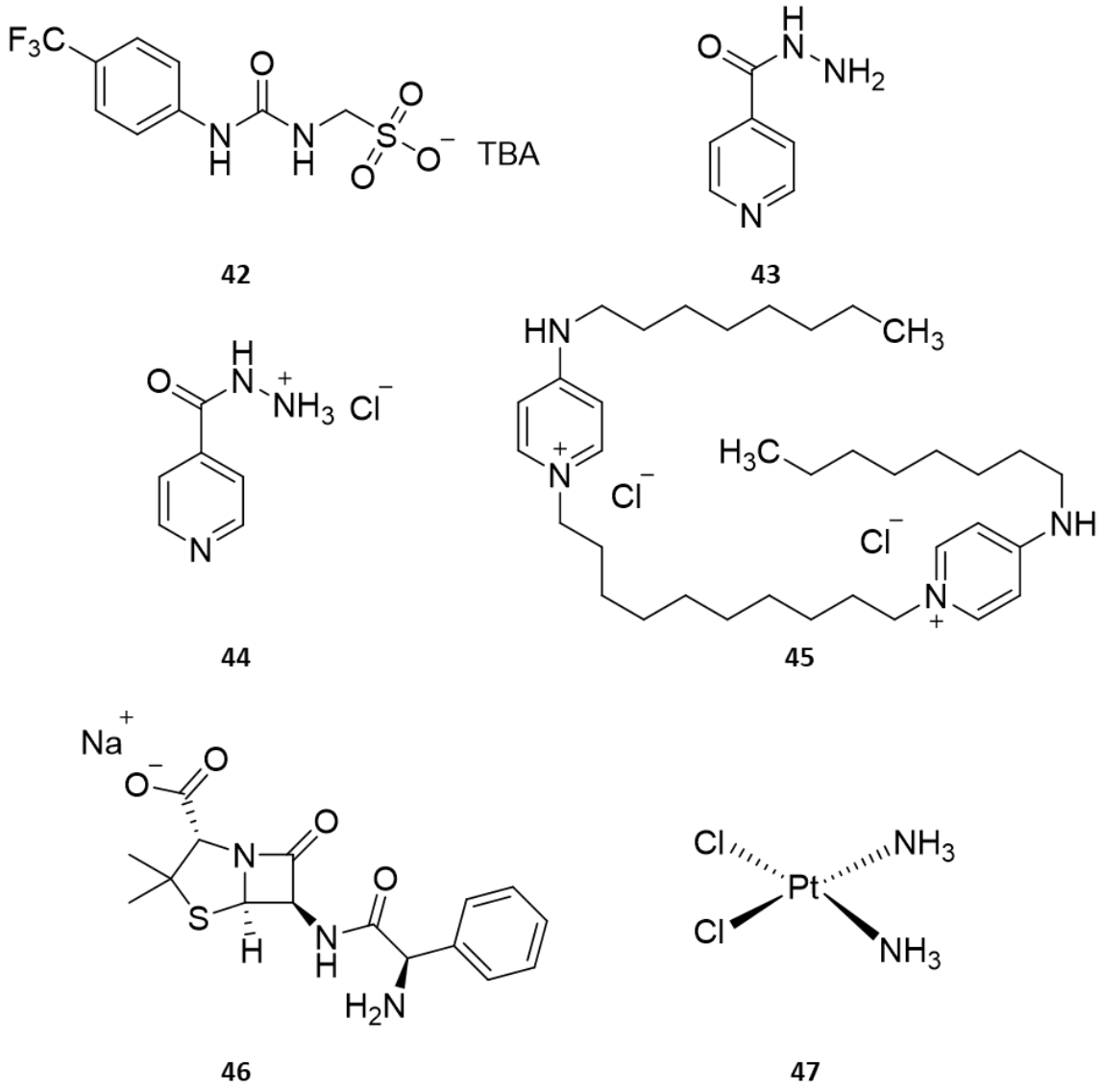

Figure 21 – Chemical structures of SSA **42** and co-formulant agents; **isoniazid** (**43**), **isoniazid hydrogen chloride** (**44**)**, octenidine dihydrochloride** (**45**), **ampicillin** (**46**) and **cisplatin** (**47**).

In line with previously published methods,[126] the SSA is supplied in a 1 : 1 molecular ratio with the secondary component, producing **co-formulations a**-**e**, as detailed in

Table 2. SSA **42** is the base structure for which all other SSAs have been derived from, it was chosen for these studies due to good solubility, comparatively low MIC_{50} value (3.85 mM against *E. coli*)[4] and low human cell toxicity.[127] Co-formulant agents (**43- 47**) were selected for the diversity in chemical structure and antimicrobial mode of action, offering an insight into the mechanism of action required for an effective SSA potentiator.

Firstly, **Isoniazid (43),** an extracellular targeting antimicrobial, traditionally used in the treatment of tuberculosis (Figure 21).[128] **Isoniazid (43)** is a prodrug, activated by the mycobacterial enzyme, and works by disrupting synthesis of both mycolic and nucleic acids, resulting in inhibition of cell wall lipid synthesis.[128] One of the most prescribed class of antibiotics are the Beta-lactam antibiotics,[129] primarily inhibiting synthesis of peptidoglycan, a vital component of the bacterial cell wall.[130] Binding to penicillin-binding proteins interrupts the final stage of peptidoglycan synthesis through acylation of the transpeptidase, an enzyme involved in the cross-linking of peptides to form peptidoglycan.[129] Beta-lactam antibiotics are characterised by a common core, a four-member beta-lactam ring,[131] one such example is **ampicillin (46)**, the structure is provided in Figure 21. **Octenidine dihydrochloride (45)**, a widely used antiseptic was chosen as a model membrane targeting antimicrobial. This agent inserts itself into the hydrophobic region of the bacterial bilayer inducing a disordered lipid arrangement, leading to loss of membrane integrity.[132] Finally, the intracellular targeting agent, **cisplatin (47)** is traditionally associated as an anticancer agent, preventing cell division through direct damage to DNA in cancer cells.[133] However, owing to potent crosslinking activity of DNA, cisplatin has been shown to promote bacterial cell death.[134] **Cisplatin (47)** was selected within the scope of this study because, at the time, preliminary data revealed potential synergistic activity between cisplatin and SSA **42** against glioblastoma cancer cells.

Table 2 - Molecular components, supplied in a 1:1 ratio, for **co-formulations a–e** discussed in this chapter.

Co-formulation	Molecular components
a	**42** + **43**
b	**42** + **44**
c	**42** + **45**
d	**42** + **46**
e	**42** + **47**

Due to the complex nature of multi-component, self-association events, the physicochemical properties of SSA coformulations **a-e** have been studied by employing a variety of complimentary techniques. The characterisation scheme is presented in Figure 22 and details methods which include quantitative ^{1}H NMR, dynamic DLS, zeta potential measurements, surface tension and CMC determination, ^{1}H NMR self-association and diffusion ordered spectroscopy (DOSY) experiments. Scanning/transmission electron microscopy (SEM/TEM) have not been attempted within the scope of these studies due to the inability of SSAs to survive the traditional sample preparation methods.[110]

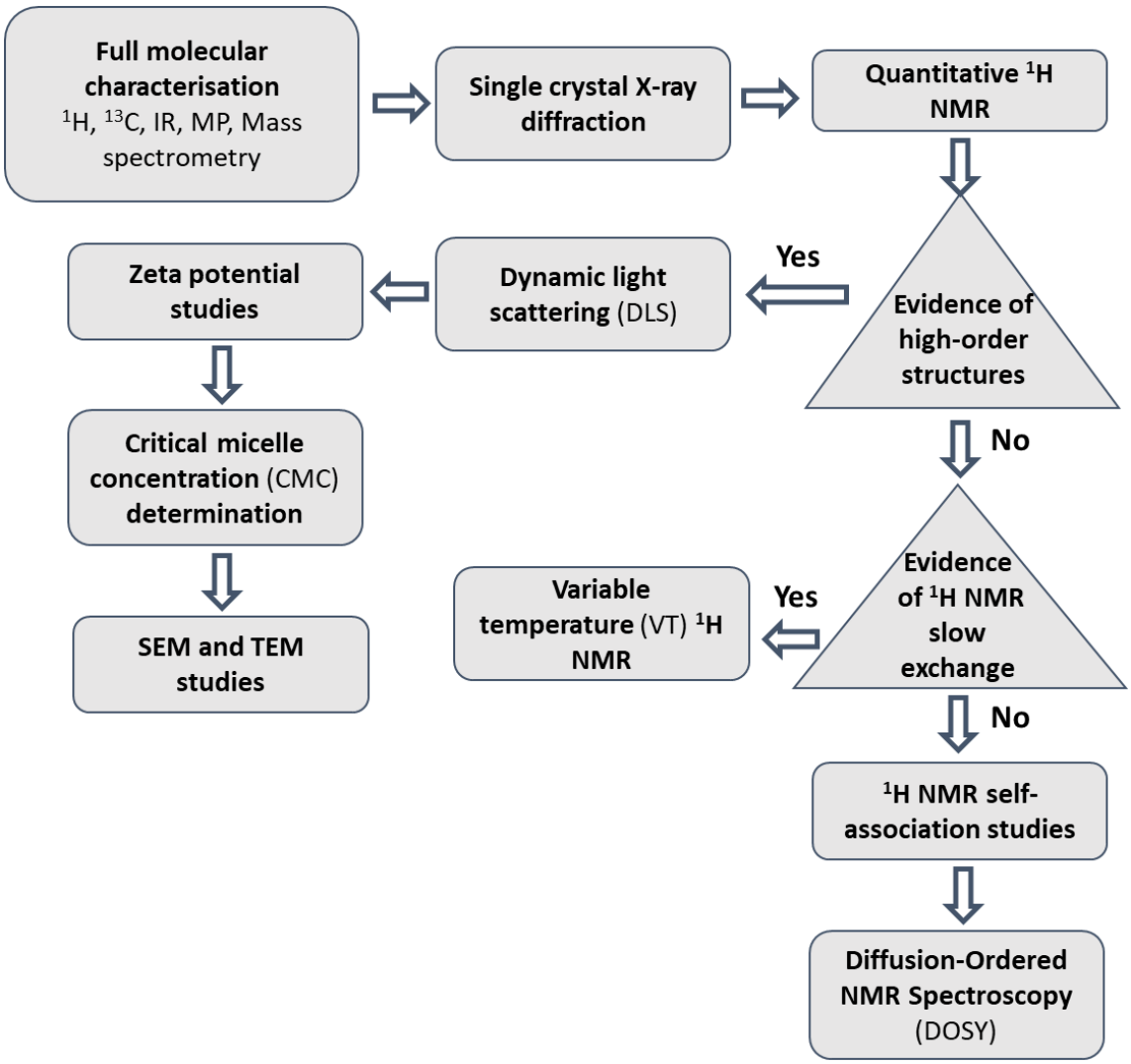

Figure 22 – A flow chart designed by Hiscock and co-workers detailing the full physicochemical characterisation of SSA systems.[126] Rectangle = action; Triangle = decision.

The work detailed in this chapter has been published within the following peer-reviewed journal article:

Supramolecular self-associating amphiphiles (SSAs) as enhancers of antimicrobial agents towards *Escherichia coli* (*E. coli*), J. E. Boles, R. J. Ellaby, H. J. Shepherd and J. R. Hiscock, *RSC Adv.*, 2021, **11**, 9550-9556.[1]

2.2. Synthesis

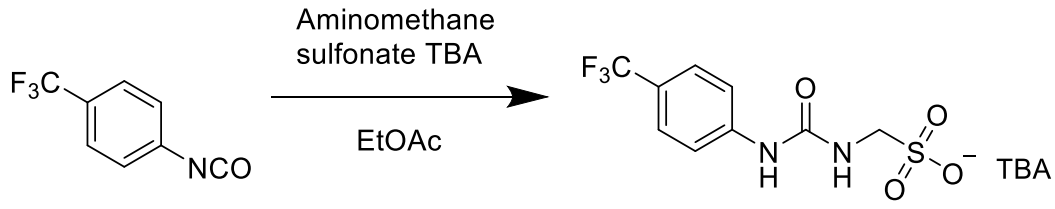

Scheme 1 – Synthesis of compound **42** discussed in this thesis.

Compound **42** was synthesised by the reaction of 1-Isocyanato-4-(trifluoromethyl)benzene with aminomethanesulfonate TBA in ethyl acetate as illustrated in Scheme 1. After purification, the pure product was obtained as a white solid in a yield of 80 %.[110]

2.3. Single crystal X-ray Diffraction

Single crystal X-ray diffraction (XRD) is a technique employed here to observe molecular self-association events occurring in the solid state. This provides an insight into the type of intermolecular interactions, for example, the hydrogen bonding modes present within a class of compounds. However this technique can not accurately predict the solution state behaviour due to the presence of solvent molecules in solution and the crystal packing forces in the solid state.[111,126] Within this study, single crystal XRD was used to investigate the effects of competitive co-formulant agent addition upon the self-association of SSA **42**.

A single crystal X-ray structure for SSA **42** has previously been published, presented in Figure 23.[111] Produced through slow evaporation of a H_2O/EtOH solution, the SSA exhibits urea-anion dimer formation stabilised by four intermolecular hydrogen bonds, formed between the HBD urea functionality and the HBA oxygen of a sulfonate group. This hydrogen bonding mode is commonly observed within SSAs in the presence of the weakly coordinating cation, TBA (Figure 23).[111]

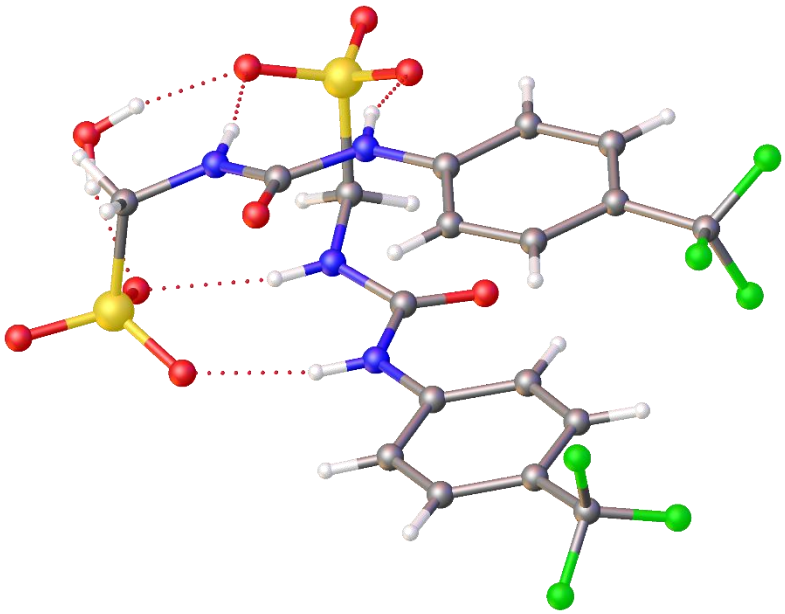

Figure 23 - A single crystal X-ray structure obtained from a single crystal sample produced from a solution of SSA **42** in H_2O:EtOH. Grey - carbon, blue - nitrogen, red - oxygen, yellow - sulfur, white - hydrogen, green - fluorine, red dashed lines - hydrogen bonds.[111]

The growth of single crystals from solutions of **co-formulations a, c-e** was unsuccessful as suitable conditions could not be found to co-crystallise both the SSA and co-formulant agent. However, slow evaporation of **co-formulation b** (SSA **42** and **isoniazid hydrogen chloride**) in acetone produced a suitable single crystal, giving the structure presented in Figure 24. This crystallography data was obtained and refined by Dr Jennifer Ruth Hiscock.

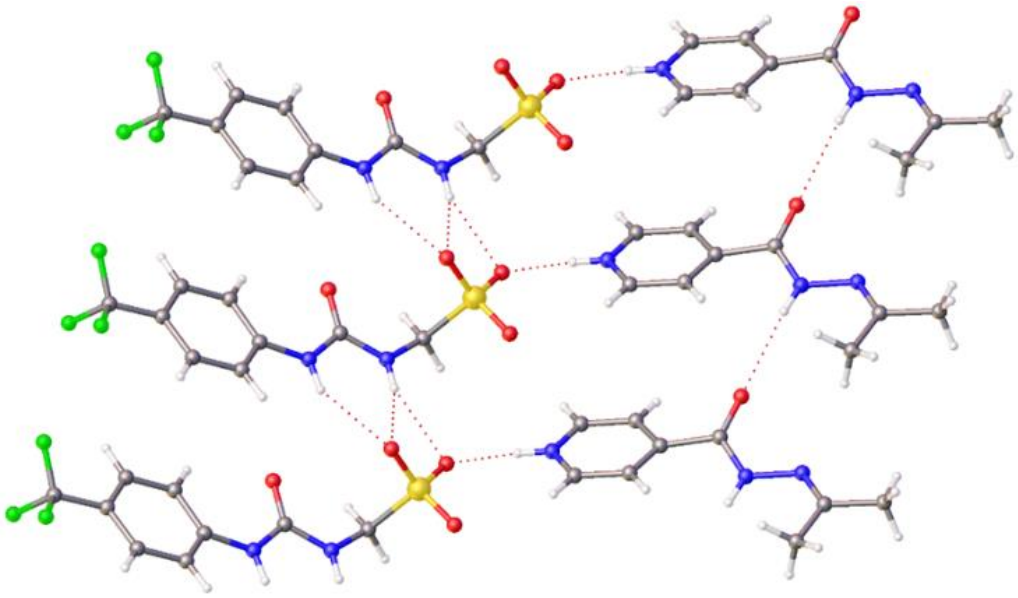

Figure 24 – A single crystal X-ray structure obtained from a single crystal sample produced from a solution of **co-formulation b** in acetone. Grey - carbon, blue - nitrogen, red - oxygen, yellow - sulfur, white - hydrogen, green - fluorine, red dashed lines - hydrogen bonds.

As described by Sarcevica *et al.*,[135] **isoniazid hydrogen chloride (44)** has undergone a reaction with acetone and in this case has replaced the TBA counter cation of SSA **42** and formed a salt via protonation of the pyridinium nitrogen on the **isoniazid (43)** derivative. In the presence of this **isoniazid (43)** derivative, the SSA anion was found to form urea-anion hydrogen bonded tapes. Figure 24 also shows the anionic sulfonate group to be involved in competitive hydrogen bonded complexation events with the pyridinium nitrogen on the co-formulant counter cation, this is thought to inhibit the formation of urea-sulfonate dimers, as observed with SSA **42.**

2.4. ^{1}H NMR Self-Association Studies

To gain an understanding of molecular level self-association interactions of SSA **42** in the presence of co-formulant agents (**43** – **47**), a series of ^{1}H NMR spectroscopy studies were performed. These experiments were undertaken in a polar organic DMSO-d_6/ 0.5 % H_2O solvent and/ or an aqueous H_2O/ 5.0 % ethanol (EtOH) solution, providing study in two competitive (both capable of forming hydrogen bonds) solvent environments and allowing for the direct observation of HBD NH resonances. From previous studies, a DMSO solvent system enables the study of the formation of individual hydrogen bonding events, whereas the aqueous system enables the study of bulk self-association studies and direct comparison against alternative solution state experiments.[112,113,136]

2.4.1. Quantitative ^{1}H NMR Spectroscopy

NMR spectroscopy is an important analytical tool for the identification of unknown compounds. Additionally, owing to the direct proportionality between signal intensity and comparative number of individual nuclei in each different environment, NMR is inherently quantitative.[137] This direct method simply requires complete solubility and a sample containing detectable nuclei.[138] For absolute quantification, the normalised ^{1}H integral signals of the analyte of interest are ratioed against the integrals of a known quantity of internal standard.

In this study, we employ absolute quantitative ^{1}H NMR analysis to provide evidence for the presence of higher order aggregate structures in contrasting solvent systems.[126] This is achieved through the ability of larger aggregate structures to adopt ‘solid-like’ properties in solution, the slow tumbling of which means their NMR signal is lost and they are deemed ‘silent’. It is therefore possible to quantify the amount of molecule involved in the construction of these higher order ‘silent’ species, given the concentration of which is above the limit of detection for the NMR spectrometer in use.

A limitation of this method arises when SSA peaks overlap with co-formulants and/or peaks owing to the internal standard.[139] For the two competitive solvent systems studied; DMSO-d_6/ 0.5 % H_2O and D_2O, dichloromethane (DCM) (1 %) and EtOH (5 %) were chosen respectively as the quantitative internal standards. These were selected as both were miscible with the deuterated solvent of choice, neither resulted in peak overlap and should have minimal interference on the observed interactions. For these experiments, relaxation times were increased to 60 seconds to ensure the entire NMR signal was collected.

Hiscock and co-workers have previously shown SSAs to form lower order species (e.g., dimers) in DMSO-d_6/ 0.5 % H_2O. This includes SSA **42** (112 mM), which when spiked with DCM resulted in a 0 % loss of anion and cation NMR signal upon comparative integration.[112] Analogous quantitative ^{1}H NMR experiments were performed on **co-formulations a**-**e** to discern the effect of the presence of co-formulant agents (**43**-**47**) on the self-associative properties of SSA **42**. In a DMSO-d_6/ 0.5 % H_2O solution, as with **42** alone, **co-formulations a**-**e** show no evidence of forming higher order aggregate structures as 0 % of material has become 'NMR silent' (Figure S2-6). A known quantity of internal standard DCM (1 %) was comparatively integrated against an isolated peak corresponding to both the anionic and cationic components of SSA and co-formulant agents. All peaks are shown to integrate for the appropriate number of protons and therefore classed as exhibiting 0 % loss of compound (Appendix 1.2), the ^{1}H NMR spectra for **co-formulation a** and internal standard DCM is shown in Figure 25. The limitation of this technique however, is the inability of the NMR to quantify any larger 'NMR silent' structures that form at a concentration below that of the limit of detection and therefore, larger aggregate structures could still be present in a negligible quantity.

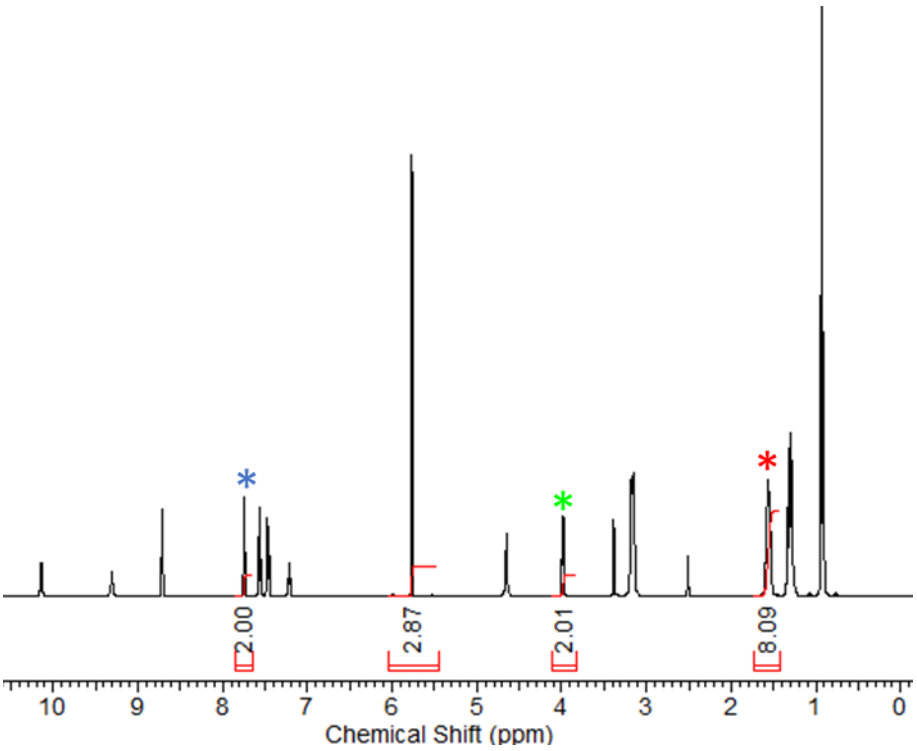

Figure 25 - ^{1}H NMR spectrum of **co-formulation a** (111.4 mM) in DMSO-d_6/ 1.0 % where comparative integration indicated 0 % of the sample has become NMR silent. (**Isoniazid (43)***, anionic component of SSA **42*** and TBA counter cation*)

Moving into an aqueous environment, quantitative ^{1}H NMR studies were also performed in a D_2O/ 5.0 % EtOH solution at 5.56 mM (Figure S7-11). A summary of these results is presented in Table 3.

Table 3 - Results from quantitative ^{1}H NMR studies obtained from D_2O standardised with 5.0 % EtOH (5.56 mM). Values are recorded in % and represent the proportion of SSA **42** (both anion and cation) and co-formulant agents **43**-**47** that is NMR silent. Coloured asterisks align with marked ^{1}H NMR spectra in main text figures and appendix.

Co-formulation	Solvent system	Anion *	Cation *	Co-formulant *
42 only[112]	D_2O	51	50	n/a
a	D_2O	56	57	50
b	D_2O	50	49	41
c	D_2O	53	29	64
d	D_2O	48	55	62
e	D_2O	65	83	*a*

a = values could not be determined due to peak overlap.

The control sample, SSA **42** alone has previously shown that under aqueous conditions, 50 % of the anionic and cationic components become incorporated into larger aggregated structures.[112] As shown in Figure 26, when SSA **42** is co-formulated with **isoniazid hydrogen chloride (44)** the proportion of anionic SSA and cationic TBA to become incorporated remains the same as with SSA only. The peak at 7.61 ppm, corresponding to the CH_2 functionality on the anionic component of SSA should integrate for 2, however in the presence of **isoniazid hydrogen chloride (44)**, this integrates comparatively for 1.01, a ≈ 50 % comparative loss. The peak at 3.14 ppm corresponding to the TBA counter cation integrates for ≈ 49 % at 4.12 ppm. Additionally, 41 % of **isoniazid hydrogen chloride (44)** becomes NMR silent, calculated from the peak at 8.12 ppm (Figure 26). Analogous NMR experiments were performed on co-formulant agents alone and were not found to exhibit the formation of any larger 'NMR silent' structures (Appendix 1.2, Figures S12-14). Therefore, **isoniazid hydrogen chloride (44)** is thought to have become incorporated into the larger aggregate structures of SSA, **42.**

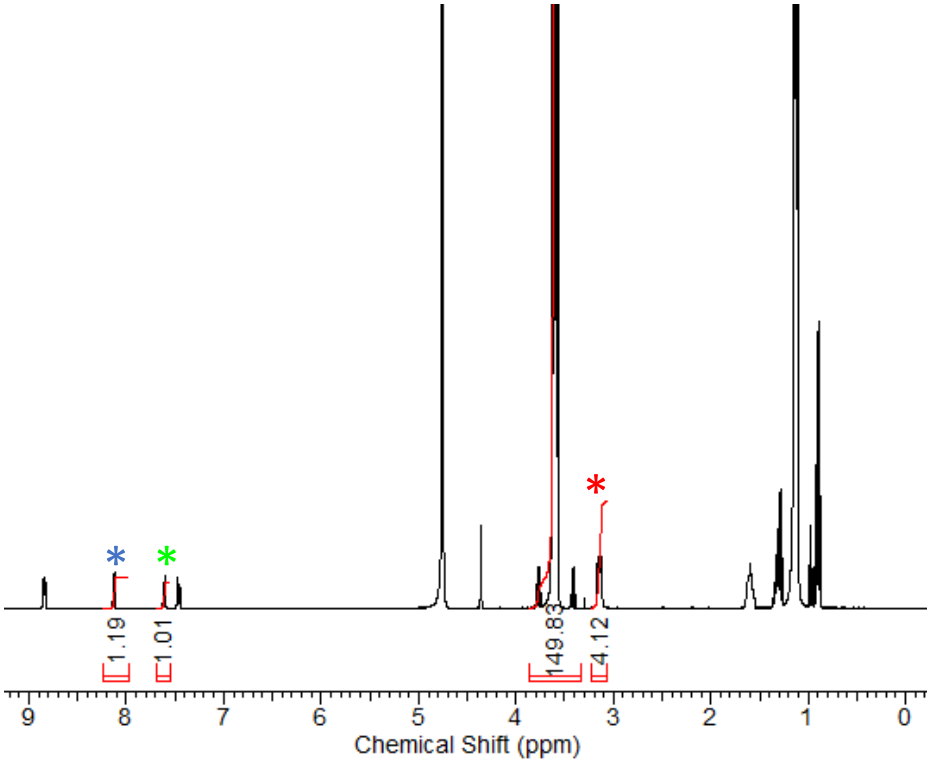

Figure 26 - ^{1}H NMR spectrum of **co-formulation b** (11.4 mM) in D_2O/5.0 % EtOH where comparative integration indicated 50 % of the anionic component of SSA **42**, 49 % of TBA countercation and 41 % of **isoniazid hydrogen chloride (44)** has become NMR silent. (**Isoniazid hydrogen chloride***, anionic component of SSA **42*** and TBA counter cation*)

When SSA **42** is co-formulated with the neutral form of **isoniazid (43)**, 5-7 % more SSA is incorporated into larger self-associated aggregates when compared to **isoniazid hydrogen chloride (44)** (Table 3). Although a small increase, the comparatively hydrophobic, uncharged **isoniazid (43)** is stabilising the formation of a higher percentage of larger aggregate structure. There is also evidence for the incorporation of **isoniazid (43)** into these aggregated species due to a 50 % 'loss' of the available co-formulant. The lack of comparative H^+ and Cl^- ions in **isoniazid (43)** maybe account for the ≈ 10 % increase in co-formulant encapsulation when compared to **isoniazid hydrogen chloride (44)**.

Similarly, the presence of **cisplatin (47)** in **co-formulation e** causes the proportion of anionic SSA involved in the formation of extended aggregate structures to increase, from 51 % to 65 % (Table 3). For the remaining co-formulations, the percentage of incorporated anion is maintained at ≈ 50 %. Whilst this remains true for **co-formulation c** (53 % of the SSA anion remains incorporated into the larger structures), the proportion of TBA drops from 50 % to 29 %. In this case, 64% of the co-formulant **octenidine (45)** is 'lost' from solution. This provides evidence to suggest **octenidine (45)** has replaced a portion of the TBA countercation involved in the higher order structures.

In summary, ^{1}H quantitative NMR analysis has shown the SSA anionic components of **co-formulations a-e to** predominantly form lower ordered structures in DMSO-d_6/0.5 % H_2O, standardised with DCM, indicated by a comparative 0 % loss of any SSA anion material from solution. However, in aqueous conditions (D_2O/ 5.0 % EtOH), the SSA anionic component retains the ability to produce larger aggregate structures in the presence of antimicrobial/therapeutic agents **43-47**. These data also revealed that a considerable portion (41 – 64 %) of these co-formulant agents becomes incorporated into these larger self-associated structures.

2.4.2. ^{1}H NMR Dilution Studies

Intermolecular, non-covalent interactions between molecules lead to the formation of self-assembled systems. One of the simplest forms of supramolecular systems to display cooperativity involve one component, one dimensional homogeneous aggregation events.[140] Self-associative binding isotherm models have been established to describe this, such models include equal *K* (EK) model, a linear aggregation model that assumes all association events to be equal. Alternatively there is the cooperative equal *K* (CoEK) model which assumes any subsequent, identical association events are different from the first.[141,142]

A series of ^{1}H NMR dilution studies were performed with **co-formulations a**-**e** in DMSO-d_6/0.5 % H_2O to both verify the presence and quantify any hydrogen bonded self-association events. A top concentration of 112 mM was selected to reproduce the experimental conditions of the quantitative ^{1}H NMR studies (Section 2.4.1). The downfield change in chemical shift for signals corresponding to NH resonances from the SSA anion and appropriate co-formulant were plotted against increasing concentration and using Bindfit v 0.5[143], these data were fitted to both EK and CoEK models, these derived values are presented in Table 4 (Figure S16-29). Given the consistently lower fitting errors and previous observations with SSAs made by Hiscock and co-workers[4,112–114,117,126], the dimerisation EK binding isotherm (K_{dim}) was chosen for these data.

Table 4 – A summary of self-association constants derived from Bindfit v 0.5[143] for SSA **42** and **co-formulations a**-**e** in DMSO-d_6/0.5 % H_2O at 298 K.

	EK model (M^{-1})		CoEK (M^{-1})		
	K_e	K_{dim}	K_e	K_{dim}	ρ
SSA 42[112]	5.3 ± 0.6 %	2.7 ± 0.3 %	13.0 ± 0.7 %	6.5 ± 0.4 %	0.5 ± 2.1 %
a	4.2 ± 2.9 %	2.1 ± 1.5 %	1.9 ± 36.3 %	0.9 ± 18.1 %	1.7 ± 45.4 %
b	8.7 ± 0.6 %	4.4 ± 0.3 %	13.4 ± 1.2 %	6.7 ± 0.6 %	0.7 ± 3.4 %
c	5.9 ± 1.6 %	2.9 0.8 %	11.3 ± 4.0 %	5.7 ± 2.0 %	0.6 ± 10.6 %
d	9.8 ± 1.0 %	4.9 0.5 %	18.1 ± 0.6 %	9.1 ± 0.3 %	0.6 ± 2.1 %
e	7.3 ± 0.76 %	3.7 ± 0.38 %	13.1 ± 1.56 %	6.6 ± 0.78 %	0.6 ± 4.42 %

The K_{dim} value for SSA **42** alone has been previously calculated to be 2.7 M^{-1}.[112] Under analogous conditions, the anionic proportion of SSA **42** in **co-formulation a** exhibited a similar K_{dim} of 2.1 M^{-1} (Table 4). As shown in Figure 27, there is a clear downfield shift in the NH resonances belonging to the urea of the SSA anion (blue and pink), however no discernible change is noted for the NH resonance associated with **isoniazid (43)** (green). It is therefore not surprising that the K_{dim} for SSA **42** remains similar as there is no evidence of co-formulant and SSA anion association in this co-formulation.

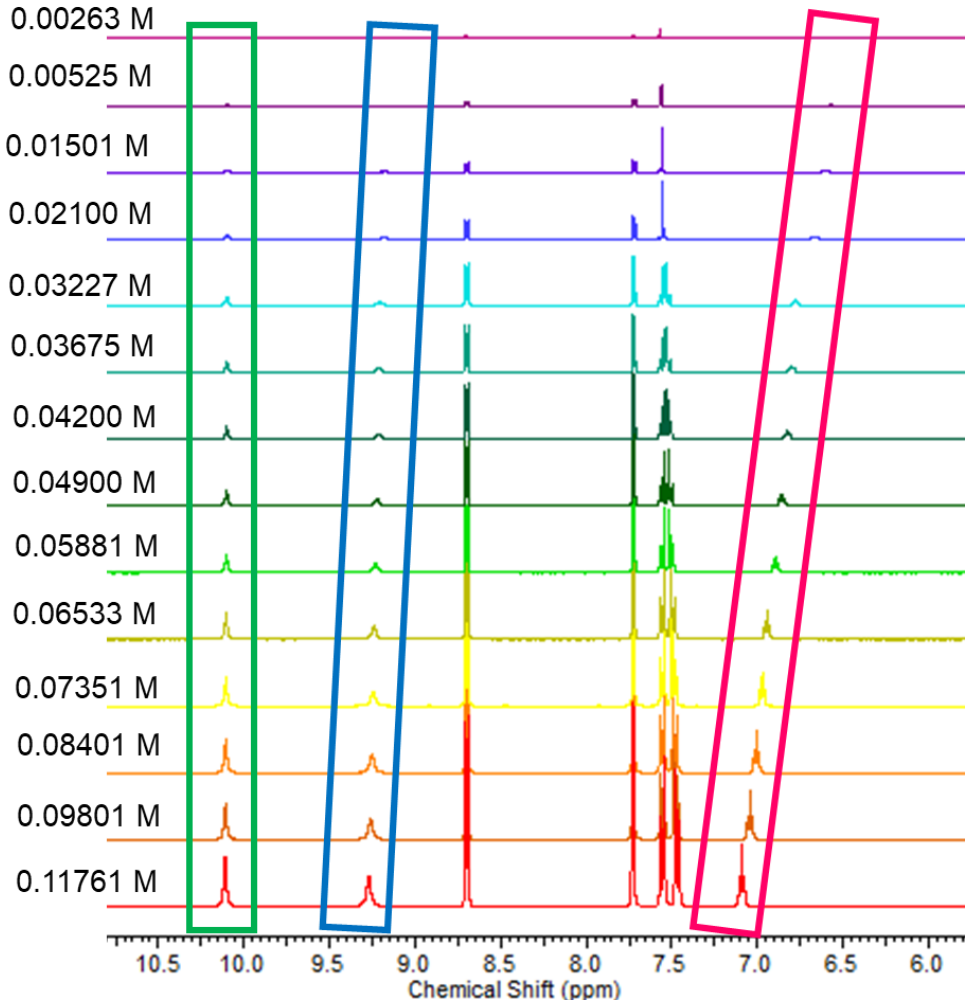

Figure 27 – ^{1}H NMR stack plot of **co-formulation a** in DMSO-d_6/ 0.5 % H_2O solution illustrating the change in chemical shift for the NH signals for SSA **42** (pink and blue) and isoniazid, **43** (green).

The K_{dim} values calculated for the SSA component of **co-formulations b** and **e** were found to increase to 4.4 and 3.7 M^{-1} respectively (Table 4). The absence of any NH within the molecular structure of co-formulant in these co-formulations meant the potential interaction of **isoniazid hydrogen chloride (44)** and **cisplatin (47)** with SSA could not be studied. It is hypothesised however that both these therapeutic agents have the potential to be involved in a complex association event with **42**. **Cisplatin (47)** is a metal complex and **isoniazid hydrogen chloride (44)** are introducing competing Cl^- ions into solution. The SSA sulfonate unit could be outcompeted by such ions to coordinate with the urea and as such, these data would no longer fulfil the 'one association event' criteria for fitting to the K_{dim} isotherm. Such values relating to **co-formulation b** and **e** in Table 4 should be therefore treated with caution.

In those co-formulations where the downfield shift of co-formulant NH resonances can be monitored, comparing the change in chemical shift values for the SSA anion and co-formulant agent can be a useful tool for identifying anion: co-formulant interactions. Figure 28 presents such graphs for **co-formulation a**, **c** and **d** respectively. As previously discussed, **co-formulation a** gives a flat line for the **isoniazid (43)**, NH resonance, indicating no association with the anionic proportion of SSA **42** (Figure 28a). In contrast, in **co-formulation c** the NH resonances associated with **octenidine (45)** and the urea of SSA **42** were found to exhibit similar profiles with increasing concentration (Figure 28b). It is therefore hypothesised in DMSO-d_6/0.5 % H_2O, **octenidine (45)** is involved in molecular association with the anionic proportion of SSA **42**.

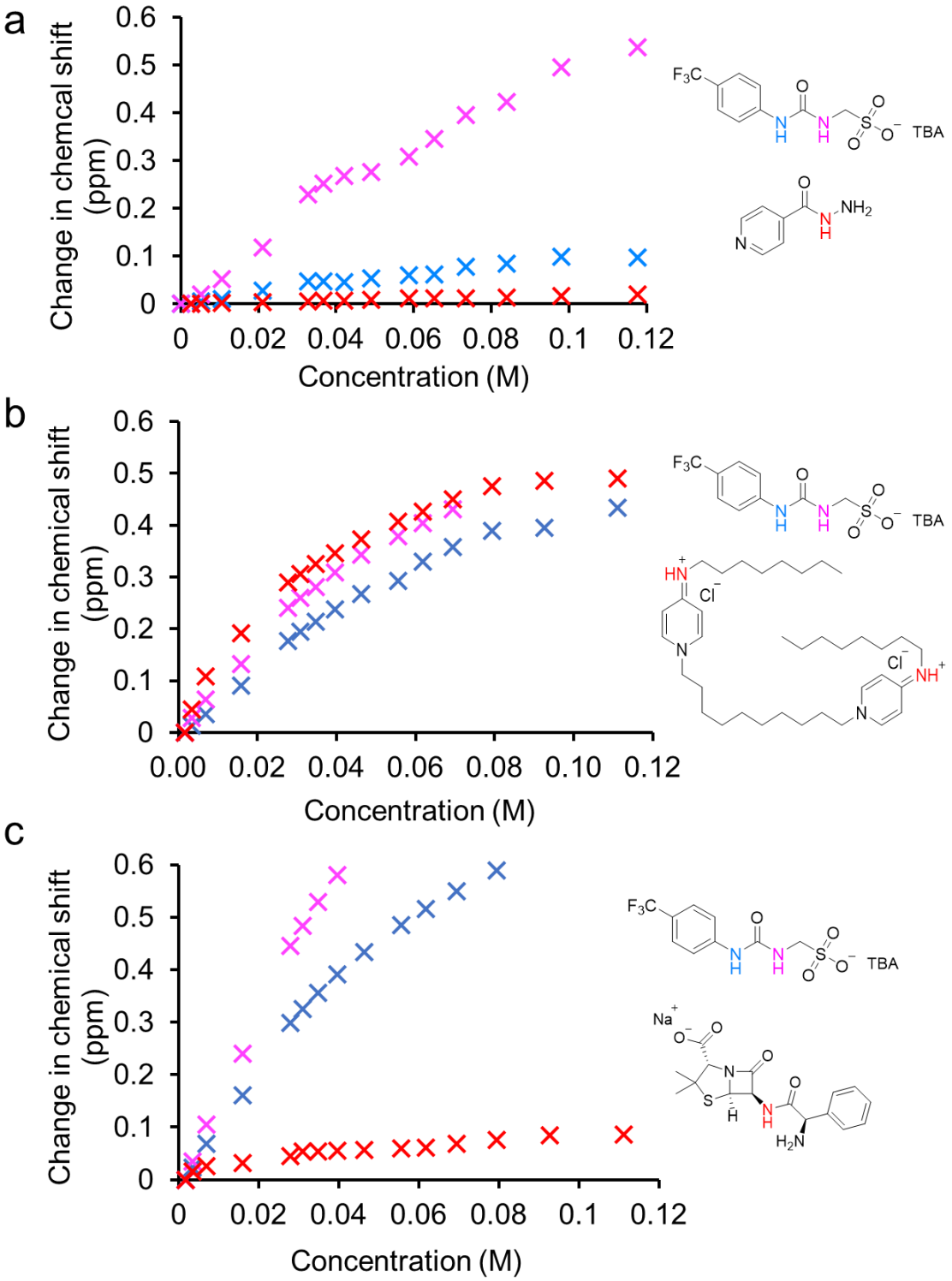

Figure 28 – The change in ^{1}H NMR chemical shift for NH resonances relating to the anionic portion of SSA **42** appropriate co-formulant in DMSO-d_6/0.5 % H_2O at 112 mM (298 K) for a) **co-formulation a**; b) **co-formulation c** and c) **co-formulation d**. The chemical structures highlight the relevant NHs plotted within these graphs.

The downfield change in chemical shift for **co-formulation d** (SSA **42** and **ampicillin (46)**) is presented in Figure 28c. The K_{dim} for the SSA anionic proportion has increased from 2.7 M^{-1} to 4.9 M^{-1} when compared to SSA **42** alone (Table 4), indicating that the presence of **ampicillin (46)** is having some effect on the self-association events of SSA **42**. The curve profile of the NH resonance monitored on **ampicillin (46)** (Figure 28c) is suggestive of a strong binding event. This antimicrobial agent contains a carboxylate functional group, known in literature to form stronger complexes with urea functionalities when compared to a sulfonate anion.[144] This suggests that **ampicillin (46)** preferentially coordinates with the anionic proportion of SSA **42**. Like **co-formation c**, these K_{dim} values should therefore be treated with caution.

In summary, ^{1}H NMR dilution studies have provided more evidence that SSA **42** in the presence of co-formulant agents (**43** – **47**) form predominantly lower order dimeric species in DMSO-d_6/0.5 % H_2O, due to the good fitting to the dimerisation EK binding isotherm (K_{dim}). Monitoring downfield change in chemical shift of the NH resonances relating to both the SSA anion and the co-formulant revealed evidence of potential complex association event association when SSA **42** is supplied in a 1:1 molecular ratio with cationic **octenidine (45)** and **ampicillin (46)**. These derived values (K_{dim}) therefore no longer fulfil the 'one component' association criteria.[140]

2.4.3. DOSY ^{1}H NMR

Diffusion Ordered Spectroscopy (DOSY) is an NMR method which reports diffusion coefficients for individual molecular components. The diffusion of molecules through a solution can be defined quantitatively by the translational diffusion coefficient (*D*), a value inversely proportional to the size of a molecule. In combination with viscosity and temperature parameters, *D* is inputted into the Stokes-Einstein Equation (Equation 1) to calculate the hydrodynamic diameter (D_H).[145]

$$\mathrm{D_H} = \frac{K_B T}{6\pi\eta D}$$

Equation 1 – The Stokes-Einstein equation where D_H is the hydrodynamic diameter, K_B is the Boltzmann constant, T is temperature η is the viscosity of the solution and D is the translational diffusion coefficient.[145]

The hydrodynamic diameter is defined as the radius of an equivalent sphere diffusing at the same rate as the particle under observation.[146] This assumes all particles are spherical in shape, whereas in reality a large proportion of particles are non-spherical or hydrated/solvated. Therefore a limitation of this technique is that only an indicative size can be calculated.[147]

DOSY experiments were performed on **co-formulations a**-**e** to determine the effect of the presence of co-formulant agents on the size of SSA aggregated species. Furthermore, comparison of diffusion coefficients can give indications of any molecular interaction/coordination. Experimental preparation was kept analogous to the ^{1}H NMR dilution studies; co-formulations were prepared in DMSO-d_6/0.5 % H_2O at 112 mM. The hydrodynamic diameters calculated for the SSA anion, cation and co-formulant agent are presented in Table 5 (Figure S30-33). Those studies with **co-formulations a**-**e** show the anionic components of SSA **42** to have hydrodynamic diameters of ≤ 1.70 nm which are sizes indicative of lower-order hydrogen bonded species. This is consistent with data gathered from quantitative ^{1}H NMR within this study and previous observations with a range of SSAs.[112–114]

Table 5 – Hydrodynamic diameters (nm) calculated for SSA **42** and **co-formulations a**-**d** in DMSO-d_6/0.5 % H_2O at 298 K.

Co-formulation	Anion (nm)	Cation (nm)	Co-formulant (nm)
SSA **42** only[112]	1.15	1.08	n/a
a	1.23	1.13	0.74
b	1.57	1.39	1.37
c	1.69	1.74	2.21
d	1.70	1.29	1.99
e	*a*	*a*	*a*

a = Experiment not performed due to peak overlap.

Although still indicative of low ordered species, there is an observed increase in the size of the anionic proportion of SSA **42** alone in the presence of co-formulant agents (**isoniazid (43), isoniazid hydrogen chloride (44)**, **octenidine (45)** and **ampicillin (46)**). Data could not be generated for **co-formulation e** (SSA **42** and **cisplatin (47)**) due to the lack of distinct isolated peaks to monitor. The diffusion of the separate molecular components of **co-formulation c** through solution is presented in Figure 29. The SSA anionic proportion of **42** (blue) is diffusing at a different rate to that of the TBA cation component (red), this is coherent with TBA being a weakly coordinating cation.[111] **Octenidine (45)** (yellow), the antimicrobial co-formulant in **c**, is also diffusing at a different rate to both the SSA anion and cation (Figure 29), suggesting these molecular components are not strongly associated with each other. This is the case for all co-formulations studied (Appendix, Figures S30-33). ^{1}H NMR dilution experiments carried out within these studies however suggest evidence for a type of hydrogen bonded association event occurring between SSA **42** and **octenidine**, as well as SSA **42** and **ampicillin (46)** (Section 2.4.2). Using this ^{1}H DOSY NMR data, it is hypothesised these molecular interaction events are transient and are not in slow exchange on the NMR timescale. The association between anionic SSA **42** and appropriate co-formulant agent is not strong enough for the two molecular components to stay bound to each other.

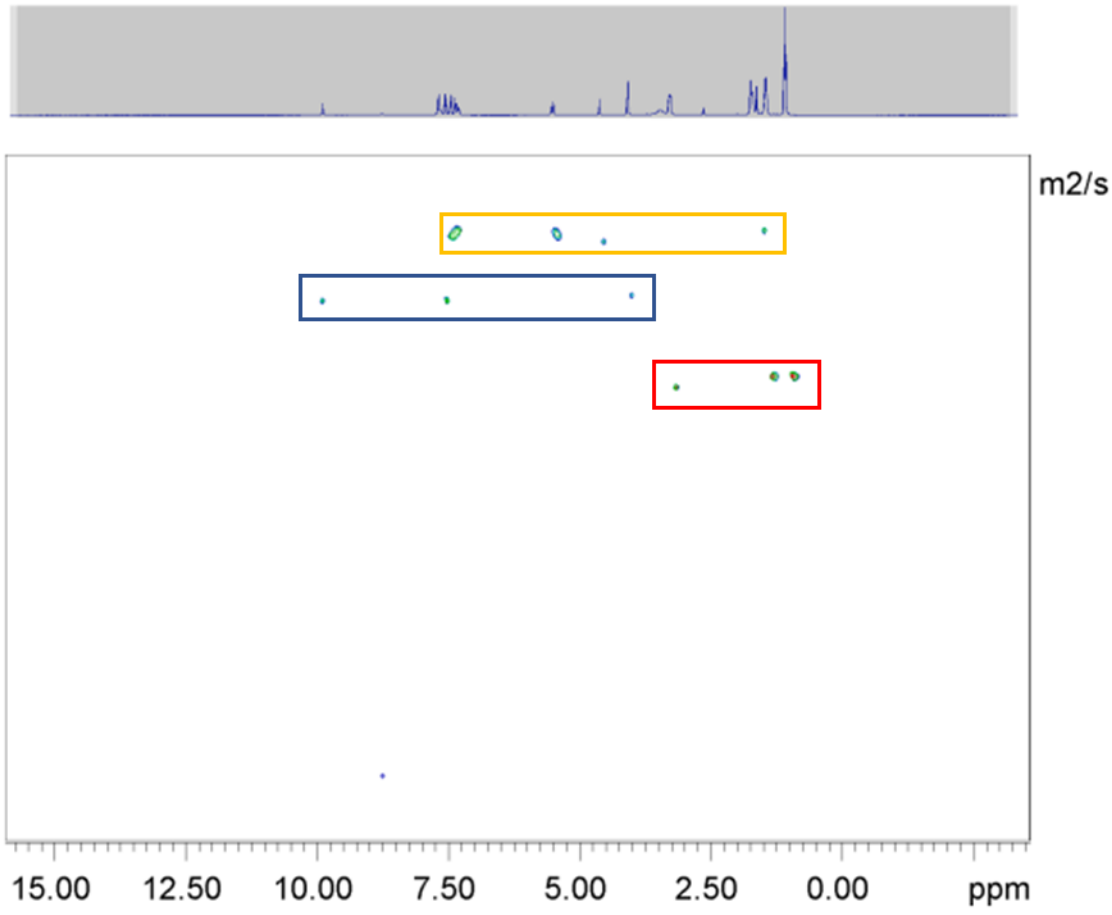

Figure 29 - ^{1}H DOSY NMR spectrum of **co-formulation c** (114.6 mM) in DMSO-d_6 at 298 K. Peaks highlighted in blue correspond to the anionic component of **d** while peaks highlighted in red correspond to the cationic component of **d**. Peaks highlighted in yellow correspond to the drug component, **ampicillin (46)**.

In summary, ^{1}H NMR DOSY experiments performed on SSA **42** in the presence of antimicrobial/ therapeutic agents indicated the presence of lower order dimeric species, ≤ 1.70 nm, correlating with both NMR quantitative and dilution studies. In **co-formulations a**-**d**, the SSA anion, TBA cation and co-formulant were found to exhibit different diffusion rates, indicating any association occurring between molecular components observed in additional experiments is a weak and transient interaction.

2.5. Solution state self-association studies

In the solution state, the type and stability of self-associated structures formed is heavily influenced by the solvent environment. More favourable solvent-solute interactions can out compete weak hydrogen bonds observed in other states, dictating the conformation of aggregates.[112,148] Exploring two contrasting solvent systems within these studies has shown the tendency for SSA **42** to form lower order species in DMSO-d_6 and higher order aggregate structures in aqueous conditions. Those solutions which were found to contain larger self-associated material not observable by ^{1}H NMR are further characterised by applying a series of complementary experimental techniques (Section 2.1, Figure 22). These include, tensiometry, DLS and zeta potential measurements.

2.5.1. Surface Tension and Critical Micelle Concentration

Surfactant molecules are amphiphilic by nature, composed of both hydrophobic and hydrophilic portions. It is this dual nature which drives the ability of surfactants to form self-associated aggregates in solution.[149] Dependent upon type of surfactant and solvent conditions, a diverse array of molecular architecture can form, a key example of which is the formation of a micelle.[150] These are closed aggregates, whereby the hydrophobic tails form the core, and the hydrophilic heads sit externally in contact with the aqueous environment.[149,150]

Critical micelle concentration (CMC) is a fundamental physicochemical parameter for the characterisation of self-assembly. It can be defined as the concentration at which the surface tension no longer decreases with an increasing concentration of surfactant molecules.[151] At low concentrations (Figure 30a), the surface tension is lowered by the presence of molecules at the water-air interface. As the surface becomes saturated, the addition of any further compound can no longer sit at the interface but instead form micellar aggregates in solution (Figure 30b).[152]

However, these stable aggregates can still form in compound concentrations below that of the CMC.[150]

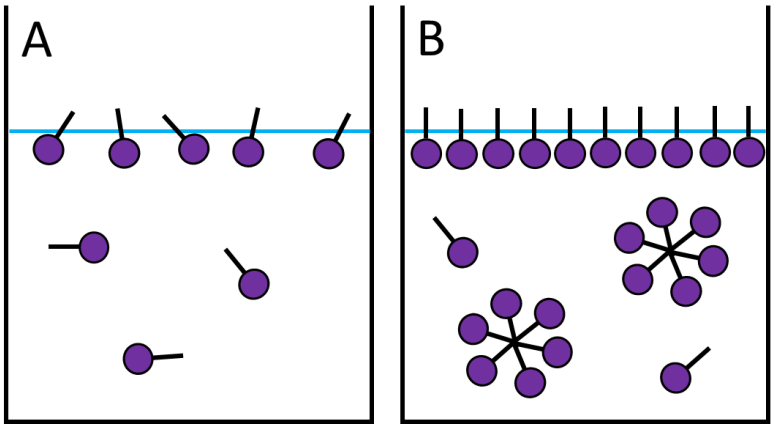

Figure 30 – Dispersal of surfactant molecules in an aqueous solution at concentrations (**A**) below and (**B**) above CMC.[152]

Practically, a surface tension-surfactant concentration graph is created, and the CMC is calculated at the point of intersection of 2 extrapolated lines with different slopes, as shown by the example tensiometry profile in Figure 31. CMC values were determined for **co-formulations a**-**e** in a H_2O/ 5.0 % EtOH solution to determine the effect of an antimicrobial/ therapeutic agent on SSA self-associated aggregation. The ethanol was included to aid SSA solubility, these results are summarised in Table 6 (Table S34-38).

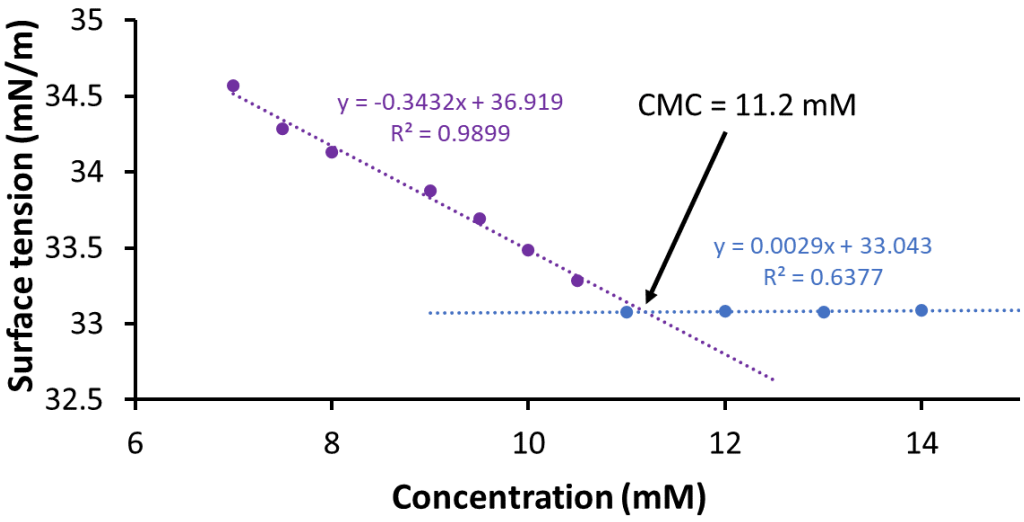

Figure 31 - Calculation of CMC (11.21 mM) for **co-formulation b** in an EtOH:H_2O 1:19 mixture using surface tension measurements.

Table 6 – Critical micelle concentration (CMC) obtained for control SSA **42** and **co-formulations a**-**e** in a H_2O/ 5.0 % EtOH solution at 298 K.

Co-formulation	CMC (mM)
42[112]	10.4
a	6.8
b	11.2
c	5.6
d	16.2
e	3.3

The CMC for control compound SSA, **42** has been previously published at a concentration of 10.4 mM.[112] **Co-formulation b**, incorporating the **isoniazid hydrogen chloride (44)**, exhibited a similar CMC value to that of SSA **42** alone, 11.2 mM (Figure 31). However, the presence of antimicrobial agents in **co-formulations a**, **c** and **e** caused a comparative drop in the CMC with values of 6.8 mM, 5.6 mM, and 3.3 mM respectively (Table 6). This is hypothesised to be due to the comparatively non-polar nature of these co-formulants.

Co-formulation d was found to exhibit a higher CMC than SSA **42** alone, 16.2 mM; this is thought to be attributed to the carboxylate moiety within the **ampicillin (46)** structure. Data generated from ^{1}H NMR dilution studies suggests this co-formulant agent perturbs the self-associative interaction of the anionic component of SSA **42**. It is theorized that the observed increase in CMC is a result of these same competitive association events.

In summary, CMC values were derived for **co-formulations a**-**e** (Table 6) and compared against a previously published value for SSA **42**[112] to investigate the effect of the presence of an antimicrobial/therapeutic agent on the concentration at which larger aggregate structures form in solution. The presence of comparatively non-polar therapeutic agents; **isoniazid (43)**, **octenidine (45)** and **cisplatin (47)** was found to lower the CMC, whereas the presence of carboxylic **ampicillin (46)** was found to increase the CMC.

2.5.2. Zeta Potential Studies

A zeta potential (ZP) describes the electrical charge at the surface of a colloidal particle, a parameter frequently employed to understand the physical stability of a sample.[153] A charged particle attracts a thin layer of oppositely charged ions to its surface, defined as a stern layer (Figure 32). An electrical double layer is created as the particle diffuses through the solution and attracts a cloud of loosely associated ions. The electrical potential of this double layer is termed the zeta potential.[154]

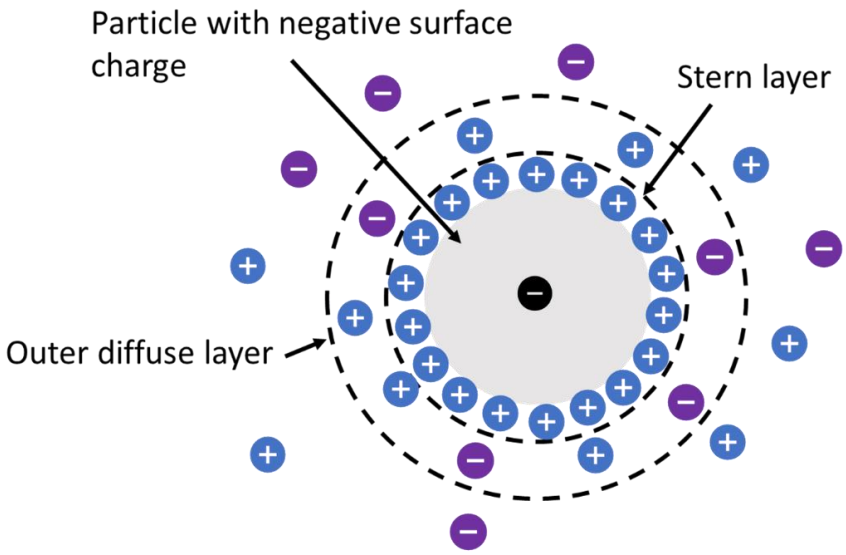

Figure 32 – An illustration of zeta potential, showing the overall surface charge, the stern layer, and the outer diffuse layer.[154]

A zeta potential value of above +30 mV or below -30 mV is generally considered electrostatically stable.[155] A sample with a value which falls within this range tend to exhibit flocculation or coagulation, resulting in poor physical stability.[156] Zeta potential measurements are greatly affected by the pH and ionic strength of solution, concentration of additives and temperature.[156]

To explore the effects of the presence of an antimicrobial/therapeutic agent on the stability of the SSA self-associated aggregates, zeta potential values were obtained for **co-formulations a-e** in a H_2O/ 5.0 % EtOH solution at 5.56 mM (Table 7) (Figures S39-44). Solubility issues

prevented zeta potential measurements of **co-formulations c** and **e** at 5.56 mM, instead these were prepared as a 10-fold dilution at 0.56 mM.

Table 7 – Overview of zeta potential measurements for control SSA **42** and **co-formulations a**-**e** in a H_2O/ 5.0 % EtOH solution at 298 K.

Co-formulation	Zeta potential (mV)
42 (5.56 mM)[112]	-76
42 (0.56 mM)	-66
a	-72
b	-22
c*	+76
d	-3
e*	-42

* Zeta potential measurements were obtained at 0.56 mM due to solubility issues.

Those larger self-associated structures produced by SSA, **42** in aqueous conditions exhibited high stability, with a previously published zeta potential measurement of -76 mV at 5.56 mM.[112] In the presence of therapeutic agents; **isoniazid (43)**, **octenidine (45)** and **cisplatin (47)**, the stability of larger SSA aggregate structures maintained a high level of stability with zeta potential measurements of -72 mV, +76 mV and -42 mV respectively (Table 7). These results correlate with a reduction in the CMC (Section 2.5.1, Table 6). Interestingly, when SSA, **42** is co-formulated with the **isoniazid hydrogen chloride (44)** (**co-formulation b**) vs the uncharged **isoniazid (43)**, a drop in stability is noted, from -72 mV to -22 mV, indicating in this case the need for a neutral co-formulant agent to maintain stability of SSA aggregates.

The greatest drop in stability was observed through the addition of **ampicillin (46)** in **co-formulation d**, with a value of -3 mV, falling considerably outside the range deemed stable for an aggregate. The lack of stable structures in solution is hypothesised to be due to the potential preferential binding of the carboxylate moiety on **ampicillin (46)** to the SSA anion, as indicated

from ^{1}H NMR dilution data. This data also correlates with CMC, where the presence of **ampicillin (46)** causes both the biggest drop in stability and the biggest increase in CMC (Section 2.5.1, Table 6).

In summary, the stability of the larger aggregate structures produced by SSA **42** in the presence of antimicrobial/therapeutic agents **43**-**47** were investigated employing zeta potential measurements. Those **co-formulations** (**a**, **c** and **e**) which exhibited reduced CMC in the tensiometry studies all contained self-associated aggregate species which maintained similar levels of stability when compared to SSA **42** alone. However, the presence of **isoniazid hydrochloric salt (44)** and **ampicillin (46)** caused the stability of those SSA self-associated structures to decrease, producing zeta potential measurements falling outside of the range deemed stable for aggregates (-30 mV ≥ ZP ≤ +30 mV).

2.5.3. Dynamic Light Scattering

Dynamic light scattering (DLS) is a used for detecting and calculating the size of aggregates in macromolecular solutions. Brownian motion of particle theory forms the basis of this technique, whereby the constant collision with solvent molecules causes particles to move in random direction.[146] A key characteristic to this theory is that small particles will diffuse faster through solution than larger ones.[157] In a DLS experiment, when a sample is irradiated with visible monochromatic light, the intensity of scattered light fluctuates over time due to the continuous motion of solute molecules.[145] This scattered light leads either to destructive interference (which will cancel out) or constructive interference, producing a detectable signal and a correlation function.[146] From this, the diffusion coefficient (*D*) is determined and inputted into the Stokes-Einstein Equation (Equation 1, Section 2.4.3) to calculate the hydrodynamic diameter.

The hydrodynamic diameter afore defined as the radius of an equivalent sphere diffusing at the same rate as the particle under observation.[146] As with ^{1}H NMR DOSY (Section 2.4.3), this technique can only provide an indicative size, as for this equation particles are assumed perfectly

speherical.[147] A further limitation relates to the 'intensity-weighted distributions' which, due to the high amount of scattered light, show an emphasis on larger particles. Volume and number-based distributions can be attained from this data, however, this technique requires further parameters, such as refractive index and therefore only intensity-weighted distributions are reported within this study of novel SSA co-formulations.

To further characterise and determine the effects of the presence of the co-formulant agents on self-associated SSA aggregates, DLS was employed to calculate hydrodynamic diameters for **co-formulations a**-**e** (Table 8) (Figures S45-60). The previously published DLS results of **42** alone have been included in this table for comparison purposes.[112] Co-formulations were prepared at 5.56 mM to mimic the zeta potential and quantitative ^{1}H NMR studies, however due to solubility issues, **co-formulations c** and **e** were prepared as a 10 fold dilution at 0.56 mM. Prior to analysis, all samples underwent an annealing process (heated to 40 °C and cooled to room temperature), to ensure all self-associated superstructures formed had achieved a thermodynamic minimum.

Table 8 – Peak maxima obtained from average intensity-weighted DLS distributions for control SSA **42** and **co-formulations a**-**e** in a H_2O/ 5.0 % EtOH solution at 298 K.

Co-formulation	D_H (nm)
42 (5.56 mM)[112]	164
42 (0.56 mM)	142
a	200
b	209
c*	240
d	136
e*	160

* DLS studies were performed at 0.56 mM due to solubility issues.

Hiscock and co-workers have previously grouped the aggregate sizes of SSAs observed by DLS into three distinct categories; 1-10 nm, 11-100 nm, and 101-550 nm.[113] Those self-associated aggregates formed by SSA **42** used in this study falls into the latter category, with an average hydrodynamic diameter of 164 nm at 5.56 mM and 142 nm at 0.56 mM.[112] With the exception of **co-formulation d**, the presence of an antimicrobial agent causes an increase in the size of self-associated aggregate formed in solution. The presence of **octenidine (45)** causes the biggest increase in aggregate size, from 142 nm to 240 nm (Table 8). As stated, the aggregates formed through the co-formulation of SSA and **ampicillin (46)** (**co-formulation d**) are smaller than those formed from SSA **42** alone, a small reduction however from 164 nm to 136 nm. As discussed earlier in this report (Section 2.5.2, Table 7), these structures also exhibit the least stability, with a zeta potential reading of -3 mV.

Interestingly, when SSA **42** is co-formulated with both the neutral form of **isoniazid (43)**, and the **hydrochloric salt (44)**, there is little difference in size of aggregate structure formed (200 nm vs 209 nm). Despite the fact those structures formed in the presence of the neutral form are considerably more unstable (-22 mv, Section 2.5.2, Table 7) compared to those formed in the presence of the hydrochloric salt (-72 mv, Section 2.5.2, Table 7) and exhibit a lower CMC (Section 2.5.1, Table 6). In summary, when SSA **42** is co-formulated with all therapeutic/antimicrobial agents, expect for **ampicillin (46)**, an increase in hydrodynamic diameter is observed, with structures measuring on average between 130-240 nm.

2.6. Antimicrobial activity testing

To assess the ability of SSA **42** to enhance the activity of antimicrobial/therapeutic agents **43-47**, *E. coli* DH10B was used. Traditionally, this *E. coli* strain is used for cloning and DNA propagation,[158] however due to lab stock availability, DH10B was employed as a model Gram-negative bacteria within the scope of this study. Owing to their distinctive outer membrane, Gram-negative bacteria are more resistant to antibiotics than their Gram-positive

counterparts,[159] and hence form the majority of the WHO's list of 'priority pathogens'.[91] The development of new treatments to combat the rising resistance to those currently marketed antimicrobials is critical, hence the decision to target *E. coli* within the scope of these studies.

In addition to chemical diversity, antimicrobial/therapeutic agents, **43-47** were selected due to the diverse range of antimicrobial mode of action. These included extracellular cell wall targeting antimicrobials **isoniazid (43)** and **ampicillin (46)**, membrane targeting antimicrobial, **octenidine dihydrochloride (45) and intracellular** DNA targeting agent, **cisplatin (47)**. Owing to the availability of **isoniazid (43)** in its neutral form, a direct comparison between co-formulation with a drug in both the neutral form (**43**) and the protonated form (**44**) could be explored. **Octenidine (45)** and **ampicillin (46)** were purchased from suppliers as the chloride and sodium salt respectively.

To elucidate the antimicrobial efficacy of **co-formulations a**-**e** compared to **43-47** alone, a microbial susceptibility assay was performed. In short, a 1:100 cell suspension (150 µL) in lysogeny broth (LB) was aliquoted into each well on a 96 well plate, a solution of **co-formulation a**-**e** (30 µL) was added to the well and incubated for 1100 mins in a plate reader, recording OD_{600} readings at 15 min intervals. The MIC_{50} for **42** has previously been published with a value of 3.85 mM,[4] for these experiments SSA **42** was kept at 2 inhibitory concentrations of 1.125 mM and 1.50 mM. Similarly, the concentrations of **2–6** were chosen to impede bacterial growth by < 30 % over 1100 min. The bacterial growth curves are provided in the appendix Figures S62-76. As observed previously,[4] the SSA appears to impede growth as the bacteria reaches stationary phase after 750 mins. We attribute this unusual observation to the change in phospholipid composition at the cell surface membrane during transition from log into stationary phase.

In addition to adding the SSA and antimicrobial agent simultaneously as a **co-formulation** (**a**-**e**), the effects of separate addition of SSA and antimicrobial agent to the bacteria was also investigated. Firstly, the SSA (**42**) was incubated with the bacterial cells for 10 mins, followed by the addition of the appropriate antimicrobial agent (**43-47**) and secondly, the

antimicrobial agent (**43 – 47**) was first incubated with cells for 10 mins, followed by the addition of SSA (**42**). A range of incubation timepoints were explored, any time > 10 mins was not found to cause any greater enhancement of drug agent. The results of these studies have revealed the ability for SSA **42** to enhance the antimicrobial activity of **octenidine**, **ampicillin (46)** and **cisplatin (47)** against *E. coli*. The key findings are summarised in Figure 33.

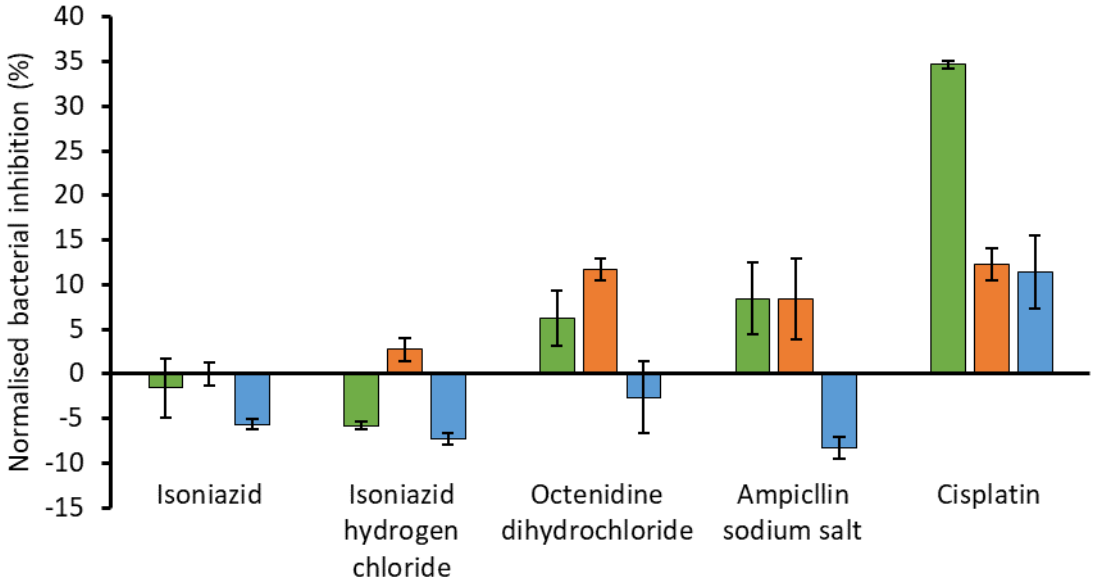

Figure 33 – Bar chart depicting the increase/decrease in efficacy of the antimicrobial agents (**43**-**47**) when delivered as a co-therapy with **42** against *E. coli* DH10B. This data has been normalised to the additive effect of agents through subtraction of any bacterial inhibition (OD_{600}) caused by the presence of SSA **42** or agents **43**-**47** alone. OD_{600} readings were attained at 1100 mins following the addition of SSA **42** (1.5 mM) and either **isoniazid (43)** (1.45 µM), **isoniazid hydrogen chloride (44)** (1.73 µM), **octenidine (45)** (0.29 µM), **ampicillin (46)** (0.89 µM) or **cisplatin (47)** (16.6 µM). Each co-therapy was supplied to the bacteria as either: i) pre-incubation of *E. coli* with SSA prior to addition of antimicrobial agent (green bars); (ii) pre-incubation of *E. coli* with antimicrobial agent prior to addition of SSA (orange bars) or iii) as a co-formulation (**a**-**e**) without prior incubation (blue bars).

Interestingly, the order in which the two agents are supplied to the bacteria has a big impact on the antimicrobial efficacy enhancement. When SSA and antimicrobial agent are supplied as a co-formulation, an antagonistic effect is observed, whereby the supply of the co-formulation to the bacteria results in enhanced bacterial growth when compared to the additive effects of SSA and antimicrobial agent alone. The opposite is true for **co-formulation e**, where supplying the SSA (**42**) and **cisplatin (47)** simultaneously to the *E. coli* bacteria results in enhanced bacterial inhibition, an agonistic effect (Figure 33).

The physicochemical studies revealed, at comparative concentrations, **co-formulation e** retained similar properties to that of SSA, **42** alone. This is hypothesised to be the reason for the observed enhanced antimicrobial activity of **co-formulation e**. Hiscock and co-workers have previously shown a decreasing MIC_{50} for *E. coli* was found to correlate with a decreasing CMC.[4] In this case, the presence of cisplatin (**47**) in **co-formulation e** drove the CMC from 10.39 mM to 3.29 mM, a possible cause for the increased SSA antimicrobial activity observed within this study. In addition, the larger self-associated structures produced by SSA **42** in the presence of **cisplatin (47)** retained similar size and stability to those produced by SSA **42** alone (Section 2.5.2, Table 7 and Section 2.5.3, Table 8).

The extracellular cell wall targeting agents were not found to have increased efficacy in the presence of SSA, either when supplied as the neutral **isoniazid (43)**, or as the **isoniazid hydrogen chloride (44)**. The only exception is the preincubation of the **isoniazid hydrogen chloride (44)** prior to the addition of SSA, this resulted in an increased bacterial inhibition, however the increase in efficacy observed was small. The most effective combination was SSA **42** and **cisplatin (47)**. A bacterial growth inhibition of 34.6 %, 12.3 % and 11.4 % was observed with pre-incubation of *E. coli* bacteria with SSA **42**, pre-incubation of *E. coli* bacteria with **cisplatin (47)** and the co-formulation of SSA and **cisplatin (47)** before addition (**co-formulation e**), respectively (Figure 33). Therefore, the greatest enhancement of antimicrobial efficacy of **cisplatin (47)** is achieved through the prior incubation of SSA with bacterial cells, prior to the addition of **cisplatin (47)** after 10 mins.

Moreover, the presence of SSA **42** was also shown to slightly improve the efficacy of both **octenidine (45)** and **ampicillin (46)**, antimicrobial effects relying on disruption of either cell wall or cell membrane, respectively. As previously stated, these effects were not detected when agents were added simultaneously, only when supplied to the bacteria separately with pre-incubation steps. Results from ^{1}H NMR dilution studies revealed that both **octenidine (45)** and **ampicillin (46)** were involved in molecular association/self-association events with SSA **42**. We

hypothesise that disruption of SSA self-association and thus multicomponent interactions are causing a smaller amount of the active form of therapeutic agent to arrive at the bacterial cell surface.

2.7. Chapter 2 conclusion

The effects of competitive antimicrobial/therapeutic agents (**43-47**) on the self-associated structures produced by SSA **42** was explored using a combination of complementary experimental techniques. In a DMSO-d_6/ 0.5 % H_2O solvent environment, no discernible loss of material from solution was noted for **co-formulations a**-**e**, aligning with previous data of SSA **42** alone,[112] hypothesising the presence of lower order dimeric species. The potential complex self-association events between co-formulant and SSA meant K_{dim} values calculated for many of the co-formulations need to be treated with caution. However, monitoring downfield change in chemical shift of the NH resonances revealed evidence of association between anionic portion of SSA **42** and the cationic **octenidine**. In contrast, no evidence of interaction was observed between SSA **42** and the neutral drug, **isoniazid (43)**. The size of structures formed by SSA **42** in DMSO-d_6 in the presence of co-formulant agents **43-47** were calculated using DOSY ^{1}H NMR experiments. The size range was indicative of lower ordered species, correlating with quantitative ^{1}H NMR studies. SSA anion, TBA cation and co-formulant agent were all found to exhibit different diffusion rates, therefore suggesting any association between molecular components is not a strong interaction.

Moving from a competitive organic solvent into aqueous conditions, quantitative ^{1}H NMR experiments revealed all co-formulations contained larger 'NMR silent' aggregate species, DLS averaged these structures to measure between 136 -240 nm. These data also showed a considerable portion (41 - 64 %) of those antimicrobial/therapeutic agents had become incorporated into those large self-associated structures. CMC values were defined in a H_2O/ 5.0 % EtOH solution, **co-formulations a**, **c** and **e** were found to have comparatively lower CMCs than

SSA **42** alone, thought to be due to the presence of comparatively non-polar therapeutic agents. However, competitive association events between the anionic proportion of **42** and **ampicillin (46)** are thought to be the cause of an increase in CMC for **co-formulation d**. Those **co-formulations** (**a**, **c**, **e**) which exhibited reduced CMC all contain aggregate structures which maintain stability when compared to SSA **42** alone, however in the presence of **isoniazid hydrogen chloride (44)** and **ampicillin (46)**, the stability of structures in solution dropped, falling outside the range deemed stable for aggregates.

In the presence of SSA **42**, the therapeutic effects of **cisplatin (47)** (intracellular DNA targeting), **ampicillin (46)** (extracellular cell wall targeting) and **octenidine (45)** (membrane disruptor) against *E. coli* DH10B were enhanced. This increased effect for **octenidine (45)** and **ampicillin (46)** was only observed however when the SSA and co-formulant agent were added separately to the bacteria. Addition as the **co-formulation** (**c** and **d**) caused an antagonistic effect, hypothesised from the physicochemical studies to be due to a combination of either constructive or destructive molecular interaction at the bacteria surface. The most effective treatment was the addition of **cisplatin (47)** following the pre-incubation of **42** with *E. coli*, resulting in a 35 % increased bacterial inhibition when compared to agents acting alone. From the evidence presented, it is concluded, SSA **42** works most effectively as an antimicrobial/therapeutic agent enhancer when supplied to the bacteria as a combination treatment, pre-incubated for 10 mins prior to an intracellular acting drug agent.

2.8. Chapter 2 Future work

The preliminary antimicrobial testing performed in this study revealed the most effective treatment to be SSA **42** and intracellular targeting antimicrobial, **cisplatin (47)**. Future work will include expanding the set of intracellular drugs tested (e.g., **novobiocin (52)** and **rifampicin (53)**) to further explore this mechanism of action hypothesis. More extensive inhibition assays will be performed, studying the antimicrobials over a larger concentration range, continuing the pre-incubation method. This future work will continue to target the Gram-negative bacteria,

expanding to include those pathogens named by the World Health Organisation as a high priority, for example, P. *aeruginosa*.[91] Much of this future work has been conducted as part of the study outlined in Chapter 3.

3. SSAs as antimicrobial potentiators against *P. aeruginosa* and *E. coli*

3.1. Introduction

The acronym 'ESKAPE' encompasses a group of six bacterial pathogens responsible for most hospital infections and are exhibiting growing multidrug resistance. These include *Staphylococcus aureus, Enterococcus faecium, Pseudomonas aeruginosa, Acinetobacter baumannii, Enterobacter* spp and *Klebsiella pneumoniae.*[160,161] The ESKAPE pathogens exhibit three main mechanisms of resistance; modification of the drug binding site, reduced intracellular accumulation or drug inactivation.[162] These bacteria have now been found to be completely resistant to the 'antibiotics of last resort', carbapenems.[163] Consequently, there is a strong clinical need not only to develop new treatments active against these infections but also to re-sensitise this bacteria to treatments already in existence.

Evident from the void in the discovery of new antibiotics since 1987,[95] the discovery of a brand new class of antimicrobial is rare and therefore the solution may reside with an antibiotic-adjuvant combination approach. An adjuvant (potentiator) is defined as an agent exhibiting little or no inherent antimicrobial activity used in combination with a drug to illicit a greater effect than that of the drug alone, this is a synergistic effect.[164,165]

Peptide based molecular constructs capable of selectively interacting with bacterial membranes are being increasingly used to enhance the permeability of Gram-negative bacteria towards poorly accumulating antimicrobial agents.[166,167] Brown and co-workers have shown the ability of a polymyxin B analogue, SPR741 (**48**, Figure 34) to potentiate various large-scaffold antibiotics in *E. coli* MC1061 bacteria. Here the authors have shown that unlike polymyxin B, which has dual action on both the outer cell membrane and the cytoplasmic membrane, SPR741 interacts solely with lipopolysaccharides on the outer membrane. This polymyxin B analogue has

been shown to improve the influx of antibiotics with inherently poor antimicrobial activity into the bacteria, improving their efficacy.[168]

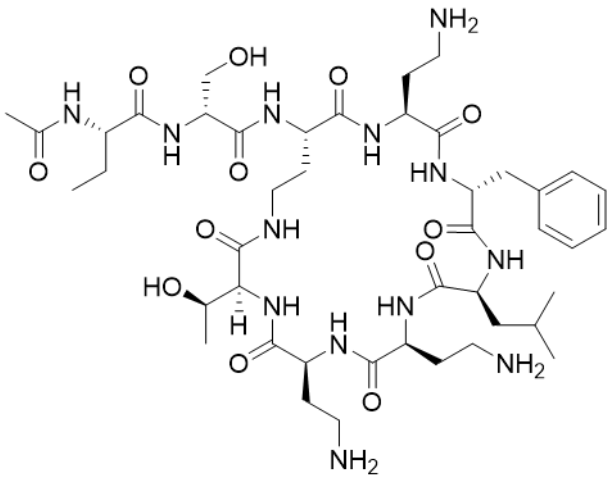

48

Figure 34 - Chemical structure of polymyxin B analogue, SPR741, **48**.[168]

Datta and co-workers also targeted *E. coli* in addition to *K. pneumoniae, P. aeruginosa,* and *A. baumannii*, revealing the potentiation potential for a class of azaindole-based small molecules (< 500 Da). This is hypothesised to be achieved via the reduction of lipopolysaccharides, reducing membrane fluidity and increasing permeability to drugs with intracellular targets. In the presence of the azaindole derivatives, antibiotics with weak innate antimicrobial activity begin to exhibit submicromolar inhibition concentrations, for example, the MIC for erythromycin decreased from 80 to 0.3 μg/mL.[169]

As previously discussed, (Section 2.1) Hiscock *et al*. have most recently focused efforts on the design of ever-more effective, next generation SSA antibacterial agents.[4,117] The antimicrobial activity of SSAs has been linked to their ability to arrive at the surface of a bacterial membrane as self-associated structures.[4,136] Using an inherently fluorescent SSA (**49**) the authors were able to visualise those self-assembled structures at the surface of both MRSA (Figure 35a) and *E. coli* (Figure 35b) bacterial cell membranes. Upon initial addition, spherical self-associated aggregates were visualised and shown to coat the external surface of the bacteria and after 30 minutes of incubation, the fluorescent SSA can be seen to internalise.

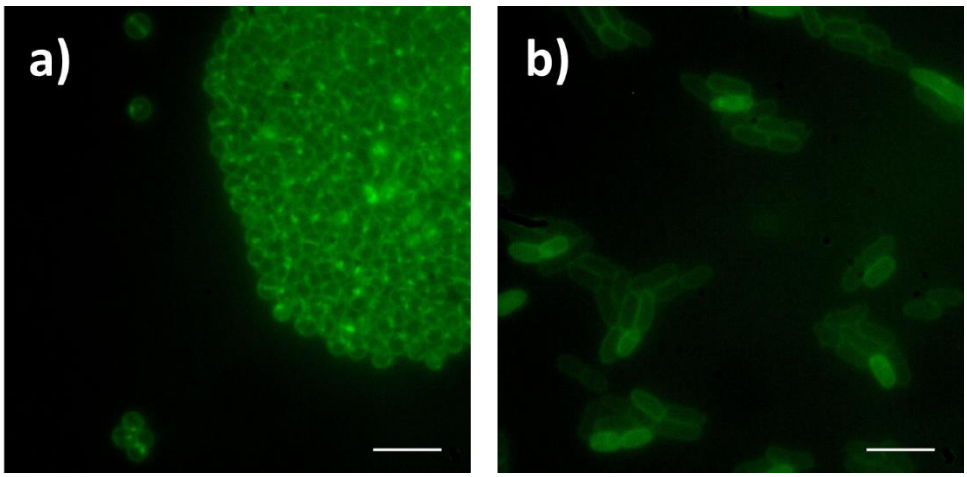

Figure 35 – Fluorescence microscopy images a) MRSA incubated with SSA **49** for 30 mins and b) *E. coli* incubated with SSA **49** for 30 mins. SSA **49** was supplied in a H_2O/ 5.0 % EtOH solution. Scale bar: 10 μM.[136]

3.1.1. Aims

Despite SSAs exhibiting antimicrobial properties, their efficacy is not yet competitive with currently marketed antimicrobials.[170] Building upon initial findings from Chapter 2, where SSA **42** was shown to be capable of enhancing the activity of the intracellular targeting anti-cancer agent **cisplatin (47)**, this chapter offers a more in-depth exploration of the ability of SSAs to act as adjuvants and to the best of our knowledge, the first anionic antimicrobial potentiators for the treatment of *P. aeruginosa*.

The SSAs studied in this chapter include **42**, **49**-**51** (Figure 36). These four, structurally related, stepwise altered SSAs will allow for the elucidation of potentiation structure-activity relationships. The CF_3 moiety within the structure of SSA **42** has been exchanged for a benzothiazole unit in both the para- and ortho- positions to give **49** and **50** respectively, both possessing intrinsic fluorescent properties.[117] Previous evidence has suggested SSAs incorporating the carboxylate moiety induce a greater antimicrobial effect against Gram-negative bacteria compared to the sulfonate anionic group.[4] To explore this with respect to antimicrobial potentiation, the carboxylate version of **42** has also be included within this series (**51**).

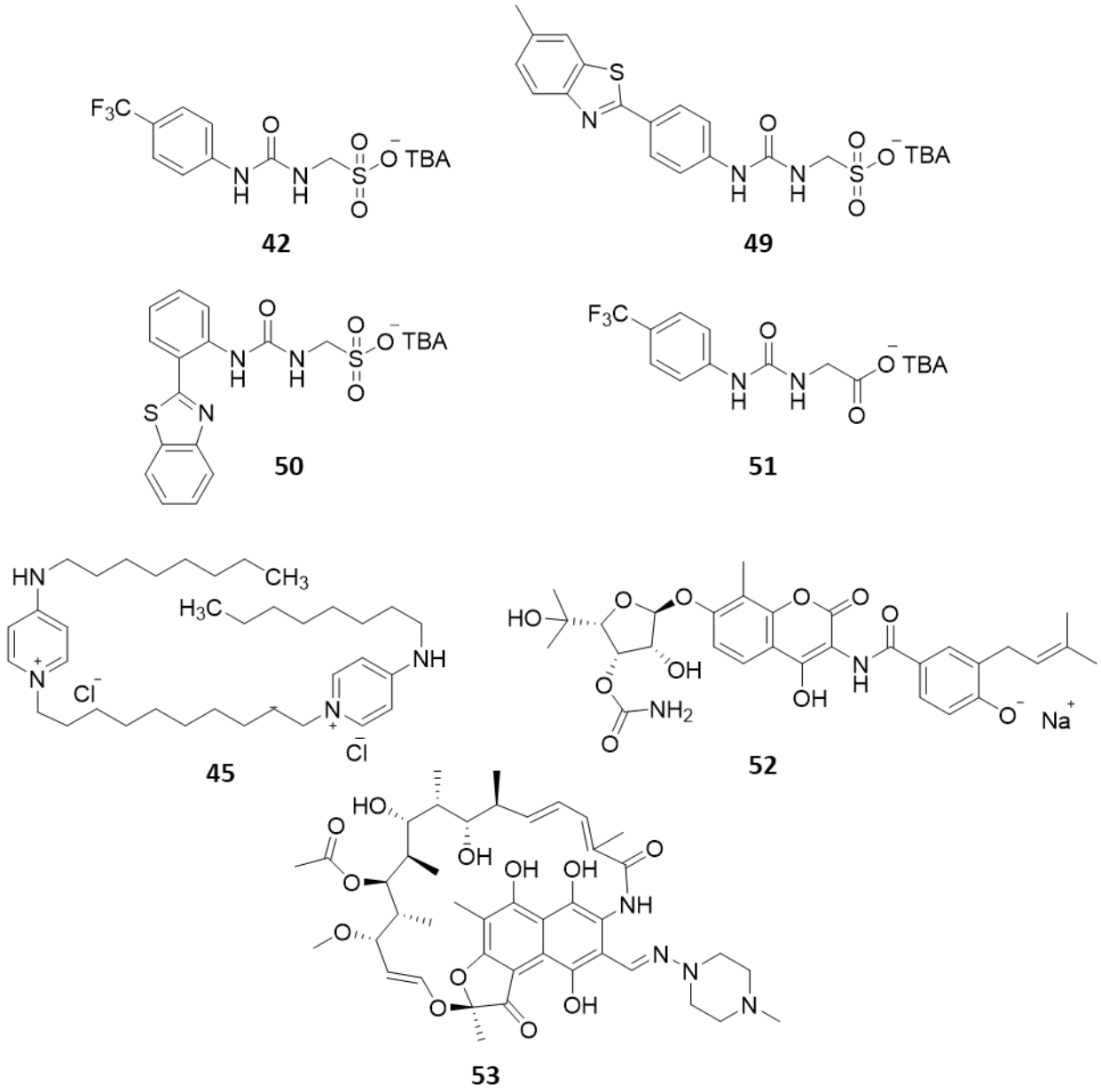

Figure 36 – Chemical structures of SSAs **42**, **49**-**51** and co-formulant agents, **octenidine dihydrochloride** (**45**)**, novobiocin (52)** and **rifampicin (53)** discussed in this chapter.

From the evidence presented in Chapter 2, the most effective therapeutic agent when supplied in combination with SSA **42** against *E. coli* DH10B was **cisplatin (47)**, an intracellular targeting drug. Accordingly, **Novobiocin (52)** and **rifampicin** (**53**) were selected as both antimicrobial agents also have intracellular molecular targets (Figure 36).[70,171,172] **Octenidine dihydrochloride (45),** a cell membrane targeting antiseptic, previously showed antagonism in combination with SSA **42** against *E. coli*, has been carried over into this study. Thus offering an

antimicrobial agent hypothesised to have the same molecular target as the SSA, providing further insight into the mechanism of action required for an effective potentiator..[132]

To verify this hypothesis, the ability of SSAs **42**, **49**-**51** to enhance the therapeutic effect of antimicrobial agents **octenidine dihydrochloride**, **novobiocin (52)** and **rifampicin (53)** will be explored through a series of modified inhibition assays against Gram-negative *E. coli* and *P. aeruginosa.* These assays monitor bacterial growth in response to the antimicrobial agents over a range of concentrations, although keeping the SSA concentration at a static, non-inhibitory concentration, as minimising the antimicrobial activity of the potentiator is vital to avoid the generation of resistance to the potentiator.[173] Sensitising Gram-negative bacteria continues to present a specific challenge to researchers in this field, owing to the robust double membrane. Consequently, this study targets both *E. coli* and 'critical priority' pathogen *P. aeruginosa*.[91] Analogous to Chapter 2, a detailed physiochemical analysis of SSA:antimicrobial co-formulations have been conducted to investigate the self-associative properties of SSAS **42**, **49**-**51** in the presence of antimicrobial agents **octenidine dihydrochloride**, **novobiocin (52)** and **rifampicin (53)**. Finally, fluorescence microscopy is employed utilising the inherently fluorescent SSA **49** and a cell-impermeable membrane staining dye to elucidate a possible SSA antimicrobial potentiation mode of action.

The work detailed in this chapter has been published within the following peer-reviewed journal article:

Anionic self-assembling supramolecular potentiators of antimicrobial activity against Gram-negative bacteria, J. E. Boles, G. T. Williams, N. Allen, L. J. White, K. L. F. Hilton, P. I. A. Popoola, D. P. Mulvihill and J. R. Hiscock, *Adv. Therap,* 2022, DOI: 10.1002/adtp.2200024.[2]

3.2. Synthesis

SSAs **42**, **49**-**51** detailed within this chapter were synthesised in-line with previously published methods.[110,112,113] The synthetic pathway for compound **42** is outlined in Scheme 1. Compound **49** was synthesised through reaction of 4-(6-methylbenzothiazol) aniline and triphosgene in ethyl acetate (EtOAc) and compound **50** was synthesised through reaction of 2-(2-Aminophenyl)benzothiazole and 1,1'-Carbonyldiimidazole (CDI) in chloroform ($CHCl_3$). (Scheme 2). Both were followed by the addition of aminomethane sulfonate TBA and following further purification were obtained as pale-yellow solids in yields 65 % and 42 % respectively.[113] Compound SSA **51** was synthesised through the reaction of 1-Isocyanato-4-(trifluoromethyl) benzene and *tert*-butyl 2-aminoacetate in $CHCl_3$. The product was deprotected using trifluoroacetic acid in DCM. The addition of TBA hydroxide produced a white solid with a yield of 65 %.[112] (Scheme 3)

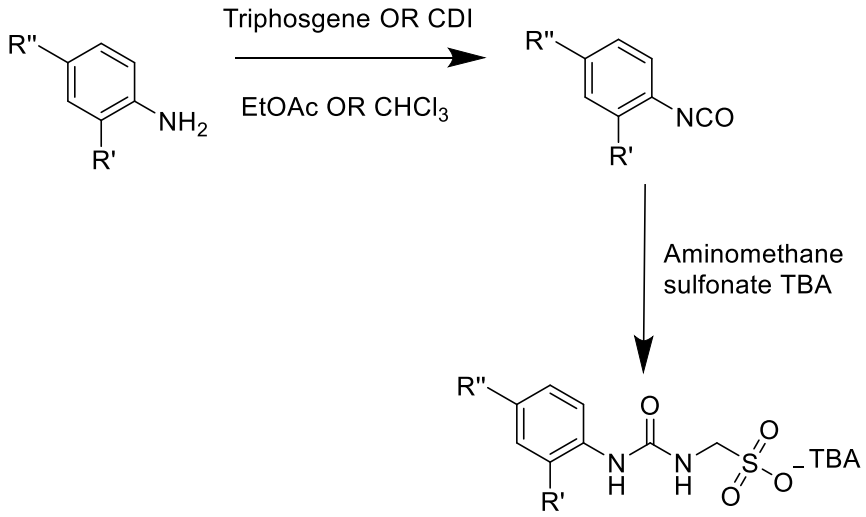

Scheme 2 - Synthesis of **49** and **50** discussed in this thesis

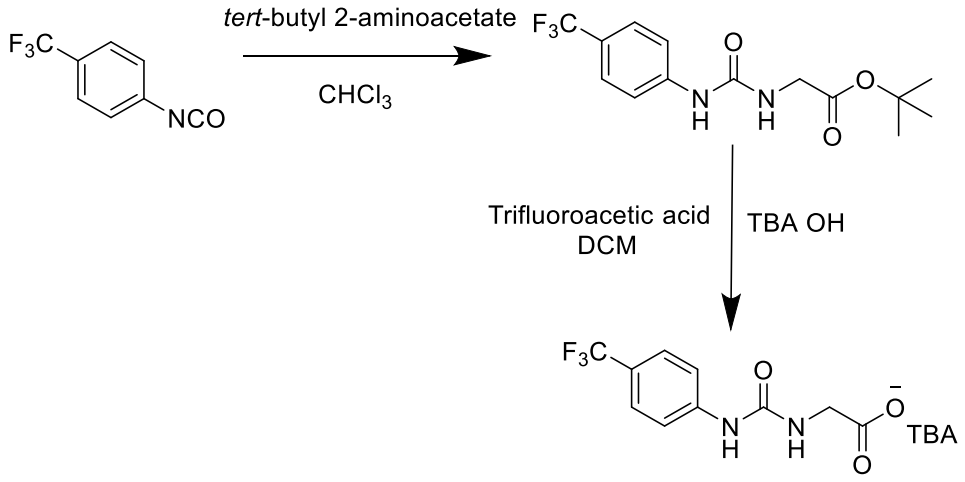

Scheme 3 - Synthesis of **51** discussed in this thesis

3.3. Physicochemical investigation

The self-association properties of SSAs **42**, **49**-**51** have been extensively studied and the resultant aggregate structures have been characterised.[112,113] In solutions of 100 % DMSO, smaller dimeric species sized < 10 nm were primarily observed, whereas larger spherical aggregates > 100 nm were identified in pure aqueous conditions. As the antimicrobial activity of SSAs has been linked to their ability to arrive at the surface of the bacterial membrane as self-associated aggregates, it is essential we understand the effect of adding competitive co-formulant species into these self-assembled systems. Due to the inherent complexities of multi-component self-association events, the physicochemical properties of these co-formulations have been studied employing a variety of complimentary techniques as previously illustrated in Section 2.1, Figure 22. Full experimental details are described in Sections 2.4 and 2.5 and methods are supplied in Section 6.2.

For the physicochemical analysis, co-formulations including SSAs **42**, **49**-**51** and antimicrobial agents **octenidine (45)**, **novobiocin (52)** and **rifampicin (53)** have been assigned an alphabetical value (**f-q**), outlined in Table 9. Data generated for **co-formulations f-q** have been compared to data generated for SSAs **42**, **49**-**51** alone under analogous experimental conditions.[112,113]

Table 9 – Summary of the results from the physicochemical analysis of co-formulations **f**-**q**, including average intensity-weighted size peak maxima (D_h) (0.56 mM), zeta potential (0.56 mM) and CMC measurements obtained for SSAs **42**, **49**-**51** alone[112,113] and co-formulations **f**-**q** in a H_2O/ 5.0 % EtOH solution at 298 K. Self-association dimerization constants (K_{dim}) obtained from fitting ^{1}H NMR dilution study data to the EK dimerization model using Bindfit v0.5[143] in a DMSO-d_6 0.5 % H_2O.

Entry	Compound combination	D_h (nm)	K_{dim} (M^{-1})	Zeta potential (mV)	CMC (mM)
42[112]	-	142	2.7	-66	10.4
49[113]	-	122	2.7	-101	0.5
50[113]	-	295	0.6	-79	9.5
51[112]	-	220	41.4	-37	11.2
f	**42** + **Octenidine**	240	2.9	+76	5.6
g	**42** + **Novobiocin**	98	2.2[c]	+1	*b*
h	**42** + **Rifampicin**	136	2.9	+6	*b*
i	**49** + **Octenidine**	391	*a*	+33	*b*
j	**49** + **Novobiocin**	240	2.1[c]	-46	3.1
k	**49** + **Rifampicin**	636	2.0[c]	-44	1.0
l	**50** + **Octenidine**	586	3.9[c]	-23	*b*
m	**50** + **Novobiocin**	160	1.3[c]	-1	2.1
n	**50** + **Rifampicin**	116	4.1[c]	-26	*b*
o	**51** + **Octenidine**	360	39.1	+44	*b*
p	**51** + **Novobiocin**	174	20.1[c]	-1	3.0
q	**51** + **Rifampicin**	160	6.6[c]	+1	*b*

a = Could not be calculated due to compound solubility; *b* = CMC is above limit of solubility; *c* = treat value with caution due to possible complex association events.

Both SSA and antimicrobial agent are supplied to the bacteria inoculum in an aqueous solvent system. To align with this, DLS, zeta potential and CMC measurements are obtained in a H_2O/ 5.0 % EtOH solution. The results from the DLS measurements revealed the presence of **octenidine (45)** to increase the size of self-associated structures produced by **42** – **51** (Figures S80-101). When comparing to analogous experimental results from SSAs alone, the hydrodynamic diameters were found to nearly double in size when co-formulated with **octenidine (45)** (**f**, **i**, **l**, **o**). In contrast, when SSAs **42**, **50** and **51** are co-formulated with **novobiocin (52)** (**g**, **m**, **p**) and **rifampicin (53)** (**h**, **n**, **q**), the hydrodynamic diameter of the anionic self-associated aggregates decreases in size. Those structures produced by SSA **49**, typically 122 nm in diameter alone, are found to increase in diameter in the presence of both **novobiocin (52)** (**j**) and **rifampicin (53)** (**k**) to 240 nm and 636 nm respectively (Table 9). These changes in hydrodynamic diameter (D_h) provided evidence for the formation of heterogeneous self-

associated SSA aggregates. Within a H_2O/ 5.0 % EtOH solution, it is hypothesised there is interaction between SSA and co-formulant, causing significant changes in the physical properties of those self-associated aggregates.

Zeta potential measurements for co-formulations **f-q** were obtained under analogous experimental conditions to the DLS studies (H_2O/ 5.0 % EtOH solution at 0.56 mM) (Figures S102-112). Those co-formulations (**g**,**h**,**m**,**n**,**p** and **q**) which resulted in the formation of smaller self-associated structures than produced by SSA alone, were all shown to be unstable (Table 9). These zeta potential measurements were between -26 and +6 mV and hence fall outside of the range deemed stable for an aggregated species (-30 mV ≥ ZP ≤ +30 mV).[155] Specifically, the presence of **novobiocin (52)** drove the stability of SSAs **42**, **50** and **51** from -66 mV, -101 mV and -37 mV to +1 mV, -1 mV and -1 mV respectively (Table 9). Out of the three antimicrobial agents co-formulated, the presence of **octenidine (45)** maintained the highest level of stability.

The CMC could not be calculated for a large proportion of the co-formulations (**g, h**, **i**, **l**, **n**, **o** and **q**) as a change in the solubility when SSAs and antimicrobial agents were combined in H_2O/ 5.0 % EtOH was observed, resulting in the CMC being above the solubility limit of these co-formulation mixtures (Figures S113-123). Of those CMCs calculated, for co-formulations incorporating SSAs **50** and **51,** the presence of **novobiocin (52)** drove down the CMC to 2.1 mM and 3.0 mM when compared to SSA alone, 9.5 mM and 11.2 mM respectively. Although, self-associated aggregates are being stabilised at lower concentrations in the presence of **novobiocin (52)**, DLS and zeta potential measurements have shown these to be comparatively smaller (160-174 nm) and less stable (-1 mV) (Table 9). Whereas, for **co-formulations j** and **k** which incorporate SSA **49**, where the presence of **novobiocin (52)** and **rifampicin (53)** was found to disrupt the self-association events and increase the CMC, albeit from an already low CMC of 0.5 mM for **SSA 2** only.

Co-formulations **f-q** were additionally studied in a competitive solvent system, DMSO-d_6/0.5 % H_2O to verify and quantify any hydrogen bonded self-association events (Figures S124-

153). Previous ^{1}H NMR dilution study and ^{1}H NMR DOSY analysis of SSAs **42** – **51** alone has supported the presence of lower order species in this solution.[112,113] Therefore, data generated from ^{1}H NMR dilution studies for **co-formulations f-q** were also fitted to the dimerization EK binding isotherm using Bindfit v.0.5 (Table 9).[143]

The K_{dim} values generated for **co-formulation f** (**42** and **octenidine** (**45**)), **g** (**42** and **novobiocin** (**52**)) and **o** (**51** and **octenidine** (**45**)) were found to reproduce those values generated for the equivalent SSA alone, (Table 9). This suggests, under these experimental conditions, that the antimicrobial co-formulant agent is not interfering or involved in any molecular association with the anionic SSA component. However, as highlighted in Table 9, fitting data from the remaining co-formulations to the dimerization (EK) binding isotherm, an increase in K_{dim} (**co-formulations l**, **m and n**) or a decrease in K_{dim} was observed (**co-formulations g**, **j**, **k**, **o**, **p**, **q**). This indicates that those antimicrobial agents are involved in a complex, molecular self-associative event with the SSA anion. As described in Section 2.4.2, fitting to this EK isotherms requires a 'one component' association event[140] and therefore these data should be treated with caution.

In summary, physiochemical characterisation was performed with **co-formulations f**-**q** to determine the effect of the presence of co-formulant agents, **octenidine (45)**, **novobiocin (52)** and **rifampicin (53)** on the self-associated structures produced by the anionic proportion of SSAs **42** -**51**. **Octenidine (45)** caused the self-associated aggregate species in H_2O/ 5.0 % EtOH to increase in size by approximately two-fold, these species were found to be the most stable when compared to the other co-formulated antimicrobial agents. The presence of **novobiocin (52)** and **rifampicin (53)** however caused a dramatic destabilisation of SSA aggregate species, generating zeta potential values outside the range deemed stable. When compared to SSAs **42**, **50** and **51** alone, these unstable structures were comparatively smaller in hydrodynamic dimeter, but interestingly caused a drop in the CMC. A change in solubility when antimicrobial agent was combined with SSA prevented the calculation of a CMC for those remaining **co-formulations f-**

q. Dimerization constants (K_{dim}) generated from ^{1}H NMR dilution studies suggested the antimicrobial agents in **co-formulation f** (**42** and **octenidine (45)**), **g** (**42** and **novobiocin (52)**) and **o** (**51** and **octenidine (45)**) are not involved in molecular association with the SSA anion in DMSO-d_6/0.5 % H_2O. However, for the remaining co-formulations, a change in is K_{dim} is indicative that conversely the antimicrobial agents are interacting/interfering with the association of SSA and therefore interpretation of such values should be done with caution. In support of the data from Chapter 2, this physicochemical analysis has provided further evidence for the separate supply of SSA and antimicrobial agent to the bacteria, both to increase co-formulation component solubility and to prevent destabilisation of the SSA self-associated structures.

3.4. Antimicrobial potentiation

From the evidence presented in Chapter 2, it was concluded that SSA **42** worked most effectively as an antimicrobial potentiator when enhancing the activity of an intracellular targeting drug agent (**cisplatin (47)**). Here, a 35 % increase in bacterial inhibition was observed when SSA **42** was pre-incubated with *E. coli* DH10B bacteria for 10 mins before addition of **cisplatin (47)** when compared to **cisplatin (47)** acting alone. To further verify the SSA potentiation of intracellular acting antimicrobials, **novobiocin (52)** and **rifampicin (53)**, were selected, both of which target the genetic machinery within the cell responsible for replication. **Novobiocin (52)** works by inhibiting the DNA gyrase, an essential bacterial enzyme responsible for the super-coiling of chromosomal DNA[171,172] and **rifampicin (53)** inhibits bacterial RNA polymerase.[70] **Octenidine (45)**, a cell membrane targeting antiseptic, previously shown (Section 2.6) to act antagonistically with SSA **42** has been carried forward into this study to offer further insight into the mechanism of action required for an effective potentiator.

Antimicrobial agents, **novobiocin (52)** and **rifampicin (53)** are known to be significantly more potent towards Gram-positive bacteria over Gram negative bacteria, hypothesized to be due to their inability to penetrate the second outer membrane and thus to reach their

intracellular targets.[169] The double layered membrane is very effective at restricting the permeability to all but the most hydrophobic of molecules,[52,174] hence the decision to target *E .coli* DH10B and *P. aeruginosa* PA01 within the scope of these studies. The aim of this work was to use SSAs **42**, **49**-**51** to increase the accessibility of these antimicrobial agents to the intracellular molecular targets.

Within Section 2.6, the method of supplying a combination of SSA and therapeutic agent to bacteria was also investigated. The highest percentage of bacterial inhibition was achieved when the SSA was pre-incubated with the *E. coli* bacteria prior to the addition of the therapeutic agent. It is hypothesised that this method enables enough time for the SSA to bind and disrupt the bacterial membrane prior to the addition of the co-formulant. Additionally, physicochemical analysis provided evidence of competitive molecular association between the two components when supplied as a co-formulation. Within this study, to prevent destabilisation of the SSA self-associated structures, increase co-formulation component solubility and maintain experimental uniformity, SSA (**42**, **49**-**51**) and antimicrobial agent (**octenidine (45)**, **novobiocin (52)** or **rifampicin (53)**) were added separately to the bacteria, with a 10-minute pre-incubation of SSA with bacteria inoculum.

3.4.1. MIC determination

Prior to antimicrobial potentiation studies, a minimum inhibitory concentration (MIC) of SSAs **42**, **49**-**51** and antimicrobial agents **octenidine (45)**, **novobiocin (52)** and **rifampicin (53)** were

determined against *E. coli* DH10B and *P. aeruginosa* PA01 (Figures S164-177). This data is presented in Table 10.

Table 10 – The MIC of SSAs **42**, **49**-**51** and antimicrobial agents, **octenidine (45)**, **novobiocin (52)** and **rifampicin (53)** against Gram negative bacteria *E. coli* DH10B and *P. aeruginosa* PA01 after 18 hours.

Compound	*E. coli* DH10B MIC (mM)	*P. aeruginosa* PA01 MIC (mM)
42	> 10[a]	> 10[a]
49	> 10[a]	> 10[a]
50	> 10[a]	> 10[a]
51	10	> 10[a]
Octenidine	0.00078	0.0031
Novobiocin	1.6	3.2
Rifampicin	0.019	0.019

[a] = maximum solubility limit at 10 mM.

The MIC was determined using the microdilution broth method as reported by a Hancock *et al.* (Section 6.2).[175] In short, all compounds were initially prepared in a H_2O/ 5.0 % EtOH solution and serially diluted across a 96 well plate (100 µL). Overnight cultures were back diluted to an OD_{600} of 0.01 (equivalent to ≈ 1 x 10^6 bacteria/mL) in LB media and an aliquot was added to each well (100 µL). Plates were incubated at 37 °C for 18 hours and the optical density (OD_{600}) was determined using a Clariostar plate reader (BMG Labtech). The MIC was defined as the lowest concentration of antimicrobial which caused no visible growth at an optical density of 600 nm, all experiments were performed in triplicate (Appendix 2.7.1).

The MIC_{50} values for SSAs **42**, **49**-**51** against *E. coli* DH10B have previously been published,[4] however for these antimicrobial potentiation studies, it was crucial a MIC value was determined as limiting the antimicrobial activity of a potentiator is vital to avoid the generation of AMR.[173] SSAs were tested at a top well concentration of 10 mM, above this exceeded the solubility limit in H_2O/ 5.0 % EtOH. Of the four SSAs analysed, only **51** displayed an inhibitory effect against *E. coli*, displaying an MIC of 10 mM (Table 10). No SSA exhibited antimicrobial activity against *P. aeruginosa* PAO1. The lack of antimicrobial activity demonstrated against both types of bacteria support the use of these SSAs as antimicrobial potentiating agents against both species of Gram-negative bacteria.

Of those antimicrobial agents tested, the membrane targeting, broad spectrum **octenidine (45)** exhibited the best antimicrobial activity against *E. coli* and *P. aeruginosa*, with MIC values of 7.8 x 10^{-4} mM and 3.1 x 10^{-3} mM respectively (Table 10). **Novobiocin (52)** was the least effective antimicrobial agent tested, with MIC values in the millimolar range (1.6 mM and 3.2 mM for *E. coli* and *P. aeruginosa* respectively), an expected result given the resistance of **novobiocin (52)** to *P. aeruginosa*.[176] Identical MIC values were obtained for the intracellular drug **rifampicin (53)**, with a value of 0.019 mM for both *E. coli* and *P. aeruginosa*. These MIC values will be used to design the antimicrobial potentiation studies whereby both SSA and drug agent will be supplied to the bacteria starting at non-inhibitory concentration.

3.4.2. *Escherichia coli* antimicrobial potentiation

To investigate the potential for SSAs **42**, **49**-**51** to enhance the antimicrobial efficacy of therapeutic agents, **octenidine (45)**, **novobiocin (52)** and **rifampicin (53)** against Gram-negative *E. coli* DH10B, a modified inhibition assay was performed. In brief, solutions of antimicrobial agents starting at 1 x MIC in LB media were serially diluted across a 96 well plate, with a final total well volume of 100 µL. Bacterial subculture (equivalent to ≈ 1 x 10^6 bacteria/mL) was pre-incubated with SSA (**42 – 51**) or control TBA Cl (**420**) at 37 °C for 10 minutes and added to each well (100 µL). Plates were incubated at 37 °C for 18 hours and OD_{600} was determined using a Clariostar plate reader (BMG Labtech). (Section 6.2)

The MICs of SSAs **42**, **49**-**51** against *E. coli* were calculated to be 10 mM and above (Section 3.4.1, Table 10). Whilst below the MIC, SSAs **42** and **51** negatively impeded bacterial growth above 0.6 mM, and as an ideal potentiator has no inherent antimicrobial effect,[177] SSAs **42** and **51** were supplied to the *E. coli* bacteria as 0.6 mM. For analogous experiments conducted with SSAs **49** and **50**, an arbitrary SSA concentration of 8 mM was selected for ease of solubility. In this inhibition assay a range of concentrations of **octenidine (45)**, **novobiocin (52)** and

rifampicin (53) are studied, starting with the MIC concentration as previously reported in Section 3.4.1, Table 10.

SSAs **42**, **49**-**51** all contain a TBA counter cation, as shown in Section 3.1, Figure 36. It has previously been documented that TBA can elicit a slight antimicrobial effect against *E. coli* DH10B, although this MIC is > 8 mM.[4] To attribute any synergistic activity to the SSA anionic portion of SSAs **42**, **49**-**51** and not the cationic TBA counter ion, antimicrobial potentiation control experiments were performed with antimicrobial agents **octenidine (45)**, **novobiocin (52)** and **rifampicin (53)** and **TBA Cl** (**54**) (Figure 37). Concentrations of **TBA Cl** were kept at 8 mM to mimic the highest concentration of SSA used in the full antimicrobial potentiation studies.

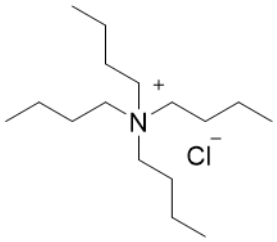

54

Figure 37 – Chemical structure of **TBA Cl** (**54**), used as a control compound to confirm synergistic behaviour of TBA counter cation on SSAs **42** – **51**.

Antimicrobial agents (**octenidine (45)**, **novobiocin (52)** and **rifampicin (53)**) in the presence of **TBA Cl** resulted in no antimicrobial enhancement with *E. coli* (Appendix, Section 2.7.3, Figures S194-196). The results from the co-therapy with **octenidine (45)** is presented in Figure 38. The OD_{600} after 15 hours of **octenidine (45)** alone was found to be within error of **octenidine (45)** in the presence of **TBA Cl**. From these data, it can be concluded that **TBA Cl** is not acting synergistically with the three drug agents selected for this study and therefore any subsequent evidence of synergy with SSAs **42** – **51** can be attributed to the anionic component.

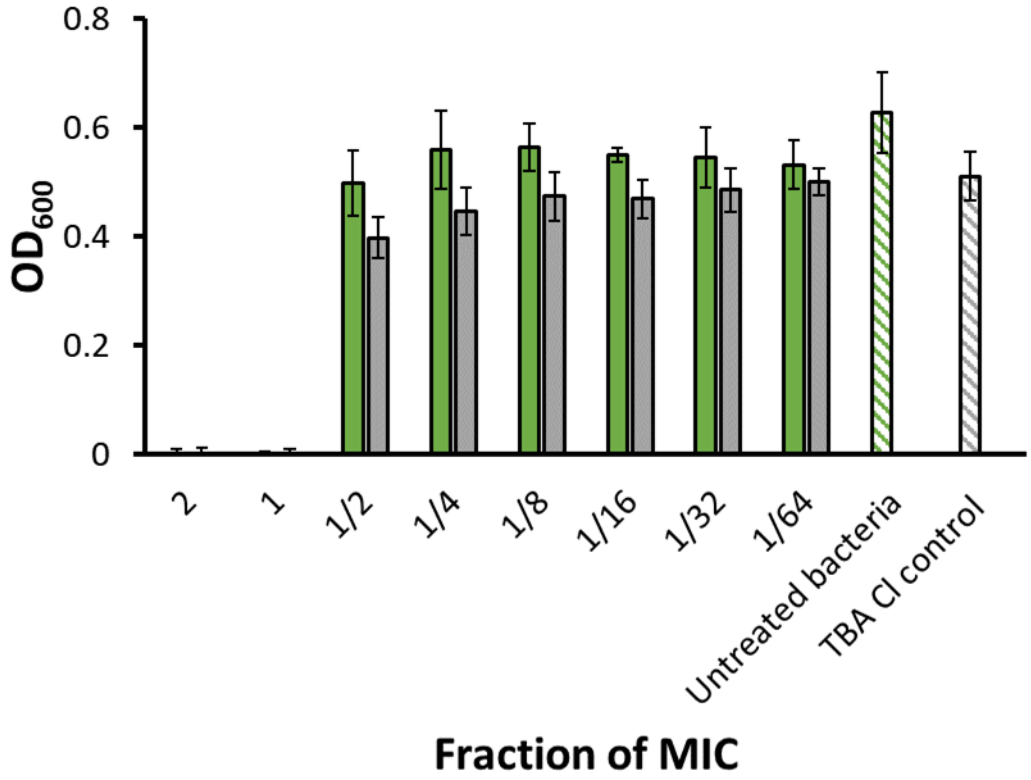

Figure 38 – A control experiment in which **TBA Cl** (8 mM) was pre-incubated with *E. coli* DH10B for ≈ 10 mins at 37 °C before the addition of **octenidine (45)** at varying concentrations. Green = **octenidine (45)** only; grey = **octenidine (45)** + **TBA Cl**.

To explore the antimicrobial efficacy of therapeutic agents, **octenidine (45)**, **novobiocin (52)** and **rifampicin (53)**, in combination with SSAs **42**, **49**-**51** compared to **42**, **49**-**51** alone, a modified inhibition assay was performed as detailed at the beginning of section 3.4.2. The key findings from these studies are summarised in Table 11 (Figures S197-208). When **octenidine (45)**, **novobiocin (52)** and **rifampicin (53)** are supplied to the bacteria following a 10-minute incubation with SSAs **42** and **51**, no antimicrobial enhancement was observed. In agreement with previous observations from Section 2.6, Figure 33 where the combination therapy of SSA **42** and **octenidine (45)** caused a negligible bacterial inhibition of > 5 %.

Table 11 – Summary of *E. coli* antimicrobial potentiation assay outcomes. Antagonism is defined when the OD_{600} of drug and SSA combined exceeds that of SSA alone. SSA was supplied to the bacteria at a non-inhibitory concentration.

Combination treatment	*E. coli* DH10B	Combination treatment	*E. coli* DH10B
f	No effect	**l**	Antagonism*
g	No effect	**m**	Antagonism*

h	No effect	**n**	Antagonism*
i	Antagonism	**o**	No effect
j	Antagonism	**p**	No effect
k	Antagonism	**q**	No effect

* = treat antagonism with caution as compound clouding may be responsible for increased OD_{600}.

In the presence of SSAs **49** and **50** however, antagonistic effects were observed when supplied 10 mins prior to antimicrobial agents **45**- **53** (Table 11). Antagonism here is assigned when the OD_{600} of cells upon exposure to drug and SSA combined exceeds that of SSA alone. With SSA **50**, media clouding was noted which could be the cause for the increase in optical density, therefore this antagonism conclusion needs to be treated with caution. However, SSA **49** did not induce media clouding, the antagonism observed with this SSA and **novobiocin (52)** is illustrated in Figure 39. At higher concentrations, **novobiocin (52)** alone is inducing an antimicrobial effect with a detected decrease in OD_{600} (green bars). However, when supplied following incubation of *E. coli* bacteria with SSA **49**, the optical density across all concentrations of **novobiocin (52)** remained the same as the untreated bacteria control, indicating the presence of SSA **49** has inhibited any antimicrobial efficacy of **novobiocin (52)**. The results of the physicochemical analysis of **co-formulations f**-**q**, as detailed in section 3.3, revealed the tendency for the self-associated structures of SSA **49** to behave differently in the presence of **novobiocin (52)** and **rifampicin (53)** compared to SSAs **42**, **50** and **51** collectively. A comparative increase in hydrodynamic diameter and an increase in CMC when compared to **SSA 49** alone was noted.

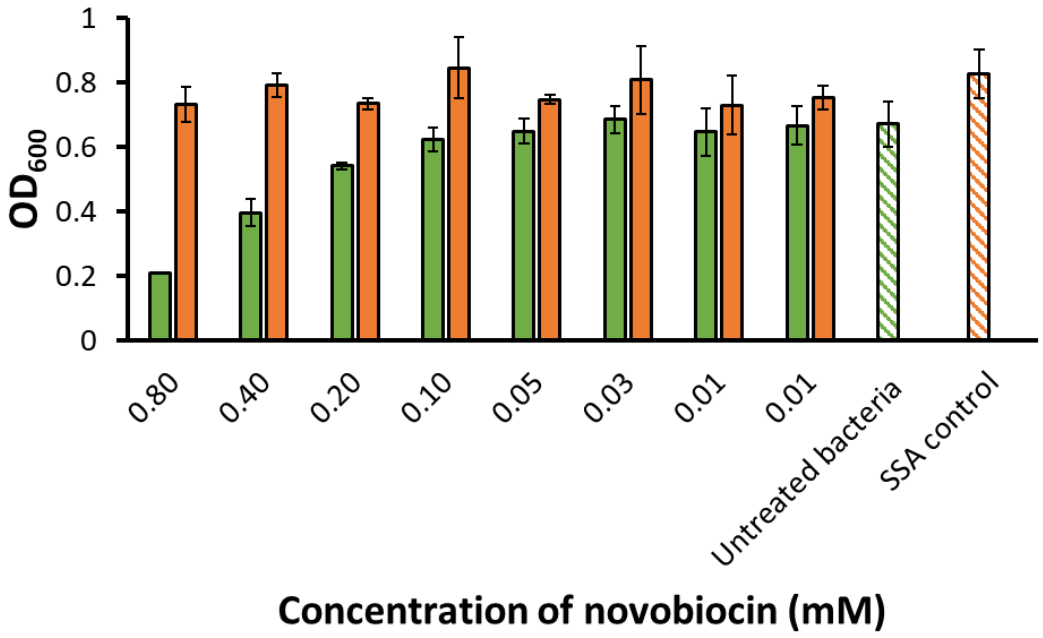

Figure 39 – OD_{600} readings of *E. coli* DH10B bacteria after 18 hours following initial pre-incubation with SSA **50** for ≈ 10 mins at 37 °C before the addition of **novobiocin (52)** at varying concentrations. Green = **novobiocin (52)** only; orange = **novobiocin (52)** + SSA (**50**).

In summary, the antimicrobial efficacy of therapeutic agents **octenidine (45)**, **novobiocin (52)** and **rifampicin (53)** are not enhanced by the presence of SSAs **42** – **51** in *E. coli* bacteria. Despite the intracellular targeting of **novobiocin (52)** and **rifampicin (53)**, the selected SSAs could not potentiate this mode of action. The inherent antimicrobial effect of **octenidine (45)**, **novobiocin (52)** and **rifampicin (53)** was impeded by the presence of SSA **49**, attributed to the opposing physicochemical studies when compared to SSAs **42**, **50** and **51.**

3.4.3. *Pseudomonas aeruginosa* antimicrobial potentiation

Gram negative *P. aeruginosa* denotes the 'P' in the ESKAPE pathogens.[161,178] The WHO have published a list of bacteria posing the greatest threat to human health, of which carbapenem-resistant *P. aeruginosa* has been placed in the highest priority category.[91] This bacteria has the ability to resist a range of currently marketed antimicrobials, including **novobiocin (52)** used

within this study,[176,179] thus acting as a good indicator for the antimicrobial potentiation ability of SSAs **42**, **49**-**51**.

Using the same biological method outline in section 3.4.2, the ability of **TBA Cl** (Figure 37), the counter cation in SSAs **42**, **49**-**51** to potentiate the antimicrobial activity of agents **octenidine (45), novobiocin (52)** and **rifampicin (53)** was ruled out before studies with SSAs were conducted. The results from the co-therapy with **novobiocin (52)** are presented in Figure 40. From these data and those presented in Appendix Section 2.7.2, it can be concluded **TBA Cl** does not enhance the efficacy of therapeutic agents **octenidine (45), novobiocin (52)** and **rifampicin (53)** against *P. aeruginosa* PA01 and therefore any subsequent evidence of synergy with SSA **42**, **49**-**51** with these antimicrobial agents can be credited to the anionic proportion of the SSA molecule.

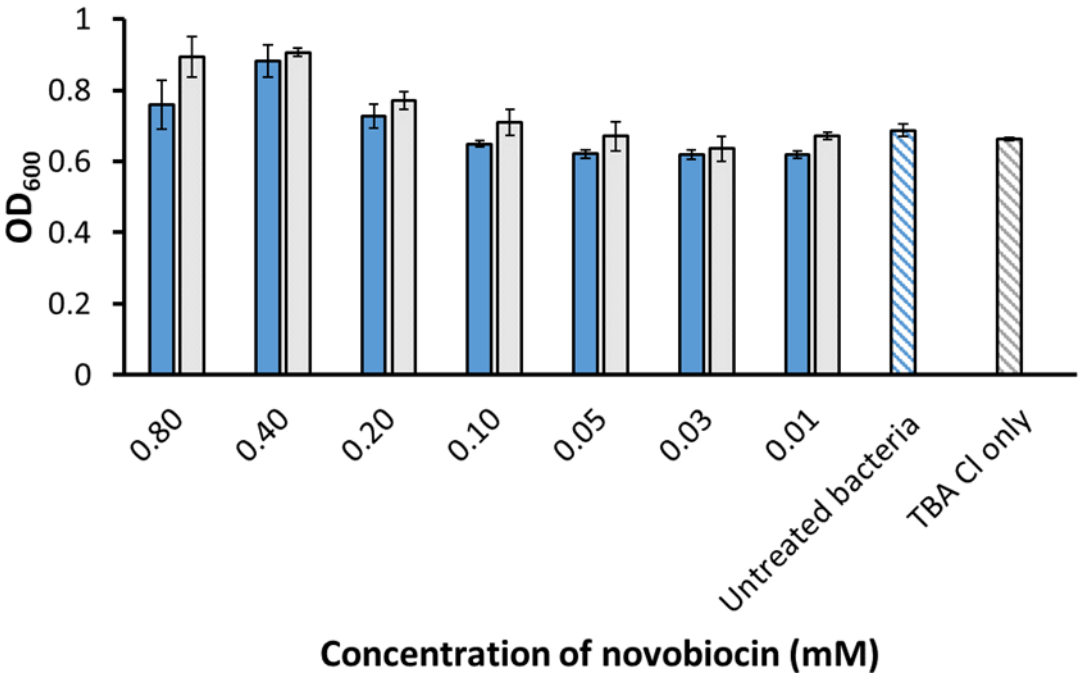

Figure 40 - A control experiment where **TBA Cl** (8 mM) was pre-incubated with *P. aeruginosa* PA01 for ≈ 10 mins at 37 °C before the addition of **novobiocin (52)** at varying concentrations. Blue = **novobiocin (52)** only; grey = **novobiocin (52)** + **TBA Cl**.

To explore the ability of SSAs **42**, **49**-**51** to enhance the antimicrobial efficacy of **octenidine (45), novobiocin (52)** and **rifampicin (53)**, the modified inhibition assay outlined in section 3.4.2 incorporating a 10-minute pre-incubation of SSA with *P. aeruginosa* inoculum was performed

(Figures S181-193). As SSAs **42** – **51** were found to exhibit no antimicrobial effect under 10 mM (Section 3.4.1, Table 10), an arbitrary SSA concentration of 8 mM was selected for ease of solubility. As with those antimicrobial potentiation studies conducted against *E. coli* DH10B (Section 3.4.2), antimicrobial agents, **octenidine (45), novobiocin (52)** and **rifampicin (53)**, are diluted starting from the appropriate MIC concentration (Section 3.4.1, Table 10). The findings from these studies are summarised in Table 12. All co-therapies containing the membrane targeting agent, **octenidine dihydrochloride (45)** exhibited antagonism, whereby the OD_{600} of **octenidine (45)** and SSA combined exceeds that of SSA alone.

Table 12 - Summary of *P. aeruginosa* antimicrobial potentiation assay outcomes. Antagonism is defined when the OD_{600} of drug and SSA combined exceeds that of SSA alone. SSA was supplied to the bacteria at a non-inhibitory concentration.

Combination treatment	*P. aeruginosa* PA01	Combination treatment	*P. aeruginosa* PA01
f	Antagonism	**l**	Antagonism*
g	Potentiation	**m**	No effect
h	Potentiation	**n**	Antagonism*
i	Antagonism	**o**	Antagonism
j	No effect	**p**	Potentiation
k	Antagonism	**q**	Potentiation

* = treat antagonism with caution as compound clouding may be responsible for increased OD_{600}.

The MIC of **octenidine (45)** against *P. aeruginosa* PA01 was previously calculated to be 3.1 µM (Section 3.4.1, Table 10), however in the presence of SSA **42**, the MIC was found to be > 40-fold higher. This is illustrated in Figure 41 where at concentrations higher than the MIC of **octenidine (45)** alone (blue), the high OD_{600} readings are indicative of live *P. aeruginosa* bacteria (purple), the presence of SSA **42** has inhibited the effectiveness of **octenidine (45)**. This effect is thought to be due to the combination of microbial surface coordination of both SSA and therapeutic agent. This further supports the theory from Section 2.6 that SSA molecules cannot potentiate those agents with analogous modes of actions to that of the SSA itself, in this case both SSA and **octenidine (45)** target the lipid membrane.

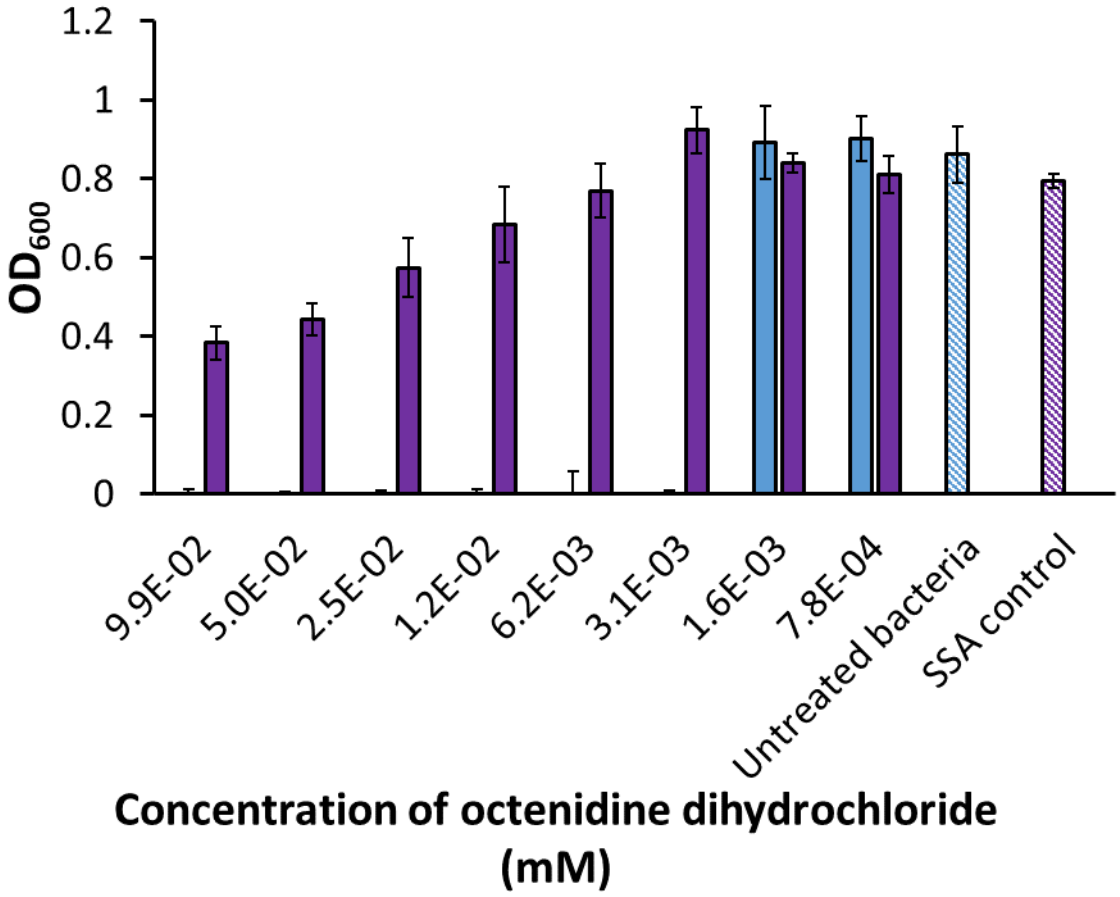

Figure 41 – OD_{600} readings of *P. aeruginosa* PA01 bacteria after 18 hours following initial pre-incubation with SSA **42** for ≈ 10 mins at 37 °C before the addition of **octenidine (45)** at varying concentrations. Blue = **octenidine (45)** only; purple = **octenidine** + SSA (**42**).

The antimicrobial effects against *P. aeruginosa* PAO1 of intracellular targeting therapeutic agents **novobiocin (52)** and **rifampicin (53)** were enhanced in the presence of SSAs **42** and **51**. As displayed in Figure 42a, the combination treatment of SSA **42** and **novobiocin (52)** offered the greatest evidence of antimicrobial potentiation with a dramatic 8-fold decrease in the MIC, from 3.2 mM (Section 3.4.1, Table 10) for **novobiocin (52)** only, to 0.4 mM in the presence of a non-inhibitory concentration of SSA **42**. An antimicrobial dose-dependent reduction in bacterial growth was also observed, with a decrease in growth detected at concentrations over 100 times lower than that of the MIC. SSA **51** showed slightly less potentiation of **novobiocin (52)** than SSA **42** but an antimicrobial dose-dependent decrease was still observed (Figure 42b). In contrast, the potentiation of the therapeutic agent, **rifampicin (53)** was near identical in the presence of both SSA **42** and **51**, producing similar antimicrobial dose dependent plots. The ability of SSAs

42 and **51** to enhance the efficacy of **rifampicin (53)** were slightly less than **novobiocin (52)**, with a reduction in bacterial growth noted only 32 times lower than the MIC (Figure 42c and d). The differences in SSA potentiator susceptibility to *P. aeruginosa* and *E. coli* could be explained by the variations in membrane phospholipid composition. The outer membrane of *P. aeruginosa* PA01 contains 59.7 % (± 2.9 %) PE, 27.1 % (± 1.7 %) PG and 13.2 % (± 2.8 %) PC, whereas *E. coli* is reported to consist of 70-80 % PE, 20–25 % PG and < 5 % cardiolipin.[180,181]

Unexpectedly, SSAs **49** and **50** did not show any antimicrobial potentiation of either **novobiocin (52)** or **rifampicin (53)** with *P. aeruginosa* PA01 (Table 12). Elucidation of basic molecular structure-antimicrobial potentiator relationships can be predicted owing to the stepwise structural alterations of SSAs **42**, **49**-**51** (Figure 36). Modification of the hydrophobic unit from a 4-trifluorophenyl moiety (**42** and **51**) to a benzothiazole derivative (**49** and **50**) causes a reduction in the potentiation ability of the SSA, this is also irrespective of the aromatic positioning of the benzothiazole unit (**49**, para and **50**, ortho). Previous evidence has indicated the carboxylate moiety induces a greater antimicrobial effect against Gram-negative bacteria over the sulfonate anionic group.[4] However, the opposite is true for antimicrobial potentiation, with a greater potentiation offered with SSA **42** (sulfonate) over **51** (carboxylate) (Figure 42a and b).

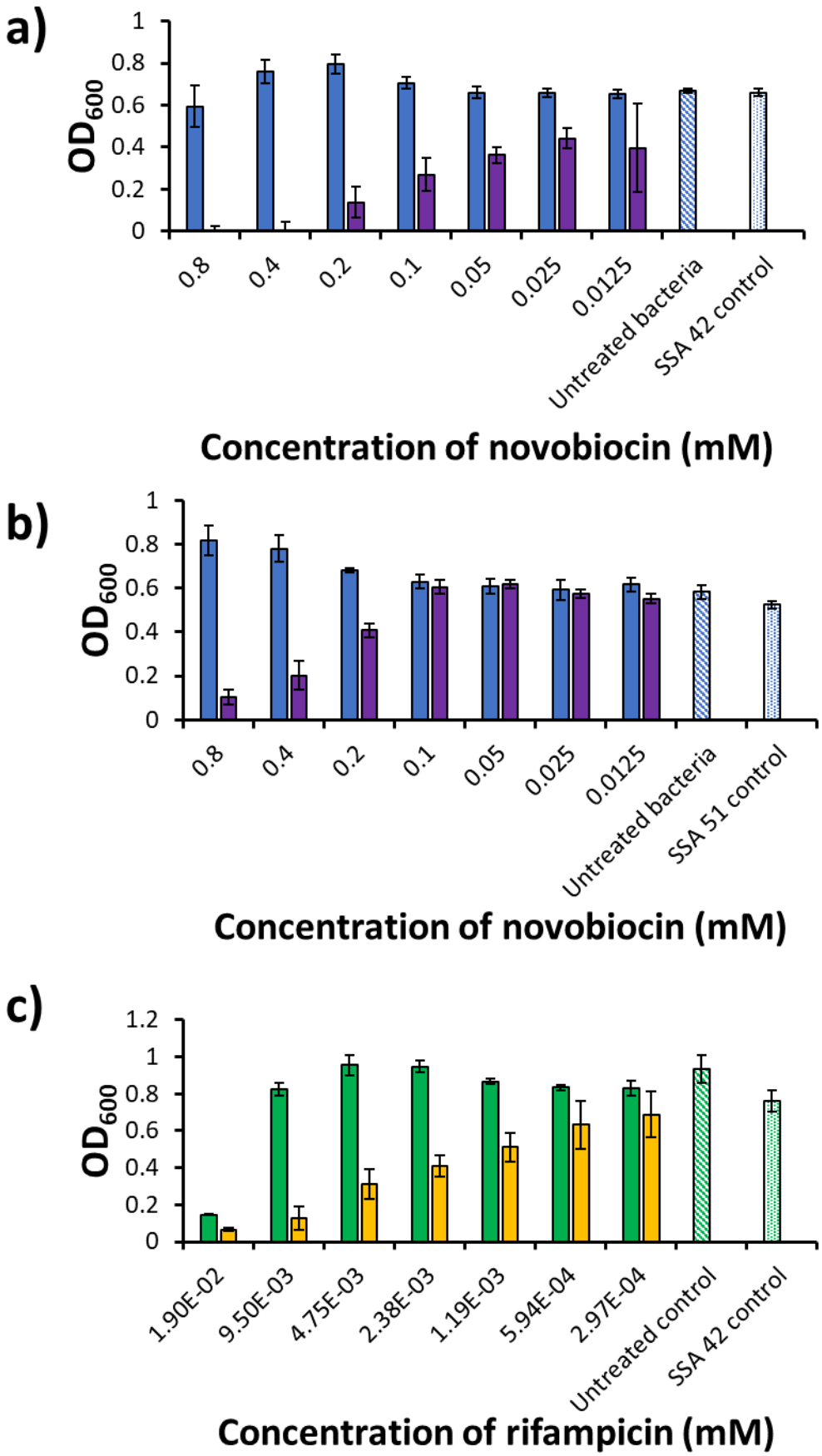
a)
OD600
1
0.8
0.6
0.4
0.2
0
0.8
0.4
0.2
0.1
0.05
0.025
0.0125
Untreated bacteria
SSA 42 control
Concentration of novobiocin (mM)
b)
OD600
1
0.8
0.6
0.4
0.2
0
0.8
0.4
0.2
0.1
0.05
0.025
0.0125
Untreated bacteria
SSA 51 control
Concentration of novobiocin (mM)
c)
OD600
1.2
1
0.8
0.6
0.4
0.2
0
1.90E-02
9.50E-03
4.75E-03
2.38E-03
1.19E-03
5.94E-04
2.97E-04
Untreated control
SSA 42 control
Concentration of rifampicin (mM)

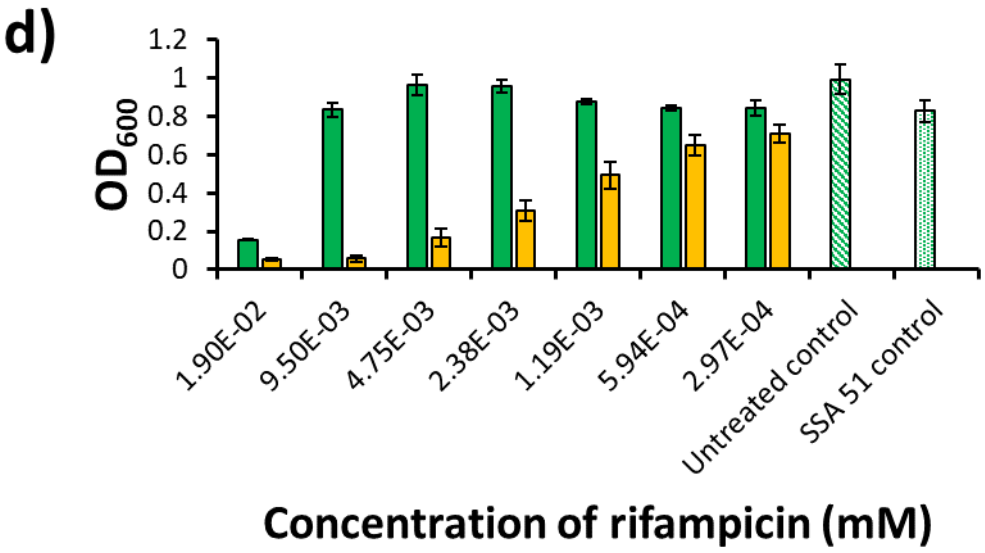

Figure 42 - OD_{600} readings of *P. aeruginosa* PA01 after 18 hours following initial pre-incubation with a) initial pre-incubation with SSA **42** followed by **novobiocin (52)**; b) initial pre-incubation with SSA **51** followed by **novobiocin (52)**; c) initial pre-incubation with SSA **42** followed by **rifampicin (53)** and d) initial pre-incubation with SSA **51** followed by **rifampicin (53).** Blue = antimicrobial agent only; orange = **novobiocin (52)** + SSA (**42** or **51**) and yellow = **rifampicin (53)** + SSA (**42** or **51**).

Interestingly, the physicochemical studies detailed in section 3.3 revealed that those co-formulations containing **octenidine (45)** maintained the highest level of stability of all co-formulations studied. The antagonistic behaviour of **octenidine (45)** in combination with SSA is suggestive of direct interaction, however physicochemical studies revealed no evidence of competitive molecular association. However, it was with these co-therapies for which antagonism was observed against *P. aeruginosa*. It is suggestive that more emphasis needs to be placed on the molecular targets of possible antimicrobials, as opposed to the physicochemical characterisation of SSAs in the presence of those antimicrobials.

The effectiveness of the combination of **novobiocin (52)**, a drug known to be ineffective against *P. aeruginosa* alone, and SSA **42** and **51** provides insight into the mechanism of potentiation. It is hypothesised the lipopolysaccharide-containing outer membrane present in Gram-negative bacteria acts as a permeability barrier for **novobiocin (52)**.[172] This indicates the SSA potentiation is mediated by the permeabilization of the outer membrane, allowing a higher cellular uptake of **novobiocin (52)** and hence a considerably lower MIC. Although,

physicochemical studies revealed potential molecular association and disruption of the larger self-associated structures in the presence of **novobiocin (52)** (Section 3.3), it is hypothesised that adding the two components to the bacteria separately offers enough time for the self-associated aggregates of SSAs **42**, **49**-**51** to act on the bacteria effectively before the addition of the potentially disruptive antimicrobial agents.

In summary, SSAs **42** and **51** can act as antimicrobial potentiators of intracellular targeting agents, **novobiocin (52)** and **rifampicin (53)** against *P. aeruginosa*. This potentiating ability has been shown to be dependent upon SSA molecular structure, with 4-trifluorophenyl substituted SSAs (**42** and **51**) offering enhancement of antimicrobial efficacy, but modification with a benzothiazole substituent (**49** and **50**) precludes all potentiation ability. Despite maintaining the highest levels of stability as a co-formulation, the presence of SSA with the membrane targeting agent **octenidine (45)** resulted in antagonistic effects whereby **octenidine (45)** was more effective alone. This work has not only expanded upon the potentiating capabilities of SSAs but has also provided evidence for the first anionic construct to effectively potentiate antimicrobial agents towards *P. aeruginosa*.

3.5. Fluorescence Microscopy studies

Fluorescence microscopy was employed to elucidate a possible SSA potentiator mechanism of action. Given that the antimicrobial agents (**octenidine (45)**, **novobiocin (52)** and **rifampicin (53)**) used in this study are not inherently fluorescent, the non-selective lipid binding fluorescent dye, **FM4-64** was utilised instead; the structure is shown in Figure 43. This dye is known to integrate into the outer leaflet of biological membranes but is unable to cross the lipophilic bacterial membranes.[182] This dye was studied in combination with SSA **49**, an inherently fluorescent molecule, employed previously within fluorescence experiments to study the coordination of SSAs to bacterial membranes.[4,117,136] Both molecules fluoresce in different

regions, allowing for the independent visualisation of each compound during the experiment with high spatiotemporal resolution.

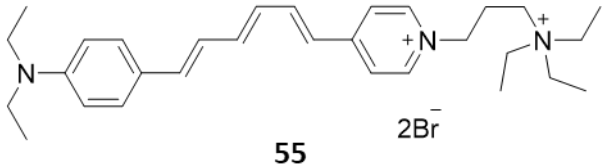

55

Figure 43 – Chemical structure of membrane binding fluorescent styryl-dye, **FM4-64**, **55.**

A competitive membrane association assay was performed. In short, *E. coli* DH10B or *P. aeruginosa* PA01 bacteria was incubated for four hours with either **FM4-64** or SSA **49** alone, or **FM4-64** and SSA **49** approximately 1 minute apart for 4 hours. Differences in excitation and emission properties allowed **FM4-64** to be visualised using a 605 nm filter and SSA **49** using a 450 nm filter. Microscopy analysis of those studies involving *P. aeruginosa* PA01 showed SSA **49** did not adhere to the microbial surface. This supports those MIC results documented in section 3.4.1, Table 10 showing the ineffectiveness of SSA **49** alone against this strain of *P. aeruginosa,* and also the antimicrobial potentiation studies in section 3.4.3 Table 12, which showed an inability of SSA **49** to enhance the efficacy of all antimicrobial agents studied. SSAs **42** and **51**, where antimicrobial potentiation was observed, are not inherently fluorescent and therefore could not be used within the scope of this study. Analogous studies with *E. coli* DH10B cells were performed by Dr Nyasha Allen, and those fluorescence images are presented in Figure 44.[4]

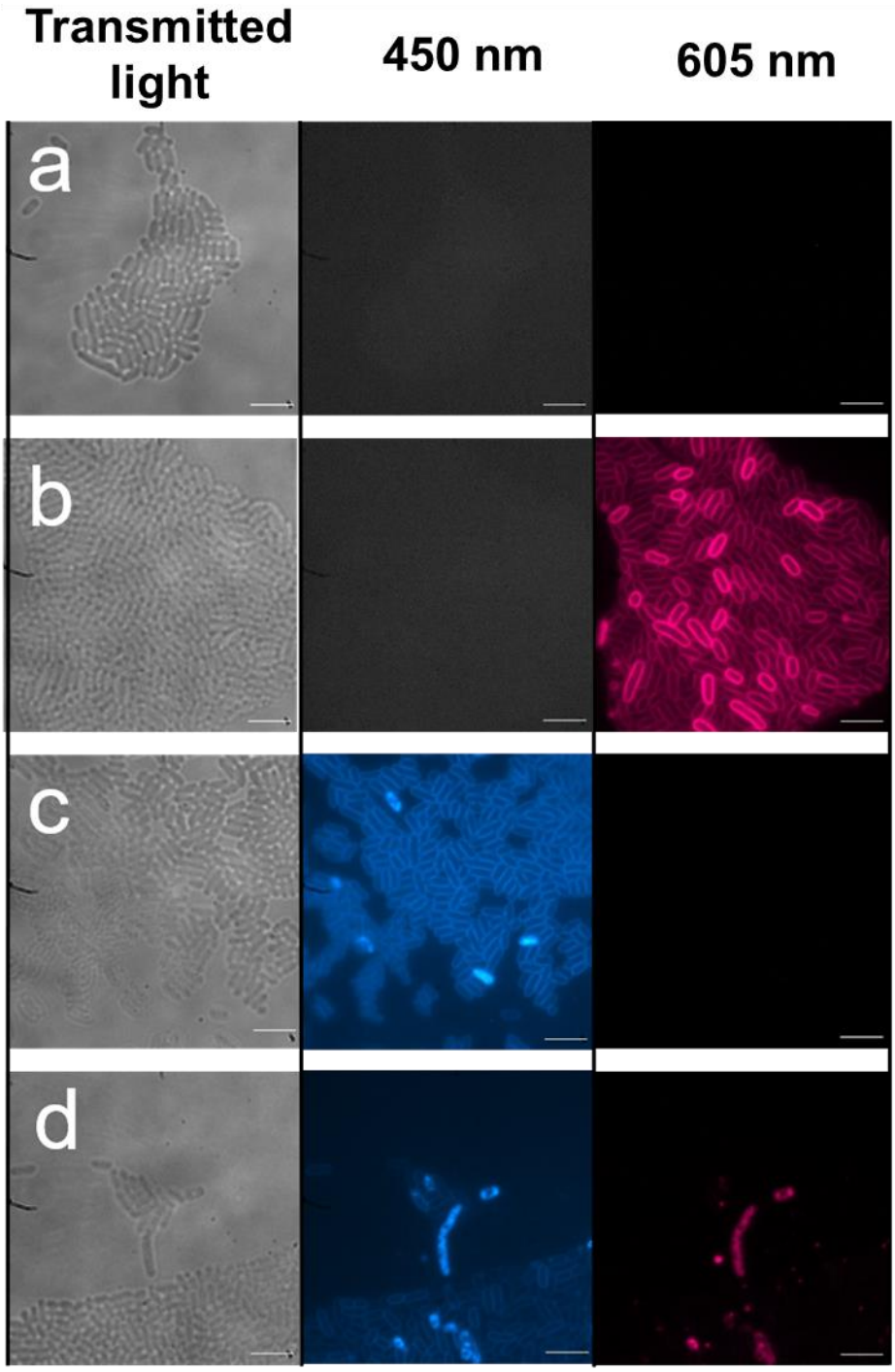

Figure 44 – Fluorescence microscopy images of E. coli DH10B; a) in the presence of no compound; b) 4 hour incubation with membrane binding compound **FM4-64**; c) 4 hour incubation with SSA **49** and d) 1 min incubation **with FM4-46** followed by addition of SSA 49 for 4 hours. Scale bar: 10 µM.[4]

The results from the studies involving *E. coli* DH10B showed that after 4 hours, SSA **49** not only adhered to the microbial surface but also internalised within the bacteria (Figure 44c). As expected, **FM4-64** was also found to adhere to the external *E. coli* bacterial surface, with no evidence of internalisation (Figure 44b). Interestingly, when both SSA **49** and **FM4-64** were

added to the *E. coli* bacteria as a combination therapy, the presence of SSA **49** was found to facilitate the internalisation of **FM4-64** (Figure 44d). Both components were then shown to co-localise within the *E. coli* bacteria itself, illustrated by an overlay fluorescence image in Figure 45.

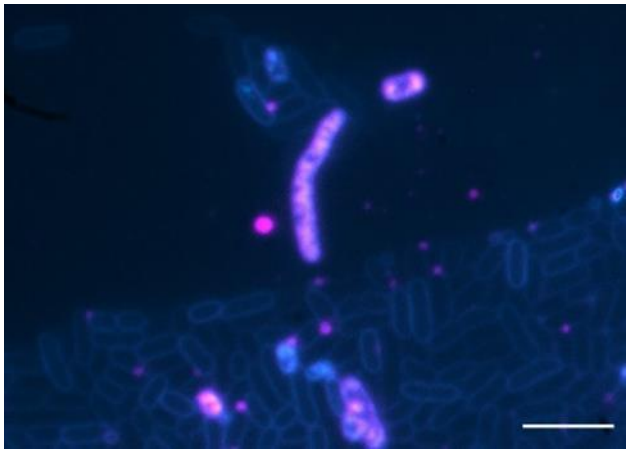

Figure 45 – An overlay fluorescence image of Figure 44b and Figure 44c showing both **FM4-64** and SSA **49** co-localising in *E. coli* bacteria following a 4 hour incubation period.[4]

In summary, fluorescence microscopy revealed the inability of inherently fluorescent SSA **49** to adhere to the bacterial membrane of *P. aeruginosa* PA01. However, this SSA was found both to adhere to the external *E. coli* membrane and internalise. SSA **49** was also found to facilitate the internalisation the cell-impermeant membrane staining dye, **FM4-64** into *E. coli* and both agents were found to co-localise within the bacterial cell. Although, results from section 3.4.2 did not show evidence of potentiator ability of SSA **49** with antimicrobial agents **octenidine (45)**, **novobiocin (52)** and **rifampicin (53)**, it is believed this fluorescence microscopy study has offered an insight into the possible potentiating mechanism of SSAs **42** and **51**.

3.6. Chapter 3 conclusion

This chapter has shown that SSAs can enhance the efficacy of two intracellular targeting antibiotics, **novobiocin (52)** and **rifampicin (53)** against *P. aeruginosa* PA01. The most effective combination was SSA **42** and **novobiocin (52)**, offering a dramatic 8-fold decrease of the MIC of **novobiocin (52)**, from 3.2 mM to 0.4 mM in the presence of **42** in concentrations that display no

effect on bacterial growth. In those SSA/antimicrobial agent combinations which showed potentiation, an antimicrobial dose-dependent reduction in bacterial growth was observed, with a decrease in growth noted at concentrations 100 times lower than the MIC. The SSA potentiator ability can be controlled through stepwise structural alterations, with 4-trifluoromethyl substituted SSAs **42** and **51** demonstrating potentiation vs benzothiazole substituted SSAs **49** and **50** causing no enhancement of antimicrobial efficacy.

In Section 2.6, the lack of potentiation observed with SSA and **octenidine (45)** against *E. coli* was thought to be since both agents had the same molecular target (cell membrane). Against *P. aeruginosa* PA01, the presence of SSAs **42 – 51** was found to inhibit the efficacy of **octenidine (45)**. The MIC of **octenidine (45)** was > 40 times higher in the presence of SSA **42** vs **octenidine (45)** alone. Interestingly, the physicochemical studies performed on all co-formulations of SSA and antimicrobial agent, revealed those co-formulations containing **octenidine (45)** maintained the highest level of stability, and unlike in the presence of **novobiocin (52)** and **rifampicin (53)**, no evidence of competitive molecular association was observed. The ability for the SSA to arrive at the bacterial membrane as a self-associated structure has been linked to the antimicrobial activity, however for SSA potentiation, it is evident the SSA and antimicrobial agents have to exhibit contrasting modes of action.[4,136]

Analogous antimicrobial potentiation studies were performed with *E. coli* DH10B, however no significant enhancement of antimicrobial agents **octenidine (45)**, **novobiocin (52)** and **rifampicin (53)** was observed. Despite this, fluorescence microscopy experiments were undertaken with inherently fluorescent SSA **49** and cell-impermeable membrane staining dye, **FM4-64**. After 4 hours, the SSA was found to adhere to the external *E. coli* membrane and consequently facilitate the internalisation of **FM4-64** where both agents were found to co-localise within the bacterial cell. This suggests a possible mode of action for those successful SSA: potentiation studies.

The variations in membrane phospholipid composition could be the cause for the differences in SSA potentiator susceptibility. The outer membrane of *P. aeruginosa* PA01 contains 59.7 % (± 2.9 %) PE, 27.1 % (± 1.7 %) PG and 13.2 % (± 2.8 %) PC, whereas *E. coli* is reported to consist of 70-80 % PE, 20–25 % PG and < 5 % CL.[180,181] This study provides the first evidence of an anionic molecular construct to potentiate antimicrobial agents towards *P. aeruginosa* PA01 and expands focus beyond cationic peptides to offer an alternative strategy in antimicrobial adjuvant design.

3.7. Chapter 3 future work

This study revealed the presence of the 4-trifluoromethyl group over the benzothiazole causes the greatest enhancement of antimicrobial efficacy against *P. aeruginosa*, whilst the carboxylate vs the sulfonate functional group causes little variation in potentiation. Expanding the diversity of SSAs tested in combination with **novobiocin (52)** and **rifampicin (53)** against *P. aeruginosa* PA01 would illicit further structure-activity relationships. It will also become valuable to conduct 'checkerboard synergy' assays to quantify the synergetic interaction between SSA and antimicrobial.[183] Direct comparison between SSAs will aid in the design and development of next-generation SSA efficacy enhancers.

Current understanding of the mode of action of the SSA potentiation of *P. aeruginosa* is that the SSAs facilitate increased penetration of the antimicrobial through the cell membrane. To provide further evidence for this hypothesis, genetically altered strains of *P. aeruginosa*, and other bacteria of interest, could be used. These 'knock-out' strains have parts of their genetic information removed, preventing them from expressing certain phenotypes.[184] The alteration in the efficacy of the antimicrobials themselves, as well as the change in the degree of potentiation of the SSAs towards these bacteria, would help to illuminate the exact mechanism of action.

These studies tested potentiation against Gram-negative *E. coli* and *P. aeruginosa*, future work will involve testing those effective SSA:drug combinations against a broader range of

bacteria to include those ESKAPE pathogens. Many of the ESKAPE bacteria have well understood phospholipid membrane compositions;[52] the degree of potentiation that each SSA can elicit in these bacteria may provide information towards the design of species and strain specific potentiators.

To establish the potential of these compounds to undergo further development as antimicrobial agents, toxicity assays will be performed. Initially, preliminary toxicity profiles will be established with our leading antimicrobial SSAs against human red blood cells. To determine the translational potential of SSAs into the clinic, a range of in vitro drug metabolism and pharmacokinetics (DMPK) studies will be conducted, specifically testing metabolic stability and mouse plasma protein binding. Based upon these results, SSAs will progress in vivo to mouse intravenous pharmacokinetic studies.

4. Establishing the selective phospholipid membrane coordination, permeation and lysis properties of SSAs

4.1. Introduction

A phospholipid bilayer membrane is a crucial component of a cell, incorporating regulatory proteins, carbohydrates and other molecular species, a fully functioning cell membrane can facilitate and control all molecular transport events and thus the intracellular composition.[55] Initially, targeting the cell membrane elucidated key understanding of biological mechanisms, however more recently application driven research has emerged,[185] specifically in the field of supramolecular chemistry, designing systems capable of selective binding,[186,187] ion transport and molecular sensing.[188,189]

Synthetic ion transporters have shown promise in the treatment of disease through manipulation of molecular transport events across the lipid membrane.[190] One such supramolecular example is a tambjamine-like anion-selective anionophore designed by Quesada and co-workers (Figure 46).[189] Anionophore **56** was found to efficiently facilitate the movement of Cl^- ions, with an EC_{50} value (concentration required for a leakage of 50 % chloride) of 16 nM. In addition, **56** demonstrated broad antibacterial activity against extensively drug-resistant clinical isolates including *A. baumannii*, *K. pneumoniae* and *E. coli* strains. This, in combination with good observed haemocompatibility demonstrates the potential for ionophore **56** to act as an effective antimicrobial agent against bacteria known to show resistance to currently marketed antibiotics.

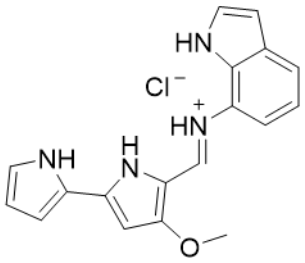

56

Figure 46 – Chemical structure of ionophore **56** designed by Quesada and co-workers.[189]

Small molecules designed to selectively bind to phospholipid headgroups are being developed by supramolecular chemists.[185] A recent body of work conducted by Busschaert and co-workers recognised the urea crown ether construct, **57** illustrated in Figure 47a, is capable of selectively targeting PE.[187] The 18-crown-6 functionality binds to the ammonium component of PE whilst the urea moiety binds to the phosphate group. A set of ^{1}H NMR titrations revealed the strength and selectivity of this construct towards PE lipids, with an association constant (*K*a) of 531 m^{-1} with PE vs 72 M^{-1} with PC. Furthermore, **57** (Figure 47a) was found to function as an effective bactericidal agent against bacteria with a high PE content, such as *Bacillus cereus* (MIC 25-30 µM), suggesting an antimicrobial mode of action involving PE lipid binding.

a)

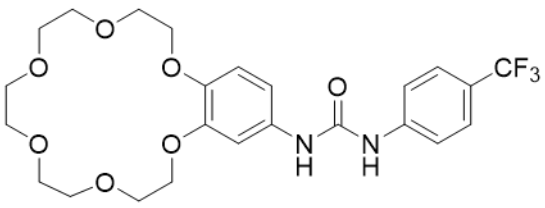

57

b)

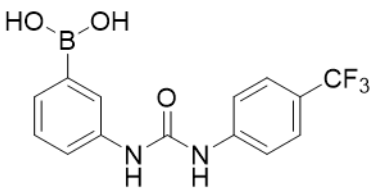

58

c)

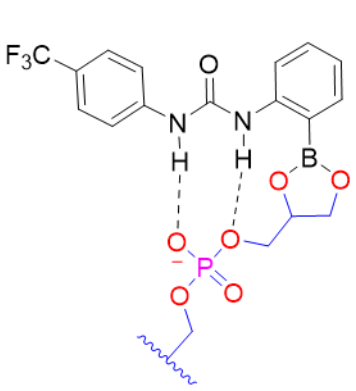

Figure 47 – Chemical structures of a) urea crown ether **57**, b) phenylboronic acid **58** synthesised and c) the complex formed between PG and **58**.[186,187]

The group went on to show the supramolecular recognition motif, **58**, is able to recognise and selectively target the glycerol portion of the PG phospholipid.[186] The binding of the phenylboronic acid molecule (**58**) to PG is shown in Figure 47c, hydrogen bonds form between the urea and the phosphate and a boronic ester is formed with the glycerol unit inherent to PG phospholipids. Association constants reveal a much stronger interaction between PG and **57** than PE and **58**, with *K*a values between 5,000-10,000 $M^{-1.}$ Compound **57** exhibited effective antimicrobial activity against Gram-positive bacteria; *S. aureus* (25 µM), *B. subtilis* (25 µM) and *E. faecalis* (50 µM), with mechanistic studies revealing the binding to PG lipids induced an increase in membrane fluidity and membrane depolarisation.[186]

Hiscock and co-workers have hypothesised that their own class of antimicrobial agents, SSAs act as bacterial membrane disruptors. This was based both on the amphiphilic nature of the molecules and the combination of HBD and HBA groups within the molecular scaffold. Proposed interactions between SSA and phospholipid head group lead to further hypothesis that SSAs could selectively interact with bacterial lipids (PE) over eukaryotic (PC); the suggested interactions are presented in Figure 48.[191]

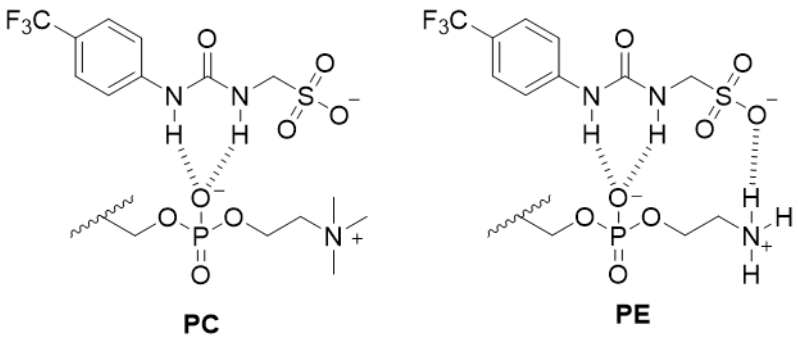

Figure 48 – The hypothesised hydrogen bonding between the anionic proportion of SSA **42** and a PC and PG phospholipid head group.

The authors developed a phospholipid nanodisc assay whereby SSA: phospholipid membrane interactions could be quantified by 1D ^{1}H NMR titration data.[191] The three SSAs tested were ranked based on the association with *E. coli* nanodiscs, **42** < **50** < **49**. SSA **49** also

exhibited high levels of selectivity towards *E. coli* nanodiscs over PC containing nanodiscs. Those SSAs containing a benzothiazole unit (SSA **50** and **49**) exhibited the strongest association towards *E. coli* nanodiscs, with the presence of the intramolecular bond in SSA **50** significantly decreasing both affinity and selectivity of SSA towards nanodisc coordination.

4.1.1. Aims

The body of work within this chapter aims to explore further into the SSA: phospholipid interactions, employing spectroscopic techniques and patch clamp technology. The ability for SSAs to permeabilise and cause lysis of a range of different phospholipid composed membranes is studied using fluorescent dye encapsulated vesicles. This data set will be correlated against a fluorescence polarisation assay whereby the selectivity and coordination of fluorescent SSAs to analogous lipid vesicles is explored to ascertain a link between membrane coordination and lysis. These data will inform the design of next generation SSAs, designed to both selectively and effectively target bacterial cell membranes. The effect of SSAs on physical membrane properties will also be explored, employing fluorescence polarisation to monitor changes in membrane fluidity, increasing understanding of the SSA antimicrobial mode of action. Finally, patch clamp technology is utilised to define a possible SSA ion transport mechanism for the co-transport of K^+/Cl^- in combination with an anionophore.

Within the scope of this study, a range of synthetic and bacterial derived vesicles were prepared, to expand upon the initial interaction studies performed by Hiscock and co-workers. The diversity of phospholipid composition was increased to include all those detailed in Table 13. A model eukaryotic cell was provided by a PC only containing membrane.[192] Typically, bacteria cell membranes are composed of mixtures of polar phospholipids PE and PG, therefore PG only and PE:PG 3:1 containing synthetic vesicles were selected. Bacterial derived *E. coli* polar and *E. coli* total lipid vesicles provided naturally derived model membranes and offered the opportunity to be compared against the commonly used synthetic alternative, PE-PG mix.[52,58]

Table 13 – Lipid compositions (%) of the vesicles used within these studies.[193,194]

Lipid vesicle	PC	PG	PE	CA	Unknown
PC	100	x	x	x	x
PG	x	100	x	x	x
PE-PG mix	x	25	75	x	x
***E. coli* polar**	x	23	67	10	x
***E. coli* total**	x	15	57	10	18

PC = phosphatidylcholine, PG = phosphatidylglycerol, PE = phosphatidylethanolamine, CA = cardiolipin

To elucidate broad structure activity relationships, an extensive and diverse group of SSAs were selected (**42, 49-51, 59-68**), the structures of which are presented in Figure 49. Stepwise structural alterations of **42** provide insight into the impact of change of cation (**60**), length of the urea-anion spacer (**59**) and incorporation of a carboxylate functionality vs a sulfonate group (**51**) on selectivity towards phospholipid compositions. Modification of the 4-trifluorophenyl moiety to a benzothiazole derivative gives rise to SSAs **49-50**, **62-66** and **67**/**68** explore the necessity of the presence of the aromatic ring system. SSAs **61**-**66** were synthesised by Kira Hilton.

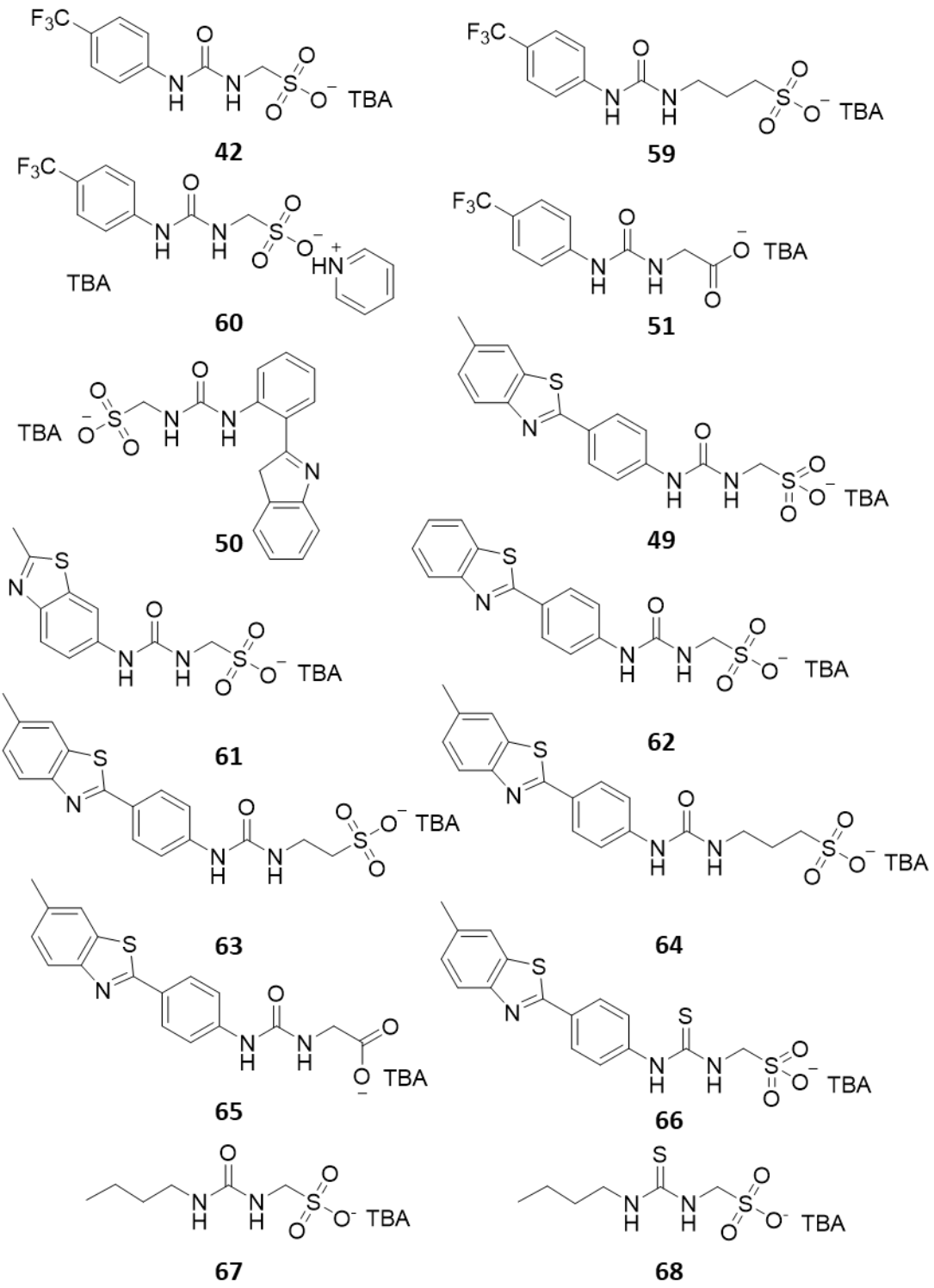

Figure 49 - Chemical structures of SSAs **42**, **49**-**51, 59**-**68**.

SSAs **42**, **49**-**51, 59**-**68** were not only chosen due to chemical diversity but also the variety of activity shown towards Gram-positive MRSA and Gram-negative *E. coli.*[4] Table 14 summarises the MIC_{50} values calculated for those SSAs which 'passed' initial antimicrobial screening at 3.3 mM, MIC_{50} data was obtained by Dr Nyasha Allen. When designing this subset of molecules, the top two most effective SSAs against MRSA (**42** and **60**) and E. coli (**64 and 59**) were added as well

as our most broad-spectrum acting antimicrobial (**51**). This table will be referred to throughout this chapter.

Table 14 – MIC_{50} values (mM) for SSAs **42, 49**-**51, 59**-**68** against MRSA USA 300 and *E. coli* DH10B after 900 mins.

SSA	MRSA	*E. coli*	SSA	MRSA	*E. coli*
42[4]	0.46	3.85	**62**	1.15	3.66
59[4]	*a*	1.48	**63**	1.20	2.16
60[4]	0.35	Fail	**64**	0.59	1.16
51[4]	1.14	1.25	**65**	*a*	*a*
50[4]	0.99	3.57	**66**	*a*	Fail
49[4]	0.93	5.02	**67**[4]	4.41	Fail
61	Fail	Fail	**68**[4]	3.07	6.03

Fail = SSA exhibited < 10 % growth inhibition of bacteria at 3.3 mM; *a* = MIC_{50} value greater than compound solubility. *b* = Estimated MIC_{50} due to data quality.

The work detailed in this chapter has been published within the following peer-reviewed journal article:

Establishing the selective phospholipid membrane coordination, permeation and lysis properties for a series of 'druggable' supramolecular self-associating antimicrobial amphiphiles, J. E. Boles, C. Bennett, J. Baker, H. A. Kotak, E. R. Clark, Y. Long, L. J. White, H. Y. Lai, C. K. Hind, J. M. Sutton, M. D. Garrett, A. Cheasty, J. L. Ortega-Roldan, M. Charles, C. J. E. Haynes and J. R. Hiscock, *Chem. Sci,* 2022, DOI:10.1039/D2SC02630A.[3]

4.2. Synthesis

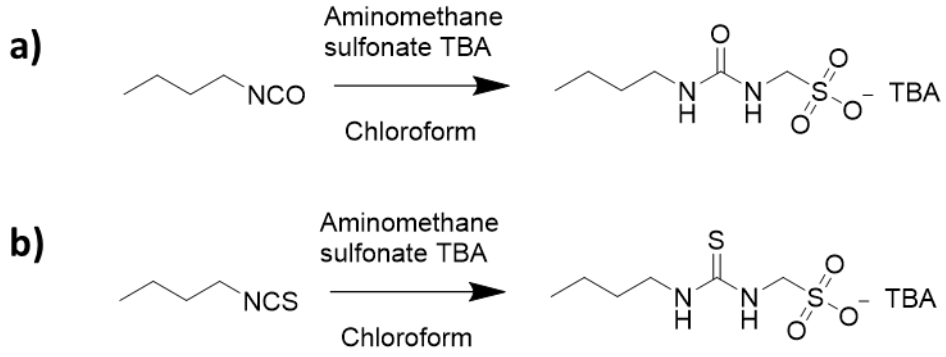

Scheme 4 – Synthesis of a) **67** and b) **68**.[4]

Compounds **67** and **68** were synthesised by the reaction of either 1-isocyanatobutane or 1-isothiocyanatobutane with aminomethanesulfonate TBA in chloroform (Scheme 4). After

purification, the pure products were obtained as opaque viscous oils in a yield of 63 % and 32 % respectively (Section 6.4).[4]

4.3. Vesicle Leakage

Within this study, fluorescence spectroscopy was employed to investigate the ability of SSAs to permeabilise/lyse a range of synthetic or bacterial derived phospholipid vesicles through a series of vesicle leakage assays. These data will contribute to determining a specific mode of action for SSAs and explore the possibility of membrane permeabilisation contributing to both the antimicrobial and potentiation properties of these molecules.

Fluorescence spectroscopy can monitor the light emitted from a fluorophore, a molecule which absorbs light at a specific wavelength and then re-emits at a different specific wavelength.[195] Calcein **69** (λ_{ex} = 495 nm, λ_{em} = 515 nm), a self-quenching fluorescent dye was chosen for this study; the chemical structure is presented in Figure 50. When a fluorophore self-quenches, the intensity of fluorescence emission decreases at high concentrations, occurring predominantly via two mechanisms; the formation of non-fluorescent dimers and/or collisions between excited fluorophores.[196] This fluorophore is well suited for such assays because at high concentrations of ≈70 mM, calcein self-quenches without altering the structural integrity of the vesicles. This dye is loaded into phospholipid vesicles of varying compositions and upon release and dilution into the surrounding buffer, a sharp increase in fluorescence emission is observed, signifying membrane disruption (Figure 51).[197,198]

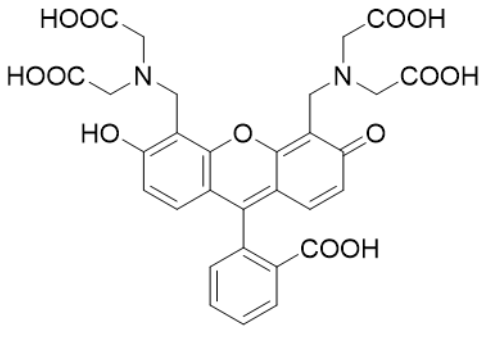

69

Figure 50 – Chemical structure of **calcein** (**69**).

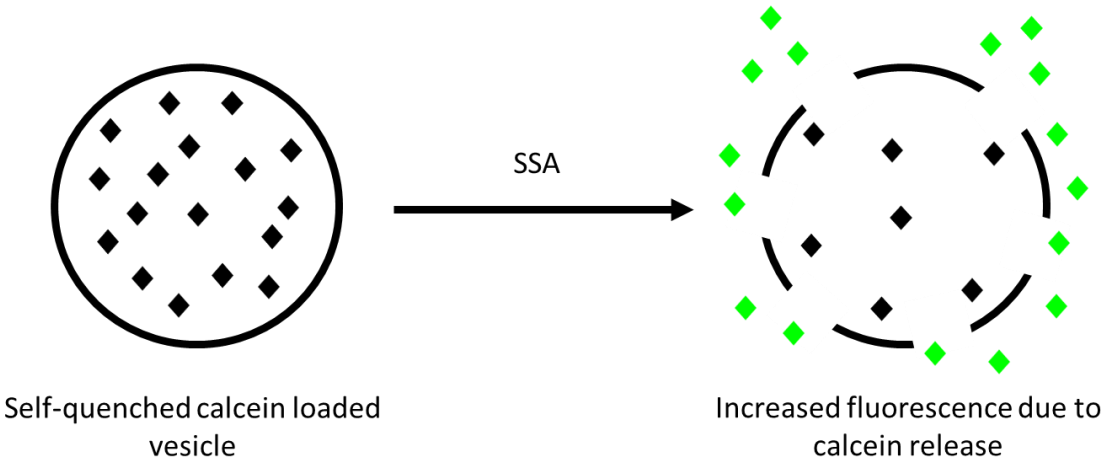

Figure 51 – A schematic showing a self-quenched calcein loaded vesicle which upon addition of an SSA is lysed, the calcein leaks out into the surrounding buffer and causes a spike in fluorescence. Black diamond = dye in self-quenching state, green diamond = dye emitting at λ_{em} = 515 nm.[197]

4.3.1. Preparation of Calcein Loaded Vesicles

Calcein loaded vesicles were prepared using a method previously described by Fiedler *et al*..[198] In summary, a thin film of the appropriate dried phospholipid/ composition was formed under reduced pressure and re-dissolved in buffer solution (70 mM calcein, 10 mM TRIS pH 8.5, 0.5 mM EDTA, 110 mM NaCl, pH adjusted to 6.5). The solution was subjected to 9 freeze-thaw cycles in liquid nitrogen and then extruded through a 200 nm polycarbonate membrane. To separate the vesicles from the free calcein, the suspension was passed through a size exclusion column packed with sephadex G-50 using buffer solution (10 mM TRIS pH 8.5, 0.5 mM EDTA, 110 mM NaCl) (Section 6.3).

To ensure the separation of free and entrapped calcein, the hydrodynamic diameter of the lipid vesicles was monitored using DLS. As the refractive index of phospholipid vesicles is known, both intensity and number-weighted distribution were employed to identify the presence of free calcein, as presented in Figure 52.

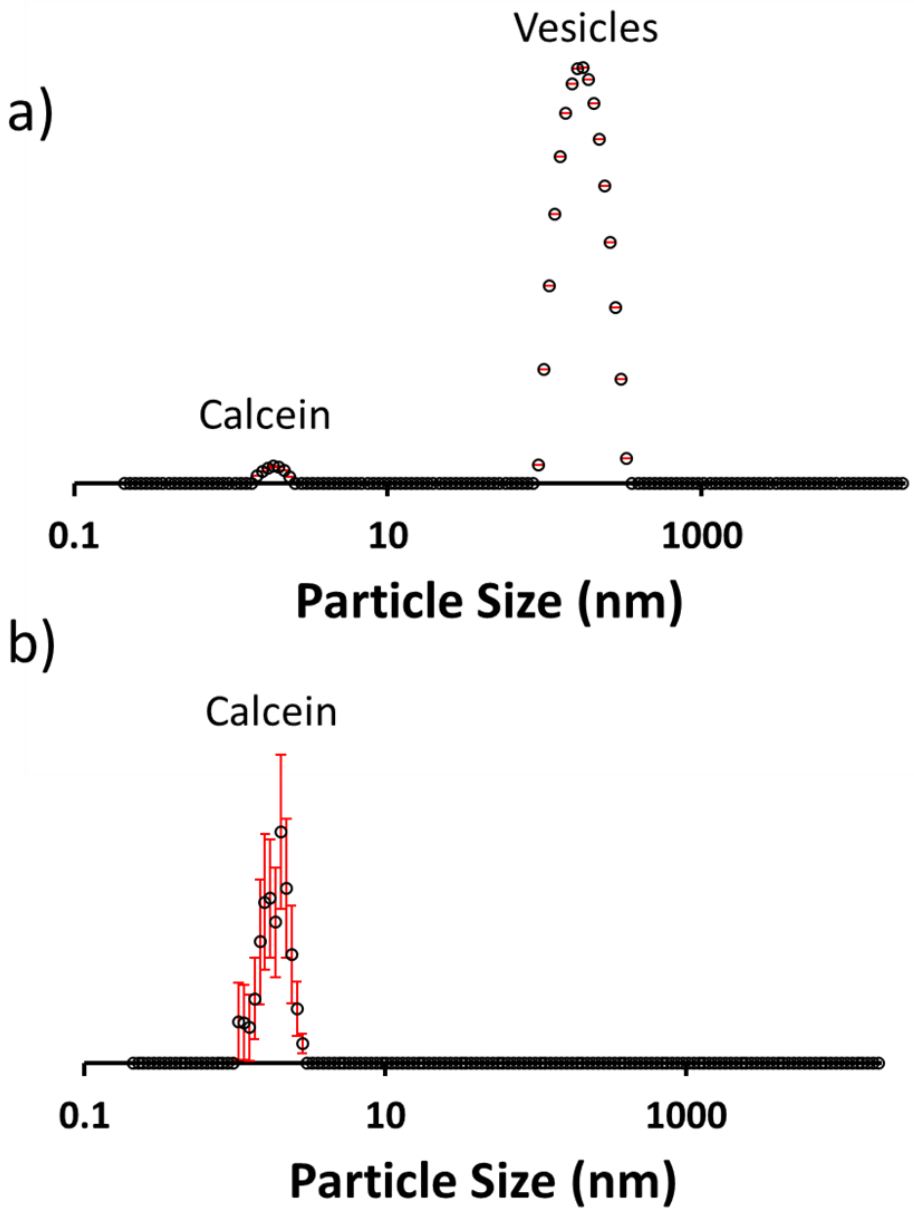

Figure 52 – a) Intensity weighted distribution of calcein, peak maxima = 188 nm and b) number weighted distribution of calcein following a size exclusion chromatography column to separate the free calcein from the calcein filled POPC vesicles, peak maxima 2 nm.

During the size exclusion chromatography purification, fractions were collected, and DLS size distribution profiles were gathered until the data shown in Figure 52 indicated lipid vesicles had been removed from the column and only free calcein remained. Figure 52a shows an intensity-weighted distribution of free calcein, whereby the intensity of scattering is proportional to $(size)^6$ according to the Rayleigh approximation, and hence shows an emphasis towards larger particles.[146] In contrast, the number-weighted distribution in Figure 52b shows a

tendency towards smaller particles, a peak at ≈ 2 nm represents the free calcein and the lack of peak at ≈ 200 nm indicates the calcein filled lipids have been removed from the column in previous fractions.

4.3.2. Vesicle Leakage Characterisation Stage 1

The amphiphilic nature of SSAs provide surfactant type properties. The ability of these molecules to lyse a diverse range of synthetic phospholipid vesicles (Table 13) was investigated using a two-phase characterisation. The first stage involved an initial fluorescence assay whereby the concentration of SSAs **42**, **49**-**51, 59**-**68** was kept at a fixed concentration of 1.5 mM (Figures S236-240). This concentration was chosen following optimisation experiments whereby an SSA concentration of 1.5 mM was shown to enable a good range of activity for SSAs **42, 49-51, 59-68** (Figures S241-245).

Fluorescence assays were conducted using a microplate reader. In summary, black bottom 96-well plates were prepared with the appropriate lipid vesicle solution (100 µL, 30 µM) in buffer solution B (10 mM TRIS pH 8.5, 0.5 mM EDTA, 110 mM NaCl) and desired SSA solution (100 µL, 1.5 mM) made in a H_2O/ 5.0 % EtOH solution. Fluorescent measurements were acquired as single points, using an excitation value of 495 mM. All experiments were performed in triplicate at 30 secs, 5 mins, 10 mins and 15 mins after addition of SSA solution to lipid vesicles.

Upon addition of SSAs **42, 49-51, 59-68** the lysis of the calcein filled phospholipid vesicles has been reported as a % vesicle leakage. Triton X-100, a non-ionic surfactant widely used for lysing cells was used as a 100 % lysis control,[199] and a solution of H_2O/ 5.0 % EtOH was used as a 0 % control. The results of these experiments are summarised in Figure 53, whereby a) presents vesicle leakage (%) after 30 secs and b) presents vesicle leakage (%) after 15 mins.

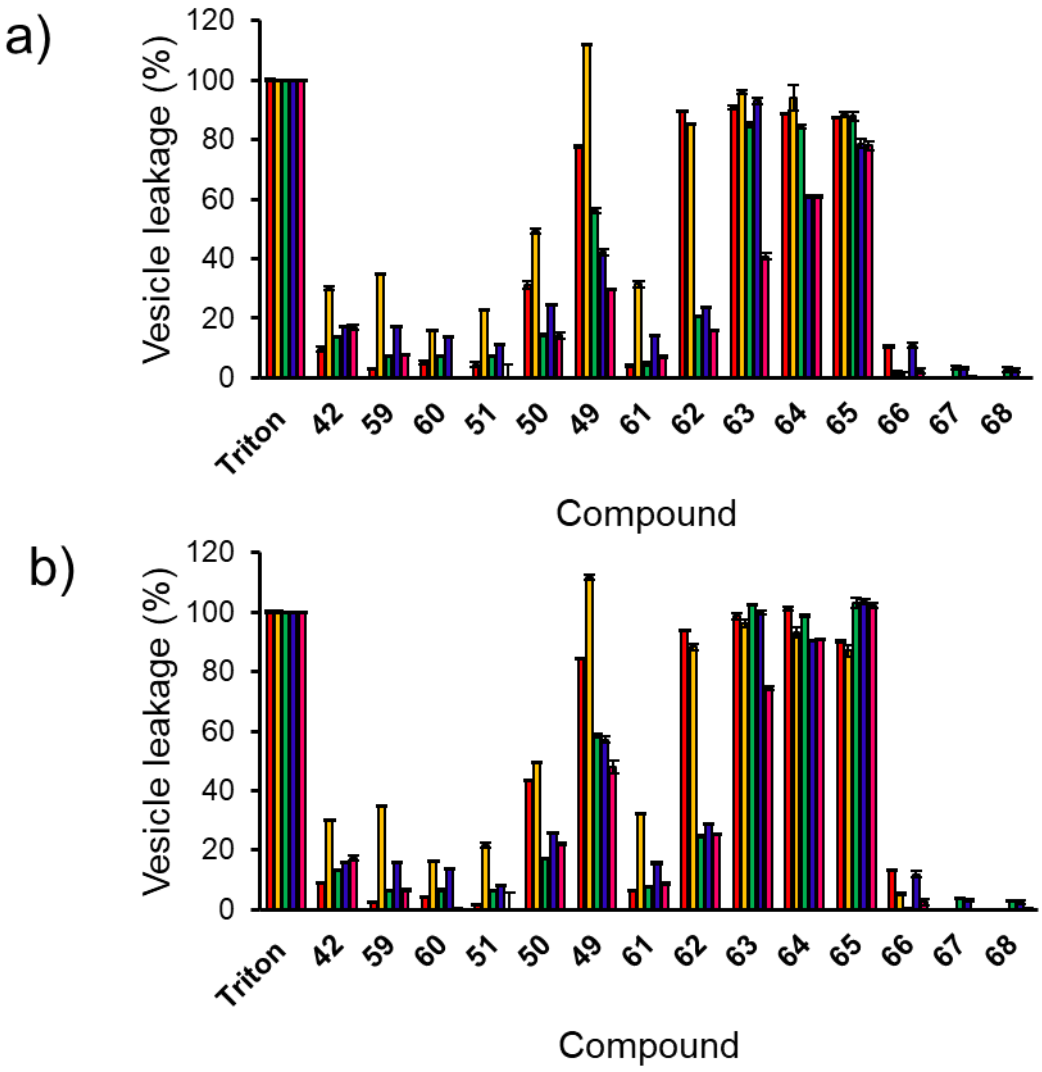

Figure 53 – The percentage lysis of 5 lipid membranes of differing composition in buffer B (10 mM TRIS pH 8.5, 0.5 mM EDTA, 110 mM NaCl), following the addition of SSAs **42**, **49**-**51, 59**-**68** (1.5 mM) after a) 30 secs and b) 15 mins. Triton X-100 (1 %) was used as a positive control for 100 % cell lysis. Data normalised to a H_2O/ 5.0 % EtOH solution. Red = PC, Yellow = PG, Green = PE-PG mix, Blue = *E. coli* polar, Pink = *E. coli* total. Error = standard error.

SSAs **42**, **49-51** and **59**-**61** show selectivity to synthetic PG vesicles over other phospholipid compositions tested, 30 secs after addition. SSAs **42**, **51**, **59** and **60** contain a para-substituted trifluoromethyl hydrophobic phenyl ring system (Figure 49). The selectivity of this class of SSAs towards PG lipid vesicles was found to be weakly influenced by type of anion (sulfonate (**42**) vs carboxylate (**51**)), counter cation (tetrabutylammonium (**42**) vs pyridinium (**60**)) or length of alkyl linker (**42** vs **59**).

The replacement of the substituted phenyl ring for an alkyl chain gives rise to SSAs **67** and **68**, this resulted in the near complete loss of any vesicle lysis activity (≤ 5 %) (Figure 53). Hiscock

and co-workers have previously demonstrated the lack of antimicrobial activity displayed by SSAs **67**- **68** against MRSA and *E. coli* when comparing to SSAs **42**, **51**, **59** and **60**, for example**,** SSAs **42**, **51**, **59** and **60** possess MIC_{50} values ≤ 1.14 mM vs **67** (4.41 mM) and **68** (3.07 mM).[4] The lack of vesicle lysis and antimicrobial activity is hypothesised to be primarily due to the deactivation of the hydrogen bond donating urea moiety and a resultant impact on the strength of the self-association properties.

In contrast, under analogous experimental conditions, the substitution of the trifluoromethyl hydrophobic phenyl ring system for a benzothiazole functionality (SSAs **49**, **50** and **62-66**) resulted in increased vesicle lysis of all five phospholipid vesicle compositions (Figure 53). A selective lysis profile similar to that generated by SSAs **42, 51**, **59** and **60** was displayed by SSA **61**, the reduction in activity compared to that of the rest of the benzothiazole family is attributed to the loss of the additional benzene ring on the structure of **61** (Figure 49). The benzothiazole unit and the additional phenyl ring system present in those urea substituted SSAs **49**, **50** and **62**-**65** are hypothesised to allow for greater stacking ability due to extra π- π stacking interactions introduced by the additional phenyl ring system. A general loss of vesicle lysis activity is also demonstrated when the urea functionality on SSA **49** is substituted for a thiourea functionality on SSA **66**. We hypothesise that this is due to the loss of molecular planarity caused by the exchange of urea (**49**) for the thiourea (**66**) functionality preventing optimal SSA self-association/integration despite the increased lipophilicity and acidity of the hydrogen bond donating thiourea over the urea moiety.

The only structural difference between SSA **49** and **62** is the removal of the methyl group from the benzothiazole ring system (Figure 49). Interestingly, a drop in the vesicle lysis properties of the SSA towards PG, PE-PG, *E. coli* polar and *E. coli* total was observed following the removal of this group. The methyl group is known to boost potency of drug candidates, with 67 % of the top selling drugs possessing a methyl group.[200,201] Out of all 14 SSAs studied, **62**

shows the greatest level of selectivity, with considerably increased activity towards PC (90 %) and PG (85 %) phospholipid vesicles (Figure 53a).

SSAs **49**, **63** and **64** were included in this series to investigate the effect of elongating the urea-anion alkyl linker on the selectivity towards different phospholipid compositions. Increasing the chain length from one to three carbons, drives an increase in the acidity of the urea group and results in a stepwise increase in the lysis of *E. coli* total lipid vesicles from 30 % to 40 % to 60% respectively. This correlates with the MIC_{50} data against *E. coli* DH10B where SSA **49** < SSA **63** < SSA **64** (Section 3.1, Table 14).

The vesicle leakage (%) was measured at four timepoints to explore the effect of time on the lysing properties of SSAs **42**, **49**-**51, 59**-**68**. As presented in Figure 53b and further summarised in Table 15, measuring the lysis at 30 secs and again at 15 mins showed some evidence of time dependent enhancement of vesicle lysis. This is particularly prevalent with the benzothiazole containing SSAs (**49**, **62**-**65**) and the *E. coli* based lipid vesicles, where SSA **64**, for example, showed a 30 % increase in vesicle lysis over 15 mins with both *E. coli* polar and *E. coli* total vesicles (Section 3.1, Table 15). This is a similar time dependence effect to that observed when Hiscock and co-workers have visualised the internalisation of SSA **49** into *E. coli* DH10B bacterial cells using fluorescence microscopy.[136] The synthetic phospholipid mixture of 3:1 PE:PG is routinely used to mimic natural *E. coli* lipid membranes.[58,59] The major difference between this and the *E. coli* derived lipid vesicles used in this study is the presence of cardiolipin (CA), a phospholipid constituent of mitochondrial membranes.[202] The presence of CA in the bacteria derived vesicles was found to inhibit the lysis effects of the SSAs with respect to time. Therefore, it could be concluded that when modelling permeation properties of small molecules, 10 % CA should also be added to the heterogeneous synthetic phospholipid mixture, PE-PG.

Table 15 – The increase in percentage lysis (%) of lipid vesicles from 30 seconds to 15 mins following the addition of SSAs **42**, **49**-**51, 59**-**68** (1.5 mM)

SSA	PC	PG	PE-PG mix	*E. coli* polar	*E. coli* total
42	< 5	< 5	< 5	< 5	< 5
59	< 5	< 5	< 5	< 5	< 5
60	< 5	< 5	< 5	< 5	< 5
51	< 5	< 5	< 5	< 5	< 5
50	**13**	< 5	< 5	**7**	< 5
49	**7**	*a*	< 5	**18**	**15**
61	< 5	< 5	< 5	< 5	< 5
62	< 5	< 5	< 5	**9**	**5**
63	**8**	*a*	**17**	**34**	**7**
64	**12**	*a*	**15**	**30**	**30**
64	< 5	< 5	**15**	**24**	**25**
66	< 5	< 5	< 5	< 5	< 5
67	< 5	< 5	< 5	< 5	< 5
68	< 5	< 5	< 5	< 5	< 5

a = vesicle lysis reached 100 % at 30 secs

In summary, the potential for surfactant SSAs **42**, **49**-**51**, **59**-**68** to selectivity lyse calcein filled bacterial/ synthetic phospholipid vesicle membranes was investigated. Those urea-based benzothiazole containing SSAs, particularly SSAs **63**, **64** and **65** caused high levels of vesicle lysis and time dependent enhancement. Selectivity of these SSAs could not be established within this study as the fixed concentration of 1.5 mM resulted in almost 100 % lysis. However, SSA **49** and **62** showed high levels of selectivity towards PC and PG synthetic phospholipid vesicles (> 90 %). The substitution of the benzothiazole moiety to a trifluoromethyl phenyl ring system (**42**, **50**, **51** and **60**) caused a reduction in the ability of the SSA to lyse lipid vesicles across all compositions and an almost complete loss of lysis activity was observed with replacement of the phenyl ring systems with an alkyl chain (≤ 5 %) (**67** and **68**).

4.3.3. Vesicle Leakage Characterisation Stage 2

The second stage of vesicle leakage experiments was performed with those SSAs which demonstrated the highest degree of lysis activity (**50**, **49**, **62**-**65**). Titration experiments were performed to determine vesicle leakage (%) at SSA concentrations ≤ 1.5 mM (Figures S241-245). These studies were particularly important to ascertain and comparatively quantify any

selectivity towards different phospholipid compositions for those SSAs which caused ≈ 100 % lysis at 1.5 mM.

Experiments incorporating PE-PG mix, *E. coli* polar and *E. coli* total phospholipid vesicles were performed with SSAs **49**, **63**-**65**, not SSAs **50** and **62** as the initial vesicle leakage assay caused > 40 % lysis (Figure 53) after 15 mins. The SSAs were added to the appropriate phospholipid vesicle (30 μM) at a starting concentration of 1.5 mM and subsequent diluted concentrations until the lysis matched that of the H_2O/ 5.0 % EtOH 0 % control. The results obtained for PE-PG mixed synthetic vesicles are presented in Figure 54. The lysis profiles for SSAs **63**, **64** and **65** are almost identical, resulting in > 80 % lysis, up until 0.5 mM where the activity is found to decrease until 0.03 mM, where no evidence of vesicle lysis is identified (0 %). Interestingly, this is at the point where the concentration of SSA matches the concentration of phospholipid. Similar profiles were obtained for *E. coli* polar and *E. coli* total bacterial lipid membranes (Appendix Figure S244-245), where SSAs **63**, **64** and **65** show higher selectivity towards these phospholipid compositions than SSA **49.** This correlates with antimicrobial data against *E. coli* DH10B where the MIC_{50} of **49** (5.02 mM) > MIC_{50} of **63** (2.16 mM) > MIC_{50} of **64** (1.16 mM) (Section 3.1, Table 14).

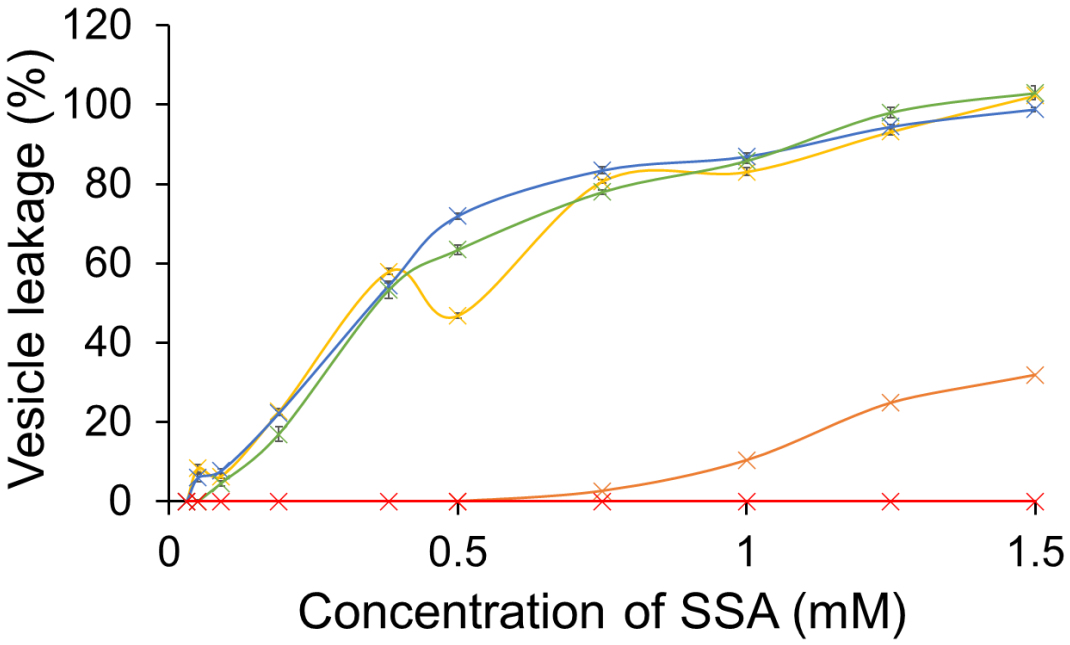

Figure 54 – The percentage lysis of PE-PG mix lipid membranes (30 µM) following addition of SSA **49** (orange), SSA **63** (yellow), SSA **64** (blue), SSA **65** (green) and control solution 5 % EtOH (red) after 15 mins. Error = standard error.

The initial fluorescence experiments conducted at 1.5 mM showed SSAs **50** and **62** to have selectivity towards PC and PG lipid vesicles (Figure 53) and therefore these SSAs were added to this titration series. These results showed some interesting SSA concentration dependent lipid selectivity, as shown in Figure 55. For experiments using PC only lipid vesicles, SSAs **63** and **64** caused 100 % lysis at concentrations ≥ 0.38 mM (Figure 55a). In analogous studies with PG only lipid vesicles, the comparative lysis activity of these SSAs was found to dramatically decrease at concentrations ≤ 0.5 mM, with a lysis percentage of ≤ 40 % at comparative concentration of 0.38 mM, demonstrating a selectivity for model human cell membranes (PC) over model bacterial cells (PG). The reverse is true however for lower concentrations of SSAs **50** and **62,** which demonstrate greater lysis activity towards PG over PC phospholipid membranes. SSAs **50** and **62** are not active against PC at concentrations ≤ 0.75 mM, however against PG, SSAs cause rupture of vesicles at concentrations ≥ 0.38 mM (Figure 55). Taking into consideration the chemical structures, it is those sulfonate anion SSAs incorporating a methyl urea-anion linker which show selectivity for PG over PC lipid membranes. An inversion of this selectivity is found at lower concentrations with a change in the length of the alkyl linking group.

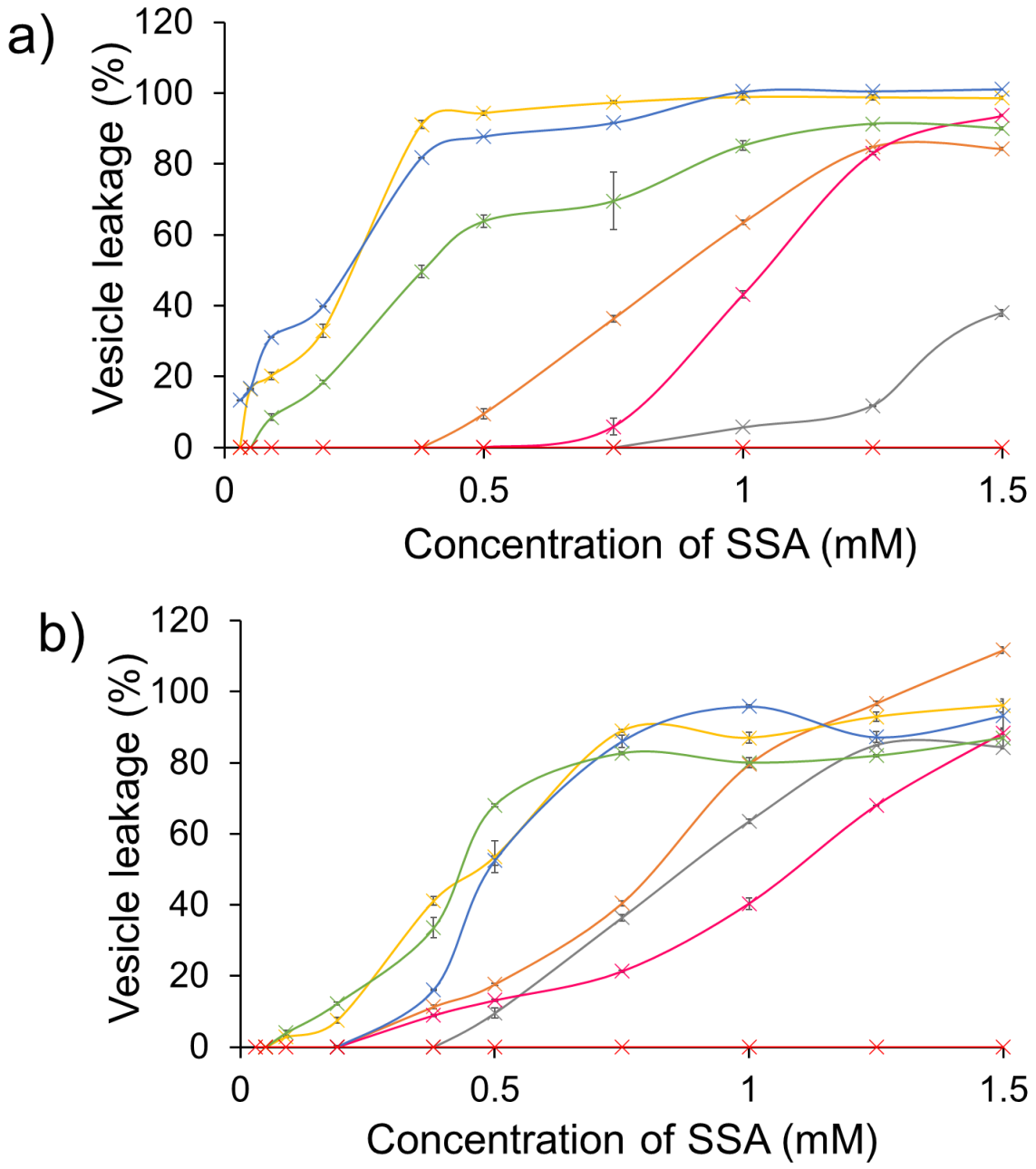

Figure 55 - The percentage lysis of a) PC and b) PG lipid membranes (30 μM) following addition of SSA **50** (grey), SSA **49** (orange), SSA **62** (pink), SSA **63** (yellow), SSA **64** (blue), SSA **65** (green) and control solution 5 % EtOH (red) after 15 mins. Error = standard error.

In summary, the effects of SSA concentration on the percentage lysis of synthetic/bacterial phospholipid membranes were investigated, focusing on those SSAs which demonstrated enhanced lysis activity (> 40 %) in initial fluorescence studies. SSAs **63**, **64** and **65** showed similar selectivity towards PE-PG mixed, *E. coli* polar and *E. coli* total lipid membranes. The increased selectivity of these SSAs to *E. coli* derived phospholipids over SSA **49** correlates

with MIC_{50} data against *E. coli* DH10B. Those urea-methyl linker sulfonate SSAs demonstrated selectivity for PG lipid vesicles over PC lipid vesicles, whilst increasing the alkyl linking chain caused a switch to human cell PC membrane lipid selectivity.

4.4. Fluorescence Polarisation

Fluorescence polarisation (FP) is a versatile solution-based method used to monitor a variety of molecular interactions.[203,204] FP is based on the physical properties related to molecular rotation; the degree of polarisation of a fluorophore is inversely proportional to the molecular rotation. The difference in emitted light parallel and emitted light perpendicular to the excitation light plane is used for the calculation of FP (Figure 56) (Equation 2).[205,206] When a fluorophore attached to a small molecule is excited with plane-polarised light, the emitted light is largely unpolarised. However, attached to a larger molecule, the fluorophore will comparatively have a slower rotation in solution and will reorient to a smaller degree, therefore the emitted light will still be polarised in the same plane as the excited light, allowing for the differentiation between different sized molecules.[207]

$$FP = \frac{I_{parallel} - I_{perpendicular}}{I_{parallel} + I_{perpendicular}}$$

Equation 2 – Fluorescence polarisation calculation, the difference between the emitted light parallel and perpendicular to the vertically polarised light, divided by the total fluorescence emission.[208]

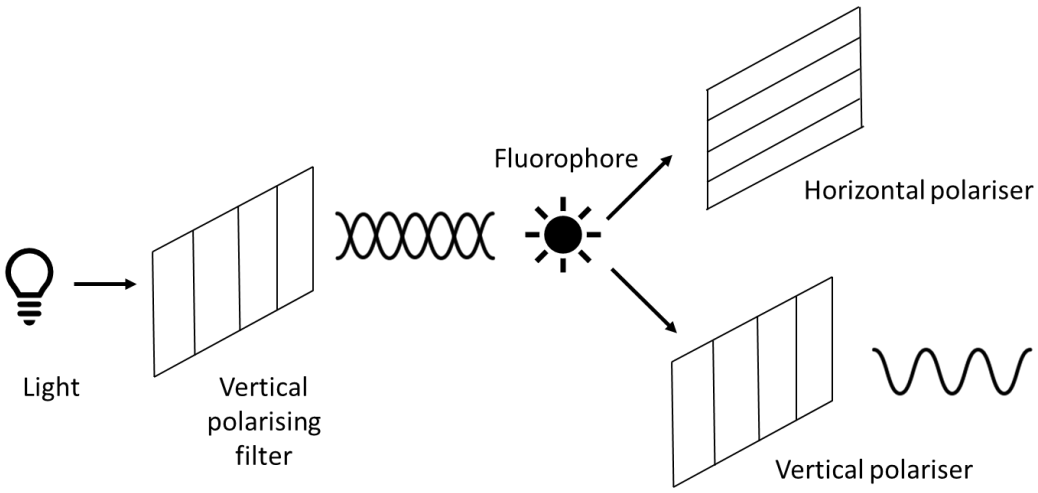

Figure 56 – The basic principle of fluorescence polarisation whereby linear polarised light excites a fluorophore, and the resultant polarised fluorescence is measured through an emission polariser, either parallel or perpendicular to the plane of polarisation of the excited light.[205]

4.4.1. Membrane Fluidity assay

In bacteria, maintaining the integrity of the cytoplasmic membrane is vital to numerous cell functions including diffusion, cell division and energy generation.[209–211] Bacteria can actively adjust membrane fluidity in response to environmental challenges and has recently emerged as an important factor in the mechanism of membrane targeting antimicrobials.[72,212] This study aims to increase understanding of the antimicrobial mechanism of action of SSAs. Membrane fluidity is broadly described as the viscosity of the cell membrane; the shifting of lipid acyl chains and the reorientation of the lipid polar head groups.[212,213] This physical property is commonly studied using fluorescence polarisation, whereby the change in mobility of a membrane bound fluorophore is caused by alterations in lipid packing. The fluorophore is excited with a polarised light, the emitted light is measured in both the parallel and perpendicular plane.[206]

This membrane fluidity study utilises the fluorescence probe, 1,6-diphenyl-hexa-1,3,5-triene (DPH) (Figure 57)**.** A symmetrical, hydrophobic molecule which inserts into the hydrophobic core of the lipid membrane, positioning itself parallel to the fatty acid tails.[209,214] As membrane fluidity increases, the DPH dye becomes more mobile and decreases the intensity of the emitted polarised light. Consequently, membrane fluidity is reciprocally related to fluorescence

polarisation. DPH is almost non-fluorescent in aqueous conditions but upon binding to the hydrophobic region of the lipid membrane, a sharp increase in the fluorescence signal is measured.[206]

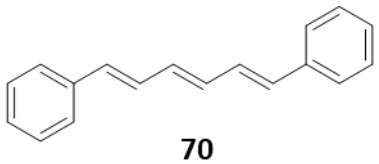

70

Figure 57 – Chemical structure of **DPH** (**70**) (1,6-diphenyl-hexa-1,3,5-triene).

Phospholipid vesicles were prepared using standard procedures described by Koulov *et al.* and labelled with DPH using a protocol detailed by BMG Labtech.[206,215] In short, a thin film of the appropriate dried phospholipid composition was formed under reduced pressure and re-dissolved in a buffer solution (150 mM KCl; 10 mM HEPES, pH 7.4; 2 mM EGTA). The solution was subjected to 9 freeze-thaw cycles in liquid nitrogen and then extruded through a 200 nm polycarbonate membrane. For fluorescent DPH labelling, phospholipid vesicles were pre-incubated with DPH (10 µM) for 1 hour at 60 °C.

4.4.1.1. Membrane Fluidity Control Experiment

To validate the membrane fluidity assay, DPH labelled DSPG vesicles were also prepared as such lipids have a well-defined gel-to-liquid crystalline phase transition temperature of 55 °C.[216] DSPG was employed here as the phospholipid vesicles used in this study have considerably lower phase transition temperatures, increasing ease of handling and preparation, and therefore were not appropriate for this validity experiment.[217] Fluorescence polarisation measurements were taken at 10 °C increments between 25 °C – 60 °C, the latter temperatures were achieved externally using a heating plate. The DPH labelled DSPG vesicles were set to an FP value of 100 mP, meaning any change in membrane fluidity would be recorded by a drop in FP (< 100 mP). The results from this validity experiment are presented in Figure 58.

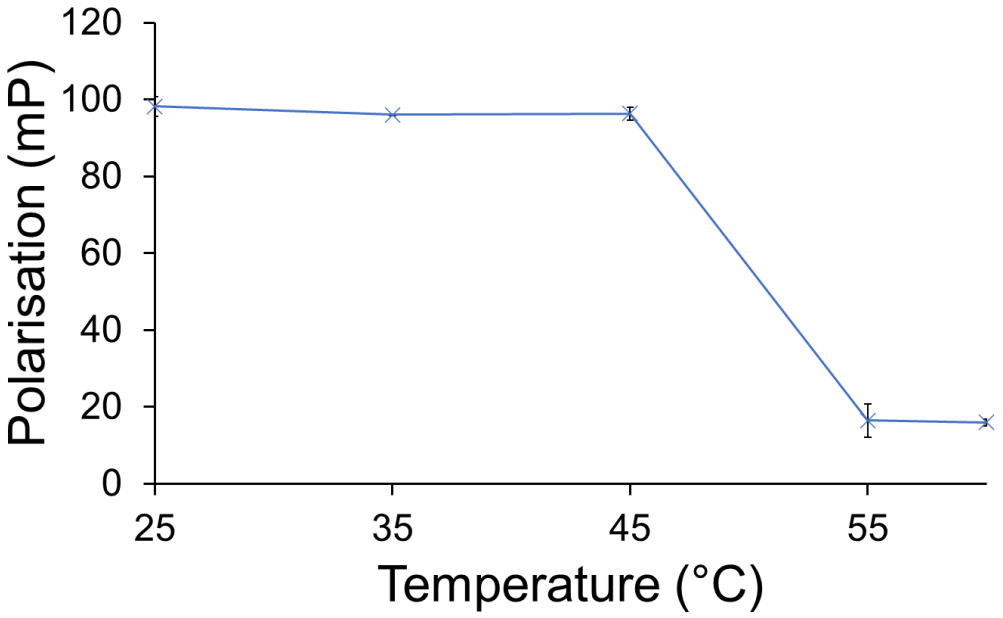

Figure 58 – Effect of temperature on the fluorescence polarisation of DPH-labelled DSPG vesicles. A target FP value of 100 mP was set to the DPH-labelled vesicles at 25 °C. Error = standard error.

As the temperature is increased from 25 °C to 45 °C, the FP value does not deviate from 100 mP, indicating a rigid ordered gel phase.[218] Increasing the temperature from 45°C to 55 °C causes a sharp decrease in FP, reflecting the expected transition to a disordered fluid crystalline phase (Figure 58). This experiment validated the preparation of the DPH- labelled vesicles.

4.4.1.2. Membrane Fluidity SSA Experiments

To further investigate the effects of SSAs on physical membrane characteristics, membrane fluidity experiments were completed with SSAs **42**, **51**, **59, 60** and **61**. Only those non-fluorescent SSAs could be used within this study due to the overlapping fluorescence properties of those benzothiazole containing SSAs (**49**, **50** and **62-66**). Additionally, due to a lack of vesicle lysis activity and the lack of inherent antimicrobial activity, SSAs **67** and **68** were also omitted from this study.[4] To keep analogous to the vesicle lysis assay, the same five lipid compositions were investigated: PC, PG, PE-PG mix, *E. coli* polar and *E. coli* total (Section 4.2, Table 13) (Figures S247-251). Each SSA was supplied to the DPH labelled vesicles in H_2O/ 5.0 %

EtOH at a top concentration of 1.5 mM (to mimic those vesicle lysis experiments) and were subsequently diluted to the lowest concentration of 0.01 mM.

As per the validation experiment, the appropriate DPH-labelled vesicles alone were set to 100 mP, therefore any evidence of membrane fluidity would be observed as a reduction in FP value. Of those SSAs tested, SSAs **42**, **59, 60** and **61** did not cause an overall change in FP > 10 % for the five types of DPH labelled vesicles studied, the results for PC lipid vesicles are presented in Figure 59.

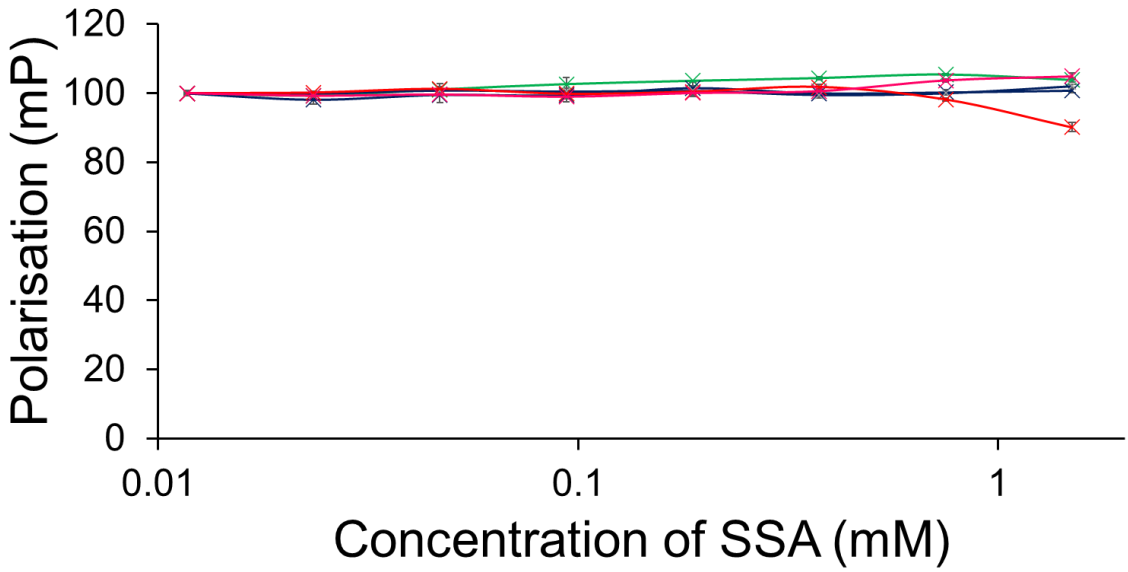

Figure 59 – The effect of varying concentrations of SSAs **42**, **51**, **59, 60** and **61** on the fluorescence polarisation of PC DPH- labelled phospholipid vesicles (30 µM) supplied in a 150 mM KCl, 10 mM HEPES, pH 7.4, 2 mM EGTA buffer. A target FP value of 100 mP was set to the DPH-labelled vesicles. Green = **42**, Yellow = **59**, Blue = **60,** Red = **51**, Pink = **61**. Error = standard error.

However, SSA **51** was found to exhibit an overall change in FP > 10 % when supplied at a concentration > 0.1 mM, except for the model human cell membrane, PC only containing vesicles (Figure 59) (Appendix, Figures S247-251). Figure 60 summarises the overall change in FP for SSA **51** against the five lipid compositions. Those bacterial derived phospholipid vesicles (*E. coli* polar, blue and *E. coli* total, pink) exhibited the greatest increase in membrane fluidity following the addition of SSA **51**, with almost identical FP profiles generated for SSA concentrations up to 0.75 mM. This provides further evidence for the importance of the addition

of 10 % CA for accurate *E. coli* membrane modelling. Of the five non-fluorescent SSAs tested, SSA **51** is the only structure to contain a carboxylate moiety, the remaining SSAs incorporate a sulfonate functionality. Additionally, the MIC_{50} values derived for SSA **51** (1.25 mM) was lower than those values calculated for SSAs **42**, **59, 60** and **61**, supporting the hypothesis that antimicrobial activity is linked to membrane activity effects (Section 3.1, Table 14).

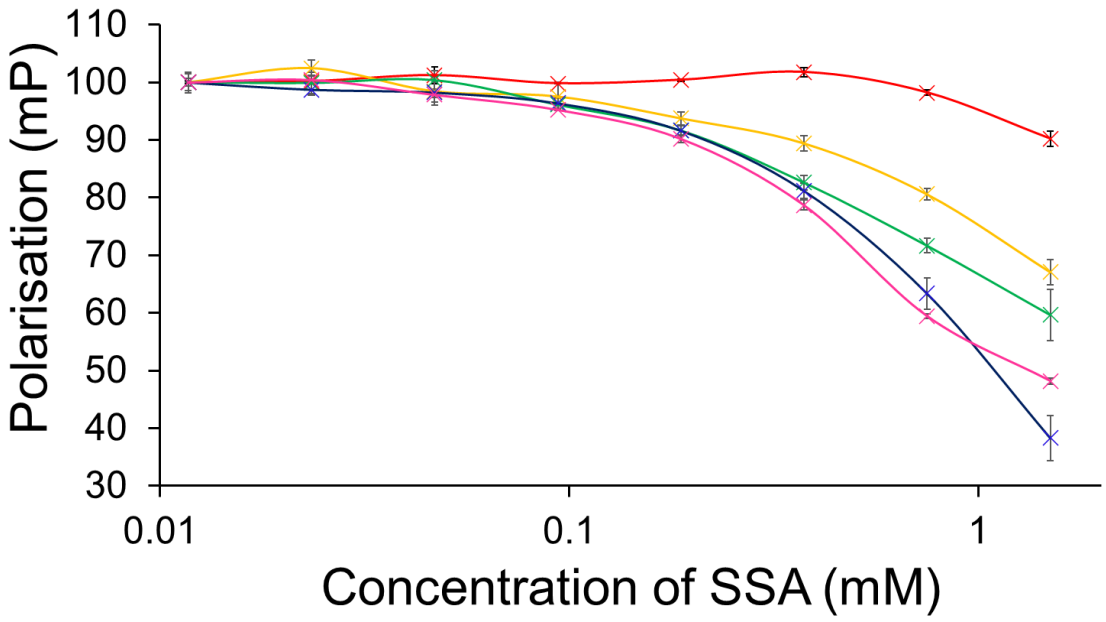

Figure 60 – The effect of varying concentrations of SSA **51** on the fluorescence polarisation of 5 types of DPH- labelled phospholipid vesicles (30 µM) supplied in a 150 mM KCl, 10 mM HEPES, pH 7.4, 2 mM EGTA buffer. A target FP value of 100 mP was set to the DPH-labelled vesicles. Red = PC, Yellow = PG, Green = PE-PG mix, Blue = *E. coli* polar, Pink = *E. coli* total vesicles. Error = standard error.

In summary, the ability of a class of non-fluorescent SSAs (**42**, **51**, **59, 60** and **61**) to induce a change on membrane fluidity on a variety of phospholipid membranes was investigated. A fluorescent probe, DPH was inserted into the vesicle membrane to enable changes in fluidity to be measured by fluorescence polarisation. The addition of SSAs **42**, **59, 60** and **61** to the DPH-labelled phospholipid vesicles did not result in any change in FP and therefore membrane fluidity. However, SSA **51**, the only carboxylate containing SSA was found to increase the membrane fluidity of PG, PE-PG mix, *E. coli* polar and *E. coli* total lipid vesicles at concentrations > 0.1 mM.

4.4.2. Fluorescence Polarisation Adhesion Assay

The interaction of those intrinsically fluorescent SSAs (**49, 50, 62-66**) with DPH-labelled phospholipid vesicles could not be conducted due to overlapping fluorescence with SSA and DPH. Instead, the SSA molecule itself was employed as the fluorophore, monitoring interaction with unlabelled phospholipid vesicles. The aim of this experiment was to study the selectivity of those fluorescent SSAs with a range of synthetic and bacterial derived vesicles with different phospholipid compositions (Table 13). These data will assist in the synthesis of next generation SSAs, designed to selectively target bacterial membranes. The ability of these SSAs to permeabilise/lyse the membranes of vesicles with analogous phospholipid compositions was studied in Section 4.3.2 and 4.3.3, these data can be compared to elucidate a possible link between coordination and permeabilization/lysis (Figures S252-258).

Phospholipid vesicles were prepared using standard procedures as described by Koulov *et al.* and buffer conditions as described in Section 4.4.1.[215] The appropriate intrinsically fluorescent SSA alone was set to 100 mP and within the scope of this experiment, an interaction between SSA and phospholipid vesicle is shown by an increase in FP, as the apparent size of the fluorescent SSA increases. As these molecules are known to self-associate into fluorescent spherical aggregates at a size similar to those vesicle membranes (100 nm – 200 nm)[4], SSAs were kept at 0.15 mM, a concentration below the CMC. These larger self-associated SSA structures would be fluorescent and therefore it was assumed, any interaction between these and similar sized vesicle membranes would not be sufficiently recorded by monitoring changes in fluorescence polarisation.

Both SSAs **62** and **64** showed very little change in FP in the presence of phospholipid vesicles of any lipid composition. As shown in Figure 61, SSA **62** maintains a constant FP of 100 mP until a lipid concentration of 0.06 mM where there is some evidence of interaction, however, this small increase in FP is suggestive of a weak SSA: phospholipid interaction. There is also no indication of selectivity to a specific phospholipid composition over another. This does not

corroborate with the vesicle leakage data in section 4.3.2 which showed the increased selectivity of SSA **62** towards synthetic PC or PG vesicles. The lack of selectivity of SSA **64** observed during the vesicle leakage experiments is supported by the lack of differentiation shown between lipid vesicles in this FP experiment. However, despite the high vesicle leakage % ability of SSA **62**, the small increases in FP are indicative of a weak SSA: phospholipid interaction (Appendix, Figure S254), suggesting interaction and resultant leakage require different mechanisms of action.

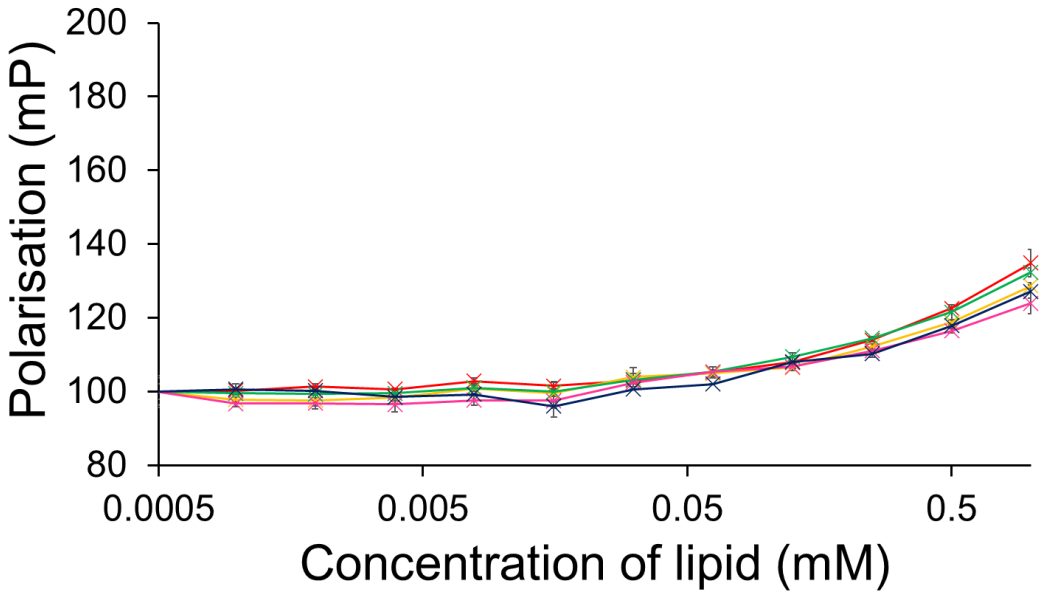

Figure 61 – The effect of a range of phospholipid vesicle compositions at varying concentrations on the FP of SSA **62** (0.15 mM). A target value of 100 mP was set to the SSA **62** alone. Red = PC, Yellow = PG, Green = PE-PG mix, Blue = *E. coli* polar, Pink = *E. coli* total.

SSAs **63** and **65** however, showed selectivity towards a single phospholipid membrane composition, *E. coli* total and synthetic PG respectively. The plotted FP profile for SSA **65** is presented in Figure 62 and shows a significant increase in FP of SSA **65** upon interaction with PG lipid vesicles (> 0.008 mM). But this strong selectivity towards this synthetic lipid composition does not result in an increased ability for SSA **65** to permeabilise/lyse the vesicle, as shown in the vesicle lysis assay (Section 4.3.2 and 4.3.3) where little selectivity is noted. Interestingly, in this FP study, SSA **63** showed increased selectivity towards *E. coli* total over the remaining lipid compositions studied (Appendix Figure S255). However, the opposite trend was observed when

studying the lysis of these vesicles, with SSA **63** causing the smallest percentage lysis for *E. coli* total lipids (≈ 50 %) compared to the remaining four compositions studied (≈ 100 %).

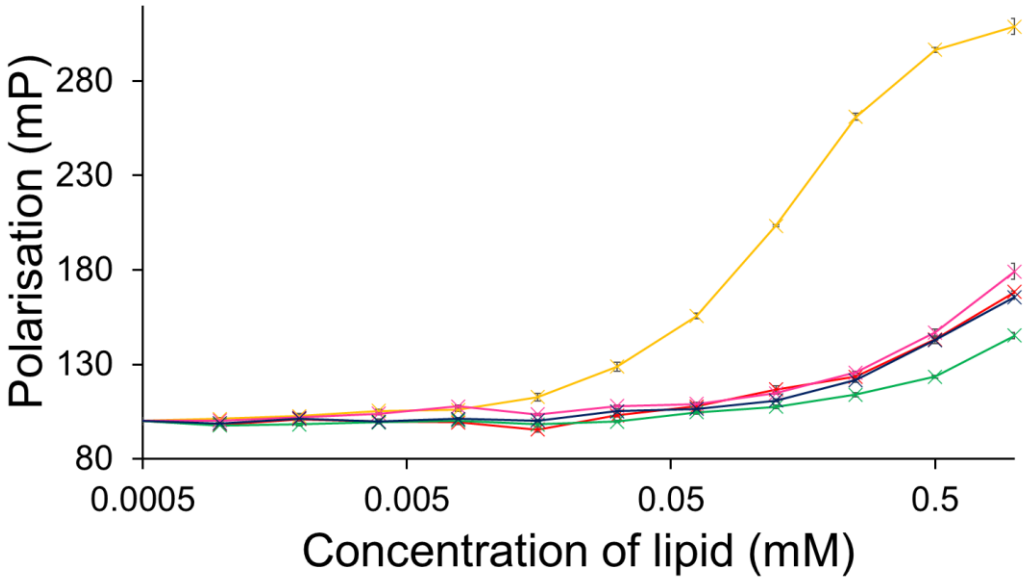

Figure 62 - The effect of a range of phospholipid vesicle compositions at varying concentrations on the FP of SSA **65** (0.15 mM). A target value of 100 mP was set to the SSA **65** alone. Red = PC, Yellow = PG, Green = PE-PG mix, Blue = *E. coli* polar, Pink = *E. coli* total.

The SSA that exhibited the strongest interaction with all phospholipid vesicles tested was SSA **66**, as shown in Figure 63. Once again, these same trends were not observed when studying vesicle lysis. SSA **66,** a thiourea benzothiazole performed the worst out of those intrinsically fluorescent molecules in the initial screening experiment, where the presence of SSA **66** resulted in < 10 % lysis of all phospholipids vesicles studied (Section 4.3.2, Figure 53). The different trends observed between the two experiments indicate the membrane interaction and the vesicle lysis are dependent upon distinct chemical/physicochemical properties.

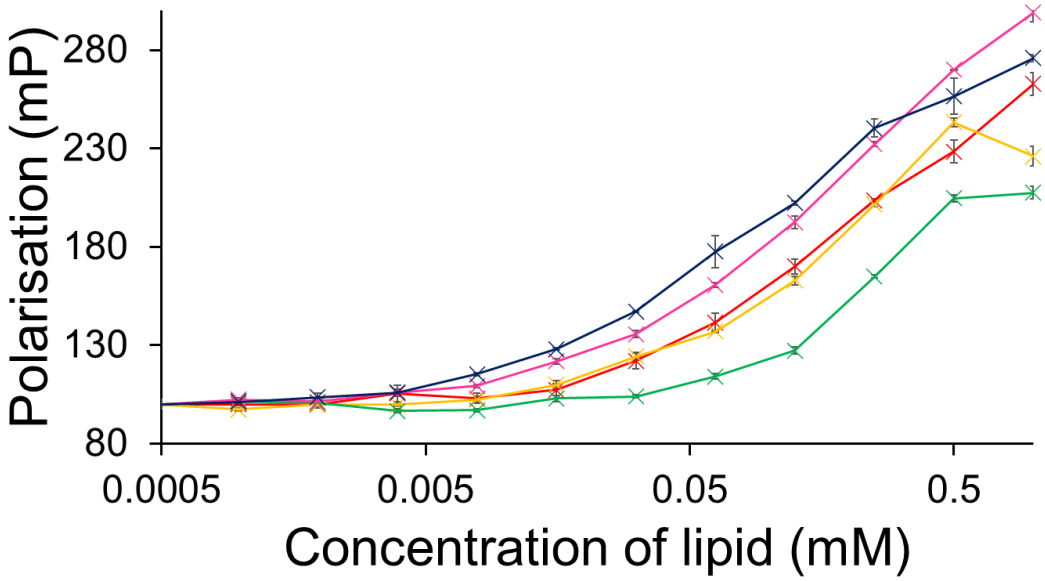

Figure 63 - The effect of a range of phospholipid vesicle compositions at varying concentrations on the FP of SSA **66** (0.15 mM). A target value of 100 mP was set to the SSA **66** alone. Red = PC, Yellow = PG, Green = PE-PG mix, Blue = *E. coli* polar, Pink = *E. coli* total.

In summary, the selectivity of a range of intrinsically fluorescent SSAs (**49, 50, 62-66**) towards five phospholipid vesicles was investigated employing fluorescence polarisation. SSAs **62** and **64** showed evidence of weak SSA: phospholipid interactions, with little selectivity towards specific membrane compositions. SSAs **63** and **65** however showed strong, single selectivity towards *E. coli* total and synthetic PG lipids respectively. The thio urea, benzothiazole SSA, **66** exhibited the strongest interactions with all phospholipid vesicles tested but performed as the least effective SSA to lyse membrane vesicles (< 10 %). Comparing the complete set of data with those vesicle lysis experiments concludes that selective SSA: phospholipid interaction and the ability to permeabilise/lyse those same model membranes are not directly linked and may rely on different mechanisms of action.

4.5. Ion Transport

A recent collaboration between the Hiscock and Haynes group sought to reveal the potential for SSAs to mediate co-transport of K^+/Cl^- in combination with a previously reported anionophore (Figure 64).[219] Using a chloride co-transport assay, SSA **50** was found to work in a

cooperative fashion with the anionophore to facilitate an overall K^+/Cl^- efflux process, functioning as a K^+ uniporter.[220]

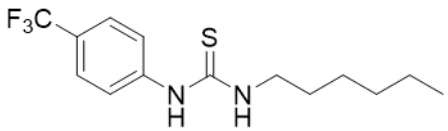

71

Figure 64 – Chemical structure of anionophore, **71**.[219,220]

This section of work investigates the ion transport mechanism of SSA **50**. The small molecular size of this SSA (> 1 nm)[113] makes the possibility of a unimolecular, membrane spanning structure unlively. Instead, given the self-associating properties of SSA **50**, the formation of a self-assembled channel seems a likely hypothesis.[113] A Port-a-Patch miniaturised patch clamp system was employed to monitor the flow of ions across a single artificial planar lipid bilayer. Figure 65 illustrates the formation of a bilayer whereby the application of negative pressure (-30 mbar) positions a single giant unilamellar vesicle (GUV) into the aperture (≈ 1 µM) of a borosilicate glass chip. As the GUV meets the glass surface of the chip, it bursts, forming a planar bilayer with a tight gigaseal (yellow section, Figure 65b). An electrical potential is applied across the membrane and changes in electrical current are monitored in response to movement of ions across the bilayer.[221,222]

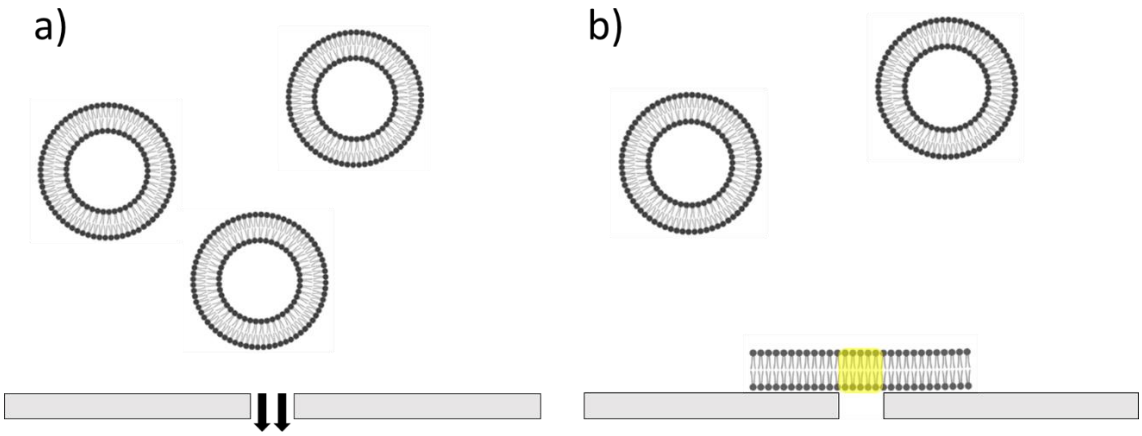

Figure 65 – The formation of a planar lipid bilayer via vesicle fusion onto a borosilicate glass chip, a) a negative pressure is applied to a GUV suspension (black arrows) and b) as a GUV touches the glass, it bursts, forming a planar bilayer. The yellow section represents the gigaseal.

4.5.1. Preparing Giant Unilamellar Vesicles (GUVs)

Giant unilamellar vesicles (GUVs) are simple model membrane systems with a cell-size diameter of > 1 µM.[223,224] In this study, GUVs were prepared using a Vesicle Prep Pro, an instrument for the automated preparation of GUVS, formed by electroswelling. This method allows for the formation of monodisperse and defect-free vesicles.[225] The ion transport studies conducted at UCL used POPC lipid vesicles, however the vesicle prep pro could not prepare stable POPC GUVs under analogous buffer conditions. Instead, 1,2-diphytanoyl-*sn*-glycero-3-phosphocholinelipid (DPhPC) lipids were used with the incorporation of 10 % cholesterol to increase the integrity and rigidity of the GUVs for subsequent bilayer formation, the structure of DPhPC is presented in Figure 66.[226]

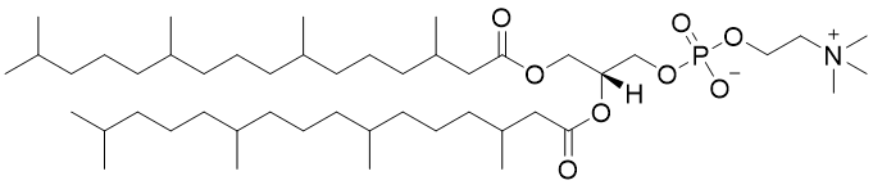

72

Figure 66 –Structure of a DPhPC lipid (**72**).[226]

To prepare the GUVS, a chloroform solution of DPhPC (10 mM) (Figure 66) with 10 % cholesterol (20 µL) was deposited onto the conducting side of an indium tin oxide (ITO) coated glass slide and left to dry to form a dehydrated thin lipid film. A filtered sucrose solution (200 mM, 275 µL) was added to the greased O-ring chamber containing the lipid film and sealed with a second ITO slide. The electro-formation protocol was carried out at 37 °C, the first AC current was applied (3 V, 5 Hz) for 2 hours, then reduced to 1.6 V,1 Hz after 30 mins and held for an hour before returning to 0 V,0 Hz after an additional 30 mins. Fluorescence microscopy images (Figure 67) were taken of DPhPC GUVs labelled with nile red dye to verify the presence and size of the vesicles. This lipophilic stain shows strong fluorescence response upon transition from an

aqueous environment to a hydrophobic one and therefore is commonly used as a fluorescent probe to visualise micelles or model membranes.[227,228] As shown in Figure 67, the DPhPC GUVs ranged in size from ≈ 1.8 – 4.5 µM.

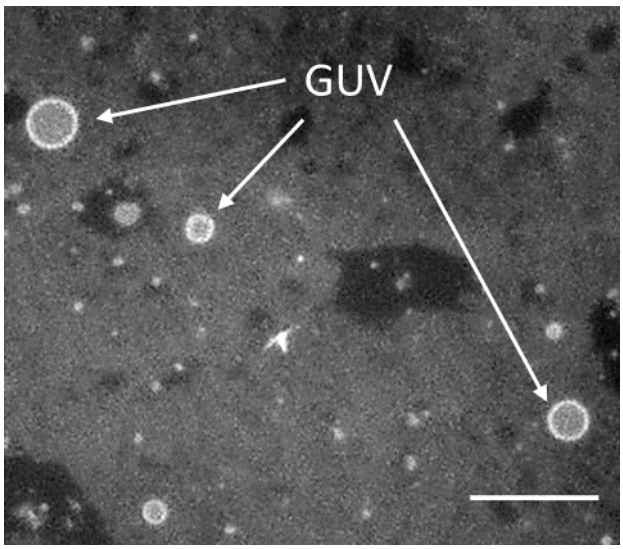

Figure 67 – Fluorescence microscopy image of a solution of Nile red labelled DPhPC GUVs in a KCl phosphate buffer made using a Nanion Vesicle Prep Pro. Scale bar = 10 µM.

4.5.2. Method Development

Planar lipid bilayers were produced from the GUVs prepared in Section 4.5.1. The ion transport studies conducted by Haynes and co-workers at UCL were performed in a phosphate buffer (pH 6.4), using the method above, single bilayers of DPhPC (10 % cholesterol) could not be stabilised under these buffer conditions for > 1 min. It was discovered, both the intravesicular and extravesicular buffer needed to be at a pH < 6 and therefore an acetate buffer (pH 5.5) was chosen, the details of which are outlined in Figure 68. Using these acetate buffer conditions, a stable planar lipid bilayer could be formed and maintained for > 6 mins, given the buffer had been freshly prepared.

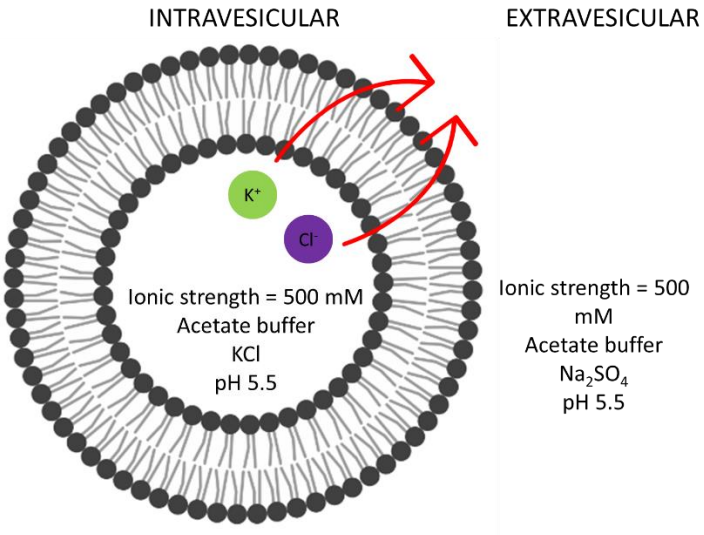

Figure 68 – A DPhPC 10 % cholesterol phospholipid vesicle showing the internal and external buffer conditions and the direction of proposed ion movement.

To establish an electrochemical gradient for the transport of ions across the DPhPC bilayer, the external buffer had to be exchanged for an alternate buffer (167 mM Na_2SO_4, acetate 5 mM, pH 5.5, ionic strength 500 mM) (Figure 68). Once the GUV is in place and the holding potential (50 mV or 100 mV) has been applied, the bilayer is extremely sensitive and therefore a quick and efficient exchange of the buffers was required. Initially, a mixing approach was investigated whereby 15 µL of the external buffer was added to the 20 µL of original buffer and GUV solution, mixed using a pipette and 15 µL was removed to return to the initial volume. However, this method weakened the bilayer and resulted in rupture of the model membrane. A more efficient approach involved the removal of 15 µL of original buffer and the subsequent addition of 15 µL of external buffer, leaving the planar bilayer in 5 µL of buffer during the exchange was found to be the lowest volume required to keep the membrane intact. This method led to the successful exchange of a buffer and the preservation of a stable lipid bilayer for < 6 mins.

To align with those ion transport studies performed by Haynes and co-workers, the SSAs were supplied to the bilayer as DMSO stocks. DMSO is known to enhance cell membrane permeability and therefore it was critical the addition of this solvent to this system was kept to a minimum volume.[229] To find the most effective method for adding compounds to the planar bilayer

system, triton x-100 (1 %) was used because if added effectively should instantly lyse/rupture the cell membrane. The first method involved adding 0.4 µL of a stock triton solution into the external buffer (20 µL); any smaller volumes with the pipettes available could be inaccurate. A selection of repeat experiments using this method are shown in Figure 69.

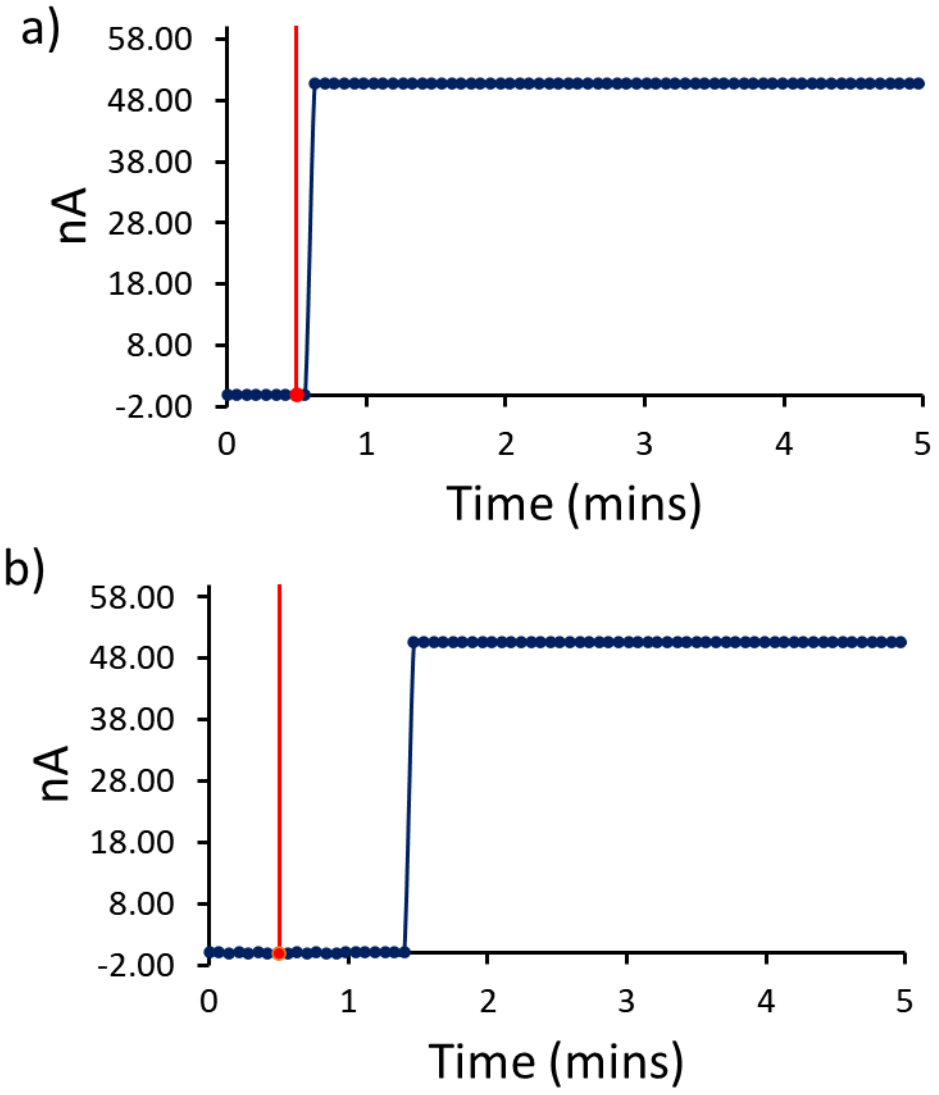

Figure 69 – Two repeat experimental recordings of a DPhPC bilayer at 100 mV, addition of triton x-100 (1 %, 0.4 µL) at 30 seconds, indicated by the red line.

As shown in Figure 69, adding the triton solution in a 0.4 µL aliquot did not produce consistent results. Both a) and b) show the DPhPC vesicle has ruptured, indicated by a maximum reading of ≈50 nA. However, the time taken for the triton x-100 to lyse the vesicle was not repeatable, with lysing a) instantaneously and b) after ≈ 50 seconds. A subsequent method was attempted

whereby a proportion of external buffer was removed from the instrument, mixed with the triton externally and replaced onto the chip. This increased the homogeneity of the triton x-100 in the external buffer and consequently lead to a consistent data set where the DPhPC vesicle was ruptured instantaneously. This method was carried forward for the addition of SSA and the anionic transporter.

4.5.3. Patch Clamp Results

To explore further into the SSA ion transport mechanism, a series of planar bilayer experiments were performed with SSAs **50**, **49** and **61** and anionophore **71** (Figure 70). To align with the methods designed by Haynes and co-workers, the anionophore (0.01 mM) was added first and then followed by SSA (0.1 – 1 mM) at 30 seconds, measurements were run for 5 mins in triplicate. Control experiments were performed (Figures S259-264); DMSO only and anionophore only controls confirmed these agents were not causing an elevated current recording over the experimental time frame when supplied alone (Appendix Section 3.7.1). Despite, anionophore **71** being a known anion antiporter, this molecule cannot mediate K^+/Cl^- symport alone.[219]

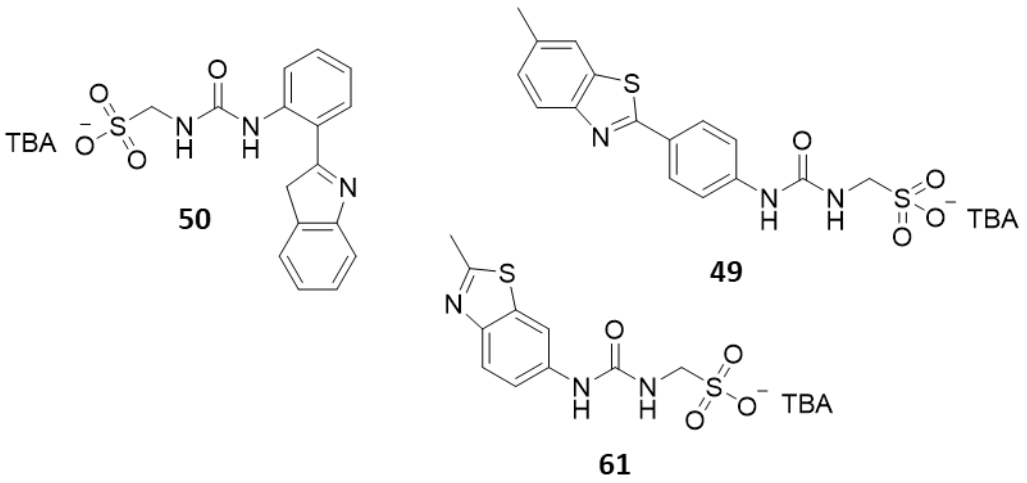

Figure 70 – Chemical structures of SSAs **50**, **49** and **61**.

Experiments were first performed with SSAs **49**, **50** and **61** alone (Figure 70). At all SSA concentrations studied (0.1 – 1 mM) there was no evidence of ion transport in the buffer

conditions studied. However, these data provided supporting evidence for the PC lysing ability of these SSAs. The addition of SSA **61** did not result in the rupture of the DPhPC lipid bilayer during the 5 mins tested. This is coherent with the data generated in the vesicle leakage assay where **61** exhibited very little leakage activity (> 6 %). Whereas the addition of SSAs **49** and **50** (≥ 0.25 mM) caused the planar lipid bilayer to rupture, the time taken between addition and rupture is presented in Table 16. Here, the SSA is acting as a simple surfactant, destroying the phospholipid bilayer.

Table 16 – The time taken (seconds) for SSA **49** and **50** to rupture a DPhPC planar bilayer.

Concentration	SSA **50**	SSA **49**
0.1	x	x
0.25	x	≈ 220
0.38	≈ 60	≈ 75
0.5	≈ 35	≈ 30
1	≈ 2	*a*

a = SSA gelates at this concentration.

Like the lysis of POPC calcein filled vesicles (Section 4.3.2), the lysis of the DPhPC lipid bilayers is a time dependent event, with the time taken decreasing as the concentration of SSA **50** and **49** increases (Table 16). The addition of SSA **49** causes rupture at lower concentrations than SSA **50**, this is again consistent with those results gathered during the vesicle leakage assays. However, both SSAs appear to lyse bilayers in the patch clamp experiment at lower concentrations than those calcein filled vesicles, this could be accounted for by the change in buffer or the solvent conditions of the stock SSA solutions (DMSO vs H_2O/ 5.0 % EtOH solution). The data for SSA **49** at 1 mM could not be obtained as addition of buffer (167 mM Na_2SO_4, acetate 5 mM, pH 5.5, ionic strength 500 mM) caused the SSA solution to form a gel. SSA **49** has been previously shown to gelate in Na_2SO_4.[136] The inherent fluorescent nature of SSA **49** allowed for the confirmation of gel fibres through fluorescence microscopy, images are presented in Figure 71.

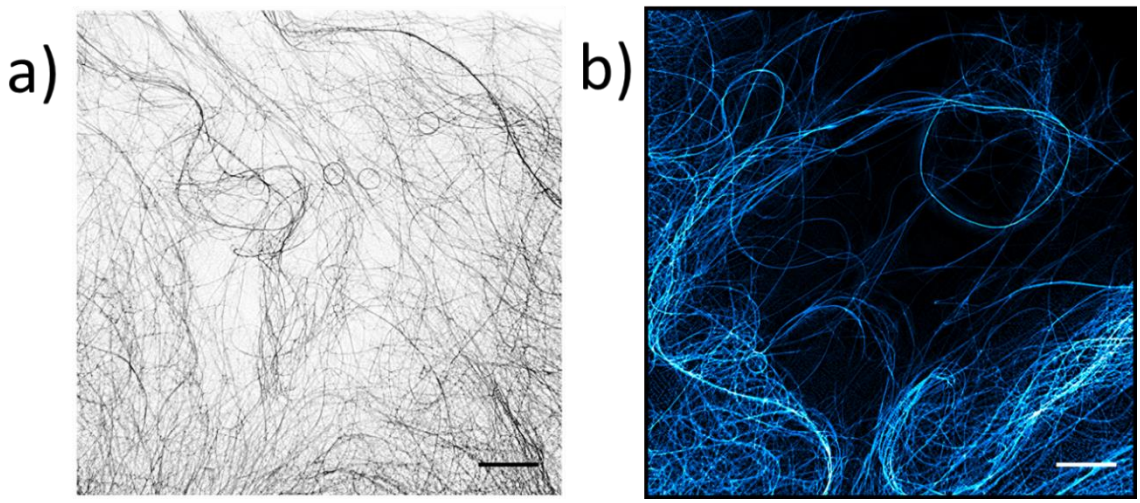

Figure 71 – a) Light microscopy and b) fluorescence microscopy images of SSA **49** (1 mM) in buffer (167 mM Na_2SO_4, acetate 5 mM, pH 5.5, ionic strength 500 mM). Scale bar = 10 µM.

Subsequently, conductance measurements were performed with SSA **49**, **50** and **61** in combination with anionophore, **71** (Figure 64). The anionophore was added initially followed by SSA after 30 secs and repeated in triplicate for 5 mins. The addition of anionophore (0.01 mM) to SSAs **49** and **61** (0.1 – 1 mM) produced conductance profiles very similar to those produced from SSAs **49** and **61** alone. Such experimental recordings either resulted in no change of current recording or indication of bilayer rupture (Appendix Sections 3.7.3 and 3.7.4), there was no evidence for ion transport. This is consistent with data generated by Haynes and co-workers whereby the addition SSAs **49** and **61** in combination with the anionophore was not found to mediate selective ion K+/Cl- transport in combination with anionophore.

However, under specific conditions, the addition of SSA **50** in combination with the anionophore produced an elevated and erratic current flow across the clamped portion of the DPhPC bilayer until eventual bilayer rupture at ≈ 210 seconds (Figure 72a). This profile was observed at an SSA **50** concentration of 0.375 mM, where when supplied in the absence of the anionophore causes bilayer rupture after ≈ 60 secs, as shown in Figure 72a.

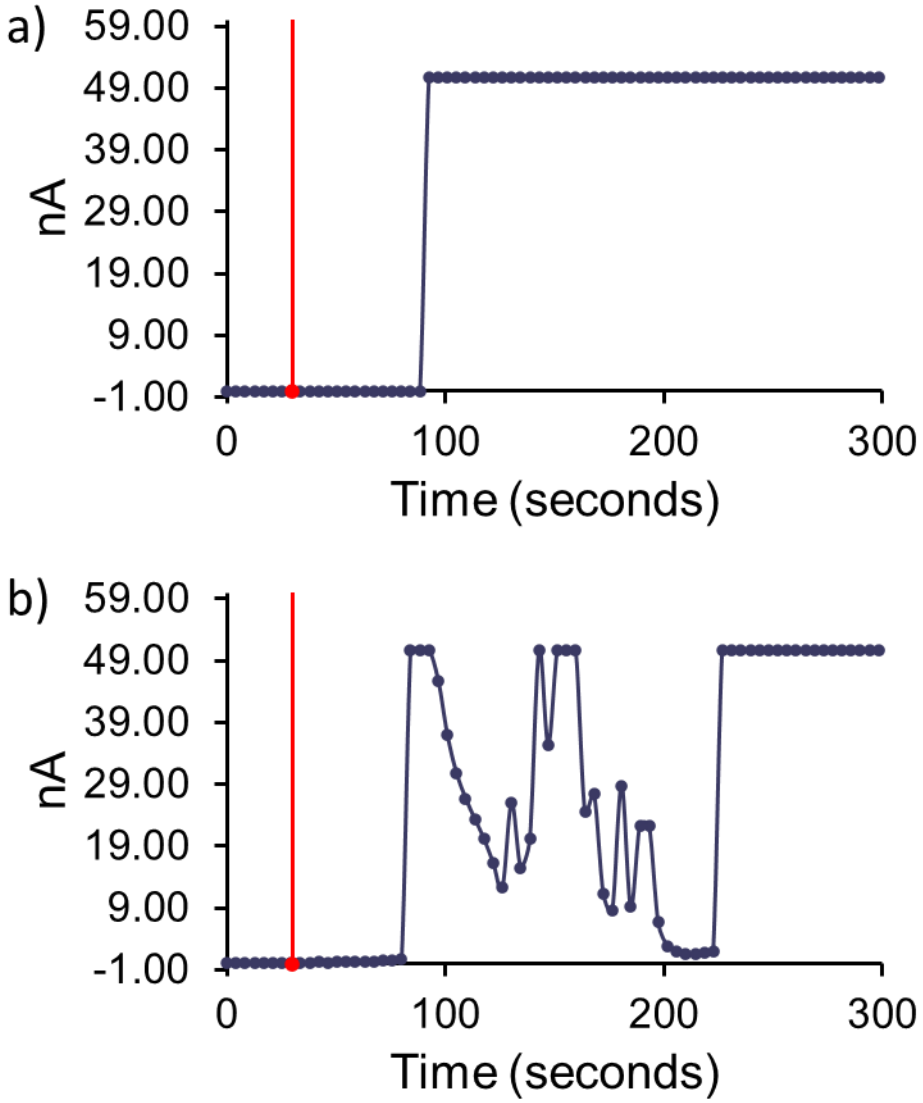

Figure 72 – Experimental recording of a DPhPC bilayer at 100 mV, addition of a) SSA **50** (0.375 mM) after 30 seconds indicated by the red line and b) anionophore (0.01 mM) at 0 seconds and SSA **50** (0.375 mM) after 30 seconds. The red line indicates the addition of SSA.

The lag phased observed between addition of SSA and change in membrane potential is hypothesised to be the time taken for SSA **50** to arrive and partition into the planar lipid bilayer. These changes are only observed at specific concentrations of SSA and therefore is suggestive that a critical concentration of SSAs is required to initiate such ion transport events. The huge changes in membrane potential (Figure 72b), measured on the nA scale prior to bilayer rupture are indicative of SSA **50** operating in combination with anionophore to initiate concentration dependent bulk ion transport events. SSA **50**, unlike **49** and **61** is not a linear molecule, an intramolecular bond forms between the HBA benzothiazole nitrogen and the HBD NH urea

group,[113] suggesting SSA **50** could facilitate ion movement through wrapping around the molecular cargo.

Conductance measurements were additionally performed with increased data points across the 5 mins, and readings were recorded ≈ every 0.7 seconds (Figure 73a). The formation of synthetic/ biological ion channels is usually observed by controlled, stepwise open/close behaviour and therefore is not consistent with this erratic current recording,[230,231] especially considering the magnitude of the current fluctuations. Instead, it is hypothesised SSA **50** could be operating in combination with anionophore through the 'carpet model', a mechanism analogous to that of some antimicrobial peptides.[232,233] Such molecules accumulate on the surface of the bilayer, forming a 'carpet', until the critical concentration is achieved, initiating membrane disruption. Figure 73b shows a magnified portion of Figure 73a, emphasising the almost instantaneous turn on/turn off change (≤ 0.7 seconds) in membrane potential at the point of critical SSA concentration.

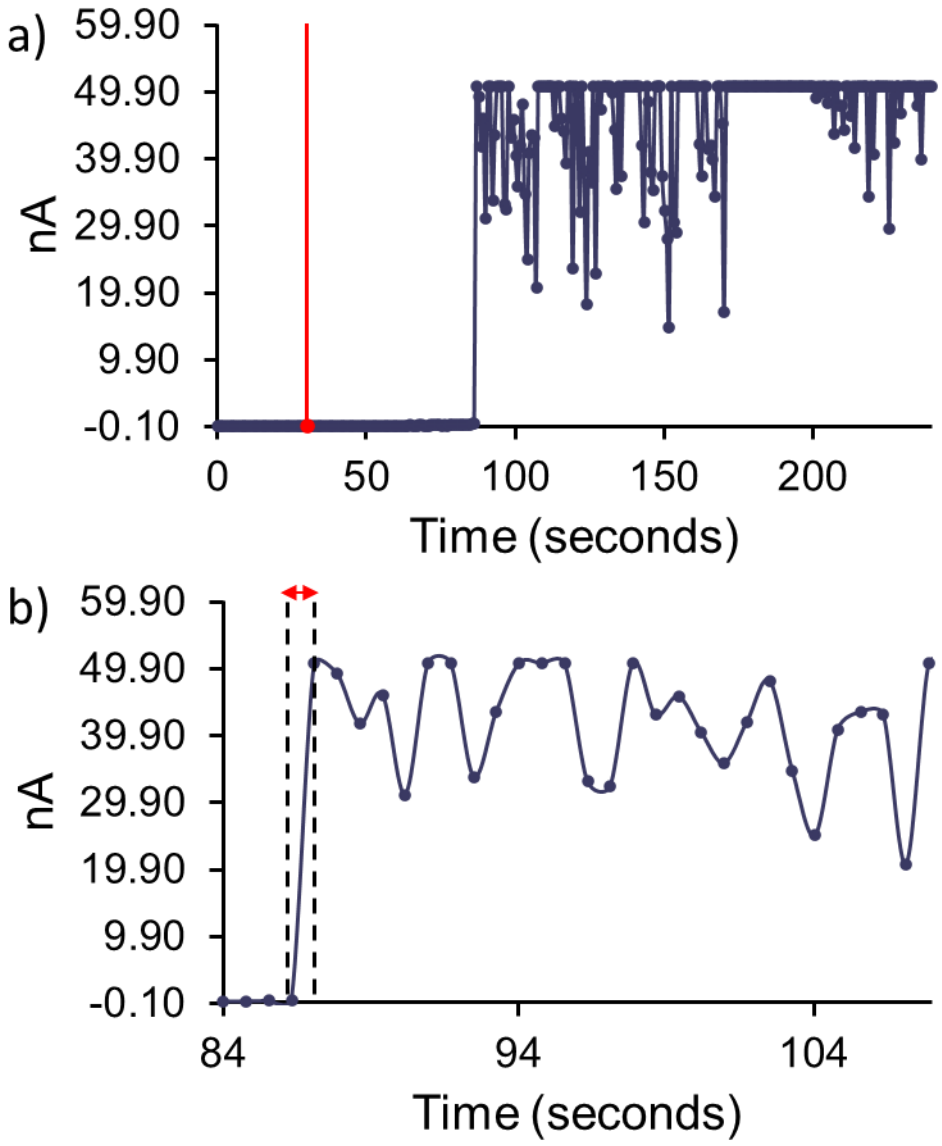

Figure 73 – Experimental recording of a DPhPC bilayer at 100 mV recorded with additional data points (every 0.7 seconds) following the addition of anionophore (0.01 mM) at 0 seconds SSA **50** (0.375 mM) after 30 seconds. The red line in (a) indicates the addition of SSA. (b) shows a magnified section of (a), emphasising the almost instantaneous turn on/turn off change in membrane potential over ≤ 0.7 seconds.

The DPhPC lipid bilayer was representative of a eukaryotic cell membrane.[192] To expand the study and monitor the ion transport across a model bacterial membrane, a range of GUVs were prepared with varying phospholipid compositions to mimic those of a bacterial cell. All GUVs were comprised of either 10 % or 20 % cholesterol to increase integrity and rigidity of any resultant bilayer. The phospholipid compositions of the planar lipid bilayers tested are outlined in Table 17. Despite the successful preparation of GUVs, stable bilayers could not be made under the buffer conditions tested.

Table 17 – Lipid composition of GUVs used to attempt to make a bacterial model planar bilayer in a KCl phosphate buffer.

Lipid composition	10 % cholesterol	20 % cholesterol
PE:PG 3:1	x	x
PG	x	x
PC:PG 1:1	x	x
PC:PG 3:1	x	x
E. coli polar	x	x
E. coli total	x	x

x = A stable lipid bilayer could not be attained.

In summary, experiments were conducted using an artificial planar lipid bilayer technique to attempt to assign a potential ion transport mechanism of SSA **50**. GUVs were prepared by an electroformation method (≈ 1.8 – 4.5 μM), composed of DPhPC lipids with 10 % cholesterol to maintain integrity and rigidity. A successful method was optimised for the formation of stable DPhPC lipid bilayers, the exchange of buffers and the addition of compound. The addition of SSAs **49**, **50** and **61** to the lipid bilayers either resulted in no change in conductance across the bilayer or complete membrane rupture. These observations correlated well with previous vesicle leakage experiments (Section 4.2). However, when SSA **50** was combined with the addition of an anionophore under specific conditions, an erratic and elevated current reading was observed, not indicative of channel formation but hypothesised to be due to a critical SSA concentration dependent bulk ion transport event.

4.6. Chapter 4 conclusion

This chapter aims to validate the hypothesis that SSAs are bacterial membrane disruptors by further exploring SSA: phospholipid interactions through the employment of fluorescence spectroscopy and patch clamp technology. A diverse selection of synthetic and bacterial derived phospholipid membranes was prepared for each study. A group of chemically and biologically diverse SSAs (**42**, **49**-**51, 59**-**68**) were chosen to elucidate structure activity relationships.

SSAs are amphiphilic in nature and therefore possess surfactant type properties. The ability of these molecules to lyse a range of calcein filled phospholipid vesicles was investigated, employing fluorescence spectroscopy. The first stage involved the addition of SSAs **42**, **49**-**51,**

59-**68** at a fixed, pre-determined concentration of 1.5 mM. Those urea benzothiazole SSAs (**63**-**65**) exhibited the highest level of broad range vesicle lysis, and this was found to be a time dependent event. Selectivity towards PC and PG synthetic vesicle membranes were observed with SSAs **49** and **62.** Exchange of the benzothiazole unit for the trifluoromethyl phenyl ring system (**42**, **50**, **51** and **60**) caused a dramatic reduction in the ability of the SSA to lyse phospholipid membranes. The replacement of the aromatic ring system for a straight alkyl chain prevented all lysing capabilities.

The second phase characterisation involved exploring effects of SSA concentration on vesicle lysis (%), this was particularly relevant to those SSAs which exhibited complete lysis (100 %) at 1.5 mM. The selectivity of SSAs towards bacterial derived *E. coli* lipid membranes correlated with the antimicrobial data against *E. coli* DH10B where the MIC_{50} of **49** > MIC_{50} of **63** > MIC_{50} of **64** (Section 3.1, Table 14). Selectivity for PG lipid vesicles over the model eukaryotic PC membranes was exhibited by those urea-methyl sulfonate SSAs. An inversion of this selectivity was observed with the structural alterations of a change in the length of the alkyl linking chain.

Membrane fluidity can be an integral factor in the mechanism of membrane targeting antimicrobials, such as the SSAs. Fluorescence polarisation was employed to investigate the potential for non-fluorescent SSAs (**42**, **51**, **59, 60** and **61**) to induce a change of the membrane fluidity in a variety of DPH-labelled phospholipid vesicles. The presence of SSAs **42, 59, 60** and **61** did not cause a change in the membrane fluidity of the five lipid vesicles studied. However, the addition of SSA **51** (> 0.1 mM), the only carboxylate containing SSA within the series, was found to increase the membrane fluidity of PG, PE-PG mix, *E. coli* polar and *E. coli* total phospholipid DPH-labelled vesicles. The MIC_{50} for SSA **51** against *E. coli* DH10B was lower than those calculated for SSAs **42, 59, 60** and **61**, indicating a potential link between membrane fluidity and antimicrobial activity.

To explore the coordination and selectivity of SSAs towards a range of synthetic and bacterial derived vesicles, those intrinsically fluorescent SSAs (**49, 50, 62-66**) were themselves utilized as the fluorophore in a fluorescence polarisation assay. Little selectivity towards specific membrane compositions and weak SSA: phospholipid interactions were detected with SSAs **62** and **64**. However, SSAs **63** and **65** exhibited a strong selectivity towards a single phospholipid composition, bacterial derived *E. coli* total and synthetic PG lipids respectively. The presence of the thio urea moiety (**66**) in this class of benzothiazole SSAs demonstrated the strongest coordination with the phospholipid vesicles tested. This FP data set was compared to the results from the vesicle leakage assay where there was found to be no correlation between selective SSA: phospholipid interaction and the ability to permeabilise/lyse model lipid membranes. The most interesting observation being SSA **66**, which exhibited the strongest coordination but performed least effectively in the lysis of comparable lipid membranes (< 10 %).

Ongoing research from Haynes and co-workers has discovered the ability for SSA **50** to work in combination with a previously reported anionophore to mediate the co-transport of K^+/Cl^-. To explore a potential SSA ion transport mechanism, experiments were designed and optimised using an artificial lipid bilayer on a patch clamp. Under the appropriate buffer conditions, only DPhPC GUVS (≈ 1.8 – 4.5 μM) could be successfully prepared, and cholesterol (10 %) was added to provide integrity and rigidity. Comparable to those chloride efflux experiments, SSAs **49** and **61** in the presence of the anionophore did not induce a change in electrical current across the membrane and therefore there was no evidence of ion exchange. However, the trends in membrane rupture correlated with those vesicle leakage experiments. Under specific concentrations of SSA **50** combined with the anionophore, an erratic and elevated current was recording, however not in the controlled, stepwise opening expected from an ion channel. It is therefore suggested SSA **50** works in combination with anionophore to initiate SSA concentration dependent bulk ion transport events.

4.7. Chapter 4 future work

Of the five structurally distinct SSAs tested, it was only **51**, the carboxylate containing SSA which was found to increase membrane fluidity of phospholipid DPH-labelled vesicles. Future work will involve expanding the carboxylate SSA series to include those shown in Figure 74. Analogous membrane fluidity studies will be performed with this set of molecules to ascertain how the presence of the carboxylate moiety alongside additional functional groups will impact on the degree of membrane fluidity. Fluorescence microscopy experiments will be performed on the DPH-labelled vesicles following exposure to SSA, this will confirm whether the dye remains embedded within the vesicles or if a displacement event with the SSA has occurred. Furthermore, imaging vesicles after exposure to SSA **51** will ascertain whether an increase in membrane fluidity induces any level of membrane disruption.

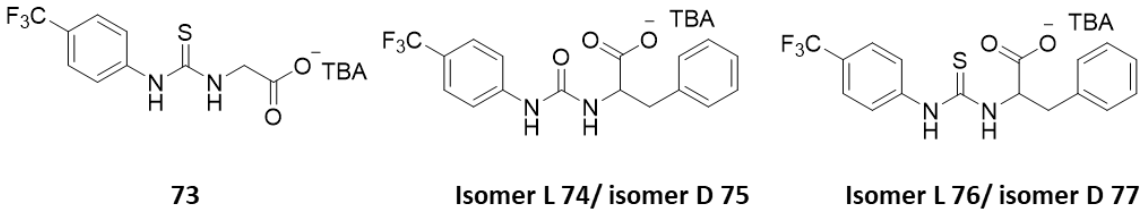

73 **Isomer L 74/ isomer D 75** **Isomer L 76/ isomer D 77**

Figure 74 – Proposed expansion of the carboxylate SSA series.

Continued collaboration with the Haynes group at UCL will further explore the cation transport ability of SSAs by expanding the phospholipid vesicles to include those representative of bacterial cells (POPG and PE-PG mix). Despite the successful preparation of GUVS made of these compositions, stable bilayers could not be formed on the patch clamp under buffer conditions analogous to the POPC experiments. Work will involve testing alternative buffer conditions to stabilise bilayer formation, especially paying attention to pH conditions. Additionally, the class of compounds tested on the patch clamp will be extended to include thio urea SSA derivatives, for example SSA **66**. These results will contribute to forming a hypothesis for the loss of vesicle lysis activity observed upon substitution of a urea for a thiourea functionality.

5. Chapter 5

5.1. Final conclusion

In response to the looming antimicrobial resistance crisis, the development of novel technologies to combat multi-drug resistant infections is critical, particularly those caused by Gram-negative bacteria. This study has shown the potential for supramolecular self-associating amphiphiles (SSAs) to act as efficacy enhancers for intracellular targeting antimicrobials against ESKAPE pathogen, *P. aeruginosa* PA01. **Novobiocin (52)**, an antimicrobial agent known to be resistant to PA01 exhibited an 8-fold decrease in MIC in the presence of an SSA. This work provides initial evidence for the potentiation of therapeutic agents using an anionic molecular construct to treat *P. aeruginosa* PA01 infections.

Due to the complex nature of multi-component, self-association events, extensive physicochemical analysis of those structures formed by SSAs in the presence of therapeutic agents was performed. These studies provided evidence for the separate supply of SSA and antimicrobial agent to the bacteria, as a result of comparative destabilisation of SSA aggregate and potential SSA: antimicrobial complex association events. Initial antimicrobial testing corroborated this theory, with antagonistic effects observed when components were added as a co-formulation vs optimal synergistic interactions observed when added separately with an SSA bacteria pre-incubation.

This work also validated the hypothesis that SSAs selectively coordinate with different phospholipid head groups. Interestingly, the trends observed from vesicle lysis and membrane coordination studies do not align, suggesting these processes rely on different mechanisms of action and SSA chemical/physicochemical properties. Investigating the effects of SSA physical membrane characteristics, the presence of a carboxylate moiety over a sulfonate was found to selectivity increase the membrane fluidity of bacterial model membranes over eukaryotic. Finally, patch clamp methods were designed to study K^+/Cl^- ion transport movement across a

single PC bilayer, revealing under specific conditions SSAs work in combination with an anionophore to initiate SSA concentration dependent bulk ion transport events.

6. Chapter 6

6.1. Experimental: Chapter 2

NMR: NMR spectra were collected using a Burker AV2 400 MHz or AVNEO 400 MHz spectrometer and processed using ACD Labs. NMR peaks were calibrated to the solvent peak and reported in parts per million (ppm), (s = singlet, d = doublet, t = triplet, q = quartet, m = multiplet).

Self-association constant calculation: Bindfit v0.5 was employed to determine self-association constants (http://app.supramolecular.org/bindfit/).

Tensiometry Studies: A Biolin Scientific Theta Attension optical tensiometer was used to gather tensiometry measurements using the pendant drop method and Biolin OneAttension software was used for data processing. Measurements were obtained in triplicate and averaged values were used to calculate the critical micelle concentration (CMC).

DLS Studies: Anton Paar LitesizerTM 500 and KalliopeTM Professional were used for data collection and processing respectively. All solvents used were filtered to remove any particulates that may interfere with the results obtained. A series of 9/10 runs were recorded at 25 °C.

Zeta Potential Studies: Anton Paar LitesizerTM 500 and KalliopeTM Professional were used for data collection and processing respectively. The final zeta potential value given is an average of 10 experiments conducted at 25 °C.

Single Crystal X-ray Studies: A suitable crystal of each amphiphile was selected and mounted on a Rigaku Oxford Diffraction Supernova diffractometer. Structures were solved with the ShelXT[234] or ShelXS structure solution programs via Direct Methods and refined with ShelXL[235] by Least Squares minimisation. Olex2[236] was used as an interface to all ShelX programs (CCDC 1999018).

6.1.1. Biological experiments

Preparation of Luria Broth (LB) media: Tryptone (10 g), yeast extract (5 g) and sodium chloride (10 g) were dissolved in dH_2O (1 L) and autoclaved.

Preparation of Luria Broth (LB) agar plates: Agar (6 g) was added to LB (400 mL), autoclaved and poured into sterile petri dishes and left to set.

Preparation of bacterial plates: *Escherichia coli* DH10B was streaked onto sterile LB agar plates then incubated at 37 °C overnight.

Preparation of Inoculum: A single colony of bacteria was added to LB media (5 mL) and incubated overnight at 37 °C. The following day, a subculture of fresh LB (5 mL) and the overnight culture (50 µL) was incubated at 37 °C until the culture had reached an optical density (OD) of 0.4 at 600 nm. Optical Density was adjusted using sterile dH_2O to equal 0.5 McFarland standard (107 – 108 cfu/mL), then a 1:10 dilution was carried out using sterile dH_2O (900 µL) and the McFarland adjusted suspension (100 µL). A final dilution (1:100) was carried using the 1:10 suspension (150 µL) and LB (14.85 mL) before use to achieve a final cell concentration of 105 cfu/mL.

Preparation of 96 well microplate for co-formulation plates: A 1:100 cell suspension (150 µL) and co-formulation solution (**a**-**e**) (30 µL) were aliquoted into each well. The plates were incubated at 37 °C for 18 hours in a Clariostar plate reader, reading OD_{600} at 15-minute intervals. Growth curves were produced, with the OD_{600} at 1100 mins used to study synergistic interactions.

Preparation of 96 well microplate for SSA preincubation plates: A 1:100 cell suspension (150 µL) and SSA solution (15 µL) were aliquoted into each well and pre-incubated at 37 °C for 10 mins before the addition of antimicrobial agents **43**-**47** (15 µL). The plates were incubated at 37 °C for 18 hours in a Clariostar plate reader, reading OD_{600} at 15-minute intervals. Growth curves were produced, with the OD_{600} at 1100 mins used to study synergistic interactions.

Preparation of 96 well microplate for drug preincubation plates: A 1:100 cell suspension (150 µL) and antimicrobial agents **43**-**47** (15 µL) were aliquoted into each well and pre-incubated at 37 °C for 10 mins before the addition of SSA solution (15 µL). The plates were incubated at 37 °C for 18 hours in a Clariostar plate reader, reading OD_{600} at 15-minute intervals. Growth curves were produced, with the OD_{600} at 1100 mins used to study synergistic interactions.

6.2. Experimental: Chapter 3

Preparation of bacterial plates: *Escherichia coli* DH10B or *Pseudomonas aeruginosa* PA01 was streaked onto sterile LB agar plates then incubated at 37 °C overnight.

Preparation of Inoculum: A single colony of bacteria was added to LB media (5 mL) and incubated overnight at 37 °C. The following day, overnight bacterial cultures were subcultured into fresh LB media to a starting OD_{600} of 0.01.

MIC determination: Compounds were serially diluted across the plate. Inoculum was added to each well giving a total well volume of 200 µL. Plates were incubated with shaking (180 rpm) at 37 °C for 18 h and the OD_{600} was determined using a Clariostar plate reader (BMG Labtech).

Preparation of well microplate co-formulation study: Antimicrobial agents (**45**, **52**-**53**) were serially diluted across the plate with a starting concentration of the minimum inhibitory concentration (MIC). Inoculum was added to SSA, 100 µL of SSA-culture was aliquoted to each well giving a total well volume of 200 µL. Plates were incubated with shaking (180 rpm) at 37 °C for 18 h and the OD_{600} was determined using a Clariostar plate reader (BMG Labtech).

6.2.1. Microscopy

Competitive Binding Assay: An overnight bacterial culture was subcultured to reach an optical density of 0.4 at 600 nm. Samples were incubated at room temperature for 30 minutes then cells were mounted onto the agarose LB pads under coverslips. Samples were visualised using

an Olympus IX71 microscope with UAPON 150x 1.45 NA Widefield fluorescence lens mounted on a PIFOC z-axis focus drive (Physik Instrumente, Karlsruhe, Germany), and illuminated using LED light sources (Cairn Research Ltd, Faversham, UK) with appropriate filters (Chroma, Bellows Falls, VT) using a Zyla 4.2 CMOS camera (Andor). The system was controlled with Metamorph software (Molecular Devices). Images were subsequently analysed using Metamorph and ImageJ software.

6.3. Experimental: Chapter 4

General remarks: All solvents and starting materials were purchased from known chemical suppliers or available stores. A Stuart SMP10 melting point apparatus was used to determine melting point. High resolution mass spectrometry was performed using a Bruker microTOF-Q mass spectrometer and spectra recorded and processed using Bruker's Compass Data Analysis software. A Shimadzu IR-Affinity-1 model spectrometer was used to obtain infrared spectra.

MIC_{50} determination: Inoculum was prepared as described in Section 6.1.1. Bacteria inoculum (150 µL) and compound (30 µL) were added to each well across a range of concentrations. Plates were incubated with shaking (180 rpm) at 37 °C in a Clariostar plate reader and the OD_{600} was taken every 15 mins for 18 hours. Growth curves were plotted using OD_{600} and inputted into Origin ® 2015. The resultant curve was normalized and fitted using the Boltzmann fit to define the MIC_{50} values for each compound.

Mass Spectrometry: A 1 mg/mL solution of compound was prepared in methanol. This solution was further diluted 100-fold before undergoing analysis where 10 µL of each sample was then injected directly into a flow of 10 mM ammonium acetate in 95 % water (flow rate = 0.02 mL/min).

Preparation of vesicles: All lipids were purchased as powder stocks from Avanti Polar Lipids. Lipid vesicles were prepared according to standard procedures.[215] Each phospholipid was dissolved in chloroform (~ 10 mL) and the solvent was removed under reduced pressure. The

thin film of dried lipid was further dried under vacuum for at least 2 hours. Lipid films were resuspended in the desired buffer and subjected to 9 freeze-thaw cycles in liquid nitrogen and extruded 20 times through a 200 nm polycarbonate membrane.

Preparation of calcein loaded vesicles: Lipid films were resuspended in buffer A (70 mM calcein, 10 mM TRIS pH 8.5, 0.5 mM EDTA, 110 mM NaCl, pH adjusted to 6-7) and subjected to 9 freeze-thaw cycles in liquid nitrogen and extruded 20 times through a 200 nm polycarbonate membrane. The suspension was run down a size exclusion column packed with sephadex G-50 using buffer B (10 mM TRIS pH 8.5, 0.5 mM EDTA, 110 mM NaCl). Phospholipid concentration was adjusted to 30 μM for vesicle leakage experiments.

Vesicle leakage assay: Black bottom 96-well plates were prepared with the appropriate lipid solution (100 μL, 30 μM) and desired SSA solution (100 μL) prepared in H_2O/ 5.0 % EtOH. Fluorescent measurements were taken at 25 °C using an excitation value of 495 nm and an optimised gain of 983. Data were acquired in endpoint mode. All experiments were repeated in triplicate to ensure experimental reproducibility.

Preparation of DPH fluorescent labelled vesicles: Lipid films were resuspended in buffer (150 mM KCl, 10 mM HEPES, pH 7.4, 2 mM EGTA) and subjected to 9 freeze-thaw cycles in liquid nitrogen and extruded 20 times through a 200 nm polycarbonate membrane. For fluorescent labelling, the desired vesicles were pre-incubated with 1,6-diphenyl-hexa-1,3,5-triene (DPH) (10 μM) at 60 °C for 1 hour.

Membrane fluidity validity assay: DPH labelled DSPG (1,2-Distearoyl-sn-glycero-3-phosphoglycerol) vesicles were prepared with a defined gel-to-liquid crystalline phase transition temperature of 55 °C. Fluorescence polarisation (FP) measurements were taken using a 355 nm filter for excitation and a 430 m for emission. The DPH labelled vesicles were set to a FP value of 100 mP. Steady state measurements were taken at 25 °C – 60 °C, the temperature on the microplate was increased in 10 °C increments until 45 °C, temperatures above this were reached

externally using a heating plate. Data were acquired in endpoint mode. All experiments were repeated in triplicate to ensure experimental reproducibility.

Membrane fluidity assay: Black bottom 96-well plates were prepared by serially diluting desired SSA in a H_2O/EtOH 95: 5 solution across the plate, the appropriate DPH labelled vesicles (100 µL, 30 µM) were added to each well to give a total well volume of 200 µL. FP measurements were taken at 25 °C using a 355 nm filter for excitation and a 430 m for emission. The DPH labelled vesicles were set to a FP value of 100 mP. Data were acquired in endpoint mode. All experiments were repeated in triplicate to ensure experimental reproducibility.

Fluorescence polarisation: Lipid films were resuspended in Buffer (150 mM KCl, 10 mM HEPES, pH 7.4, 2 mM EGTA) and subjected to 9 freeze-thaw cycles in liquid nitrogen and extruded 20 times through a 200 nm polycarbonate membrane. Black bottom 96-well plates were prepared by serially diluting desired vesicle solution across the plate, the appropriate SSA solution (100 µL, 0.15 mM) was added to each well to give a total well volume of 200 µL. FP measurements were taken at 25 °C. Fluorescent SSA solutions were set to a FP value of 100 mP. Data were acquired in endpoint mode. All experiments were repeated in triplicate to ensure experimental reproducibility.

6.3.1. Patch clamp

Vesicle formation: Giant unilamellar Vesicles (GUVS) were prepared using the electroformation method using the Nanion VesiclePrepPro setup. A solution of 1,2-diphytanoyl-sn-glycero-3-phosphocholine (DPhPC) (10 mM) with 10 % cholesterol in chloroform (20 mL) was deposited on the ITO-coated glass surface to create a dehydrated thin lipid film. A greased O-ring is filled with sucrose (200 mM, 275 mL) and sealed with a second ITO-slide. AC current (3 V, 5 Hz) was then applied. After 2 h the voltage and the frequency were reduced in steps, first to 1.6 V,1 Hz, after 30 min and held for 1 h and to the final values 0V,0 Hz after 30 mins.

Patch clamp measurements: Patch clamp experiments were performed with the Port-a-Patch (Nanion Technologies), using borosilicate glass chips with an aperture diameter of approximately 1 µm. The GUVS were positioned into the aperture in the chip by application of negative pressure (-30 mbar), with symmetrical buffer solutions (489 mM KCl, acetate 5 mM, pH 5.5, ionic strength 500 mM). The external buffer was exchanged (167 mM Na_2SO_4, acetate 5 mM, pH 5.5, ionic strength 500 mM). A single GUV forms a planar bilayer upon contact with the glass surface of the chip. The holding potential was set to 50 or 100 mV. Anionophore (0.01 mM) was added at t = 0 s and the SSA (0.1 - 1 mM) was subsequently added at t = 30 s. The sweep interval was set to 1 s, and the protocol was run for a total of 5 mins in triplicate.

6.4. Synthetic procedures

Compound 42: This compound was synthesised in line with our previously published methods. Proton NMR were found to match our previously published.[113] ^{1}H NMR (400 MHz, 298 K, DMSO-d_6): δ: 9.27 (s, 1H), 7.53 (dd, *J* = 23.76, 8.44 Hz, 4H), 6.97 (t, *J* = 5.52 Hz, 1H), 3.94 (d, *J* = 5.68 Hz, 2H), 3.19 - 3.15 (m, 8H), 1.57 (m, 8H), 1.31 - 1.28 (m, 8H), 0.93 (t, *J* = 7.24 Hz, 12H).

Compound 59: This compound was synthesised in line with our previously published methods. Proton NMR were found to match or previously published.[112] ^{1}H NMR (400 MHz, 298 K, DMSO-d_6): δ: 8.94 (s, 1H), 7.56 (dd, *J* = 18.08, 8.96 Hz, 4H), 6.38 (t, *J* = 5.68 Hz, 1H), 3.15 (m, 10H), 2.46 (m, 2H), 1.74 (m, 2H), 1.57 – 1.54 (m, 8H), 1.31 - 1.29 (m, 8H), 0.93 (t, *J* = 7.40 Hz, 12H).

Compound 60: This compound was synthesised in line with our previously published methods. Proton NMR were found to match our previously published.[112] ^{1}H NMR (400 MHz, 298 K, DMSO-d_6): δ: 9.18 (s, 1H), 8.90 (d, *J* = 5.00 Hz, 2H), 8.55 (t, *J* = 6.41 Hz, 1H), 8.27 (s, 1H), 8.01 (t, *J* = 7.56 Hz, 2H), 7.55 (s, 4H), 6.70 (s, 1H), 3.90 (d, *J* = 5.24 Hz, 2H).

Compound 51: This compound was synthesised in line with our previously published methods. Proton NMR were found to match our previously published.[112] ^{1}H NMR (400 MHz, 298 K, DMSO-

d_6): δ: 10.27 (s, 1H), 7.68 (d, *J* = 8.52 Hz, 2H), 7.50 (d, *J* = 8.72 Hz, 2H), 6.76 (s, 1H), 3.17-3.13 (m, 8H), 1.59 - 1.54 (m, 8H), 1.31 - 1.25 (m, 8H), 0.92 (t, *J* = 7.34 Hz, 12H).

Compound 50: This compound was synthesised in line with our previously published methods. Proton NMR were found to match our previously published.[113] ^{1}H NMR (400 MHz, 298 K, DMSO-d_6): δ: 10.64 (s, 1H) 8.44 (d, *J* = 7.77 Hz, 1H), 8.30 (d, *J* = 7.79 Hz, 1H), 8.15 (d, *J* = 7.80 Hz, 1H), 7.84 (d, *J* = 7.88 Hz, 2H), 7.57 (t, *J* = 7.80 Hz, 1H), 7.48 (m, 2H), 7.09 (t, *J* = 7.80 Hz, 1H), 3.96 (s, 2H), 3.18 – 3.13 (m, 8H), 1.60 – 1.56 (m, 8H), 1.31 – 1.29 (m, 8H), 0.92 (t, *J* = 7.28 Hz, 12H).

Compound 49: This compound was synthesised in line with our previously published methods. Proton NMR were found to match our previously published.[113] ^{1}H NMR (400 MHz, 298 K, DMSO-d_6): δ: 9.22 (s, 1H), 7.91 – 7.84 (m, 4H), 7.57 (d, *J* = 8.64 Hz, 2H), 7.32 – 7.30 (m, 1H), 6.94 (t, *J* = 5.11 Hz, 1H), 3.93 (d, *J* = 5.40 Hz, 2H), 3.15 – 3.12 (m, 8H), 2.43 (s, 3H), 1.54 (m, 8H), 1.30 – 1.28 (m, 8H), 0.91 (t, *J* = 7.16 Hz, 12H).

Compound 61: Aminomethansulfonic acid (0.22 g**,** 2.00 mmol) was dissolved in tetrabutylammonium in methanol (2 mL, 2 mmol) with excess methanol (15 mL) to aid dissolving before being taken to complete dryness. A mixture of 2-Aminobenzothiazole (0.33 g, 2.00 mmol) and 1,1'-Carbonyldiimidazole (0.33 g, 2.00 mmol) were heated at reflux at 80 °C for 4 hours in chloroform (20 mL). Tetrabutylammonium aminomethanesulfonate (2.00 mmol) was dissolved in chloroform (2 mL) and added to the original reaction mixture and heated at reflux at 80 °C overnight. The solvent was removed and the resulting oil dissolved in ethyl acetate (15 mL), producing the pure product as a white solid with a yield of 91 % (0.99 g, 1.82 mmol); melting point: > 200 °C ^{1}H NMR (400 MHz, 298 K, DMSO-d_6): δ: 10.52 (s, 1H), 7.67 (s, 1H), 7.50 (d, *J* = 8.16 Hz, H), 7.17 – 7.11 (m, 2H), 3.91 (d, *J* = 5.88 Hz, 2H), 3.17 – 3.13 (m, 8H), 2.37 (s, 3H), 1.59 – 1.52 (m, 8H), 1.35 – 1.25 (m, 8H), 0.93 (t, *J* = 7.24 Hz, 12H);); ^{13}C{^{1}H} NMR (100 MHz, 298K, DMSO-d_6): δ: 158.7 (ArC), 153.3 (ArC), 147.1 (ArC), 132.0 (ArC), 131.7 (ArC), 127.0 (ArCH), 121.1 (ArCH), 119.4 (ArCH), 57.5 (CH_2), 55.9 (CH_2), 23.1 (CH_2), 21.0 (CH_3), 19.2 (CH_2), 19.2 (CH_2), 13.5,

(CH_3); IR (film): ν (cm^{-1}) = 3345 (NH stretch), 1697 (C=O stretch), 1038 (CN stretch); HRMS for the sulfonate-urea ion ($C_{10}H_{10}N_3O_4S_2^-$) (ESI^-): m/z: act: 300.0133 [M] cal: 300.0118 [M].

Compound 62: Aminomethansulfonic acid (0.22 g**,** 2.00 mmol) was dissolved in tetrabutylammonium in methanol (2.00 mL, 2.00 mmol) with excess methanol to aid dissolving before being taken to complete dryness. A mixture of 4-(benzothiazol-2-yl)aniline (0.45 g, 2.00 mmol) and triphosgene (0.30 g, 1 mmol) was heated at reflux for 4 hours in ethyl acetate (20 mL). Tetrabutylammonium aminomethanesulfonate (2.00 mmol) was dissolved in ethyl acetate (2.00 mL) and added to the original reaction mixture and heated at reflux overnight. Resulting in the clean product as a white solid with a yield of 67 % (0.81 g, 1.34 mmol); melting point: 195 °C; ^{1}H NMR (400 MHz, 298 K, DMSO-d_6): δ: 9.28 (s, 1H), 8.05 (d, *J* = 7.92 Hz, 1H), 8.00 – 7.90 (m, 3H), 7.59 (d, *J* = 8.56 Hz, 2H), 7.50 (t, *J* = 7.84 Hz, 1H), 7.40 (t, *J* = 7.76 Hz, 1H), 7.06 (s, 1H), 3.98 (d, *J* = 5.80 Hz, 2H), 3.15 – 3.11 (m, 8H), 1.53 (m, 8H), 1.29 (m, 8H), 0.91 (t, *J* = 7.24, 12H); ^{13}C{^{1}H} NMR (100 MHz, 298 K, DMSO-d_6): δ: 167.4 (C=O), 154.2 (ArC), 153.7 (ArC), 143.7 (ArC), 134.1 (ArC), 128.0 (ArCH), 126.5 (ArCH), 125.4 (ArC), 125.0 (ArCH), 122.4 (ArCH), 122.2 (ArCH), 117.6 (ArCH), 57.4 (CH_2), 56.0 (CH_2), 23.1 (CH_2), 19.2 (CH_2), 13.5 (CH_3); IR (film): ν (cm^{-1}) = 3267 (NH stretch), 1697 (C=O stretch), 1327 (S=O stretch), 1038 (CN stretch); HRMS for the sulfonate-urea ion ($C_{15}H_{12}N_3O_4S_2^-$) (ESI^-): m/z: act: 390.2425 [M + C_2H_4] cal: 362.0275 [M].

Compound 63: Aminomethansulfonic acid (0.22 g**,** 2.00 mmol) was dissolved in tetrabutylammonium in methanol (2.00 mL, 2 mmol) with excess methanol (15 mL) to aid dissolving before being taken to complete dryness. A mixture of 4-(benzothiazol-2-yl)aniline (0.48 g, 2 mmol) and triphosgene (0.30 g, 1 mmol) was heated at reflux for 4 hours in ethyl acetate (20 mL). Tetrabutylammonium aminomethanesulfonate (2 mmol) was dissolved in ethyl acetate (2.00 mL) and added to the original reaction mixture and heated at reflux overnight. Resulting in the clean product as a white solid with a yield of 64 % (0.81 g, 1.28 mmol); melting point: 195 °C; ^{1}H NMR (400 MHz, 298 K, DMSO-d_6): δ: 9.30 (s, 1H), 7.92 – 7.85 (m, 4H), 7.59 (d*, J* = 8.64 Hz, 2H), 7.32 (d, *J* = 10 Hz, 1H), 6.51 (t, *J* = 5.60 Hz, 1H), 3.39 (q, *J* = 6.40 Hz, 2H), 3.18 –

3.14 (m, 8H), 2.57 (t, *J* = 6.04 Hz, 2H), 2.45 (s, 3H), 1.54 (m, 8H), 1.32 – 1.26 (m, 8H), 0.93 (t, J = 7.32, 12H); $^{13}C\{^{1}H\}$ NMR (100 MHz, 298 K, DMSO-d_6): δ: 166.3 (C=O), 154.7 (ArC), 151.9 (ArC), 143.9 (ArC), 134.7 (ArC), 134.3 (ArC), 127.8 (ArCH), 127.7 (ArCH), 125.3 (ArC), 121.9 (ArCH), 121.7 (ArCH), 117.5 (ArCH), 57.5 (CH_2), 50.9 (CH_2), 36.1 (CH_2), 23.1 (CH_2), 21.0 (CH_3), 19.2 (CH_2), 13.5 (CH_3); IR (film): ν (cm^{-1}) = 3267 (NH stretch), 1697 (C=O stretch), 1327 (S=O stretch), 1038 (CN stretch); HRMS for the sulfonate-urea ion ($C_{15}H_{12}N_3O_4S_2^-$) (ESI^-): m/z: act: 390.0575 [M] cal: 390.0588 [M].

Compound 64: This compound was synthesised in line with our previously published methods. Proton NMR were found to match our previously published.[237] ^{1}H NMR (298 K, 400 MHz, DMSO-d_6): δ: 9.11 (s, 1H), 7.90-7.83 (m, 4H), 7.61 (d, *J* = 8.72 Hz, 2H), 7.30 (d, *J* = 8.32 Hz, 1H), 6.73 (t, *J* = 5.52 Hz, 1H), 3.21-3.10 (m, 10H), 2.56 (t, *J* = 7.7 Hz, 2H), 2.43 (s, 3H), 1.83-1.80 (m, 2H), 1.53 (m, 8H), 1.29-1.23 (m, 8H), 0.94 (t, *J* = 7.34 Hz, 12H).

Compound 65: A mixture of 4-(6-methylbenzothiazole-2-yl)aniline (0.48 g, 2.00 mmol) and triphosgene (0.30 g, 1.00 mmol) were heated at reflux for 4 hours in ethyl acetate (10.00 mL), then tert-butyl 2-amino-acetate (0.26 g, 2.00 mmol) was added to the original reaction mixture and heated at reflux overnight. The crude precipitate was removed. The precipitate was dissolved in chloroform (5.00 mL), triflouroacetic acid (1.50 mL) added and the resulting solution left to stir at RT for 30 minutes. NaOH (6 M) was then added dropwise, testing pH until neutral and the deprotected product precipitates out. Dissolve product in methanol (10 mL) and add tetrabutylammonium hydroxide in excess (2.00 mL, 2.00 mmol). Remove precipitate and take the filtrate to dryness and titrate with water. Filter to produce pure product as a white solid with a yield of 27 % (0.23 g, 0.39 mmol), melting point: 86 °C; ^{1}H NMR (400 MHz, 298 K, DMSO-d_6): δ: 10.49 (s, 1H), 7.89 – 7.85 (m, 4H), 7.74 – 7.71 (d, *J* = 8.76 Hz, 2H), 7.31 (d, *J* = 8.52 Hz, 1H), 6.92 (s, 1H), 3.39 (d, *J* = 3.52 Hz , 2H) 3.16 – 3.12 (m, 8H), 2.44 (s, 3H), 1.54 (m, 8H), 1.32 – 1.30 (m, 8H), 0.92 (t, *J* = 7.36, 12H); $^{13}C\{^{1}H\}$ NMR (100 MHz, 298 K, DMSO-d_6): δ: 13.5 (CH_3), 19.2 (CH_2), 21.0 (CH_3), 23.0 (CH_2), 45.0 (CH_2), 57.5 (CH_2), 117.1 (ArCH), 121.7 (ArCH), 121.8 (ArCH), 124.6

(ArC), 127.7 (ArCH), 127.8 (ArCH), 134.2 (ArC), 134.5 (ArC), 144.8 (ArC), 151.9 (ArC), 154.8 (ArC), 166.5 (C=O), 170.4 (C=O); IR (film): ν (cm^{-1}) 3331 (NH stretch), 2961 (OH stretch), 1699 (C=O stretch), 1331 (S=0 stretch), 1177 (CN stretch); HRMS for the sulfonate-urea ion ($C_{17}H_{14}N_3O_3S^-$) (ESI^-): m/z: act 340.2244 [M], cal: 340.0761 [M].

Compound 66: A mixture of 4-(6-methylbenzothiazole-2-yl)aniline (0.48 g, 2.00 mmol) and thiophosgene (0.15 mL, 2 mmol) as a two phase solution of dichloromethane (20 mL) and saturated sodium hydrogen carbonate (20 mL) was stirred for 4 hours at room temperature, then transferred to separation funnel, the organic layer was separated and taken to dryness. Then it was re-dissolved in ethyl acetate (30 mL) and tetrabutylammonium aminomethanesulfonate (2.00 mmol) was added and the solution left to reflux overnight. The ethyl acetate was decanted out, the oil taken to dryness, re-dissolved in methanol (5 mL) and ran down an ion exchange column. Ammonia was used to remove the product, with 50 % loss of tetrabutylammonium. The product was then re-dissolved in methanol (10 mL) and excess tetrabutylammonium (2 mL, 2 mmol) was then added and taken to dryness. The oil was re-dissolved in chloroform (30 mL) and water washed (30 mL). The organic layer was taken to dryness leaving a yellow solid as the clean product with a yield of 28 % (0.35 g, 0.55 mmol); melting point: >200 °C; ^{1}H NMR (400 MHz, 333 K, DMSO-d_6): δ: 10.33 (s, 1H), 7.99-7.80 (m, 7H), 7.33 (m, 1H), 4.25 (s, 2H), 3.20 – 3.17 (m, 8H), 2.47 (s, 3H), 1.63 – 1.61 (m, 8H), 1.36 – 1.32 (m, 8H), 0.96 (t, *J* = 7.24, 12H). ^{13}C{^{1}H} NMR (100 MHz, 298 K, DMSO-d_6): δ: 179.8 (C=O), 165.8 (ArC), 151.8 (ArC), 142.6 (ArC), 135.0 (ArC), 134.5 (ArC), 128.0 (ArC), 127.3 (ArCH), 127.1 (ArCH), 122.2 (ArCH), 121.8 (ArCH), 121.6 (ArCH), 60.2 (CH_2), 57.5 (CH_2), 23.0 (CH_2), 21.1 (CH_3), 19.2 (CH_2), 13.5 (CH_3); IR (film): ν (cm^{-1}) 3242 (NH stretch), 1325 (S=O stretch), 1223 (CN stretch), 1036 (S=O stretch); HRMS for the sulfonate-urea ion ($C_{16}H_{14}N_3O_3S_3^-$) (ESI^-): m/z: act: 391.1053 [M^-], cal: 392.0203 [M].

Compound 67: Aminomethane sulfonic acid (0.16 g, 1.50 mmol) was dissolved in tetrabutylammonium in methanol (1.50 mL, 1.50 mmol) with excess methanol to aid dissolving

before being taken to complete dryness. Tetrabutylammonium aminomethane sulfonate (1.50 mmol) was dissolved in chloroform (12.5 mL) and left overnight in a sealed vial with 1-isocyanatobutane (0.15 g, 1.50 mmol). The resulting solution was taken to dryness, re-dissolved in ethyl acetate (15 mL) and extracted with water (15 mL). The pure product was obtained by flash chromatography 100 % ethyl acetate followed by 100 % methanol. The methanol fraction was taken to dryness to give the pure product as an opaque viscous oil with a yield of 63 % (0.28 g, 0.62 mmol); melting Point: 131 °C; ^{1}H NMR (400 MHz, 298 K, DMSO-d_6): δ: 6.16 (s, 1H), 6.05 (t, *J* = 5.52 Hz, 1H), 3.75 (d, *J* = 5.96 Hz, 2H), 3.16 (t, *J* = 8.24 Hz, 8H), 2.96 (q, *J* = 5.96 Hz, 2H), 1.56 (m, 8H), 1.30 (m, 12H), 0.93 (t, *J* = 6.88 Hz, 12H), 0.86 (t, *J* = 6.84 Hz, 3H); ^{13}C{^{1}H} NMR (100 MHz, 298 K, DMSO-d_6): δ: 13.5 (CH_3), 13.5 (CH_3), 19.2 (CH_2), 19.3 (CH_2), 23.1 (CH_2), 32.2 (CH_2), 48.6 (CH_2), 56.7 (CH_2), 57.5 (CH_2), 157.5 (CO); IR (film): ν (cm^{-1}) = 3317 (NH stretch), 1658, 1170, 1035, 883; HRMS for the sulfonate-urea ion ($C_6H_{13}N_2O_4S^-$) (ESI^-): m/z: act: 209.0602 $[M]^-$ cal: 209.0587 [M]-.

Compound 68: Aminomethane sulfonic acid (0.16 g, 1.50 mmol) was dissolved in tetrabutylammonium in methanol (1.50 mL, 1.50 mmol) with excess methanol to aid dissolving before being taken to complete dryness. Tetrabutylammonium aminomethane sulfonate (1.50 mmol) was dissolved in chloroform (12.5 mL) and left overnight in a sealed vial with 1-isothiocyanatobutane (0.18 mL, 1.50 mmol). The resulting solution was taken to dryness, re-dissolved in ethyl acetate (15 mL) and extracted with water (15 mL). The pure product was obtained by flash chromatography 100 % ethyl acetate followed by 100 % methanol. The methanol fraction was taken to dryness to give the pure product as an opaque viscous oil with a yield of 32 % (0.21 g, 0.45 mmol); melting Point: 129 °C; ^{1}H NMR (400 MHz, 333 K, DMSO-d_6): δ: 7.98 (s, 1H), 7.33 (s, 1H), 4.09 (d, *J* = 3.68 Hz, 2H), 3.40 (q, *J* = 8.24 Hz, 2H), 3.19 (t, *J* = 7.80 Hz, 8H), 1.63 (m, 8H), 1.47 (m, 2H), 1.33 (m, 10H), 0.93 (m, 15 H); ^{13}C{^{1}H} NMR (100 MHz, 298 K, DMSO-d_6): δ: 13.6 (CH_3), 13.8 (CH_3), 19.2 (CH_2), 19.7 (CH_2), 23.1 (CH_2), 30.8 (CH_2), 43.5 (CH_2), 57.5 (CH_2), 60.6 (CH_2), 182.5 (CS); IR (film): ν (cm^{-1}) = 3263 (NH stretch), 1556, 1211, 1166, 881; HRMS for the sulfonate-urea ion ($C_6H_{13}N_2O_3S_2^-$) (ESI^-): m/z: act: 225.0373 $[M]^-$ cal: 225.0360 $[M]^-$.

7. References

1 J. E. Boles, R. J. Ellaby, H. J. Shepherd and J. R. Hiscock, *RSC Adv.*, 2021, **11**, 9550–9556.

2 J. E. Boles, G. T. Williams, N. Allen, L. J. White, K. L. F. Hilton, P. I. A. Popoola, D. P. Mulvihill and J. R. Hiscock, *Adv. Ther.*, , DOI:10.1002/adtp.202200024.

3 J. E. Boles, C. Bennett, J. Baker, K. L. F. Hilton, H. A. Kotak, E. R. Clark, Y. Long, L. J. White, H. Y. Lai, C. K. Hind, J. M. Sutton, M. D. Garrett, A. Cheasty, J. L. Ortega-Roldan, M. Charles, C. J. E. Haynes and J. R. Hiscock, , DOI:10.1039/d2sc02630a.

4 N. Allen, L. J. White, J. E. Boles, G. T. Williams, D. F. Chu, R. J. Ellaby, H. J. Shepherd, K. K. L. Ng, L. R. Blackholly, B. Wilson, D. P. Mulvihill and J. R. Hiscock, *ChemMedChem*, 2020, **15**, 2193–2205.

5 T. D. James, *Front. Chem.*, 2017, **5**, 83.

6 J. -M Lehn, *Angew. Chemie Int. Ed. English*, 1988, **27**, 89–112.

7 J. W. Steed, D. R. Turner and K. J. Wallace, *Core concepts in Supramolecular Chemistry and Nanochemistry*, Wiley, Chichester, 1st edn., 2007.

8 T. D. Pollard, W. C. Earnshaw, J. Lippincott- Schwartz and G. T. Johnson, *Biophysical Principles*, Elsevier, Philadelphia, 3rd edn., 2017.

9 M. O. Sinnokrot and C. D. Sherrill, *J. Phys. Chem. A*, 2006, **110**, 10656–10668.

10 R. Thakuria, N. K. Nath and B. K. Saha, *Cryst. Growth Des.*, 2019, **19**, 523–528.

11 C. A. Hunter and J. K. M. Sanders, *J. Am. Chem. Soc.*, 2002, **112**, 5525–5534.

12 P. D. Beer, P. A. Gale and D. K. Smith, *Supramolecular Chemistry: 74*, Oxford Chemistry Press, Oxford, 1st edn., 1999.

13 M. Grzelczak, J. Vermant, E. M. Furst and L. M. Liz-Marzán, *ACS Nano*, 2010, **4**, 3591–

3605.

14 K. Szalewicz, *Hydrogen Bond*, Elsevier, California, 3rd edn., 2003.

15 J. W. Steed, J. L. Atwood and P. A. Gale, *Supramolecular Chemistry*, John Wiley & Sons, Ltd, Chichester, 2nd edn., 2012.

16 A. Klug, *Nature*, 1968, **219**, 808–844.

17 C. F. Matta, N. Castillo and R. J. Boyd, *J. Phys. Chem. B*, 2005, **110**, 563–578.

18 C. K. Mc Laughlin, G. D. Hamblin and H. F. Sleiman, *Chem. Soc. Rev.*, 2011, **40**, 5647–5656.

19 N. C. Seeman, *Nature*, 2003, **421**, 427–431.

20 C. Lin, Y. Liu and H. Yan, *Biochemistry*, 2009, **48**, 1663–1674.

21 D. Lombardo, M. A. Kiselev, S. Magazù and P. Calandra, *Adv. Condens. Matter Phys.*, , DOI:10.1155/2015/151683.

22 Y. Nakama, *Cosmetic Science and Technology: Theoretical Principles and Applications*, Elsevier Inc., Amsterdam, 1st edn., 2017.

23 S. Ghosh, A. Ray and N. Pramanik, *Biophys. Chem.*, , DOI:10.1016/J.BPC.2020.106429.

24 C. A. M. Bondi, J. L. Marks, L. B. Wroblewski, H. S. Raatikainen, S. R. Lenox and K. E. Gebhardt, *Environ. Health Insights*, 2015, **9**, 27.

25 R. De Cássia, C. Wagner and I. Joekes, *Colloids Surfaces B Biointerfaces*, 2005, **41**, 7–14.

26 K. A. Natarajan, *Biotechnology of metals : Principles, recovery methods, and environmental concerns*, Elsevier, Amsterdam, 1st edn., 2018.

27 A. Moretti, R. M. Weeks, M. Chikindas and K. E. Uhrich, *Langmuir*, 2019, **35**, 5557–5567.

28 B. Findlay, G. G. Zhanel and F. Schweizer, *Antimicrob. Agents Chemother.*, 2010, **54**,

4049–4058.

29 Y. Zhang, A. Algburi, N. Wang, V. Kholodovych, D. O. Oh, M. Chikindas and K. E. Uhrich, *Nanomedicine Nanotechnology, Biol. Med.*, 2017, **13**, 343–352.

30 T. J. Moyer, J. A. Finbloom, F. Chen, D. J. Toft, V. L. Cryns and S. I. Stupp, *J. Am. Chem. Soc.*, 2014, **136**, 14746–14752.

31 W. Kim, J. Thévenot, E. Ibarboure, S. Lecommandoux and E. L. Chaikof, *Angew. Chemie Int. Ed.*, 2010, **49**, 4257–4260.

32 M. Qi and Y. Zhou, *Mater. Chem. Front.*, 2019, **3**, 1994–2009.

33 M. Ghezzi, S. Pescina, C. Padula, P. Santi, E. Del Favero, L. Cantù and S. Nicoli, *J. Control. Release*, 2021, **332**, 312–336.

34 J. Kaur, V. Mishra, S. K. Singh, M. Gulati, B. Kapoor, D. K. Chellappan, G. Gupta, H. Dureja, K. Anand, K. Dua, G. L. Khatik and K. Gowthamarajan, *J. Control. Release*, 2021, **334**, 64–95.

35 Y. Deng, J. Wei, Z. Sun and D. Zhao, *Chem. Soc. Rev.*, 2013, **42**, 4054–4070.

36 C. Oelschlaeger, P. Suwita and N. Willenbacher, *Langmuir*, 2010, **26**, 7045–7053.

37 M. Elsabahy and K. L. Wooley, *Chem. Soc. Rev.*, 2012, **41**, 2545–2561.

38 Y. Geng, P. Dalhaimer, S. Cai, R. Tsai, M. Tewari, T. Minko and D. E. Discher, *Nat. Nanotechnol.*, 2007, **2**, 249–255.

39 C. Shan, X. Huang, H. Wei, W. Wei, H. Sun and X. Tang, *RSC Adv.*, 2014, **4**, 11216–11218.

40 Y. Kang, C. Wang, K. Liu, Z. Wang and X. Zhang, *Langmuir*, 2012, **28**, 14562–14566.

41 G. Yu, K. Jie and F. Huang, *Chem. Rev.*, 2015, 115, 7240–7303.

42 F. Huang and X. Zhang, *Mater. Chem. Front.*, 2020, **4**, 11.

43 X. Zhang, Z. Chen and F. Wü, *J. Am. Chem. Soc.*, 2007, **129**, 4886–4887.

44 Y. Chen, X. H. Pang and C. M. Dong, *Adv. Funct. Mater.*, 2010, **20**, 579–586.

45 C. Park, H. Lee, S. Lee, Y. Song, M. Rhue and C. Kim, *PNAS*, 2006, **103**, 1199–1203.

46 M. Rajagopal and S. Walker, *Curr. Top. Microbiol. Immunol.*, 2017, **404**, 1–44.

47 R. Coico, *Curr. Protoc. Microbiol.*, , DOI:10.1002/9780471729259.

48 T. J. Silhavy, *J. Bacteriol.*, 2016, **198**, 201.

49 W. Vollmer, D. Blanot and M. A. De Pedro, *FEMS Microbiol. Rev.*, 2008, **32**, 149–167.

50 S. Brown, J. P. Santa Maria and S. Walker, *Annu. Rev. Microbiol.*, 2013, **67**, 313–336.

51 N. Malanovic and K. Lohner, *Biochim. Biophys. Acta - Biomembr.*, 2016, **1858**, 936–946.

52 K. L. F. Hilton, C. Manwani, J. E. Boles, L. J. White, S. Ozturk, M. D. Garrett and J. R. Hiscock, *Chem. Sci.*, 2021, **12**, 13273–13282.

53 C. Sohlenkamp and O. Geiger, *FEMS Microbiol. Rev.*, 2016, **8**, 133–159.

54 B. Alberts, A. Johnson, J. Lewis, M. Raff, K. Roberts and P. Walter, *Molecular biology of the cell*, Garland Science, New York, 3rd edn., 2002.

55 J. Gruenberg and M. J. Clague, *Curr. Opin. Cell Biol.*, 1992, **4**, 593–599.

56 T. Harayama and H. Riezman, *Nat. Rev. Mol. Cell Biol.*, 2018, **19**, 281–296.

57 M. Aktas, L. Danne, P. Möller and F. Narberhaus, *Front. Plant Sci.*, 2014, **5**, 1–13.

58 H. Goldfine, *J. Lipid Res.*, 1984, **25**, 1501–1507.

59 K. Murzyn, T. Róg and M. Pasenkiewicz-Gierula, *Biophys. J.*, 2005, **88**, 1091–1103.

60 P. H. Ray and D. C. White, *J. Bacteriol.*, 1972, **109**, 668–677.

61 E. Deschamps, A. Schaumann, I. Schmitz-Afonso, C. Afonso, E. Dé, C. Loutelier-Bourhis and S. Alexandre, *Biochim. Biophys. Acta - Biomembr.*, 2021, **1863**, 183482.

62 C. Le Sénéchal, M. Crouzet, P. Costaglioli, C. Barthe, C. Buré and S. Vilain, *Lipids*, 2019, **54**, 519–529.

63 J. Gidden, J. Denson, R. Liyanage, D. M. Ivey and J. O. Lay, *Int. J. Mass Spectrom.*, 2009, **283**, 178–184.

64 S. Furse, H. Wienk, R. Boelens, A. I. P. M. De Kroon and J. A. Killian, *FEBS Lett.*, 2015, **589**, 2726–2730.

65 A. Okabe, Y. Hirai, H. Hayashi and Y. Kanemasa, *Biochim. Biophys. Acta - Lipids Lipid Metab.*, 1980, **617**, 28–35.

66 A. Fleming, *Bull. World Health Organ.*, 2001, **79**, 780–790.

67 C. L. Ventola, *Pharm. Ther.*, 2015, **40**, 277.

68 K. F. Kong, L. Schneper and K. Mathee, *APMIS*, 2010, **118**, 1–36.

69 S. Arenz and D. N. Wilson, *Cold Spring Harb. Perspect. Med.*, 2016, **6**, 1–10.

70 E. A. Campbell, N. Korzheva, A. Mustaev, K. Murakami, S. Nair, A. Goldfarb and S. A. Darst, *Cell*, 2001, **104**, 901–912.

71 A. Fàbrega, S. Madurga, E. Giralt and J. Vila, *Microb. Biotechnol.*, 2009, **2**, 40.

72 R. M. Epand, C. Walker, R. F. Epand and N. A. Magarvey, *Biochim. Biophys. Acta - Biomembr.*, 2016, **1858**, 980–987.

73 P. Brown and M. J. Dawson, *Nat. Publ. Gr.*, 2017, **70**, 386–394.

74 A. P. Zavascki, L. Z. Goldani, J. Li and R. L. Nation, *J. Antimicrob. Chemother.*, 2007, **60**, 1206–1215.

75 H. Ullah and S. Ali, *Classification of Anti-Bacterial Agents and Their Functions*, IntechOpen, London, 1st edn., 2017.

76 C. Dias and A. P. Rauter, *Future Med. Chem.*, 2019, **11**, 211–228.

77 J. Lei, L. C. Sun, S. Huang, C. Zhu, P. Li, J. He, V. Mackey, D. H. Coy and Q. Y. He, *Am. J. Transl. Res.*, 2019, **11**, 3919.

78 A. A. Bahar and D. Ren, *Pharmaceuticals*, 2013, **6**, 1543.

79 J. Li, J. J. Koh, S. Liu, R. Lakshminarayanan, C. S. Verma and R. W. Beuerman, *Front. Neurosci.*, , DOI:10.3389/FNINS.2017.00073.

80 E. V. K. Ledger, A. Sabnis and A. M. Edwards, *Microbiology*, 2022, **168**, 1136.

81 R. M. Humphries, S. Pollett and G. Sakoulas, *Clin. Microbiol. Rev.*, 2013, **26**, 759–780.

82 J. Micklefield, *Chem. Biol.*, 2004, **11**, 887–888.

83 G. M. Matar, J. Fishovitz, B. Bakhshi, E. Adel Rahal, N. Rizk, J. Legault JeanLegault, H. Côté, A. Pichette, F. Simard, M.-E. Ouellette, L. Ripoll, M. Mihoub, D. Grimard and J. Legault, , DOI:10.3389/fmicb.2019.02341.

84 N. Rosenblatt-Farrell, *Environ. Health Perspect.*, 2009, **117**, 244.

85 E. D. Brown and G. D. Wright, *Nature*, 2016, 529, 336–343.

86 L. J. Shallcross and D. S. C. Davies, *Br. J. Gen. Pract.*, 2014, **64**, 604–605.

87 C. Llor and L. Bjerrum, *Ther. Adv. Drug Saf.*, 2014, **5**, 229–241.

88 C. Manyi-Loh, S. Mamphweli, E. Meyer and A. Okoh, *Molecules*, 2018, **4**, 23.

89 J. O'Neill, *Rev. Antimicrob. Resist.*, 2016, **1**, 1–16.

90 C. J. Murray, K. S. Ikuta, F. Sharara, L. Swetschinski and G. Robles Aguilar, *Lancet*, 2022, **399**, 629–655.

91 WHO publishes list of bacteria for which new antibiotics are urgently needed, https://www.who.int/news/item/27-02-2017-who-publishes-list-of-bacteria-for-which-new-antibiotics-are-urgently-needed, (accessed 20 April 2022).

92 A. K. Sarmah, M. T. Meyer and A. B. A. Boxall, *Chemosphere*, 2006, **65**, 725–759.

93 B. M. Marshall and S. B. Levy, *Clin. Microbiol. Rev.*, 2011, **24**, 718–733.

94 E. Charani and A. Holmes, *Antibiotics*, 2019, 8, 1–9.

95 L. L. Silver, *Clin. Microbiol. Rev.*, 2011, **24**, 71–109.

96 M. J. Renwick, D. M. Brogan and E. Mossialos, *J. Antibiot. (Tokyo).*, 2016, **69**, 73–88.

97 J. M. Munita and C. A. Arias, *Microbiol. Spectr.*, 2016, **23**, 464–472.

98 W. C. Reygaert, *AIMS Microbiol.*, 2018, **4**, 482.

99 D. Sharma, L. Misba and A. U. Khan, *Antimicrob. Resist. Infect. Control 2019 81*, 2019, **8**, 1–10.

100 E. Peterson and P. Kaur, *Front. Microbiol.*, 2018, **9**, 2928.

101 J. B. McPhee, S. Tamber, M. D. Brazas, S. Lewenza and R. E. W. Hancock, *Antimicrob. Drug Resist.*, 2009, 97–110.

102 M. Zhang, P.-P. Zhu, P. Xin, W. Si, Z.-T. Li and J.-L. Hou, *Angew. Chemie Int. Ed.*, 2017, **56**, 2999–3003.

103 H. S. El-Sheshtawy, S. Chatterjee, K. I. Assaf, M. N. Shinde, W. M. Nau and J. Mohanty, *Sci. Rep.*, 2018, **8**, 13925.

104 C. Limban, M. C. Chifiriuc, M. T. Caproiu, F. Dumitrascu, M. Ferbinteanu, L. Pintilie, A. Stefaniu, I. M. Vlad, C. Bleotu, L. G. Marutescu and D. C. Nuta, *Molecules*, 2020, **25**, 1478.

105 M. Patil, A. Noonikara-Poyil, S. D. Joshi, S. A. Patil, S. A. Patil and A. Bugarin, *Antibiotics*, 2019, **8**, 4.

106 K. Pandurangan, J. A. Kitchen, S. Blasco, F. Paradisi and T. Gunnlaugsson, *Chem. Commun.*, 2014, **50**, 10819–10822.

107 A. Scozzafava, A. Mastrolorenzo, C. T. Supuran, A. Mastrolorenzob and C. T. Supljran, *Journnl Enzym. Inhib.*, 2010, **16**, 425432.

108 C. M. C. Faustino, A. R. T. Calado and L. Garcia-Rio, *J. Phys. Chem. B*, 2009, **113**, 977–982.

109 C. Faustino, C. Serafim, I. Ferreira, L. Pinheiro and A. Calado, *Colloids Surfaces A Physicochem. Eng. Asp.*, 2015, **480**, 426–432.

110 J. R. Hiscock, G. P. Bustone, B. Wilson, K. E. Belsey and L. R. Blackholly, *Soft Matter*, 2016, **12**, 4221–4228.

111 L. R. Blackholly, H. J. Shepherd and J. R. Hiscock, *CrystEngComm*, 2016, **37**, 7021–7028.

112 L. J. White, S. N. Tyuleva, B. Wilson, H. J. Shepherd, K. K. L. Ng, S. J. Holder, E. R. Clark and J. R. Hiscock, *Chem. - A Eur. J.*, 2018, **24**, 7761–7773.

113 L. J. White, N. J. Wells, L. R. Blackholly, H. J. Shepherd, B. Wilson, G. P. Bustone, T. J. Runacres and J. R. Hiscock, *Chem. Sci.*, 2017, **8**, 7620–7630.

114 K. K. L. Ng, M. Dimitrovski, J. E. Boles, R. J. Ellaby, L. J. White and J. R. Hiscock, *Supramol. Chem.*, 2020, **32**, 414–424.

115 L. J. White, J. E. Boles, M. Clifford, B. L. Patenall, K. H. L. F. Hilton, K. K. L. Ng, R. J. Ellaby, C. K. Hind, D. P. Mulvihill and J. R. Hiscock, *Chem. Commun.*, 2021, **57**, 11839–11842.

116 J. J. P. Stewart, *J. Mol. Model.*, 2007, **13**, 1173–1213.

117 S. N. Tyuleva, N. Allen, L. J. White, H. J. Shepherd, P. J. Saines, R. J. Ellaby, D. P. Mulvihill and J. R. Hiscock, 2019, **2**, 95–98.

118 B. Mott, D. Payne, M. Riley, A. Rubio, S. Therapeutics, L. Silver, L. Silver Consulting, J. Silverman, J. Sutcliffe, T. Pharmaceuticals, A. Tomaras, R. Tommasi, E. Therapeutics and D. Zurawski, *A report from A Scientific Roadmap for Antibiotic Discovery*, 2016.

119 L. Bock, C. Hind, J. Sutton, M. Wand, M. Wand and L. J. Bock, *Lett. Appl. Microbiol.*, 2018, **66**, 368–377.

120 J. P. Torella, R. Chait and R. Kishony, *PLoS Comput Biol*, 2010, **6**, 1000796.

121 Q. Yu, T. Deng, F. C. Lin, B. Zhang and J. I. Zink, *ACS Nano*, 2020, **14**, 5926–5937.

122 F. Wu, D. He, L. Chen, F. Liu, H. Huang, J. Dai, S. Zhang and J. You, *RSC Adv.*, 2018, **8**, 20829–20835.

123 W. Sim, R. T. Barnard, M. A. T. Blaskovich and Z. M. Ziora, *Antibiotics*, 2018, 7, 93–99.

124 C. Aisenbrey, M. Amaro, M. Hof and & B. Bechinger, 2020, **10**, 11652.

125 K. Matsuzaki, Y. Mitani, K. Y. Akada, O. Murase, S. Yoneyama, M. Zasloff and K. Miyajima, *Biochemistry*, 1998, **37**, 15144–15153.

126 L. J. White, J. E. Boles, K. L. F. Hilton, R. J. Ellaby and J. R. Hiscock, *Molecules*, 2020, **25**, 4126.

127 N. O. Dora, E. Blackburn, J. E. Boles, G. T. Williams, L. J. White, S. E. G. Turner, J. D. Hothersall, T. Askwith, J. A. Doolan, D. P. Mulvihill, M. D. Garrett and J. R. Hiscock, *RSC Adv.*, 2021, **11**, 14213–14217.

128 G. S. Timmins and V. Deretic, *Mol. Microbiol.*, 2006, 62, 1220–1227.

129 N. Pandey and M. Cascella, *Antibiot. Discov. Dev.*, 2022, **9781461414001**, 79–117.

130 D. Kaushik, M. Mohan, D. M. Borade and O. C. Swami, *J. Clin. Diagnostic Res.*, 2014, **8**, 1–3.

131 X. Zeng and J. Lin, *Front. Microbiol.*, 2013, **4**, 128.

132 N. Malanovic, A. Ön, G. Pabst, A. Zellner and K. Lohner, *Int. J. Antimicrob. Agents*, 2020, **56**, 106146.

133 S. Dasari and P. Bernard Tchounwou, *Eur. J. Pharmacol.*, 2014, **740**, 364.

134 N. Chowdhury, T. L. Wood, M. Martínez-Vázquez, R. García-Contreras and T. K. Wood, *Biotechnol. Bioeng.*, 2016, **113**, 1984–92.

135 I. Sarcevica, L. Orola, M. V. Veidis and S. Belyakov, *Acta Crystallogr. Sect. C Struct. Chem.*, 2014, **70**, 392–395.

136 L. J. White, J. E. Boles, N. Allen, L. S. Alesbrook, J. M. Sutton, C. K. Hind, K. L. F. Hilton, L. R. Blackholly, R. J. Ellaby, G. T. Williams, D. P. Mulvihill and J. R. Hiscock, *J. Mater. Chem. B*, 2020, **8**, 4694–4700.

137 A. A. Crook and R. Powers, *Molecules*, 2020, **25**, 5128–5133.

138 B. U. Jaki, A. Bzhelyansky and G. F. Pauli, *Magn. Reson. Chem.*, 2021, **59**, 7–15.

139 S. K. Bharti and R. Roy, *TrAC Trends Anal. Chem.*, 2012, **35**, 5–26.

140 L. K. S. Von Krbek, C. A. Schalley and P. Thordarson, *Chem. Soc. Rev.*, 2017, 46, 2622–2637.

141 M. P. Evstigneev, A. S. Buchelnikov, V. V. Kostjukov, I. S. Pashkova and V. P. Evstigneev, *Supramol. Chem.*, 2013, **25**, 199–203.

142 R. B. Martin, *Chem. Rev.*, 1996, **96**, 3043–3064.

143 Supramolecular.org - Binding Constant Calculators, http://supramolecular.org/, (accessed 1 June 2020).

144 P. A. Gale, J. R. Hiscock, N. Lalaoui, M. E. Light, N. J. Wells and M. Wenzel, *Org. Biomol. Chem.*, 2012, **10**, 5909–5915.

145 B. Lorber, F. Fischer, M. Bailly, H. Roy and D. Kern, *Biochem. Mol. Biol. Educ.*, 2012, **40**, 372–382.

146 J. Stetefeld, S. A. McKenna and T. R. Patel, *Biophys. Rev.*, 2016, 8, 409–427.

147 S. Bhattacharjee, *J. Control. Release*, 2016, 235, 337–351.

148 R. Papadakis and I. Deligkiozi, *Solvent Effects in Supramolecular Systems*, IntechOpen, London, 1st edn., 2020.

149 D. R. Perinelli, M. Cespi, N. Lorusso, G. F. Palmieri, G. Bonacucina and P. Blasi, *Langmuir*, 2020, **36**, 5745–5753.

150 E. Ruckenstein and R. Nagarajan, *J. Phys. Chem.*, 1975, **79**, 2622–2626.

151 Á. Piñeiro, X. Banquy, S. Pérez-Casas, E. Tovar, A. García, A. Villa, A. Amigo, A. E. Mark and M. Costas, *J. Phys. Chem. B*, 2007, **111**, 4383–4392.

152 J. J. Sheng, *Modern Chemical Enhanced Oil Recovery*, Elsevier, Amsterdam, 1st edn., 2011.

153 S. G. Patel, M. D. Patel, A. J. Patel, M. B. Chougule and H. Choudhury, *Nanotechnology-Based Target. Drug Deliv. Syst. Brain Tumors*, 2018, **59**, 191–244.

154 A. J. Shnoudeh, I. Hamad, R. W. Abdo, L. Qadumii, A. Y. Jaber, H. S. Surchi and S. Z. Alkelany, *Synthesis, Characterization, and Applications of Metal Nanoparticles*, Academic Press, Cambridge, 2019.

155 J. D. Clogston and A. K. Patri, *Methods Mol. Biol.*, 2011, **697**, 63–70.

156 G. W. Lu and P. Gao, *Emulsions and Microemulsions for Topical and Transdermal Drug Delivery*, William Andrew Publishing, Norwcih, 1st edn., 2010.

157 N. Raval, R. Maheshwari, D. Kalyane and R. K.Tekade, *Basic Fundamentals of Drug Delivery*, Academic Press, Cambridge, 1st edn., 2019.

158 F. Huang, J. R. Spangler and A. Y. Huang, *PLoS One*, 2017, **12**, e0183974.

159 Z. Breijyeh, B. Jubeh and R. Karaman, *Molecules*, 2020, 25, 1340.

160 E. Tacconelli, E. Carrara, A. Savoldi, S. Harbarth and M. Mendelson, *Lancet Infect. Dis.*, 2018, **18**, 318–327.

161 R. Thombre, V. Tiwari, R. Bhalchandra Patwardhan, K. R. Pardesi, M. S. Mulani, E. E. Kamble, S. N. Kumkar and M. S. Tawre, *Front. Microbiol.*, 2019, **1**, 539.

162 S. Santajit and N. Indrawattana, *Biomed Res. Int.*, 2016, **2016**, 2475067.

163 K. M. Papp-Wallace, A. Endimiani, M. A. Taracila and R. A. Bonomo, *Antimicrob. Agents Chemother.*, 2011, **55**, 4943.

164 P. Bernal, C. Molina-Santiago, A. Daddaoua and M. A. Llamas, *Microb. Biotechnol.*, 2013, **6**, 445.

165 C. González-Bello, *Bioorg. Med. Chem. Lett.*, 2017, **27**, 4221–4228.

166 L. W. Chan, K. E. Hern, C. Ngambenjawong, K. Lee, E. J. Kwon, D. T. Hung and S. N. Bhatia, *ACS Infect. Dis.*, 2021, **7**, 721–732.

167 W. C. Wimley, *ACS Chem. Biol*, 2010, **5**, 905–917.

168 S. French, M. Farha, M. J. Ellis, Z. Sameer, J. P. Côté, N. Cotroneo, T. Lister, A. Rubio and E. D. Brown, *ACS Infect. Dis.*, 2020, **6**, 1405–1412.

169 S. Sharma, R. Rao, S. M. Reeve, G. A. Phelps, N. Bharatham, N. Katagihallimath, V. Ramachandran, S. Raveendran, M. Sarma, A. Nath, T. Thomas, D. Manickam, S. Nagaraj, V. Balasubramanian, R. E. Lee, S. Hameed P and S. Datta, *ACS Infect. Dis.*, 2021, **7**, 3009–3024.

170 G. Dimopoulos, G. De Pascale, A. Afonso, G. Poulakou, I. Karaiskos, S. Lagou, K. Pontikis and V. Rapti, *Front. Public Heal. | www.frontiersin.org*, 2019, **1**, 151.

171 S. M. Opal and A. Pop-Vicas, *Mand. Douglas, Bennett's Princ. Pract. Infect. Dis.*, 2015, **1**, 235-251.e3.

172 J. M. May, T. W. Owens, M. D. Mandler, B. W. Simpson, M. B. Lazarus, D. J. Sherman, R. M. Davis, S. Okuda, W. Massefski, N. Ruiz and D. Kahne, *J. Am. Chem. Soc.*, 2017, **139**, 17221–17224.

173 Y. Liu, R. Li, X. Xiao and Z. Wang, *Crit Rev Microbiol.*, 2019, **45**, 301–314.

174 M. Bassetti, A. Vena, A. Croxatto, E. Righi and B. Guery, *Drugs Context.*, 2018, **7**, 25–31.

175 I. Wiegand, K. Hilpert and R. E. W. Hancock, *Nat. Protoc.*, 2008, **3**, 163–175.

176 R. Srikumar, T. Kon, N. Gotoh and K. Poole, *Antimicrob. Agents Chemother.*, 1998, **42**, 65–71.

177 A. Sugino, N. P. Higginst, P. 0 Brownt, C. L. Peeblesf and N. R. Cozzarellitf, *Biochemistry*, 1978, **75**, 4838–4842.

178 H. W. Boucher, G. H. Talbot, J. S. Bradley, J. E. Edwards, D. Gilbert, L. B. Rice, M. Scheld, B. Spellberg and J. Bartlett, *Clin. Infect. Dis.*, 2009, **48**, 1–12.

179 Z. Pang, R. Raudonis, B. R. Glick, T. J. Lin and Z. Cheng, *Biotechnol. Adv.*, 2019, **37**, 177–192.

180 Y. Tashiro, A. Inagaki, M. Shimizu, S. Ichikawa, N. Takaya, T. Nakajima-Kambe, H. Uchiyama and N. Nomura, *Biosci. Biotechnol. Biochem.*, 2011, **75**, 605–607.

181 S. Hiraoka, H. Matsuzaki and I. Shibuya, *FEBS Lett.*, 1993, **336**, 221–224.

182 J. Pogliano, N. Osborne, M. D. Sharp, A. A. De Mello, A. Perez, Y. L. Sun and K. Pogliano, *Mol. Microbiol.*, 1999, **31**, 1149–1159.

183 G. Orhan, A. Bayram, Y. Zer and I. Balci, *J. Clin. Microbiol.*, 2005, **43**, 140–143.

184 P. Wah Tang, P. San Chua, S. Kee Chong, M. Saberi Mohamad, Y. Wen Choon, S. Deris, S. Omatu, J. Manuel Corchado, W. Howe Chan and R. Abdul Rahim, *Recent Pat. Biotechnol.*, 2016, **9**, 176–197.

185 L. E. Bickerton, T. G. Johnson, A. Kerckhoffs and M. J. Langton, *Chem. Sci.*, 2021, **12**, 11252–11274.

186 E. S. Williams, H. Gneid, S. R. Marshall, M. J. González, J. A. Mandelbaum and N.

Busschaert, *Org. Biomol. Chem.*, , DOI:10.1039/d1ob02298a.

187 S. R. Herschede, H. Gneid, T. Dent, E. B. Jaeger, L. B. Lawson and N. Busschaert, *Org. Biomol. Chem.*, 2021, **19**, 3838–3843.

188 J. Lou, X. Zhang and M. D. Best, *Chem. – A Eur. J.*, 2019, **25**, 20–25.

189 I. Carreira-Barral, C. Rumbo, M. Mielczarek, D. Alonso-Carrillo, E. Herran, M. Pastor, A. Del Pozo, C. Marí A Garcí A-Valverde and R. Quesada, *Chem. Commun*, 2019, **55**, 10080.

190 P. A. Gale, J. T. Davis and R. Quesada, *Chem. Soc. Rev.*, 2017, **46**, 2497–2519.

191 G. Townshend, G. S. Thompson, L. J. White, J. R. Hiscock and J. L. Ortega-Roldan, *Chem. Commun.*, 2020, **56**, 4015–4018.

192 M. Aktas, M. Wessel, S. Hacker, S. Klüsener, J. Gleichenhagen and F. Narberhaus, *Eur. J. Cell Biol.*, 2010, **89**, 888–894.

193 E. coli Extract Polar, https://avantilipids.com/product/100600, (accessed 1 March 2022).

194 E. coli Extract Total, https://avantilipids.com/product/100500, (accessed 1 March 2022).

195 M. Sauer, J. Hofkens and J. Enderlein, *Handbook of Fluorescence Spectroscopy and Imaging: From Single Molecules to Ensembles*, Hoboken, Wiley., 2011.

196 W. Bae, T. Y. Yoon and C. Jeong, *PLoS One*, 2021, **16**, 1–8.

197 S. Dutta, B. Watson, S. Mattoo and J.-C. Rochet, *Bio-protocol*, 2020, **10**, 3690.

198 S. Fiedler and H. Heerklotz, *Biophys. J.*, 2015, **109**, 2079–89.

199 D. Koley and A. J. Bard, *Proc. Natl. Acad. Sci. U. S. A.*, 2010, **107**, 16783–16787.

200 K. Feng, R. E. Quevedo, J. T. Kohrt, M. S. Oderinde, U. Reilly and M. C. White, *Nature*, 2020, **580**, 621–627.

201 H. Schönherr and T. Cernak, *Angew. Chem. Int. Ed. Engl.*, 2013, **52**, 12256–12267.

202 J. Dudek, *Front. Cell Dev. Biol.*, 2017, **5**, 90.

203 M. D. Hall, A. Yasgar, T. Peryea, J. C. Braisted, A. Jadhav, A. Simeonov and N. P. Coussens, *Methods Appl. Fluoresc.*, 2016, 4, 2–8.

204 O. D. Hendrickson, N. A. Taranova, A. V Zherdev, B. B. Dzantiev and S. A. Eremin, *Sensors*, 2020, **20**, 7132.

205 W. A. Lea and A. Simeonov, *Expert Opin. Drug Discov.*, 2011, **6**, 17–32.

206 Membrane Fluidity Measurements on a Plate Reader, BMG LABTECH, https://www.bmglabtech.com/membrane-fluidity-measurement-using-uv-fluorescence-polarization/, (accessed 4 March 2022).

207 N. J. Moerke, *Curr. Protoc. Chem. Biol.*, 2009, **1**, 1–15.

208 J. R. Lakowicz, *Principles of fluorescence spectroscopy*, Springer, New York, 3rd edn., 2006.

209 N. C. S. Mykytczuk, J. T. Trevors, L. G. Leduc and G. D. Ferroni, *Prog. Biophys. Mol. Biol.*, 2007, **95**, 60–82.

210 W. Dowhan, *Annu. Rev. Biochem.*, 1997, **66**, 199–232.

211 M. K. Choi, S. Son, M. Hong, M. S. Choi, J. Y. Kwon and J. Lee, *Genetics*, 2016, **202**, 1411–1420.

212 A. B. Schäfer and M. Wenzel, *Front. Cell. Infect. Microbiol.*, 2020, **10**, 540898.

213 M. Kates and L. A. Manson, *Membrane fluidity*, Springer, New York, 1st edn., 1984.

214 M. Adler and T. R. Tritton, *Biophys. J.*, 1988, **53**, 989–1005.

215 A. V. Koulov, T. N. Lambert, R. Shukla, M. Jain, J. M. Boon, B. D. Smith, H. Li, D. N. Sheppard, J. B. Joos, J. P. Clare and A. P. Davis, *Angew. Chem. Int. Ed. Engl.*, 2003, **42**,

4931–4933.

216 J. Pan, F. A. Heberle, S. Tristram-Nagle, M. Szymanski, M. Koepfinger, J. Katsaras and N. Kučerka, *Biochim. Biophys. Acta - Biomembr.*, 2012, **1818**, 2135–2148.

217 Phase Transition Temperatures for Glycerophospholipids | Avanti Polar Lipids, https://avantilipids.com/tech-support/physical-properties/phase-transition-temps, (accessed 4 March 2022).

218 W. Chen, F. Duša, J. Witos, S. K. Ruokonen and S. K. Wiedmer, *Sci. Rep.*, 2018, **8**, 14815.

219 S. J. Moore, M. Wenzel, M. E. Light, R. Morley, S. J. Bradberry, P. Gómez-Iglesias, V. Soto-Cerrato, R. Pérez-Tomás and P. A. Gale, *Chem. Sci.*, 2012, **3**, 2501–2509.

220 K. Yang, J. E. Boles, L. J. White, K. L. F. Hilton, H. Y. Lai, Y. Long, J. R. Hiscock and C. J. E. Haynes, *ChemRxiv*, , DOI:10.26434/CHEMRXIV-2021-RPXHS-V2.

221 M. Kreir, C. Farre, M. Beckler, M. George and N. Fertig, *Lab Chip*, 2008, **8**, 587–595.

222 A. Molleman, *Patch Clamping*, Wiley, New Jersey, 1st edn., 2002.

223 T. Bhatia, P. Husen, J. Brewer, L. A. Bagatolli, P. L. Hansen, J. H. Ipsen and O. G. Mouritsen, *Biochim. Biophys. Acta - Biomembr.*, 2015, **1848**, 3175–3180.

224 H. Stein, S. Spindler, N. Bonakdar, C. Wang and V. Sandoghdar, *Front. Physiol.*, 2017, **8**, 63–66.

225 V. Pereno, D. Carugo, L. Bau, E. Sezgin, J. Bernardino De La Serna, C. Eggeling and E. Stride, *ACS Omega*, 2017, **2**, 994–1002.

226 S. Kara, S. Afonin, O. Babii, A. N. Tkachenko, I. V. Komarov and A. S. Ulrich, *Biochim. Biophys. Acta - Biomembr.*, 2017, **1859**, 1828–1837.

227 L. Sessa, S. Concilio, M. Di Martino, A. M. Nardiello, Y. Miele, F. Rossi, J. Brunetti, B. Panunzi and S. Piotto, *Dye. Pigment.*, 2021, **196**, 109759.

228 T. H. Steinberg, *Methods Enzymol.*, 2009, **463**, 541–563.

229 M. A. de Ménorval, L. M. Mir, M. L. Fernández and R. Reigada, *PLoS One*, 2012, **7**, 41733.

230 N. W. Davies, in *Encyclopedia of Biophysics*, Springer, Berlin, 1st edn., 2013, pp. 1825–1832.

231 B. A. Maki, K. A. Cummings, M. A. Paganelli, S. E. Murthy and G. K. Popescu, *J. Vis. Exp.*, 2014, **88**, 51629.

232 E. Gazit, I. R. Miller, P. C. Biggin, M. S. P. Sansom and Y. Shai, *J. Mol. Biol.*, 1996, **258**, 860–870.

233 K. A. Brogden, *Nat. Rev. Microbiol.*, 2005, **3**, 238–250.

234 G. M. Sheldrick, *Acta Crystallogr. Sect. A Found. Crystallogr.*, 2015, **71**, 3–8.

235 G. M. Sheldrick, *Acta Crystallogr. Sect. C Struct. Chem.*, 2015, **71**, 3–8.

236 O. V. Dolomanov, L. J. Bourhis, R. J. Gildea, J. A. K. Howard and H. Puschmann, *J. Appl. Crystallogr.*, 2009, **42**, 339–341.

237 A. Rutkauskaite, L. J. White, K. L. F. Hilton, G. Picci, L. Croucher, C. Caltagirone and J. R. Hiscock, *Org. Biomol. Chem.*, , DOI:10.1039/d2ob00066k.

Appendix

Table of contents

1 Chapter 2 Appendix

1.1 Characterisation NMR

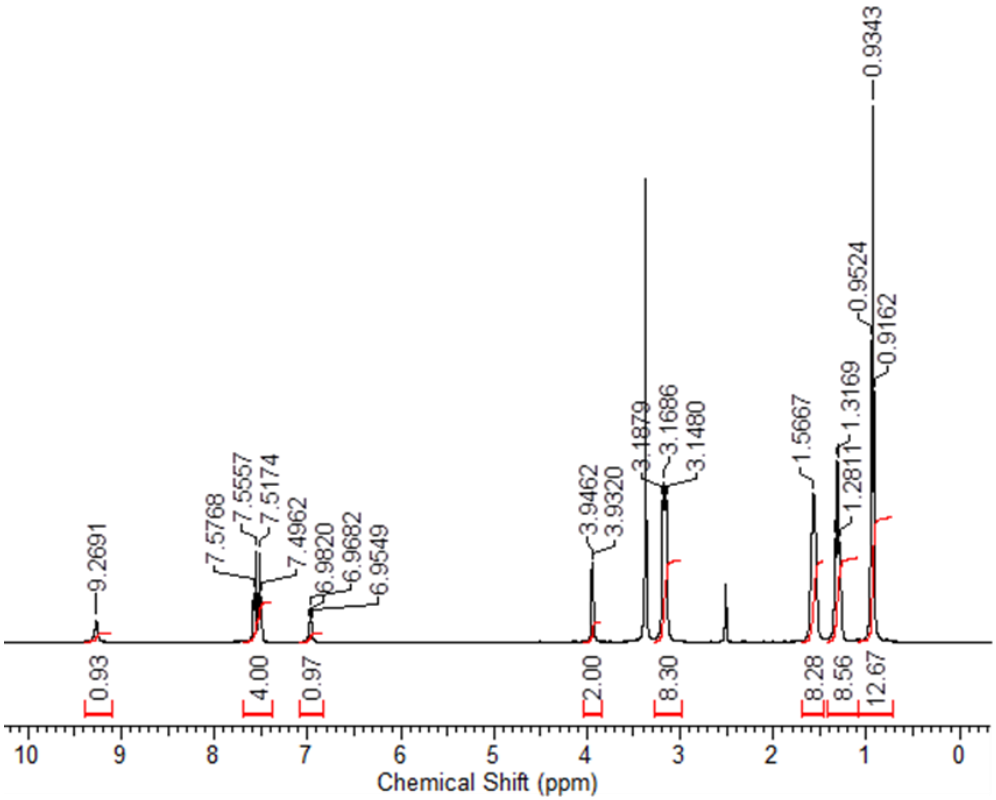

Figure S1 - ^{1}H NMR of compound **42** in DMSO-d_6 conducted at 298 K.

1.2 Quantitative ^{1}H NMR Spectroscopy

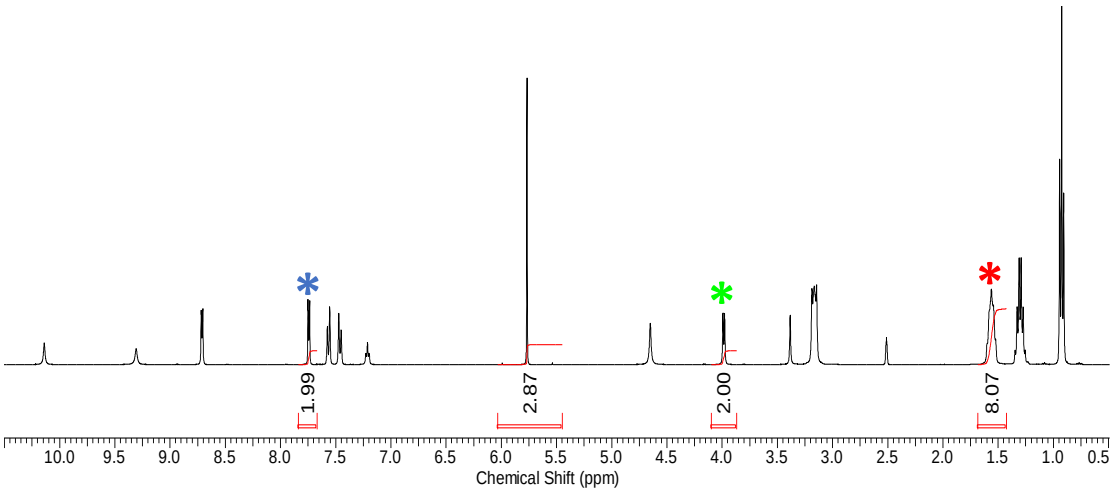

Figure S2 - ^{1}H NMR spectrum with a delay (d_1 = 60 s) of co-formulation **a** (111.4 mM) in DMSO-d_6/ 1.0 % DCM. Comparative integration indicated 0 % of the sample has become NMR silent. (**Isoniazid***, anionic component of SSA **42***, TBA counter cation*).

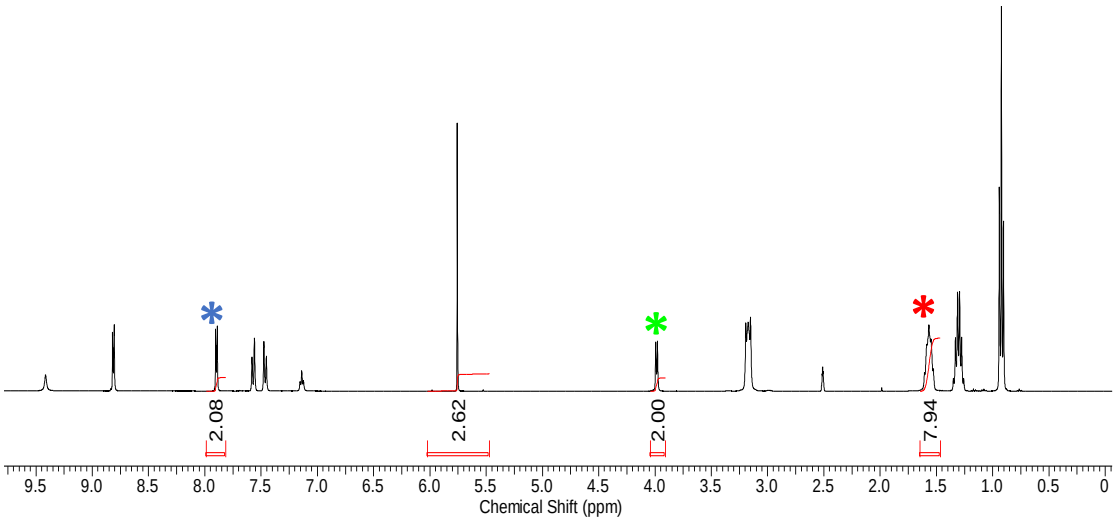

Figure S3 - ^{1}H NMR spectrum with a delay (d_1 = 60 s) of co-formulation **b** (122.1 mM) in DMSO-d_6/ 1.0 % DCM. Comparative integration indicated 0 % of the sample has become NMR silent. (**Isoniazid hydrogen chloride***, anionic component of SSA **42***, TBA countercation*).

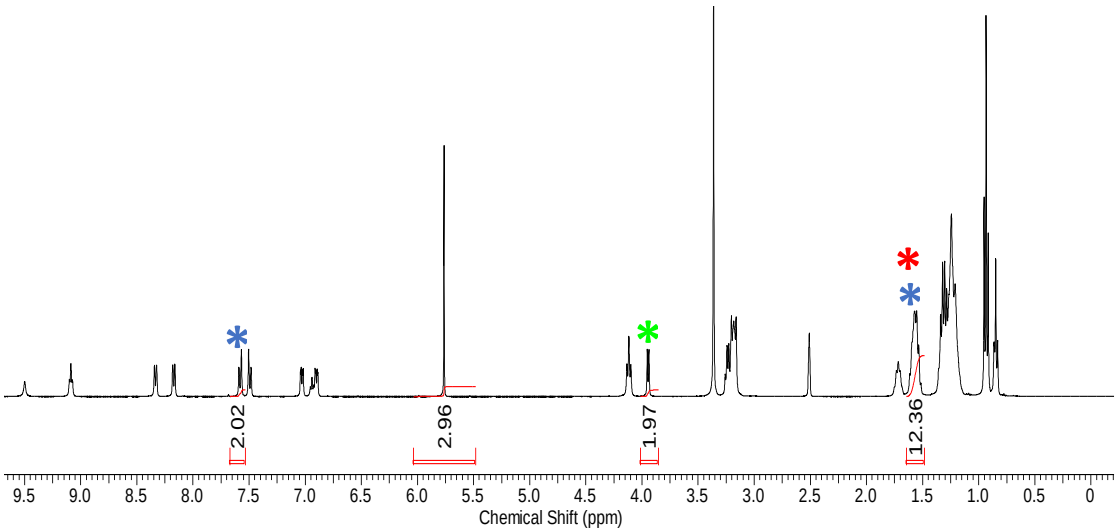

Figure S4 - ^{1}H NMR spectrum with a delay (d_1 = 60 s) of co-formulation **c** (108.1 mM) in DMSO-d_6/ 1.0 % DCM. Comparative integration indicated 0 % of the sample has become NMR silent. (**Octenidine dihydrochloride***, anionic component of SSA **42***, TBA countercation*).

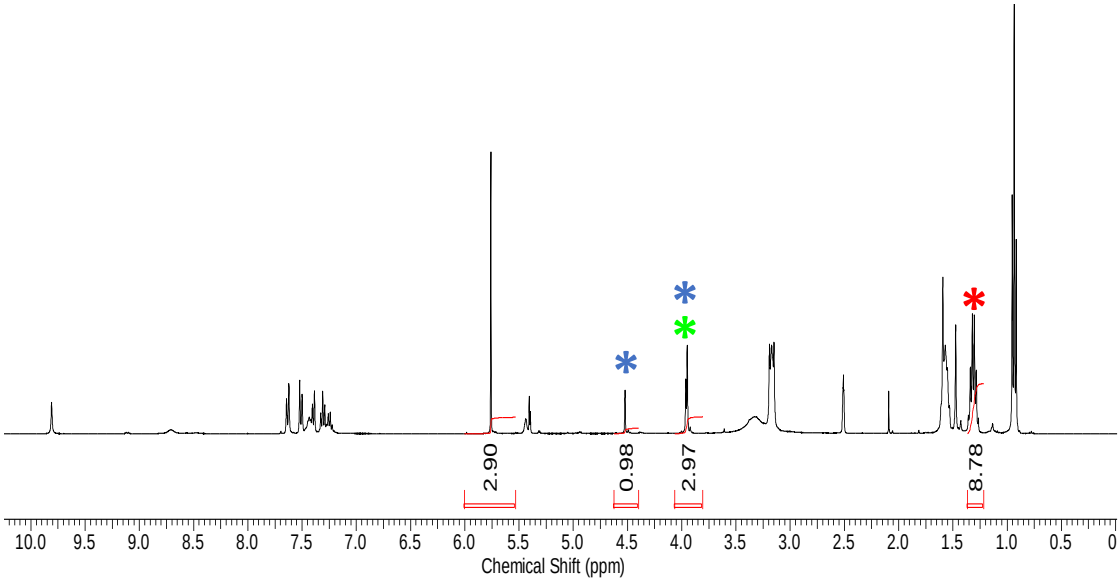

Figure S5 - ^{1}H NMR spectrum with a delay (d_1 = 60 s) of co-formulation **d** (110.0 mM) in DMSO-d_6/ 1.0 % DCM. Comparative integration indicated 0 % of the sample has become NMR silent. (**Ampicillin***, anionic component of SSA **42***, TBA countercation*).

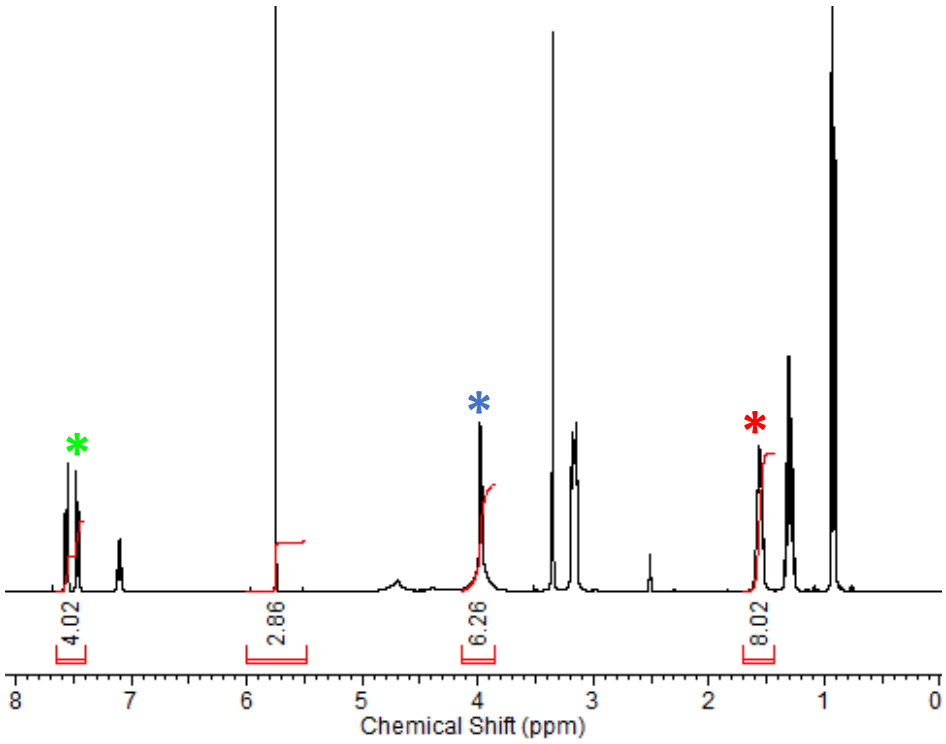

Figure S6 - ^{1}H NMR spectrum with a delay (d_1 = 60 s) of co-formulation **e** (111.8 mM) in DMSO-d_6/ 1.0 % DCM. Comparative integration indicated 0 % of sample has become NMR silent (anionic component SSA **42***, TBA countercation* and **cisplatin***).

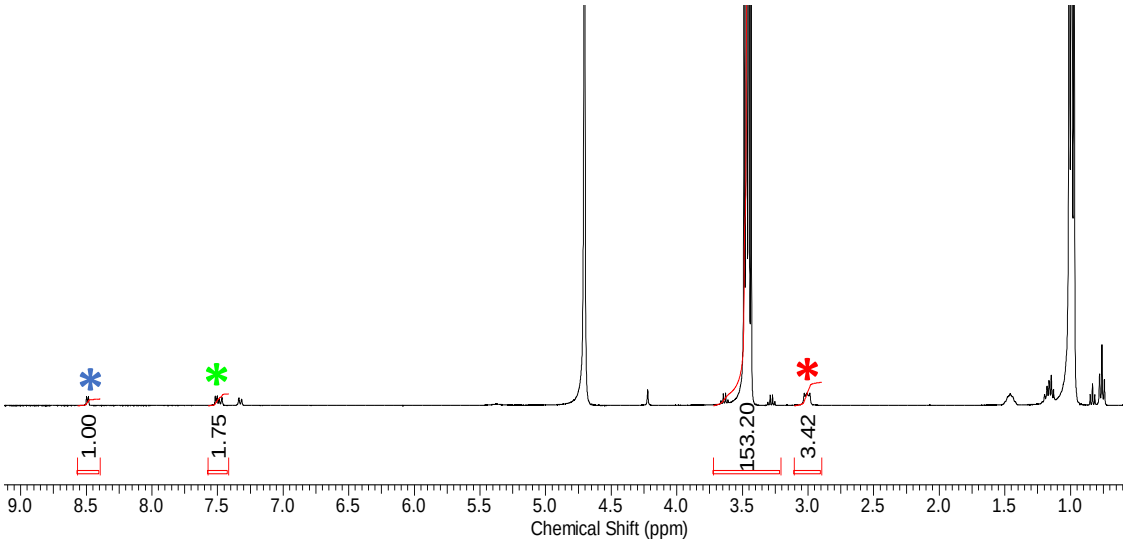

Figure S7 - ^{1}H NMR spectrum with a delay (d_1 = 60 s) of co-formulation **a** (5.61 mM) in D_2O/ 5.0 % EtOH. Comparative integration indicated 56 % of the anionic component of the SSA, 57 % of TBA countercation and 50 % of the isoniazid has become NMR silent. (**Isoniazid***, anionic component of the SSA*, TBA countercation*).

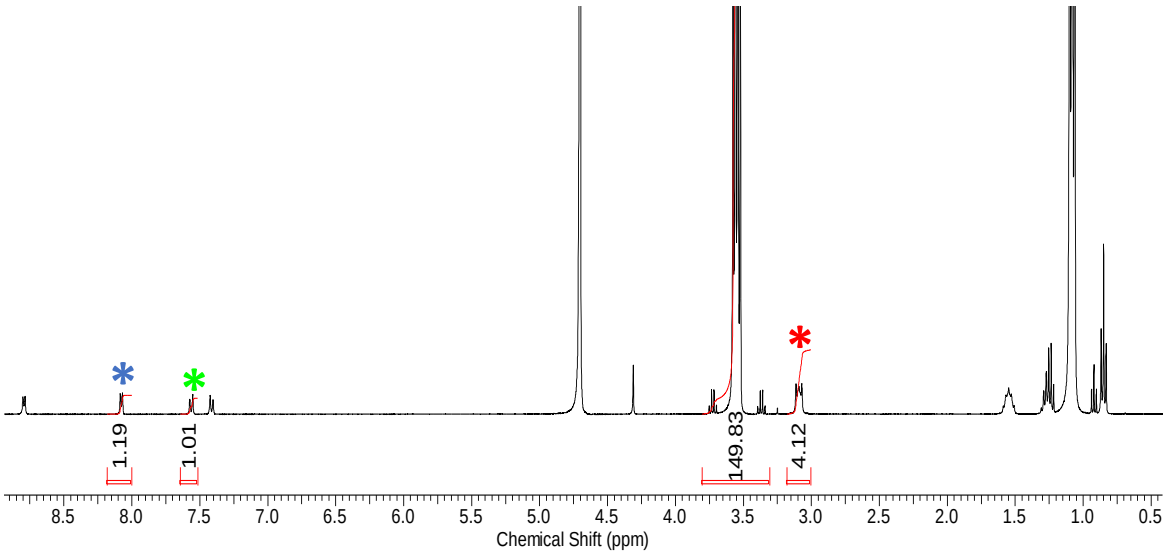

Figure S8 - ^{1}H NMR spectrum with a delay (d_1 = 60 s) of co-formulation **b** (5.61 mM) in D_2O/ 5.0 % EtOH. Comparative integration indicated 50 % of the anionic component of the SSA, 49 % of TBA countercation and 41 % of the **isoniazid hydrogen chloride** has become NMR silent. (**Isoniazid hydrogen chloride***, anionic component of SSA **42***, TBA countercation*).

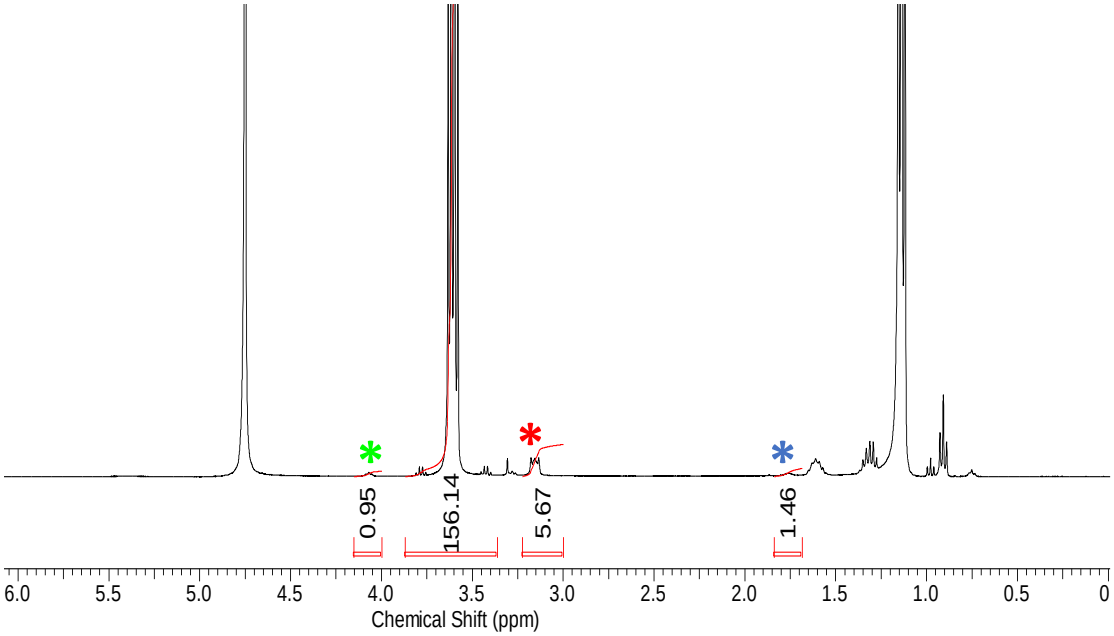

Figure S9 - ^{1}H NMR spectrum with a delay (d_1 = 60 s) of co-formulation **c** (5.51 mM) in D_2O/ 5.0 % EtOH. Comparative integration indicated 53 % of the anionic component of the SSA, 29 % of TBA countercation and 64 % of the **octenidine dihydrochloride** has become NMR silent. (**Octenidine dihydrochloride***, anionic component of SSA **42***, TBA countercation*).

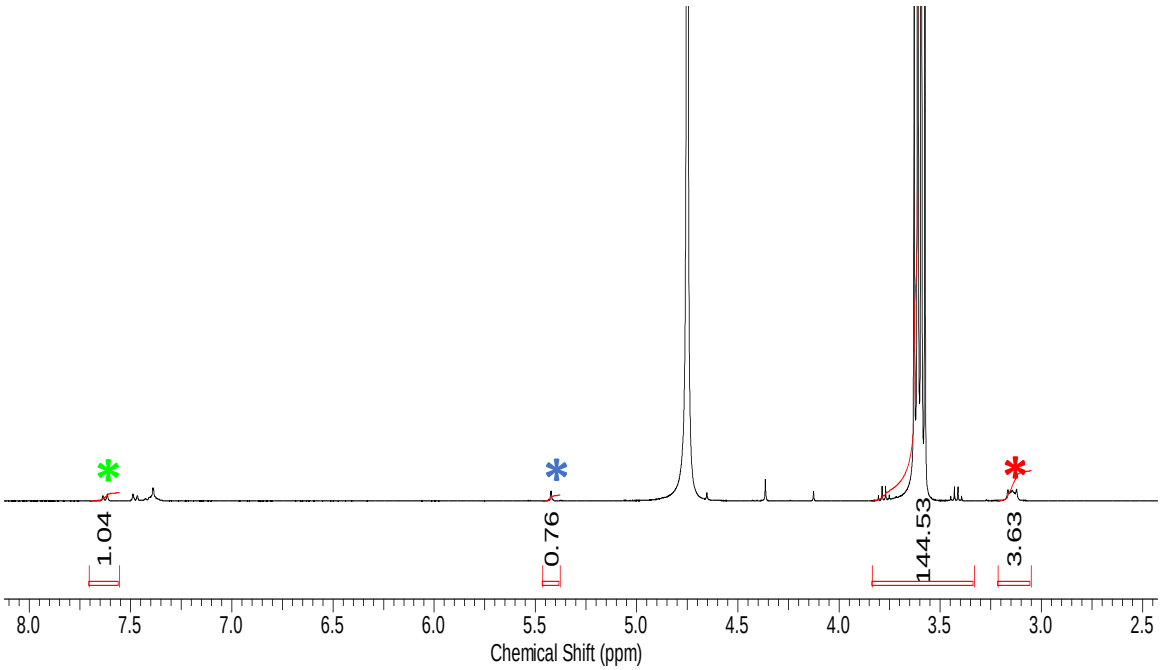

Figure S10 - ^{1}H NMR spectrum with a delay (d_1 = 60 s) of co-formulation **d** (5.95 mM) in D_2O/ 5.0 % EtOH. Comparative integration indicated 48 % of the anionic component of the SSA, 55 % of TBA countercation and 62 % of the **ampicillin** has become NMR silent. (**Ampicillin***, anionic component of SSA **42***, TBA countercation*).

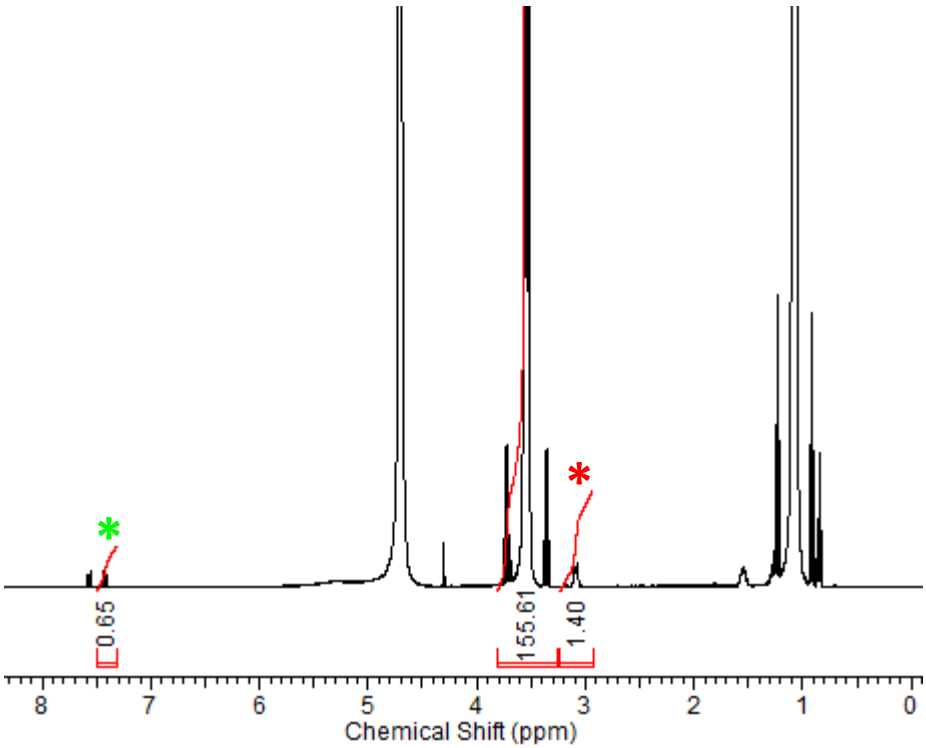

Figure S11 - ^{1}H NMR spectrum with a delay (d_1 = 60 s) of co-formulation **e** (5.53 mM) in D_2O/ 5.0 % EtOH. Comparative integration indicated 65 % of the anionic component of the SSA and 83 % of TBA counteraction has become NMR silent. (Anionic component of SSA **42** and TBA countercation*).

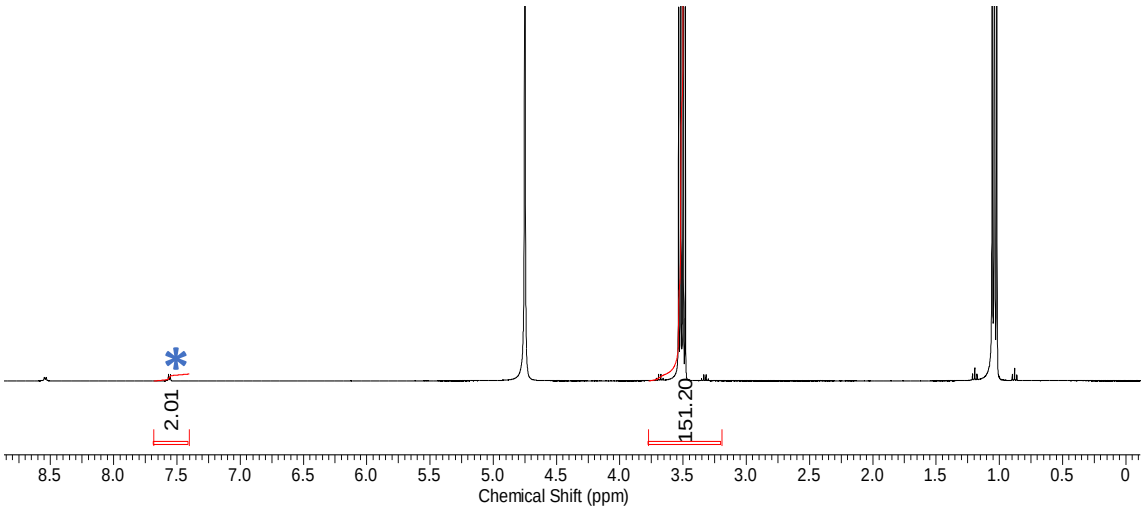

Figure S12 - ^{1}H NMR spectrum with a delay (d_1 = 60 s) of **Isoniazid** (5.29 mM) in D_2O/ 5.0 % EtOH. Comparative integration indicated 0 % of the isoniazid has become NMR silent. (**Isoniazid***).

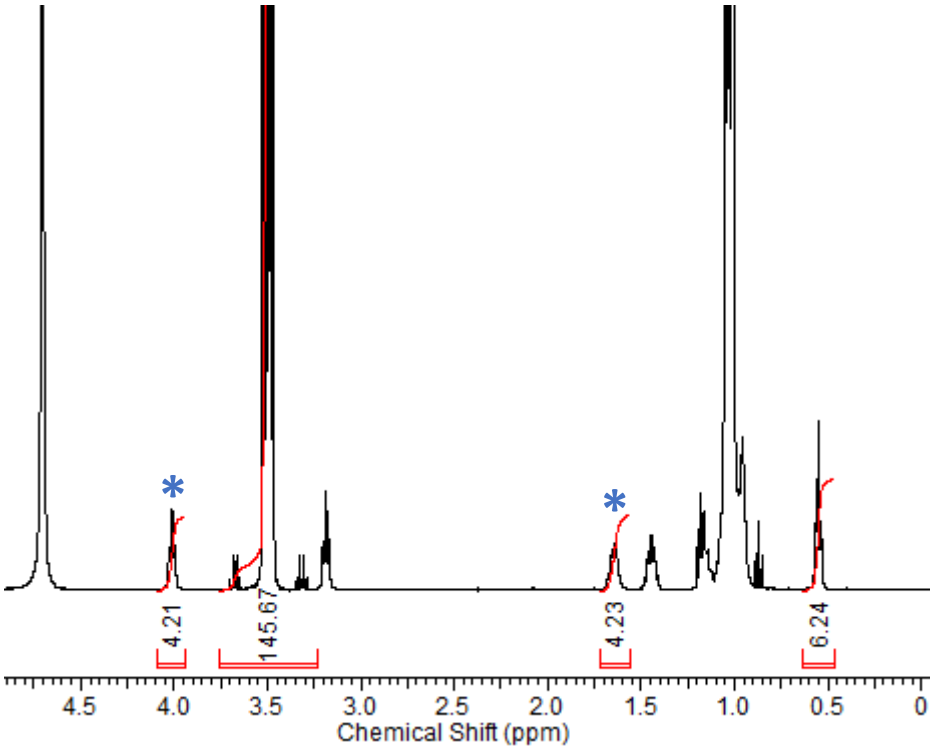

Figure S13 - ^{1}H NMR spectrum with a delay (d_1 = 60 s) of **octenidine dihydrochloride** (5.93 mM) in D_2O/ 5.0 % EtOH. Comparative integration indicated 0 % of the octenidine has become NMR silent. (**Octenidine dihydrochloride***).

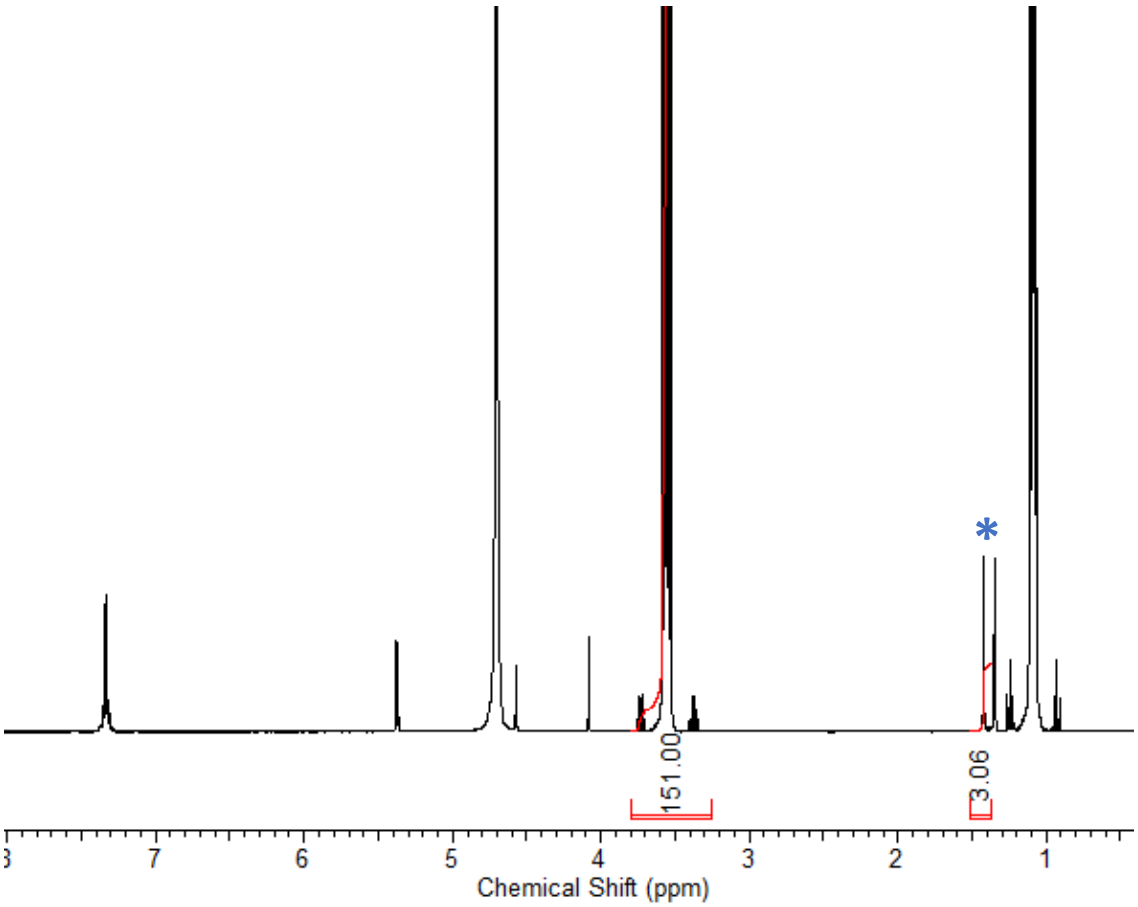

Figure S14 - ^{1}H NMR spectrum with a delay (d_1 = 60 s) of **ampicillin** (5.69 mM) in D_2O/ 5.0 % EtOH. Comparative integration indicated 0 % of the **ampicillin** has become NMR silent. (**Ampicillin***).

1.3 ^{1}H NMR Dilution Studies

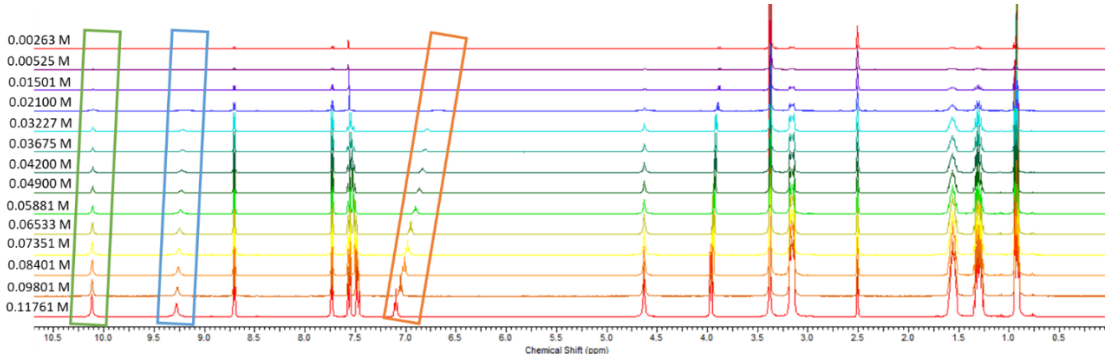

Figure S15 - ^{1}H NMR stack plot of co-formulation **a** in DMSO-d_6 0.5 % H_2O solution. Samples were prepared in series with an aliquot of the most concentrated solution undergoing serial dilution.

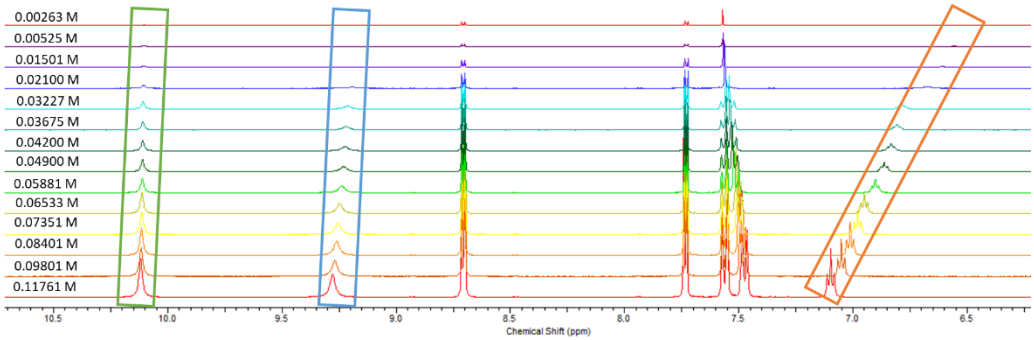

Figure S16 - Enlarged ^{1}H NMR stack plot of co-formulation **a** in DMSO-d_6 0.5 % H_2O solution. Samples were prepared in series with an aliquot of the most concentrated solution undergoing serial dilution.

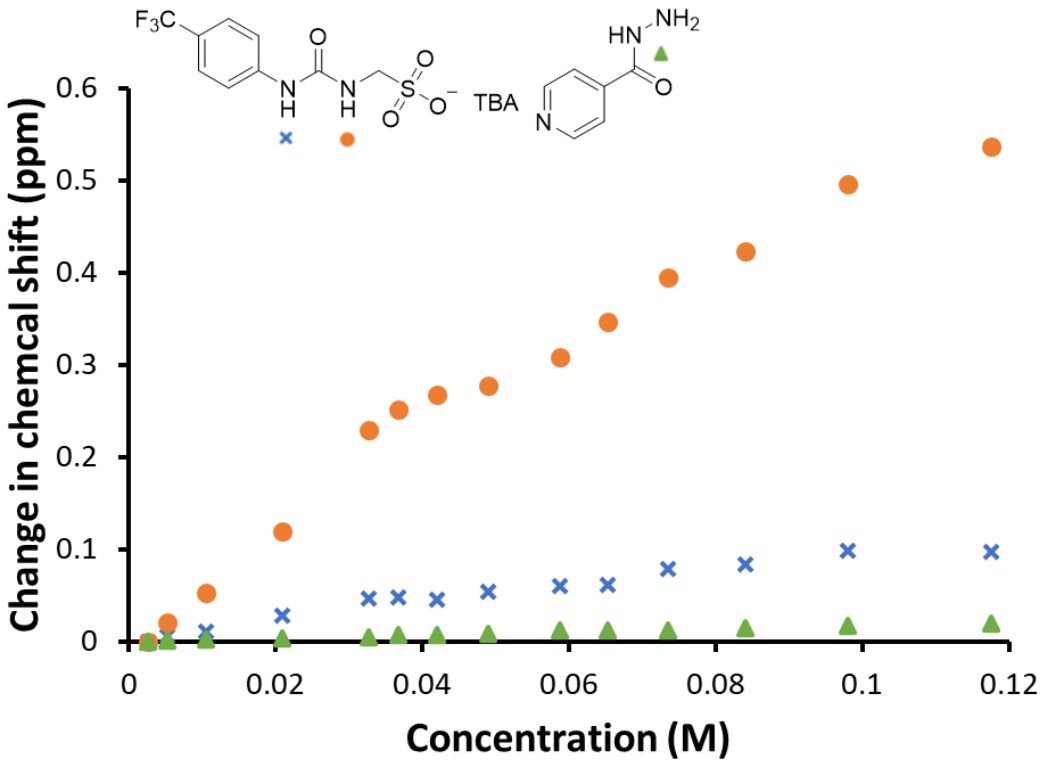

Figure S17 - Graph illustrating the ^{1}H NMR down-field change in chemical shift of urea NH resonances with increasing concentration of co-formulation **a** in DMSO-d_6 0.5 % H_2O (298 K).

Self-association constant calculation

Co-formulation **a** - Dilution study in DMSO-d_6 5 % H_2O. Values calculated from data gathered from both NH 1 and 2.

Equal K/Dimerization model

K_e =4.18 M^{-1} ± 2.9347 % K_{dim} = 2.09 M^{-1} ± 1.4673 %

http://app.supramolecular.org/bindfit/view/af60fbcd-6906-4279-8651-4a153e3f9d7e

CoEK model

K_e = 1.88 M^{-1} ± 36.2950 % K_{dim} = 0.94 M^{-1} ± 18.1475 % ρ = 1.70 ± 45.4394 %

http://app.supramolecular.org/bindfit/view/8483344b-5f77-4661-adff-f15e4b0f2e8a

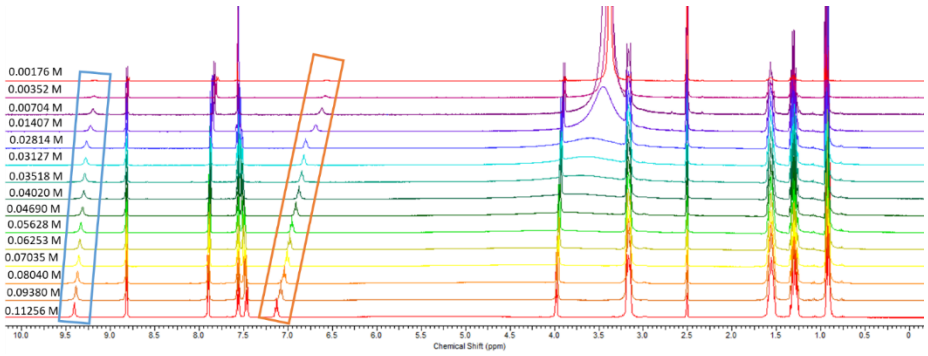

Figure S18 - ^{1}H NMR stack plot of co-formulation **b** in DMSO-d_6 0.5 % H_2O solution. Samples were prepared in series with an aliquot of the most concentrated solution undergoing serial dilution.

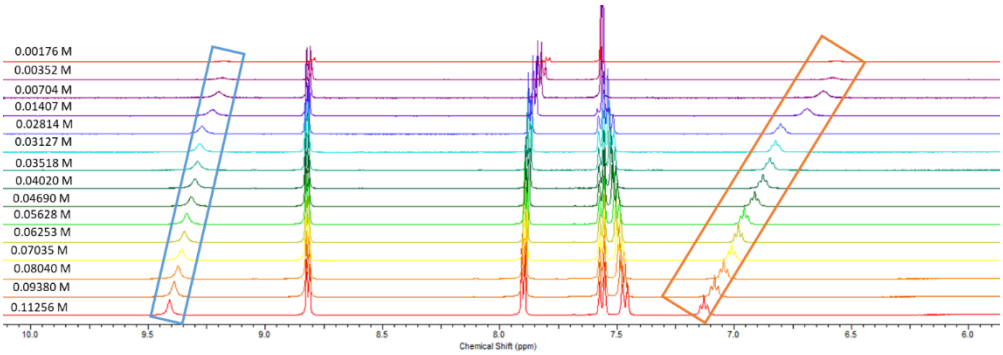

Figure S19 - Enlarged ^{1}H NMR stack plot of co-formulation **b** in DMSO-d_6 0.5 % H_2O solution. Samples were prepared in series with an aliquot of the most concentrated solution undergoing serial dilution.

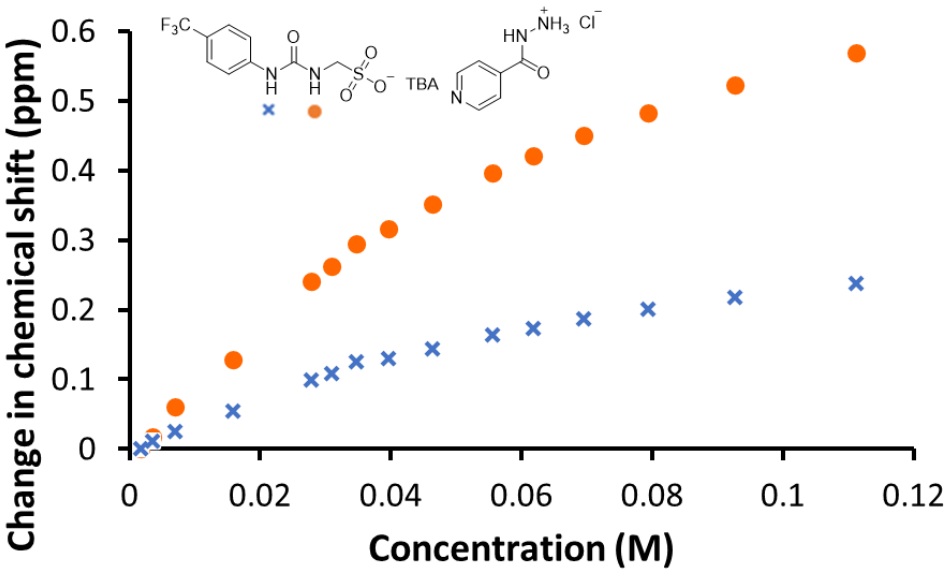

Figure S20 - Graph illustrating the ^{1}H NMR down-field change in chemical shift of urea NH resonances with increasing concentration of co-formulation **b** in DMSO-d_6 0.5 % H_2O (298 K).

Self-association constant calculation

Co-formulation **b** - Dilution study in DMSO-d_6 5 % H_2O. Values calculated from data gathered from both NH 1 and 2.

Equal K/Dimerization model

K_e = 8.73 M^{-1} ± 0.6136 % K_{dim} = 4.37 M^{-1} ± 0.3068 %

http://app.supramolecular.org/bindfit/view/93f0636d-94f2-4837-b515-131a8b317641

CoEK model

K_e = 13.37 M^{-1} ± 1.1955 % K_{dim} = 6.69 M^{-1} ± 0.5978 % ρ = 0.70 ± 3.4165 %

http://app.supramolecular.org/bindfit/view/a23baa7c-f28d-4b37-92f1-11c47e1b5412

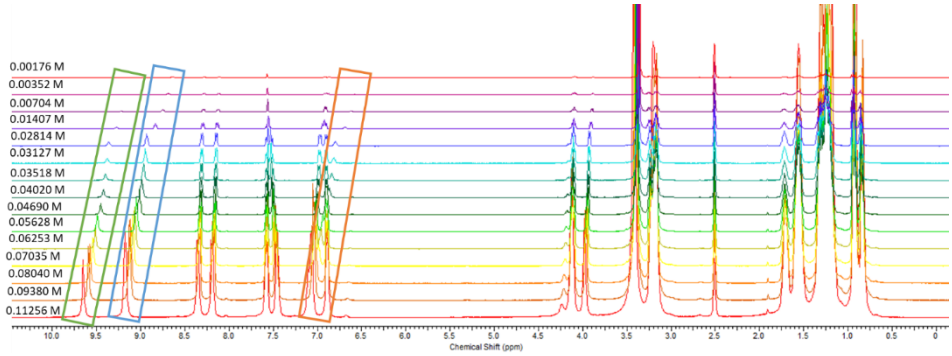

Figure S21 - ^{1}H NMR stack plot of co-formulation **c** in DMSO-d_6 0.5 % H_2O solution. Samples were prepared in series with an aliquot of the most concentrated solution undergoing serial dilution.

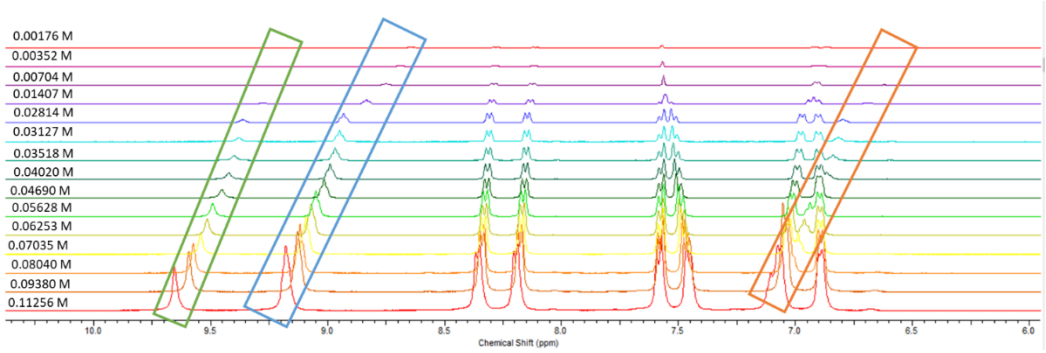

Figure S22 -Enlarged ^{1}H NMR stack plot of co-formulation **c** in DMSO-d_6 0.5 % H_2O solution. Samples were prepared in series with an aliquot of the most concentrated solution undergoing serial dilution.

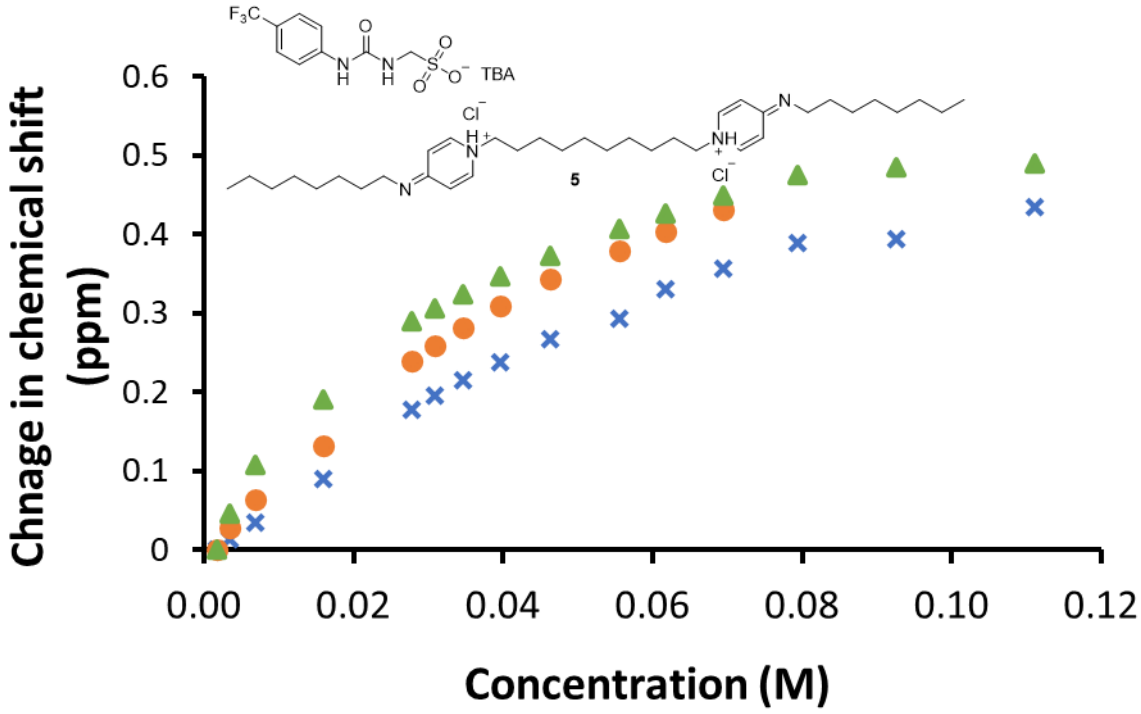

Figure S23 - Graph illustrating the ^{1}H NMR down-field change in chemical shift of urea NH resonances with increasing concentration of co-formulation **c** in DMSO-d_6 0.5 % H_2O (298 K).

Self-association constant calculation

Co-formulation **c** - Dilution study in DMSO-d_6 0.5 % H_2O. Values calculated from data gathered from NH 1.

Equal K/Dimerization model

K_e = 5.85 M^{-1} ± 1.5916 % K_{dim} = 2.92 M^{-1} 0.7958 %

http://app.supramolecular.org/bindfit/view/e15303e8-eb56-4dca-b782-c28be7611357

CoEK model

K_e = 11.30 M^{-1} ± 3.9459 % K_{dim} = 5.65 M^{-1} ± 1.9730 % ρ = 0.60 ± 10.5806 %

http://app.supramolecular.org/bindfit/view/dcaf8e9c-6662-4c84-b1e6-3981726939d

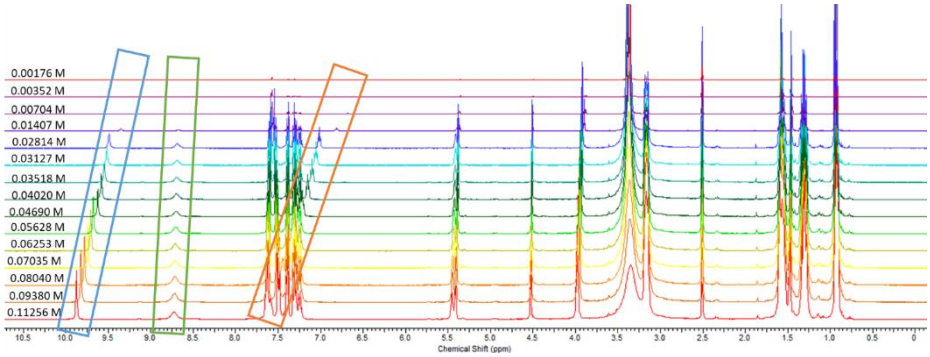

Figure S24 - ^{1}H NMR stack plot of co-formulation **d** in DMSO-d_6 0.5 % H_2O solution. Samples were prepared in series with an aliquot of the most concentrated solution undergoing serial dilution.

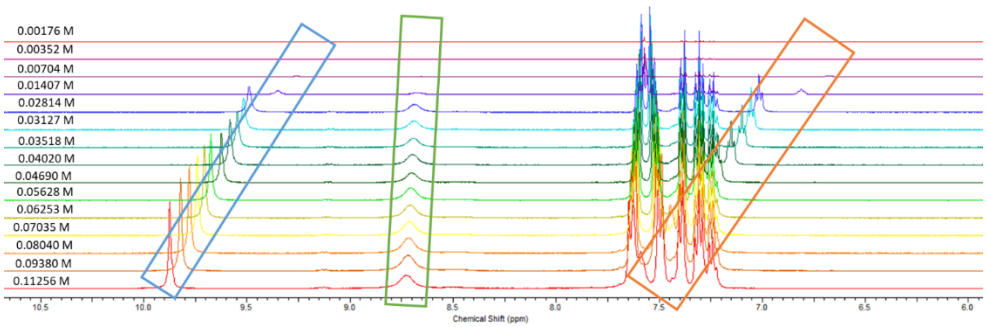

Figure S25 - Enlarged ^{1}H NMR stack plot of co-formulation **d** in DMSO-d_6 0.5 % H_2O solution. Samples were prepared in series with an aliquot of the most concentrated solution undergoing serial dilution.

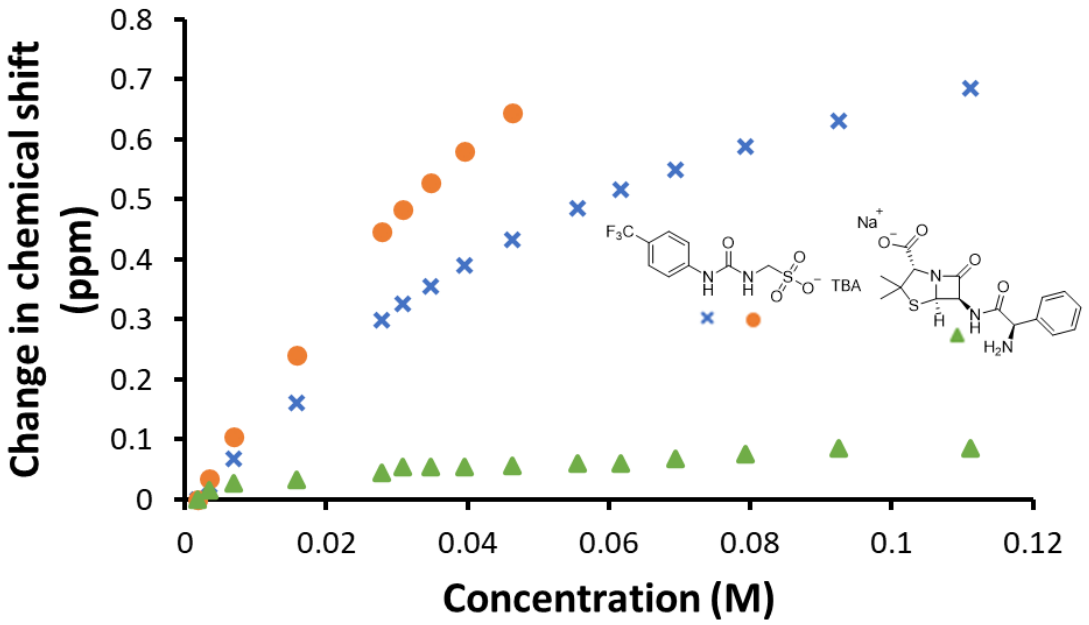

Figure S26 - Graph illustrating the ^{1}H NMR down-field change in chemical shift of urea NH resonances with increasing concentration of co-formulation **d** in DMSO-d_6 0.5 % H_2O (298 K).

Self-association constant calculation

Co-formulation **d** - Dilution study in DMSO-d_6 5 % H_2O. Values calculated from data gathered from NH 1.

Equal K/Dimerization model

K_e = 9.81 M^{-1} ± 0.9962 % K_{dim} = 4.91 M^{-1} 0.4981 %

http://app.supramolecular.org/bindfit/view/2865831b-c5e4-4eb4-a97d-e3f1a955de0b

CoEK model

K_e = 18.10 M^{-1} ± 0.5718 % K_{dim} = 9.05 M^{-1} ± 0.2859 % ρ = 0.55 ± 2.0789 %

http://app.supramolecular.org/bindfit/view/b5e2838a-37d6-40a4-bee9-e033afb6bba2

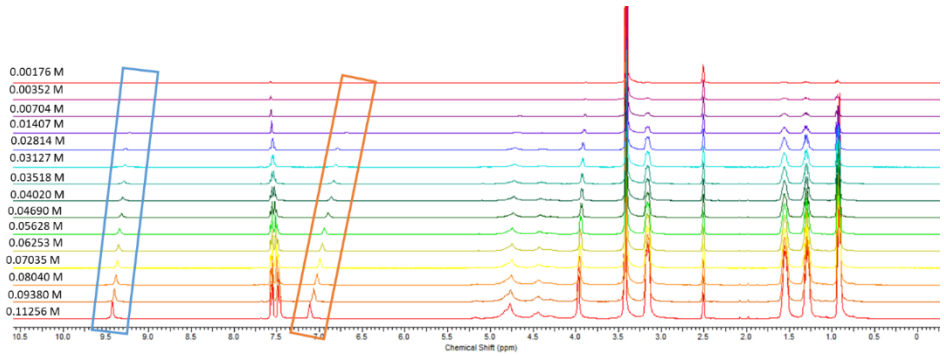

Figure S27 - ^{1}H NMR stack plot of co-formulation **e** in DMSO-d_6 0.5 % H_2O solution. Samples were prepared in series with an aliquot of the most concentrated solution undergoing serial dilution.

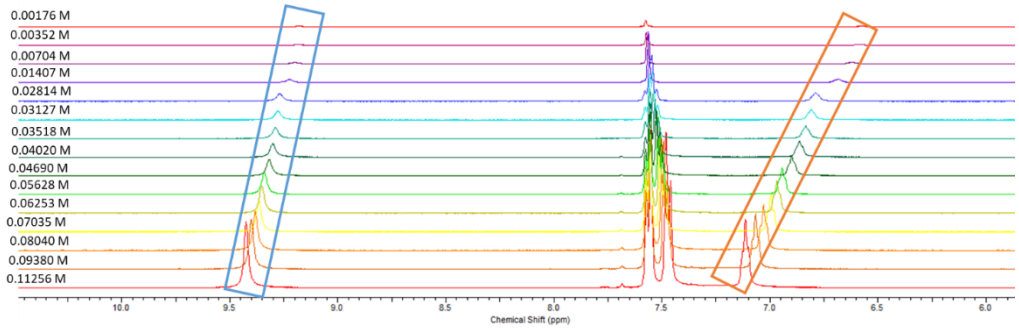

Figure S28 -Enlarged ^{1}H NMR stack plot of co-formulation **e** in DMSO-d_6 0.5 % H_2O solution. Samples were prepared in series with an aliquot of the most concentrated solution undergoing serial dilution.

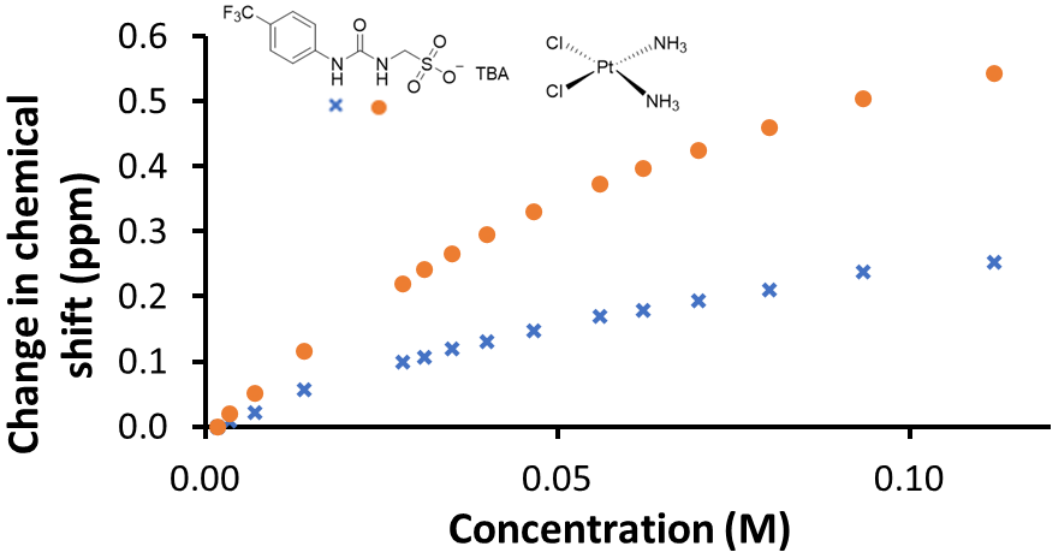

Figure S29 - Graph illustrating the ^{1}H NMR down-field change in chemical shift of urea NH resonances with increasing concentration of co-formulation **e** in DMSO-d_6 0.5 % H_2O (298 K).

Self-association constant calculation

Co-formulation **e** - Dilution study in DMSO-d_6 5 % H_2O. Values calculated from data gathered from both NH 1 and 2.

Equal K/Dimerization model

K_e = 7.34 M^{-1} ± 0.7666 % K_{dim} = 3.67 M^{-1} ± 0.3833 %

http://app.supramolecular.org/bindfit/view/9a4e48ba-c79c-48cf-8ef9-70df96f1595e

CoEK model

K_e = 13.11 M^{-1} ± 1.5699 % K_{dim} = 6.55 M^{-1} ± 0.7849 % ρ = 0.62 ± 4.4228 %

http://app.supramolecular.org/bindfit/view/a686415f-cefd-4e16-b9e8-3670179f4e3a

1.4 ^{1}H NMR DOSY experiments

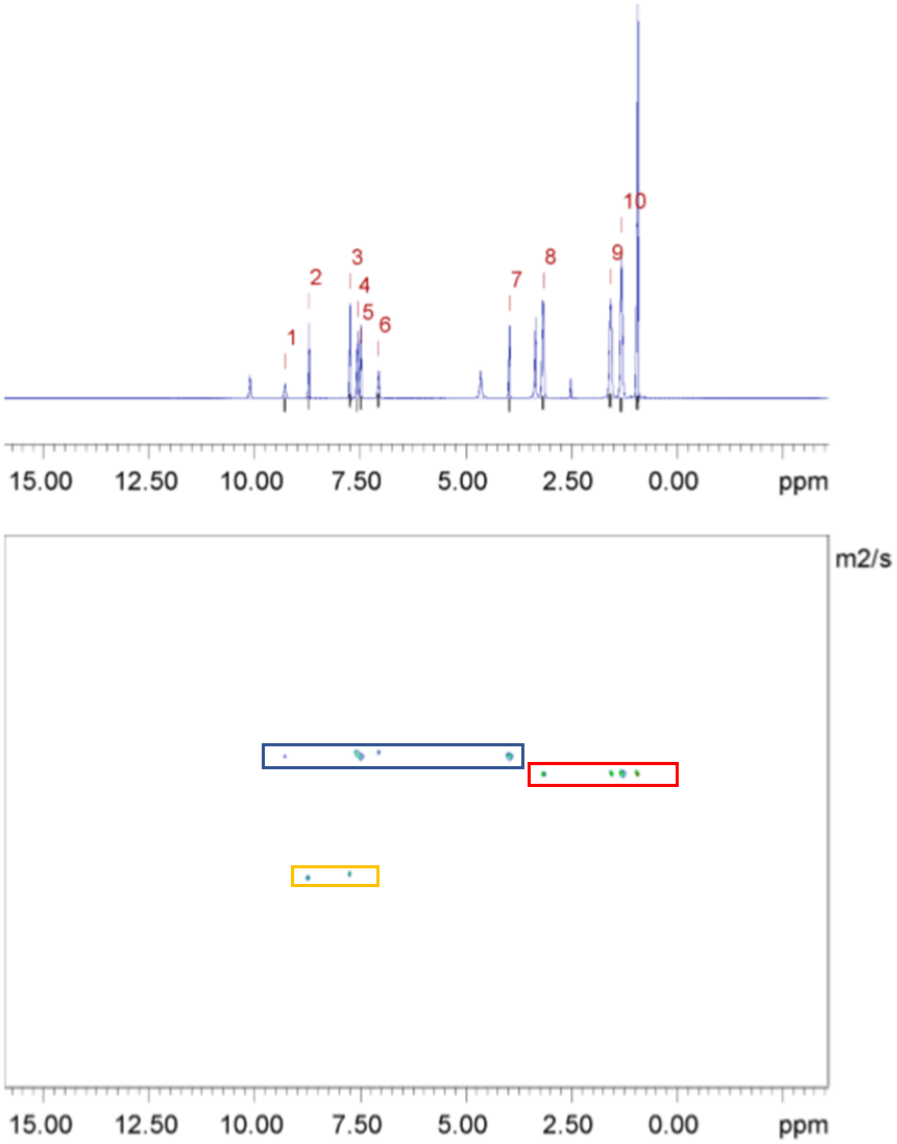

Peak name	F2 [ppm]	Io	error	D [m2/s]	error
1	9.279	1.15e+09	1.246e+05	1.80e-10	4.258e-14
2	8.709	3.61e+09	1.181e+05	2.95e-10	2.042e-14
3	7.739	4.13e+09	1.179e+05	2.94e-10	1.777e-14
4	7.566	3.96e+09	1.054e+05	1.79e-10	1.041e-14
5	7.482	4.24e+09	1.151e+05	1.80e-10	1.063e-14
6	7.067	1.76e+09	1.185e+05	1.79e-10	2.641e-14
7	3.964	3.76e+09	1.046e+05	1.79e-10	1.090e-14
8	3.166	1.12e+10	1.425e+05	1.95e-10	5.354e-15
9	1.567	1.16e+10	1.467e+05	1.94e-10	5.306e-15
10	1.309	1.47e+10	1.466e+05	1.94e-10	4.212e-15
11	0.935	2.61e+10	1.377e+05	1.94e-10	2.218e-15

Figure S30 - ^{1}H DOSY NMR spectrum of co-formulation **a** (112.6 mM) in DMSO-d_6 at 298 K and a table reporting the diffusion constants calculated for each peak used to determine the hydrodynamic diameter of the anionic components of **a** (d_H = 1.23 nm). Peaks 1, 4-7 correspond to the anionic component of **a** while peaks 8-11 correspond to the cationic component of **a**. Peaks 2-3 correspond to the drug component, **Isoniazid**.

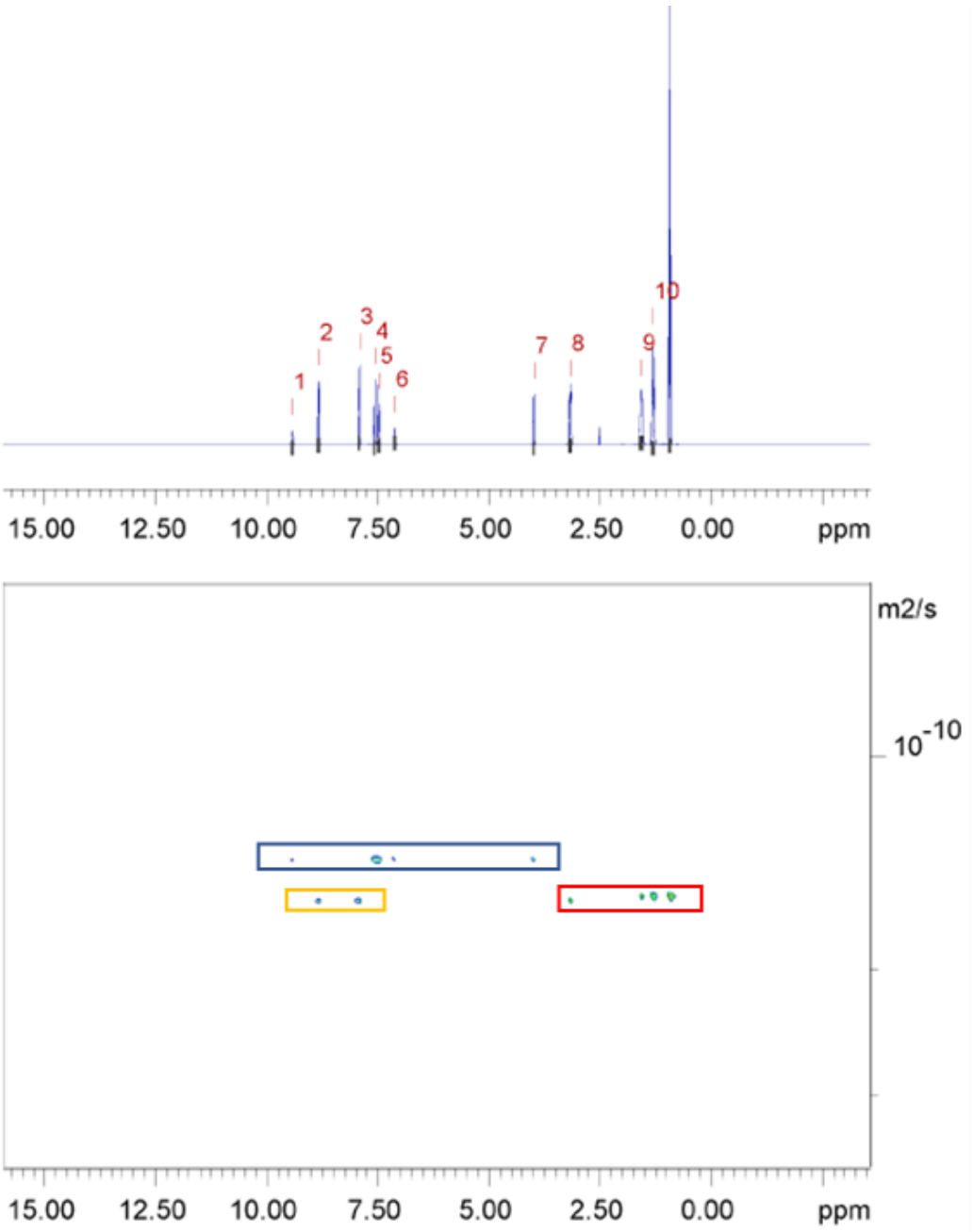

Peak name	F2 [ppm]	Io	error	D [m2/s]	error
1	9.417	7.53e+08	5.190e+04	1.40e-10	2.112e-14
2	8.827	3.04e+09	5.390e+04	1.60e-10	6.127e-15
3	7.915	3.18e+09	4.951e+04	1.60e-10	5.382e-15
4	7.564	2.74e+09	5.699e+04	1.40e-10	6.358e-15
5	7.470	2.69e+09	5.580e+04	1.40e-10	6.348e-15
6	7.110	9.24e+08	6.292e+04	1.40e-10	2.083e-14
7	3.981	2.33e+09	5.582e+04	1.40e-10	7.347e-15
8	3.166	6.32e+09	8.105e+04	1.59e-10	4.417e-15
9	1.560	7.36e+09	9.104e+04	1.57e-10	4.196e-15
10	1.300	9.69e+09	9.271e+04	1.57e-10	3.248e-15
11	0.911	1.62e+10	7.274e+04	1.57e-10	1.517e-15

Figure S31 - ^{1}H DOSY NMR spectrum of co-formulation **b** (112.6 mM) in DMSO-d_6 at 298 K and a table reporting the diffusion constants calculated for each peak used to determine the hydrodynamic diameter of the anionic components of **b** (d_H = 1.57 nm). Peaks 1, 4-7 correspond to the anionic component of **b** while peaks 8-11 correspond to the cationic component of **b**. Peaks 2-3 correspond to the drug component, **Isoniazid hydrogen chloride**.

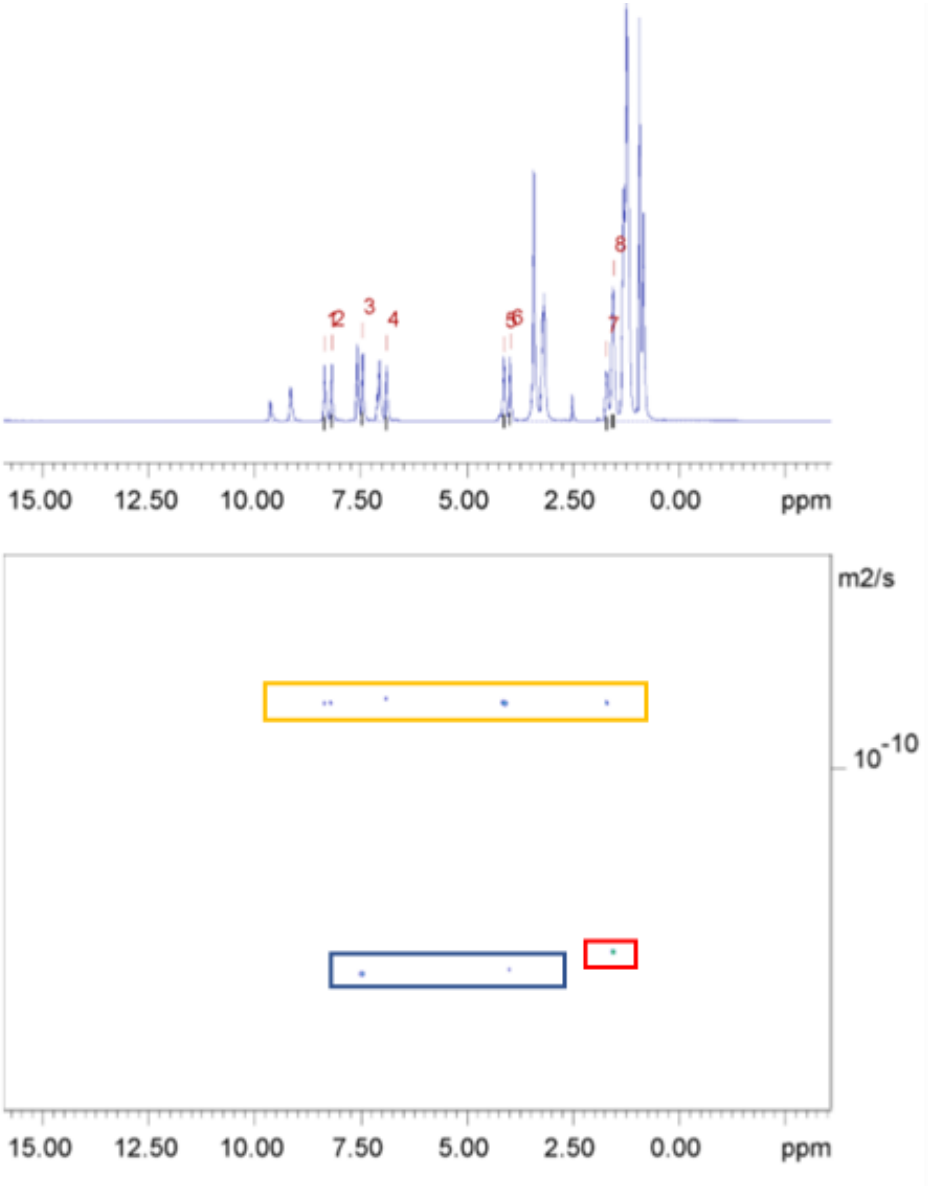

Peak name	F2 [ppm]	Io	error	D [m2/s]	error
1	8.353	3.85e+09	1.722e+05	9.22e-11	8.818e-15
2	8.190	3.82e+09	1.680e+05	9.18e-11	8.652e-15
3	7.461	5.06e+09	1.861e+05	1.30e-10	1.002e-14
4	6.893	3.64e+09	1.602e+05	9.17e-11	8.649e-15
5	4.118	4.86e+09	1.725e+05	9.17e-11	6.977e-15
6	3.982	3.77e+09	1.734e+05	1.30e-10	1.251e-14
7	1.703	4.83e+09	1.881e+05	9.17e-11	7.652e-15
8	1.550	1.78e+10	2.490e+05	1.26e-10	3.714e-15

Figure S32 - ^{1}H DOSY NMR spectrum of co-formulation **c** (112.6 mM) in DMSO-d_6 at 298 K and a table reporting the diffusion constants calculated for each peak used to determine the hydrodynamic diameter of the anionic components of **c** (d_H = 1.69 nm). Peaks 3 and 6 correspond to the anionic component of **c** while peak 8 corresponds to the cationic component of **c**. Peaks 1-2, 4-5 and 7 correspond to the drug component, **octenidine dihydrochloride**. Note, some signals were excluded due to poor fitting.

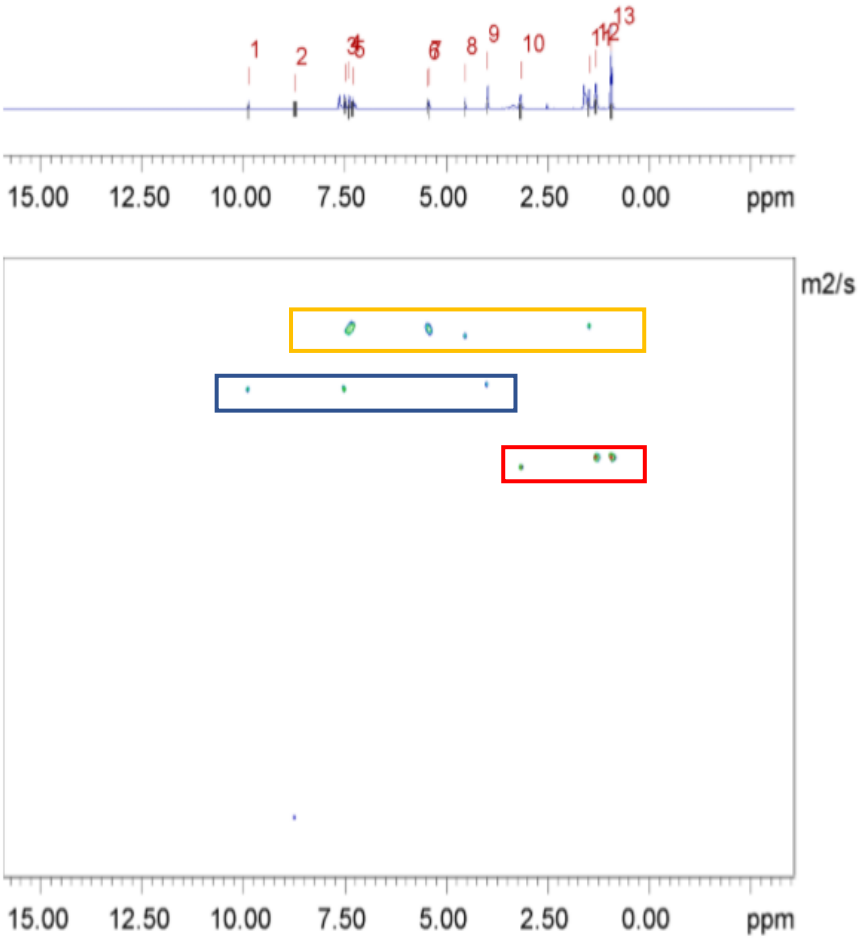

Peak name	F2 [ppm]	Io	error	D [m2/s]	error
1	9.877	1.83e+09	1.042e+05	1.30e-10	1.622e-14
2	8.724	5.43e+08	2.410e+05	4.48e-10	4.091e-13
3	7.496	4.92e+09	1.111e+05	1.30e-10	6.406e-15
4	7.395	4.16e+09	9.989e+04	1.10e-10	5.864e-15
5	7.307	4.70e+09	1.206e+05	1.09e-10	6.226e-15
6	5.455	1.62e+09	8.172e+04	1.09e-10	1.220e-14
7	5.414	1.77e+09	7.367e+04	1.11e-10	1.018e-14
8	4.526	1.54e+09	6.384e+04	1.12e-10	1.028e-14
9	3.988	1.26e+09	4.928e+04	1.28e-10	1.092e-14
10	3.167	8.88e+09	1.335e+05	1.64e-10	5.325e-15
11	1.483	3.42e+09	7.567e+04	1.09e-10	5.351e-15
12	1.308	1.48e+10	1.487e+05	1.59e-10	3.447e-15
13	0.928	2.62e+10	1.280e+05	1.59e-10	1.676e-15

Figure S33 - ^{1}H DOSY NMR spectrum of co-formulation **d** (112.6 mM) in DMSO-d_6 at 298 K and a table reporting the diffusion constants calculated for each peak used to determine the hydrodynamic diameter of the anionic components of **d** (d_H = 1.70 nm). Peaks 1, 3 and 9 correspond to the anionic component of **6** while peaks 10, 12-13 correspond to the cationic component of **d**. Peaks 4-8 and 11 correspond to the drug component, **Ampicillin**.

1.5 Surface Tension and Critical Micelle Concentration

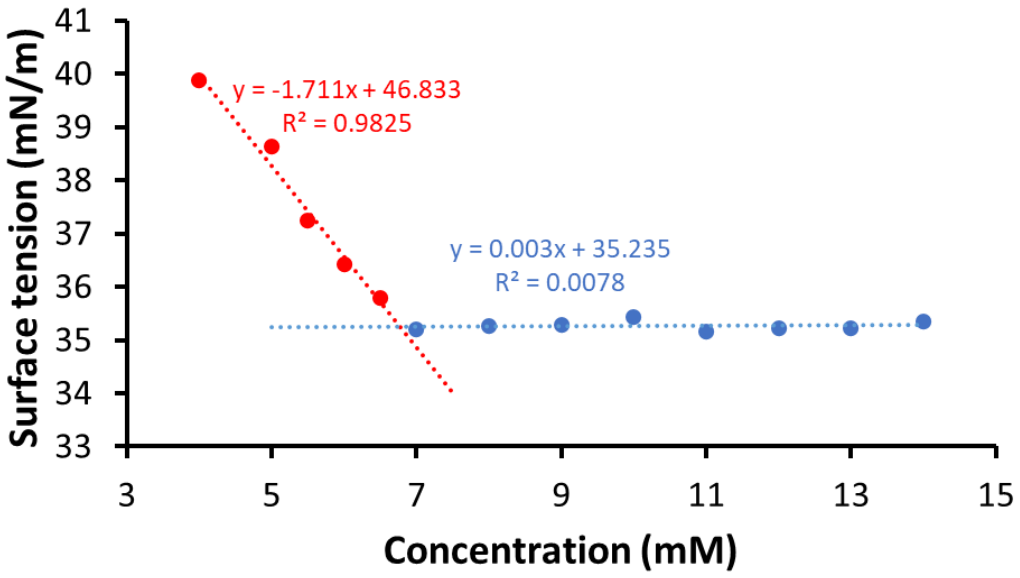

Figure S34 - Calculation of CMC (6.76 mM) for co-formulation **a** in an EtOH:H_2O 1:19 mixture using surface tension measurements.

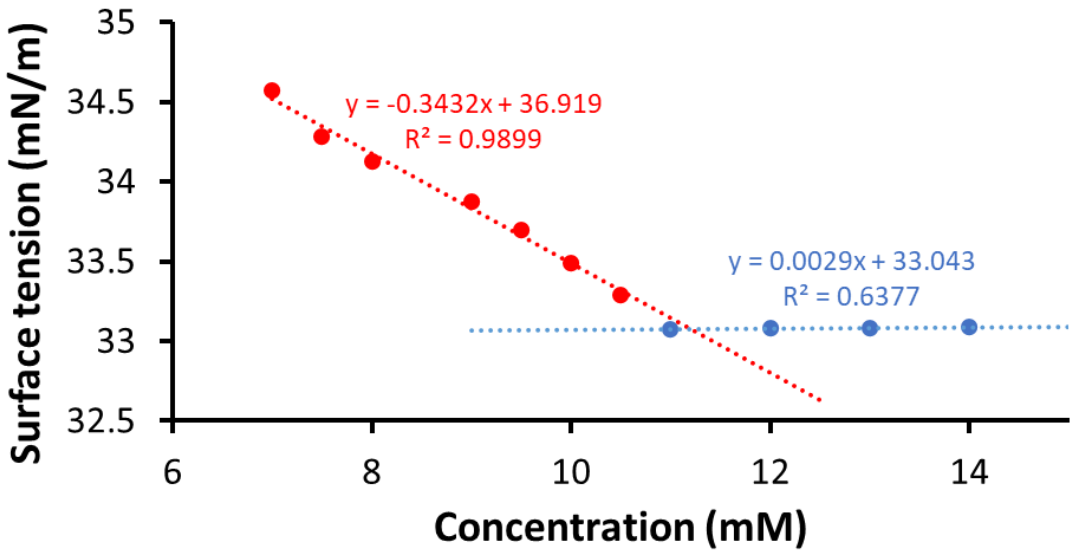

Figure S35 - Calculation of CMC (11.21 mM) for co-formulation **b** in an EtOH:H_2O 1:19 mixture using surface tension measurements.

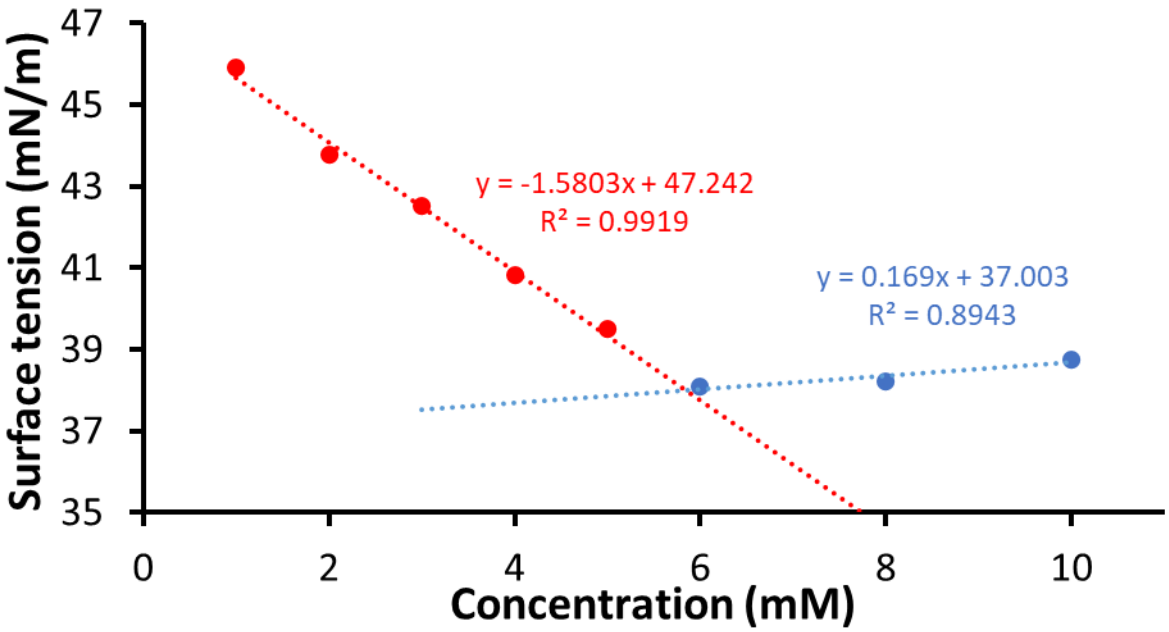

Figure S36 - Calculation of CMC (5.58 mM) for co-formulation **c** in an EtOH:H_2O 1:19 mixture using surface tension measurements.

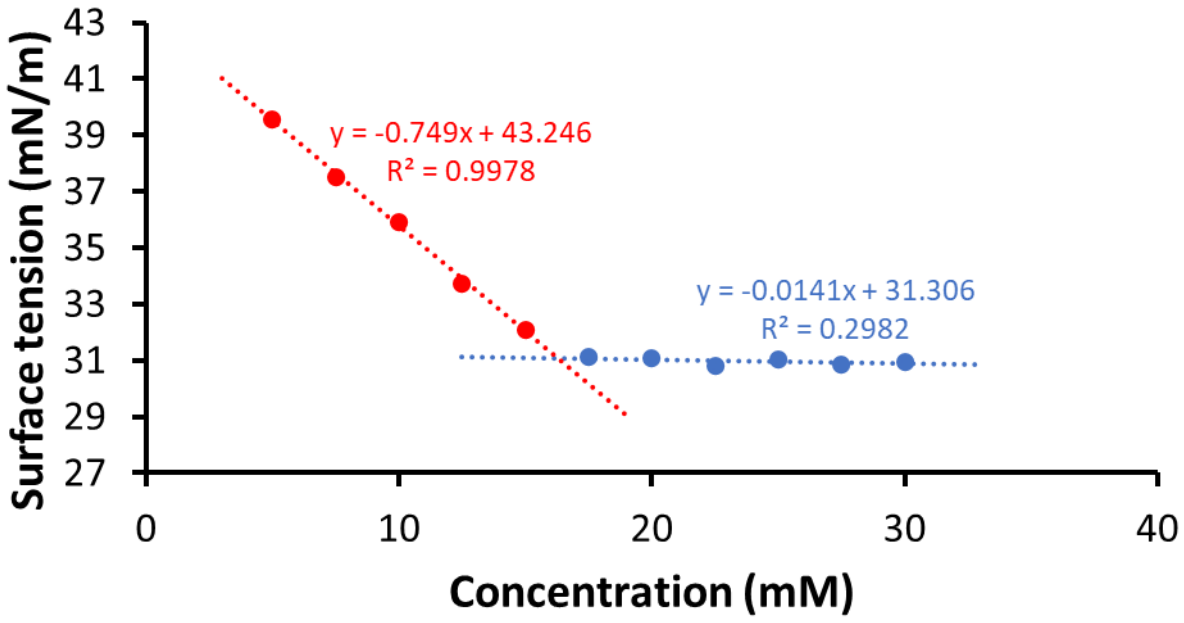

Figure S37 - Calculation of CMC (16.24 mM) for co-formulation **d** in an EtOH:H_2O 1:19 mixture using surface tension measurements.

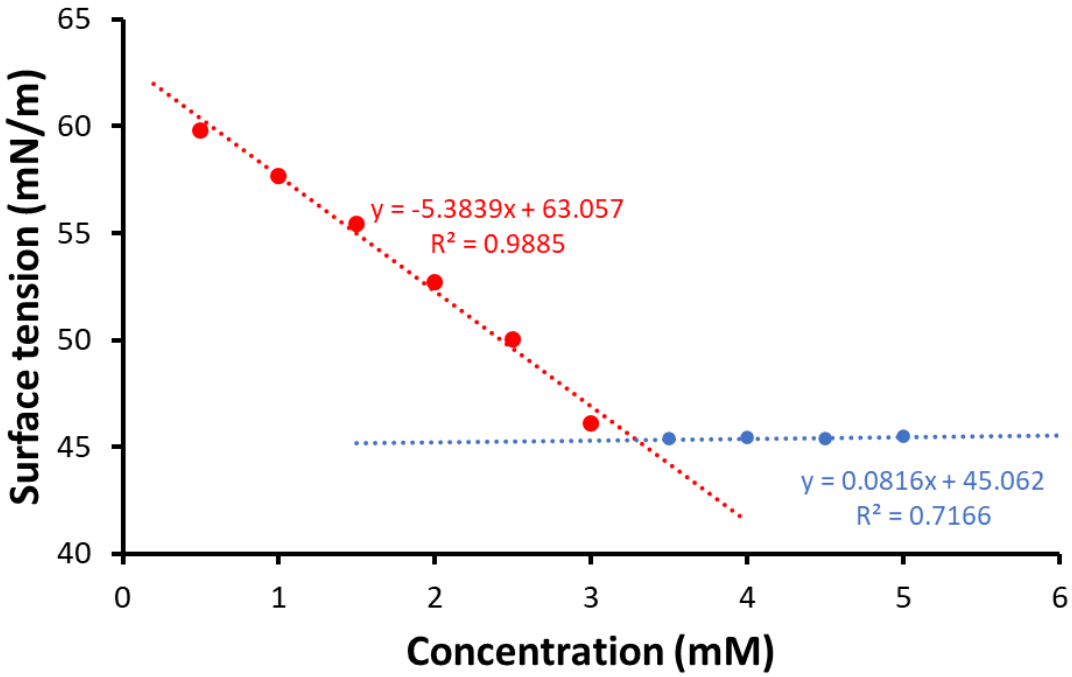

Figure S38 - Calculation of CMC (3.29 mM) for co-formulation **e** in an EtOH:H_2O 1:19 mixture using surface tension measurements.

1.6 Zeta Potential Studies

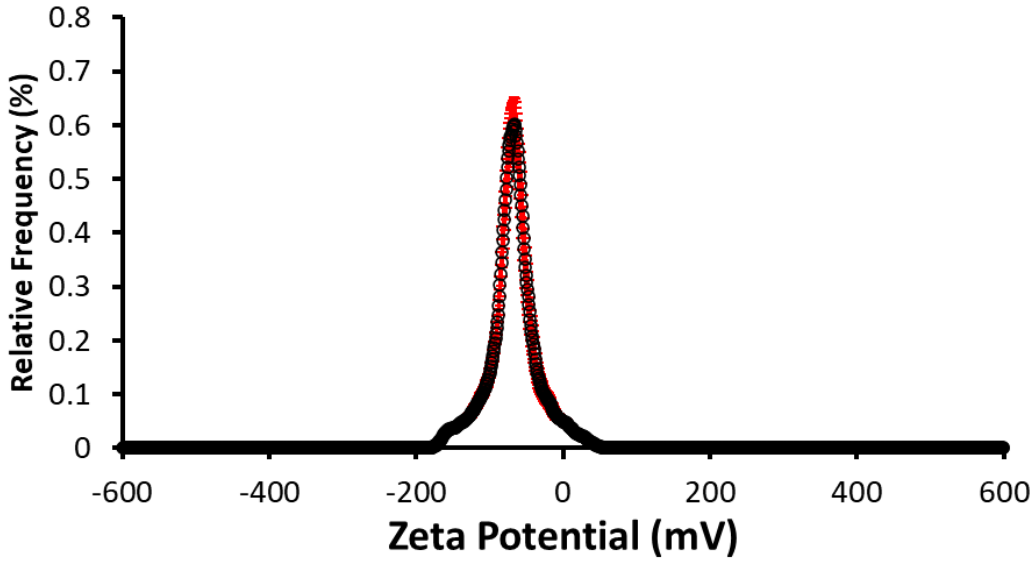

Figure S39 - The average zeta potential distribution calculated using 10 runs for compound **42** (0.56 mM) in an EtOH:H_2O (1:19) solution at 298 K. Average measurement value -66.8 mV.

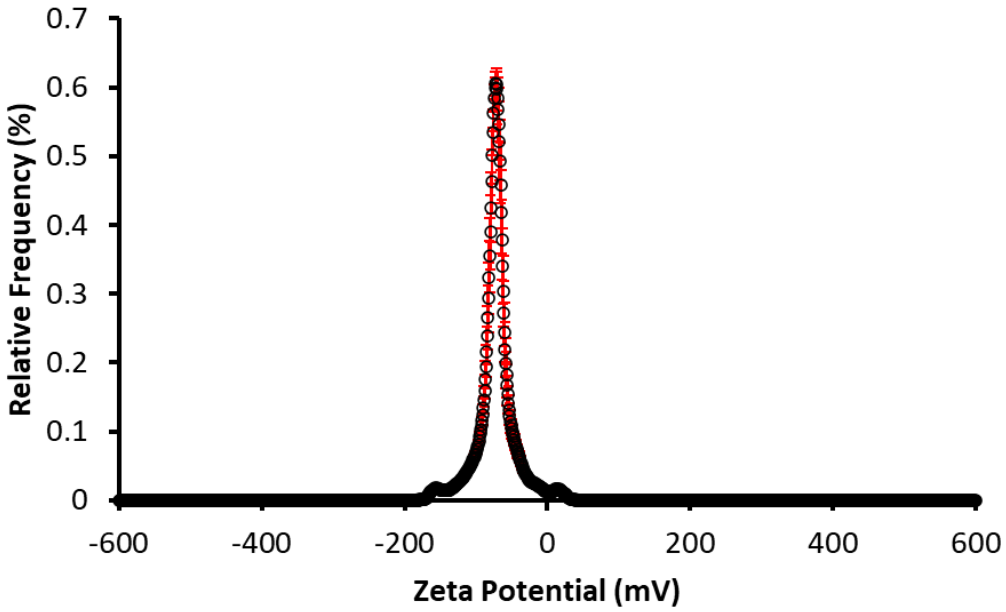

Figure S40 - The average zeta potential distribution calculated using 10 runs for co-formulation **a** (5.56 mM) in an EtOH: H_2O (1:19) solution at 298 K. Average measurement value -71.8 mV.

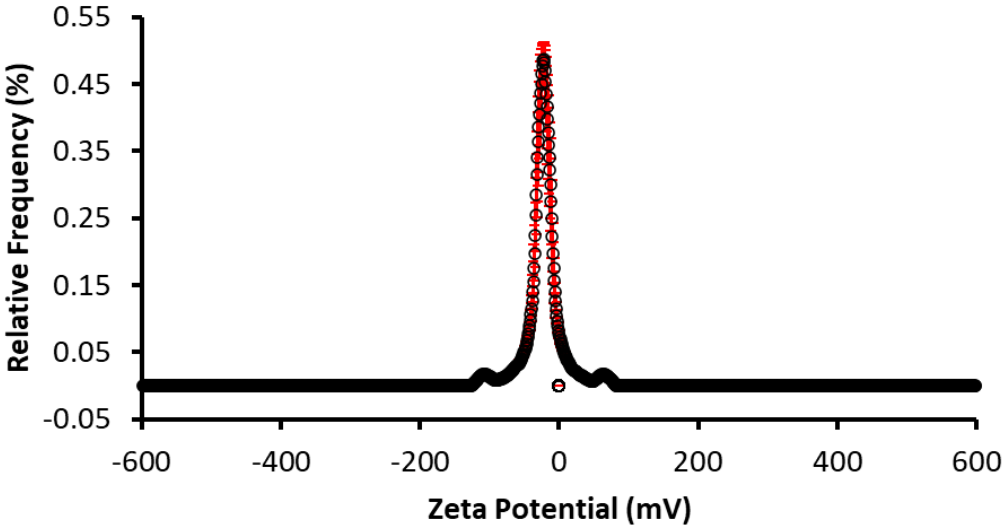

Figure S41 - The average zeta potential distribution calculated using 10 runs for co-formulation **b** (5.56 mM) in an EtOH: H_2O (1:19) solution at 298 K. Average measurement value -22.0 mV.

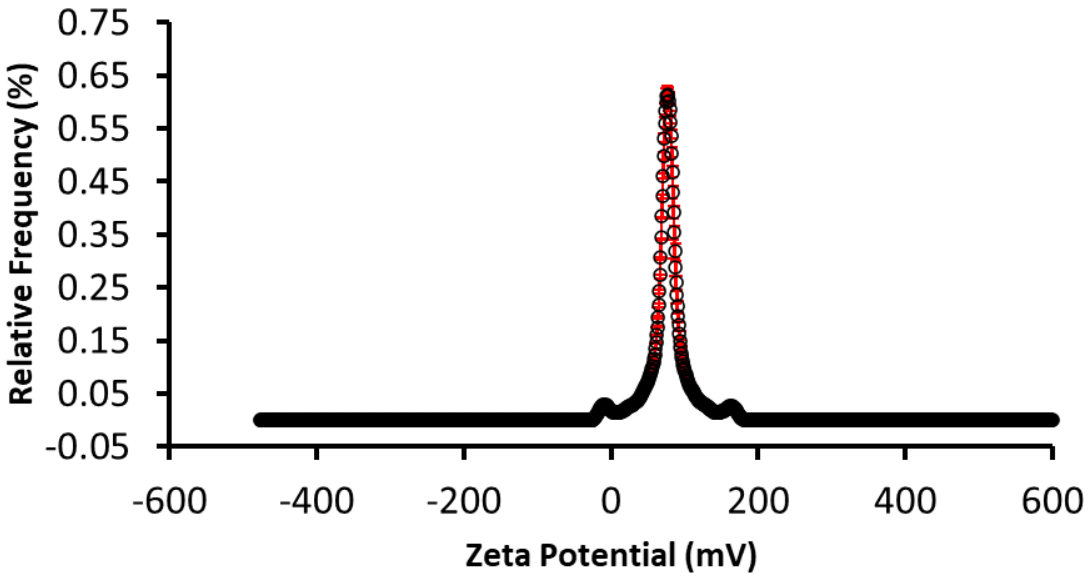

Figure S42 - The average zeta potential distribution calculated using 10 runs for co-formulation **c** (0.56 mM) in an EtOH: H_2O (1:19) solution at 298 K. Average measurement value 76.27 mV.

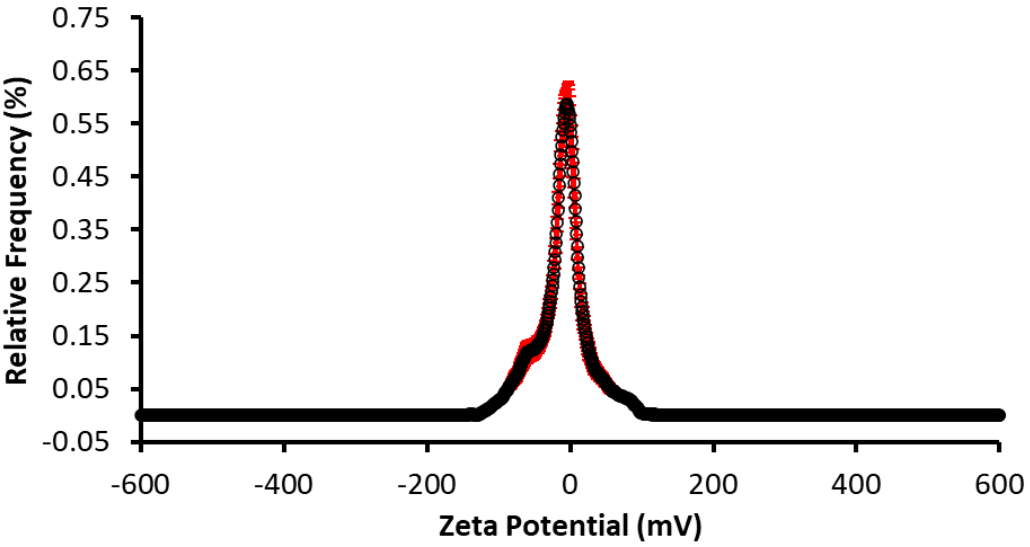

Figure S43 - The average zeta potential distribution calculated using 10 runs for co-formulation **d** (5.56 mM) in an EtOH: H_2O (1:19) solution at 298 K. Average measurement value -2.62 mV.

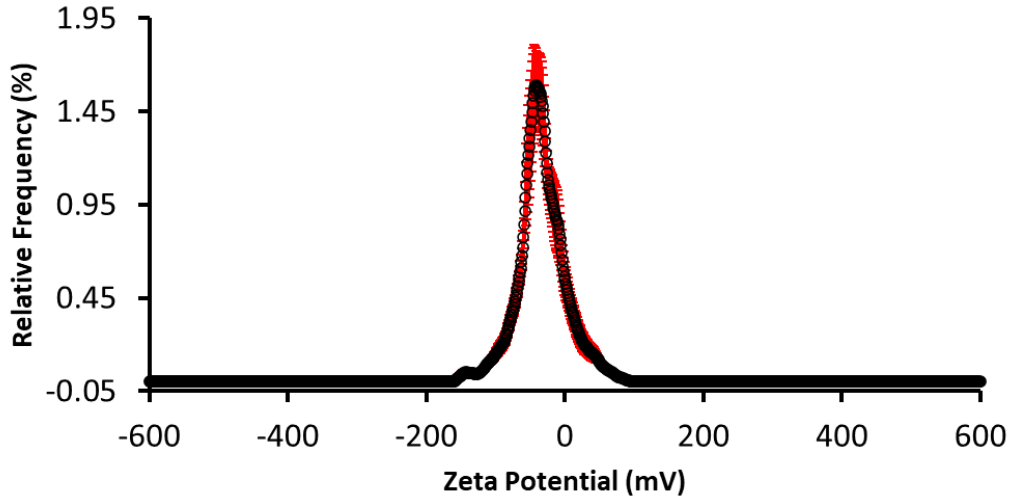

Figure S44 - The average zeta potential distribution calculated using 10 runs for co-formulation **e** (0.56 mM) in an EtOH: H_2O (1:19) solution at 298 K. Average measurement value -42.16 mV.

1.7 Dynamic Light Scattering

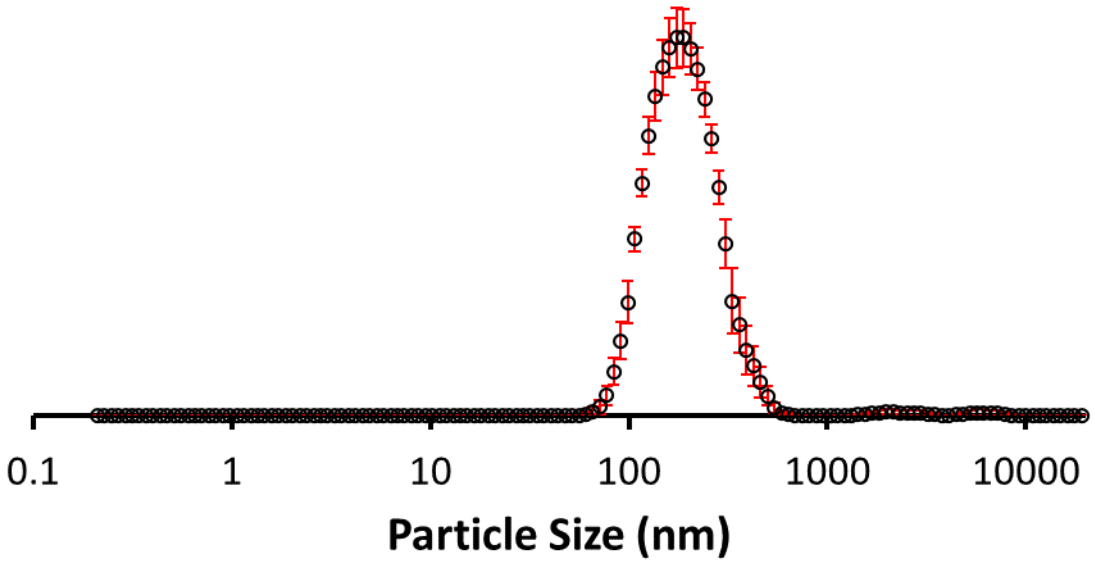

Figure S45 - The average intensity particle size distribution calculated using 10 DLS runs for co-formulation **a** (5.56 mM) in an EtOH: H_2O (1:19) solution at 298 K.

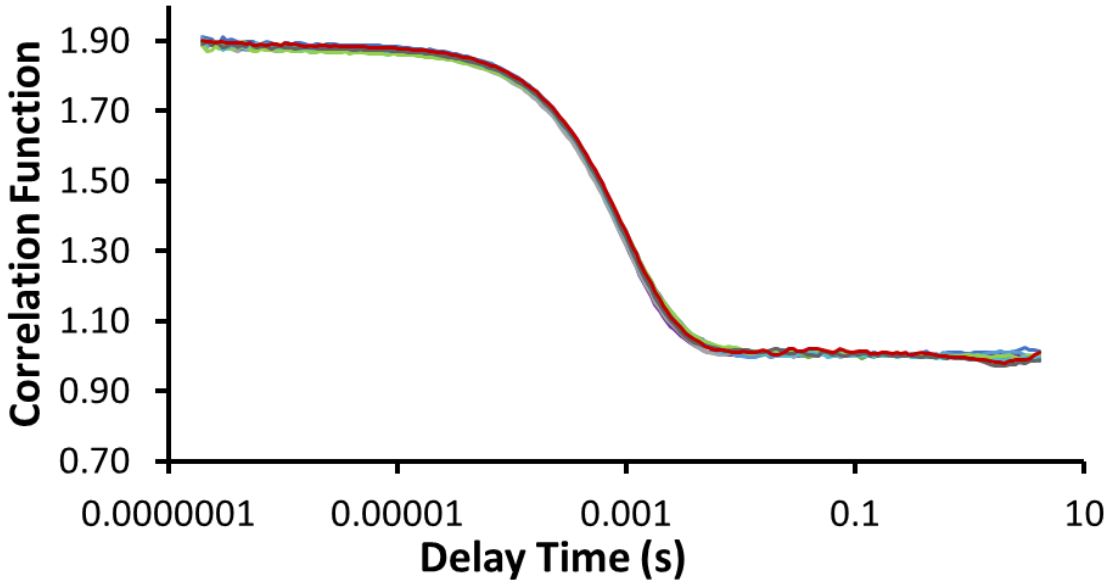

Figure S46 - Correlation function data for 10 DLS runs of co-formulation **a** (5.56 mM) in an EtOH: H_2O (1:19) solution at 298 K.

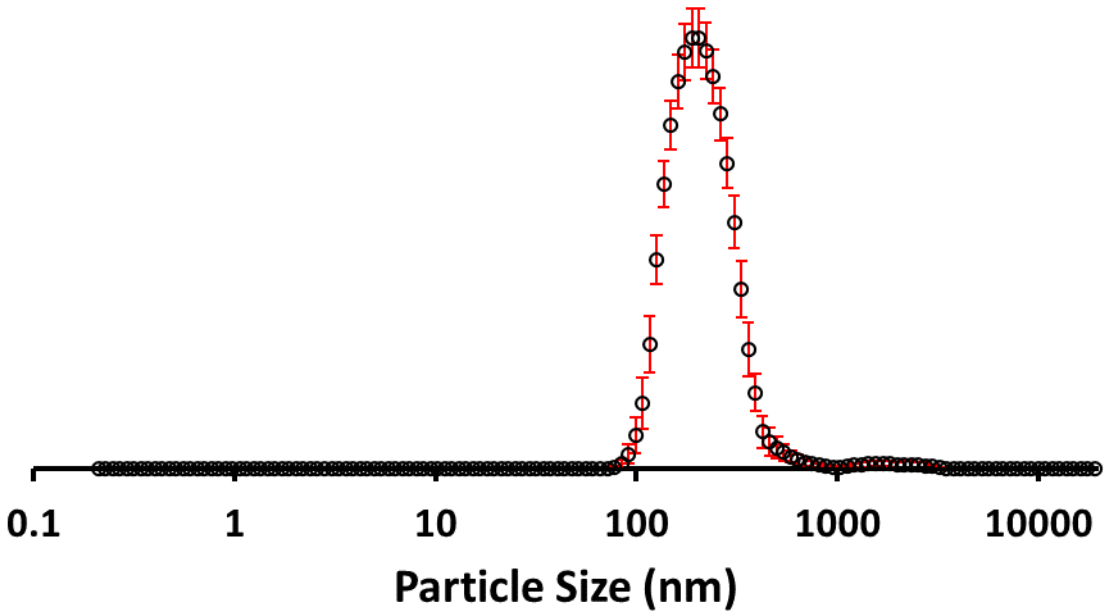

Figure S47 - The average intensity particle size distribution calculated using 10 DLS runs for co-formulation **a** (0.56 mM) in an EtOH: H_2O (1:19) solution at 298 K.

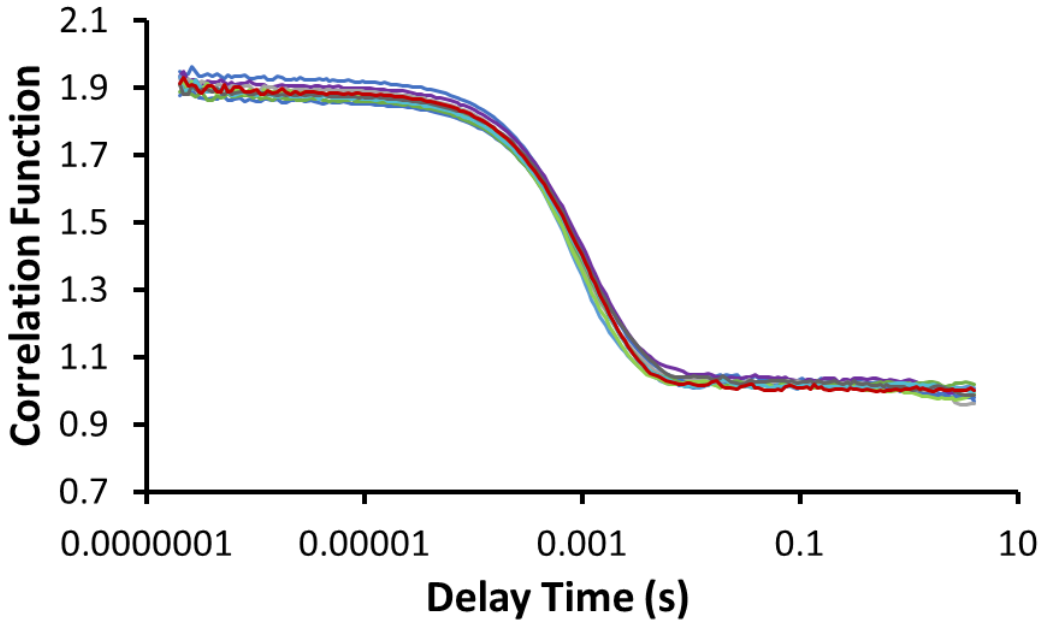

Figure S48 - Correlation function data for 10 DLS runs of co-formulation **a** (0.56 mM) in an EtOH: H_2O (1:19) solution at 298 K.

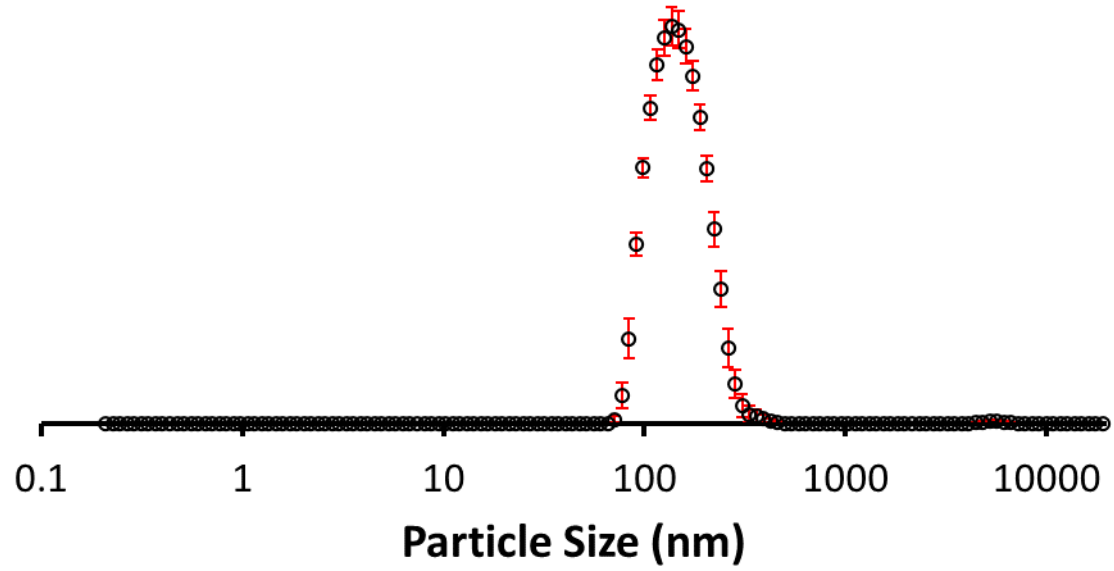

Figure S49 - The average intensity particle size distribution calculated using 10 DLS runs for co-formulation **b** (5.56 mM) in an EtOH: H_2O (1:19) solution at 298 K.

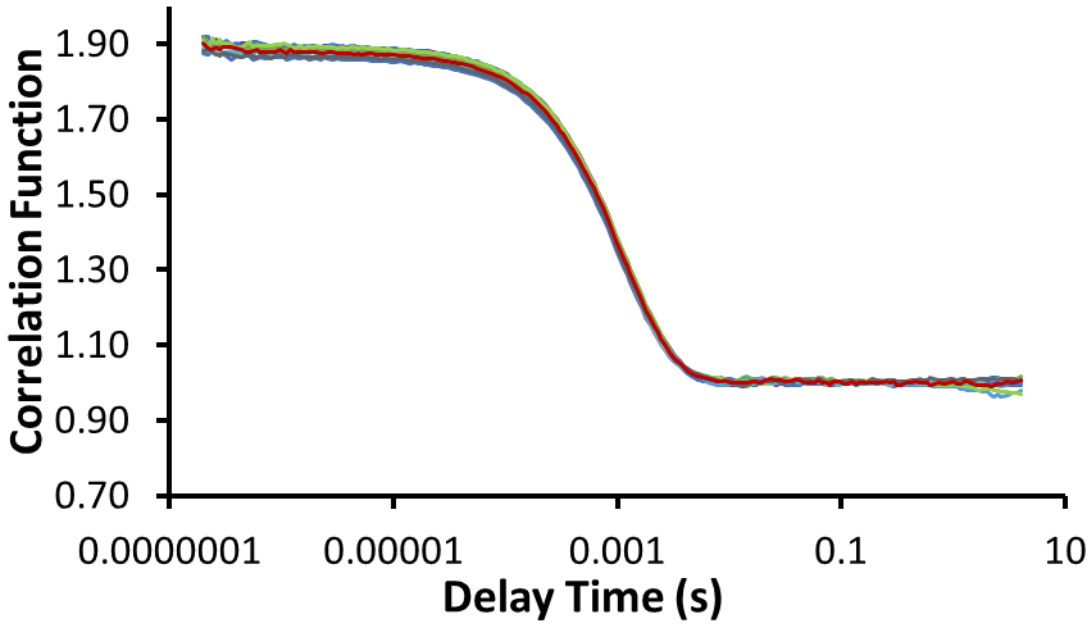

Figure S50 - Correlation function data for 10 DLS runs of co-formulation **b** (5.56 mM) in an EtOH: H_2O (1:19) solution at 298 K.

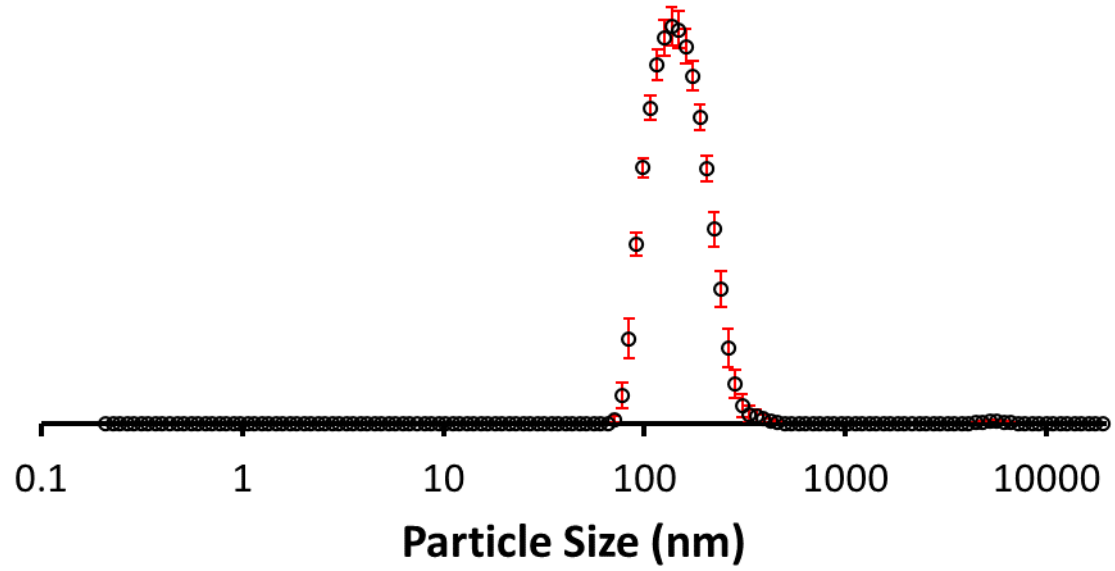

Figure S51 - The average intensity particle size distribution calculated using 10 DLS runs for co-formulation **b** (0.56 mM) in an EtOH: H_2O (1:19) solution at 298 K.

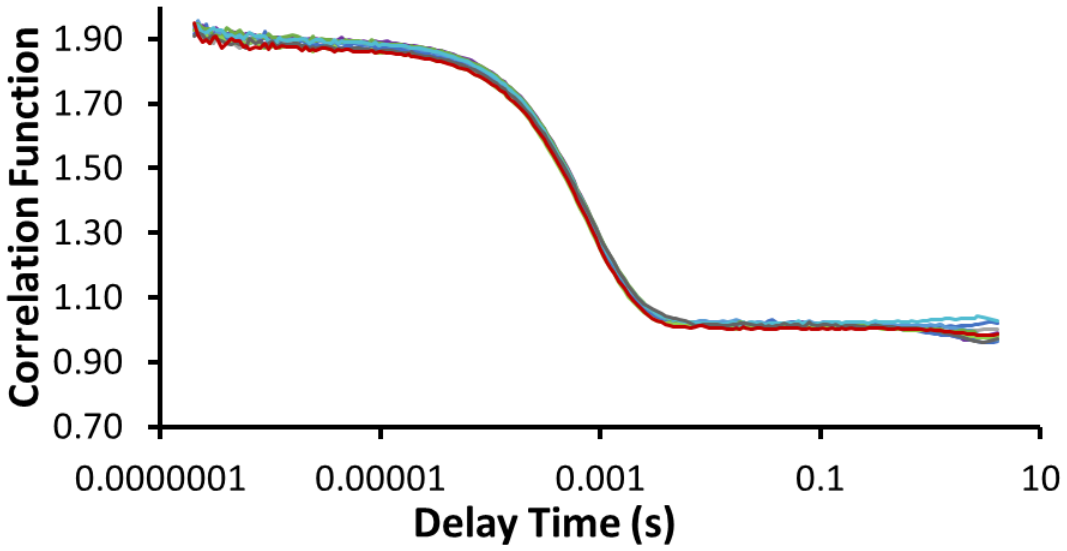

Figure S52 - Correlation function data for 10 DLS runs of co-formulation **b** (0.56 mM) in an EtOH: H_2O (1:19) solution at 298 K.

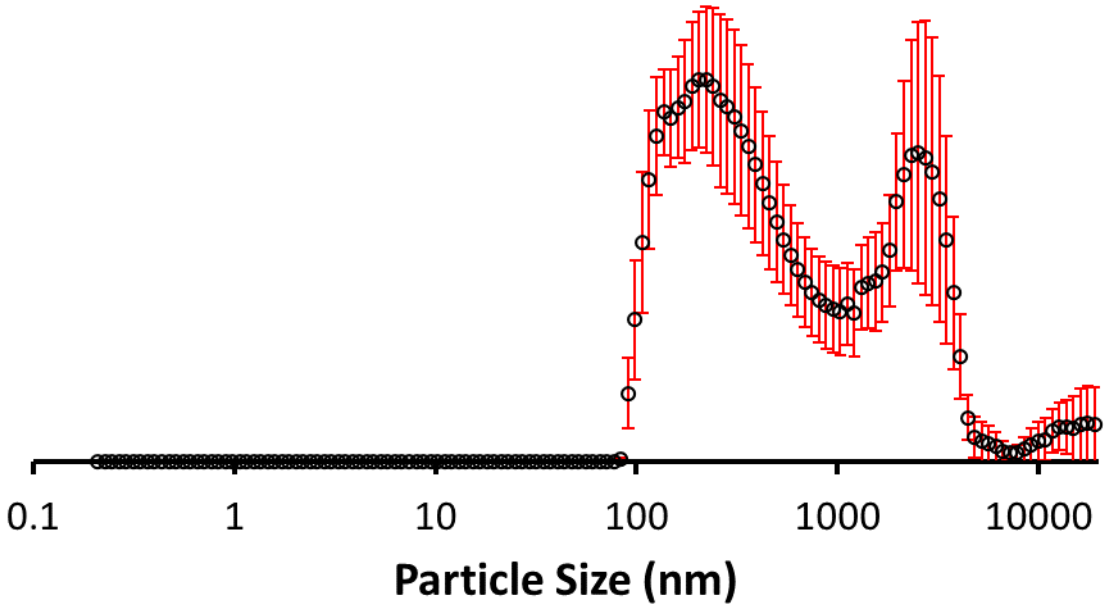

Figure S53 - The average intensity particle size distribution calculated using 10 DLS runs for co-formulation **c** (0.56 mM) in an EtOH: H_2O (1:19) solution at 298 K.

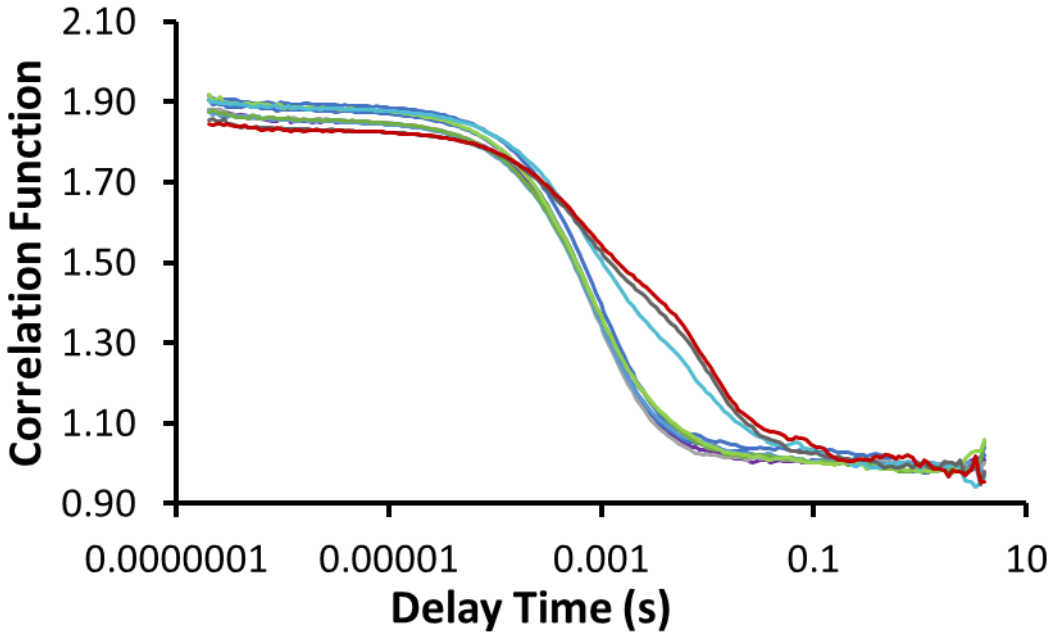

Figure S54 - Correlation function data for 10 DLS runs of co-formulation **c** (0.56 mM) in an EtOH: H_2O (1:19) solution at 298 K.

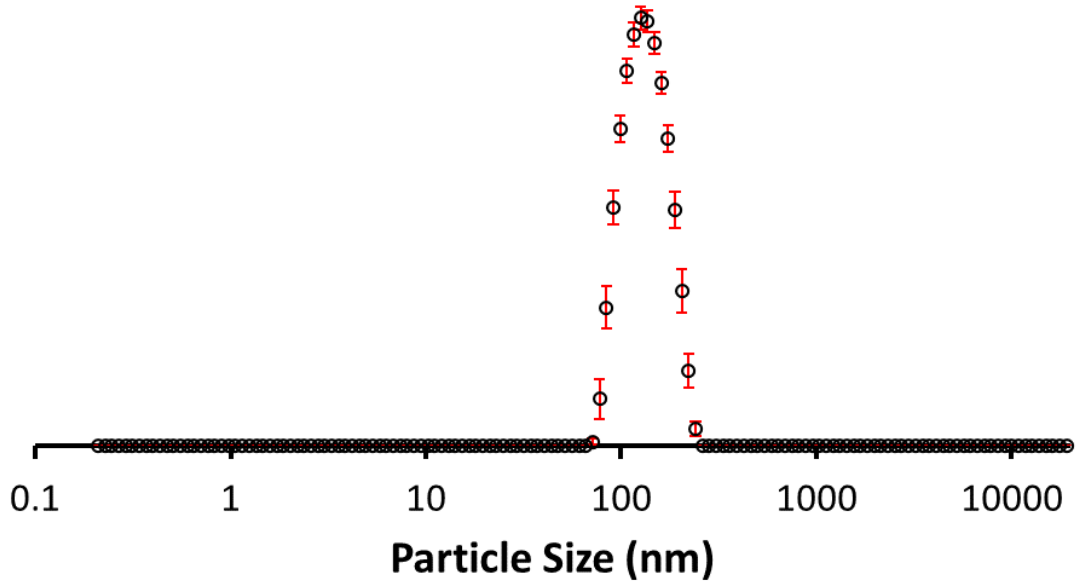

Figure S55 - The average intensity particle size distribution calculated using 10 DLS runs for co-formulation **d** (5.56 mM) in an EtOH: H_2O (1:19) solution at 298 K.

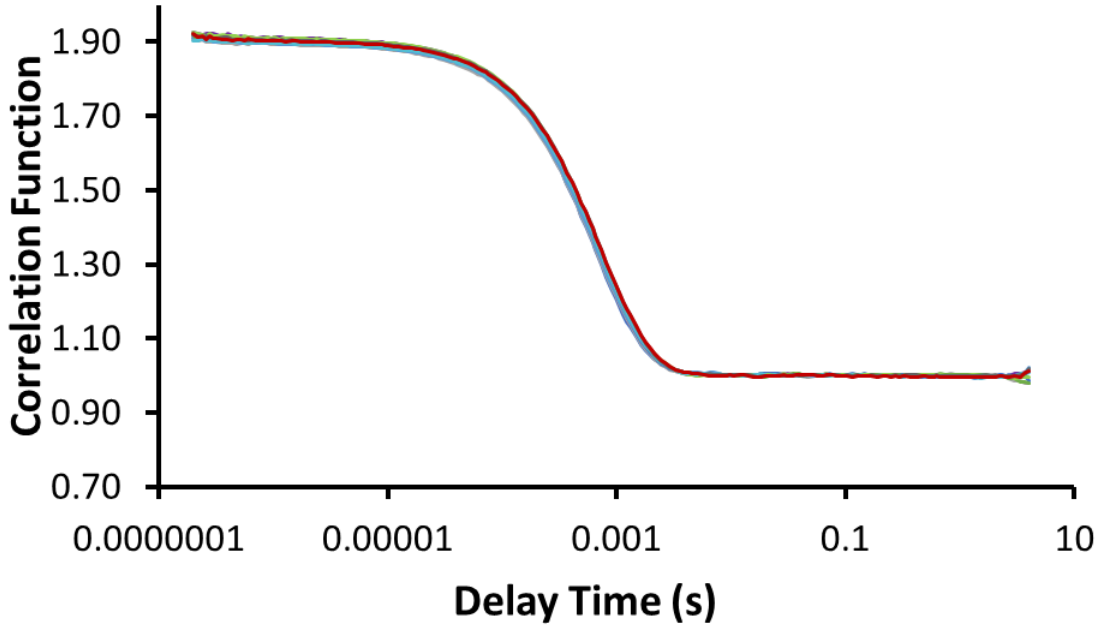

Figure S56 - Correlation function data for 10 DLS runs of co-formulation **d** (5.56 mM) in an EtOH: H_2O (1:19) solution at 298 K.

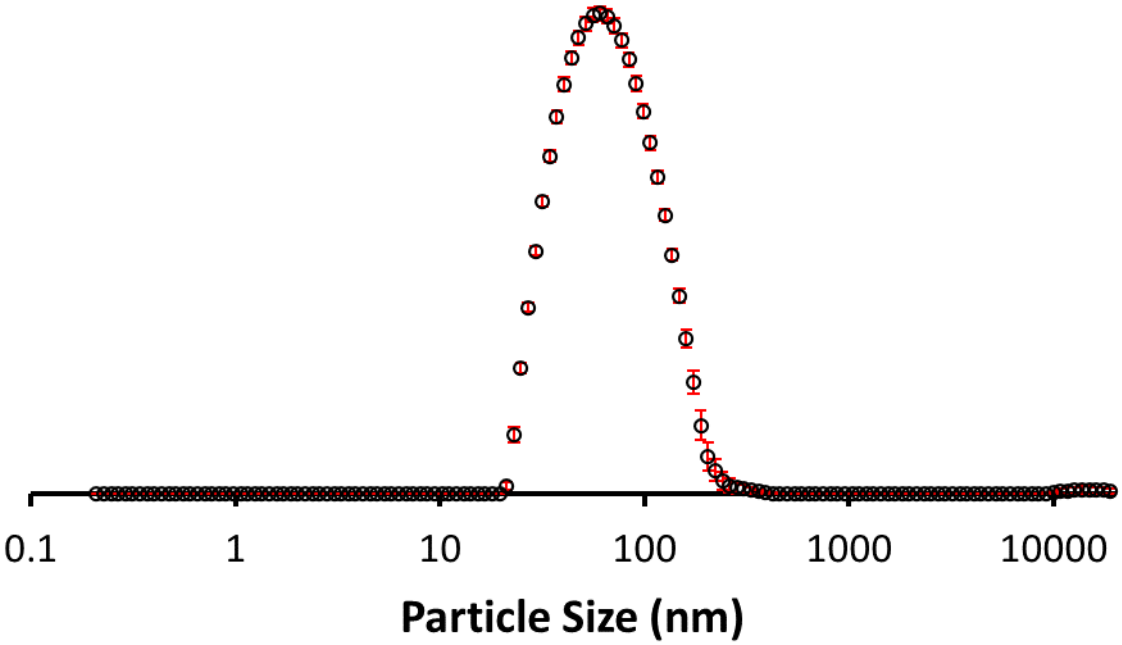

Figure S57 - The average intensity particle size distribution calculated using 10 DLS runs for co-formulation **d** (0.56 mM) in an EtOH: H_2O (1:19) solution at 298 K.

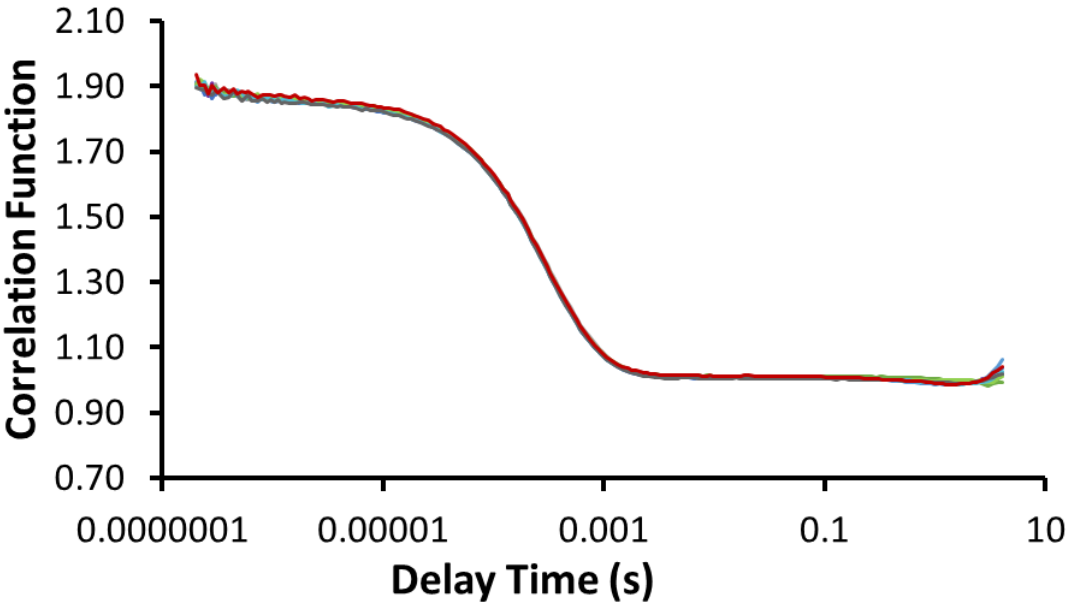

Figure S58 - Correlation function data for 10 DLS runs of co-formulation **d** (0.56 mM) in an EtOH: H_2O (1:19) solution at 298 K.

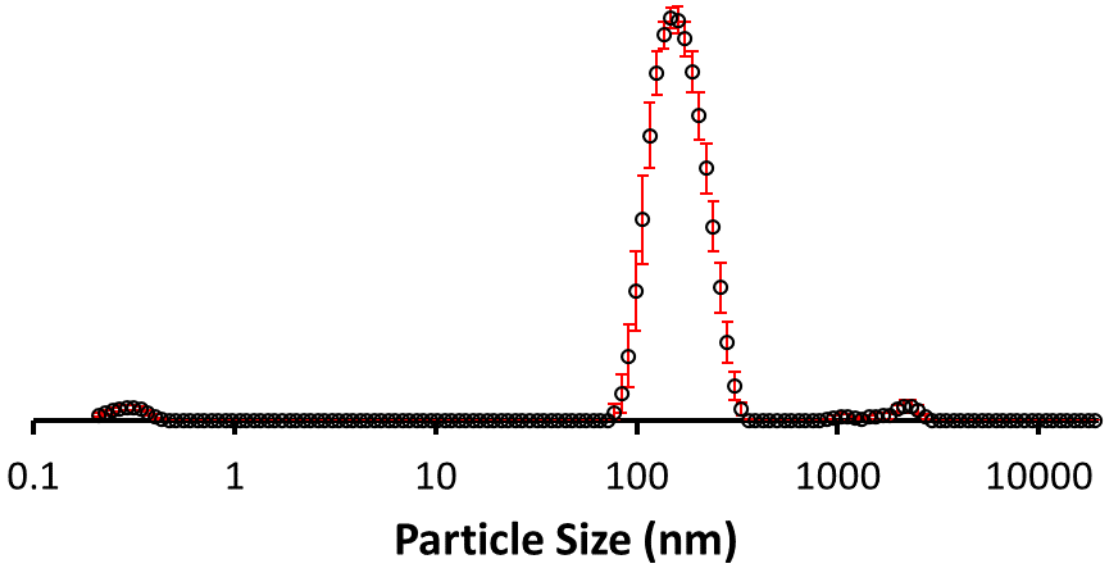

Figure S59 - The average intensity particle size distribution calculated using 9 DLS runs for co-formulation **e** (0.56 mM) in an EtOH: H_2O (1:19) solution at 298 K.

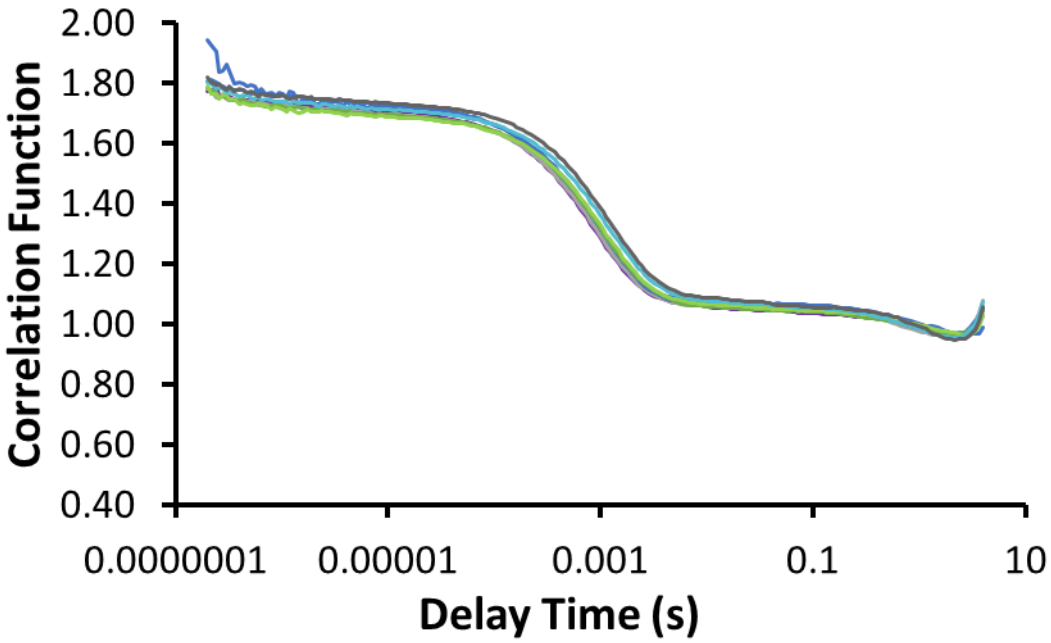

Figure S60 - Correlation function data for 9 DLS runs of co-formulation **e** (0.56 mM) in an EtOH: H_2O (1:19) solution at 298 K.

1.8 Antimicrobial Efficacy Testing

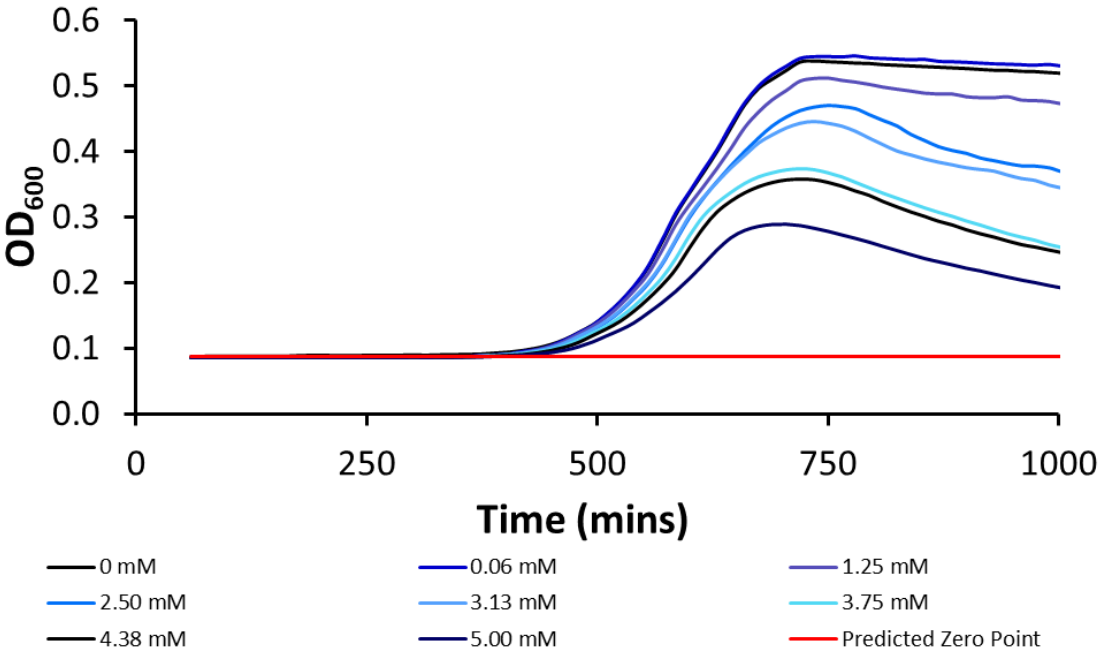

Figure S61 - Averaged growth curves created from absorbance readings of *E.coli* DH10B in the presence of compound **42** at varying concentrations.

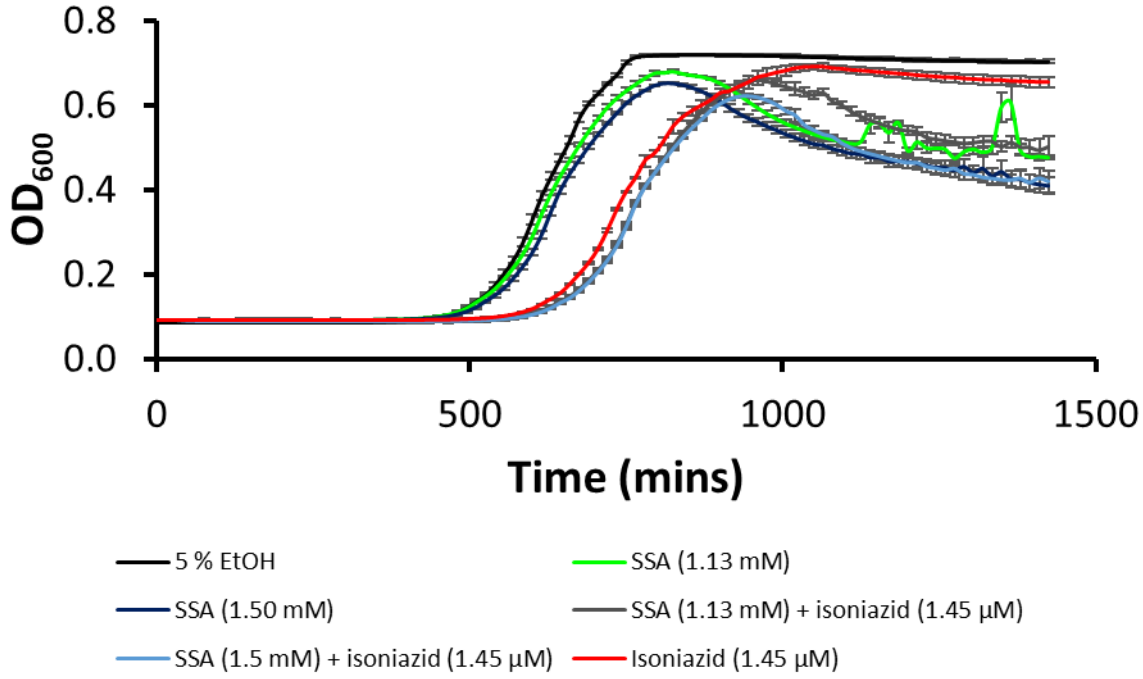

Figure S62 - Averaged growth curves created from absorbance readings of *E. coli* DH10B in the presence of SSA **42**, **isoniazid** (1.45 µM) and co-formulated systems with no prior incubation.

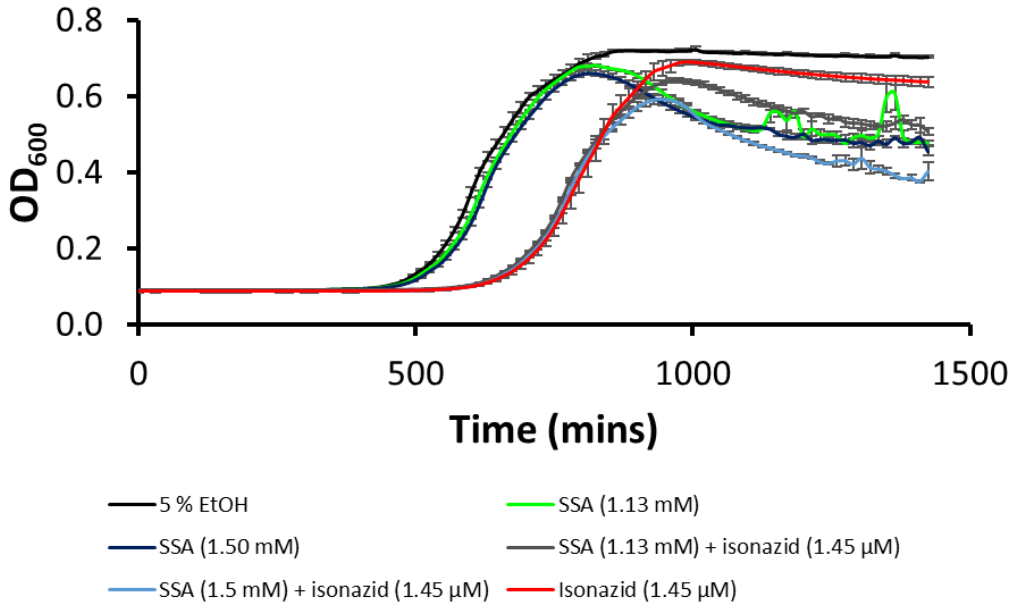

Figure S63 - Averaged growth curves created from absorbance readings of *E. coli* DH10B in the presence of SSA **42**, **isoniazid** (1.45 µM) and co-formulated systems following a 10 min incubation of **isoniazid** prior to the addition of the SSA.

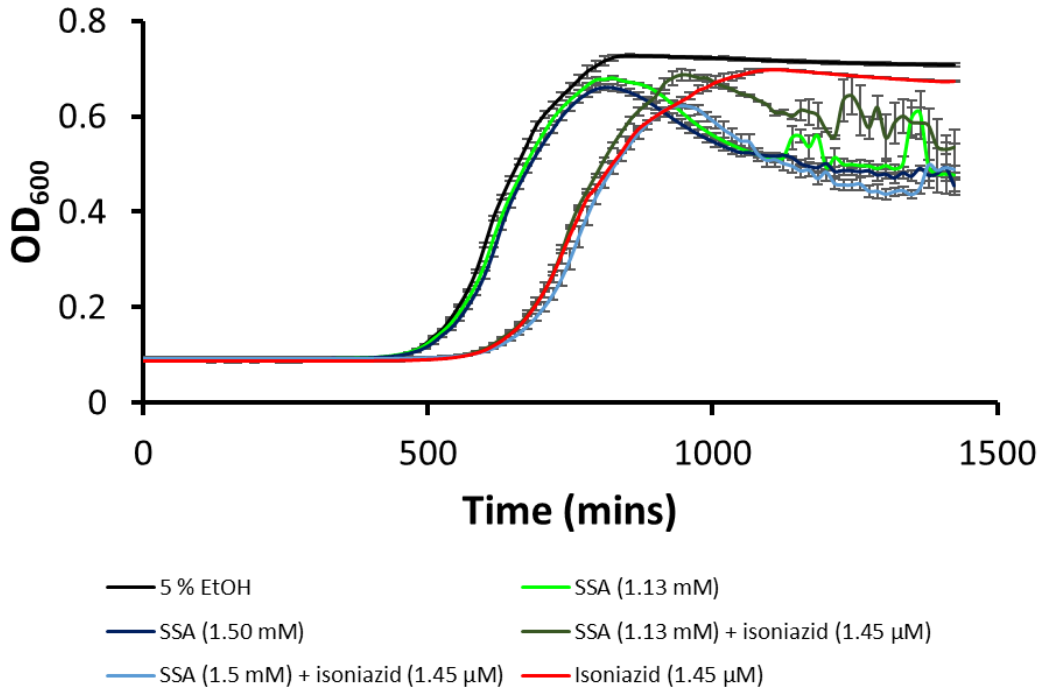

Figure S64 - Averaged growth curves created from absorbance readings of *E. coli* DH10B in the presence of SSA **42**, **isoniazid** (1.45 µM) and co-formulated systems following a 10 min incubation of SSA prior to the addition of the **isoniazid**.

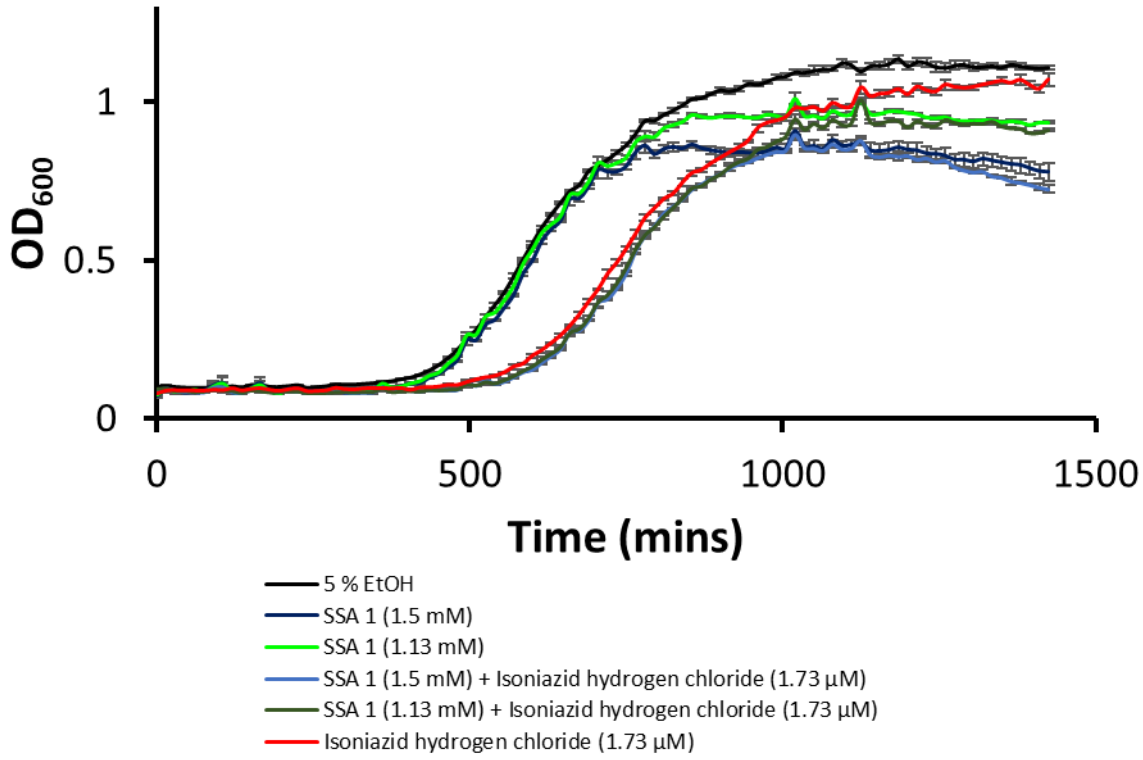

Figure S65 - Averaged growth curves created from absorbance readings of *E. coli* DH10B in the presence of SSA **42**, **isoniazid hydrogen chloride** (1.73 µM) and co-formulated systems with no prior incubation.

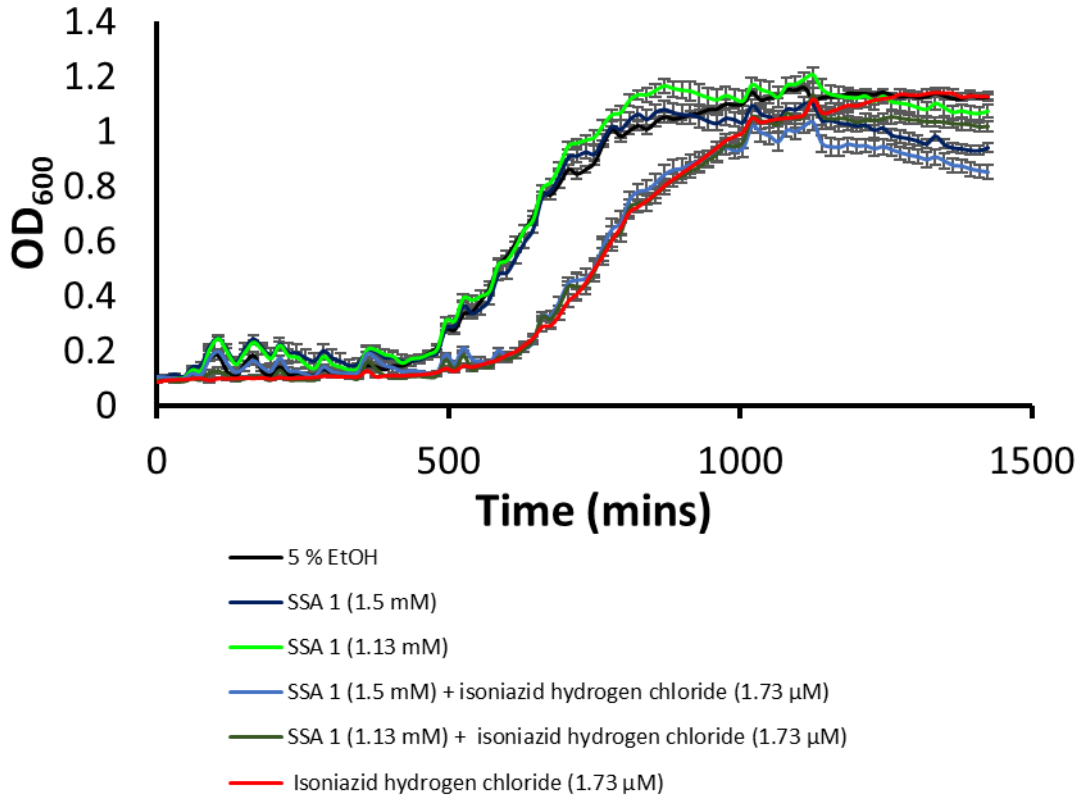

Figure S66 - Averaged growth curves created from absorbance readings of *E. coli* DH10B in the presence of SSA **42**, **isoniazid hydrogen chloride** (1.73 µM) and co-formulated systems following a 10 min incubation of **isoniazid hydrogen chloride** prior to the addition of the SSA.

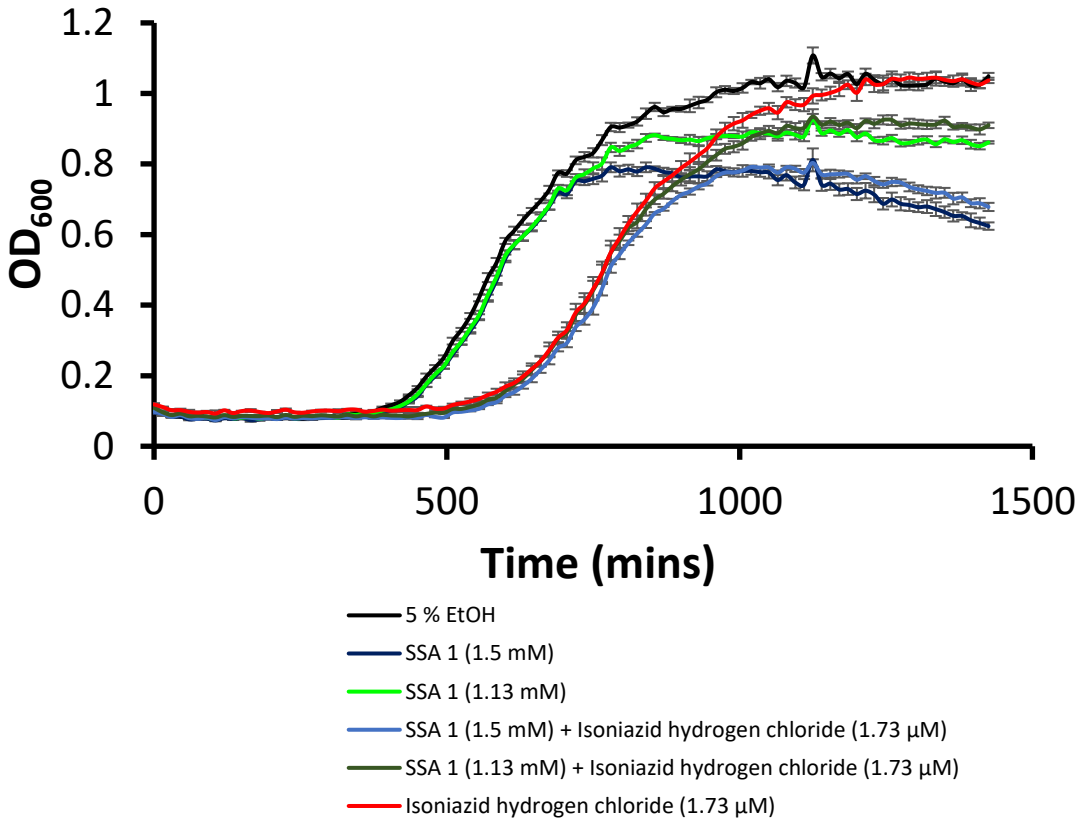

Figure S67 - Averaged growth curves created from absorbance readings of *E. coli* DH10B in the presence of SSA **42**, **isoniazid hydrogen chloride** (1.73 µM) and co-formulated systems following a 10 min incubation of SSA prior to the addition of the **isoniazid hydrogen chloride**.

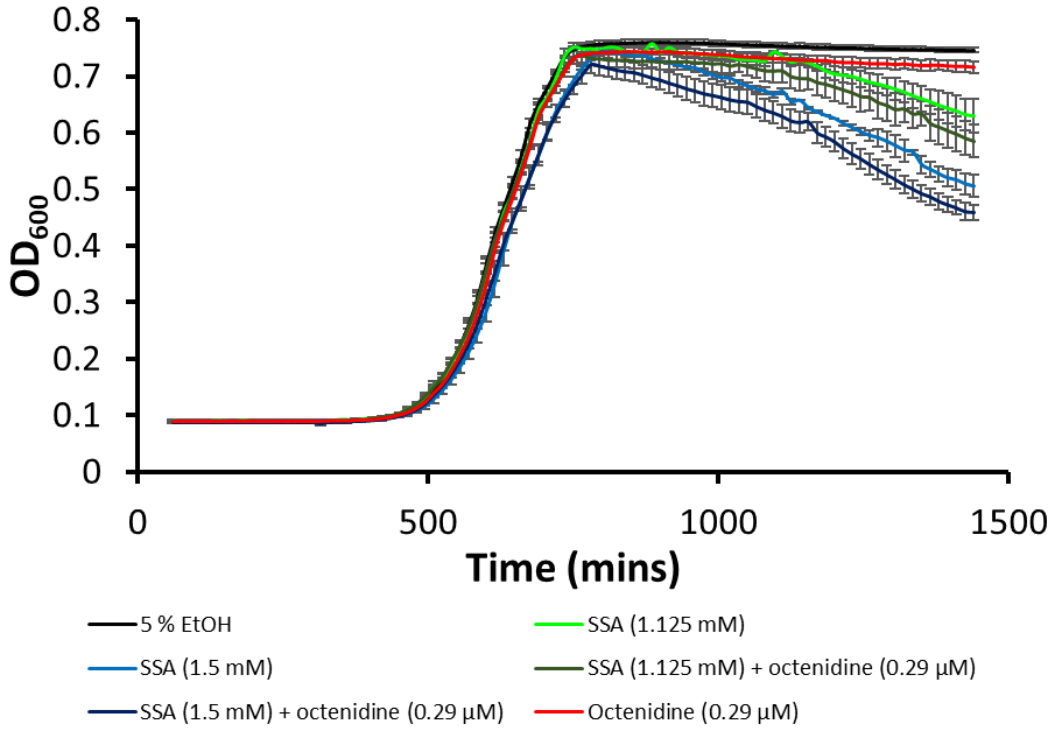

Figure S68 - Averaged growth curves created from absorbance readings of *E. coli* DH10B in the presence of SSA **42**, **octenidine** (0.29 µM) and co-formulated systems following a 10 min incubation of SSA prior to the addition of the **octenidine**.

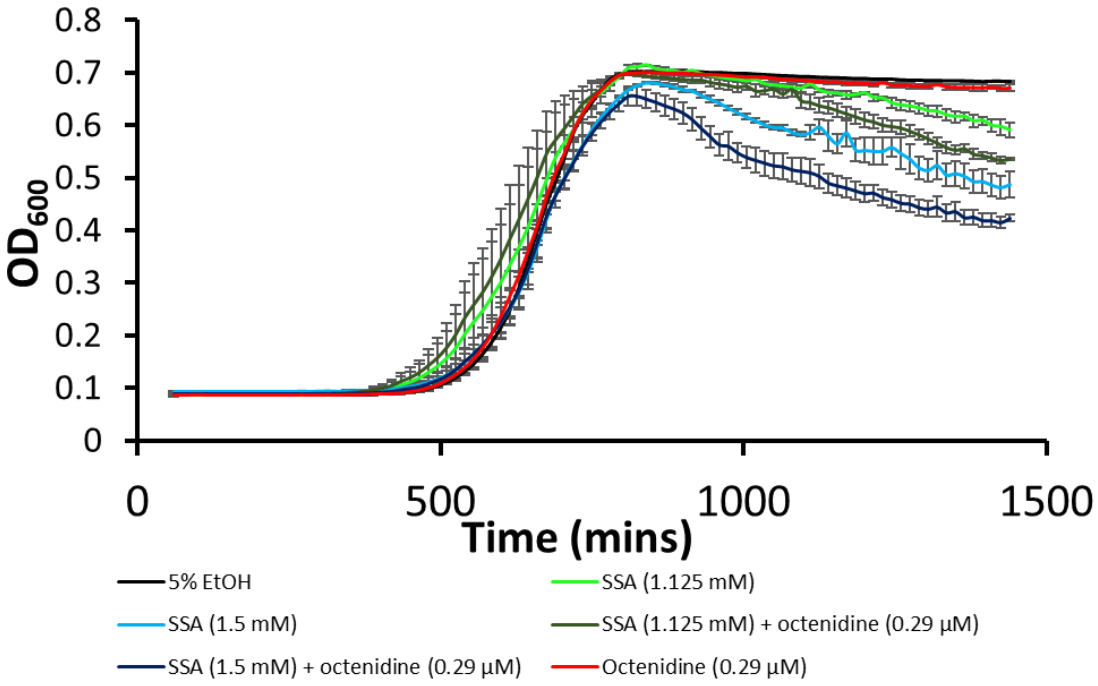

Figure S69 - Averaged growth curves created from absorbance readings of *E. coli* DH10B in the presence of SSA **42**, **octenidine** (0.29 µM) and co-formulated systems following a 10 min incubation of **octenidine** prior to the addition of the SSA.

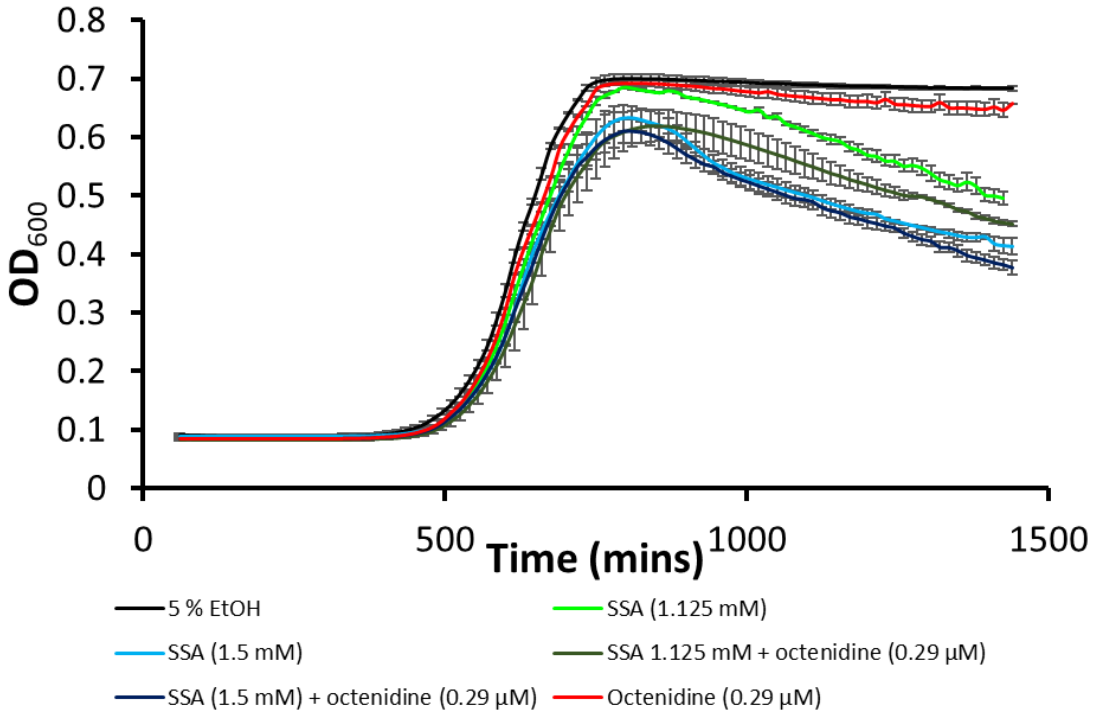

Figure S70 -Averaged growth curves created from absorbance readings of *E. coli* DH10B in the presence of SSA **42**, **octenidine** (0.29 µM) and co-formulated systems with no prior incubation.

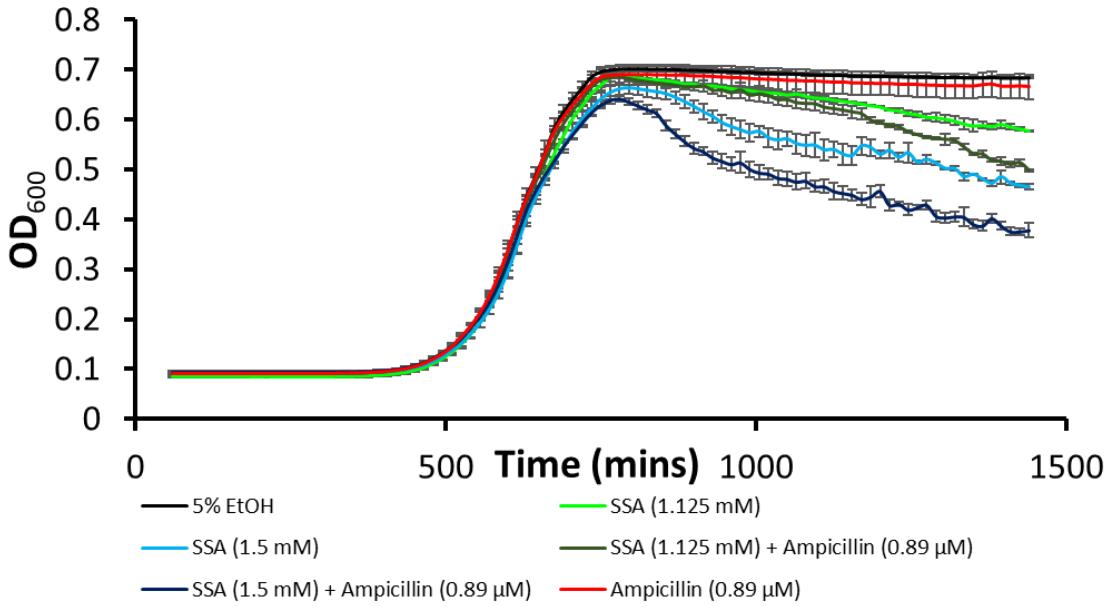

Figure S71 - Averaged growth curves created from absorbance readings of *E. coli* DH10B in the presence of SSA **42**, **ampicillin** (0.89 µM) and co-formulated systems following a 10 min incubation of SSA prior to the addition of the **ampicillin**.

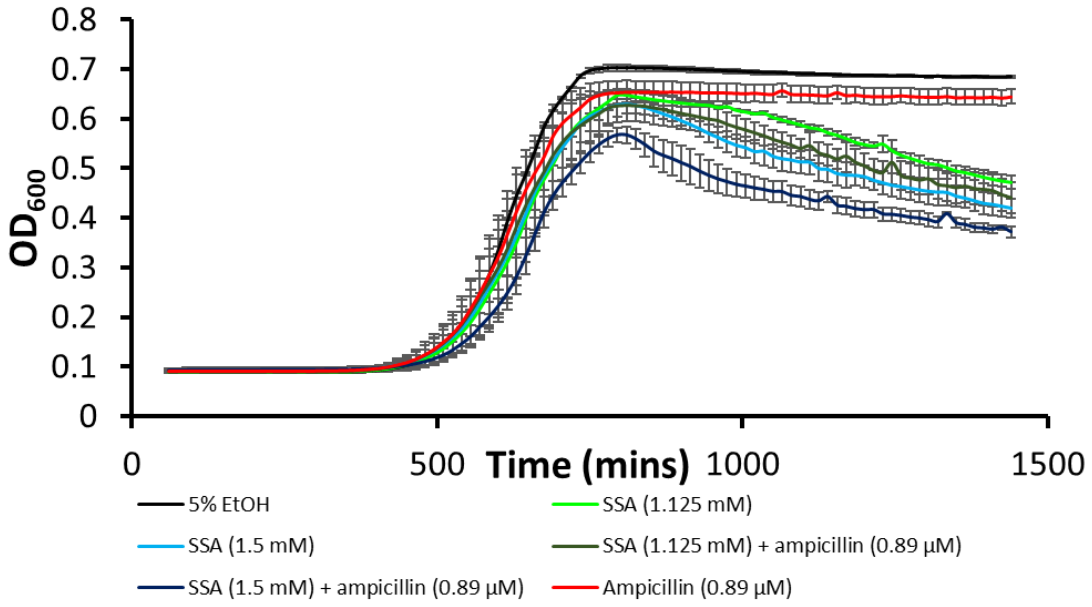

Figure S72 - Averaged growth curves created from absorbance readings of *E. coli* DH10B in the presence of SSA **42**, **ampicillin** (0.89 µM) and co-formulated systems following a 10 min incubation of **ampicillin** prior to the addition of the SSA.

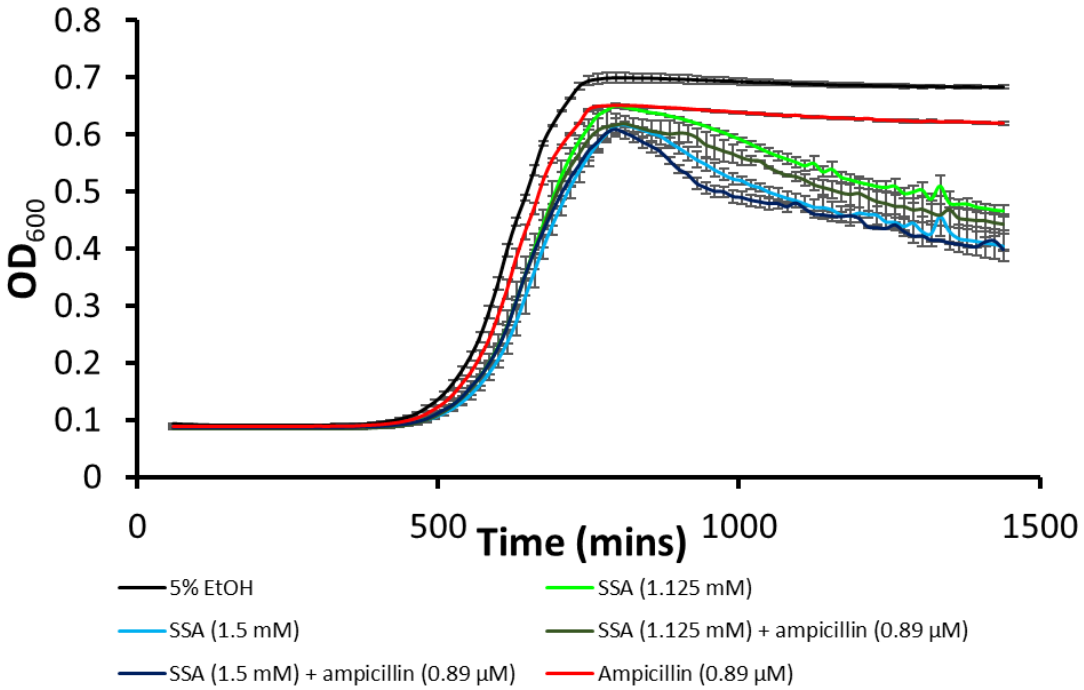

Figure S73 - Averaged growth curves created from absorbance readings of *E. coli* DH10B in the presence of SSA **42**, **ampicillin** (0.89 µM) and co-formulated systems with no prior incubation.

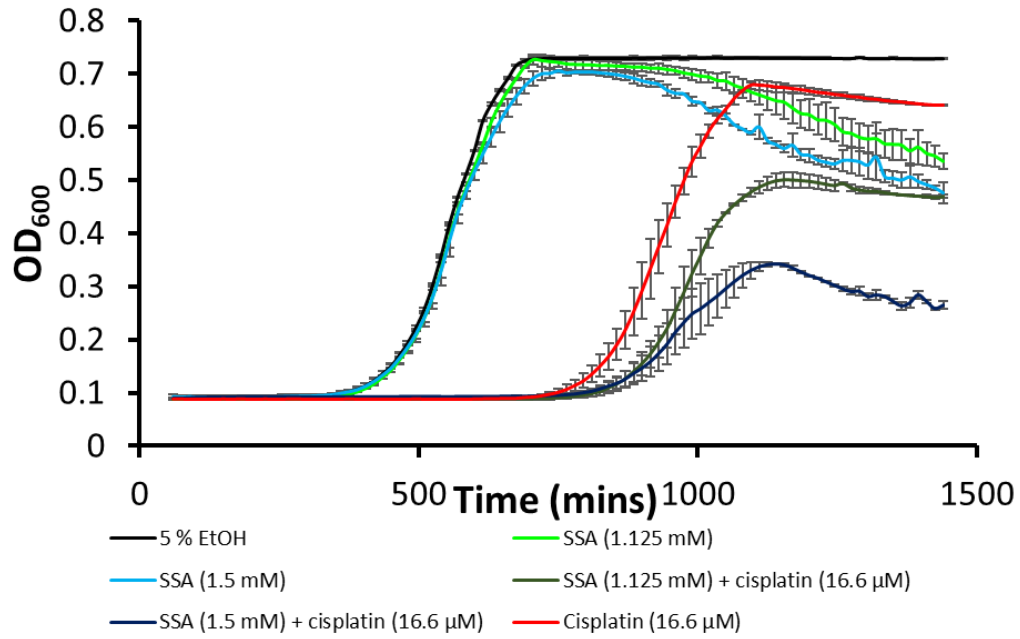

Figure S74 - Averaged growth curves created from absorbance readings of *E. coli* DH10B in the presence of SSA **42**, **cisplatin** (16.6 µM) and co-formulated systems following a 10 min incubation of SSA prior to the addition of the **cisplatin**.

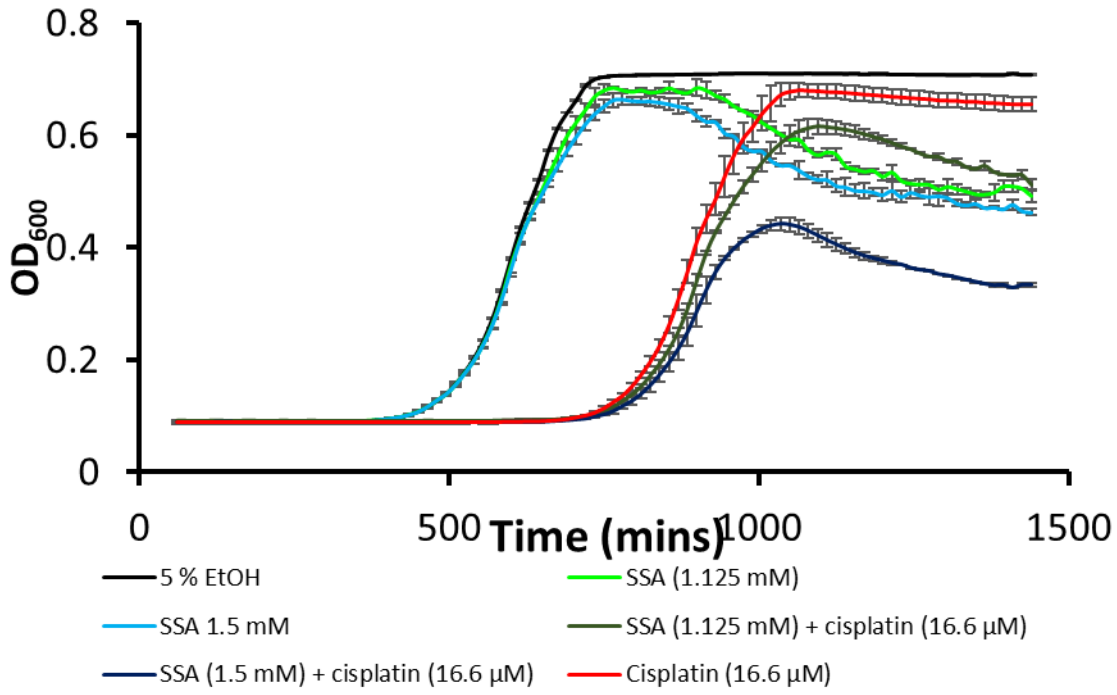

Figure S75 - Averaged growth curves created from absorbance readings of *E. coli* DH10B in the presence of SSA **42**, **cisplatin** (16.6 µM) and co-formulated systems following a 10 min incubation of **cisplatin** prior to the addition of the SSA.

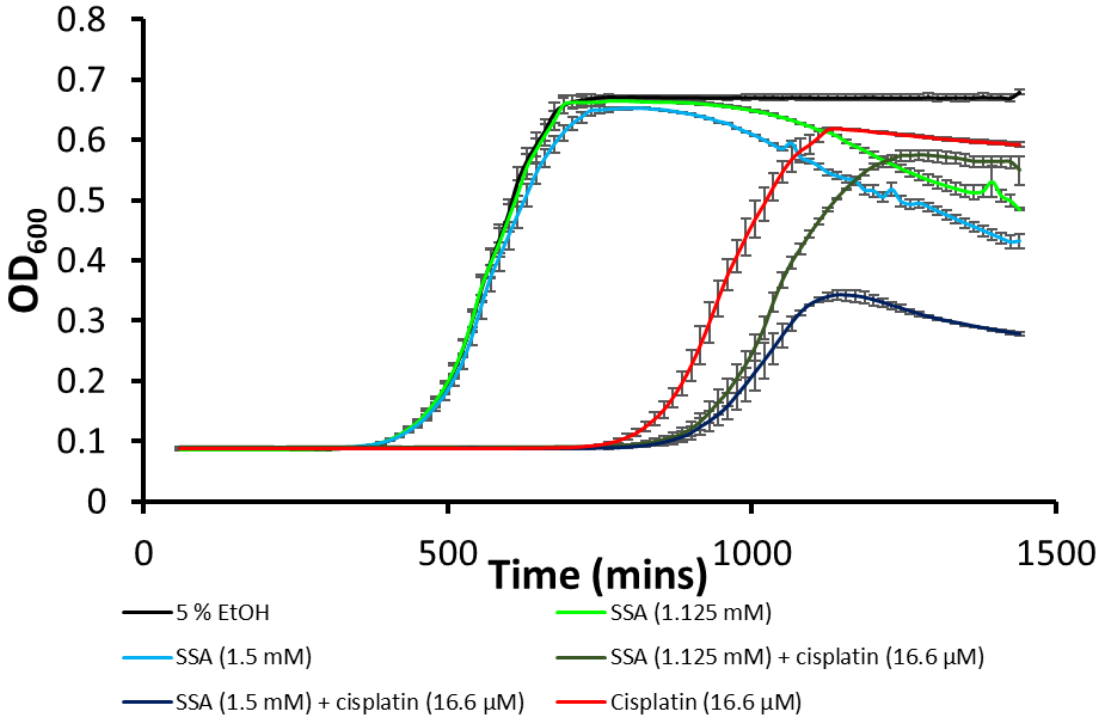

Figure S76 - Averaged growth curves created from absorbance readings of *E. coli* DH10B in the presence of SSA **42**, **cisplatin** (16.6 µM) and co-formulated systems with no prior incubation.

2 Chapter 3 Appendix

2.1 Characterisation NMR

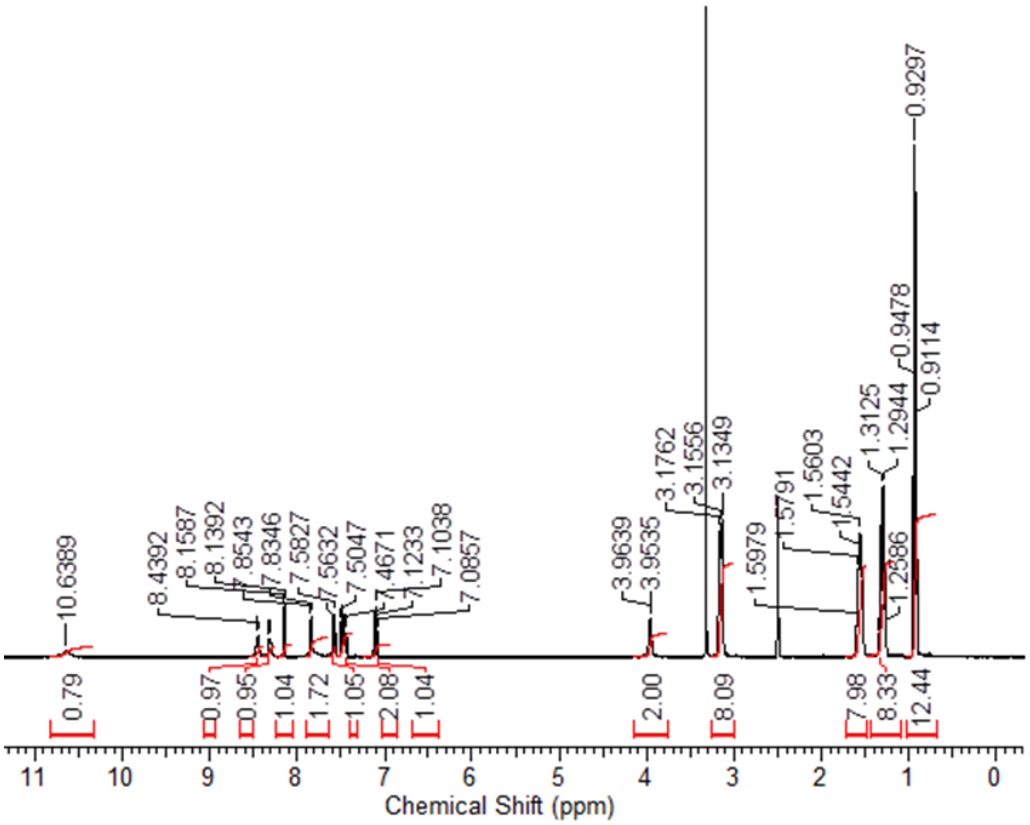

Figure S77 - ^{1}H NMR of compound **49** in DMSO-d_6 conducted at 298 K.

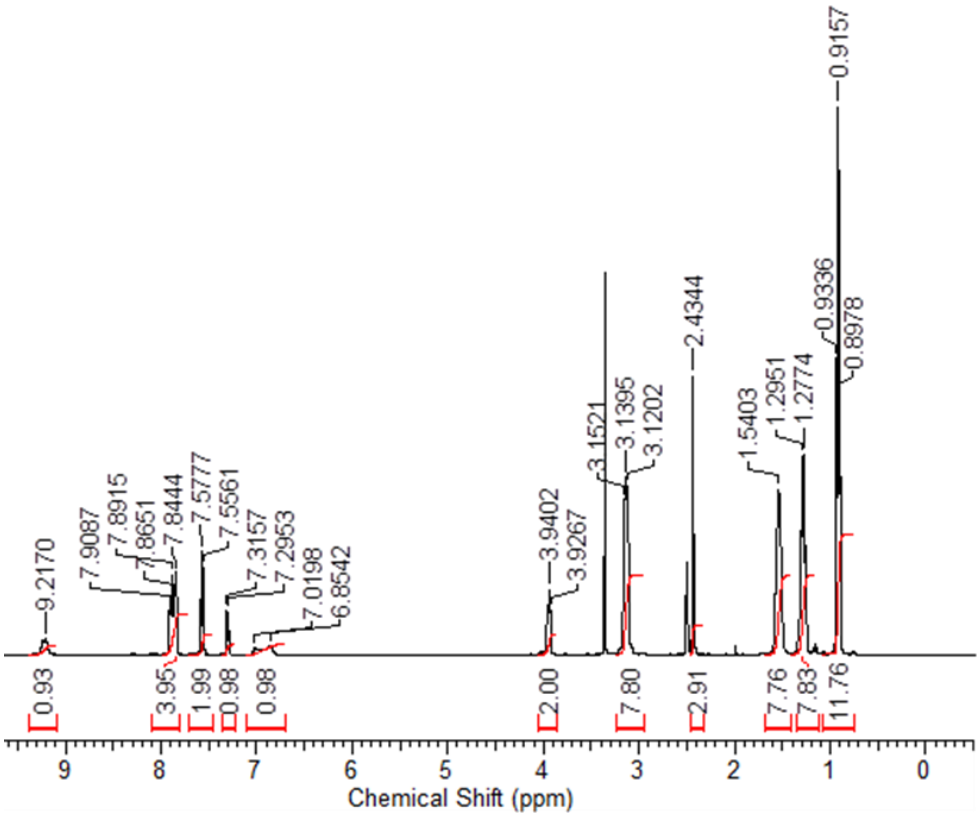

Figure S78 - ^{1}H NMR of compound **50** in DMSO-d_6 conducted at 298 K.

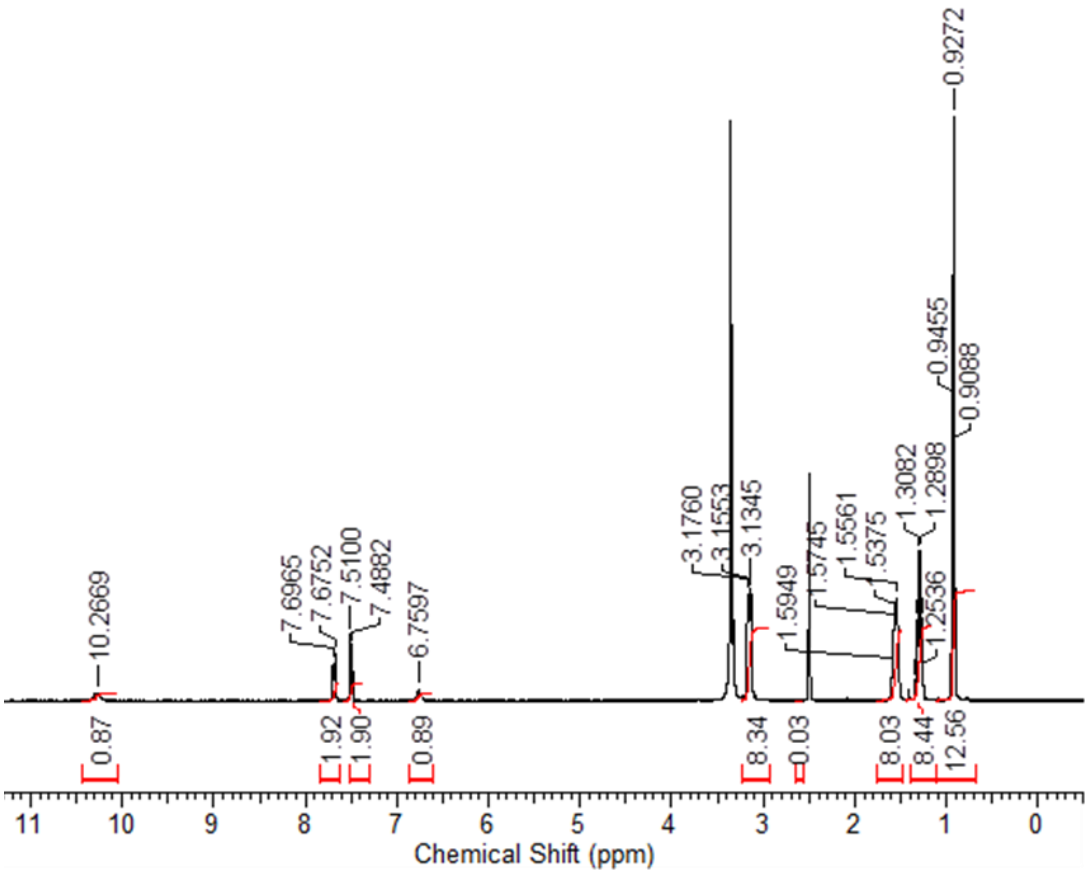

Figure S79 - ^{1}H NMR of compound **51** in DMSO-d_6 conducted at 298 K.

2.2 Dynamic Light Scattering

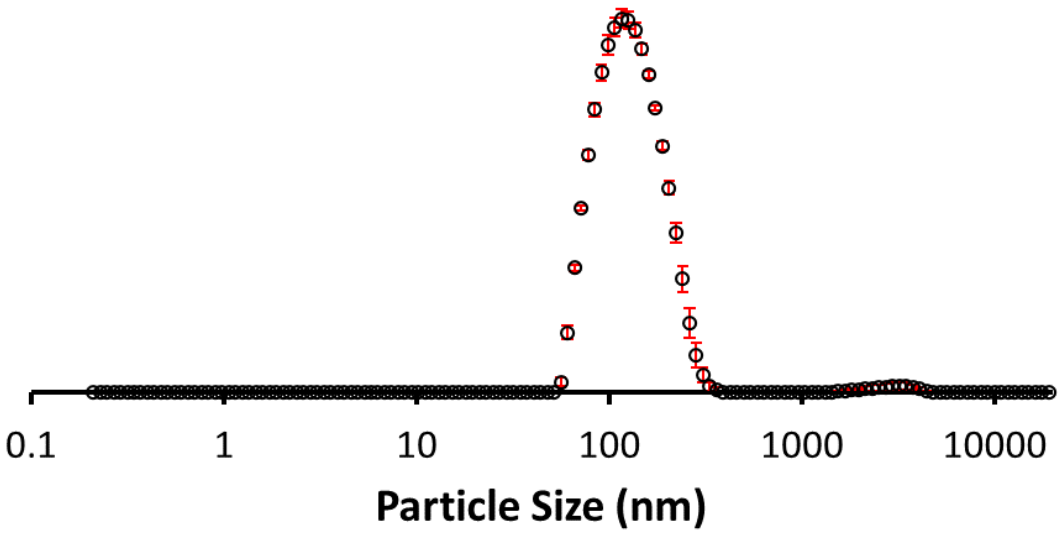

Figure S80 - The average intensity particle size distribution calculated using 9 DLS runs for co-formulation **g** (0.56 mM) in an EtOH: H_2O (1:19) solution at 298 K.

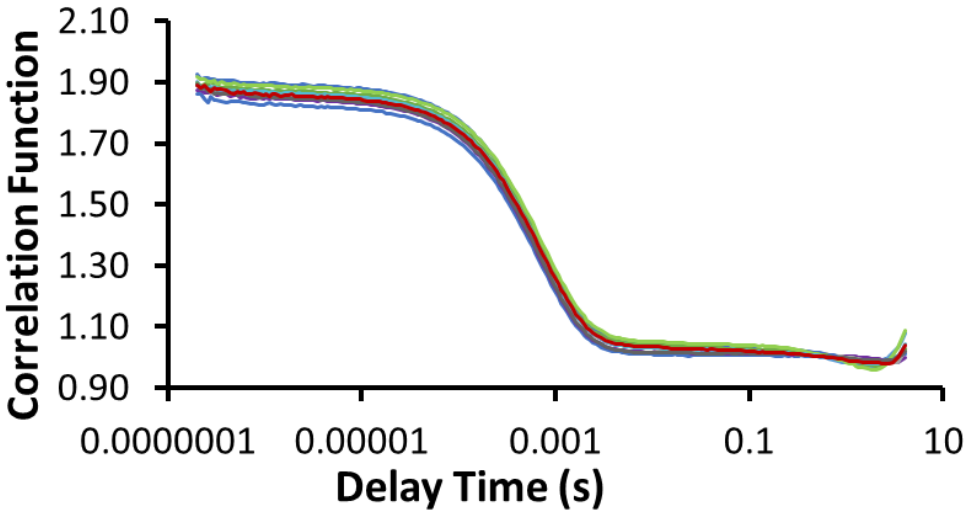

Figure S81 - Correlation function data for 9 DLS runs of co-formulation **g** (0.56 mM) in an EtOH: H_2O (1:19) solution at 298 K.

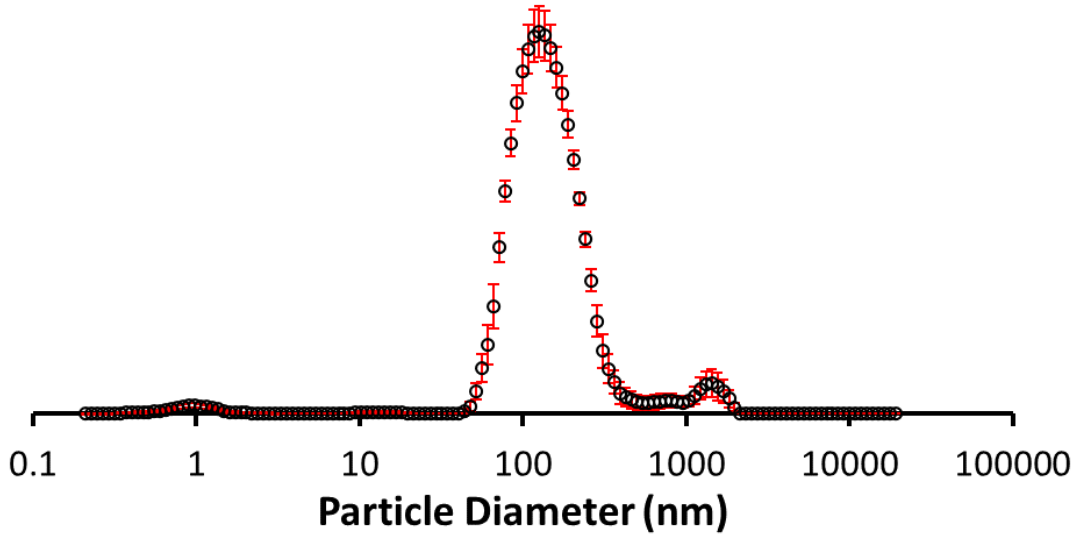

Figure S82 - The average intensity particle size distribution calculated using 9 DLS runs for co-formulation **h** (0.56 mM) in an EtOH: H_2O (1:19) solution at 298 K.

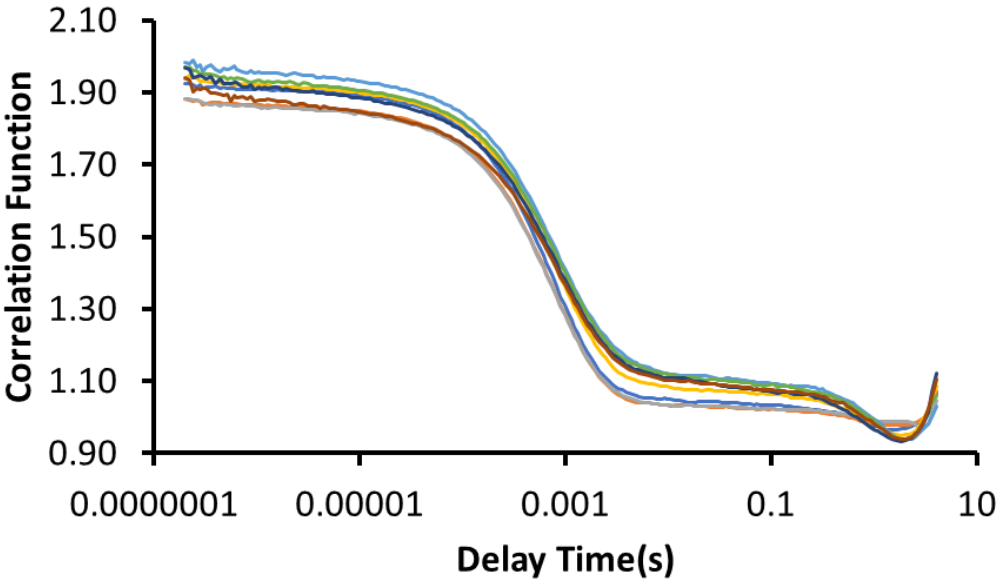

Figure S83 - Correlation function data for 9 DLS runs of co-formulation **h** (0.56 mM) in an EtOH: H_2O (1:19) solution at 298 K.

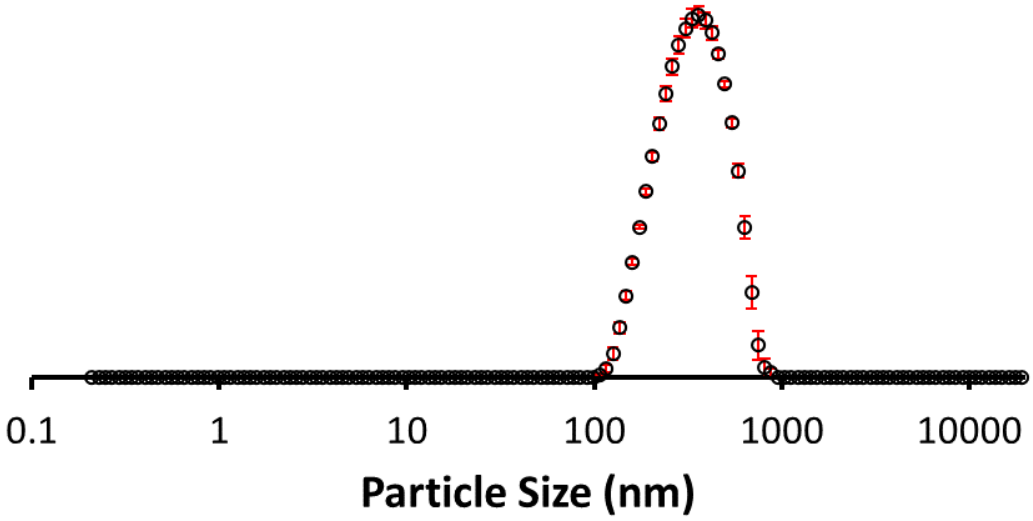

Figure S84 - The average intensity particle size distribution calculated using 9 DLS runs for co-formulation **i** (0.56 mM) in an EtOH: H_2O (1:19) solution at 298 K.

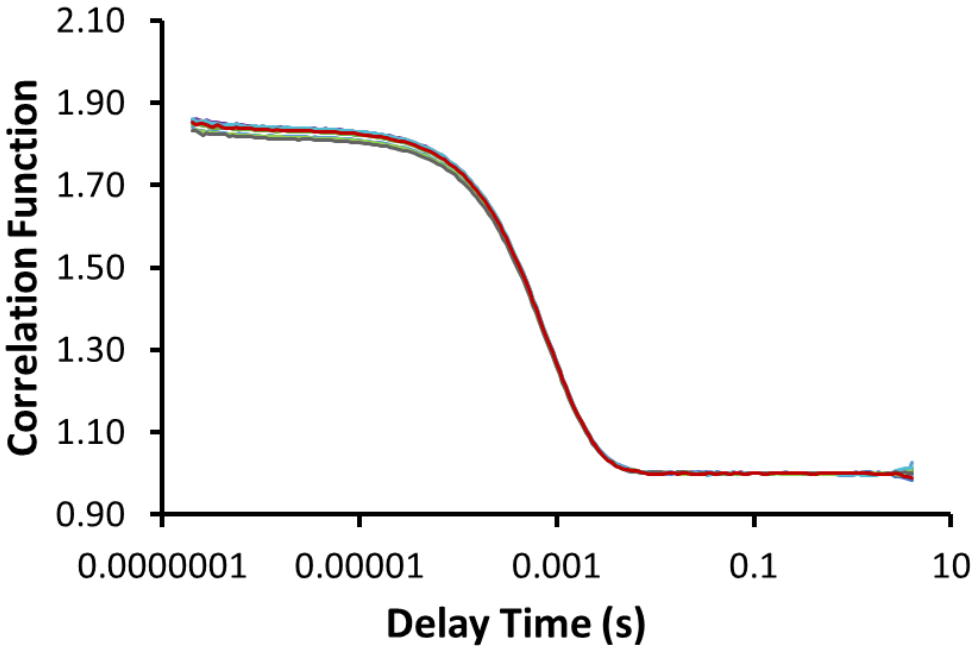

Figure S85 - Correlation function data for 9 DLS runs of co-formulation **i** (0.56 mM) in an EtOH: H_2O (1:19) solution at 298 K.

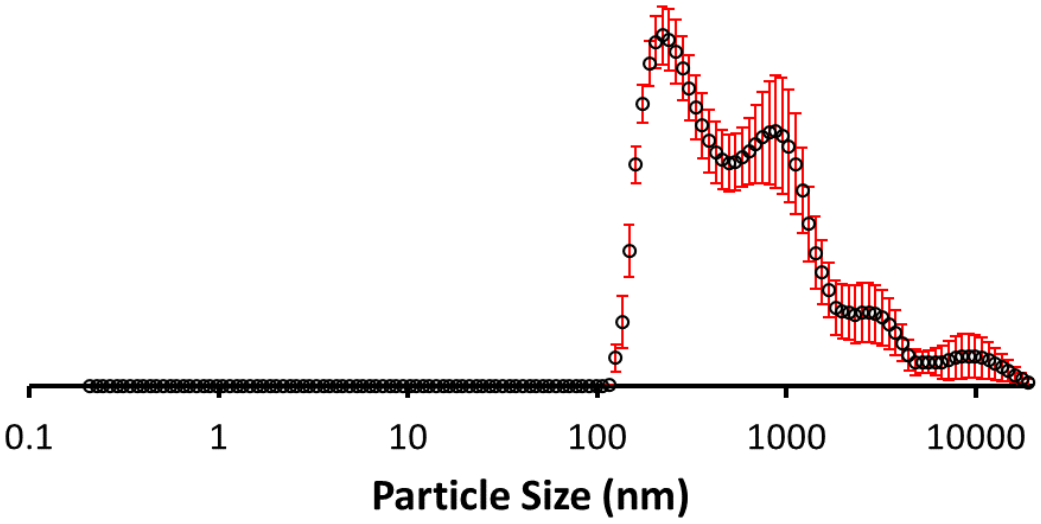

Figure S86 - The average intensity particle size distribution calculated using 9 DLS runs for co-formulation **j** (0.56 mM) in an EtOH: H_2O (1:19) solution at 298 K.

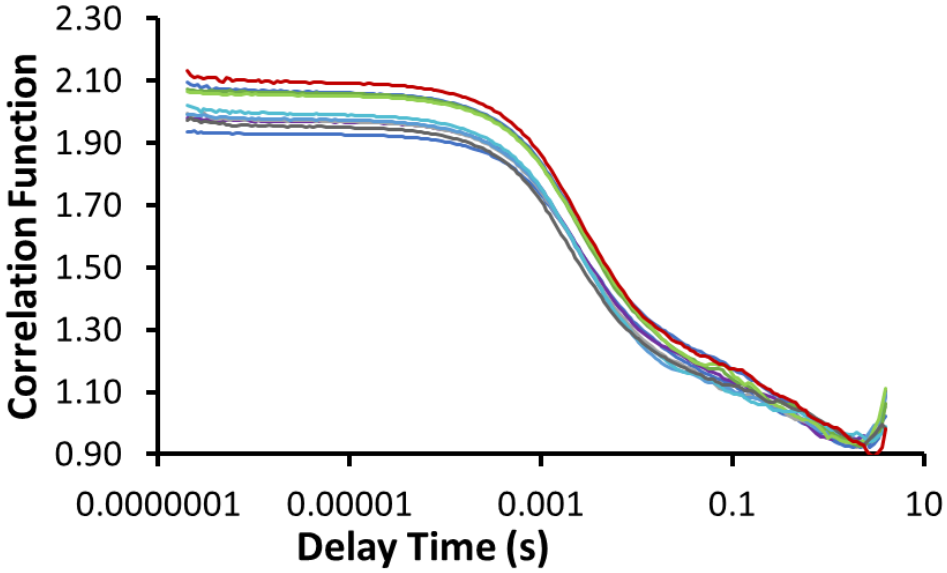

Figure S87 - Correlation function data for 9 DLS runs of co-formulation **j** (0.56 mM) in an EtOH: H_2O (1:19) solution at 298 K.

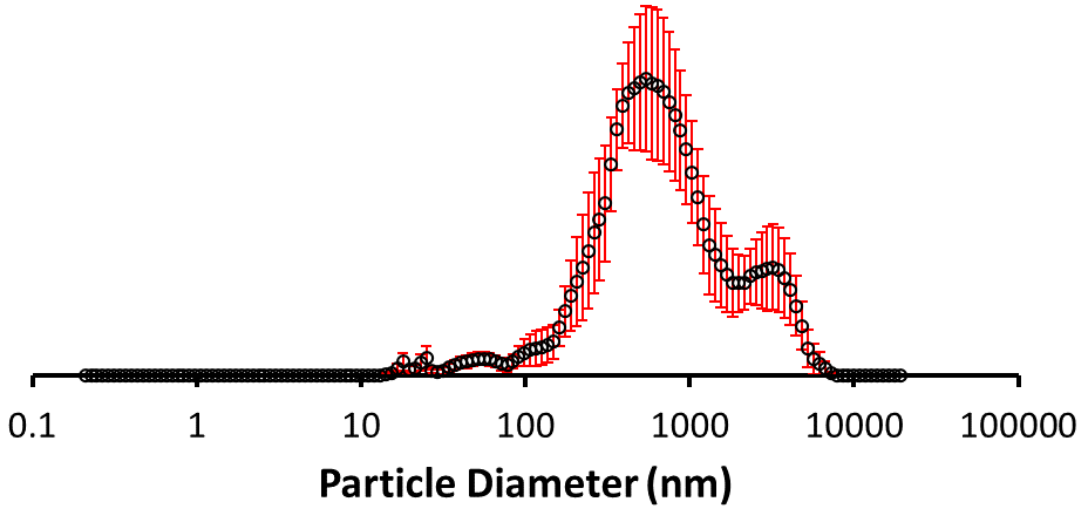

Figure S88 - The average intensity particle size distribution calculated using 9 DLS runs for co-formulation **k** (0.56 mM) in an EtOH: H_2O (1:19) solution at 298 K.

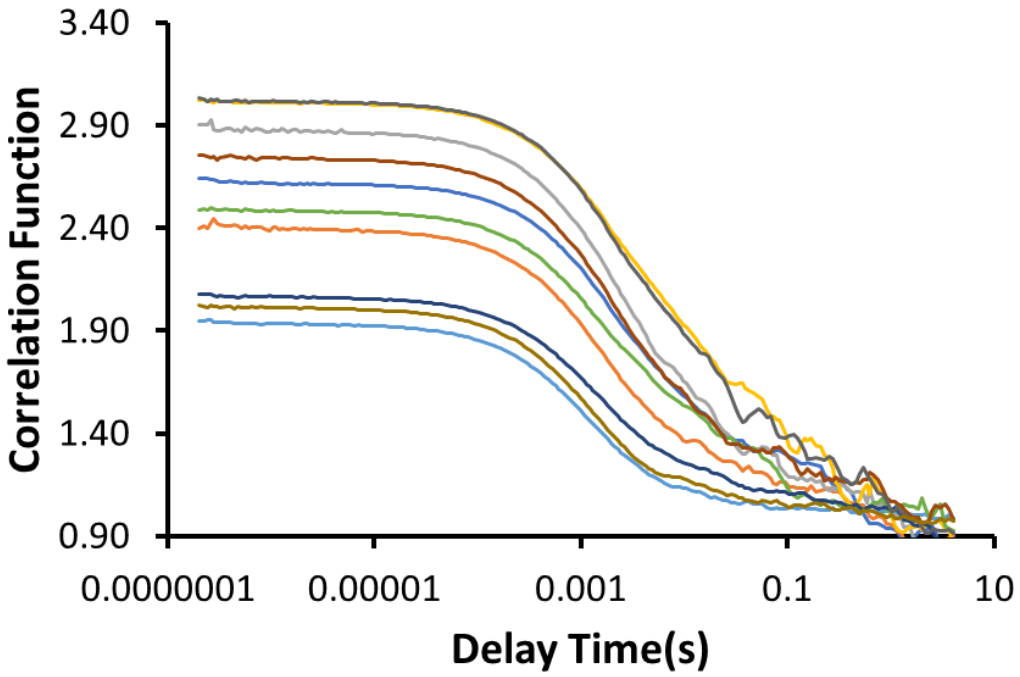

Figure S89 - Correlation function data for 9 DLS runs of co-formulation **k** (0.56 mM) in an EtOH: H_2O (1:19) solution at 298 K.

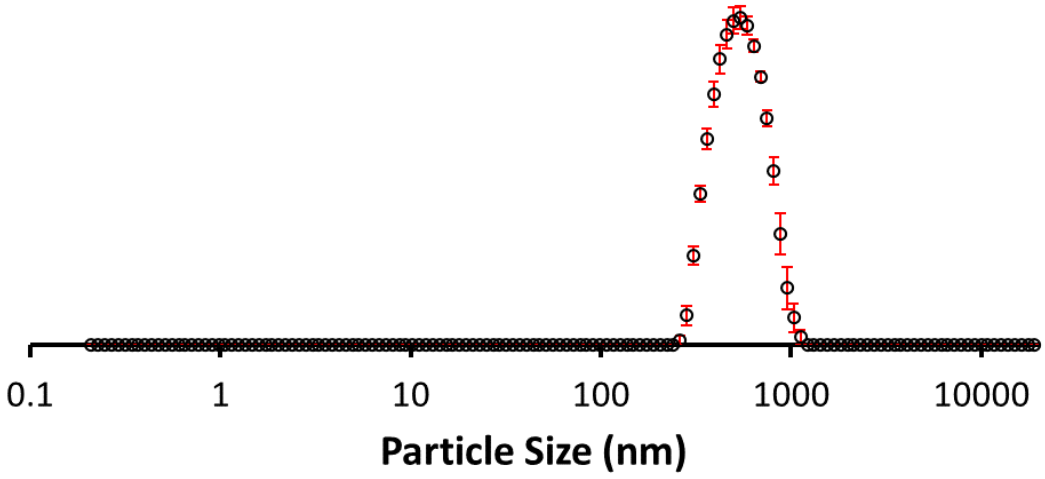

Figure S90 - The average intensity particle size distribution calculated using 9 DLS runs for co-formulation **I** (0.56 mM) in an EtOH: H_2O (1:19) solution at 298 K.

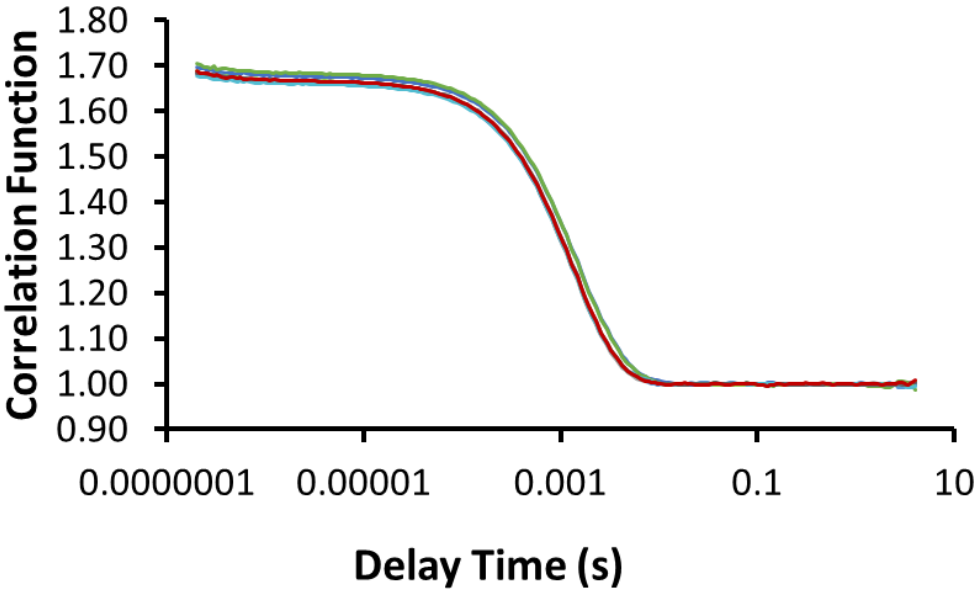

Figure S91 - Correlation function data for 9 DLS runs of co-formulation **I** (0.56 mM) in an EtOH: H_2O (1:19) solution at 298 K.

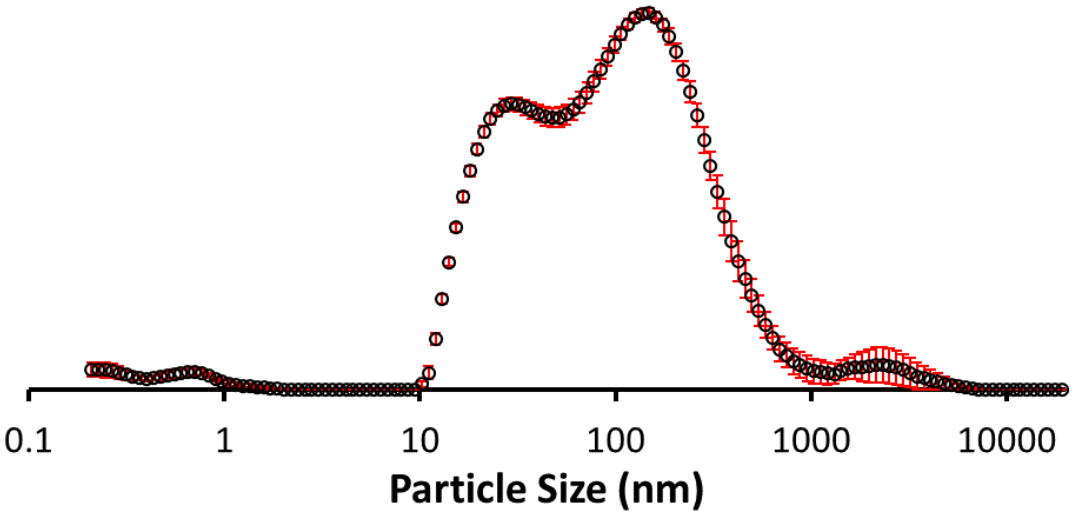

Figure S92 - The average intensity particle size distribution calculated using 9 DLS runs for co-formulation **m** (0.56 mM) in an EtOH: H_2O (1:19) solution at 298 K.

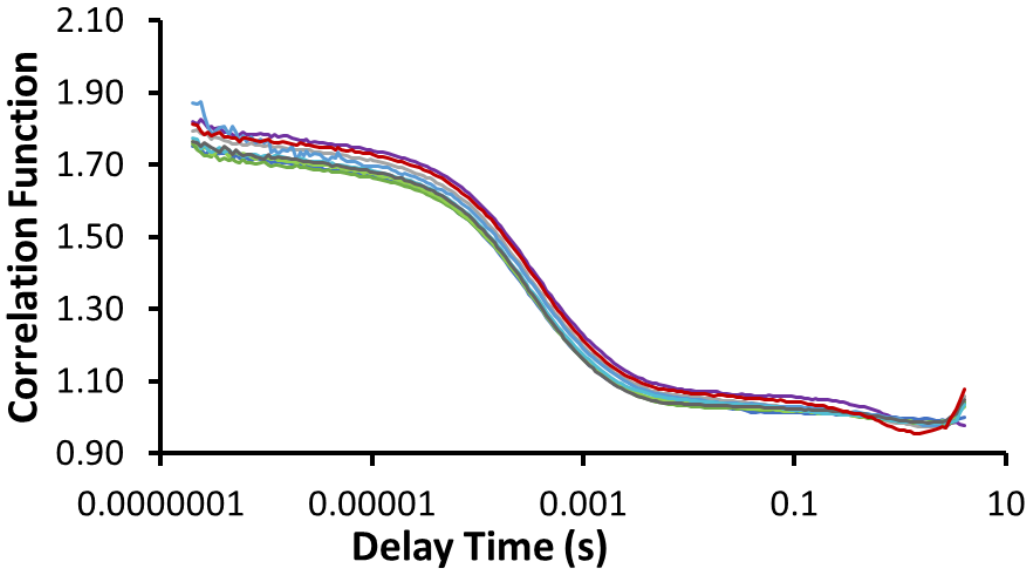

Figure S93 - Correlation function data for 9 DLS runs of co-formulation **m** (0.56 mM) in an EtOH: H_2O (1:19) solution at 298 K.

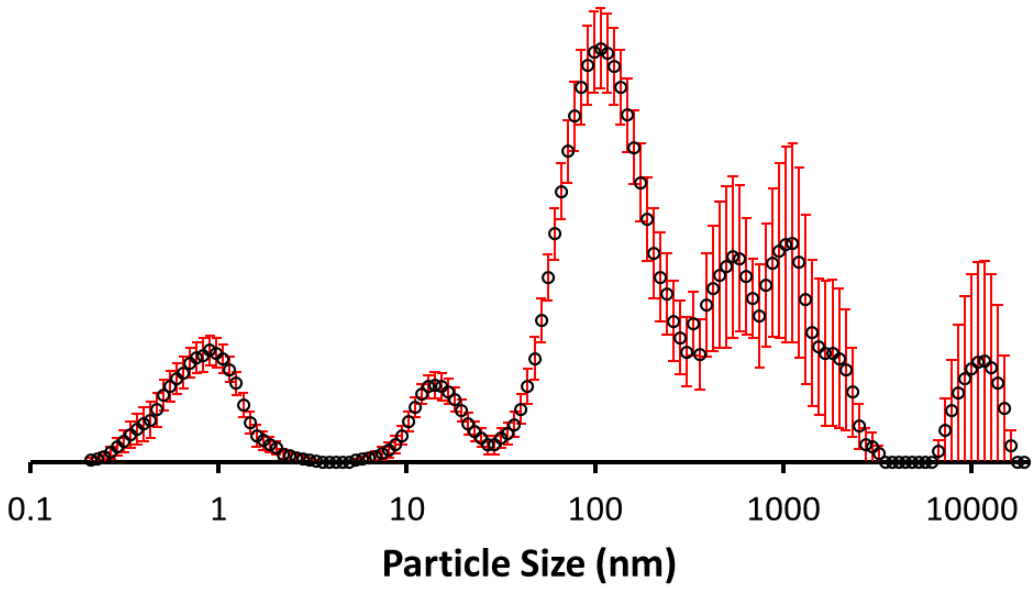

Figure S94 - The average intensity particle size distribution calculated using 9 DLS runs for co-formulation **n** (0.56 mM) in an EtOH: H_2O (1:19) solution at 298 K.

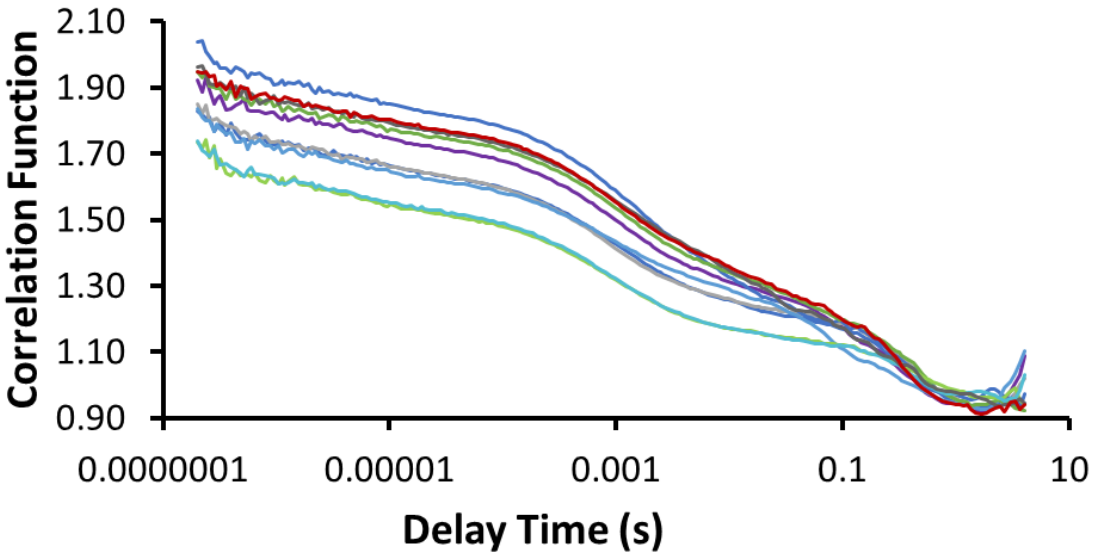

Figure S95 - Correlation function data for 9 DLS runs of co-formulation **n** (0.56 mM) in an EtOH: H_2O (1:19) solution at 298 K.

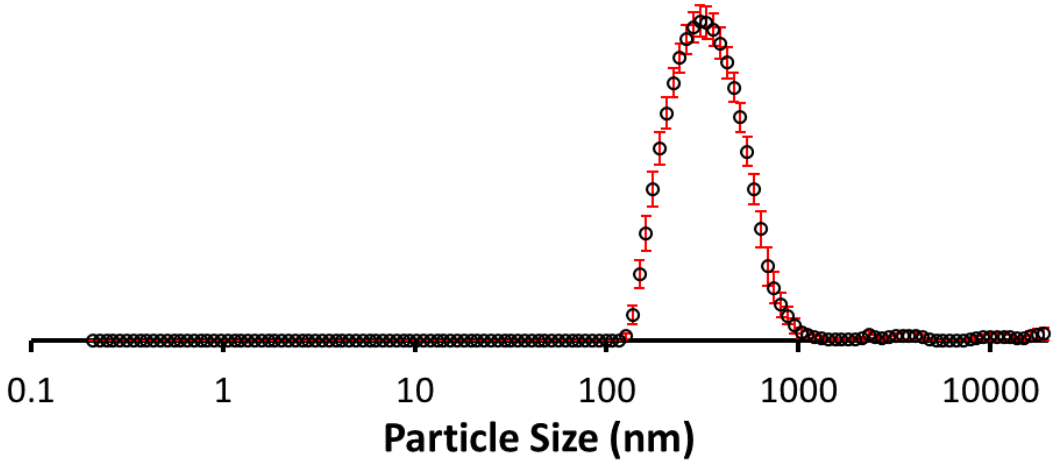

Figure S96 - The average intensity particle size distribution calculated using 9 DLS runs for co-formulation **o** (0.56 mM) in an EtOH: H_2O (1:19) solution at 298 K.

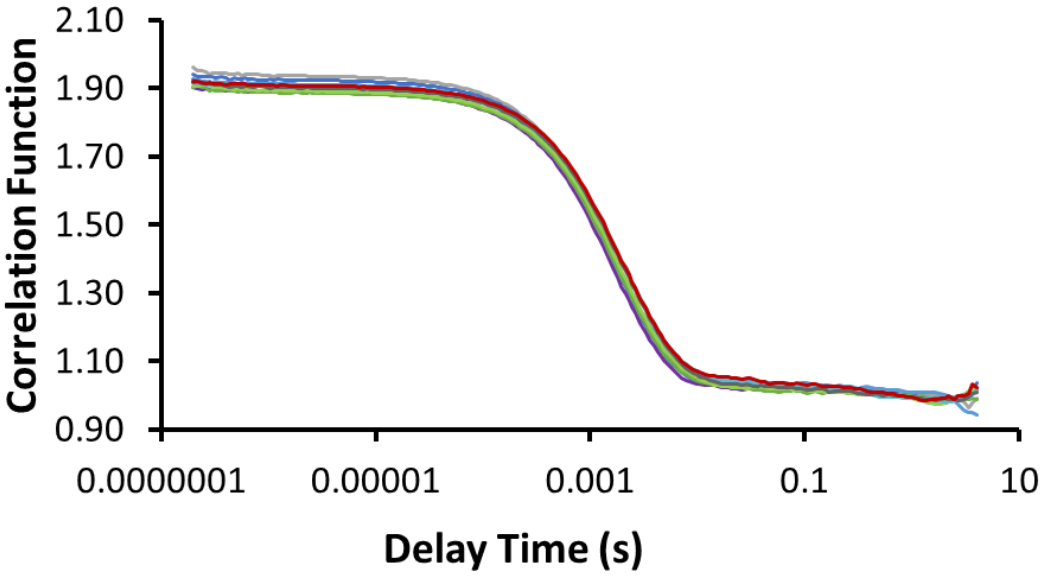

Figure S97 - Correlation function data for 9 DLS runs of co-formulation **o** (0.56 mM) in an EtOH: H_2O (1:19) solution at 298 K.

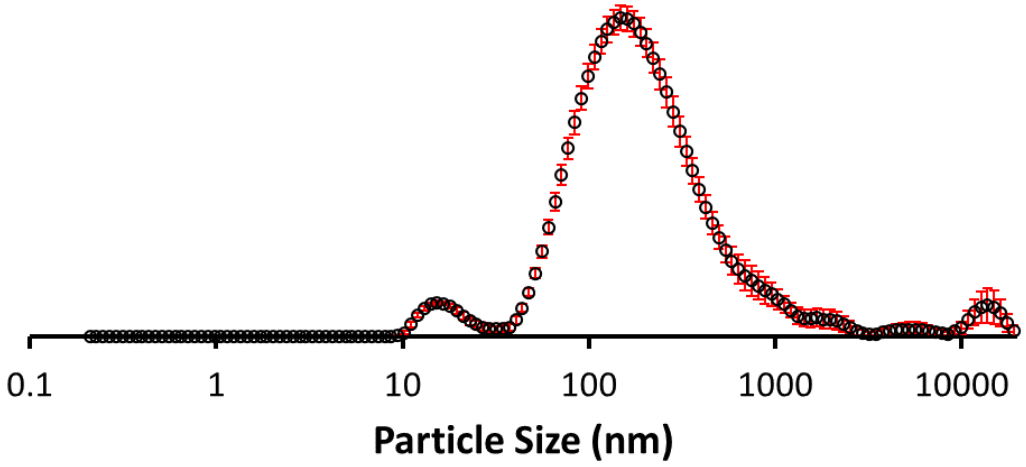

Figure S98 - The average intensity particle size distribution calculated using 9 DLS runs for co-formulation **p** (0.56 mM) in an EtOH: H_2O (1:19) solution at 298 K.

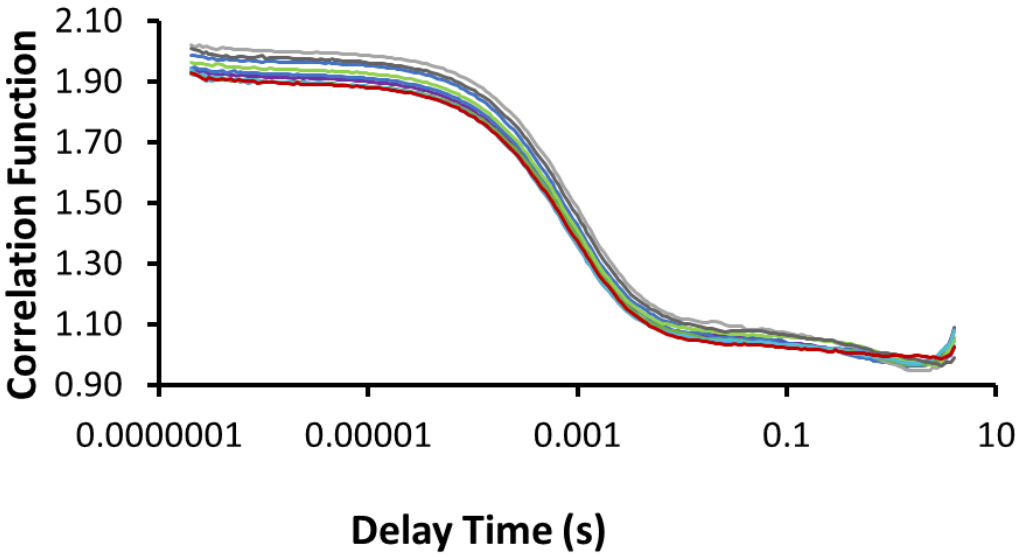

Figure S99 - Correlation function data for 9 DLS runs of co-formulation **p** (0.56 mM) in an EtOH: H_2O (1:19) solution at 298 K.

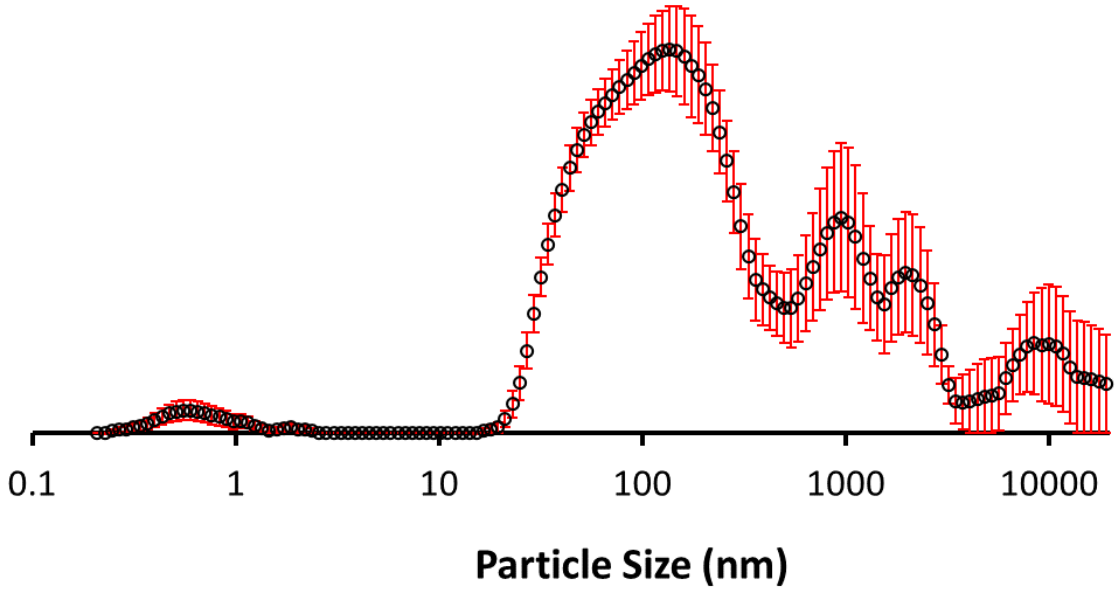

Figure S100 - The average intensity particle size distribution calculated using 9 DLS runs for co-formulation **q** (0.56 mM) in an EtOH: H_2O (1:19) solution at 298 K.

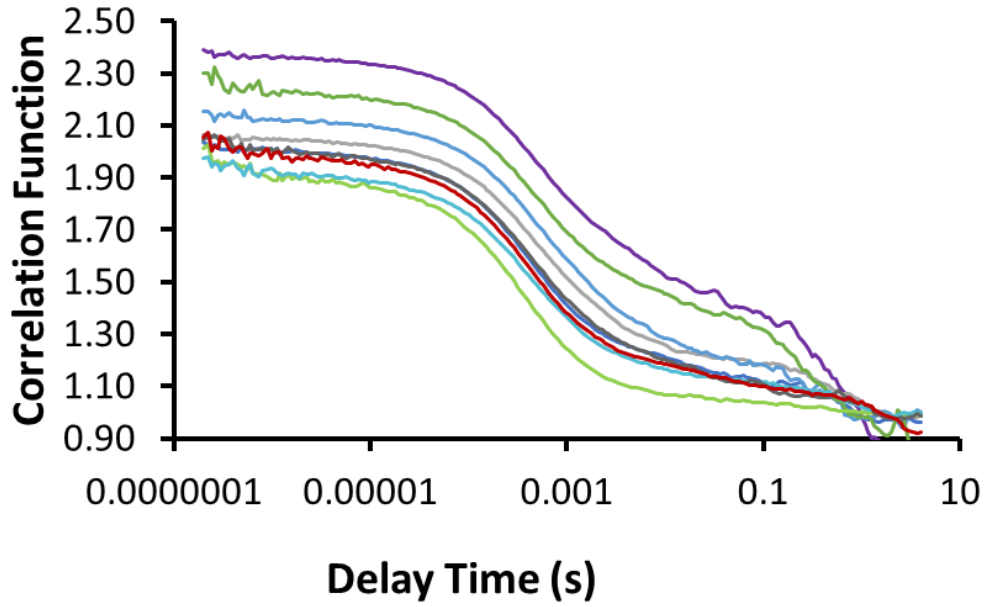

Figure S101 - Correlation function data for 9 DLS runs of co-formulation **q** (0.56 mM) in an EtOH: H_2O (1:19) solution at 298 K.

2.3 Zeta Potential studies

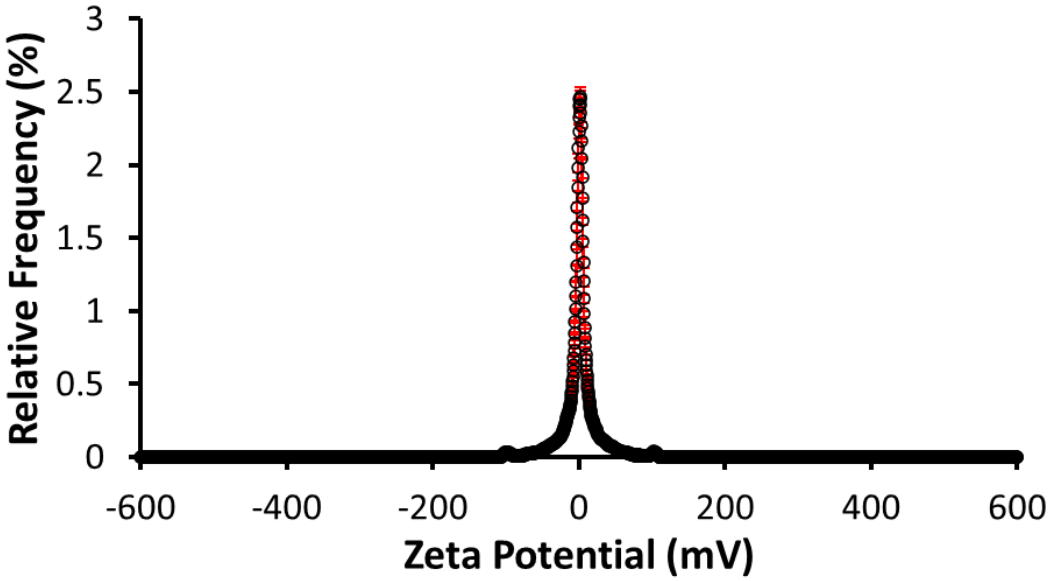

Figure S102 - The average zeta potential distribution calculated using 9 runs for co-formulation **g** (0.56 mM) in an EtOH:H_2O (1:19) solution at 298 K. Average measurement value +1 mV.

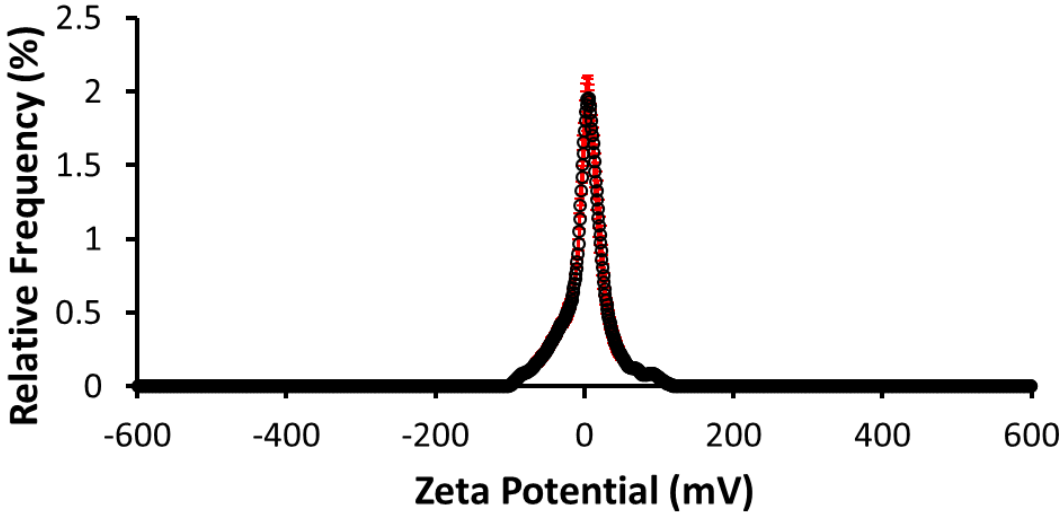

Figure S103 - The average zeta potential distribution calculated using 9 runs for co-formulation **h** (0.56 mM) in an EtOH:H_2O (1:19) solution at 298 K. Average measurement value +6 mV.

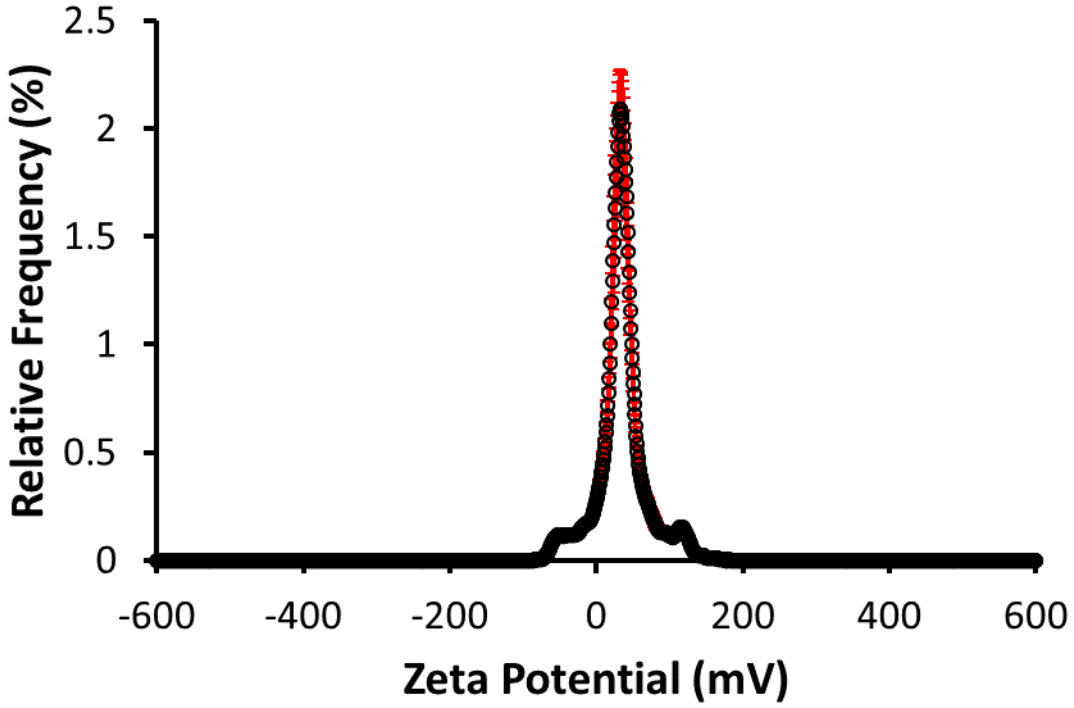

Figure S104 - The average zeta potential distribution calculated using 9 runs for co-formulation **i** (0.56 mM) in an EtOH:H_2O (1:19) solution at 298 K. Average measurement value +33 mV.

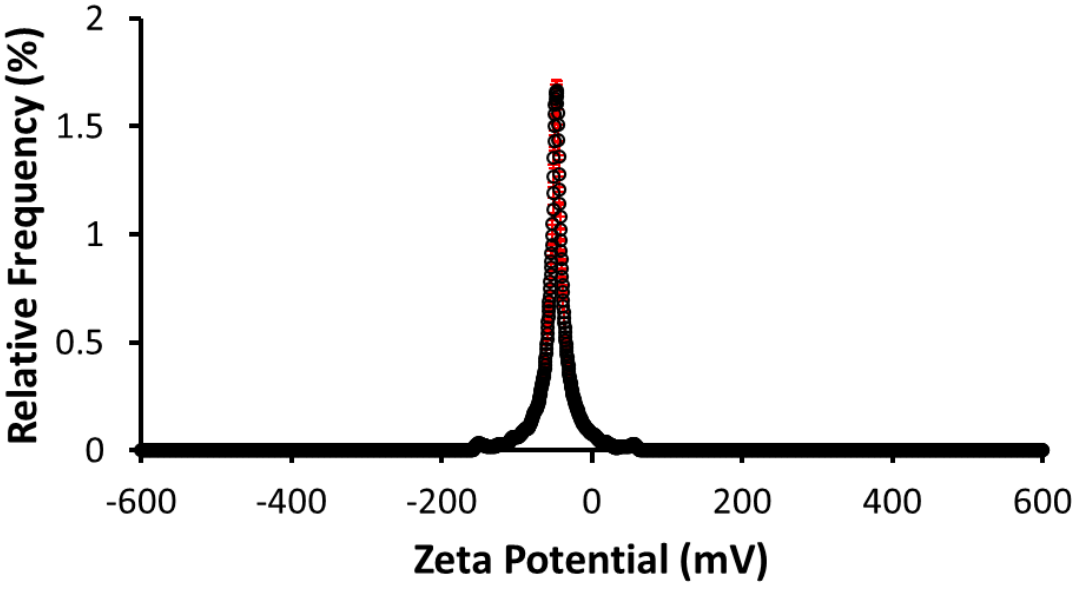

Figure S105 - The average zeta potential distribution calculated using 9 runs for co-formulation **j** (0.56 mM) in an EtOH:H_2O (1:19) solution at 298 K. Average measurement value -46 mV.

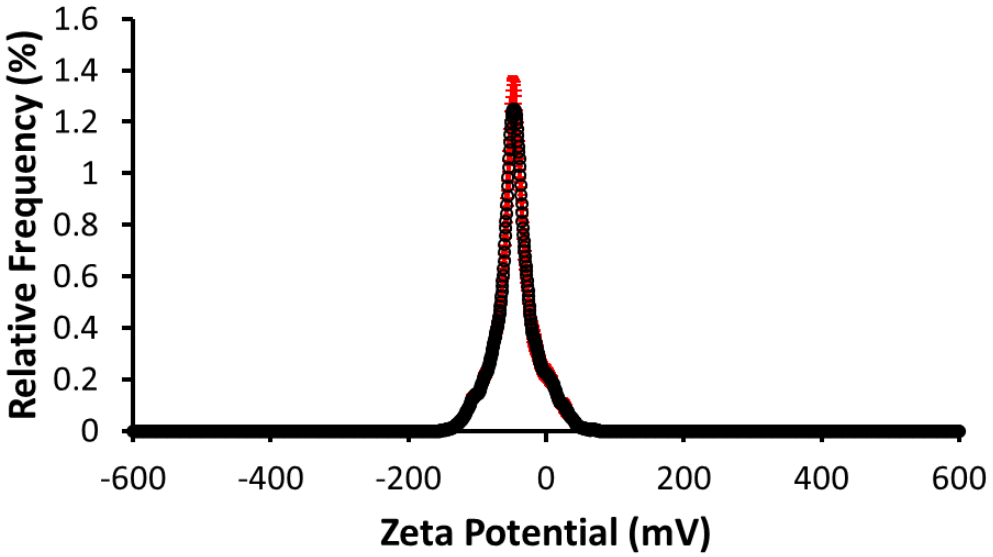

Figure S106 - The average zeta potential distribution calculated using 9 runs for co-formulation **k** (0.56 mM) in an EtOH:H_2O (1:19) solution at 298 K. Average measurement value -44 mV.

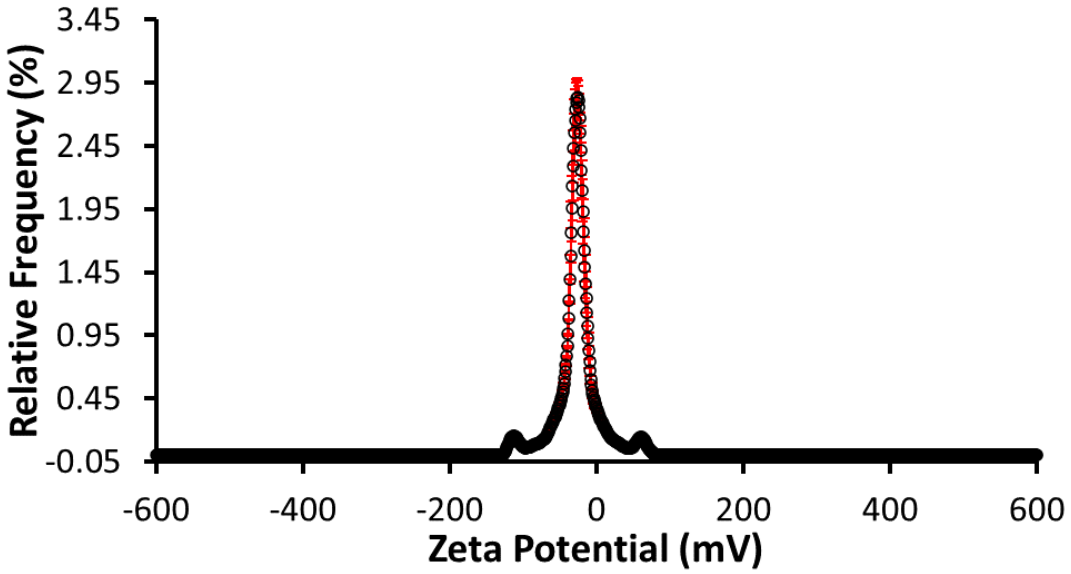

Figure S107 - The average zeta potential distribution calculated using 9 runs for co-formulation **l** (0.56 mM) in an EtOH:H_2O (1:19) solution at 298 K. Average measurement value -23 mV.

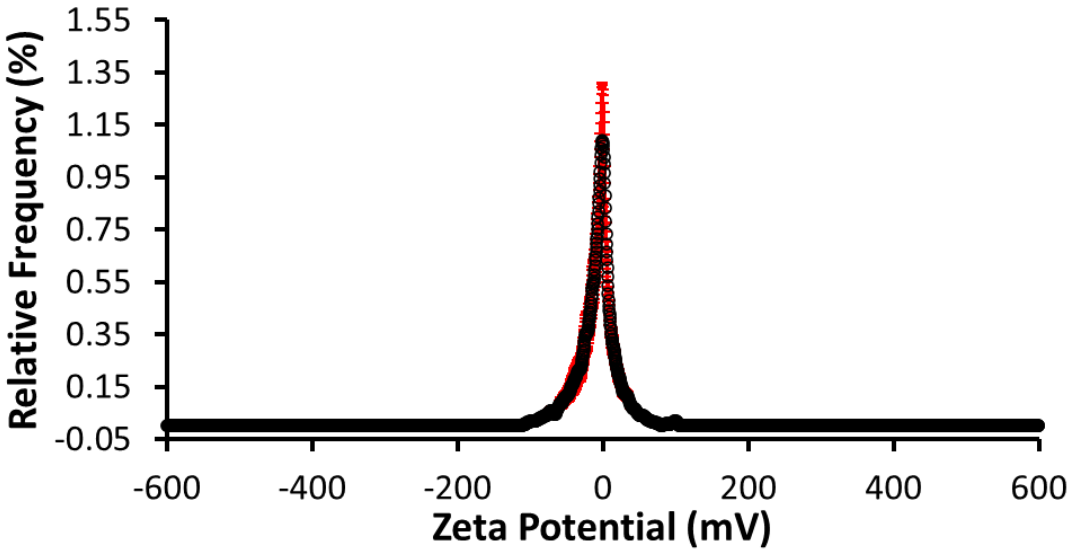

Figure S108 - The average zeta potential distribution calculated using 9 runs for co-formulation **m** (0.56 mM) in an EtOH:H_2O (1:19) solution at 298 K. Average measurement value -1 mV.

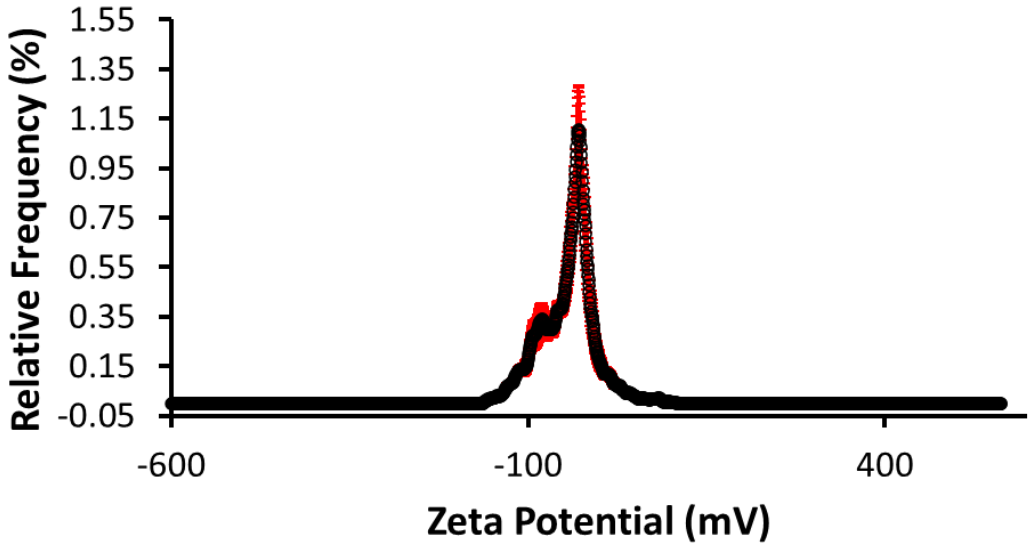

Figure S109 - The average zeta potential distribution calculated using 9 runs for co-formulation **n** (0.56 mM) in an EtOH:H_2O (1:19) solution at 298 K. Average measurement value -26 mV.

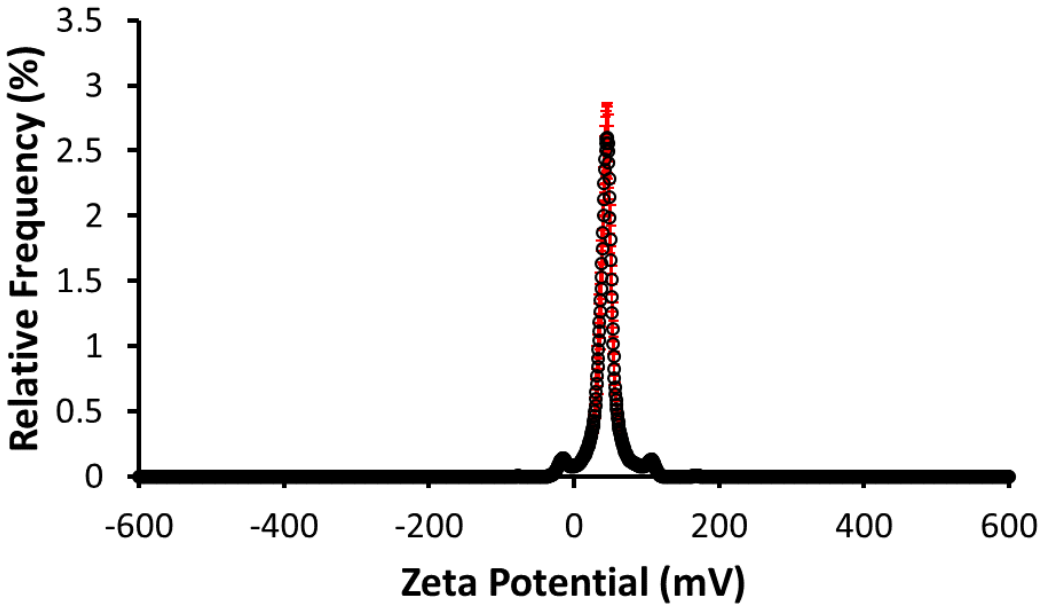

Figure S110 - The average zeta potential distribution calculated using 9 runs for co-formulation **o** (0.56 mM) in an EtOH:H_2O (1:19) solution at 298 K. Average measurement value +44 mV.

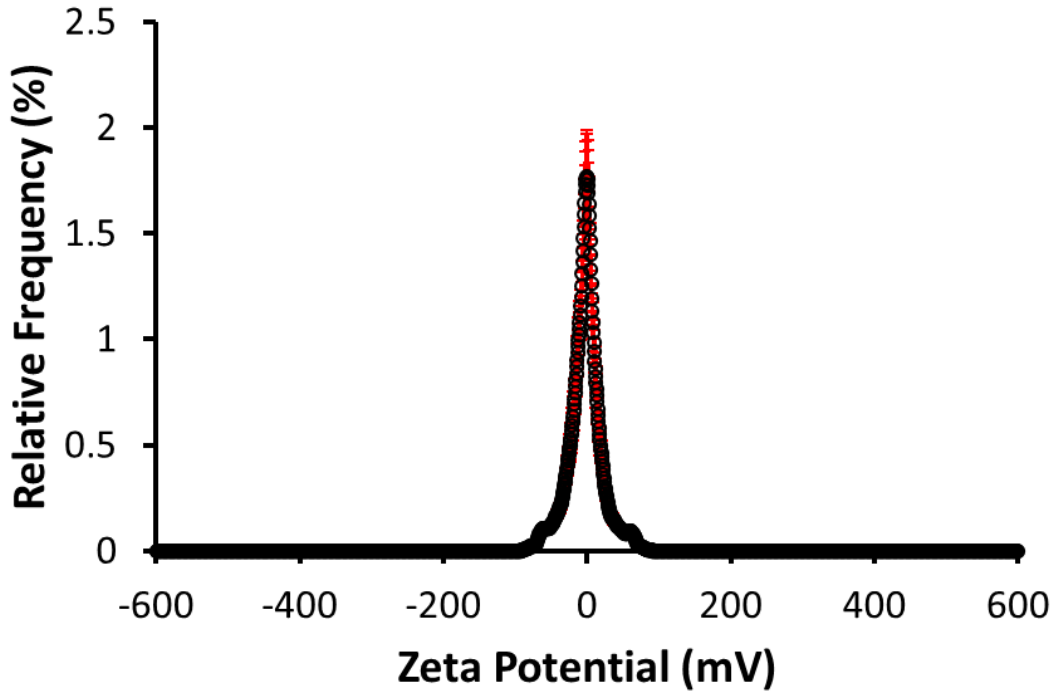

Figure S111 - The average zeta potential distribution calculated using 9 runs for co-formulation **p** (0.56 mM) in an EtOH:H_2O (1:19) solution at 298 K. Average measurement value -1 mV.

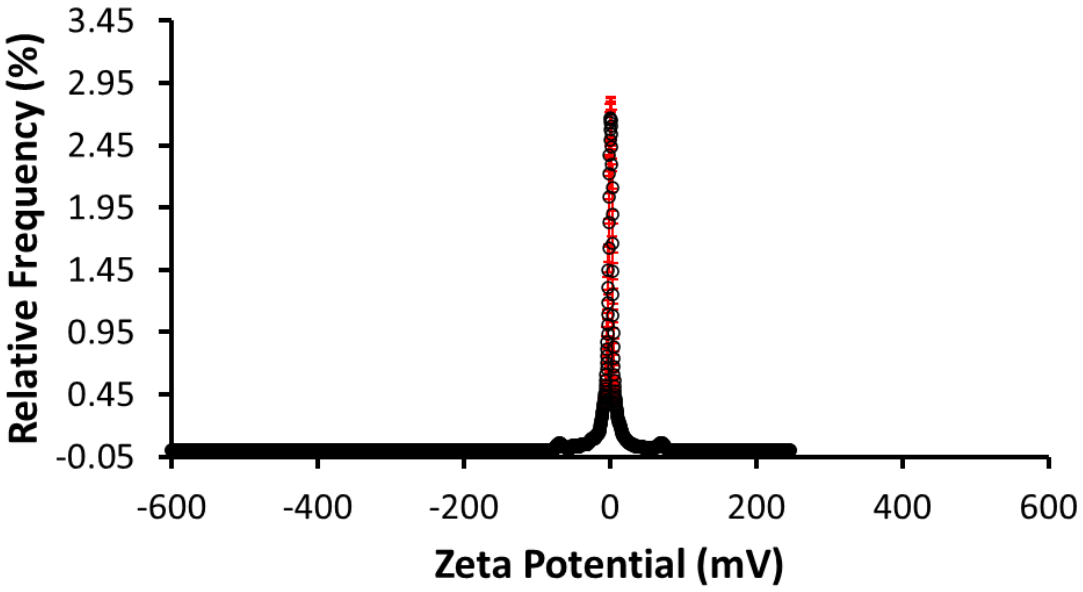

Figure S112 - The average zeta potential distribution calculated using 9 runs for co-formulation **q** (0.56 mM) in an EtOH:H_2O (1:19) solution at 298 K. Average measurement value +1 mV.

2.4 Surface Tension and Critical Micelle Concentration

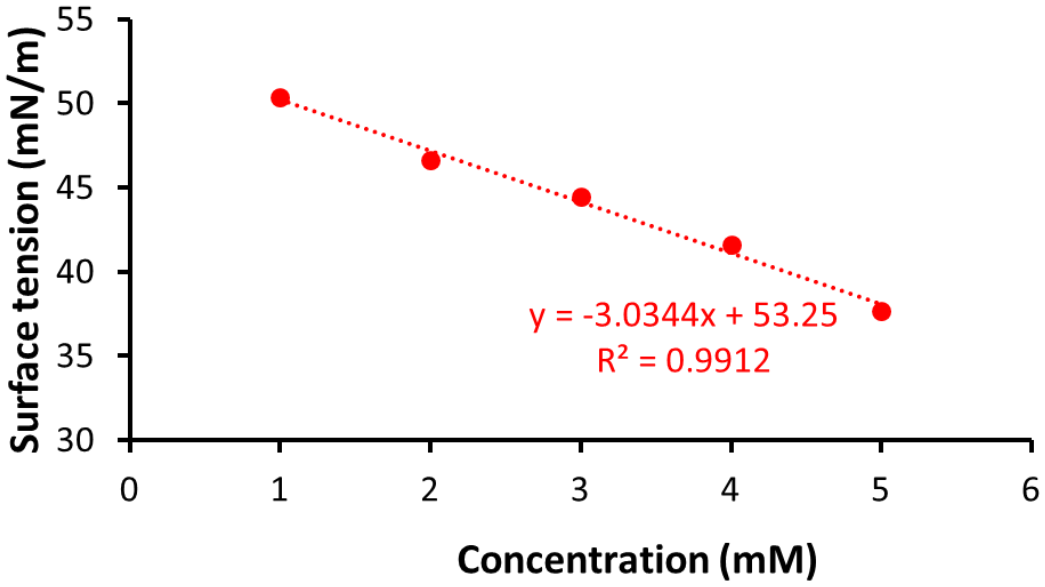

Figure S113 - Calculation of CMC for co-formulation **g** in an EtOH:H_2O 1:19 mixture using surface tension measurements. A CMC could not be calculated as solubility limits were reached.

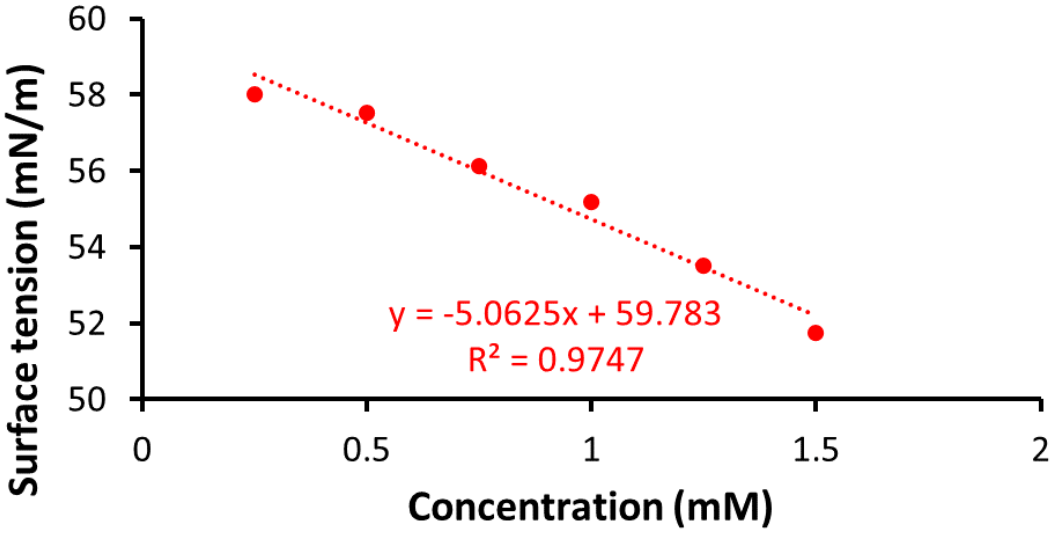

Figure S114 - Calculation of CMC for co-formulation **h** in an EtOH:H_2O 1:19 mixture using surface tension measurements. A CMC could not be calculated as solubility limits were reached.

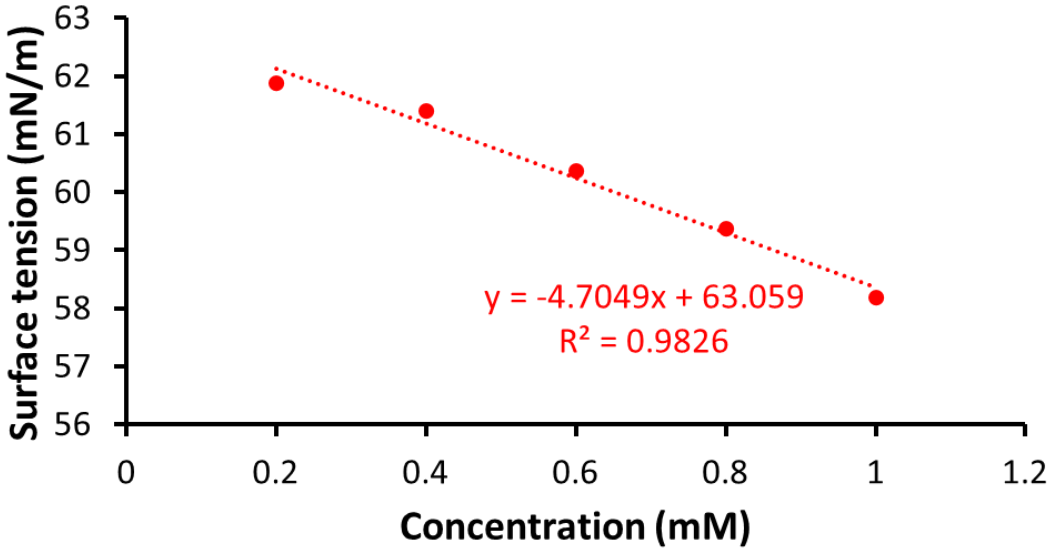

Figure S115 - Calculation of CMC for co-formulation **i** in an EtOH:H_2O 1:19 mixture using surface tension measurements. A CMC could not be calculated as solubility limits were reached.

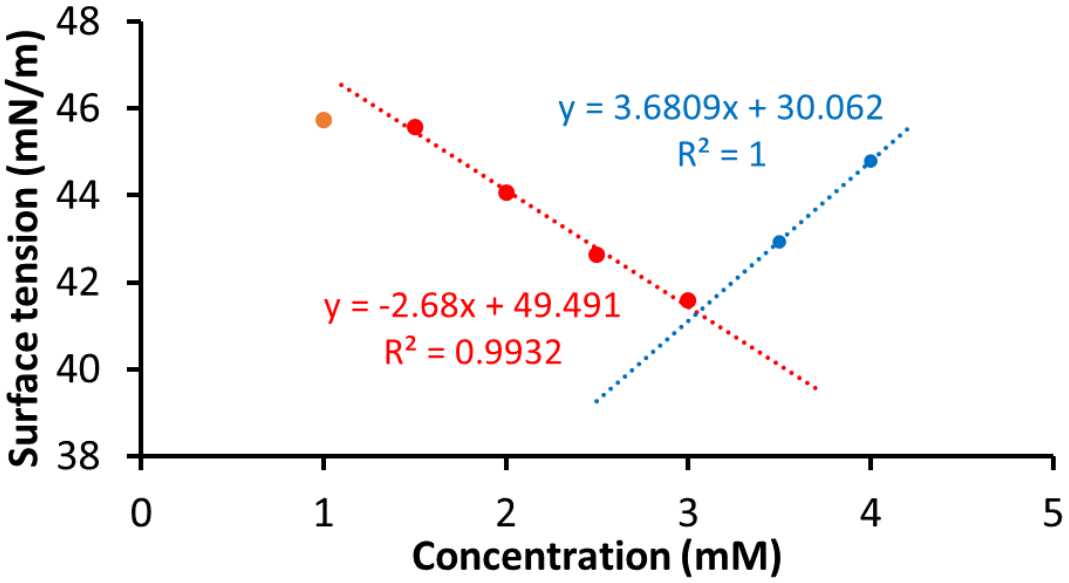

Figure S116 – Calculation of CMC (3.1 mM) for co-formulation **j** in an EtOH:H_2O 1:19 mixture using surface tension measurements.

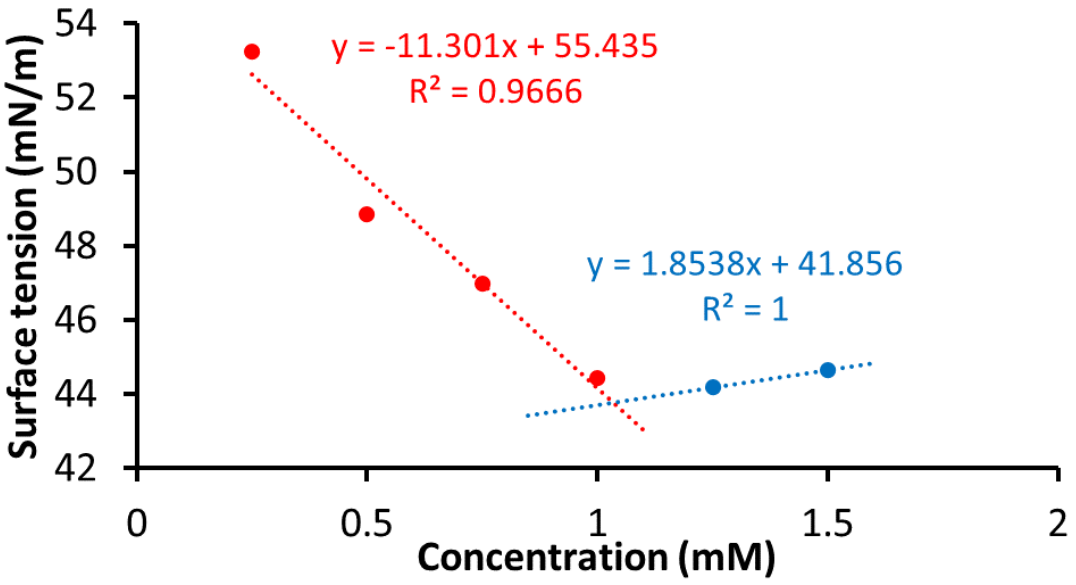

Figure S117 - Calculation of CMC (1.0 mM) for co-formulation **k** in an EtOH:H_2O 1:19 mixture using surface tension measurements.

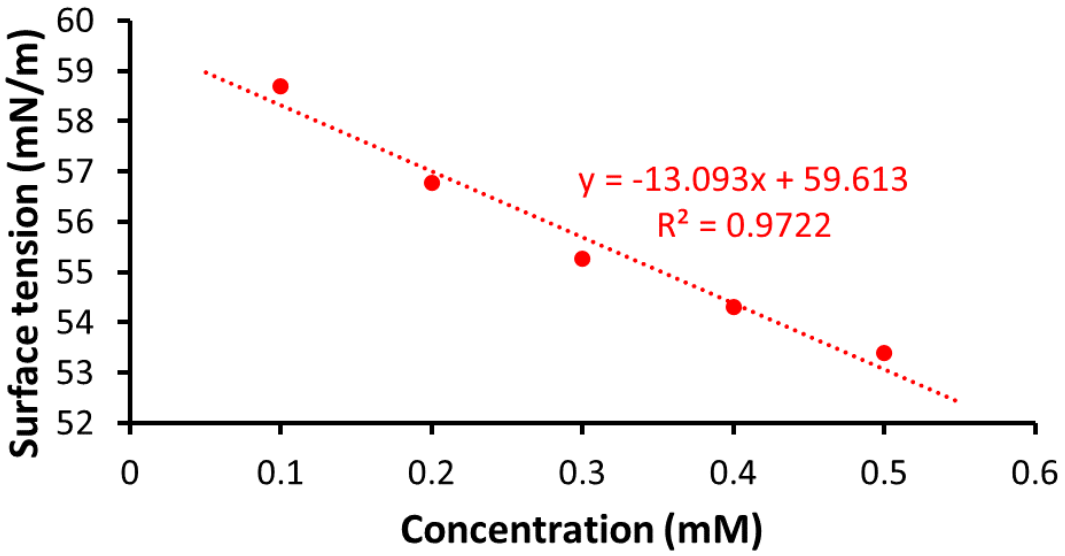

Figure S118 - Calculation of CMC for co-formulation **l** in an EtOH:H_2O 1:19 mixture using surface tension measurements. A CMC could not be calculated as solubility limits were reached.

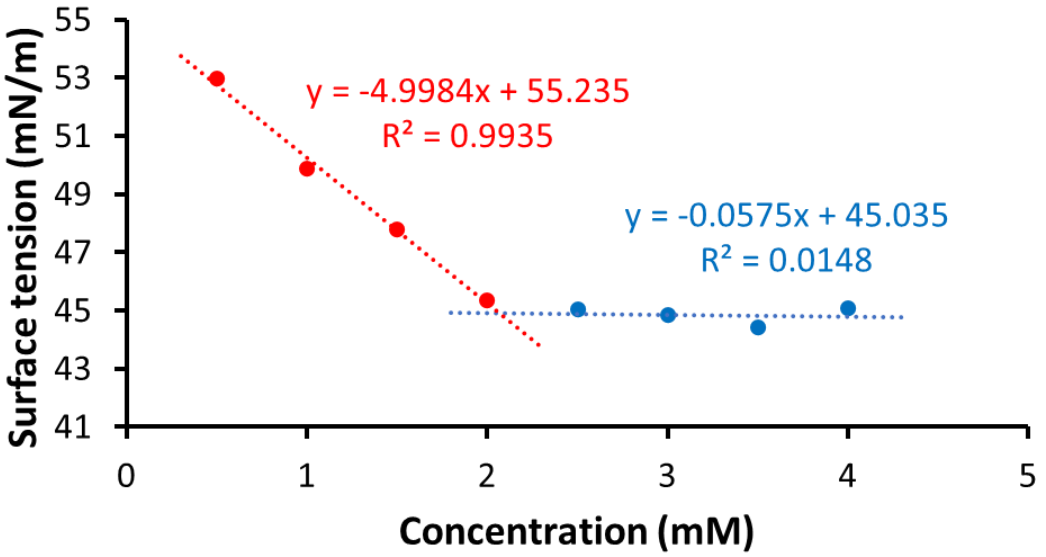

Figure S119 - Calculation of CMC (2.1 mM) for co-formulation **m** in an EtOH:H_2O 1:19 mixture using surface tension measurements.

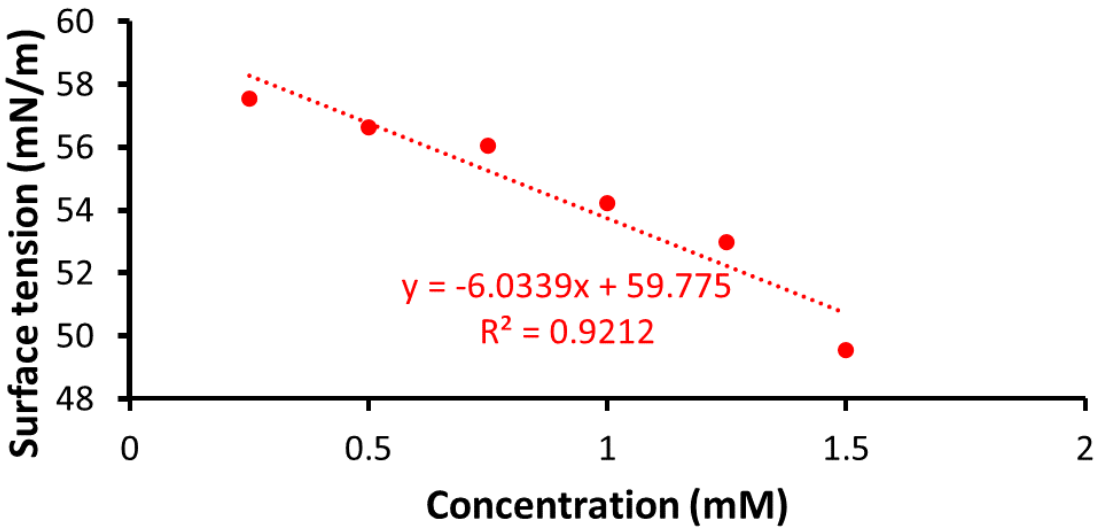

Figure S120 - Calculation of CMC for co-formulation **n** in an EtOH:H_2O 1:19 mixture using surface tension measurements. A CMC could not be calculated as solubility limits were reached.

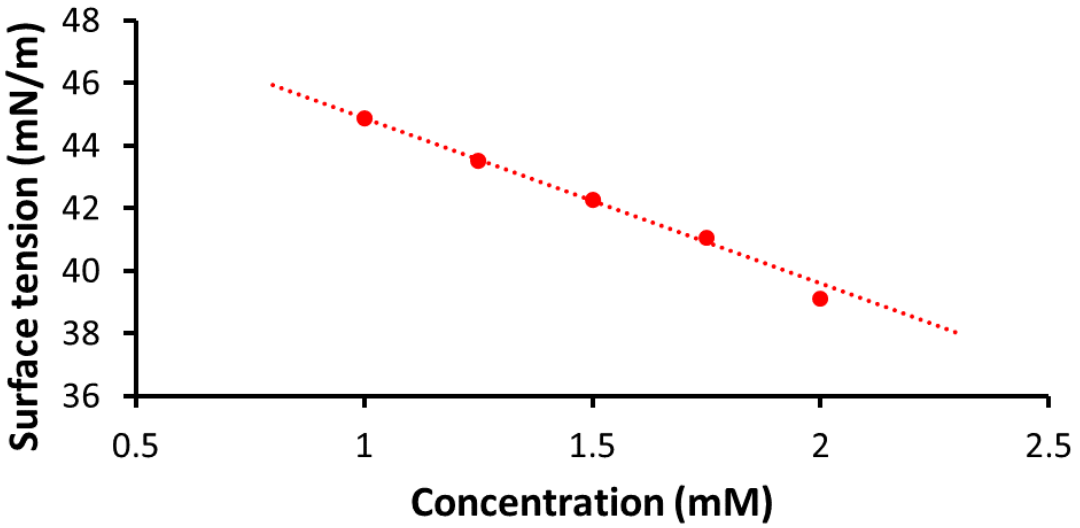

Figure S121 - Calculation of CMC for co-formulation **o** in an EtOH:H_2O 1:19 mixture using surface tension measurements. A CMC could not be calculated as solubility limits were reached.

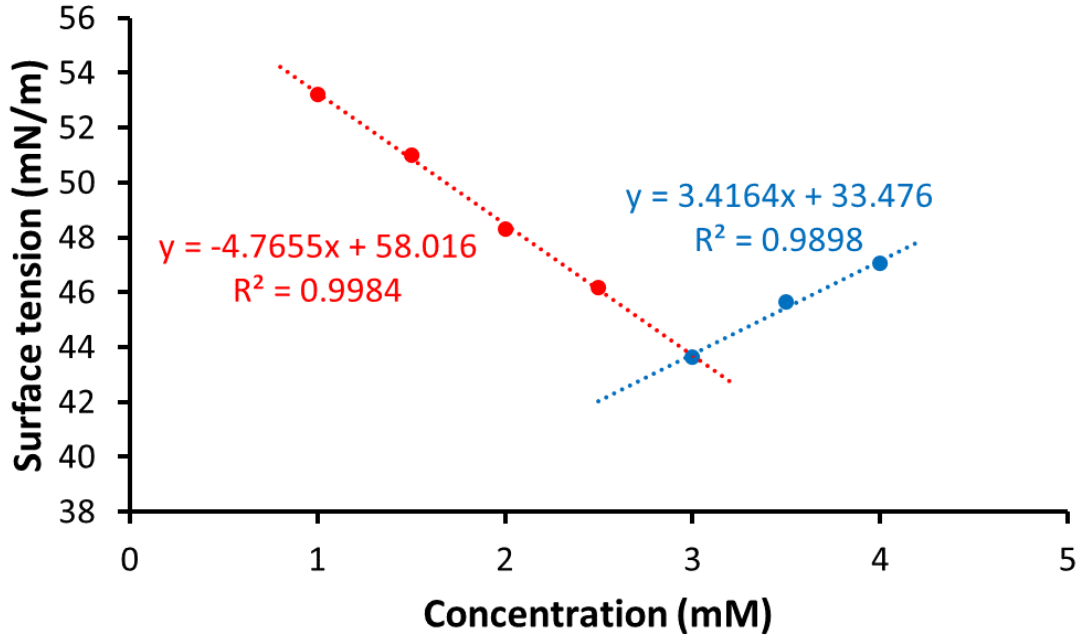

Figure S122 - Calculation of CMC (3.0 mM) for co-formulation **p** in an EtOH:H_2O 1:19 mixture using surface tension measurements.

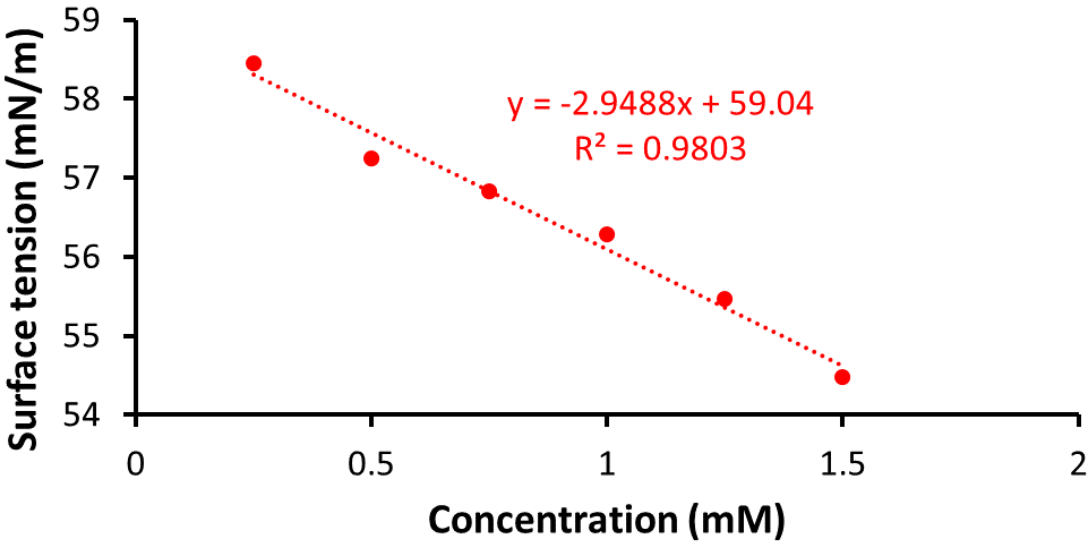

Figure S123 - Calculation of CMC for co-formulation **q** in an EtOH:H_2O 1:19 mixture using surface tension measurements. A CMC could not be calculated as solubility limits were reached.

2.5 ^{1}H NMR Dilution Studies

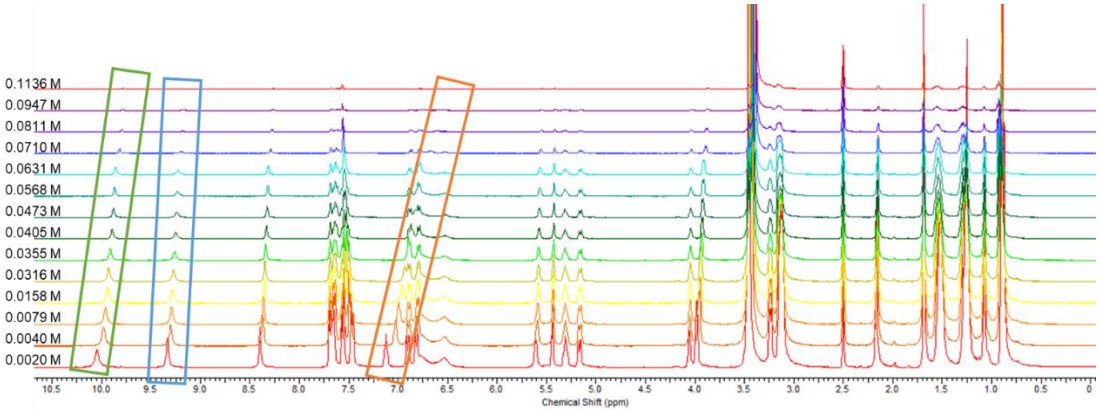

Figure S124 - ^{1}H NMR stack plot of co-formulation **g** in DMSO-d_6 0.5 % H_2O solution. Samples were prepared in series with an aliquot of the most concentrated solution undergoing serial dilution.

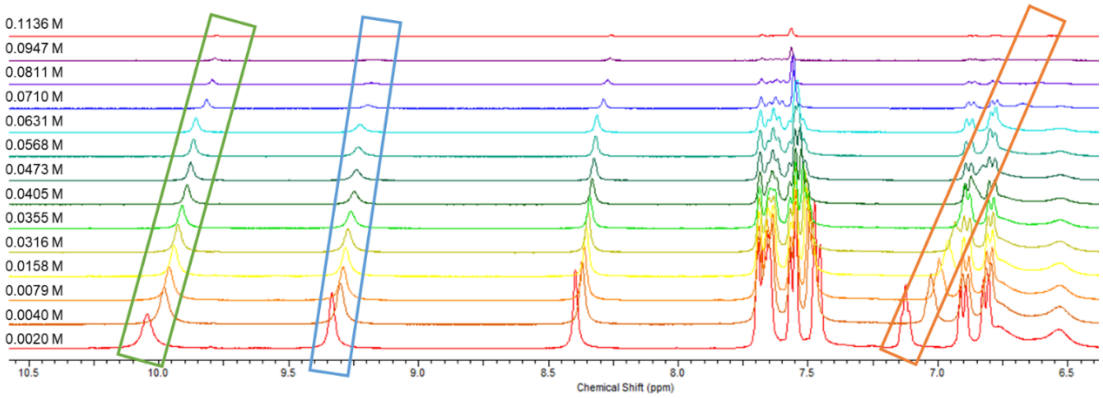

Figure S125 – Enlarged ^{1}H NMR stack plot of co-formulation **g** in DMSO-d_6 0.5 % H_2O solution. Samples were prepared in series with an aliquot of the most concentrated solution undergoing serial dilution.

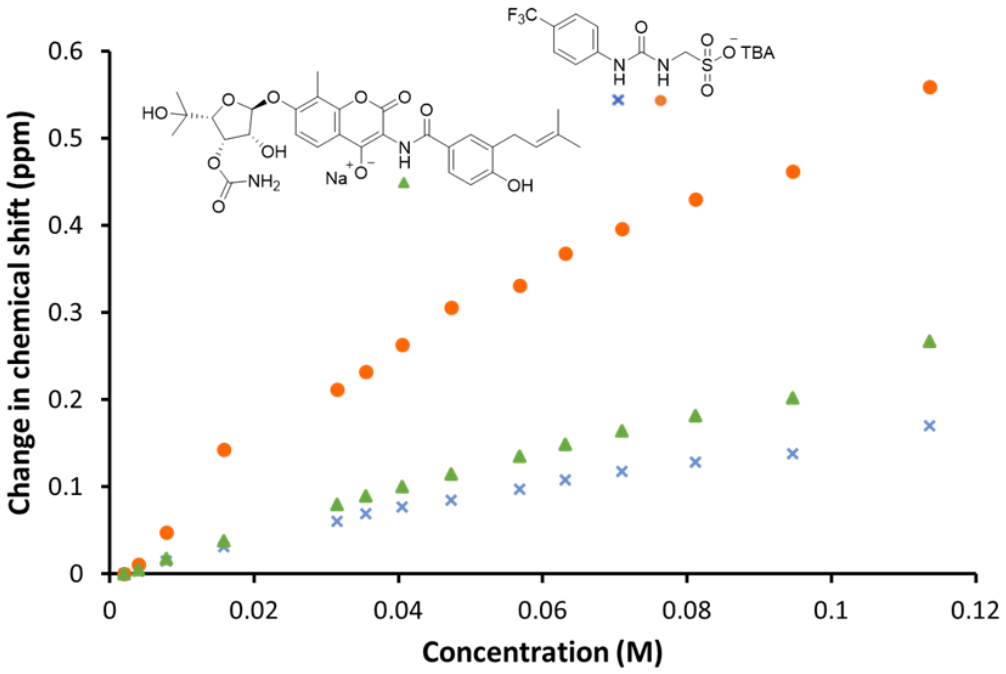

Figure S126 - Graph illustrating the ^{1}H NMR down-field change in chemical shift of SSA urea and appropriate co-formulant NH resonances with increasing concentration of co-formulation **g** in DMSO-d_6 0.5 % H_2O (298 K).

Self-association constant calculation

Co-formulation **g** - Dilution study in DMSO-d_6 5 % H_2O. Values calculated from data gathered from SSA NH urea resonances.

Equal K/Dimerization model

K_e = 4.44 M^{-1} ± 2.4373 % K_{dim} = 2.22 M^{-1} ± 1.2186 %

http://app.supramolecular.org/bindfit/view/d528c451-f9ed-4fe4-bf73-f39aa5c592bf

CoEK model

K_e = 2.02 M^{-1} ± 29.3231 % K_{dim} = 1.01 M^{-1} ± 14.6615 % ρ = 1.70 ± 37.0358 %

http://app.supramolecular.org/bindfit/view/5ddfdfe5-b8e5-47be-ba51-def3ad11860e

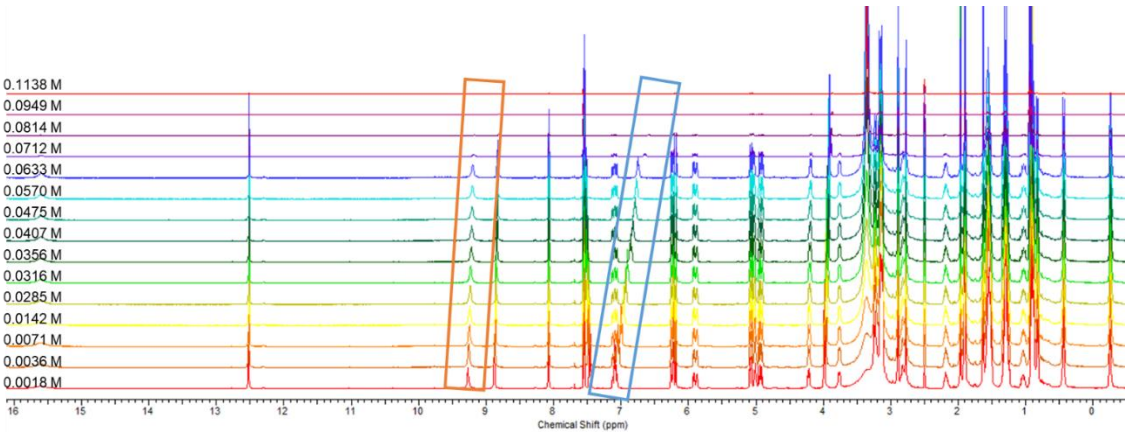

Figure S127 - ^{1}H NMR stack plot of co-formulation **h** in DMSO-d_6 0.5 % H_2O solution. Samples were prepared in series with an aliquot of the most concentrated solution undergoing serial dilution.

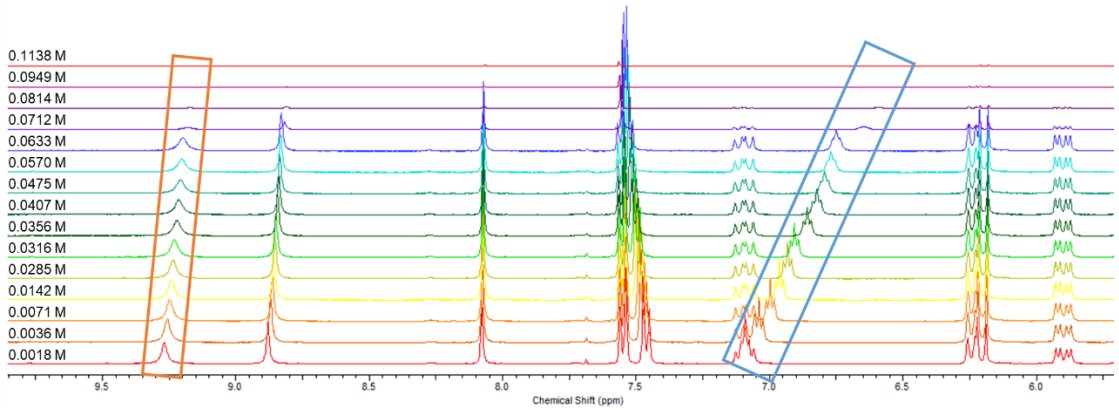

Figure S128 – Enlarged ^{1}H NMR stack plot of co-formulation **h** in DMSO-d_6 0.5 % H_2O solution. Samples were prepared in series with an aliquot of the most concentrated solution undergoing serial dilution.

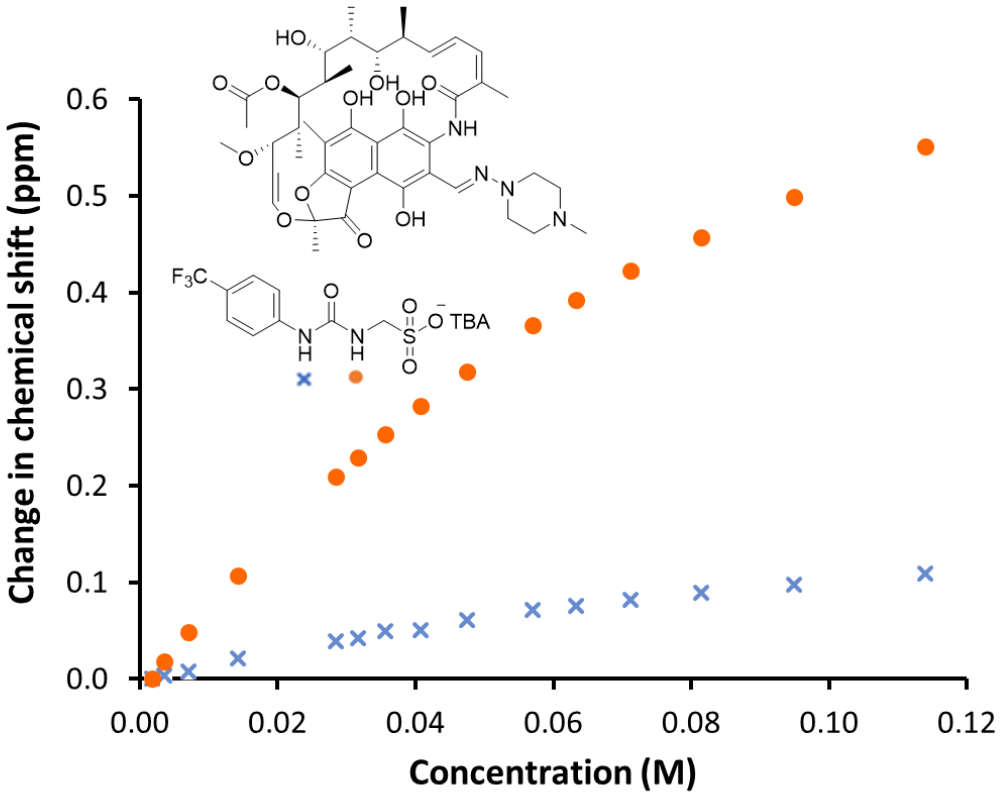

Figure S129 - Graph illustrating the ^{1}H NMR down-field change in chemical shift of SSA urea with increasing concentration of co-formulation **h** in DMSO-d_6 0.5 % H_2O (298 K).

Self-association constant calculation

Co-formulation **h** - Dilution study in DMSO-d_6 5 % H_2O. Values calculated from data gathered from SSA NH urea resonances.

Equal K/Dimerization model

K_e = 5.78 M^{-1} ± 0.5468 % K_{dim} = 2.89 M^{-1} ± 0.2734 %

http://app.supramolecular.org/bindfit/view/128fcf54-1d84-4c76-b841-506e2dd801fa

CoEK model

K_e = 12.34 M^{-1} ± 0.7699 % K_{dim} = 6.17 M^{-1} ± 0.3849 % ρ = 0.55 ± 2.1754 %

http://app.supramolecular.org/bindfit/view/e75b12af-e538-4af5-85f2-b0c654c2e343

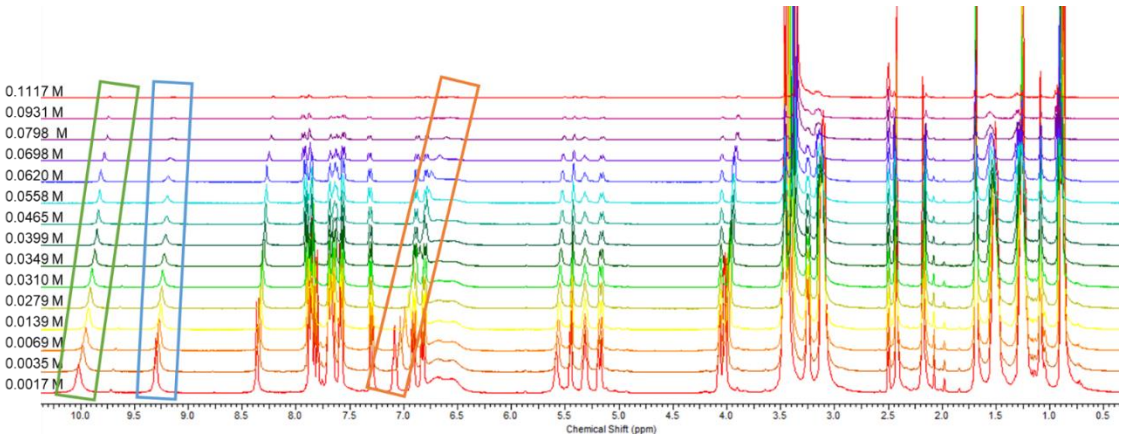

Figure S130 - ^{1}H NMR stack plot of co-formulation **j** in DMSO-d_6 0.5 % H_2O solution. Samples were prepared in series with an aliquot of the most concentrated solution undergoing serial dilution.

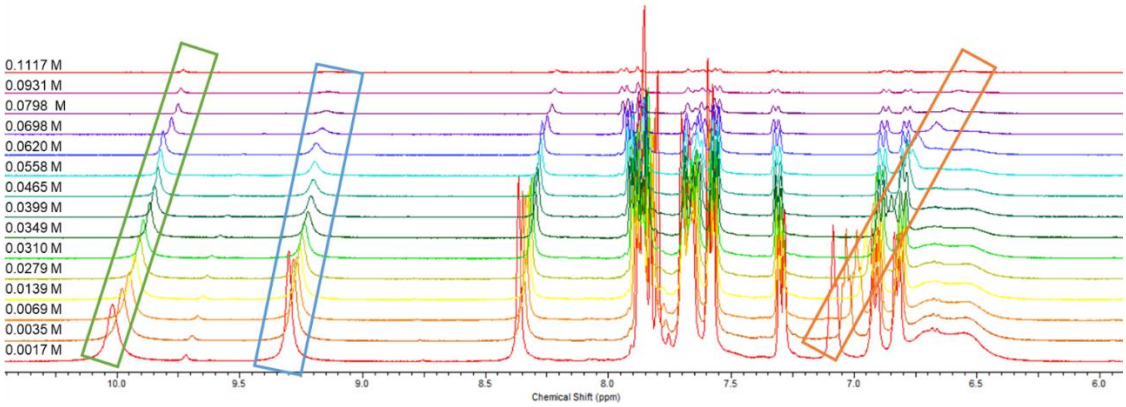

Figure S131 – Enlarged ^{1}H NMR stack plot of co-formulation **j** in DMSO-d_6 0.5 % H_2O solution. Samples were prepared in series with an aliquot of the most concentrated solution undergoing serial dilution.

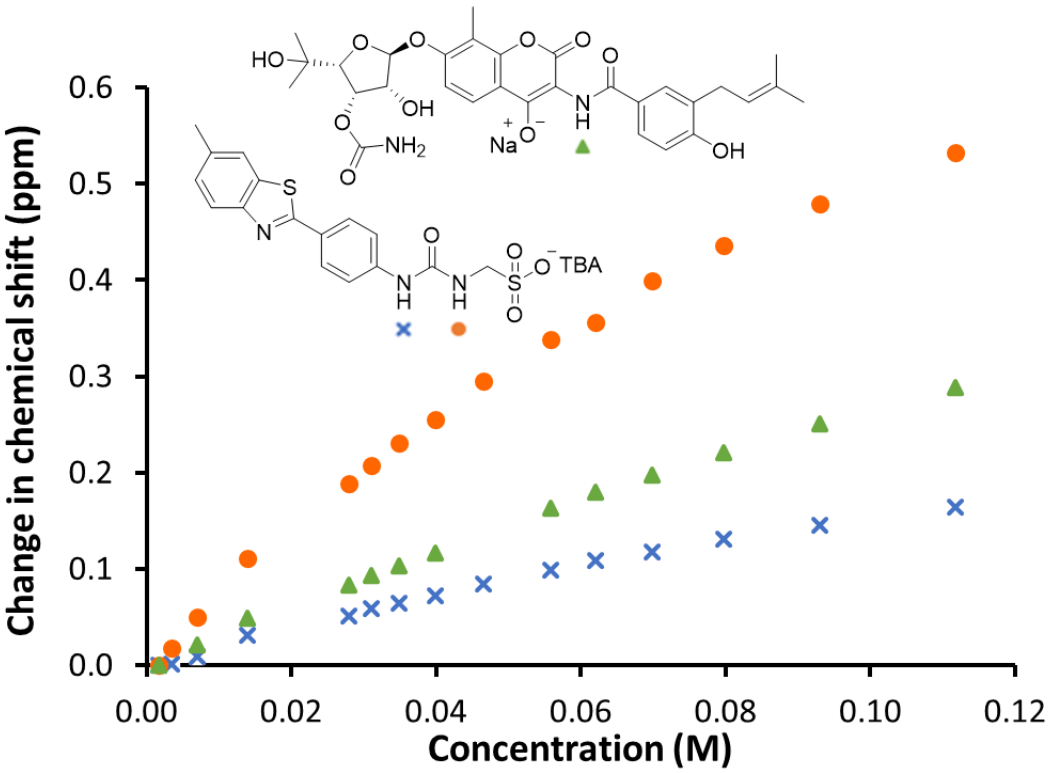

Figure S132 - Graph illustrating the ^{1}H NMR down-field change in chemical shift of SSA urea and appropriate co-formulant NH resonances with increasing concentration of co-formulation **j** in DMSO-d_6 0.5 % H_2O (298 K).

Self-association constant calculation

Co-formulation **j** - Dilution study in DMSO-d_6 5 % H_2O. Values calculated from data gathered from SSA NH urea resonances.

Equal K/Dimerization model

K_e = 4.14 M^{-1} ± 0.8909 % K_{dim} = 2.07 M^{-1} ± 0.4454 %

http://app.supramolecular.org/bindfit/view/1e3ce722-9bcf-4c91-82dd-973c24a00099

CoEK model

K_e = 3.17 M^{-1} ± 7.0724 % K_{dim} = 1.59 M^{-1} ± 3.5362 % ρ = 1.18 ± 9.9785 %

http://app.supramolecular.org/bindfit/view/4c23c35a-32cc-4aa1-9fc8-d839cfaafa88

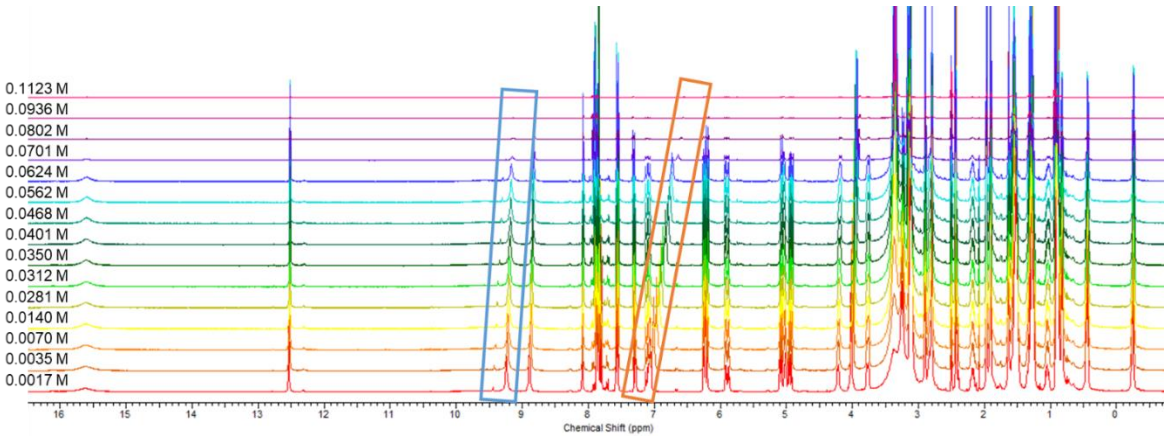

Figure S133 - ^{1}H NMR stack plot of co-formulation **k** in DMSO-d_6 0.5 % H_2O solution. Samples were prepared in series with an aliquot of the most concentrated solution undergoing serial dilution.

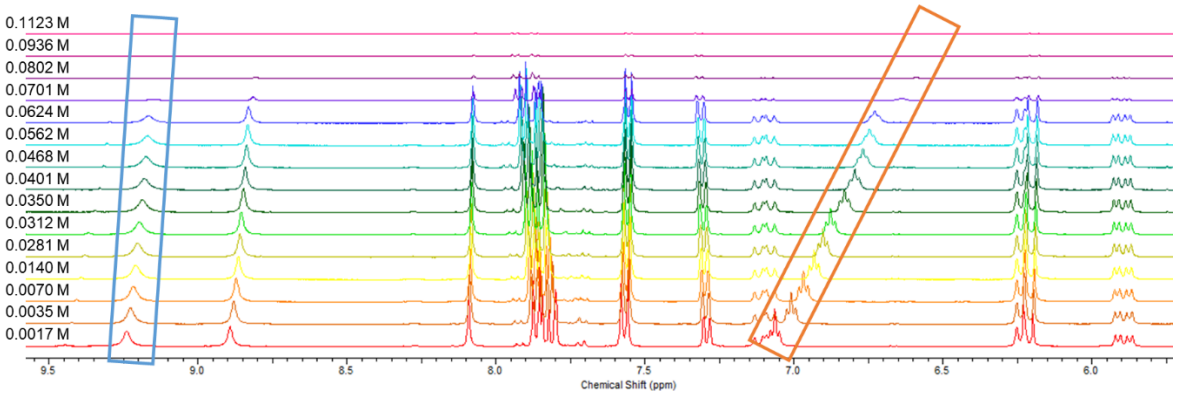

Figure S134 – Enlarged ^{1}H NMR stack plot of co-formulation **k** in DMSO-d_6 0.5 % H_2O solution. Samples were prepared in series with an aliquot of the most concentrated solution undergoing serial dilution.

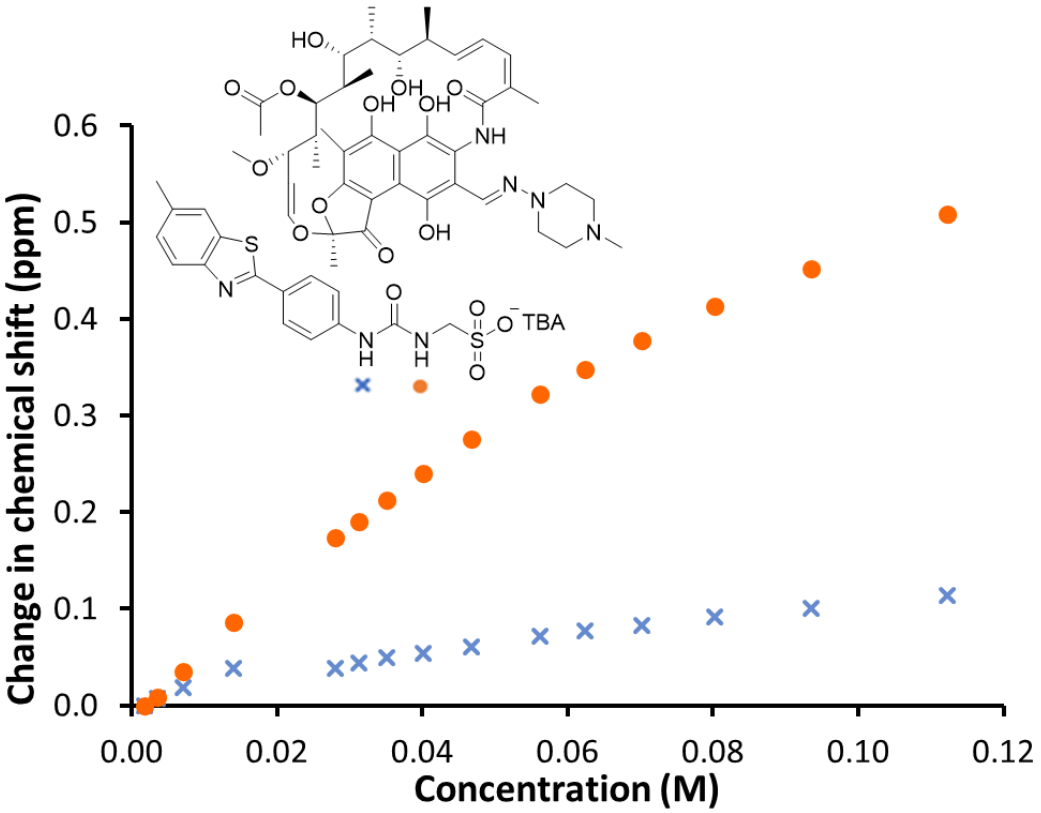

Figure S135 - Graph illustrating the ^{1}H NMR down-field change in chemical shift of SSA urea with increasing concentration of co-formulation **k** in DMSO-d_6 0.5 % H_2O (298 K).

Self-association constant calculation

Co-formulation **k** - Dilution study in DMSO-d_6 5 % H_2O. Values calculated from data gathered from SSA NH urea resonances.

Equal K/Dimerization model

K_e = 4.06 M^{-1} ± 1.0701 % K_{dim} = 2.03 M^{-1} ± 0.5351 %

http://app.supramolecular.org/bindfit/view/abc8136b-927a-49bb-b2f7-ea2de7deb2db

CoEK model

K_e = 10.39 M^{-1} ± 2.7627 % K_{dim} = 5.19 M^{-1} ± 1.3813 % ρ = 0.52 ± 7.1161 %

http://app.supramolecular.org/bindfit/view/09420342-ea5a-48b5-aeef-92529c0aa3ac

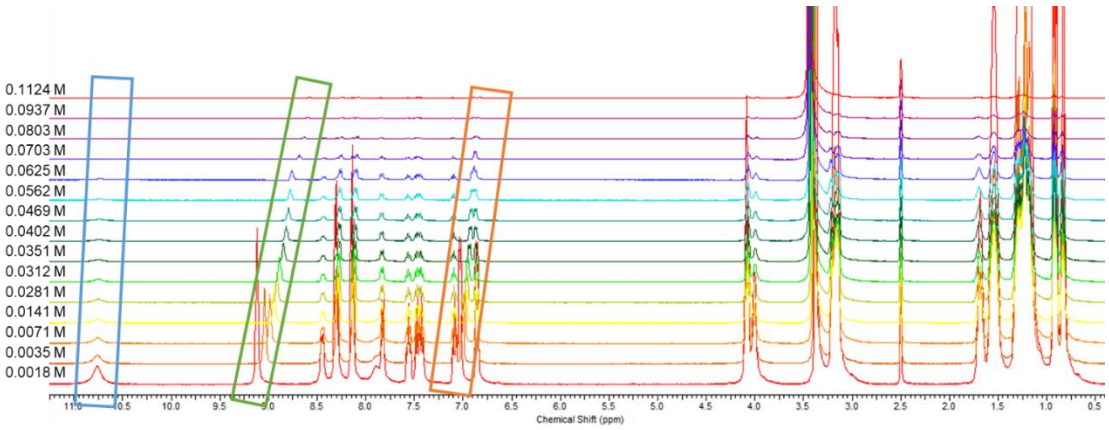

Figure S136 - ^{1}H NMR stack plot of co-formulation **I** in DMSO-d_6 0.5 % H_2O solution. Samples were prepared in series with an aliquot of the most concentrated solution undergoing serial dilution.

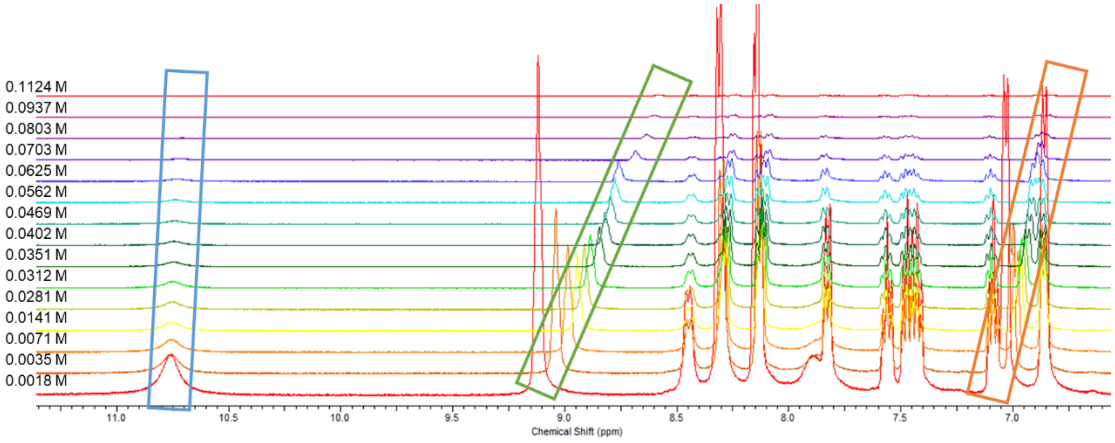

Figure S137 – Enlarged ^{1}H NMR stack plot of co-formulation **I** in DMSO-d_6 0.5 % H_2O solution. Samples were prepared in series with an aliquot of the most concentrated solution undergoing serial dilution.

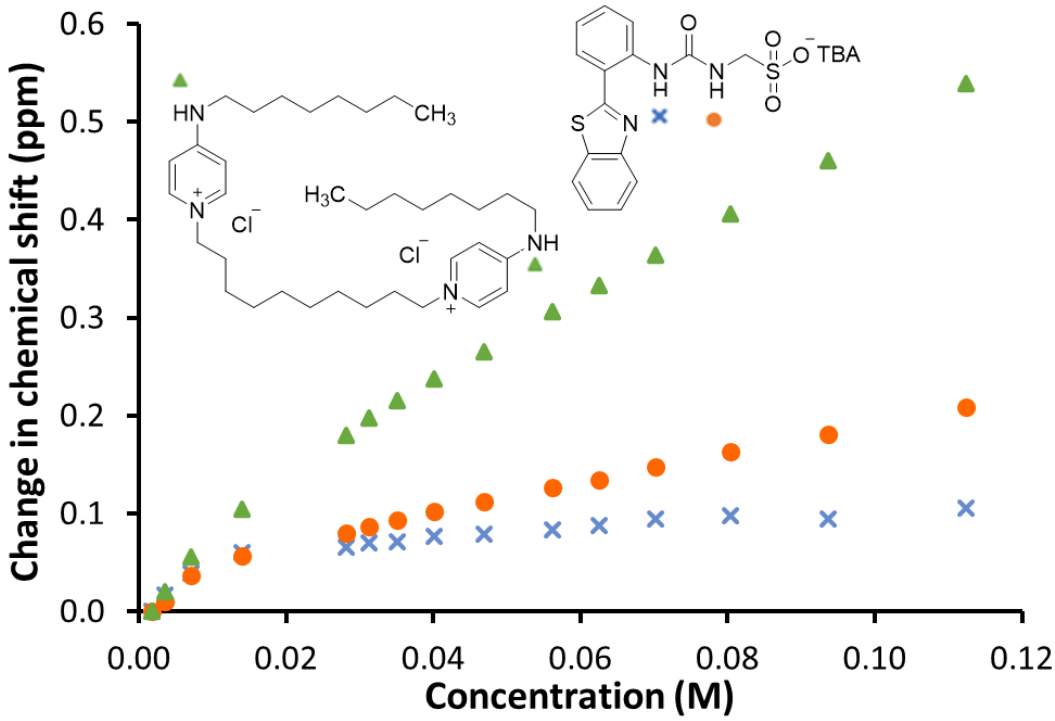

Figure S138 - Graph illustrating the ^{1}H NMR down-field change in chemical shift of SSA urea and appropriate co-formulant NH resonances with increasing concentration of co-formulation **I** in DMSO-d_6 0.5 % H_2O (298 K).

Self-association constant calculation

Co-formulation **I** - Dilution study in DMSO-d_6 5 % H_2O. Values calculated from data gathered from SSA NH urea resonances.

Equal K/Dimerization model

K_e = 7.81 M^{-1} ± 6.1958 % K_{dim} = 3.91 M^{-1} ± 3.0879 %

http://app.supramolecular.org/bindfit/view/1d3fc1ee-462a-443a-ae55-7750fd96893f

CoEK model

K_e = 3.59 M^{-1} ± 45.2451 % K_{dim} = 1.80 M^{-1} ± 22.6225 % ρ = 1.77 ± 63.8361 %

http://app.supramolecular.org/bindfit/view/219d4bd1-121d-4e51-8835-175a1e5b6add

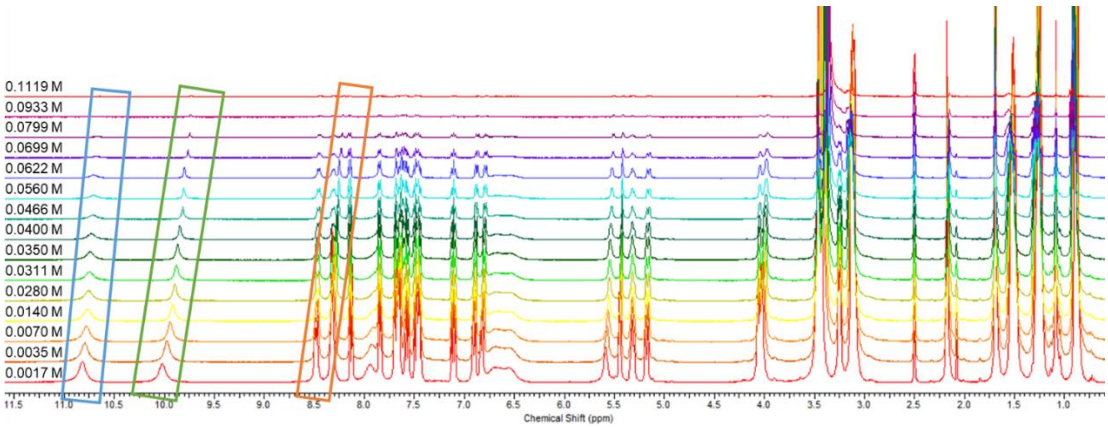

Figure S139 - ^{1}H NMR stack plot of co-formulation **m** in DMSO-d_6 0.5 % H_2O solution. Samples were prepared in series with an aliquot of the most concentrated solution undergoing serial dilution.

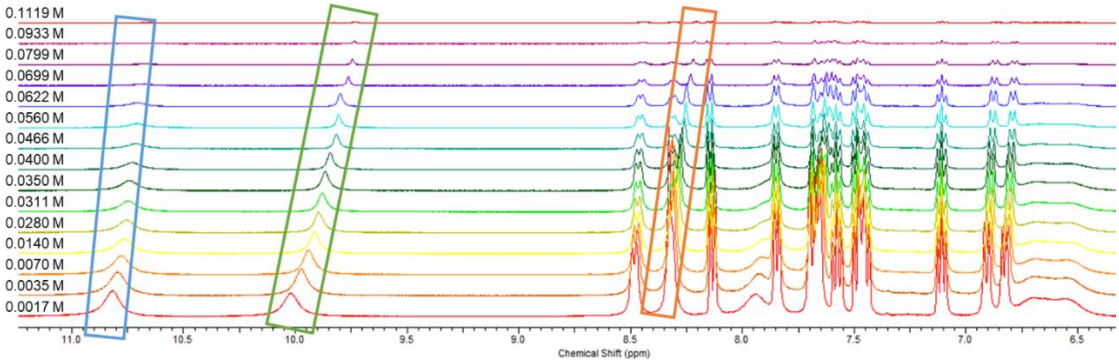

Figure S140 -Enlarged ^{1}H NMR stack plot of co-formulation **m** in DMSO-d_6 0.5 % H_2O solution. Samples were prepared in series with an aliquot of the most concentrated solution undergoing serial dilution.

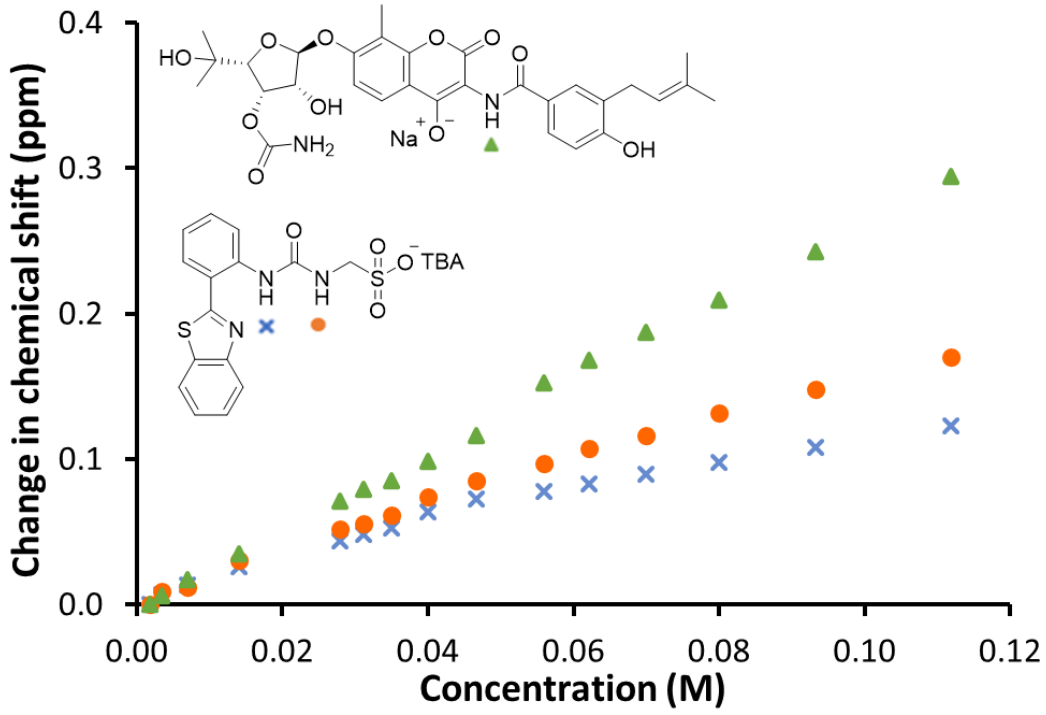

Figure S141 - Graph illustrating the ^{1}H NMR down-field change in chemical shift of SSA urea and appropriate co-formulant NH resonances with increasing concentration of co-formulation **m** in DMSO-d_6 0.5 % H_2O (298 K).

Self-association constant calculation

Co-formulation **m** - Dilution study in DMSO-d_6 5 % H_2O. Values calculated from data gathered from SSA NH urea resonances.

Equal K/Dimerization model

K_e = 2.63 M^{-1} ± 1.7535 % K_{dim} = 1.31 M^{-1} ± 0.8767 %

http://app.supramolecular.org/bindfit/view/a594f18d-322d-4fee-8ac5-d1c0f1e5578a

CoEK model

K_e = 1.23 M^{-1} ± 32.4964 % K_{dim} = 0.62 M^{-1} ± 16.2482 % ρ = 1.62 ± 37.8928 %

http://app.supramolecular.org/bindfit/view/fe0afc63-7cb1-4aeb-8e96-9fbf369b169a

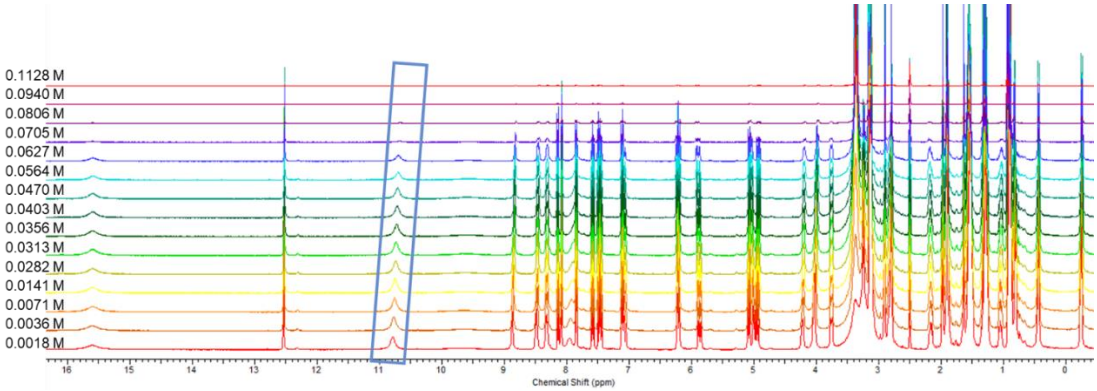

Figure S142 - ^{1}H NMR stack plot of co-formulation **n** in DMSO-d_6 0.5 % H_2O solution. Samples were prepared in series with an aliquot of the most concentrated solution undergoing serial dilution.

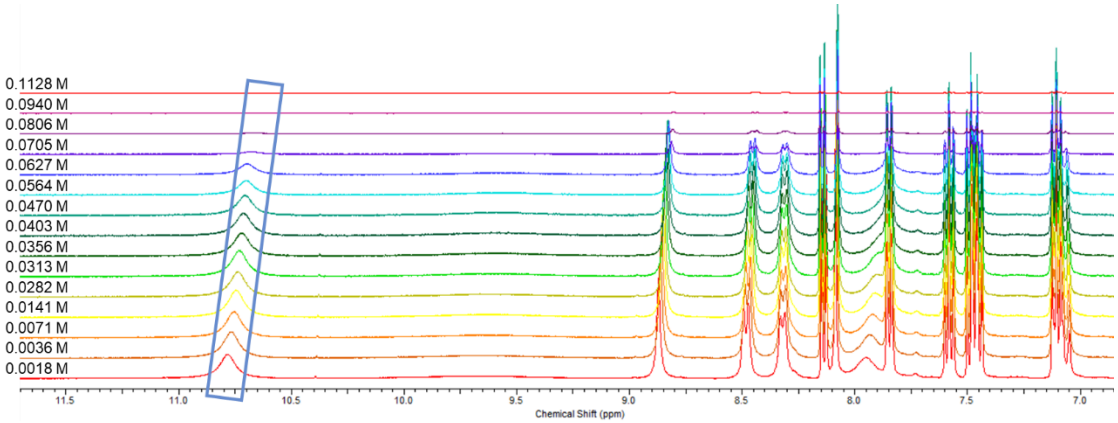

Figure S143 – Enlarged ^{1}H NMR stack plot of co-formulation **n** in DMSO-d_6 0.5 % H_2O solution. Samples were prepared in series with an aliquot of the most concentrated solution undergoing serial dilution.

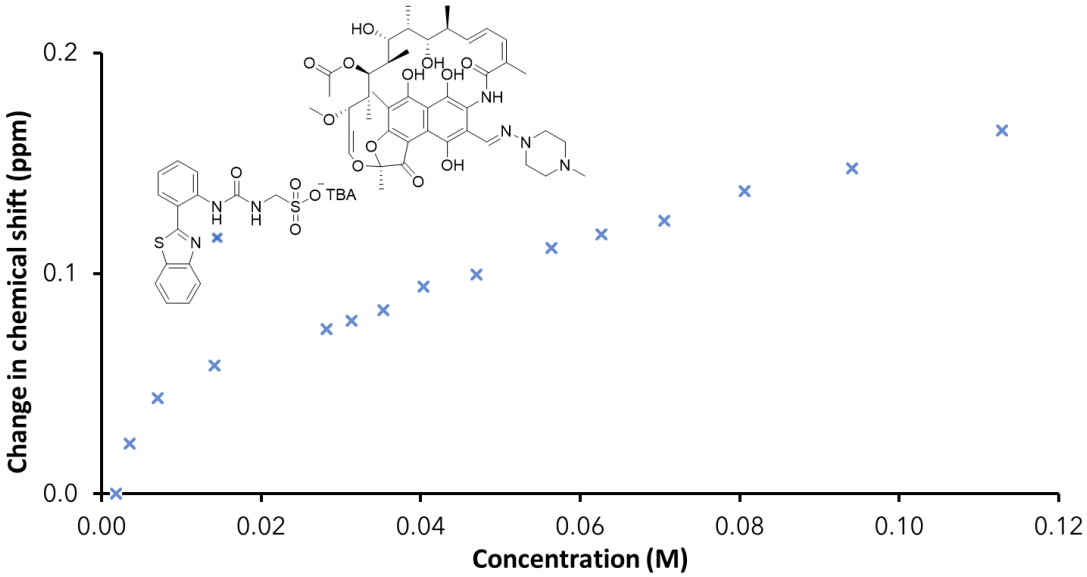

Figure S144 - Graph illustrating the ^{1}H NMR down-field change in chemical shift of SSA urea and appropriate co-formulant NH resonances with increasing concentration of co-formulation **n** in DMSO-d_6 0.5 % H_2O (298 K).

Self-association constant calculation

Co-formulation **n** - Dilution study in DMSO-d_6 5 % H_2O. Values calculated from data gathered from a single SSA NH urea resonance.

Equal K/Dimerization model

K_e = 8.17 M^{-1} ± 7.7895 % K_{dim} = 4.09 M^{-1} ± 3.8948 %

http://app.supramolecular.org/bindfit/view/b48e0b8d-253e-4047-847d-d41aacb47b7a

CoEK model

K_e = 3.80 M^{-1} ± 55.5630 % K_{dim} = 1.90 M^{-1} ± 27.7815 % ρ = 1.77 ± 79.6074 %

http://app.supramolecular.org/bindfit/view/4be487b0-6863-4881-88a7-d8304669766c

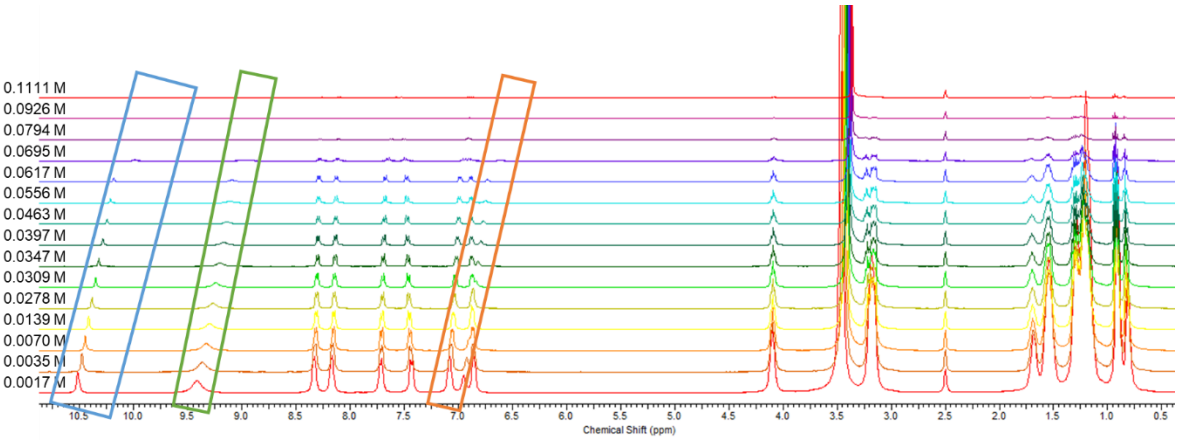

Figure S145 - ^{1}H NMR stack plot of co-formulation **o** in DMSO-d_6 0.5 % H_2O solution. Samples were prepared in series with an aliquot of the most concentrated solution undergoing serial dilution.

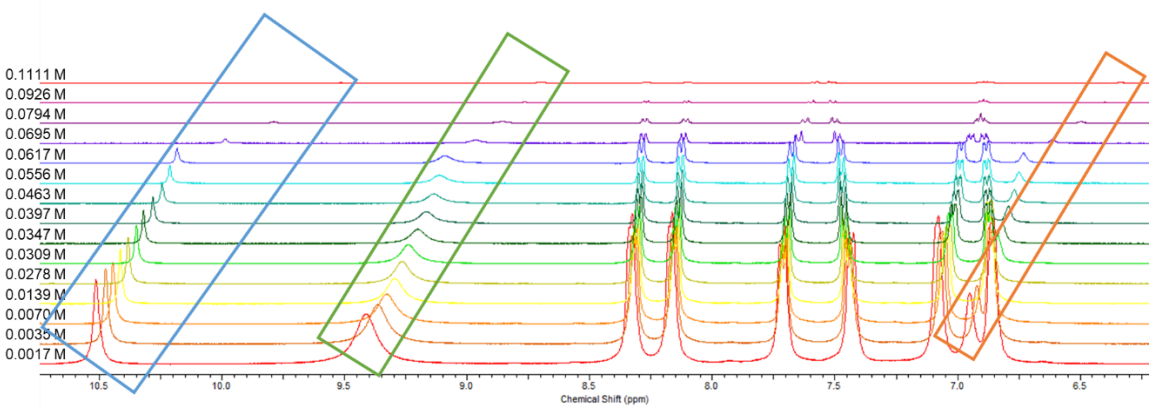

Figure S146 – Enlarged ^{1}H NMR stack plot of co-formulation **o** in DMSO-d_6 0.5 % H_2O solution. Samples were prepared in series with an aliquot of the most concentrated solution undergoing serial dilution.

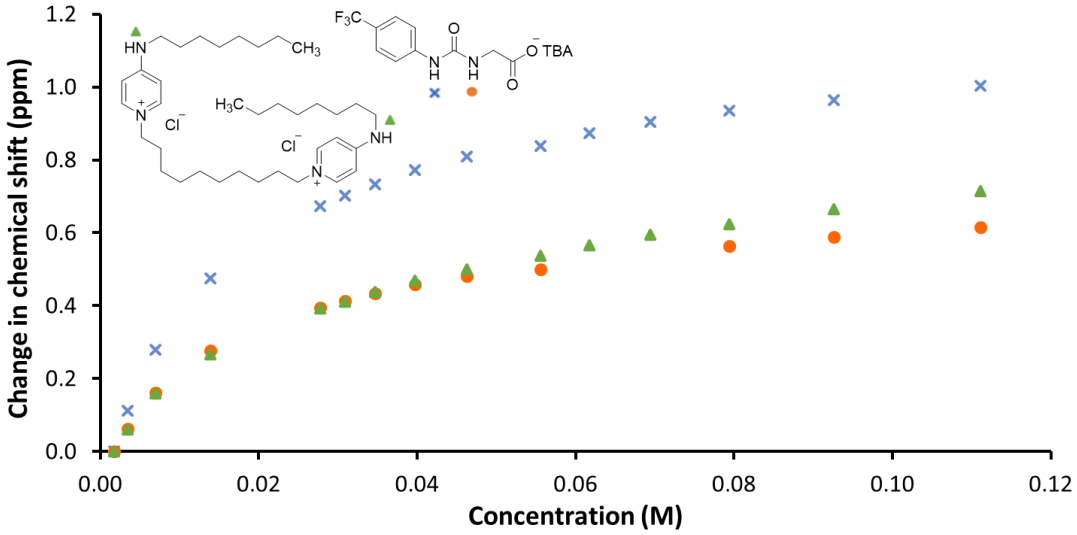

Figure S147 - Graph illustrating the ^{1}H NMR down-field change in chemical shift of SSA urea and appropriate co-formulant NH resonances with increasing concentration of co-formulation **o** in DMSO-d_6 0.5 % H_2O (298 K).

Self-association constant calculation

Co-formulation **o** - Dilution study in DMSO-d_6 5 % H_2O. Values calculated from data gathered from a single SSA NH urea resonance.

Equal K/Dimerization model

K_e = 78.18 M^{-1} ± 1.2112 % K_{dim} = 39.09 M^{-1} ± 0.6056 %

http://app.supramolecular.org/bindfit/view/23183f48-d5fc-4d1a-afa7-f904f88b887b

CoEK model

K_e = 81.59 M^{-1} ± 1.1801 % K_{dim} = 40.80 M^{-1} ± 0.5900 % ρ = 0.84 ± 3.8983 %

http://app.supramolecular.org/bindfit/view/dc86b128-752c-437e-86d3-ab349697afac

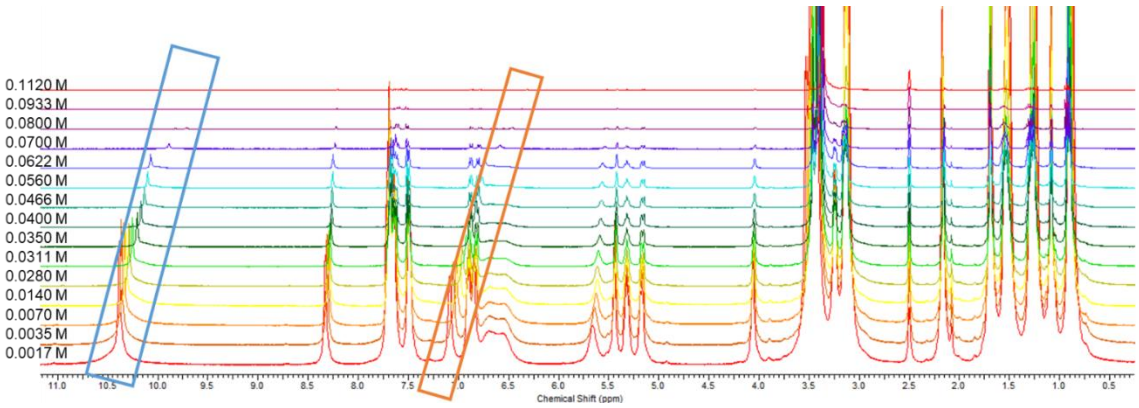

Figure S148- ^{1}H NMR stack plot of co-formulation **p** in DMSO-d_6 0.5 % H_2O solution. Samples were prepared in series with an aliquot of the most concentrated solution undergoing serial dilution.

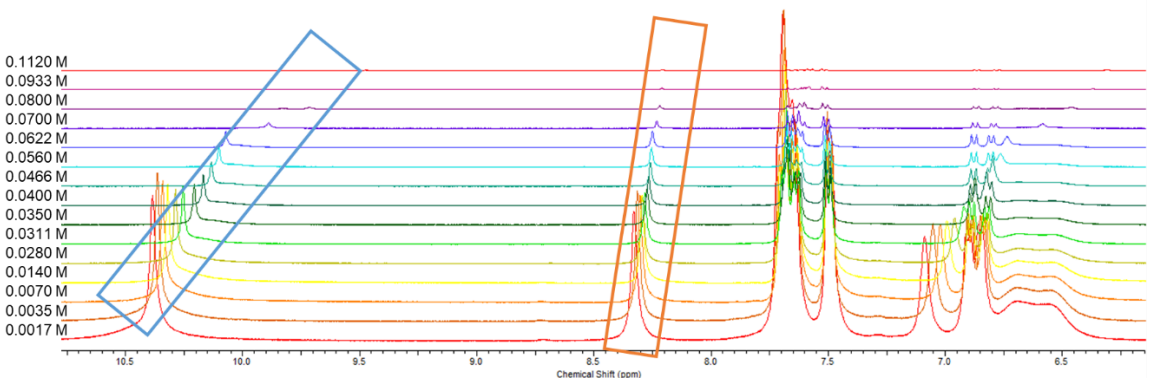

Figure S149 – Enlarged ^{1}H NMR stack plot of co-formulation **p** in DMSO-d_6 0.5 % H_2O solution. Samples were prepared in series with an aliquot of the most concentrated solution undergoing serial dilution.

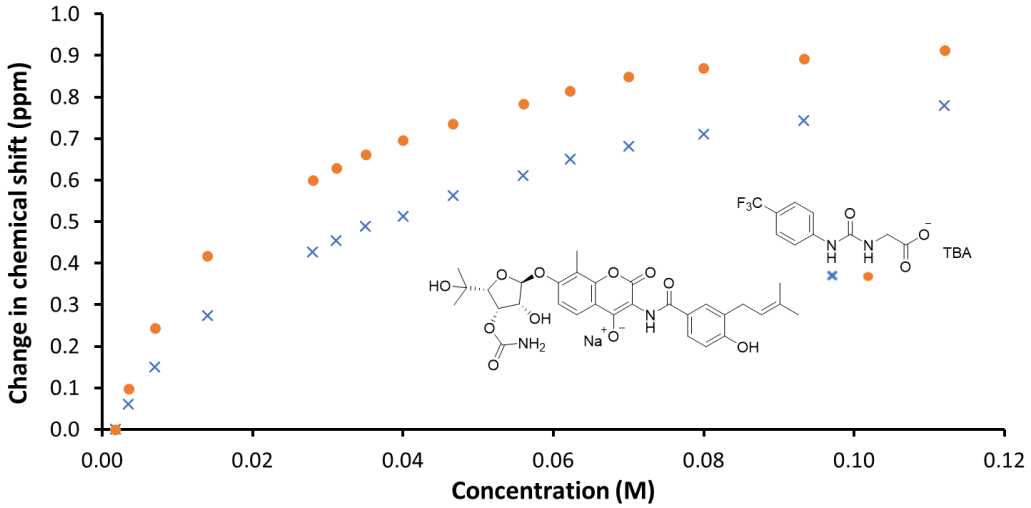

Figure S150 - Graph illustrating the ^{1}H NMR down-field change in chemical shift of SSA urea and appropriate co-formulant NH resonances with increasing concentration of co-formulation **p** in DMSO-d_6 0.5 % H_2O (298 K).

Self-association constant calculation

Co-formulation **p** - Dilution study in DMSO-d_6 5 % H_2O. Values calculated from data gathered from SSA NH urea resonances.

Equal K/Dimerization model

K_e = 41.90 M^{-1} ± 3.1148 % K_{dim} = 20.95 M^{-1} ± 1.5574 %

http://app.supramolecular.org/bindfit/view/efb348f6-f123-492f-9a9d-632c43cabdac

CoEK model

K_e = 42.06 M^{-1} ± 3.3053 % K_{dim} = 21.03 M^{-1} ± 1.6526 % ρ = 0.99 ± 12.5209 %

http://app.supramolecular.org/bindfit/view/f5957374-1a78-4b1b-8bd2-044b20adffae

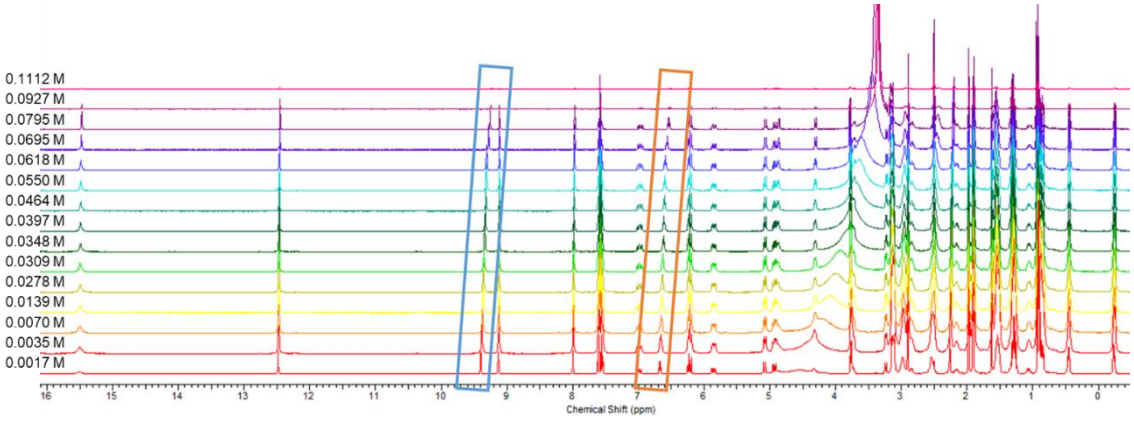

Figure S151 - ^{1}H NMR stack plot of co-formulation **q** in DMSO-d_6 0.5 % H_2O solution. Samples were prepared in series with an aliquot of the most concentrated solution undergoing serial dilution.

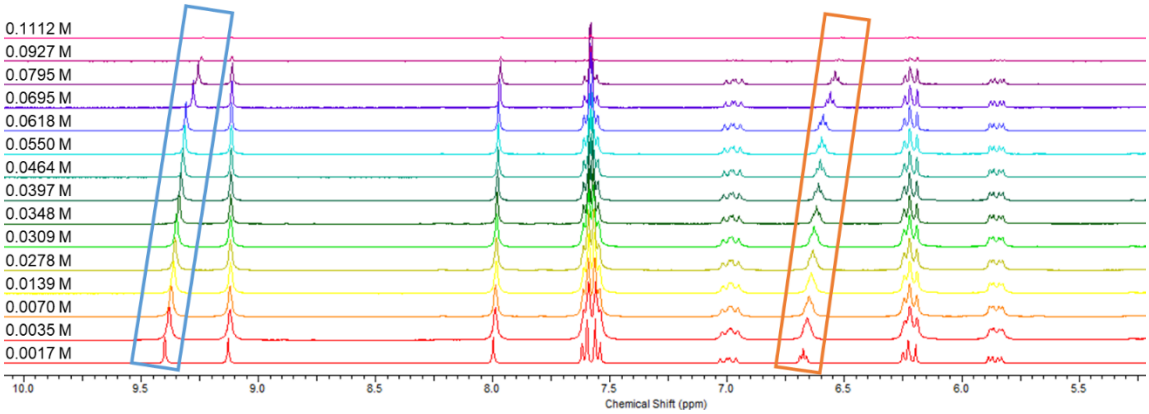

Figure S152 – Enlarged ^{1}H NMR stack plot of co-formulation **q** in DMSO-d_6 0.5 % H_2O solution. Samples were prepared in series with an aliquot of the most concentrated solution undergoing serial dilution.

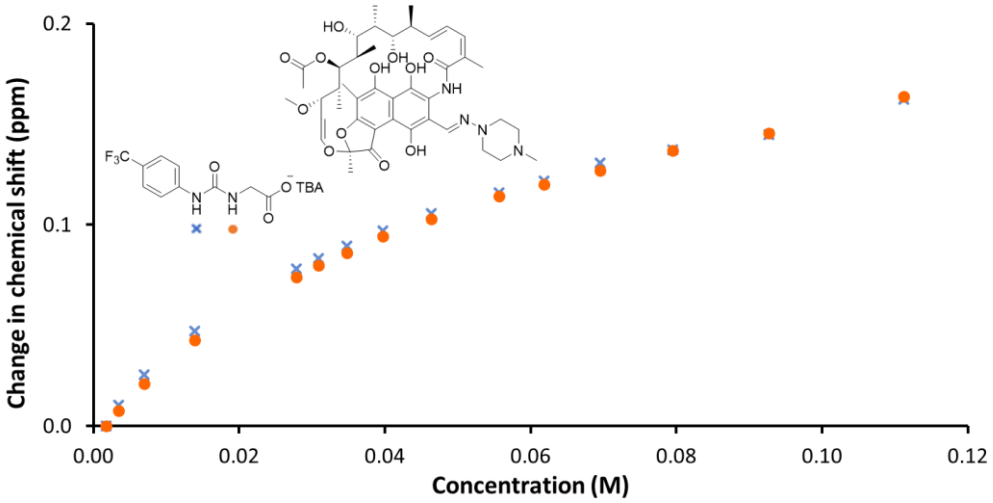

Figure S153 - Graph illustrating the ^{1}H NMR down-field change in chemical shift of SSA urea and appropriate co-formulant NH resonances with increasing concentration of co-formulation **q** in DMSO-d_6 0.5 % H_2O (298 K).

Self-association constant calculation

Co-formulation **q** - Dilution study in DMSO-d_6 5 % H_2O. Values calculated from data gathered from a single SSA NH urea resonance.

Equal K/Dimerization model

K_e = 13.23 M^{-1} ± 1.2414 % K_{dim} = 6.62 M^{-1} ± 0.6207 %

http://app.supramolecular.org/bindfit/view/54ae6033-228a-49fc-a0be-7a4cbfa2477c

CoEK model

K_e = 5.44 M^{-1} ± 5.8420 % K_{dim} = 2.72 M^{-1} ± 2.9210 % ρ = 1.96 ± 9.1254 %

http://app.supramolecular.org/bindfit/view/8ced8d04-5a65-41f1-9f90-1766f092c834

2.6 ^{1}H NMR DOSY experiments

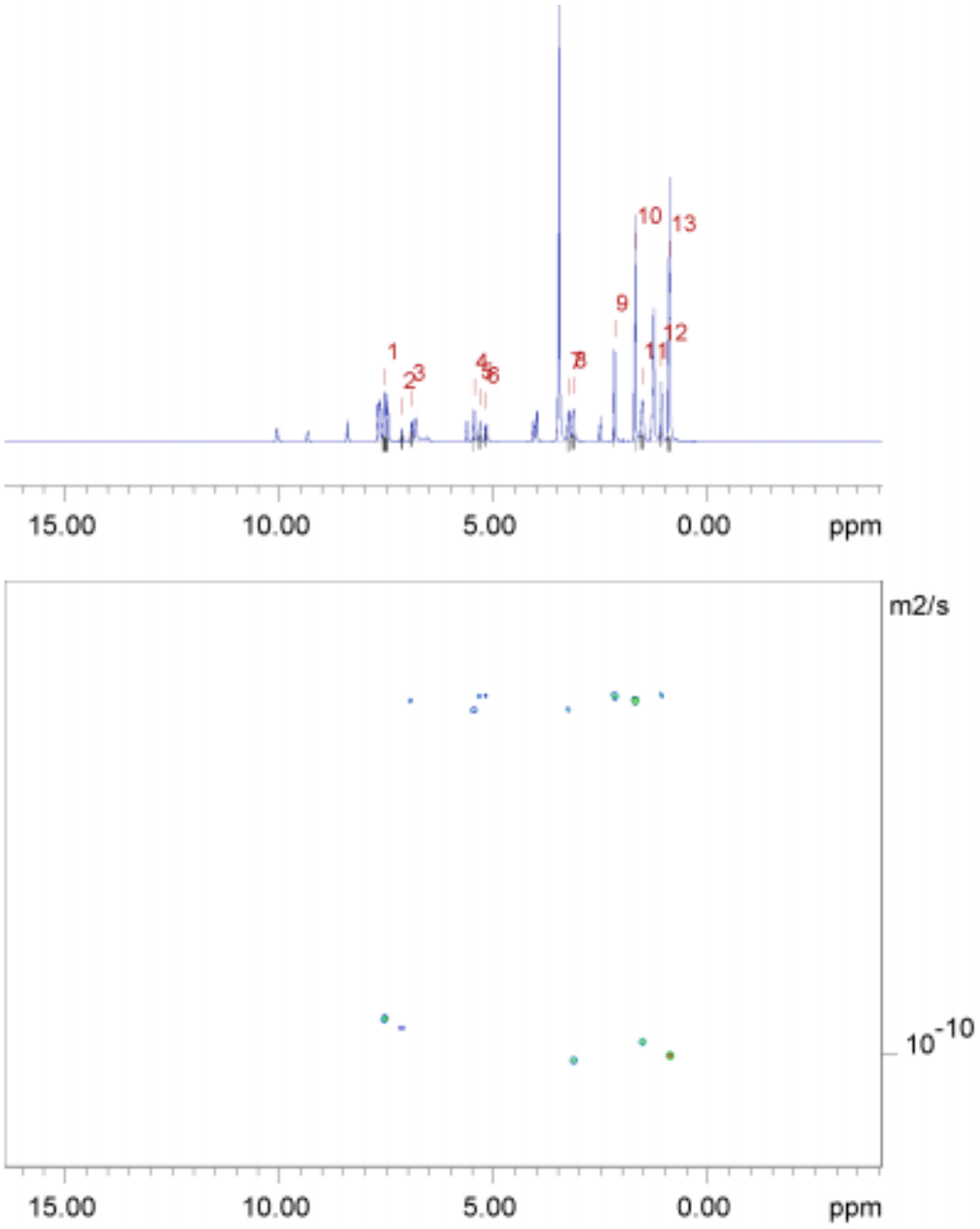

Peak name	F2 [ppm]	Io	error	D [m2/s]	error
1	7.521	8.23e+09	2.509e+05	9.46e-11	5.902e-15
2	7.133	1.02e+09	1.345e+05	9.57e-11	2.569e-14
3	6.912	1.78e+09	1.178e+05	5.58e-11	7.750e-15
4	5.450	1.62e+09	9.453e+04	5.69e-11	6.980e-15
5	5.317	2.02e+09	1.320e+05	5.57e-11	7.647e-15
6	5.174	1.32e+09	1.061e+05	5.55e-11	9.419e-15
7	3.247	2.70e+09	1.109e+05	5.67e-11	4.901e-15
8	3.135	4.31e+09	1.615e+05	1.01e-10	7.723e-15
9	2.174	4.47e+09	9.331e+04	5.56e-11	2.442e-15
10	1.690	9.88e+09	8.911e+04	5.58e-11	1.057e-15
11	1.526	5.97e+09	1.743e+05	9.77e-11	5.831e-15
12	1.083	2.61e+09	8.386e+04	5.56e-11	3.759e-15
13	0.896	2.31e+10	1.685e+05	1.01e-10	1.497e-15

Figure S154 - ^{1}H DOSY NMR spectrum of co-formulation **g** (113.6 mM) in DMSO-d_6 at 298 K and a table reporting the diffusion constants calculated for each peak used to determine the hydrodynamic diameter of the anionic components of **g** (d_H = 2.30 nm). Peaks 1 and 2 correspond to the anionic component of **g** while peaks 8, 11 and 13 correspond to the cationic component of **g**. Peaks 3-7, 9-10 and 12 correspond to the drug component, **novobiocin**.

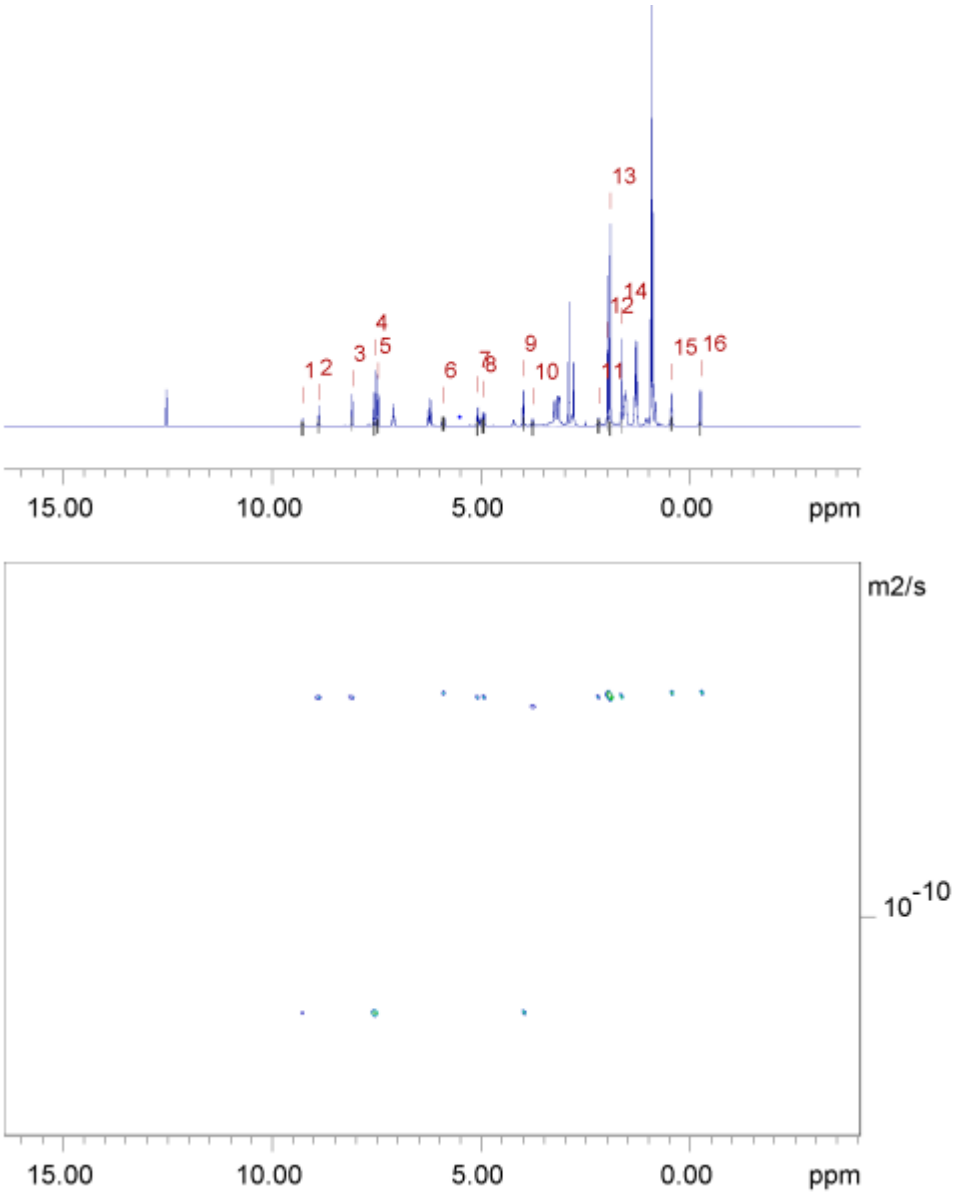

Peak name	F2 [ppm]	Io	error	D [m2/s]	error
1	9.277	6.02e+08	8.989e+04	1.15e-10	3.330e-14
2	8.888	8.50e+08	6.143e+04	7.25e-11	1.059e-14
3	8.087	7.15e+08	3.676e+04	7.24e-11	7.531e-15
4	7.558	2.26e+09	6.896e+04	1.15e-10	6.758e-15
5	7.474	2.38e+09	7.662e+04	1.15e-10	7.160e-15
6	5.907	1.02e+09	8.179e+04	7.23e-11	1.176e-14
7	5.093	1.01e+09	6.962e+04	7.25e-11	1.011e-14
8	4.947	1.19e+09	8.367e+04	7.28e-11	1.033e-14
9	3.994	1.67e+09	6.381e+04	1.15e-10	8.493e-15
10	3.770	6.22e+08	5.942e+04	7.38e-11	1.423e-14
11	2.192	9.73e+08	7.863e+04	7.28e-11	1.190e-14
12	1.973	3.30e+09	4.950e+04	7.23e-11	2.197e-15
13	1.916	6.01e+09	5.691e+04	7.25e-11	1.387e-15
14	1.643	1.99e+09	4.046e+04	7.26e-11	2.988e-15
15	0.448	2.21e+09	6.356e+04	7.20e-11	4.199e-15
16	-0.243	1.77e+09	4.914e+04	7.21e-11	4.064e-15

Figure S155 - ^{1}H DOSY NMR spectrum of co-formulation **h** (113.8 mM) in DMSO-d_6 at 298 K and a table reporting the diffusion constants calculated for each peak used to determine the hydrodynamic diameter of the anionic components of **h** (d_H = 1.91 nm). Peaks 1, 4-5 and 9 correspond to the anionic component of **h** while peaks 2-3, 6-8 and 10-16 and 12 correspond to the cationic component of **h** and drug component, **rifampicin**.

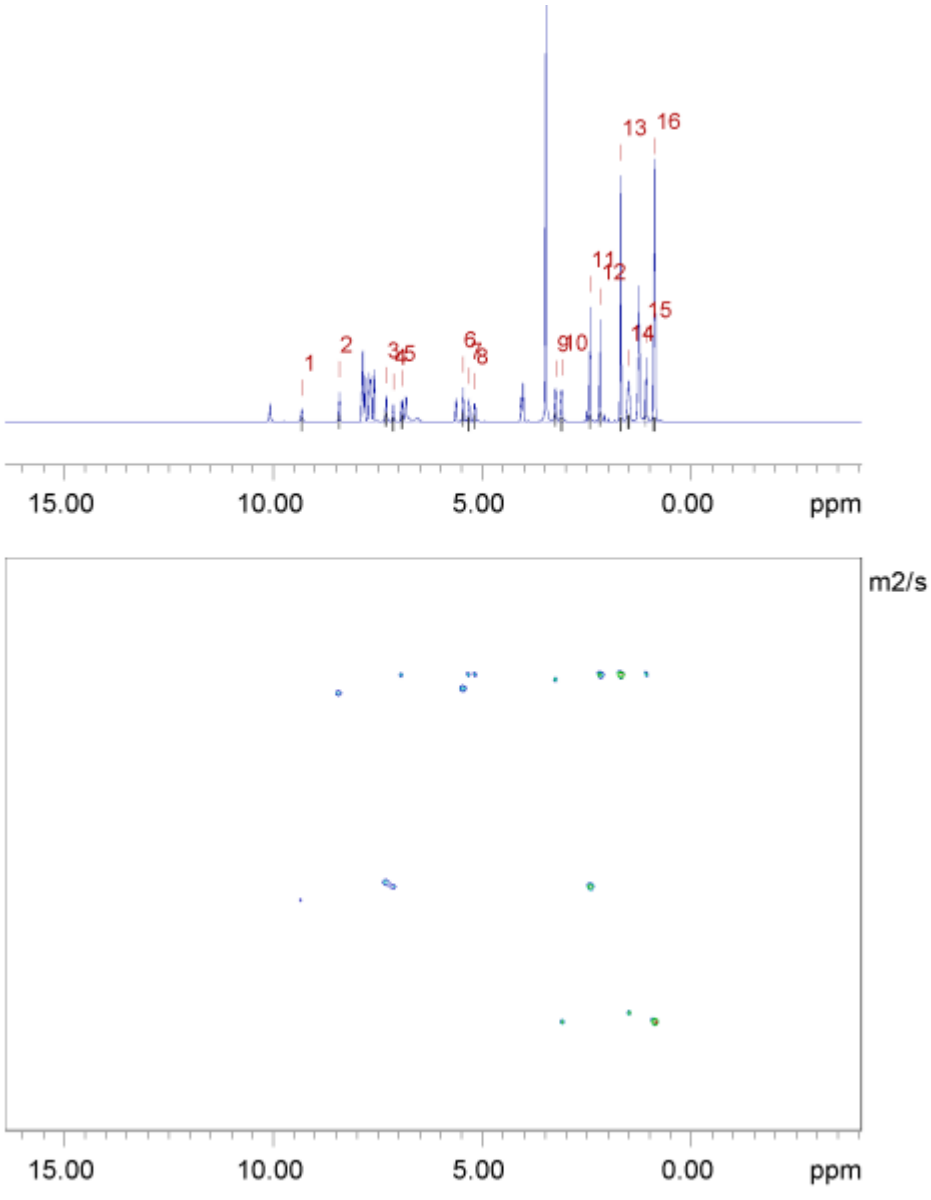

Peak name	F2 [ppm]	Io	error	D [m2/s]	error
1	9.315	9.58e+08	1.111e+05	7.12e-11	1.755e-14
2	8.421	1.69e+09	9.619e+04	5.04e-11	6.237e-15
3	7.299	2.06e+09	1.139e+05	6.90e-11	8.137e-15
4	7.128	1.36e+09	1.174e+05	6.97e-11	1.279e-14
5	6.918	2.17e+09	1.155e+05	4.92e-11	5.722e-15
6	5.458	1.99e+09	9.663e+04	5.03e-11	5.310e-15
7	5.318	1.87e+09	1.063e+05	4.89e-11	6.084e-15
8	5.185	1.62e+09	1.059e+05	4.90e-11	6.987e-15
9	3.246	3.05e+09	1.067e+05	4.96e-11	3.782e-15
10	3.101	4.37e+09	1.510e+05	8.68e-11	6.313e-15
11	2.422	6.12e+09	1.099e+05	6.97e-11	2.664e-15
12	2.185	5.70e+09	9.899e+04	4.89e-11	1.858e-15
13	1.689	1.36e+10	1.025e+05	4.90e-11	8.084e-16
14	1.500	5.80e+09	1.566e+05	8.55e-11	4.865e-15
15	1.084	2.58e+09	7.081e+04	4.92e-11	2.949e-15
16	0.880	2.43e+10	1.550e+05	8.73e-11	1.173e-15

Figure S156 - ^{1}H DOSY NMR spectrum of co-formulation **j** (111.7 mM) in DMSO-d_6 at 298 K and a table reporting the diffusion constants calculated for each peak used to determine the hydrodynamic diameter of the anionic components of **j** (d_H = 3.2 nm). Peaks 1, 3-4 and 11 correspond to the anionic component of **j** while peaks 10, 14 and 16 correspond to the cationic component of **j**. Peaks 2, 5-9, 12-13 and 15 correspond to the drug component, **novobiocin**.

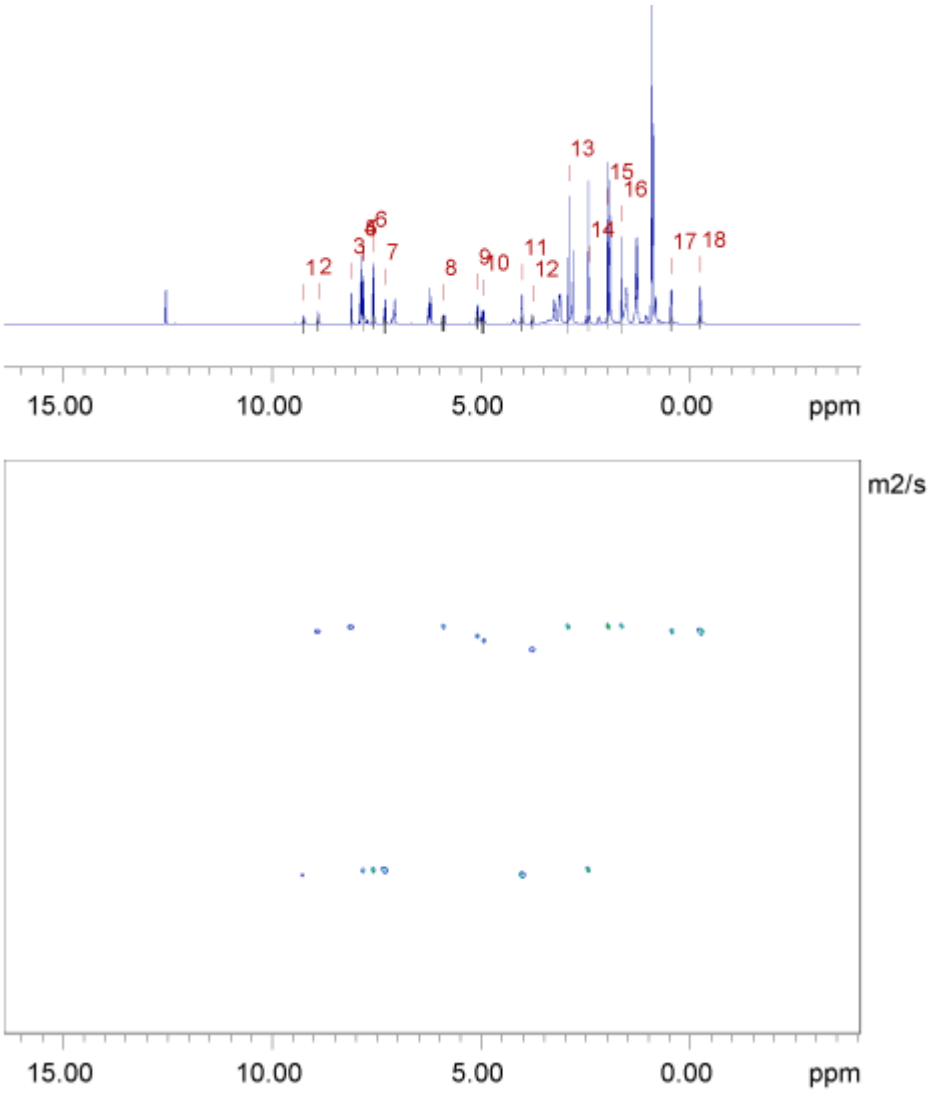

Peak name	F2 [ppm]	Io	error	D [m2/s]	error
1	9.249	6.91e+08	9.627e+04	8.89e-11	2.282e-14
2	8.903	8.99e+08	9.291e+04	6.76e-11	1.317e-14
3	8.101	9.83e+08	6.439e+04	6.73e-11	8.309e-15
4	7.832	7.04e+08	4.731e+04	8.85e-11	1.095e-14
5	7.809	1.46e+09	5.957e+04	8.86e-11	6.638e-15
6	7.577	3.36e+09	1.013e+05	8.86e-11	4.910e-15
7	7.303	1.72e+09	1.013e+05	8.84e-11	9.576e-15
8	5.902	1.44e+09	1.336e+05	6.74e-11	1.179e-14
9	5.092	1.35e+09	9.797e+04	6.79e-11	9.249e-15
10	4.957	1.29e+09	1.155e+05	6.83e-11	1.150e-14
11	4.026	2.38e+09	9.485e+04	8.91e-11	6.534e-15
12	3.775	8.73e+08	9.761e+04	6.89e-11	1.448e-14
13	2.913	3.76e+09	7.021e+04	6.73e-11	2.367e-15
14	2.435	3.92e+09	6.623e+04	8.85e-11	2.749e-15
15	1.976	3.93e+09	6.064e+04	6.73e-11	1.955e-15
16	1.643	2.19e+09	5.157e+04	6.72e-11	2.986e-15
17	0.457	2.53e+09	8.354e+04	6.75e-11	4.205e-15
18	-0.236	2.64e+09	8.213e+04	6.76e-11	3.961e-15

Figure S157 - ^{1}H DOSY NMR spectrum of co-formulation **k** (112.3 mM) in DMSO-d_6 at 298 K and a table reporting the diffusion constants calculated for each peak used to determine the hydrodynamic diameter of the anionic components of **k** (d_H = 2.53 nm). Peaks 1, 4-7, 11 and 14 correspond to the anionic component of **k** while peaks 2-3, 8-10, 12-13 and 15-18 correspond to the cationic component of **k** and the drug component, **rifampicin.**

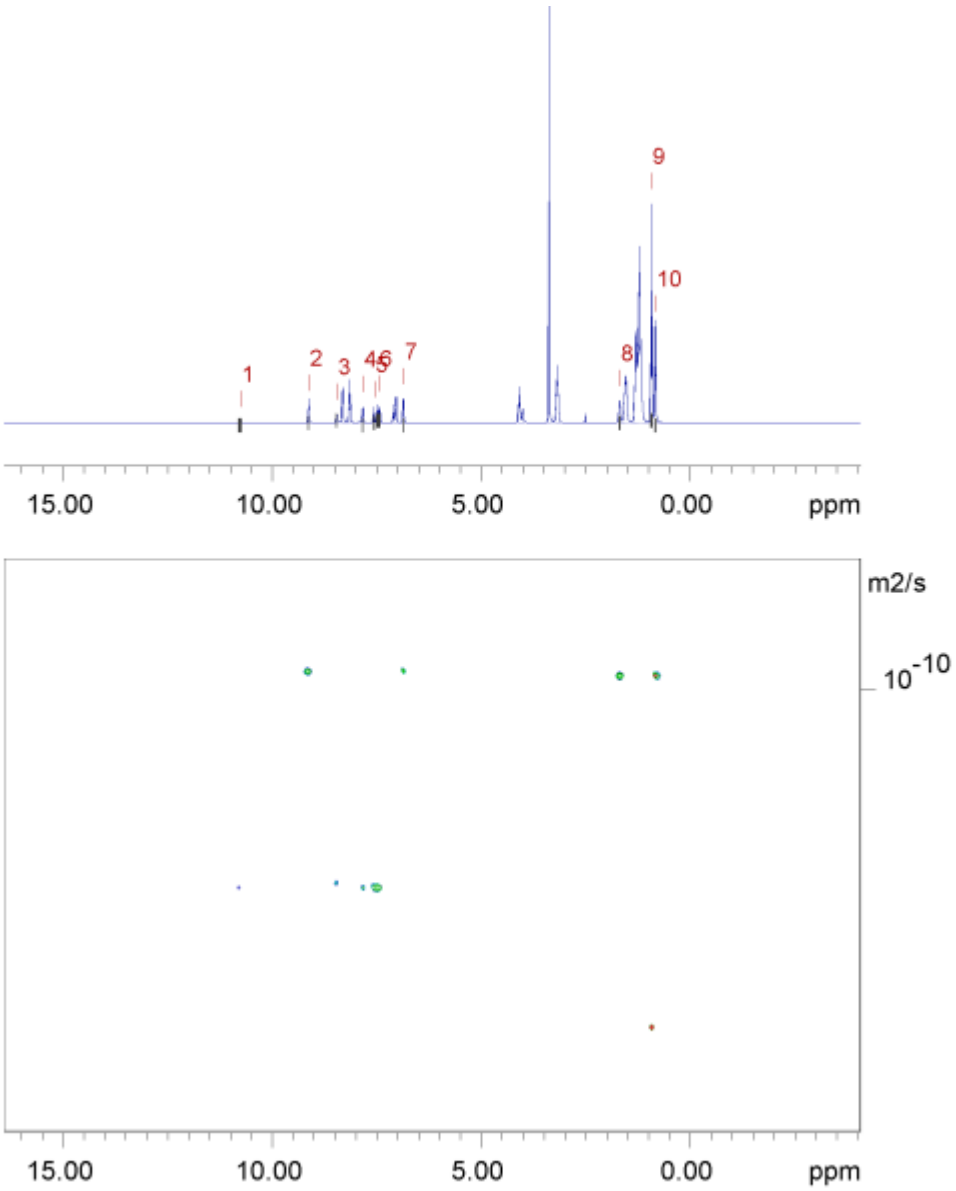

Peak name	F2 [ppm]	Io	error	D [m2/s]	error
1	10.768	2.39e+08	1.807e+05	1.40e-10	2.292e-13
2	9.129	1.70e+09	1.050e+05	9.73e-11	1.337e-14
3	8.457	6.71e+08	1.049e+05	1.39e-10	4.705e-14
4	7.832	9.00e+08	9.914e+04	1.39e-10	3.333e-14
5	7.562	1.18e+09	1.353e+05	1.39e-10	3.466e-14
6	7.460	2.64e+09	1.913e+05	1.39e-10	2.185e-14
7	6.864	2.17e+09	1.046e+05	9.74e-11	1.040e-14
8	1.693	2.45e+09	1.179e+05	9.76e-11	1.043e-14
9	0.926	1.49e+10	1.505e+05	1.75e-10	3.814e-15
10	0.831	6.87e+09	1.138e+05	9.82e-11	3.609e-15

Figure S158 - ^{1}H DOSY NMR spectrum of co-formulation **I** (112.4 mM) in DMSO-d_6 at 298 K and a table reporting the diffusion constants calculated for each peak used to determine the hydrodynamic diameter of the anionic components of **I** (d_H = 1.14 nm). Peaks 1 and 3-6 correspond to the anionic component of **I** while peak 9 corresponds to the cationic component of **I**. Peaks 2, 7-8 and 10 correspond to the drug component, **octenidine**.

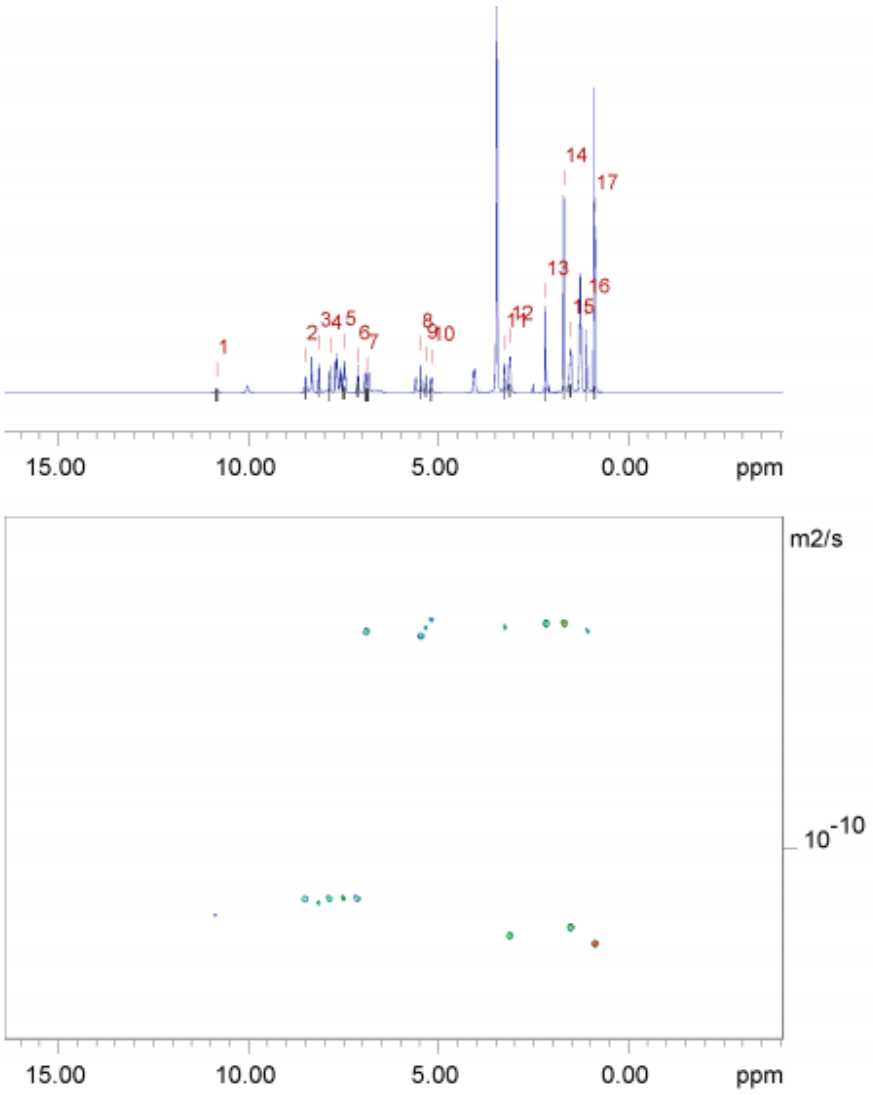

Peak name	F2 [ppm]	Io	error	D [m2/s]	error
1	10.835	4.34e+08	1.706e+05	1.13e-10	9.421e-14
2	8.496	1.65e+09	1.218e+05	1.10e-10	1.727e-14
3	8.145	1.99e+09	1.114e+05	1.11e-10	1.319e-14
4	7.858	1.85e+09	1.066e+05	1.10e-10	1.348e-14
5	7.480	4.31e+09	1.583e+05	1.09e-10	8.551e-15
6	7.122	1.98e+09	1.261e+05	1.10e-10	1.488e-14
7	6.881	3.57e+09	1.711e+05	6.74e-11	7.109e-15
8	5.458	1.40e+09	7.845e+04	6.79e-11	8.330e-15
9	5.333	1.45e+09	9.931e+04	6.68e-11	1.003e-14
10	5.193	1.30e+09	9.537e+04	6.62e-11	1.072e-14
11	3.261	2.63e+09	9.936e+04	6.69e-11	5.555e-15
12	3.127	4.92e+09	1.365e+05	1.17e-10	6.892e-15
13	2.185	4.13e+09	8.289e+04	6.63e-11	2.932e-15
14	1.697	1.05e+10	9.543e+04	6.63e-11	1.326e-15
15	1.523	6.54e+09	1.455e+05	1.16e-10	5.461e-15
16	1.100	1.94e+09	5.612e+04	6.76e-11	4.306e-15
17	0.895	2.18e+10	1.289e+05	1.19e-10	1.488e-15

Figure 159 - ^{1}H DOSY NMR spectrum of co-formulation **m** (111.9 mM) in DMSO-d_6 at 298 K and a table reporting the diffusion constants calculated for each peak used to determine the hydrodynamic diameter of the anionic components of **m** (d_H = 1.99 nm). Peaks 1-6 correspond to the anionic component of **m** while peaks 12, 15 and 17 correspond to the cationic component of **m.** Peaks 2, 7-11, 13-14 and 16 correspond to the drug component, **novobiocin**.

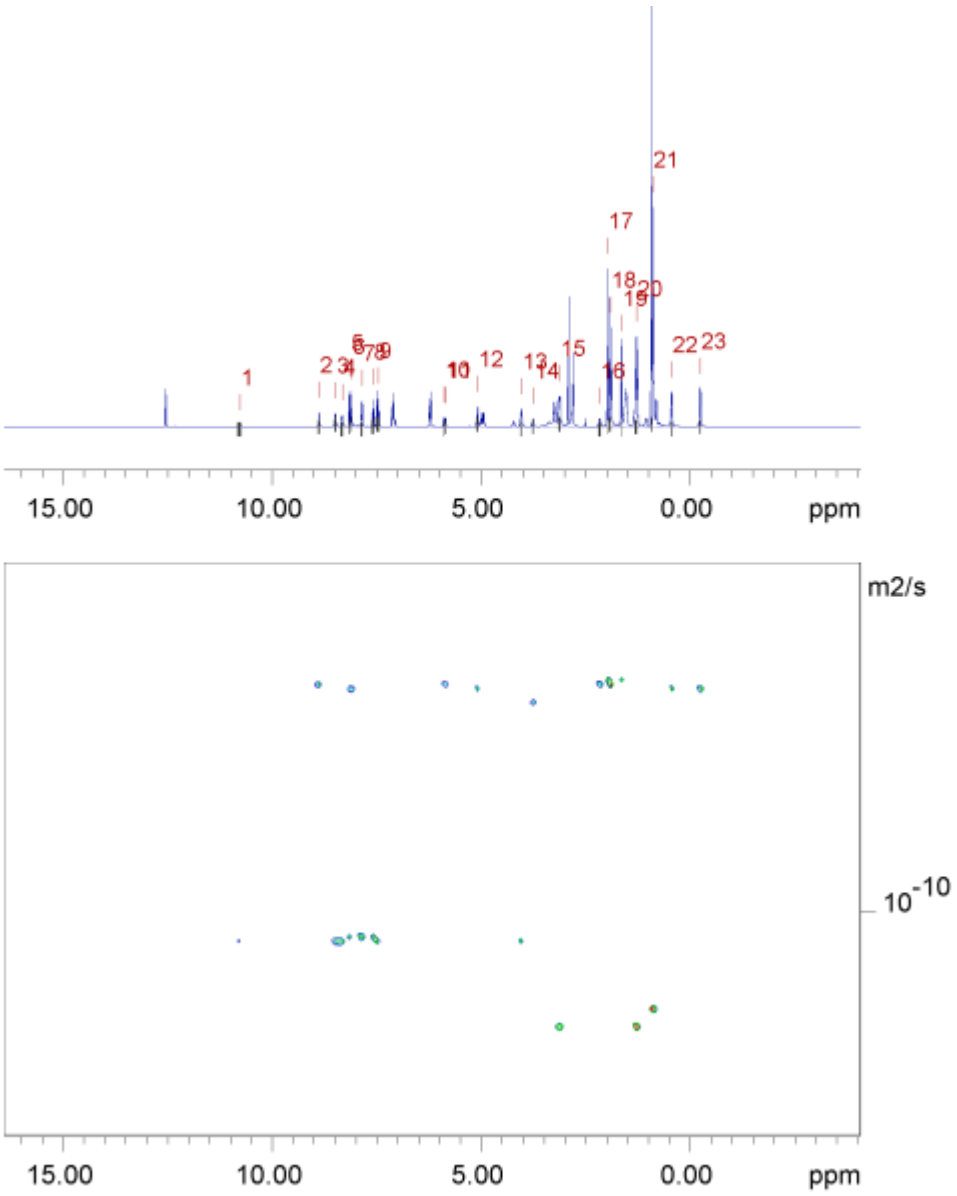
21
17
18
19
20
1
2
3
4
5
6
7
8
9
10
12
13
14
15
16
22
23
15.00
10.00
5.00
0.00
ppm
m2/s
10-10
15.00
10.00
5.00
0.00
ppm

Peak name	F2 [ppm]	Io	error	D [m2/s]	error
1	10.783	2.31e+08	1.245e+05	1.05e-10	1.017e-13
2	8.880	7.39e+08	8.608e+04	6.89e-11	1.464e-14
3	8.480	8.01e+08	8.587e+04	1.05e-10	2.018e-14
4	8.328	1.03e+09	1.028e+05	1.04e-10	1.869e-14
5	8.146	1.02e+09	6.752e+04	1.04e-10	1.236e-14
6	8.096	4.93e+08	3.402e+04	6.90e-11	8.688e-15
7	7.855	1.16e+09	7.555e+04	1.04e-10	1.219e-14
8	7.593	1.10e+09	9.144e+04	1.04e-10	1.554e-14
9	7.478	2.61e+09	1.153e+05	1.05e-10	8.306e-15
10	5.891	3.73e+08	5.629e+04	6.89e-11	1.899e-14
11	5.855	3.90e+08	5.888e+04	6.88e-11	1.895e-14
12	5.090	8.62e+08	6.993e+04	6.91e-11	1.022e-14
13	4.044	1.12e+09	7.561e+04	1.05e-10	1.265e-14
14	3.758	5.68e+08	7.072e+04	7.05e-11	1.599e-14
15	3.130	2.92e+09	9.613e+04	1.20e-10	7.110e-15
16	2.167	6.91e+08	8.140e+04	6.87e-11	1.477e-14
17	1.984	2.09e+09	3.800e+04	6.80e-11	2.254e-15
18	1.911	4.81e+09	7.398e+04	6.87e-11	1.928e-15
19	1.648	1.47e+09	3.807e+04	6.83e-11	3.232e-15
20	1.293	6.30e+09	1.047e+05	1.21e-10	3.611e-15
21	0.910	9.92e+09	7.863e+04	1.17e-10	1.665e-15
22	0.444	1.38e+09	5.363e+04	6.91e-11	4.909e-15
23	-0.241	1.57e+09	5.637e+04	6.92e-11	4.526e-15

Figure S160 - ^{1}H DOSY NMR spectrum of co-formulation **n** (112.8 mM) in DMSO-d_6 at 298 K and a table reporting the diffusion constants calculated for each peak used to determine the hydrodynamic diameter of the anionic components of **n** (d_H = 2.09 nm). Peaks 1, 3-5, 7-9 and 13 correspond to the anionic component of **n** while peaks 15 and 20-21 correspond to the cationic component of **n**. Peaks 2, 6, 10-12, 14, 16-19 and 22-23 correspond to the drug component, **rifampicin**.

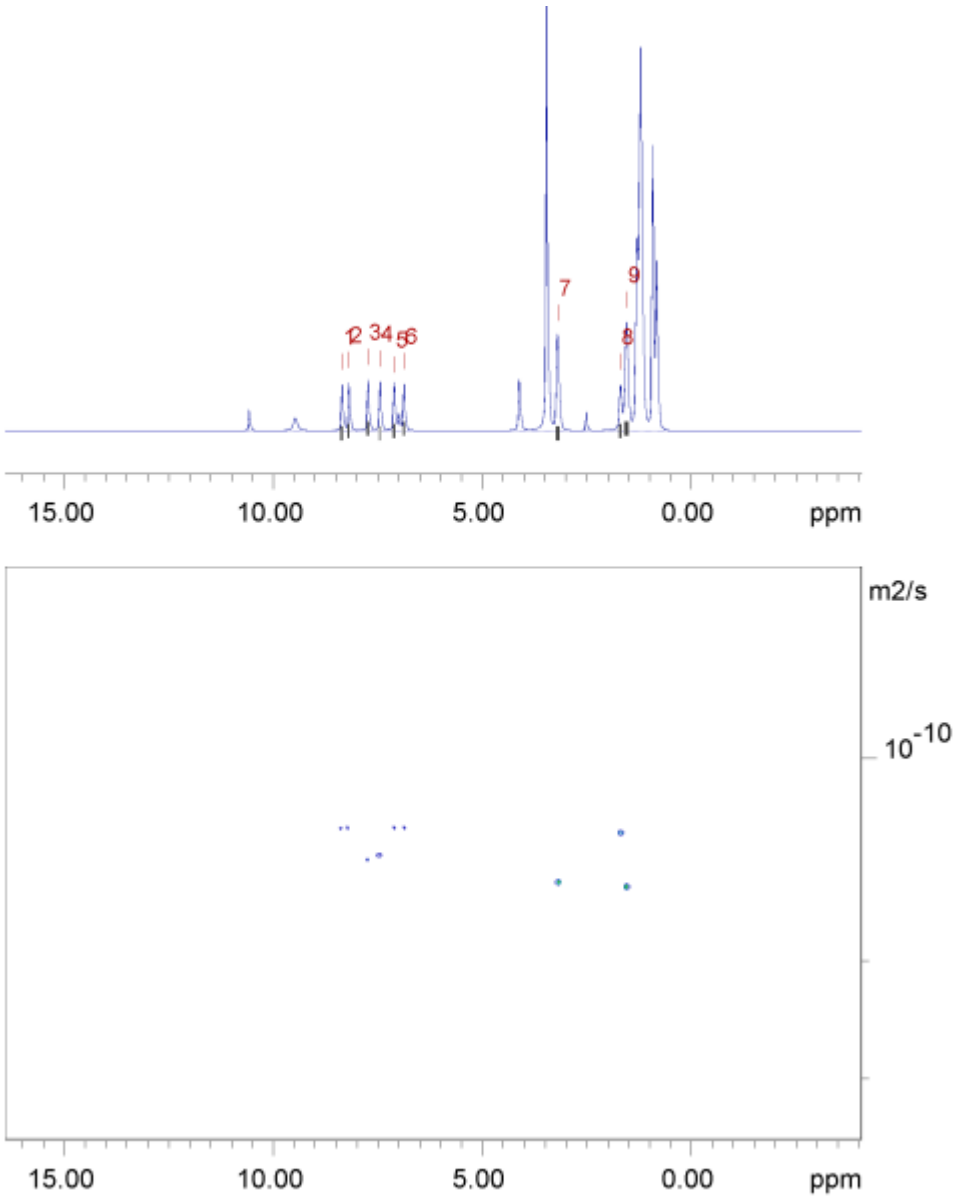

Peak name	F2 [ppm]	Io	error	D [m2/s]	error
1	8.356	4.56e+09	2.299e+05	1.27e-10	1.360e-14
2	8.192	4.07e+09	1.992e+05	1.26e-10	1.314e-14
3	7.738	4.61e+09	2.223e+05	1.41e-10	1.435e-14
4	7.450	4.06e+09	1.984e+05	1.40e-10	1.445e-14
5	7.107	4.45e+09	2.096e+05	1.28e-10	1.275e-14
6	6.875	4.38e+09	2.116e+05	1.26e-10	1.294e-14
7	3.194	1.63e+10	3.089e+05	1.53e-10	6.099e-15
8	1.696	5.65e+09	2.341e+05	1.29e-10	1.136e-14
9	1.552	1.98e+10	3.220e+05	1.56e-10	5.347e-15

Figure S161 - ^{1}H DOSY NMR spectrum of co-formulation **o** (111.1 mM) in DMSO-d_6 at 298 K and a table reporting the diffusion constants calculated for each peak used to determine the hydrodynamic diameter of the anionic components of **o** (d_H = 1.57 nm). Peaks 3 and 4 correspond to the anionic component of **o** while peaks 7 and 9 corresponds to the cationic component of **o**. Peaks 1-2, 5-6 and 8 correspond to the drug component, **octenidine**.

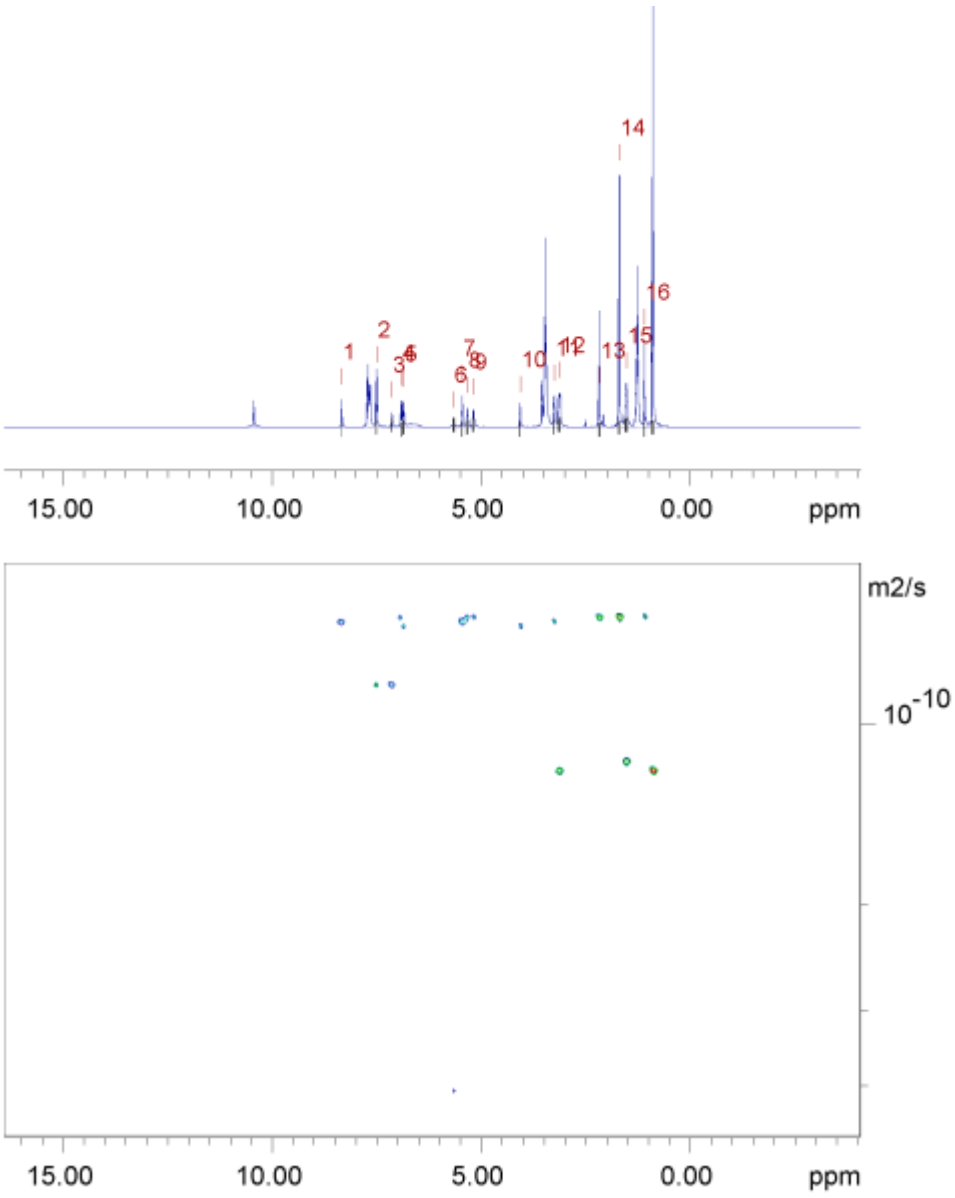
14
16
2
1
15
13
10
15.00
10.00
5.00
0.00
ppm
m2/s
10^{-10}
15.00
10.00
5.00
0.00
ppm

Peak name	F2 [ppm]	Io	error	D [m2/s]	error
1	8.337	1.22e+09	8.599e+04	6.78e-11	1.012e-14
2	7.503	3.57e+09	1.124e+05	8.53e-11	5.613e-15
3	7.138	1.19e+09	1.248e+05	8.59e-11	1.888e-14
4	6.913	1.77e+09	1.074e+05	6.60e-11	8.545e-15
5	6.860	1.97e+09	1.145e+05	6.91e-11	8.507e-15
6	5.661	7.51e+08	2.778e+05	4.11e-10	2.943e-13
7	5.458	1.68e+09	9.951e+04	6.79e-11	8.514e-15
8	5.334	2.01e+09	1.326e+05	6.60e-11	9.258e-15
9	5.188	1.67e+09	1.184e+05	6.60e-11	9.962e-15
10	4.073	1.70e+09	1.135e+05	6.81e-11	9.661e-15
11	3.259	2.70e+09	1.051e+05	6.78e-11	5.606e-15
12	3.135	5.89e+09	1.764e+05	1.18e-10	7.308e-15
13	2.176	5.47e+09	1.206e+05	6.58e-11	3.089e-15
14	1.700	1.22e+10	1.130e+05	6.60e-11	1.304e-15
15	1.532	7.05e+09	1.735e+05	1.16e-10	5.887e-15
16	1.097	2.96e+09	7.419e+04	6.63e-11	3.537e-15
17	0.899	2.45e+10	1.592e+05	1.20e-10	1.602e-15

Figure S162 - ^{1}H DOSY NMR spectrum of co-formulation **p** (112.0 mM) in DMSO-d_6 at 298 K and a table reporting the diffusion constants calculated for each peak used to determine the hydrodynamic diameter of the anionic components of **p** (d_H = 2.56 nm). Peaks 2 and 3 correspond to the anionic component of ***k*** while peaks 12, 15 and 17 correspond to the cationic component of **p.** Peaks 1, 4-5, 7-11, 13-14 and 16 correspond to the drug component, **novobiocin**.

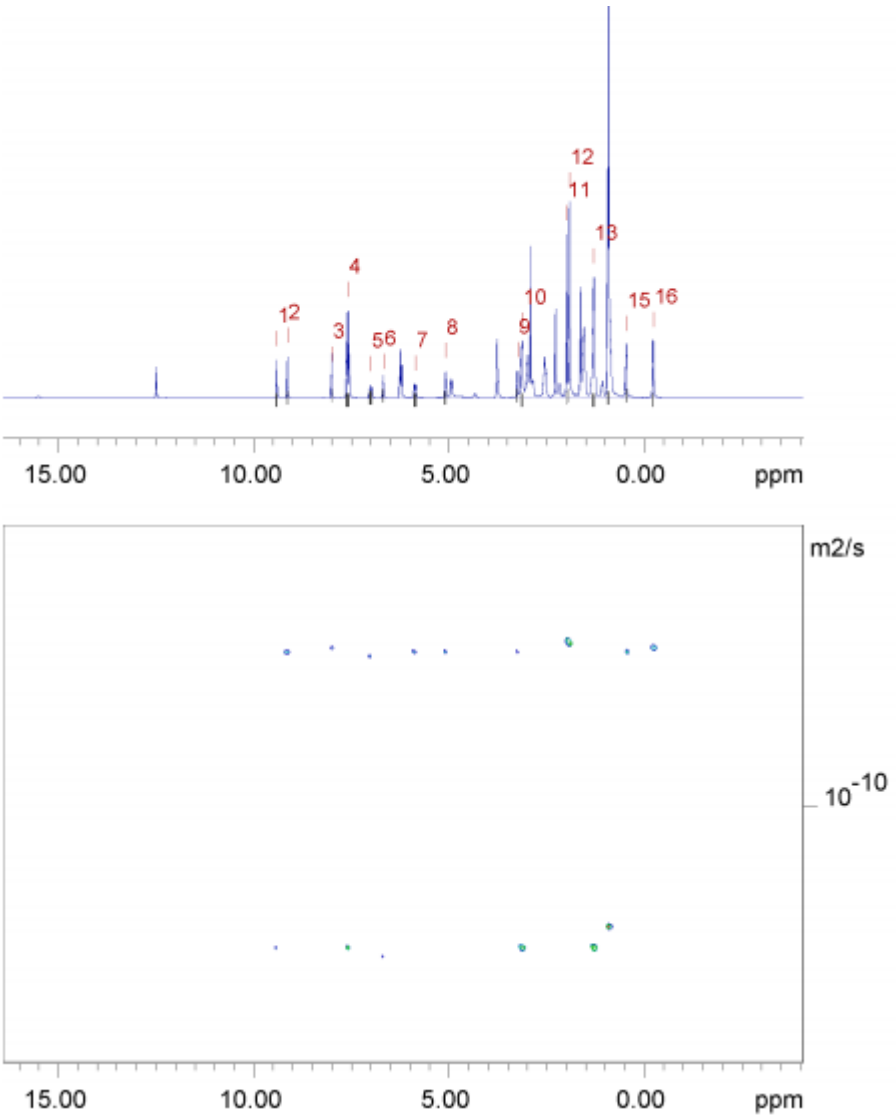

Peak name	F2 [ppm]	Io	error	D [m2/s]	error
1	9.408	1.51e+09	1.373e+05	1.27e-10	2.159e-14
2	9.132	1.76e+09	1.323e+05	7.78e-11	1.121e-14
3	8.002	1.44e+09	9.378e+04	7.73e-11	9.710e-15
4	7.590	9.75e+09	2.334e+05	1.27e-10	5.688e-15
5	7.000	1.69e+09	1.930e+05	7.83e-11	1.716e-14
6	6.681	1.25e+09	1.349e+05	1.28e-10	2.588e-14
7	5.865	1.80e+09	1.685e+05	7.77e-11	1.398e-14
8	5.088	1.81e+09	1.329e+05	7.78e-11	1.097e-14
9	3.246	1.27e+09	1.018e+05	7.78e-11	1.197e-14
10	3.127	6.50e+09	1.748e+05	1.26e-10	6.348e-15
11	1.983	4.70e+09	8.064e+04	7.62e-11	2.522e-15
12	1.916	8.68e+09	9.356e+04	7.67e-11	1.593e-15
13	1.298	1.22e+10	1.807e+05	1.26e-10	3.489e-15
14	0.916	2.57e+10	1.619e+05	1.22e-10	1.444e-15
15	0.461	3.61e+09	1.146e+05	7.74e-11	4.732e-15
16	-0.229	2.91e+09	9.806e+04	7.71e-11	4.995e-15

Figure S163 - ^{1}H DOSY NMR spectrum of co-formulation **q** (111.2 mM) in DMSO-d_6 at 298 K and a table reporting the diffusion constants calculated for each peak used to determine the hydrodynamic diameter of the anionic components of **q** (d_H = 1.72 nm). Peaks 1, 3-5, 7-9 and 13 correspond to the anionic component of **q** while peaks 15 and 20-21 correspond to the cationic component of **q**. Peaks 2, 6, 10-12, 14, 16-19 and 22-23 correspond to the drug component, **rifampicin**.

2.7 Biological experiments

2.7.1 MIC determination

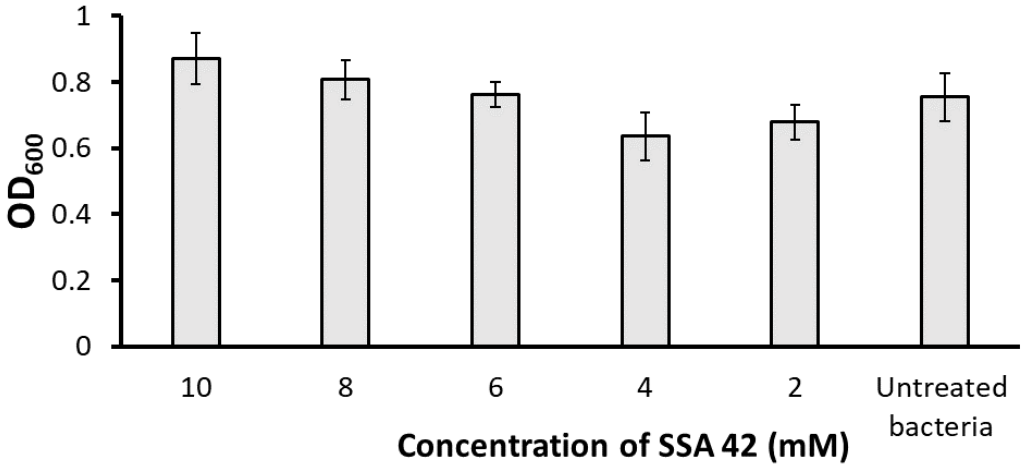

Figure S164 – Determination of minimum inhibitory concentration of SSA **42** against *P. aeruginosa* PA01.

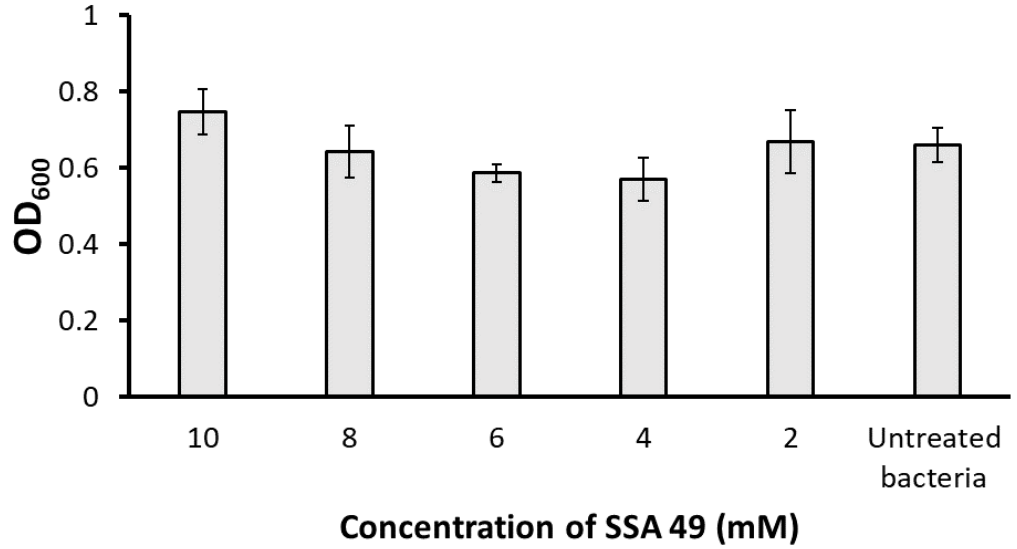

Figure S165 - Determination of inhibitory concentration of SSA **49** against *P. aeruginosa* PA01.

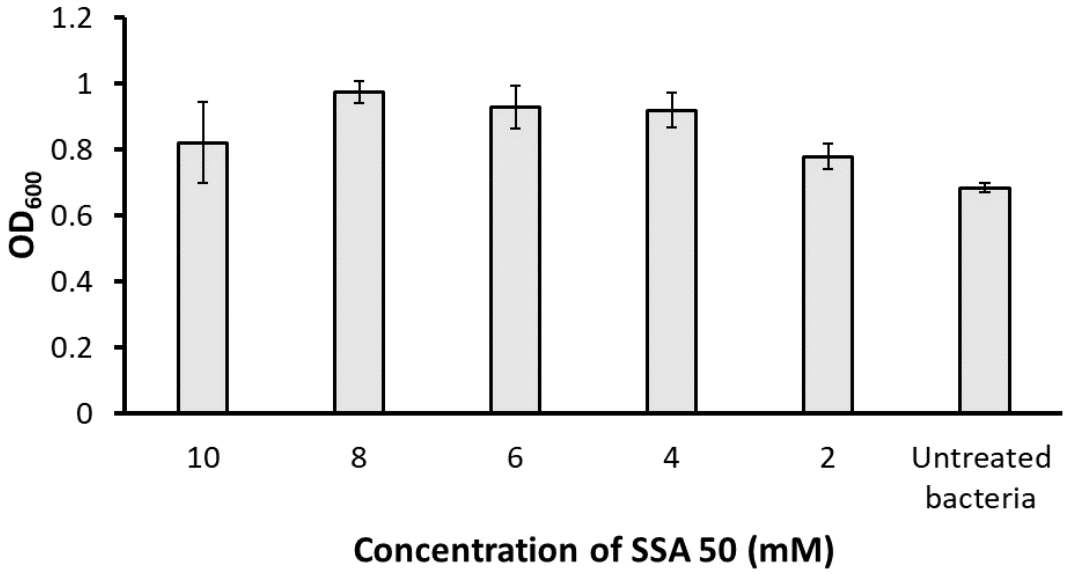

Figure S166 - Determination of inhibitory concentration of SSA **50** against *P. aeruginosa* PA01.

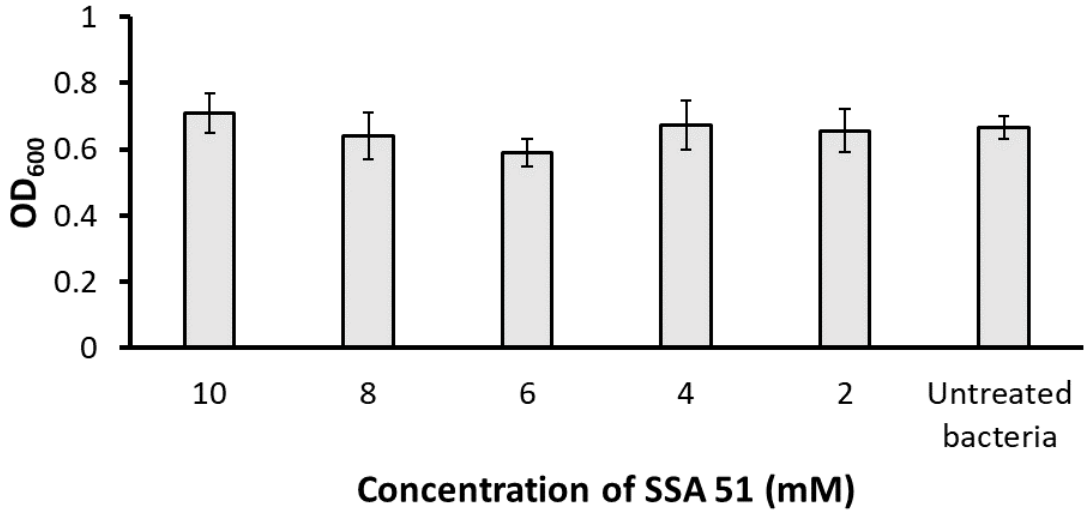

Figure S167 - Determination of inhibitory concentration of SSA **51** against *P. aeruginosa* PA01.

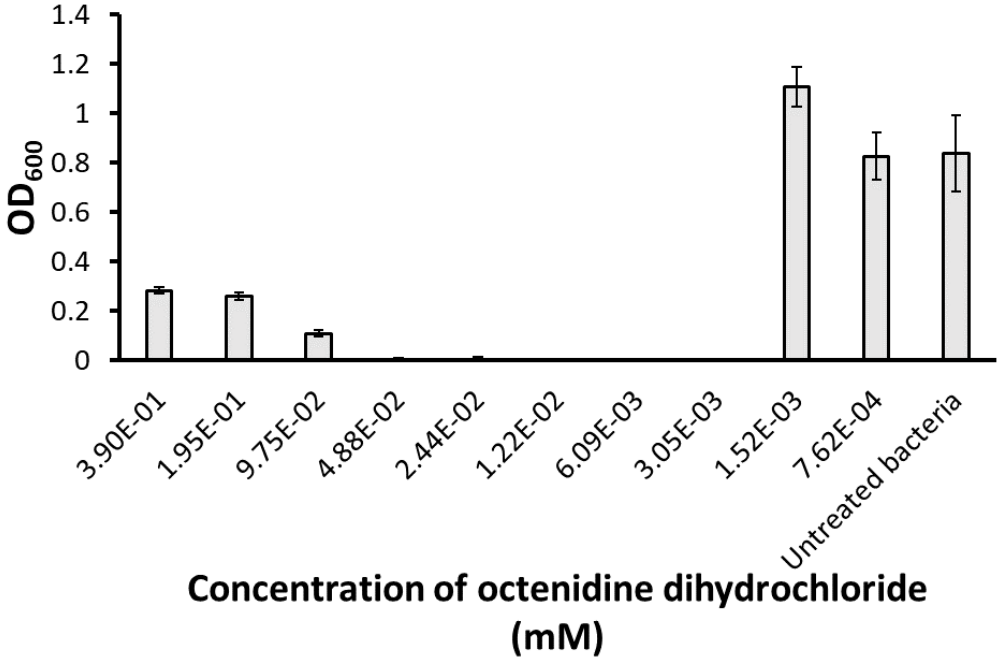

Figure S168 - Determination of the minimum inhibitory concentration (MIC) of **octenidine dihydrochloride** against *P. aeruginosa* PAO1. At higher concentrations, compound clouding caused increase in OD.

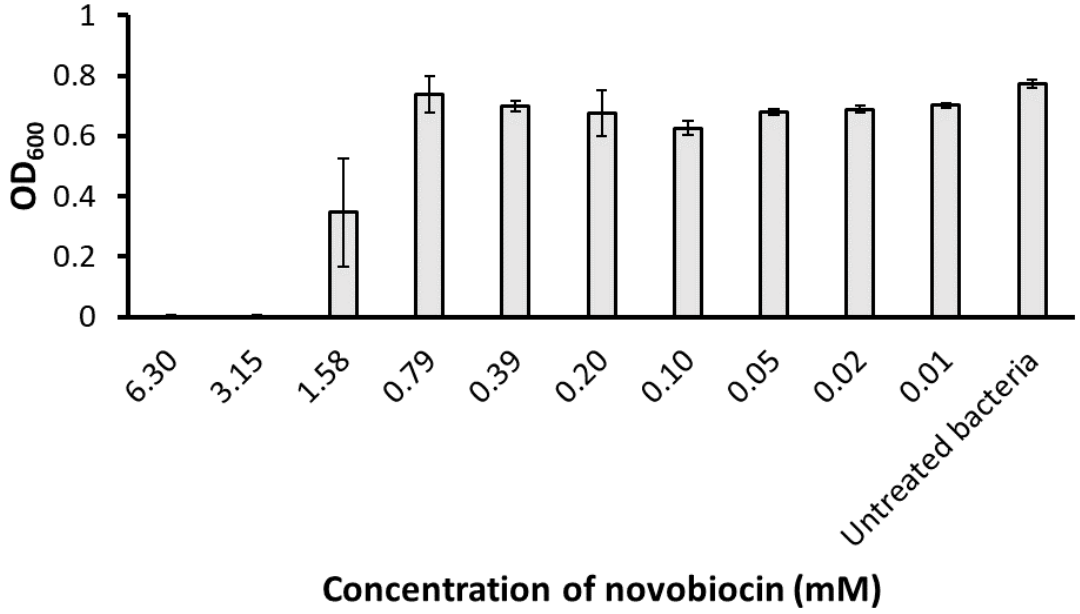

Figure S169 - Determination of the minimum inhibitory concentration (MIC) of **novobiocin** against *P. aeruginosa* PAO1.

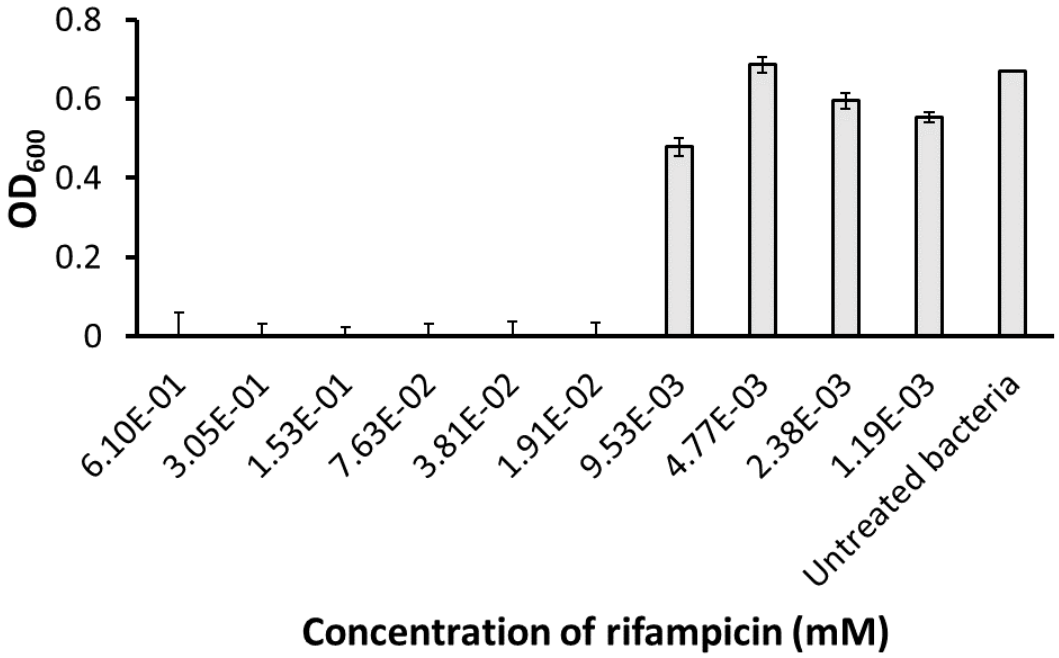

Figure S170 - Determination of the minimum inhibitory concentration (MIC) of **rifampicin** against *P. aeruginosa* PAO1.

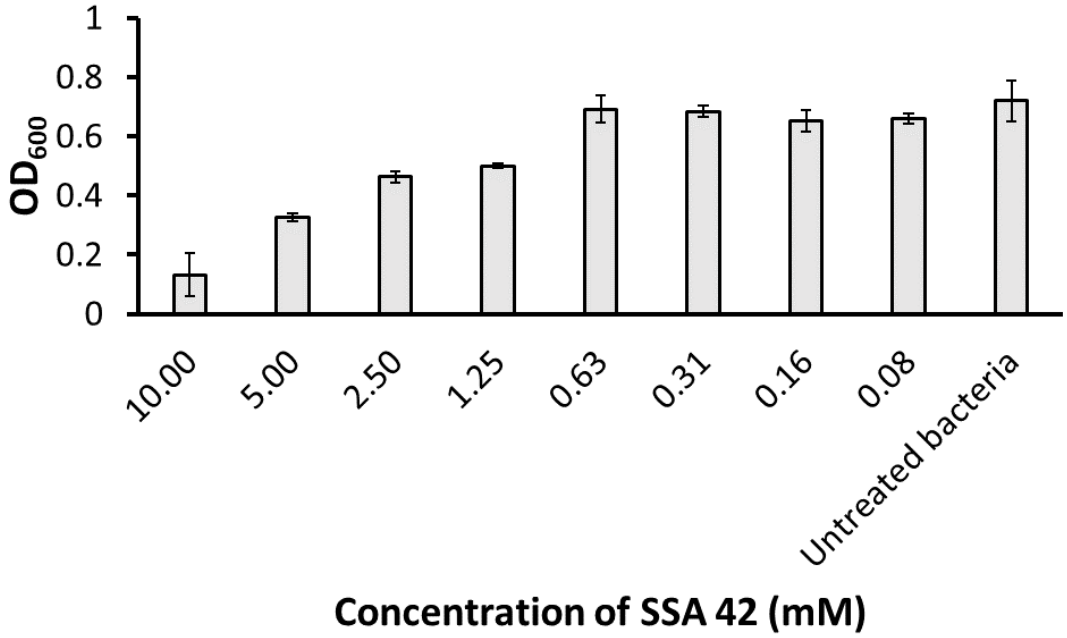

Figure S171 - Determination of minimum inhibitory concentration of SSA **42** against *E. coli* DH10B.

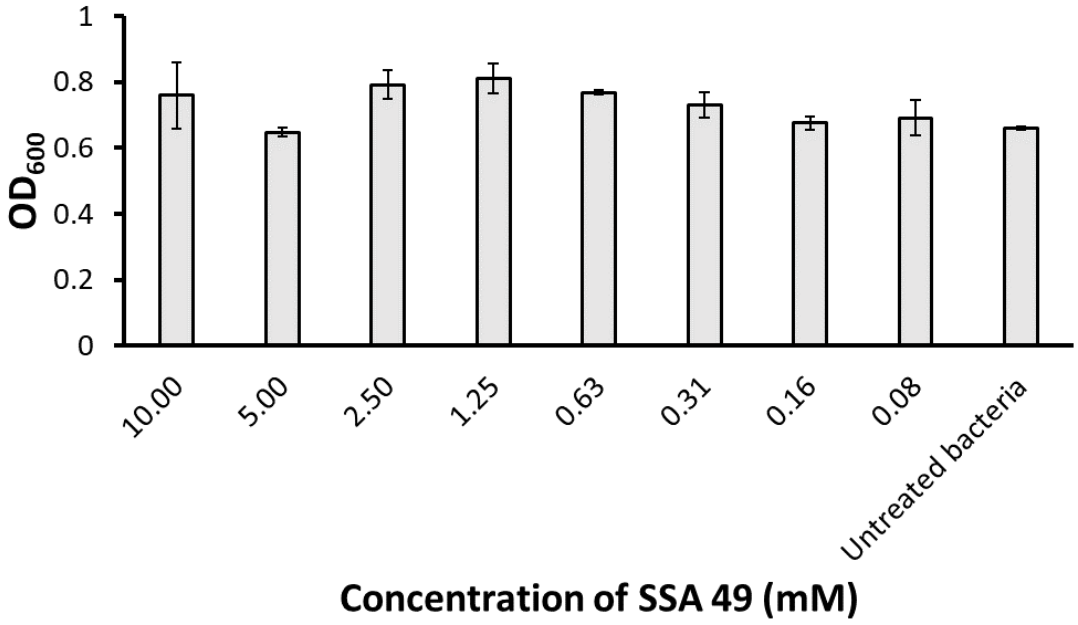

Figure S172 - Determination of minimum inhibitory concentration of SSA **49** against *E. coli* DH10B.

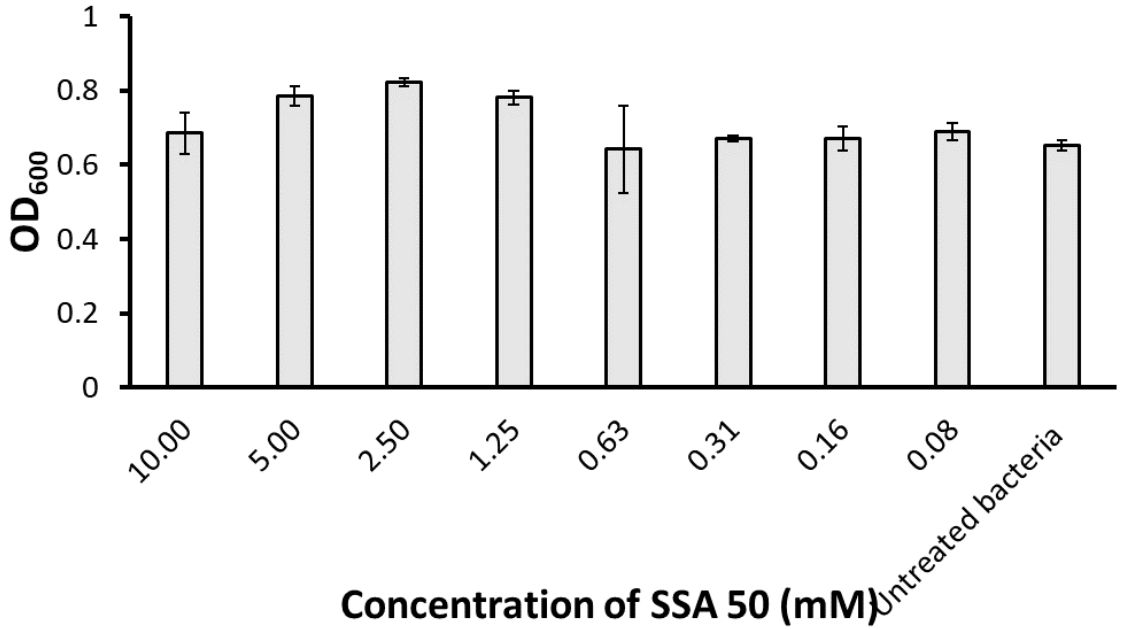

Figure S173 - Determination of minimum inhibitory concentration of SSA **50** against *E. coli* DH10B.

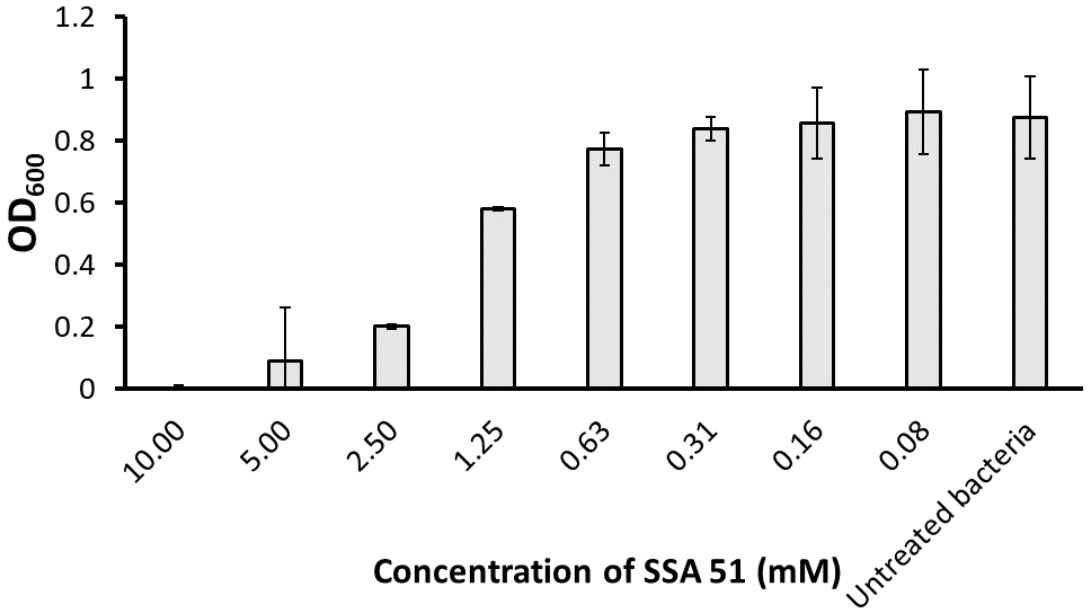

Figure S174 - Determination of minimum inhibitory concentration of SSA **51** against *E. coli* DH10B.

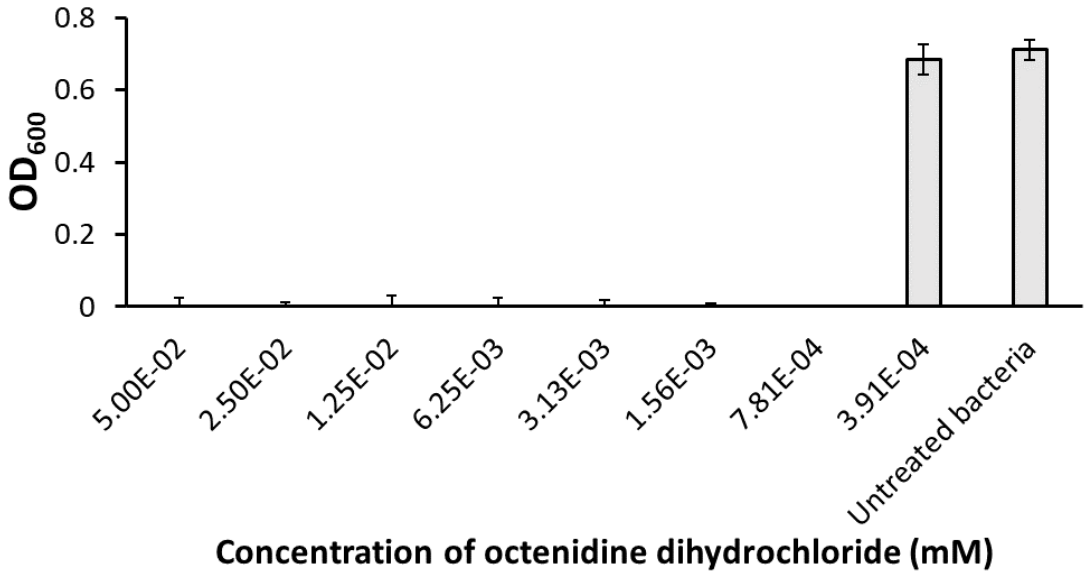

Figure S175 - Determination of the minimum inhibitory concentration (MIC) against **octenidine dihydrochloride** for *E. coli* DH10B.

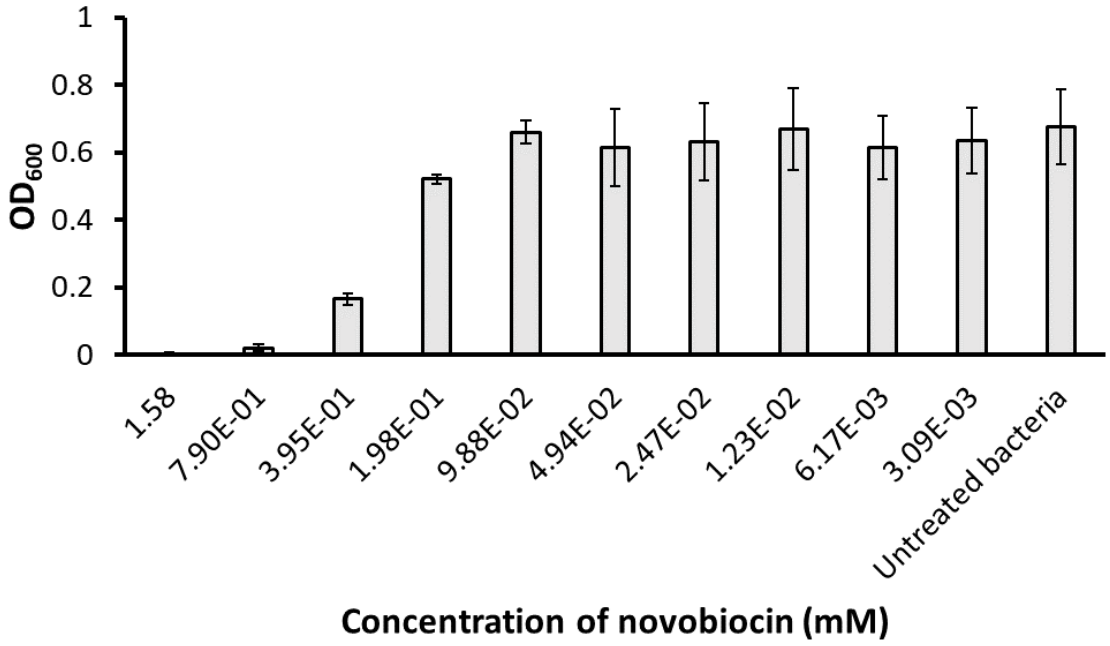

Figure S176 - Determination of the minimum inhibitory concentration (MIC) against **novobiocin** for *E. coli* DH10B.

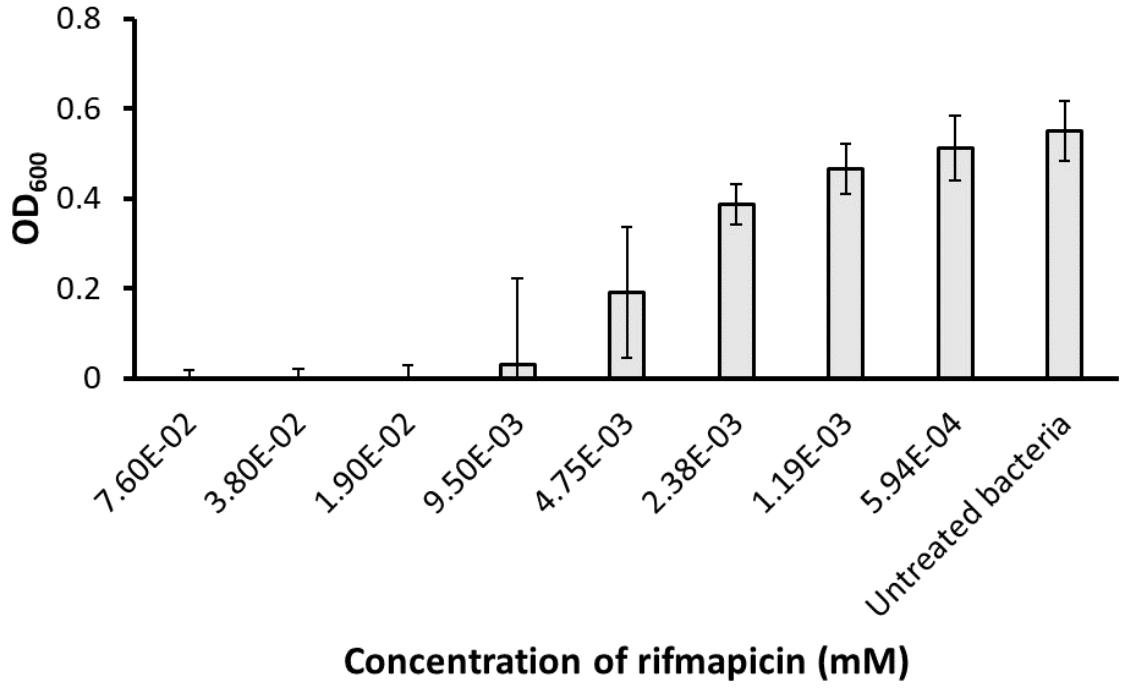

Figure S177 - Determination of the minimum inhibitory concentration (MIC) against **rifampicin** for *E. coli* DH10B.

2.7.2 Antimicrobial potentiation *P. aeruginosa*

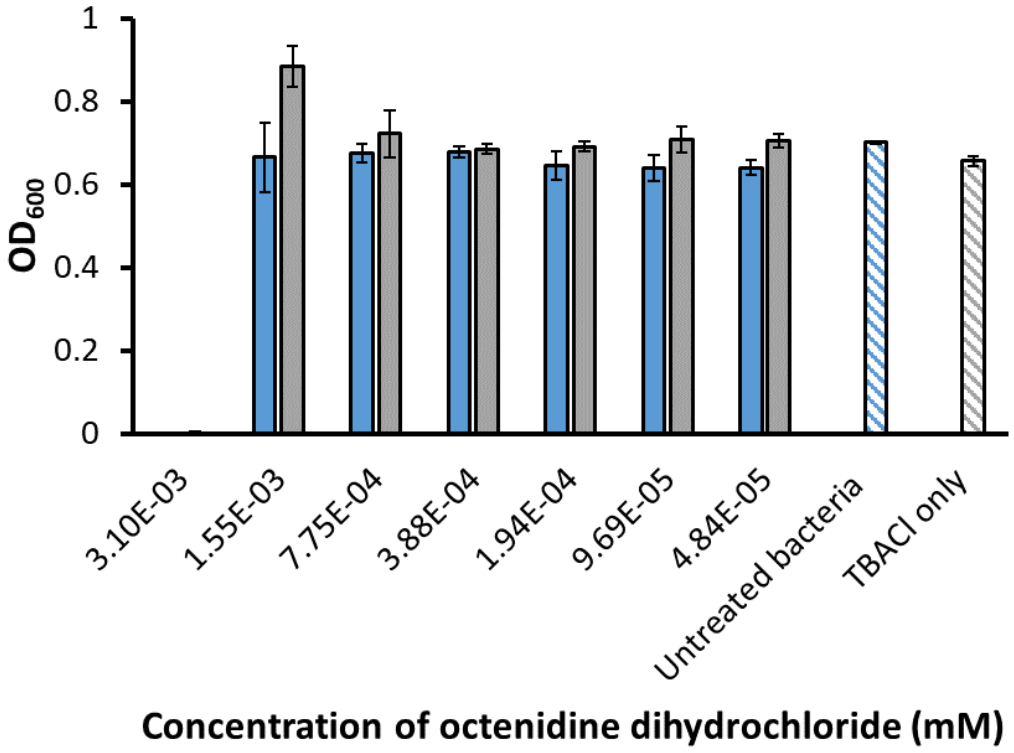

Figure S178 – A control experiment where **TBACl** at 8 mM was incubated with *P. aeruginosa* PA01 for ≈ 10 minutes before being added to a well containing **octenidine dihydrochloride** at varying concentrations. Blue = **octenidine dihydrochloride** only, Grey = **octenidine dihydrochloride** + **TBACl.**

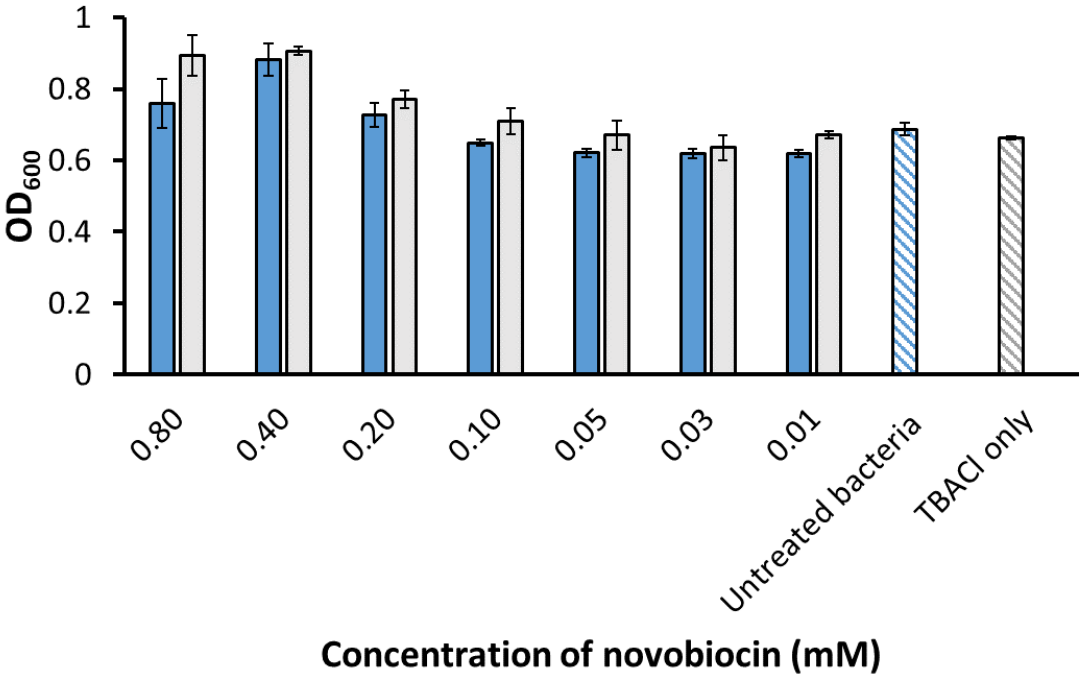

Figure S179 - A control experiment where **TBACl** at 8 mM was incubated with *P. aeruginosa* PA01 for ≈ 10 minutes before being added to a well containing **novobiocin** at varying concentrations. Blue = **novobiocin** only, Grey = **novobiocin** + **TBACl.**

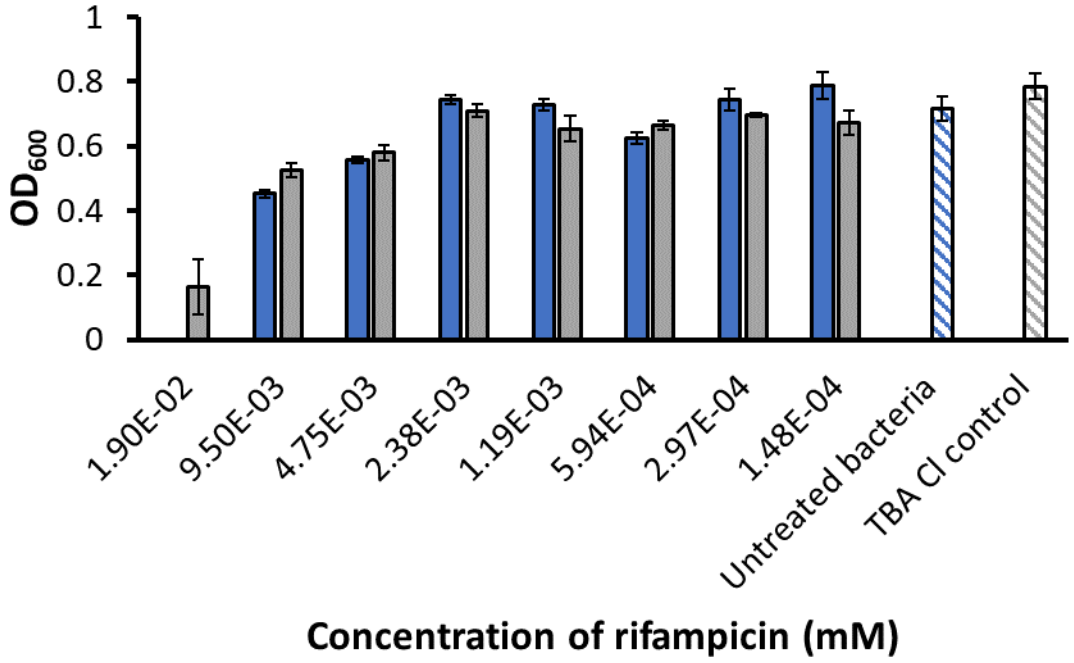

Figure S180 - A control experiment where **TBACl** at 8 mM was incubated with *P. aeruginosa* PA01 for ≈ 10 minutes before being added to a well containing **rifampicin** at varying concentrations. Blue = **rifampicin** only, Grey = **rifampicin** + **TBACl.**

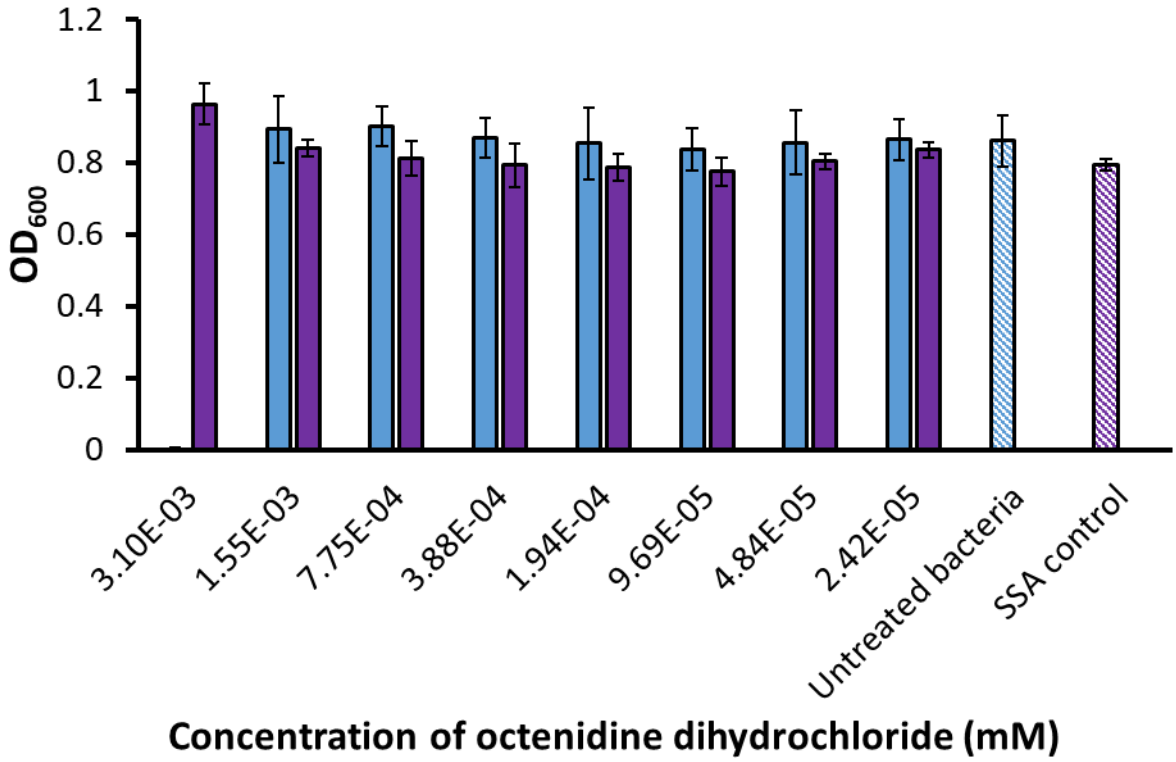

Figure S181 - SSA **42** (8 mM) was incubated with *P. aeruginosa* PA01 for ≈ 10 minutes before being added to a well containing **octenidine dihydrochloride** at varying concentrations. Purple = **octenidine dihydrochloride** + SSA **42** (co-formulation **f**), Blue = **octenidine dihydrochloride.**

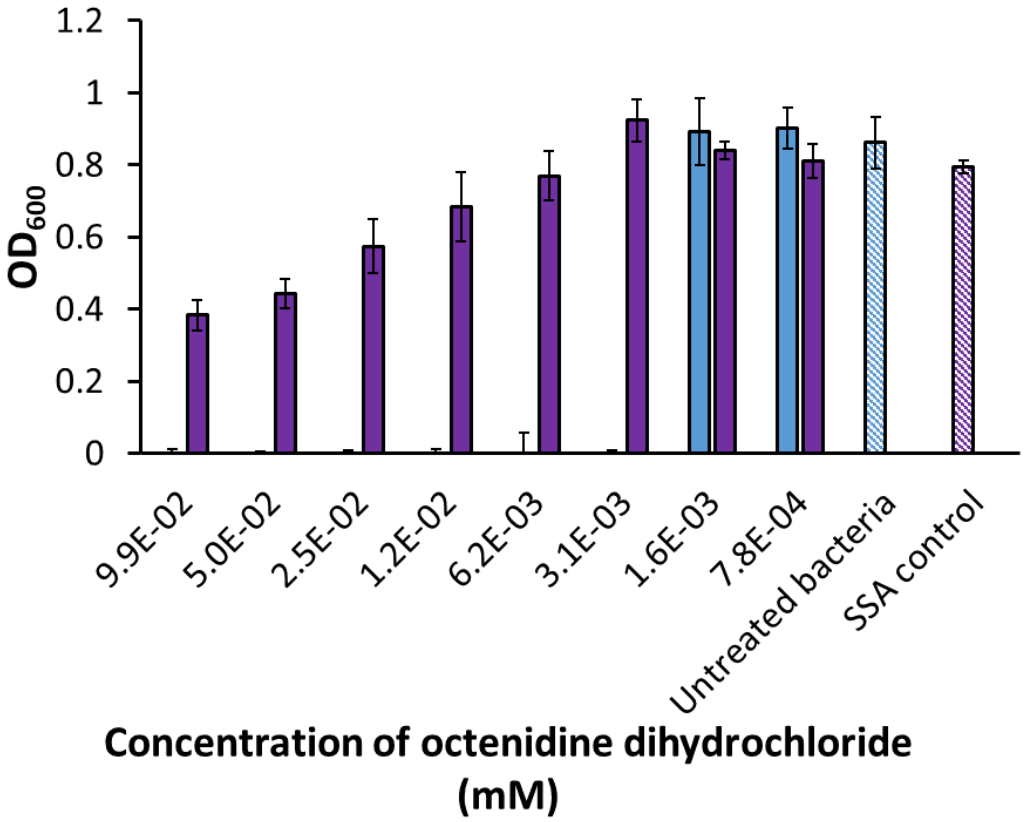

Figure S182 - SSA **42** (8 mM) was incubated with *P. aeruginosa* PA01 for ≈ 10 minutes before being added to a well containing **octenidine dihydrochloride** at varying concentrations. Concentration of **octenidine dihydrochloride** was increased until solubility limit was reached to further investigate antagonism. Purple = **octenidine dihydrochloride** + SSA **42** (co-formulation **f**), Blue = **octenidine dihydrochloride.**

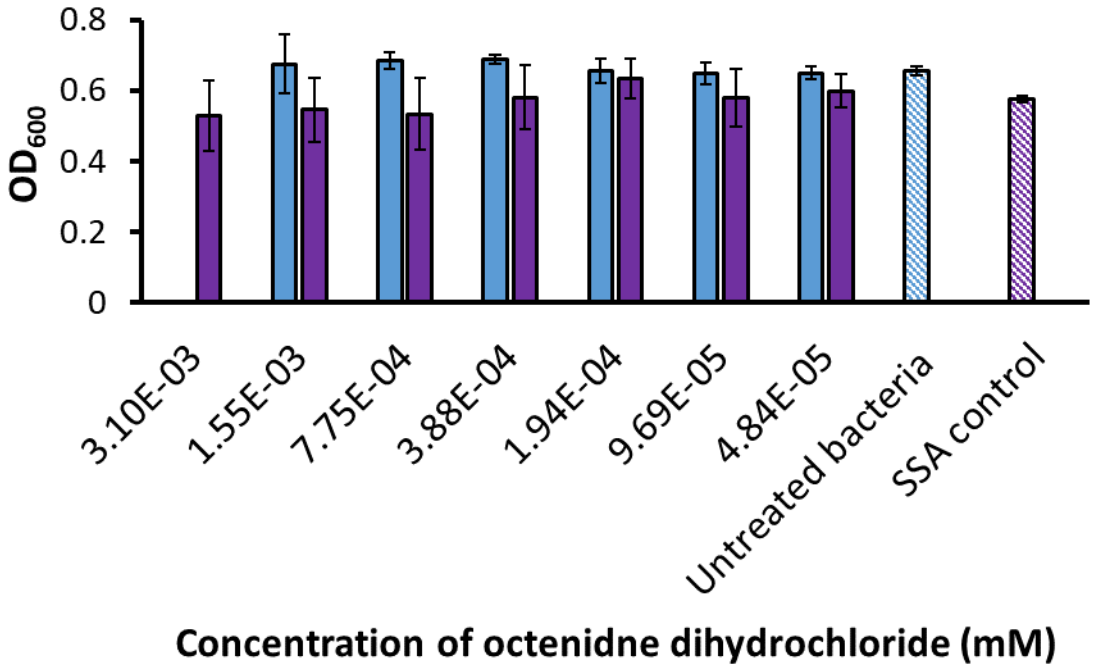

Figure S183 - SSA **49** (8 mM) was incubated with *P. aeruginosa* PA01 for ≈ 10 minutes before being added to a well containing **octenidine dihydrochloride** at varying concentrations. Purple = **octenidine dihydrochloride** + SSA **49** (co-formulation **i**), Blue = **octenidine dihydrochloride.**

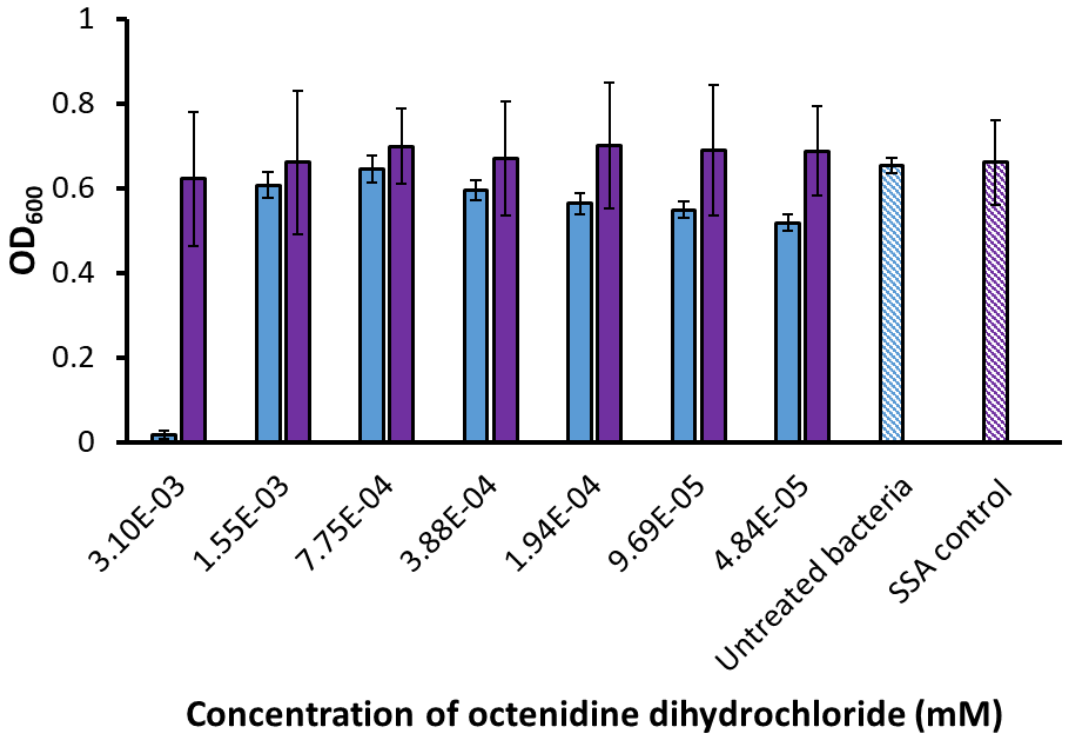

Figure S184 - SSA **50** (8 mM) was incubated with *P. aeruginosa* PA01 for ≈ 10 minutes before being added to a well containing **octenidine dihydrochloride** at varying concentrations. Purple = **octenidine dihydrochloride** + SSA **50** (co-formulation **l**), Blue = **octenidine dihydrochloride.**

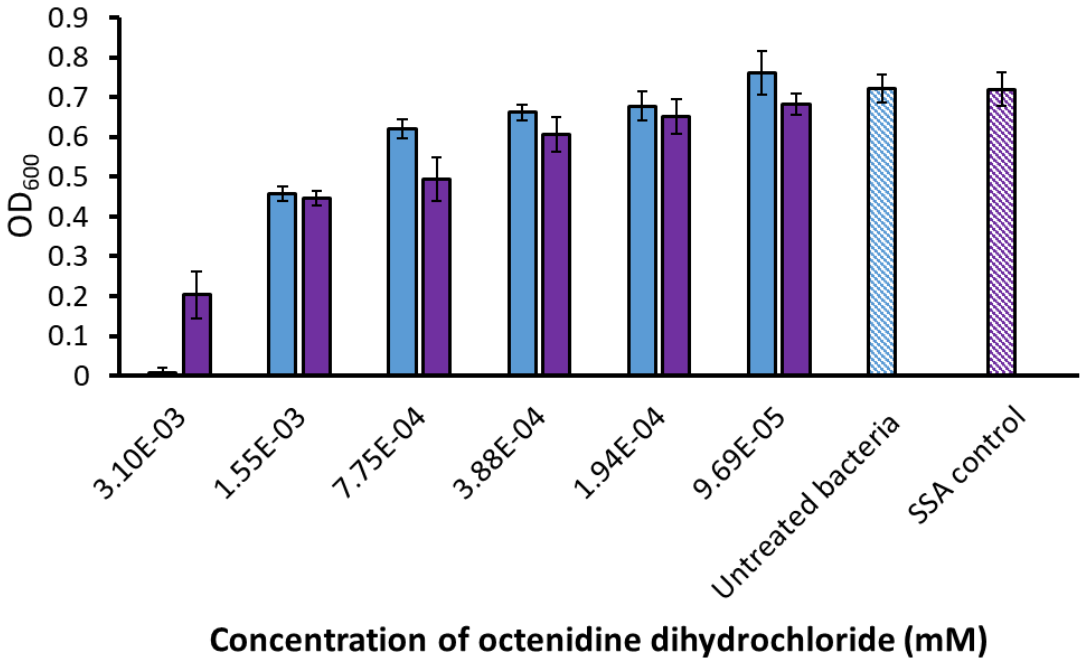

Figure S185 - SSA **51** (8 mM) was incubated with *P. aeruginosa* PA01 for ≈ 10 minutes before being added to a well containing **octenidine dihydrochloride** at varying concentrations. Purple = **octenidine dihydrochloride** + SSA **51** (co-formulation **o**), Blue = **octenidine dihydrochloride.**

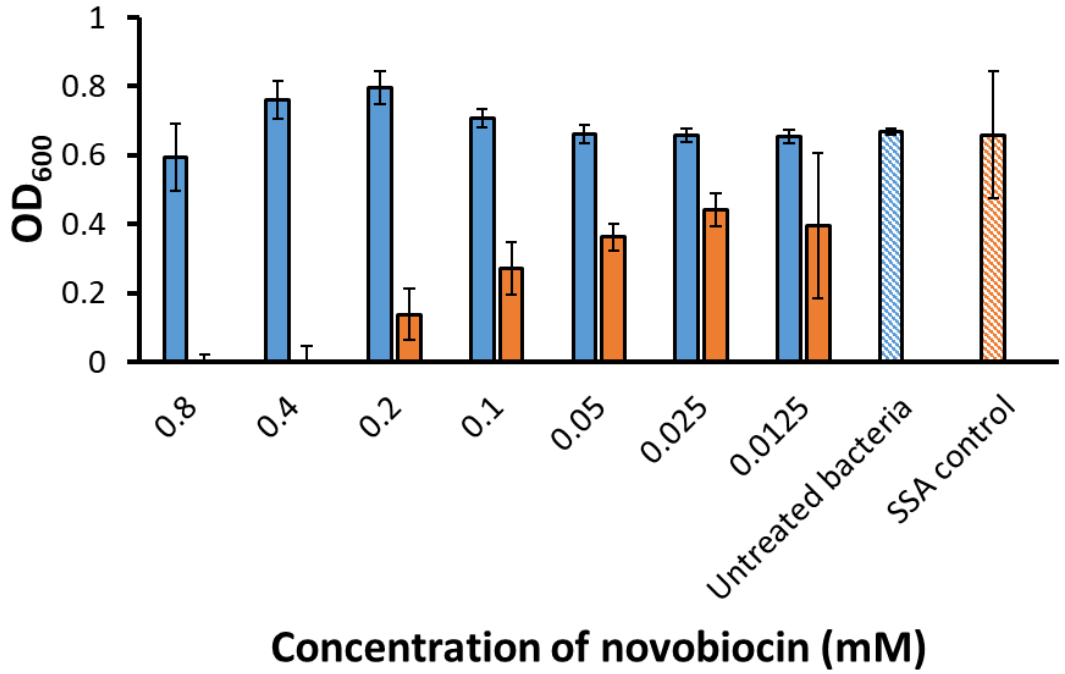

Figure S186 - SSA **42** (8 mM) was incubated with *P. aeruginosa* PA01 for ≈ 10 minutes before being added to a well containing **novobiocin** at varying concentrations. Orange = **novobiocin** + SSA **42** (co-formulation **g**), Blue = **novobiocin.**

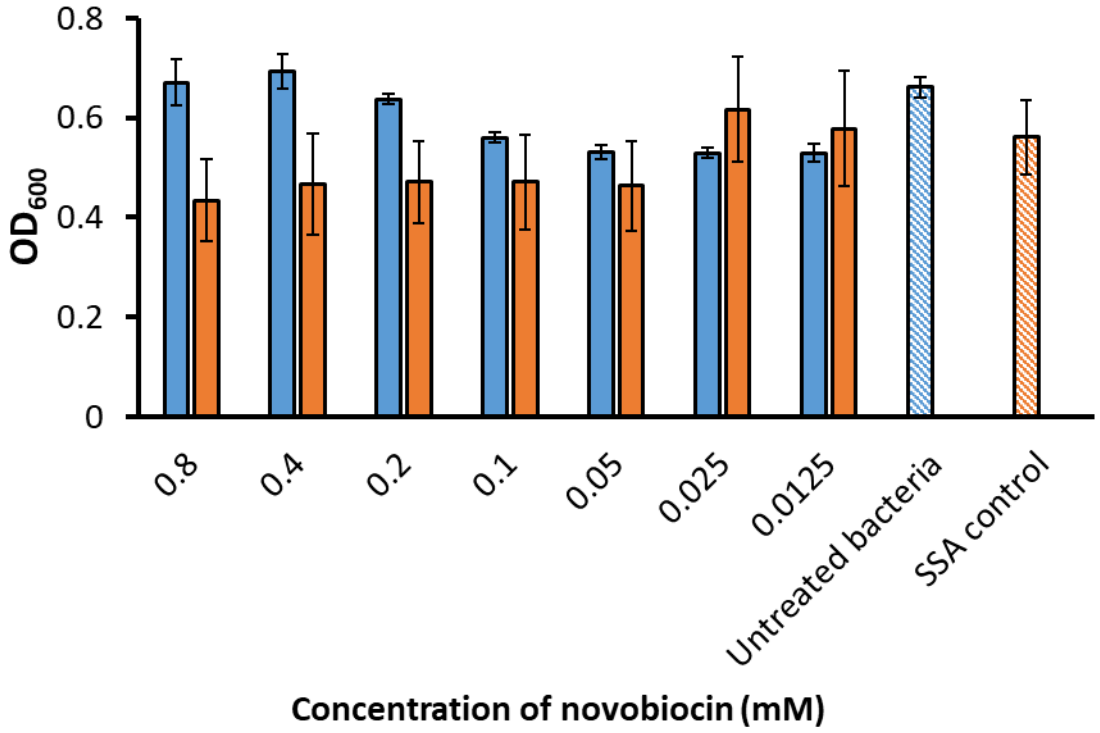

Figure S187 - SSA **49** (8 mM) was incubated with *P. aeruginosa* PA01 for ≈ 10 minutes before being added to a well containing **novobiocin** at varying concentrations. Orange = **novobiocin** + SSA **49** (co-formulation **j**), Blue = **novobiocin.**

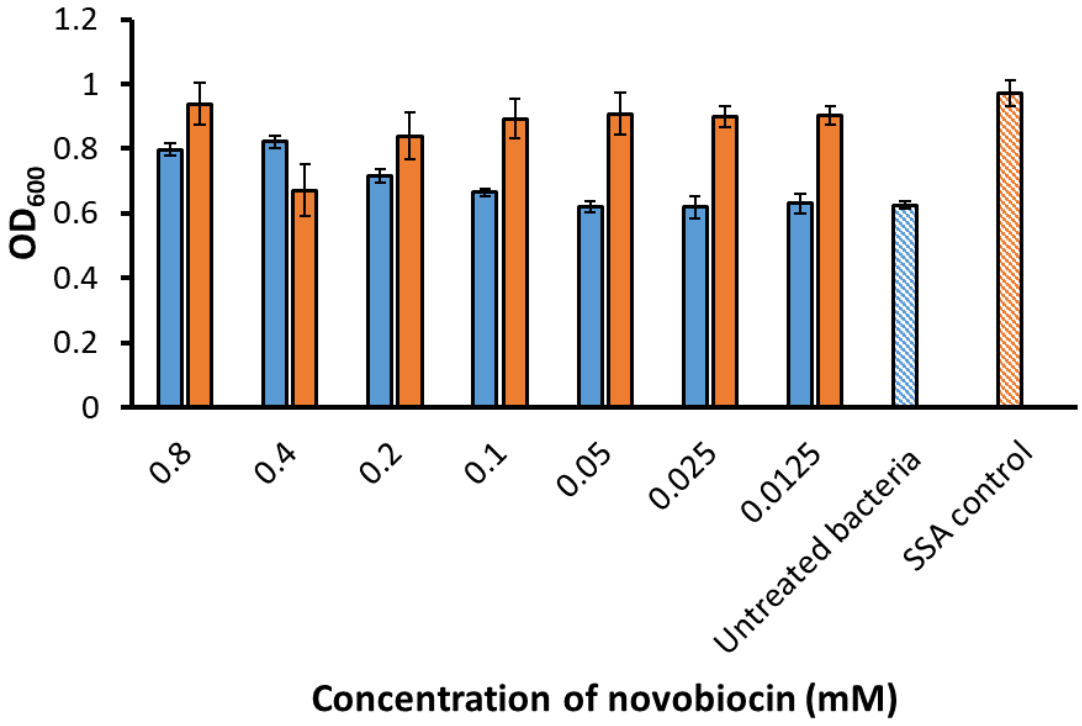

Figure S188 - SSA **50** (8 mM) was incubated with *P. aeruginosa* PA01 for ≈ 10 minutes before being added to a well containing **novobiocin** at varying concentrations. Orange = **novobiocin** + SSA **50** (co-formulation **m**), Blue = **novobiocin.**

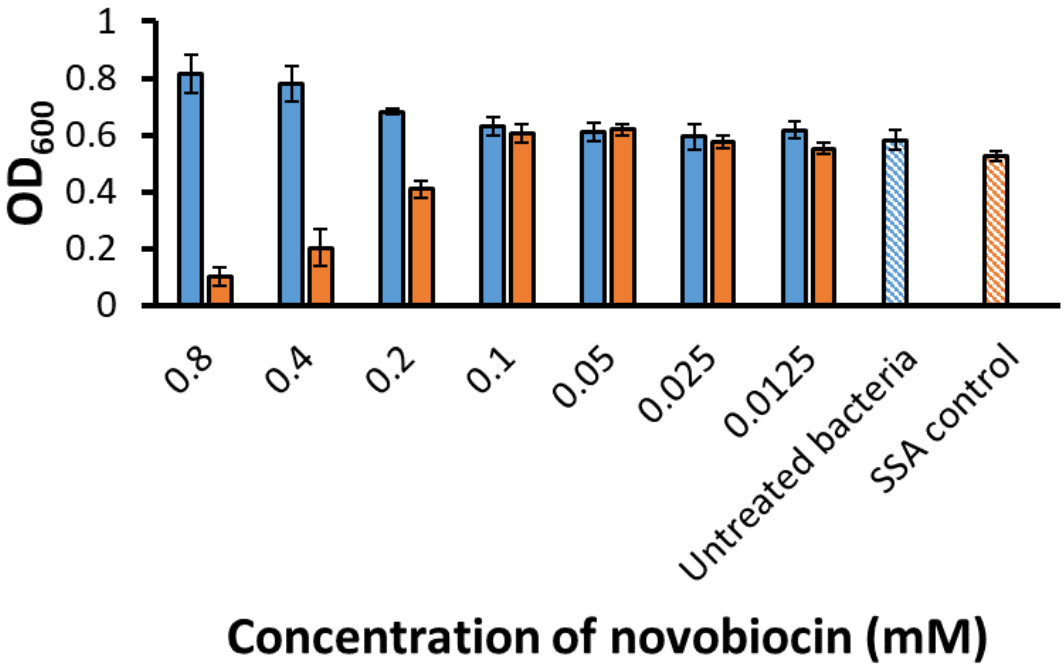

Figure S189 - SSA **51** (8 mM) was incubated with *P. aeruginosa* PA01 for ≈ 10 minutes before being added to a well containing **novobiocin** at varying concentrations. Orange = **novobiocin** + SSA **51** (co-formulation **p**), Blue = **novobiocin.**

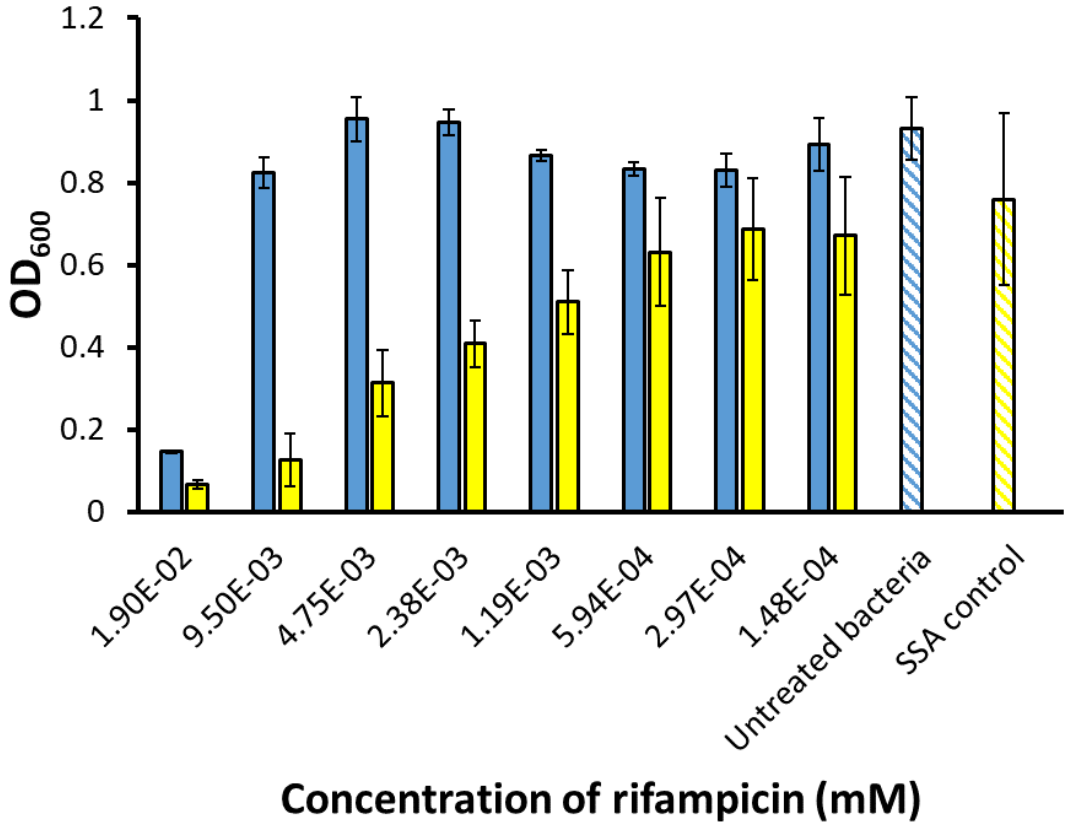

Figure S190 – SSA **42** (8 mM) was incubated with *P. aeruginosa* PA01 for ≈ 10 minutes before being added to a well containing **rifampicin** at varying concentrations. Yellow = **rifampicin** + SSA **42** (co-formulation **h**), Blue = **rifampicin.**

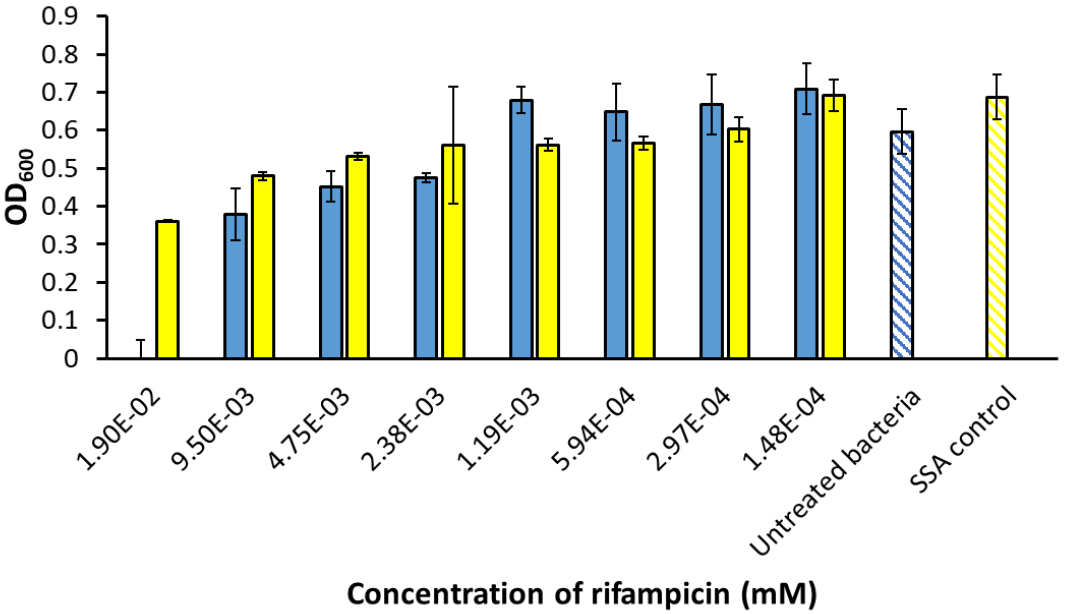

Figure S191 - SSA **49** (8 mM) was incubated with *P. aeruginosa* PA01 for ≈ 10 minutes before being added to a well containing **rifampicin** at varying concentrations. Yellow = **rifampicin** + SSA **49** (co-formulation **k**), Blue = **rifampicin.**

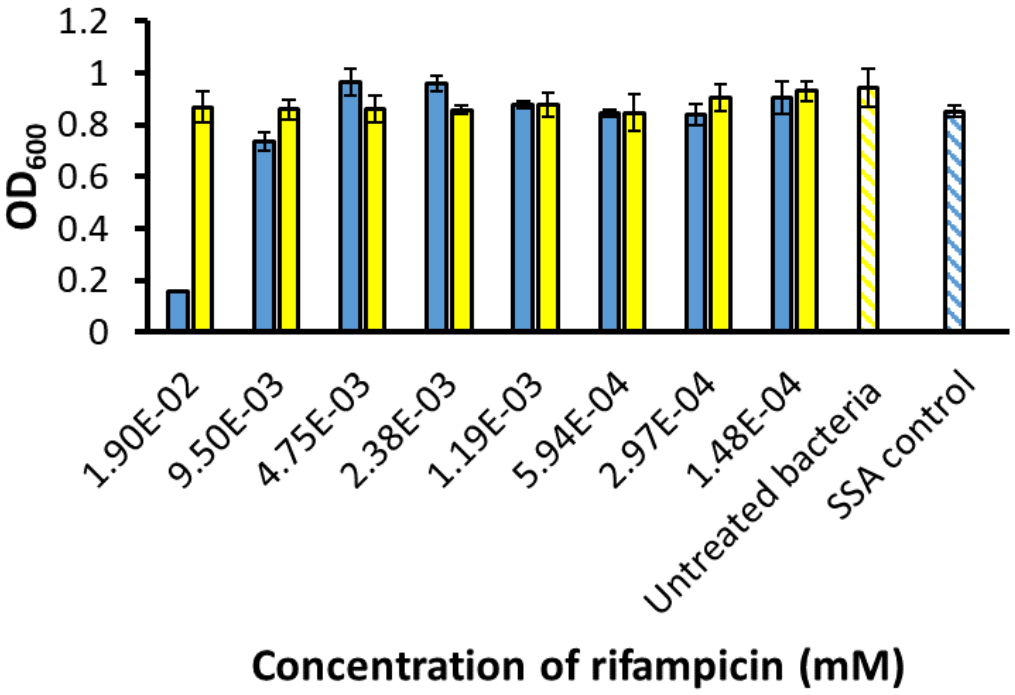

Figure 192 - SSA **50** (8 mM) was incubated with *P. aeruginosa* PA01 for ≈ 10 minutes before being added to a well containing **rifampicin** at varying concentrations. Yellow = **rifampicin** + SSA **50** (co-formulation **n**), Blue = **rifampicin.**

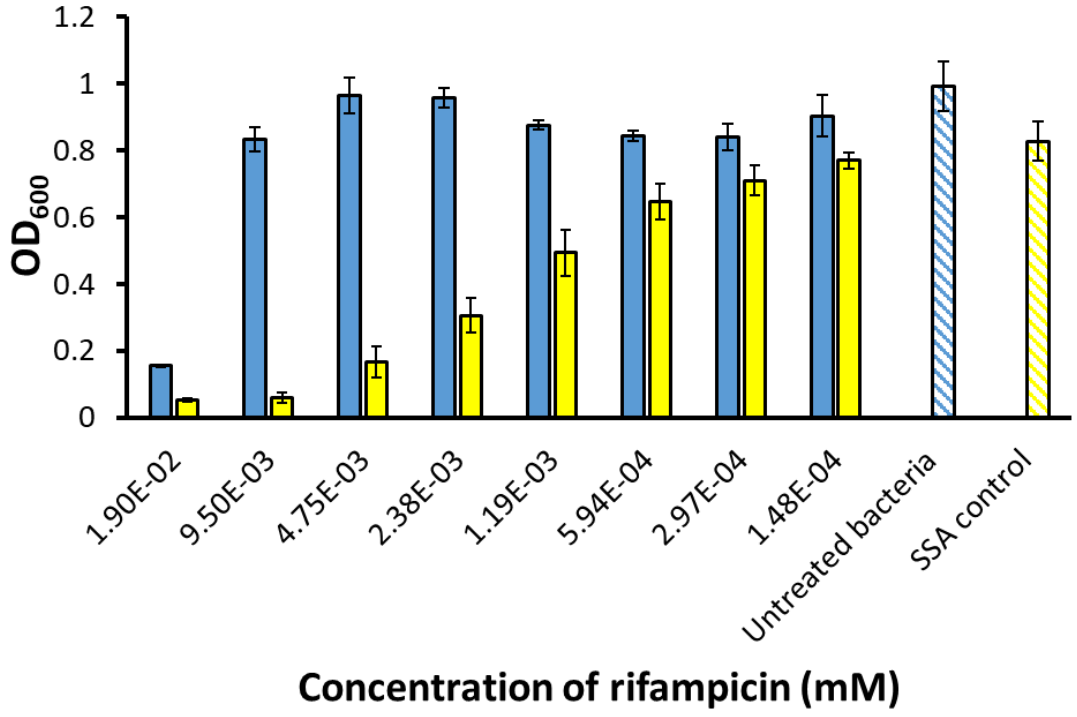

Figure S193 - SSA **51** (8 mM) was incubated with *P. aeruginosa* PA01 for ≈ 10 minutes before being added to a well containing **rifampicin** at varying concentrations. Yellow = **rifampicin** + SSA **51** (co-formulation **q**), Blue = **rifampicin.**

2.7.3 Antimicrobial potentiation *E. coli*

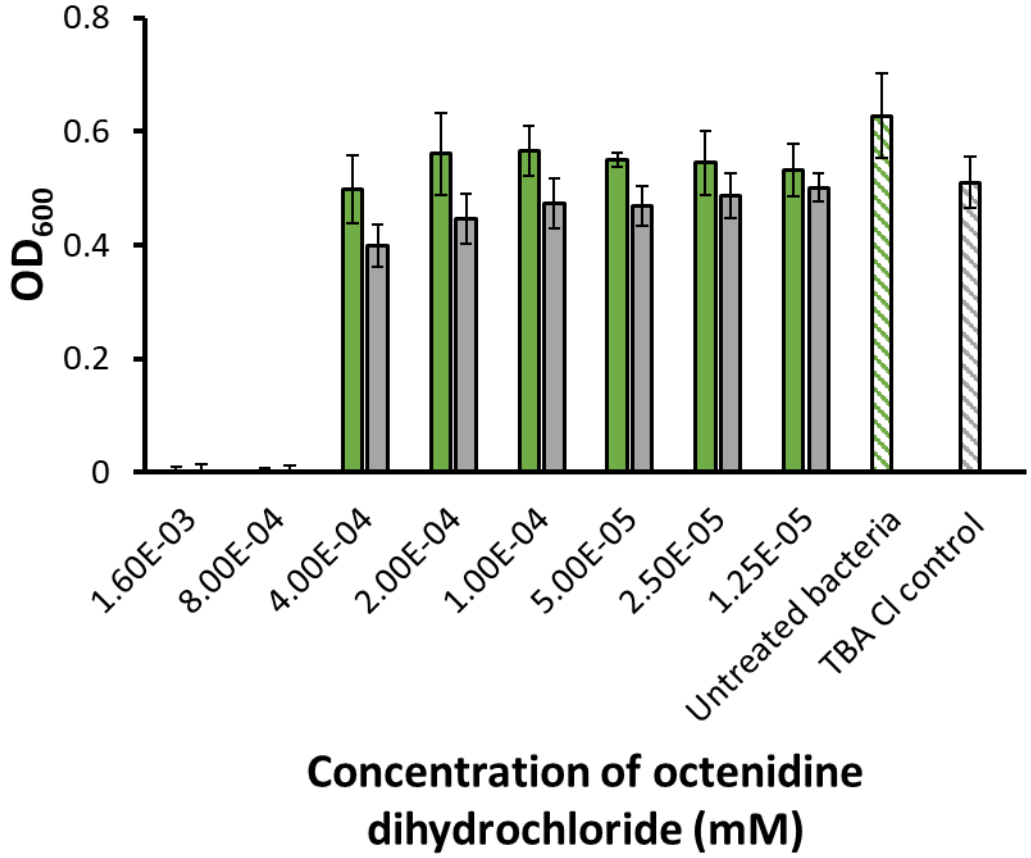

Figure S194 - A control experiment where **TBACl** at 8 mM was incubated with *E. coli* DH10B for ≈ 10 minutes before being added to a well containing **octenidine dihydrochloride** at varying concentrations. Green = **octenidine dihydrochloride** only, Grey = **octenidine dihydrochloride** + **TBACl.**

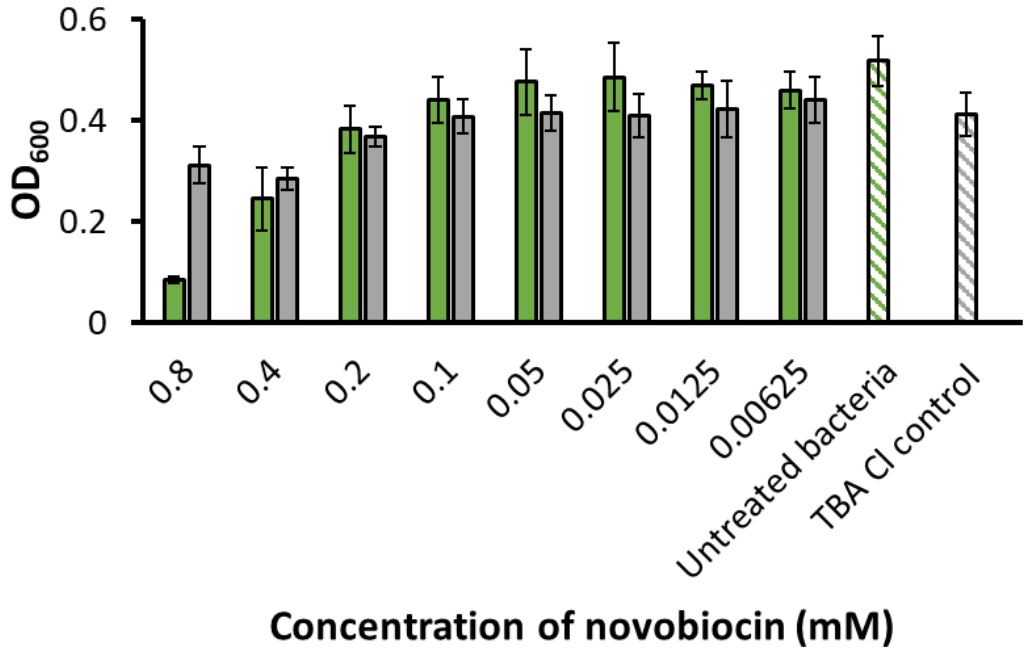

Figure S195 - A control experiment where **TBACl** at 8 mM was incubated with *E. coli* DH10B for ≈ 10 minutes before being added to a well containing **novobiocin** at varying concentrations. Green = **novobiocin** only, Grey = **novobiocin** + **TBACl.**

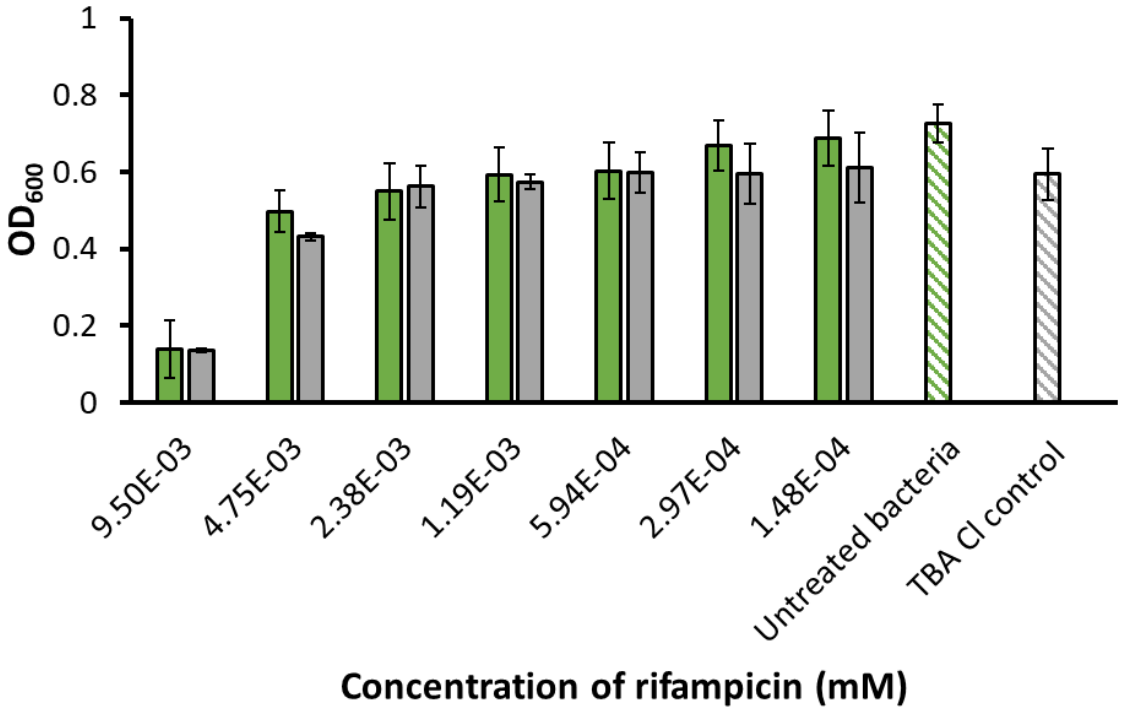

Figure S196 - A control experiment where **TBACl** at 8 mM was incubated with *E. coli* DH10B for ≈ 10 minutes before being added to a well containing **rifampicin** at varying concentrations. Green = **rifampicin** only, Grey = **rifampicin** + **TBACl.**

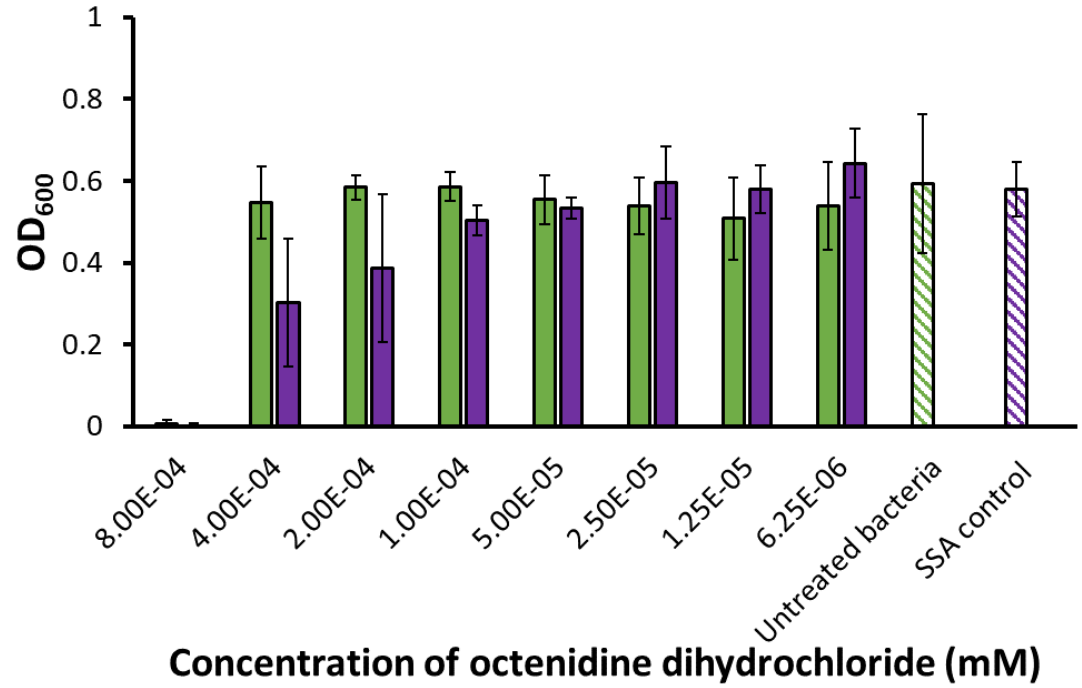

Figure S197 - SSA **42** (8 mM) was incubated with *E. coli* DH10B for ≈ 10 minutes before being added to a well containing **octenidine dihydrochloride** at varying concentrations. Purple = **octenidine dihydrochloride** + SSA **42** (co-formulation **f**), Green = **octenidine dihydrochloride.**

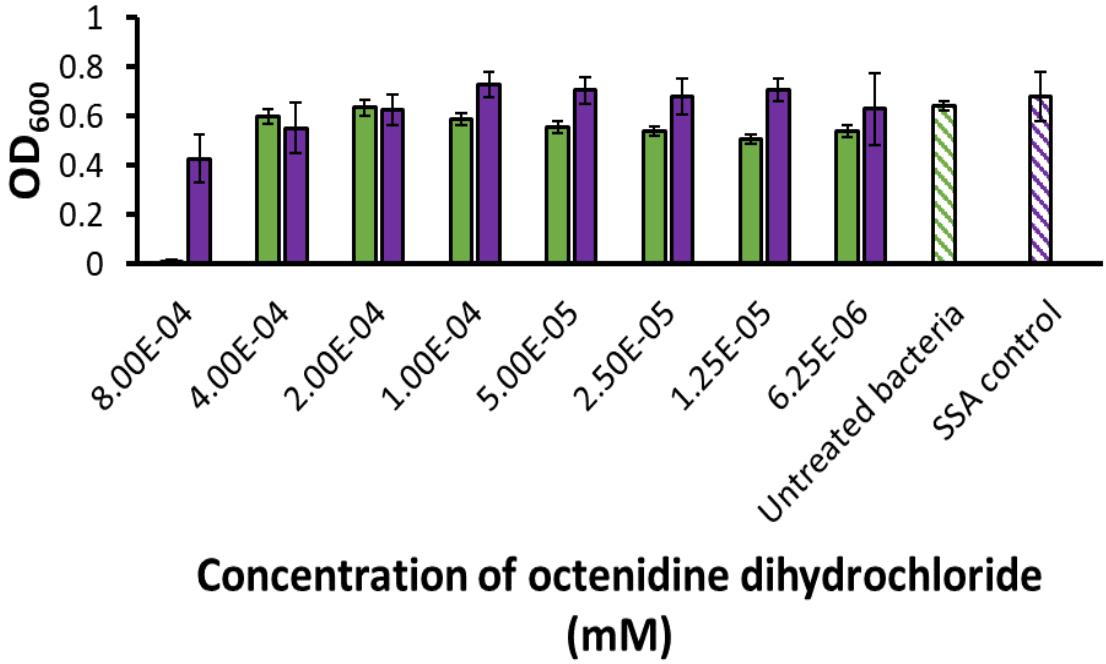

Figure S198 - SSA **49** (8 mM) was incubated with *E. coli* DH10B for ≈ 10 minutes before being added to a well containing **octenidine dihydrochloride** at varying concentrations. Purple = **octenidine dihydrochloride** + SSA **49** (co-formulation **i**), Green = **octenidine dihydrochloride.**

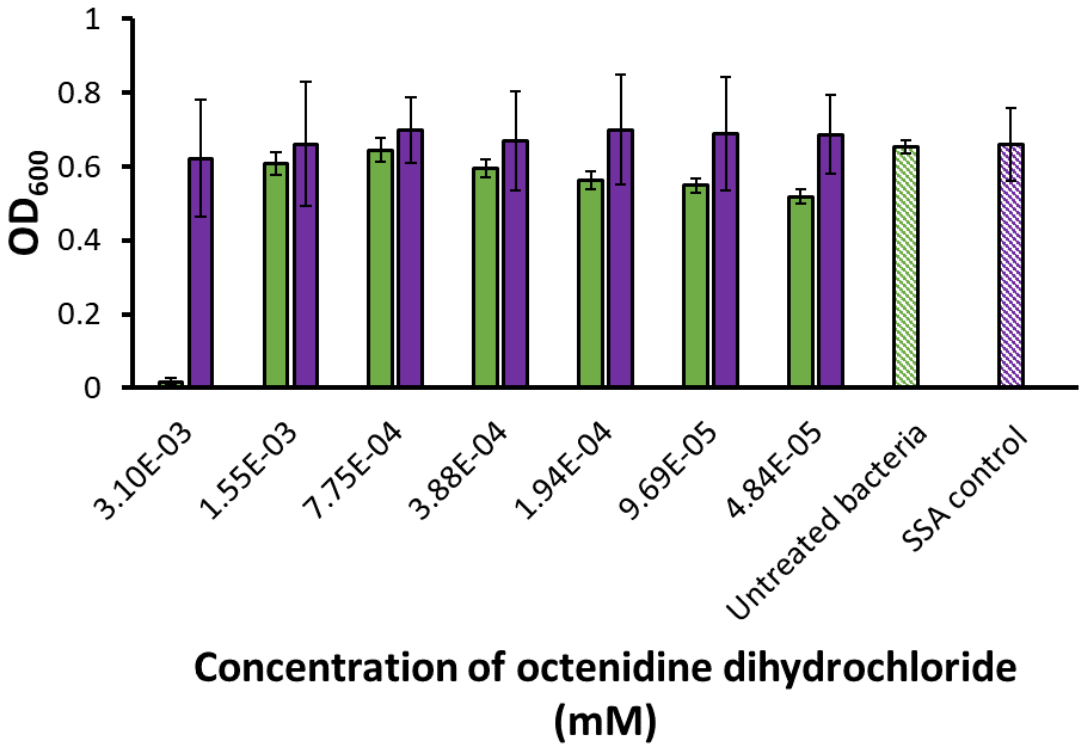

Figure S199 - SSA **50** (8 mM) was incubated with *E. coli* DH10B for ≈ 10 minutes before being added to a well containing **octenidine dihydrochloride** at varying concentrations. Purple = **octenidine dihydrochloride** + SSA **50** (co-formulation **I**), Green = **octenidine dihydrochloride.**

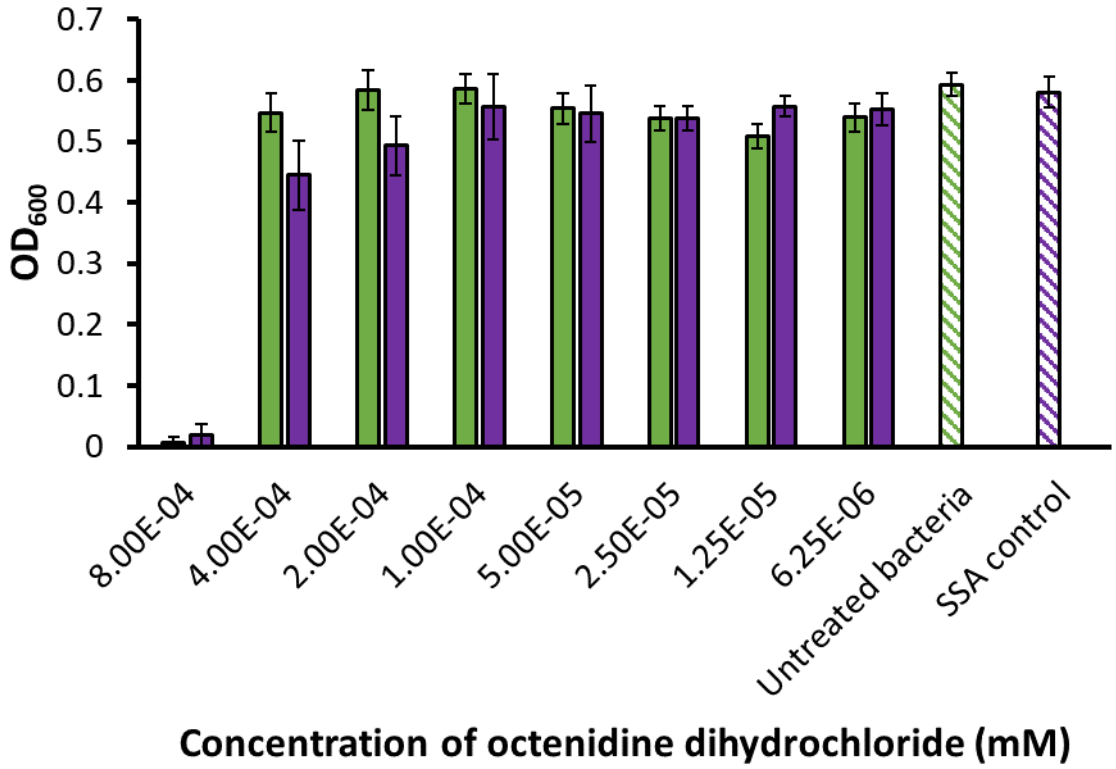

Figure S200 - SSA **51** (8 mM) was incubated with *E. coli* DH10B for ≈ 10 minutes before being added to a well containing **octenidine dihydrochloride** at varying concentrations. Purple = **octenidine dihydrochloride** + SSA **51** (co-formulation **o**), Green = **octenidine dihydrochloride.**

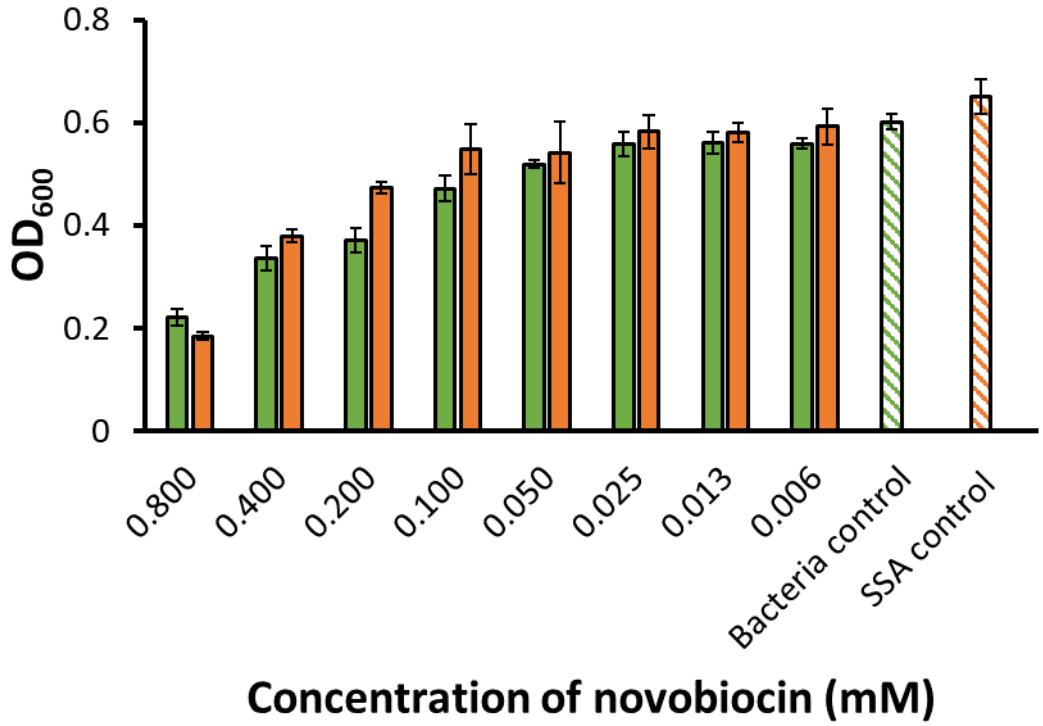

Figure S201 - SSA **42** (8 mM) was incubated with *E. coli* DH10B for ≈ 10 minutes before being added to a well containing **novobiocin** at varying concentrations. Orange = **novobiocin** + SSA **42** (co-formulation **g**), Green = **novobiocin.**

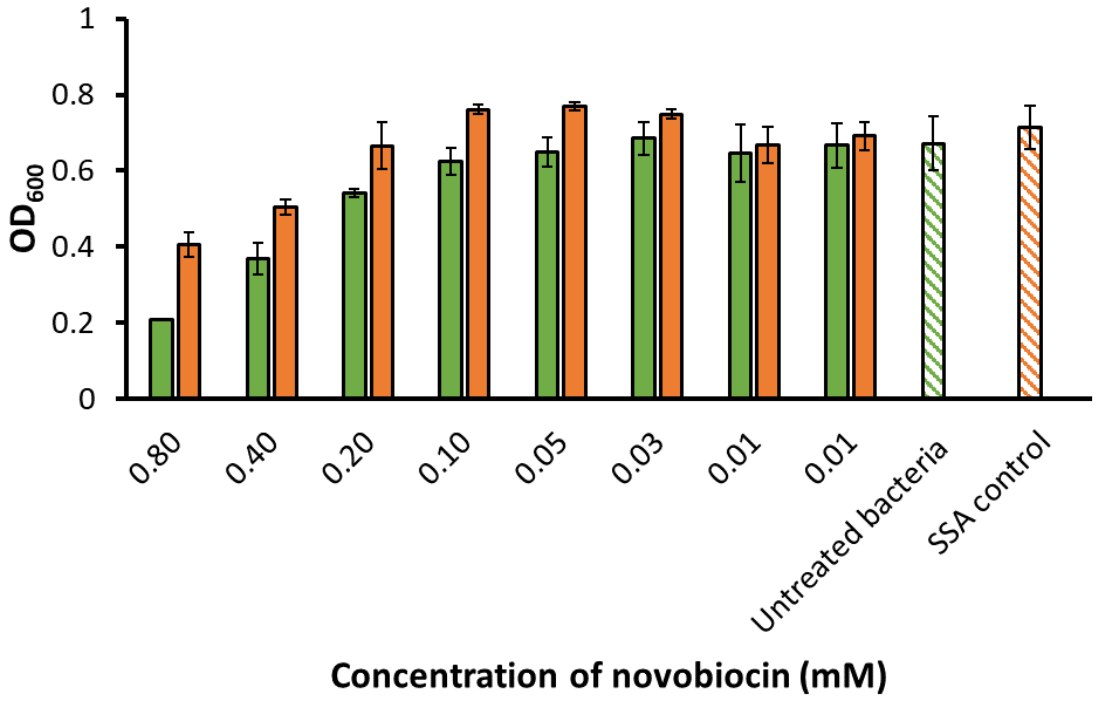

Figure S202 - SSA **49** (8 mM) was incubated with *E. coli* DH10B for ≈ 10 minutes before being added to a well containing **novobiocin** at varying concentrations. Orange = **novobiocin** + SSA **49** (co-formulation **j**), Green = **novobiocin.**

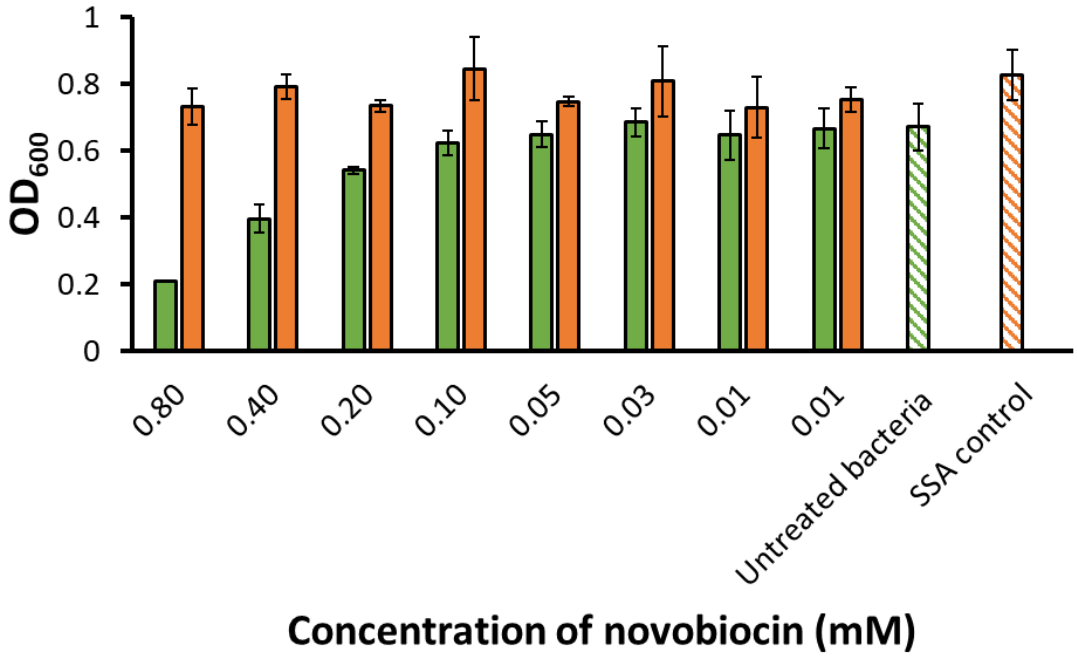

Figure S203 - SSA **50** (8 mM) was incubated with *E. coli* DH10B for ≈ 10 minutes before being added to a well containing **novobiocin** at varying concentrations. Orange = **novobiocin** + SSA **50** (co-formulation **m**), Green = **novobiocin.**

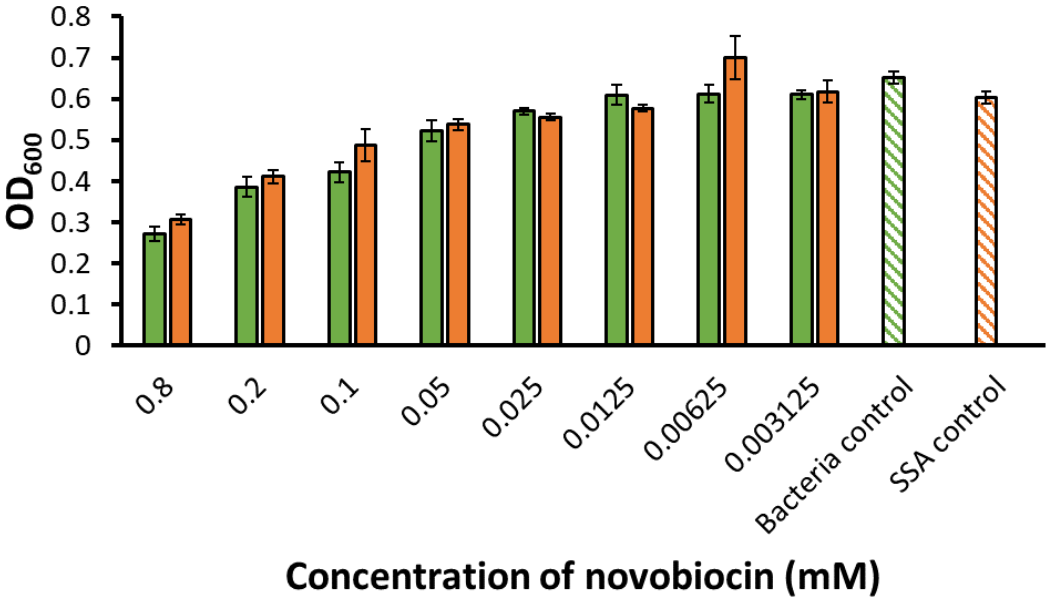

Figure S204 - SSA **51** (8 mM) was incubated with *E. coli* DH10B for ≈ 10 minutes before being added to a well containing **novobiocin** at varying concentrations. Orange = **novobiocin** + SSA **51** (co-formulation **p**), Green = **novobiocin.**

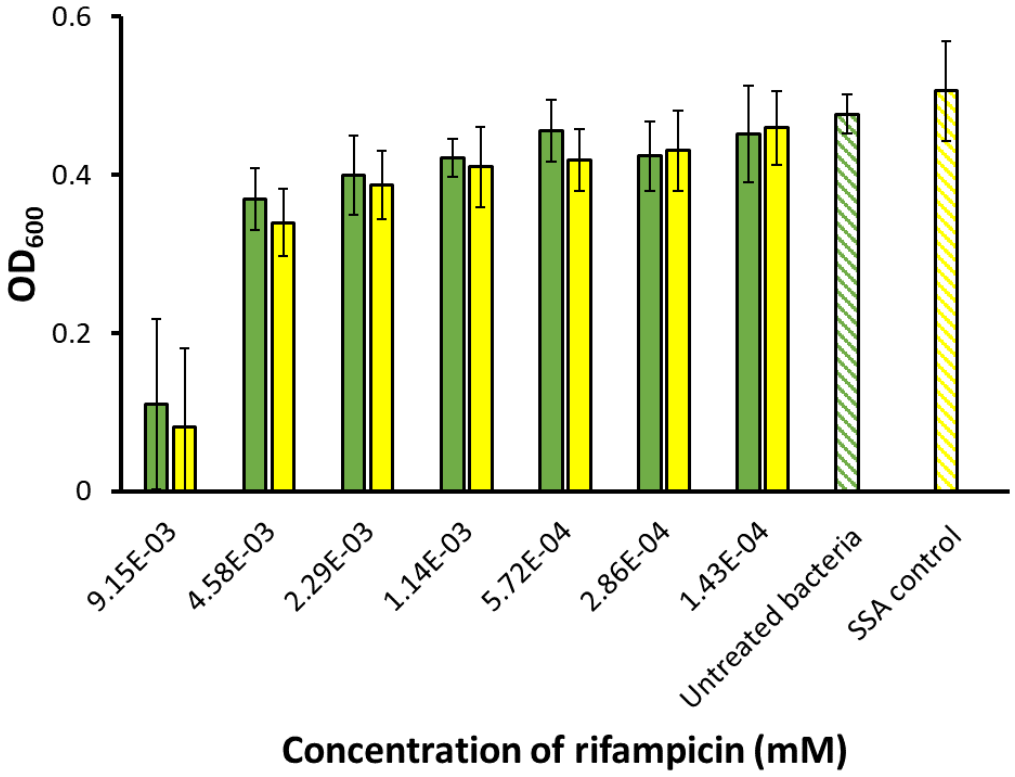

Figure S205 - SSA **42** (8 mM) was incubated with *E. coli* DH10B for ≈ 10 minutes before being added to a well containing **novobiocin** at varying concentrations. Yellow = **rifampicin** + SSA **42** (co-formulation **h**), Green = **rifampicin.**

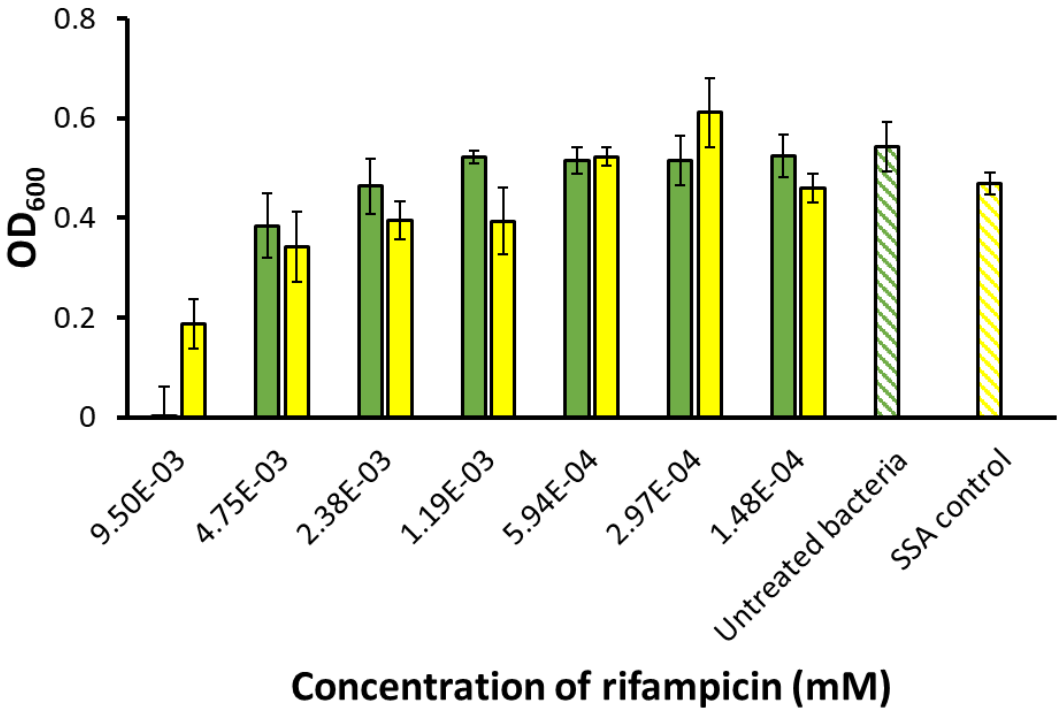

Figure S206 - SSA **49** (8 mM) was incubated with *E. coli* DH10B for ≈ 10 minutes before being added to a well containing **novobiocin** at varying concentrations. Yellow = **rifampicin** + SSA **49** (co-formulation **k**), Green = **rifampicin.**

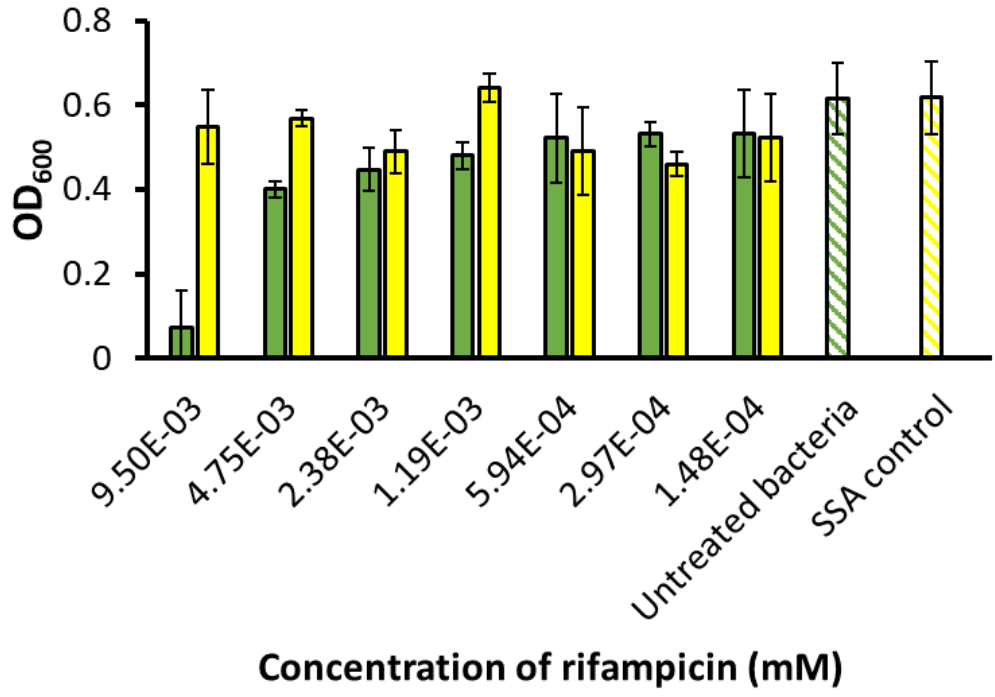

Figure S207 - SSA **50** (8 mM) was incubated with *E. coli* DH10B for ≈ 10 minutes before being added to a well containing **novobiocin** at varying concentrations. Yellow = **rifampicin** + SSA **50** (co-formulation **n**), Green = **rifampicin.**

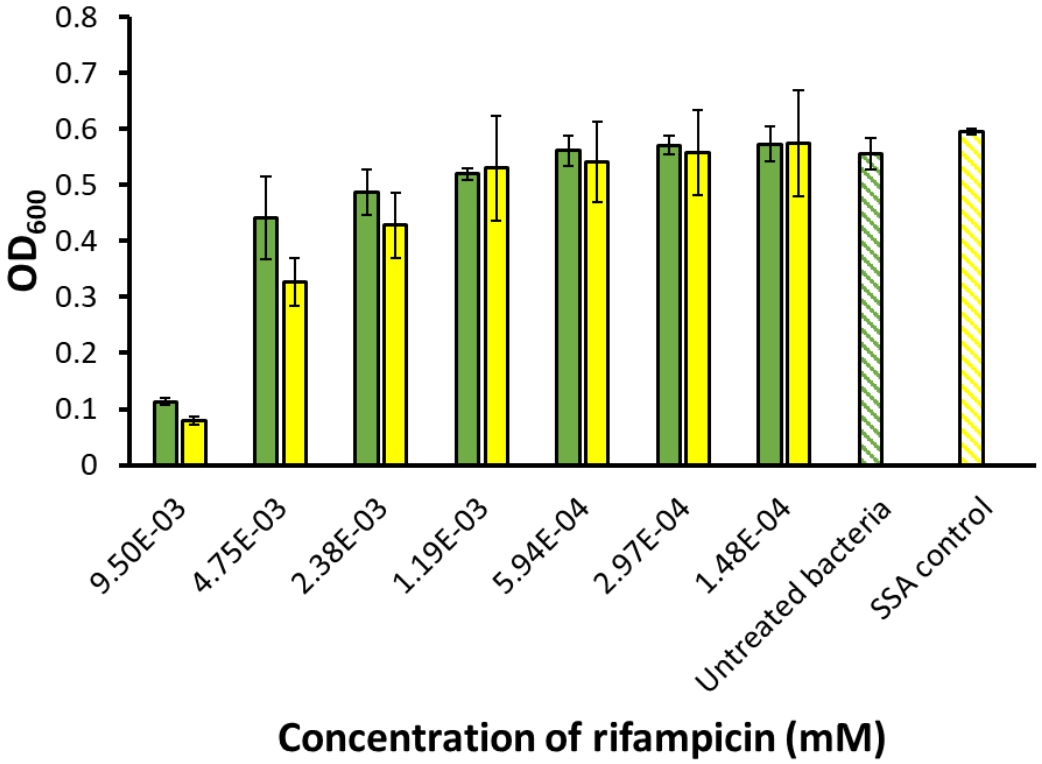

Figure S208 - SSA **51** (8 mM) was incubated with *E. coli* DH10B for ≈ 10 minutes before being added to a well containing **novobiocin** at varying concentrations. Yellow = **rifampicin** + SSA **51** (co-formulation **q**), Green = **rifampicin.**

3 Chapter 4 Appendix

3.1 Characterisation NMR

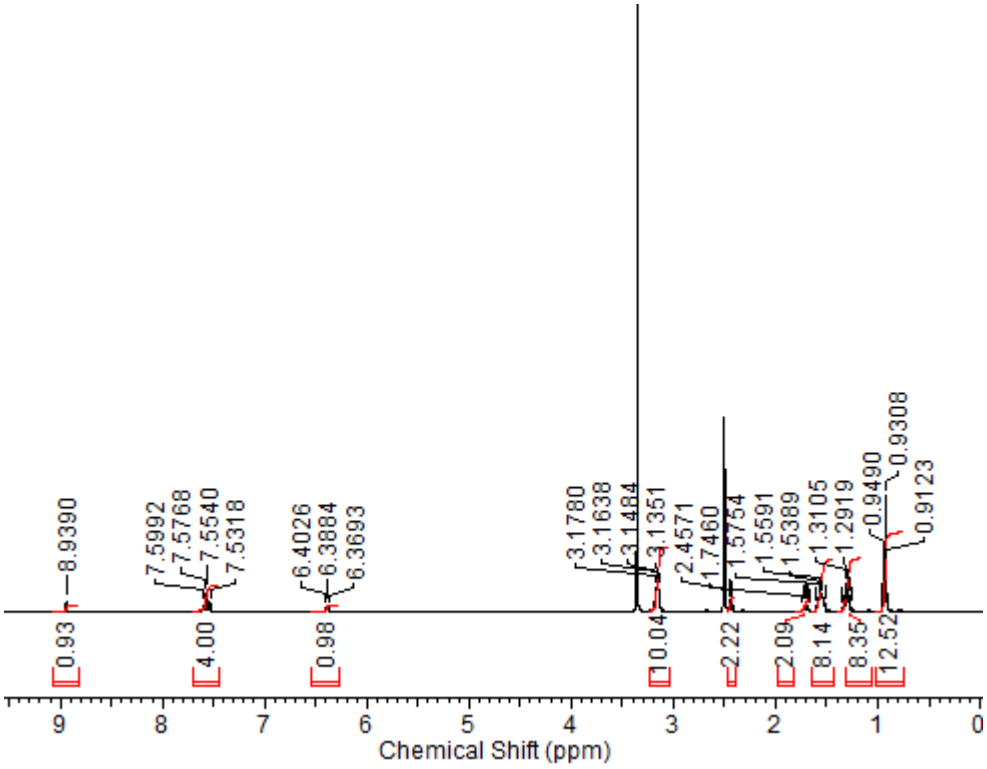

Figure S209 - ^{1}H NMR of compound **59** in DMSO-d_6 conducted at 298 K.

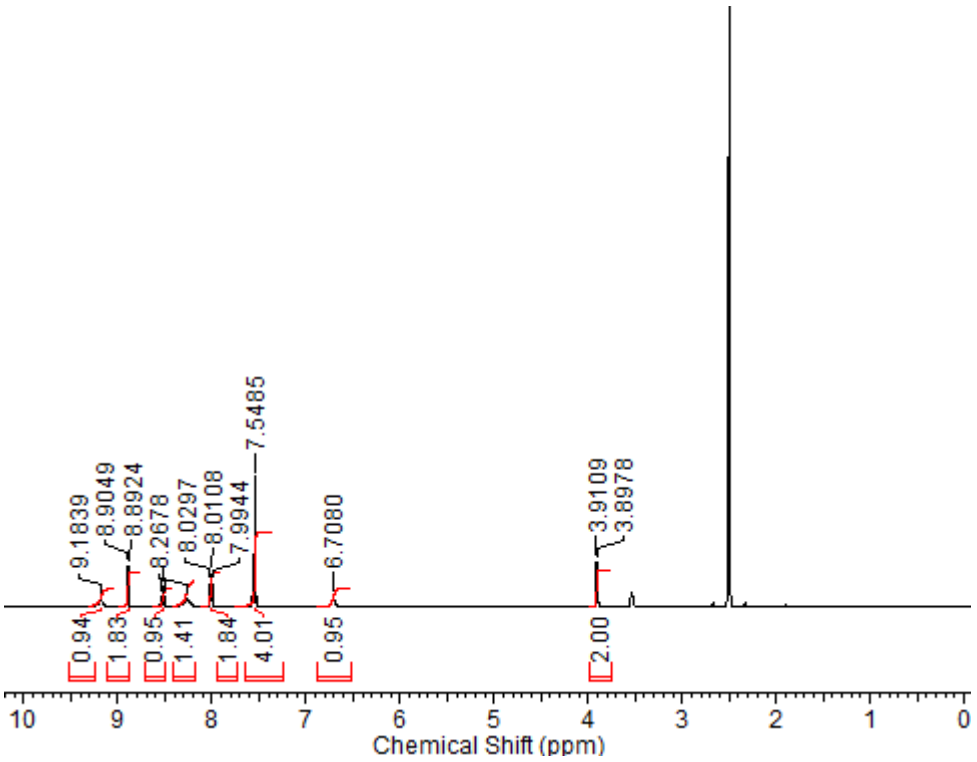

Figure S210 - ^{1}H NMR of compound **60** in DMSO-d_6 conducted at 298 K.

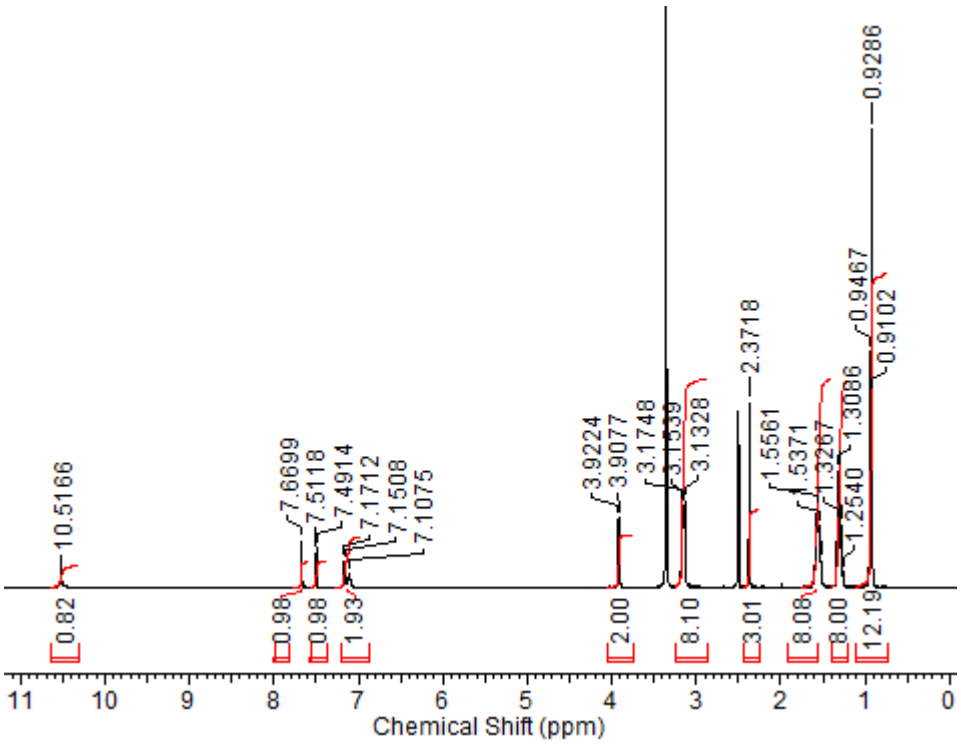

Figure S211 - ^{1}H NMR of compound **61** in DMSO-d_6 conducted at 298 K.

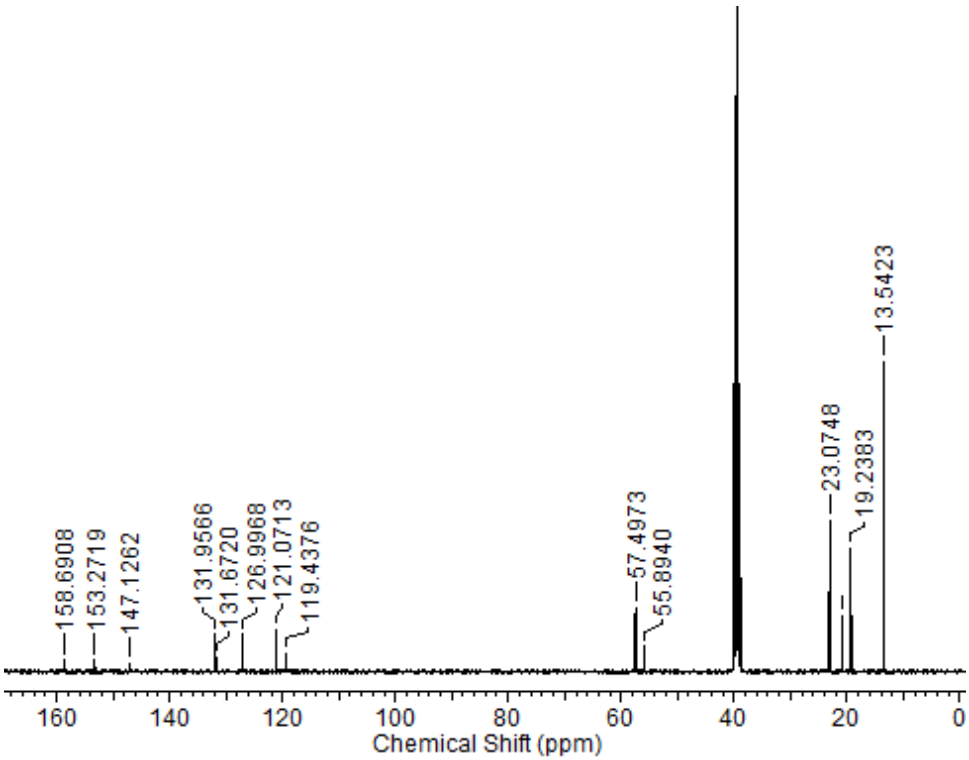

Figure S212 - ^{13}C NMR of compound **61** in DMSO-d_6 conducted at 298 K.

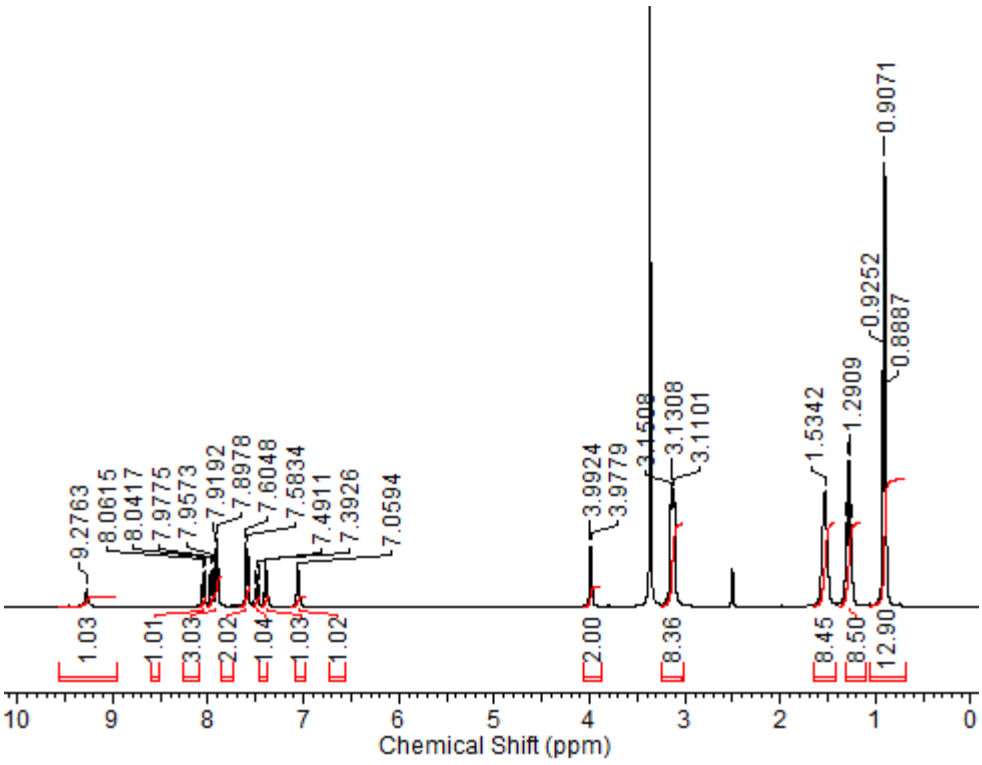

Figure S213 - ^{1}H NMR of compound **62** in DMSO-d_6 conducted at 298 K.

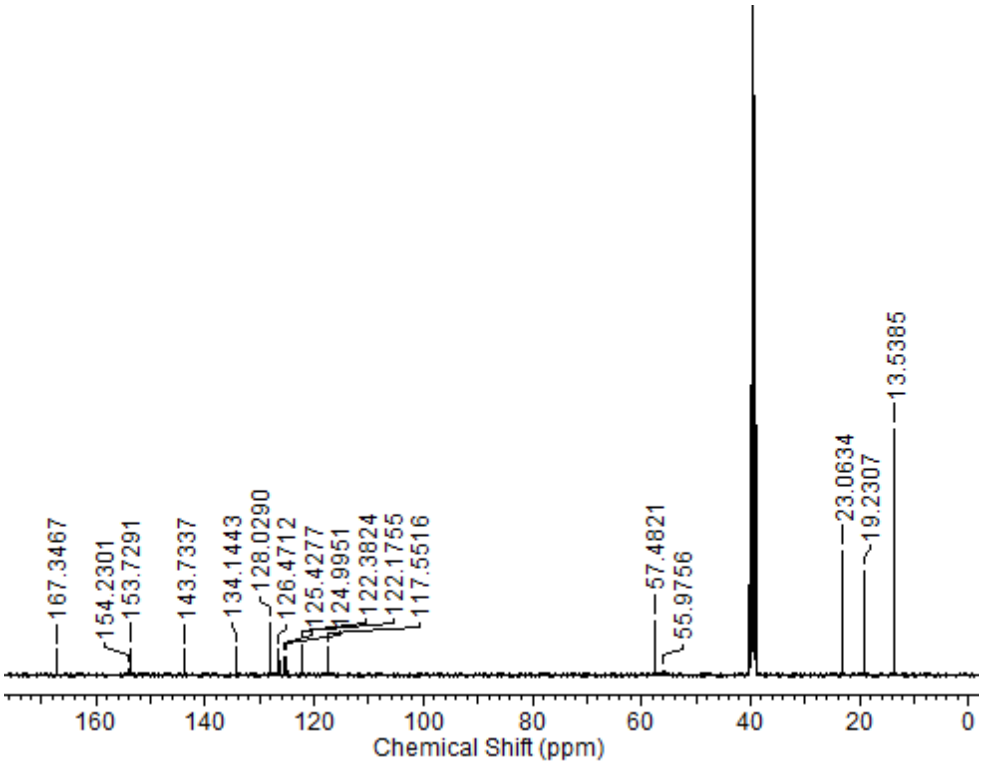

Figure S214 - ^{13}C NMR of compound **62** in DMSO-d_6 conducted at 298 K.

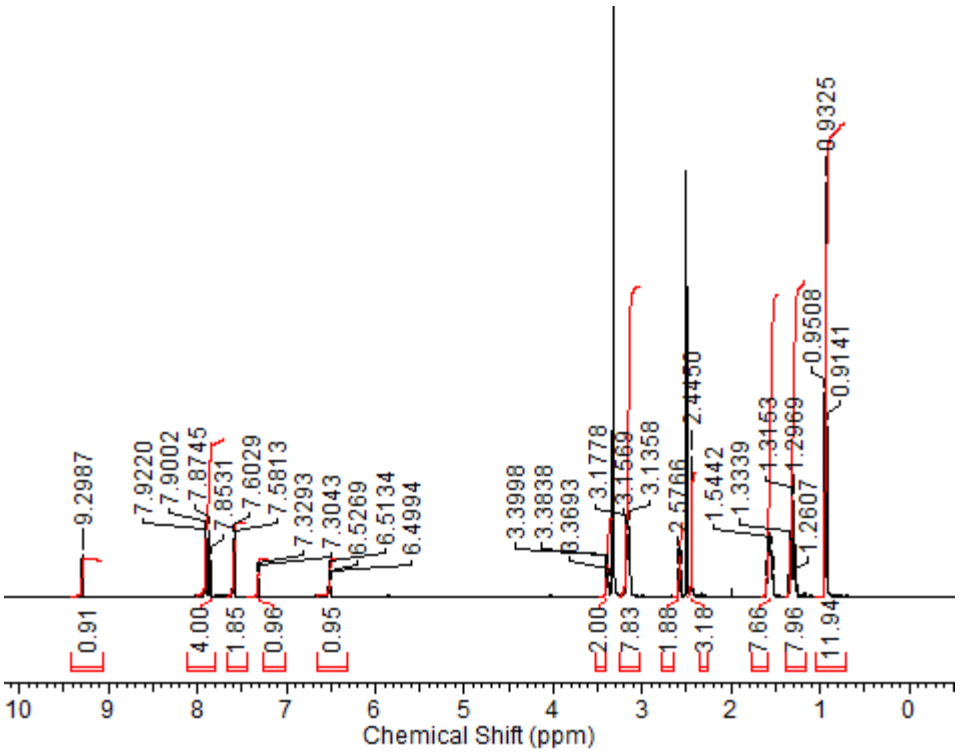

Figure S215 - ^{1}H NMR of compound **63** in DMSO-d_6 conducted at 298 K.

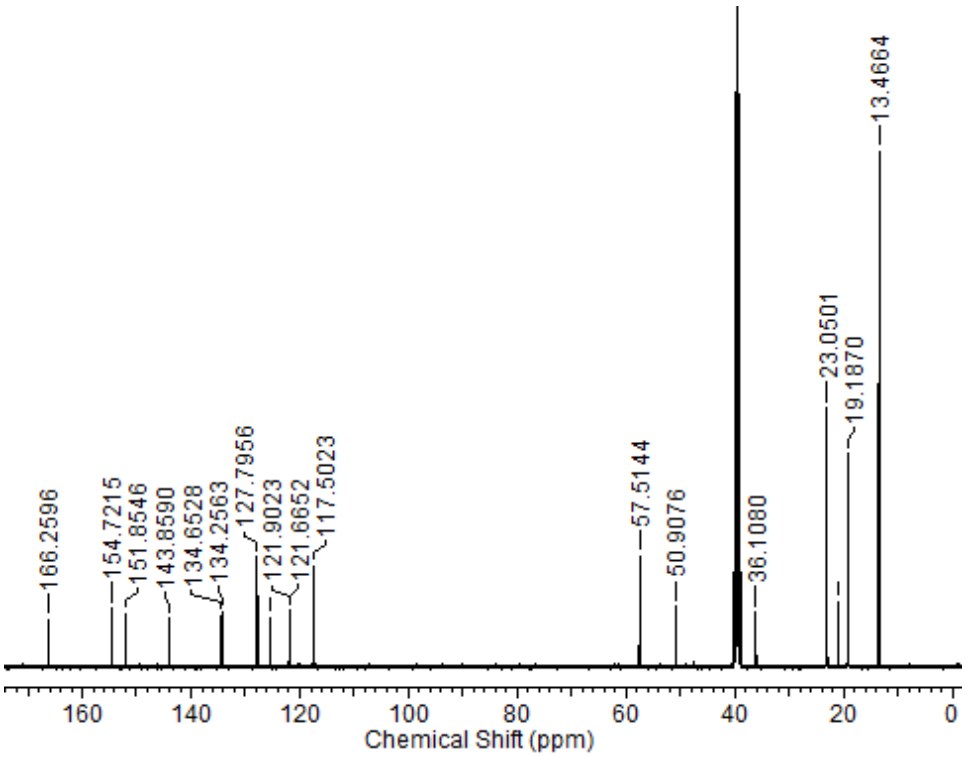

Figure S216 - ^{13}C NMR of compound **63** in DMSO-d_6 conducted at 298 K.

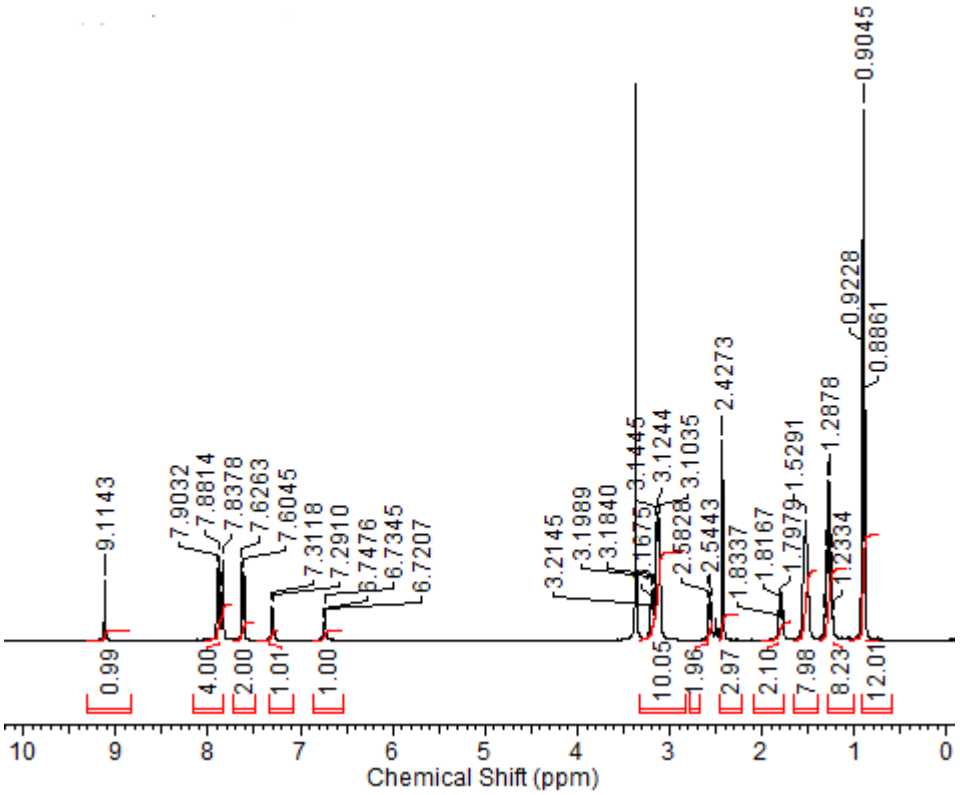

Figure S217 - ^{1}H NMR of compound **64** in DMSO-d_6 conducted at 298 K.

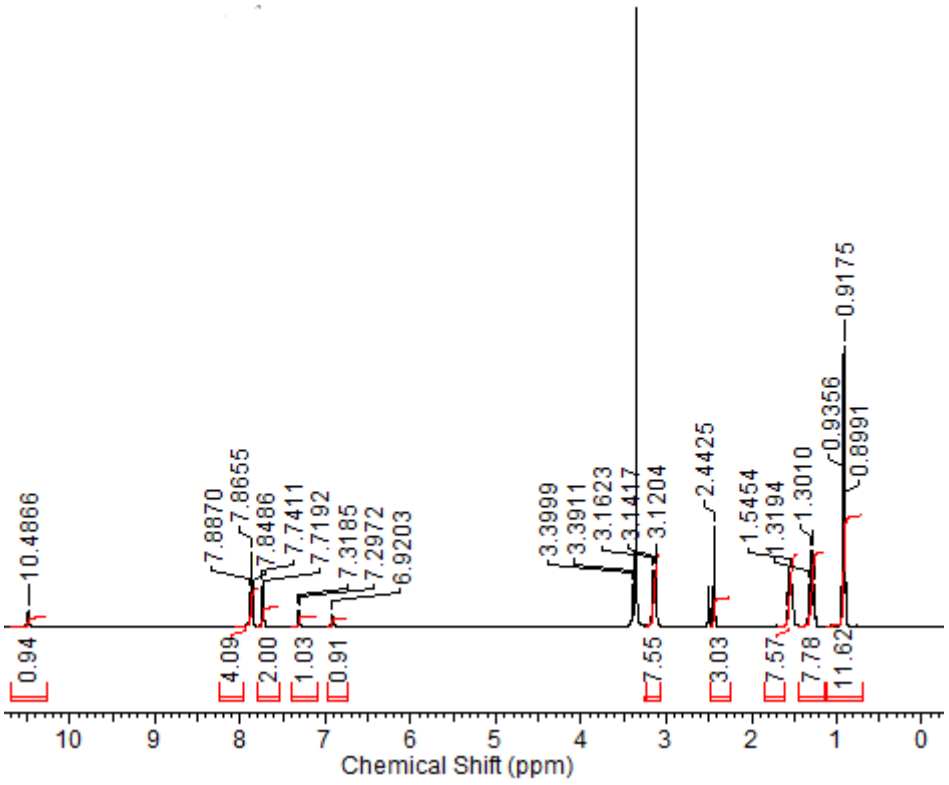

Figure S218 - ^{1}H NMR of compound **65** in DMSO-d_6 conducted at 298 K.

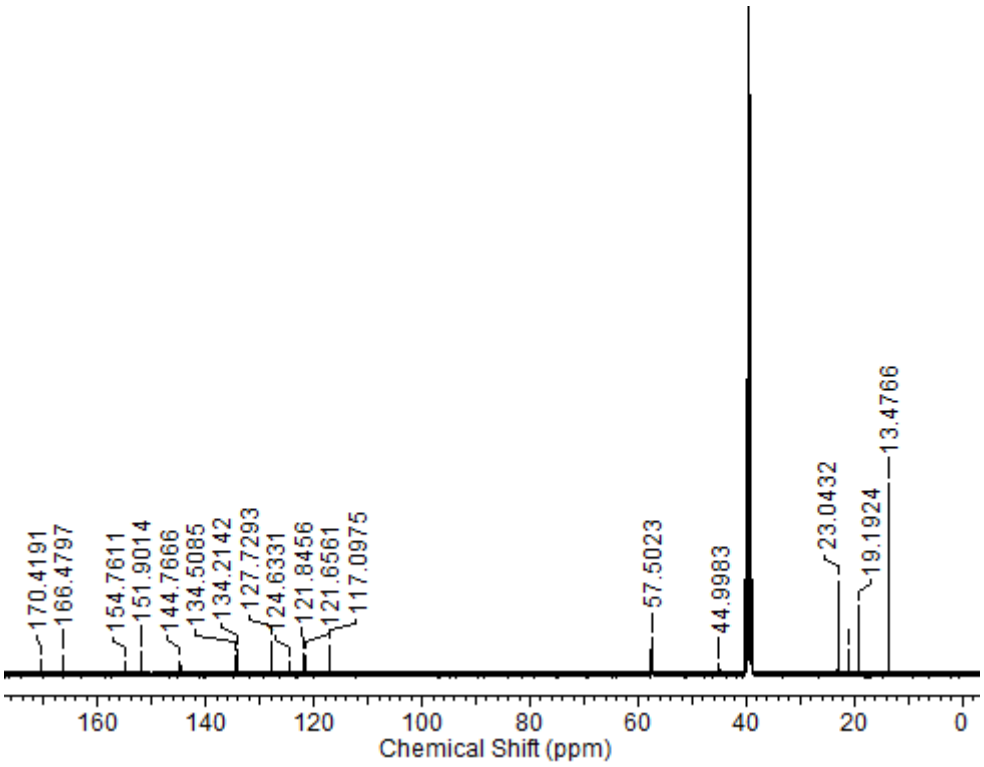

Figure S219 - ^{13}C NMR of compound **65** in DMSO-d_6 conducted at 298 K.

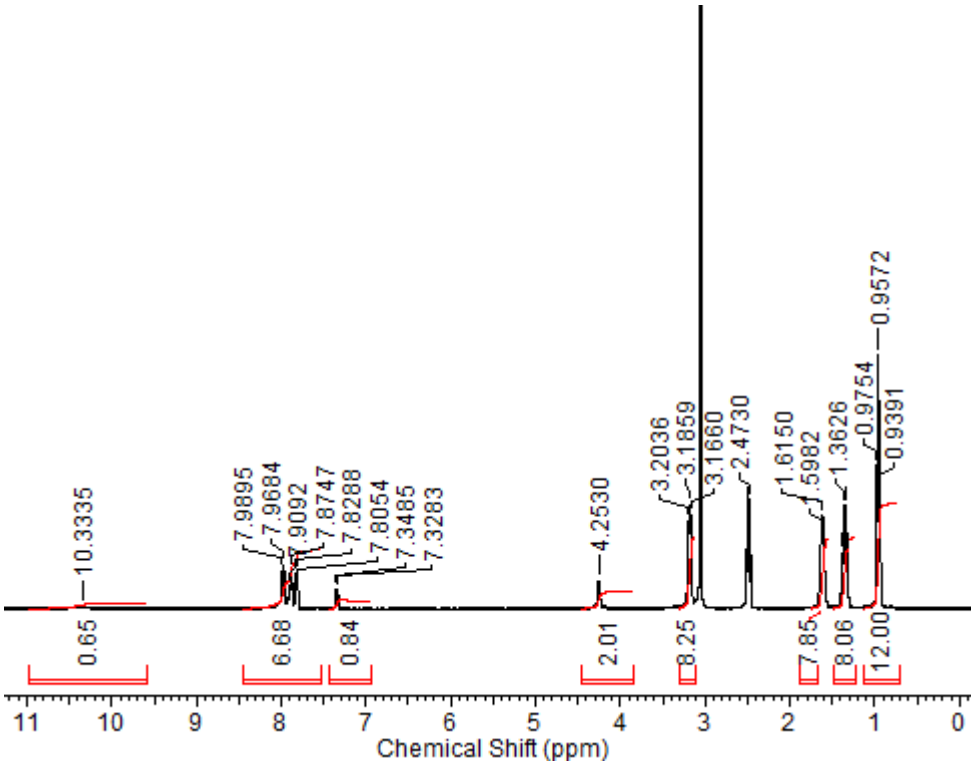

Figure S220 - ^{1}H NMR of compound **66** in DMSO-d_6 conducted at 333 K.

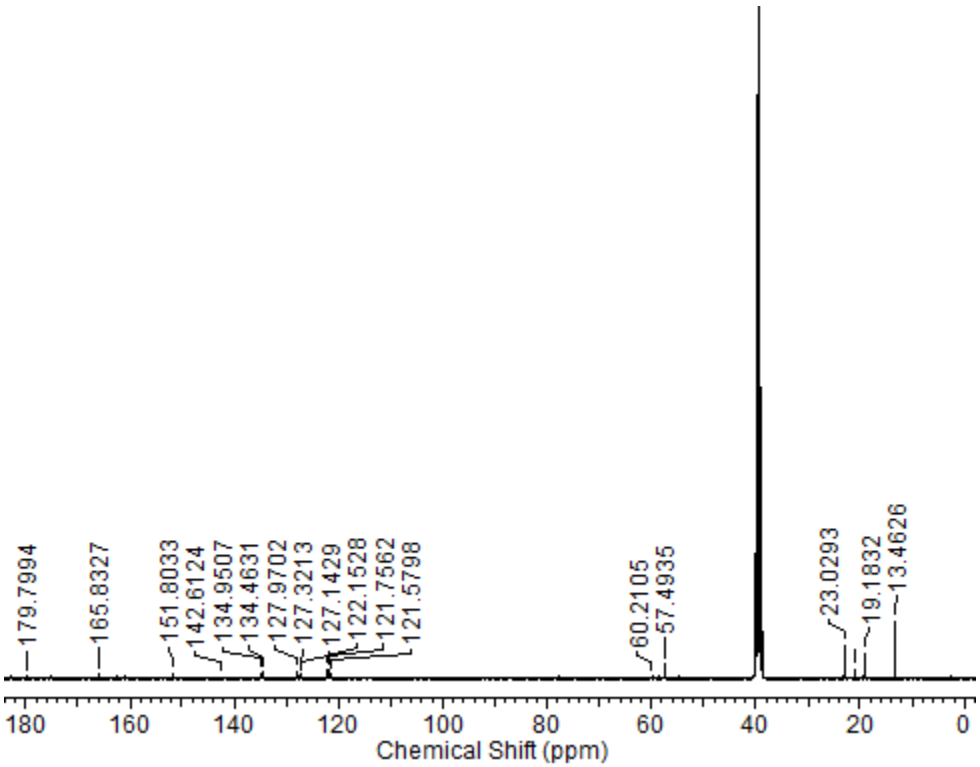

Figure S221 - ^{13}C NMR of compound **66** in DMSO-d_6 conducted at 298 K.

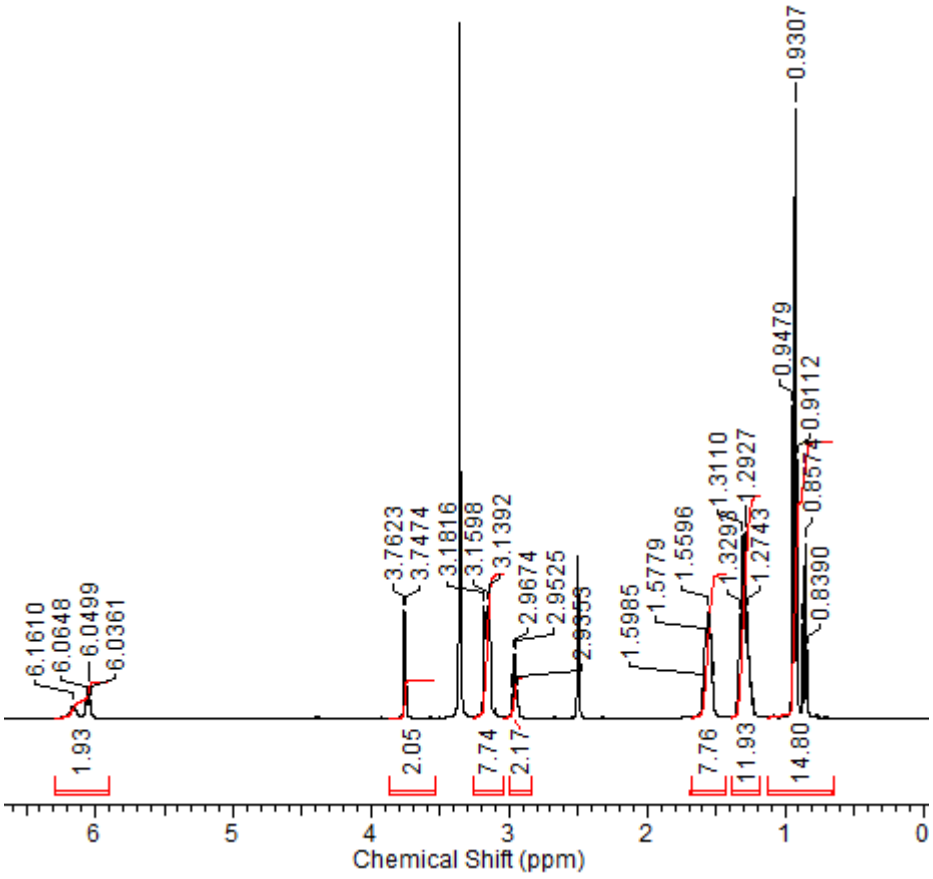

Figure S222 - ^{1}H NMR of compound **67** in DMSO-d_6 conducted at 298 K.

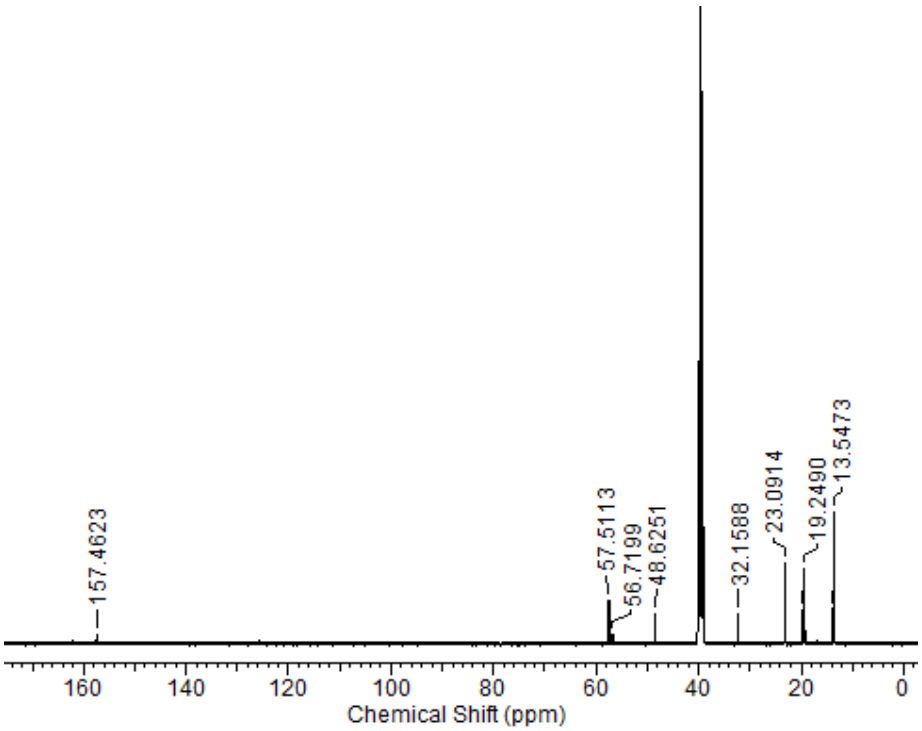

Figure S223 - ^{13}C NMR of compound **67** in DMSO-d_6 conducted at 298 K.

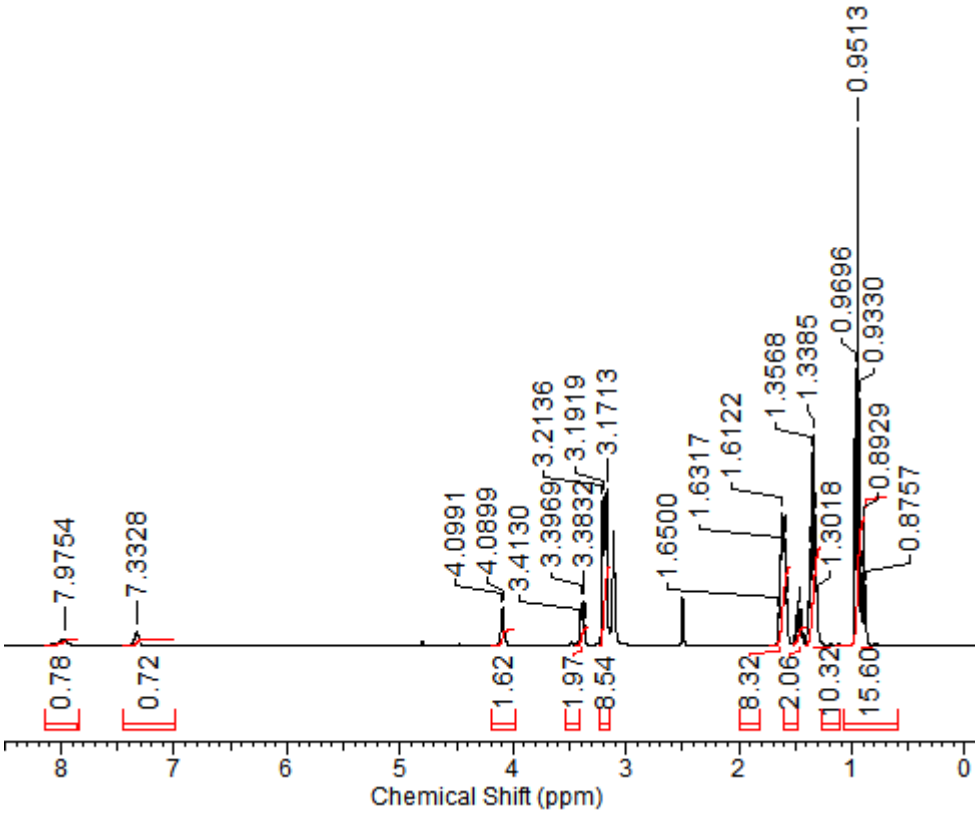

Figure S224 - ^{1}H NMR of compound **68** in DMSO-d_6 conducted at 333 K.

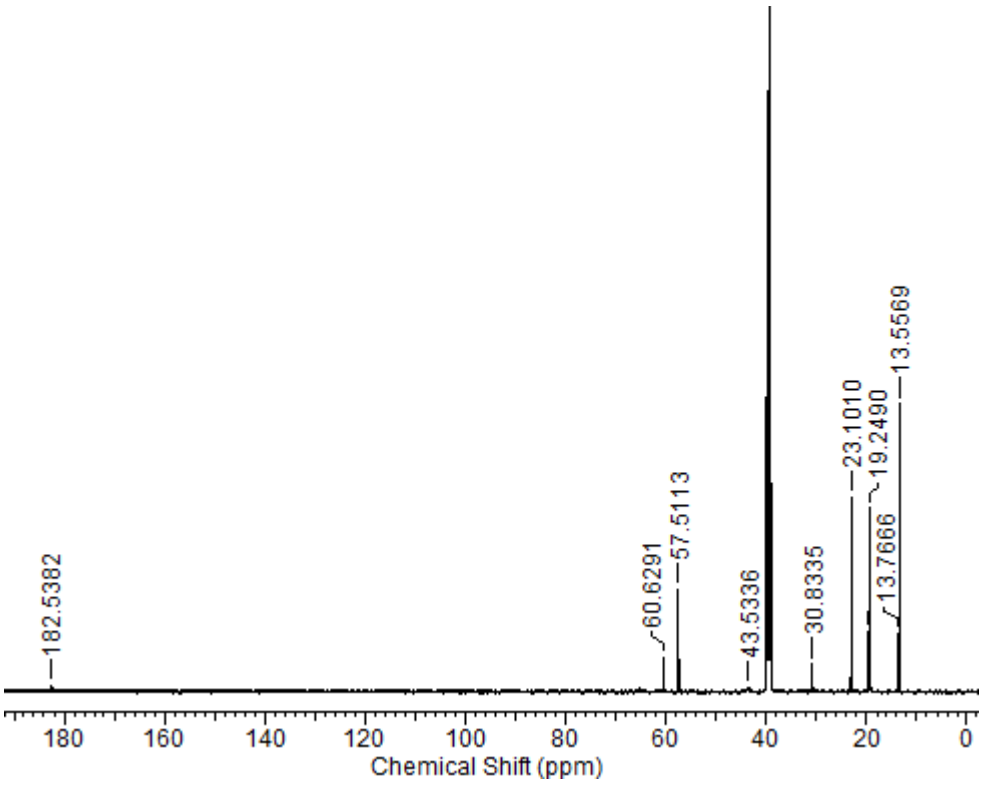

Figure S225 - ^{13}C NMR of compound **68** in DMSO-d_6 conducted at 298 K.

3.2 Mass Spectrometry

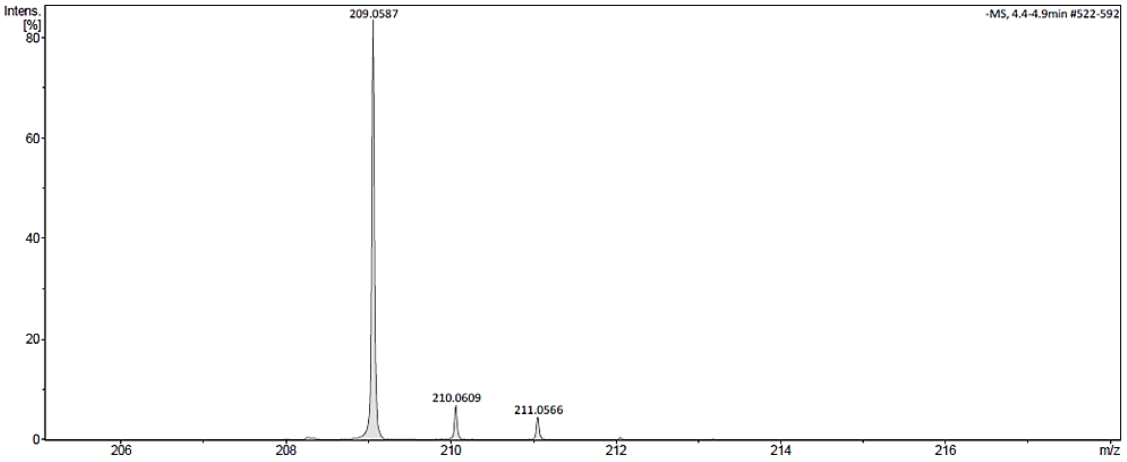

Figure S226 - A high-resolution mass spectrum (ESI^-) obtained for compound **67** in methanol.

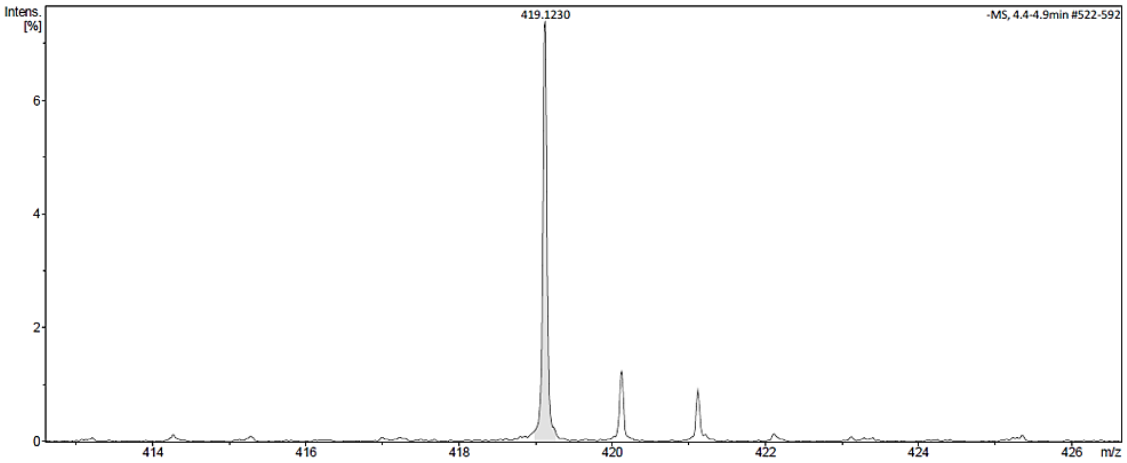

Figure S227 - A high-resolution mass spectrum (ESI^-) obtained for dimeric species of compound **67** in methanol, m/z $[M + M + H^+]^-$.

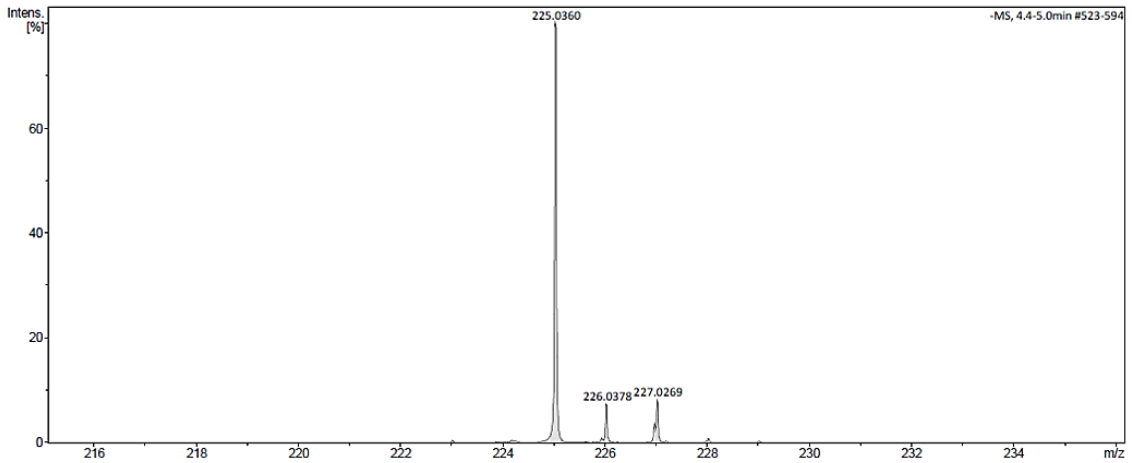

Figure S228 - A high-resolution mass spectrum (ESI^-) obtained for compound **68** in methanol.

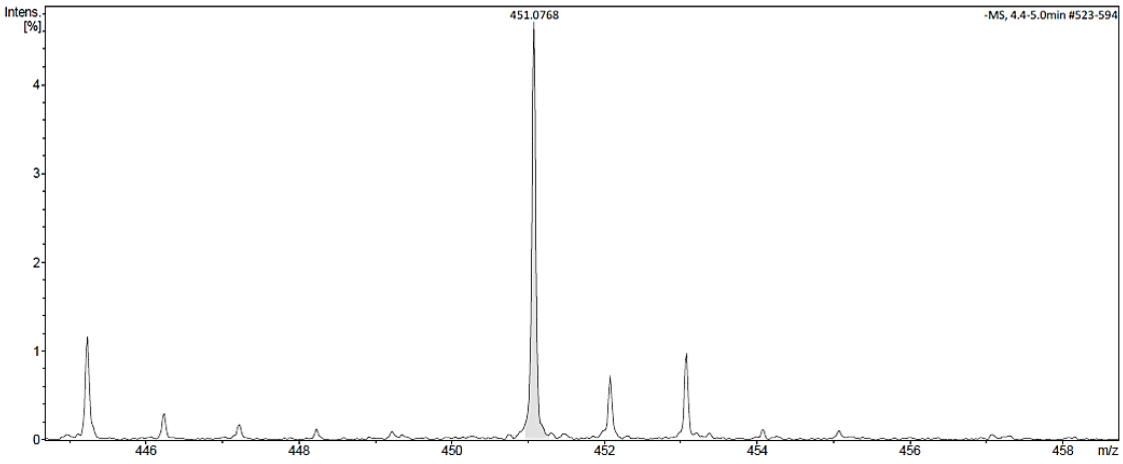

Figure S229 - A high-resolution mass spectrum (ESI^-) obtained for dimeric species of compound **68** in methanol, m/z $[M + M + H^+]^-$.

3.3 MIC_{50} determination

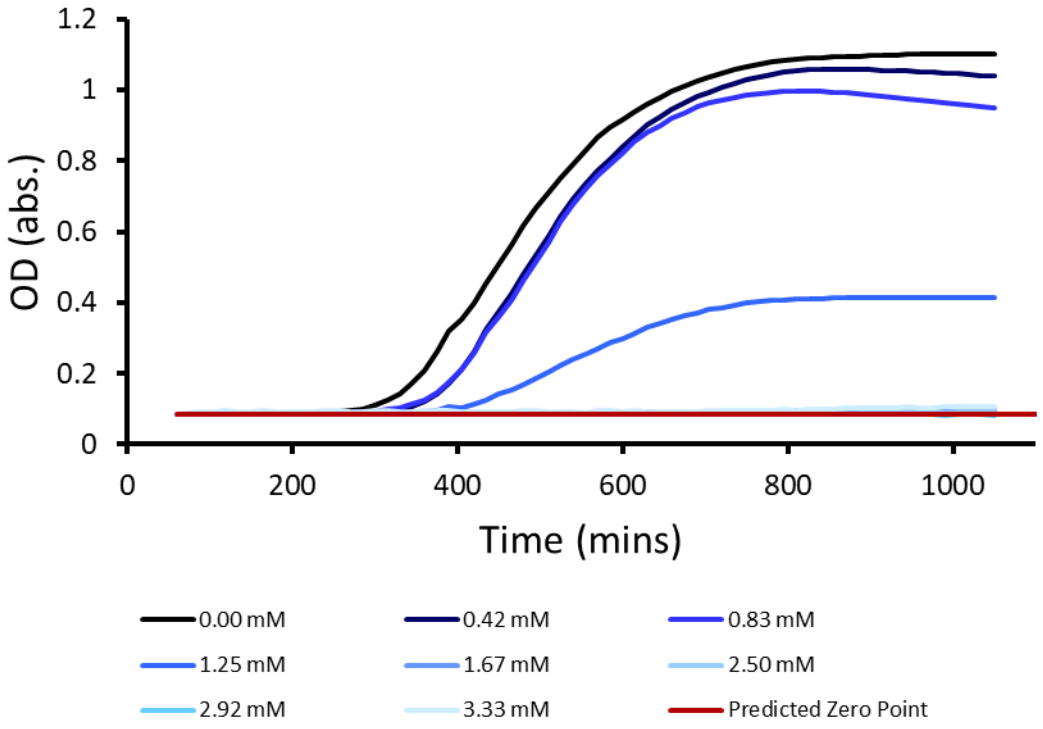

Figure S230 - MRSA USA 300 growth curves created from an average of 6 optical density readings for each concentration in the presence of compound **62** at varying concentrations.

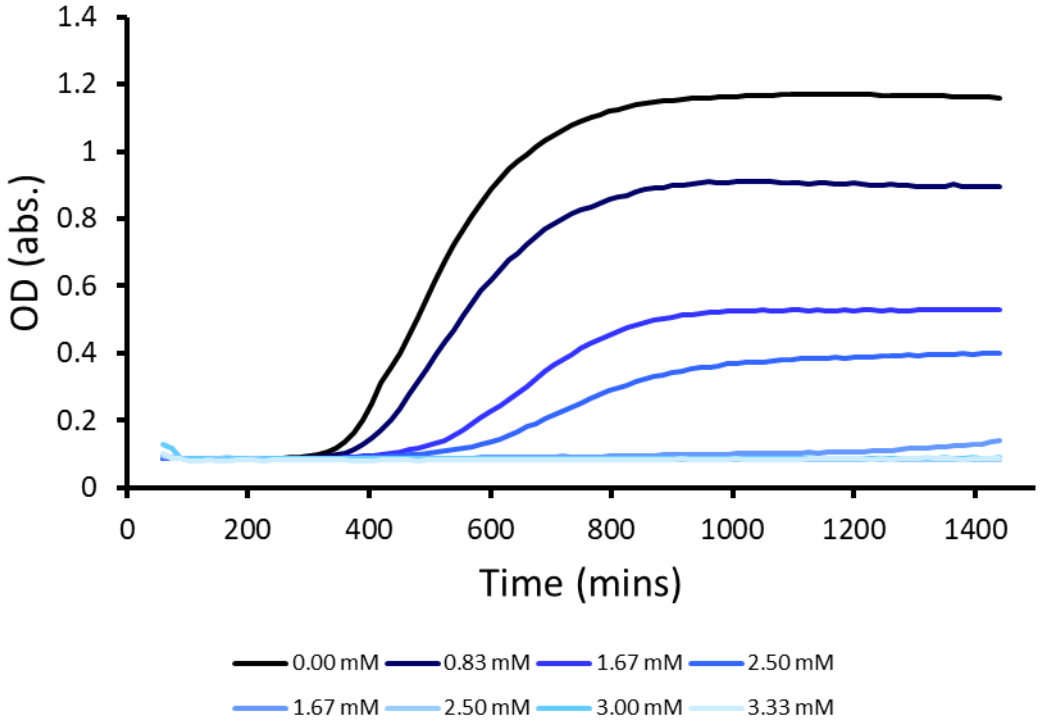

Figure S231 - MRSA USA 300 growth curves created from an average of 6 optical density readings for each concentration in the presence of compound **63** at varying concentrations.

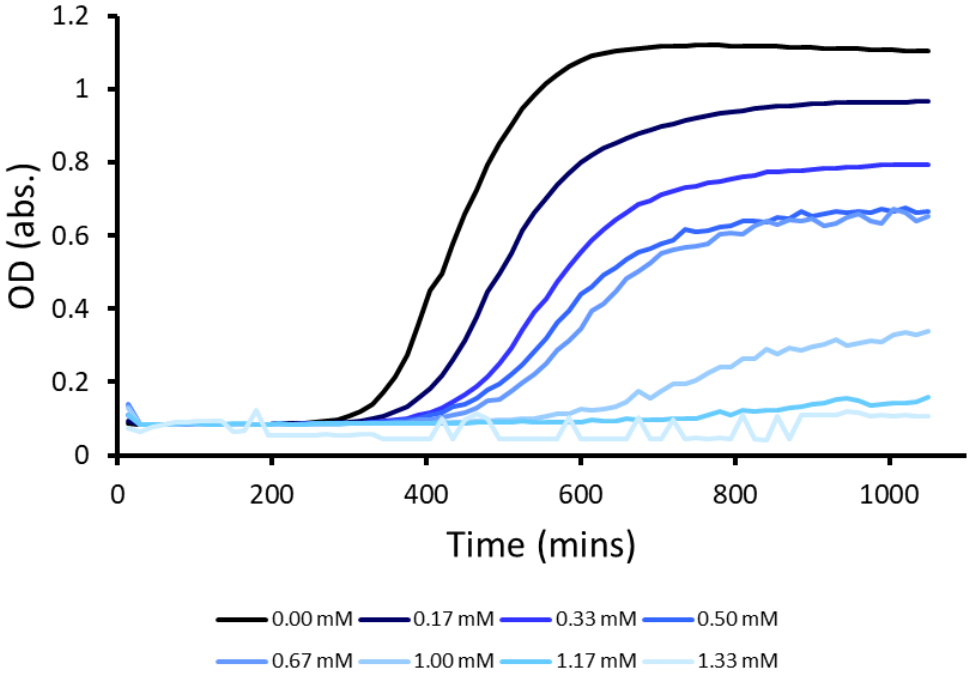

Figure S232 - MRSA USA 300 growth curves created from an average of 6 optical density readings for each concentration in the presence of compound **64** at varying concentrations.

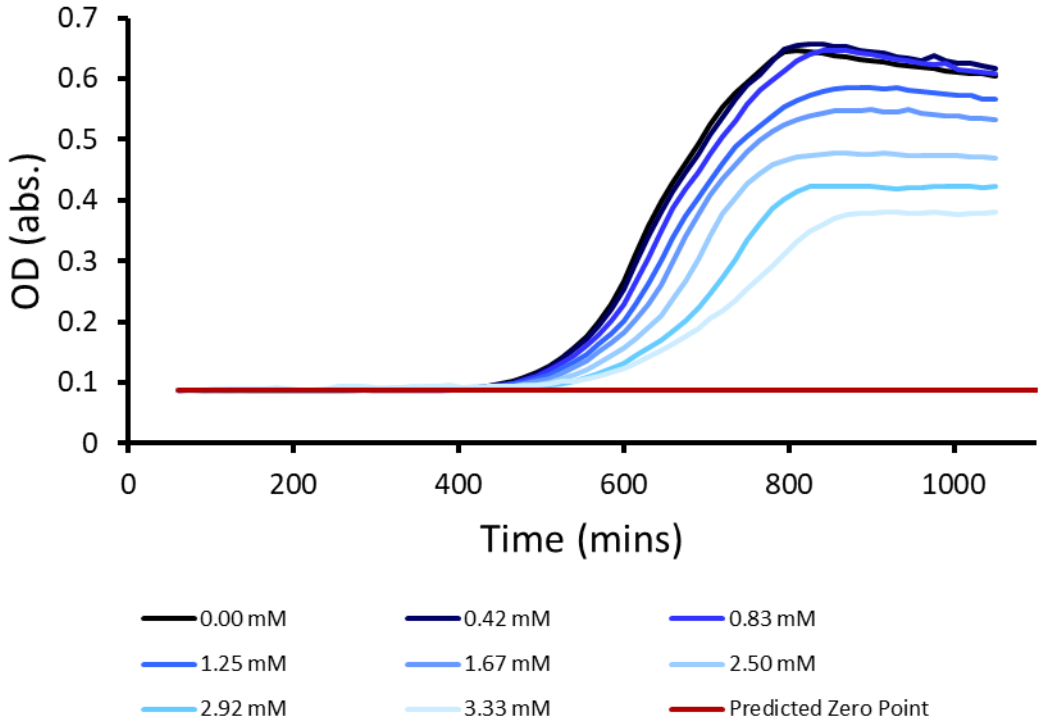

Figure S233 - *E. coli* DH10B growth curves created from an average of 6 optical density readings for each concentration in the presence of compound **62** at varying concentrations.

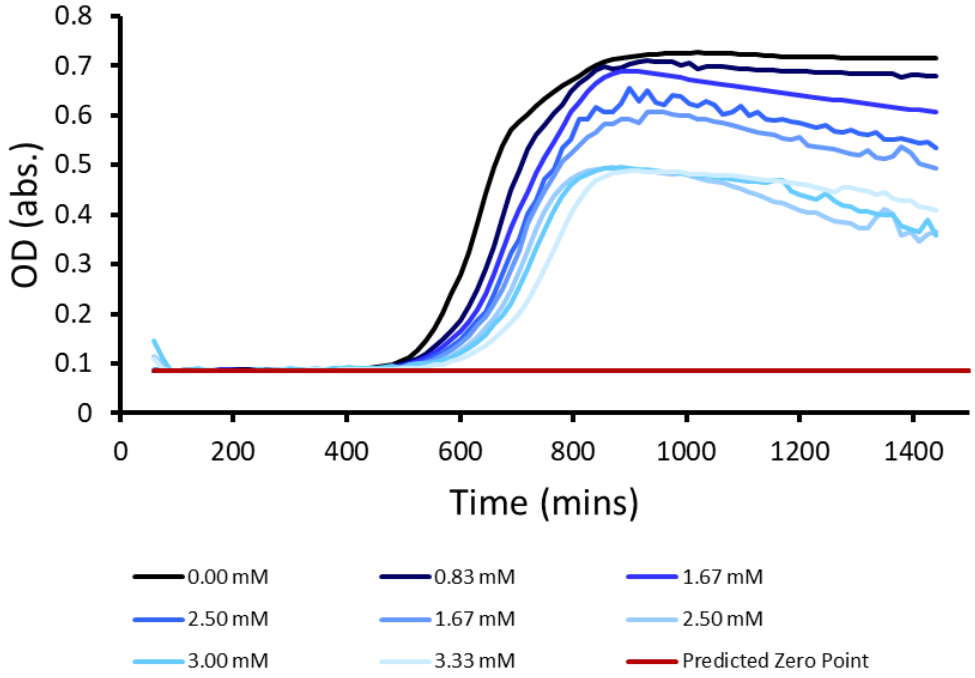

Figure S234 - *E. coli* DH10B growth curves created from an average of 6 optical density readings for each concentration in the presence of compound **63** at varying concentrations.

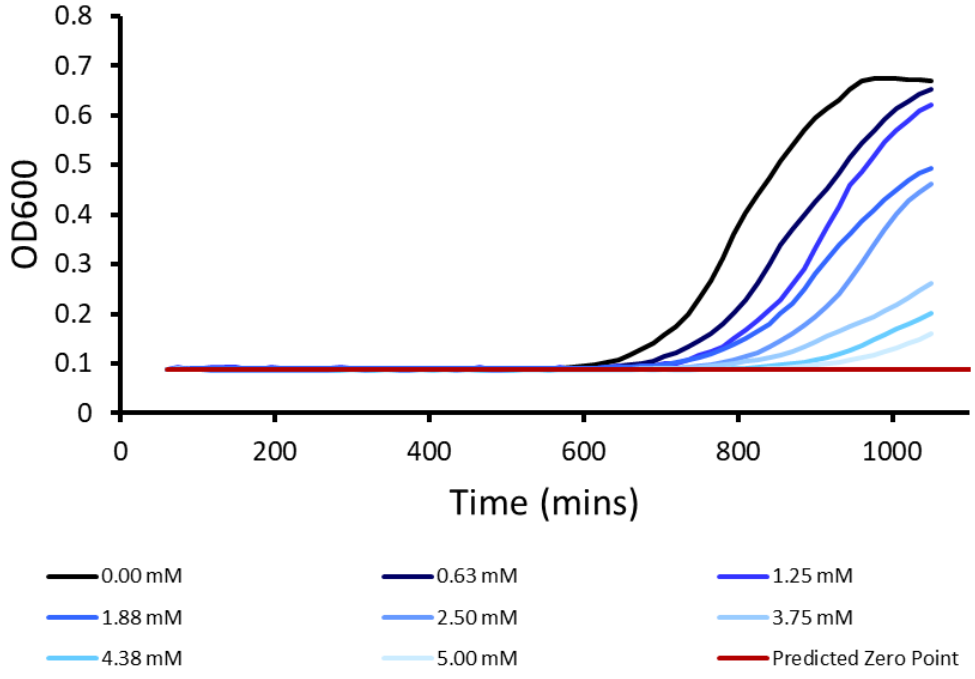

Figure S235 - *E. coli* DH10B growth curves created from an average of 6 optical density readings for each concentration in the presence of compound **64** at varying concentrations.

3.4 Vesicle Leakage assay

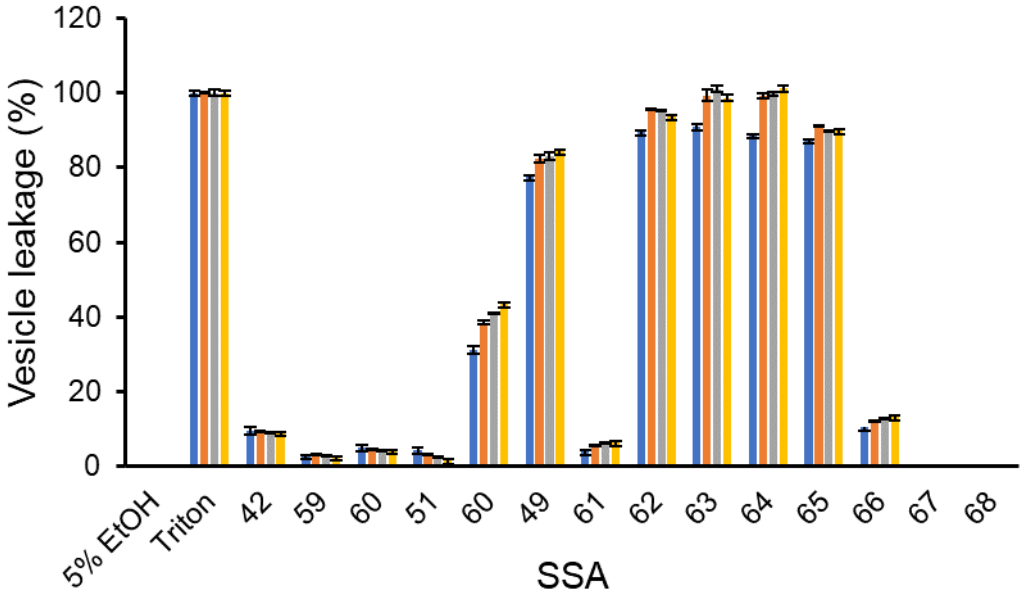

Figure S236 – The percentage lysis of PC lipid membranes (λ_{em} = 515 nm) following the addition of a series of SSAs (1.5 mM). Blue = 30 secs, Orange = 5 mins, Grey = 10 mins and Yellow = 15 mins. Triton X-100 (1 %) was used as a positive control for 100 % cell lysis.

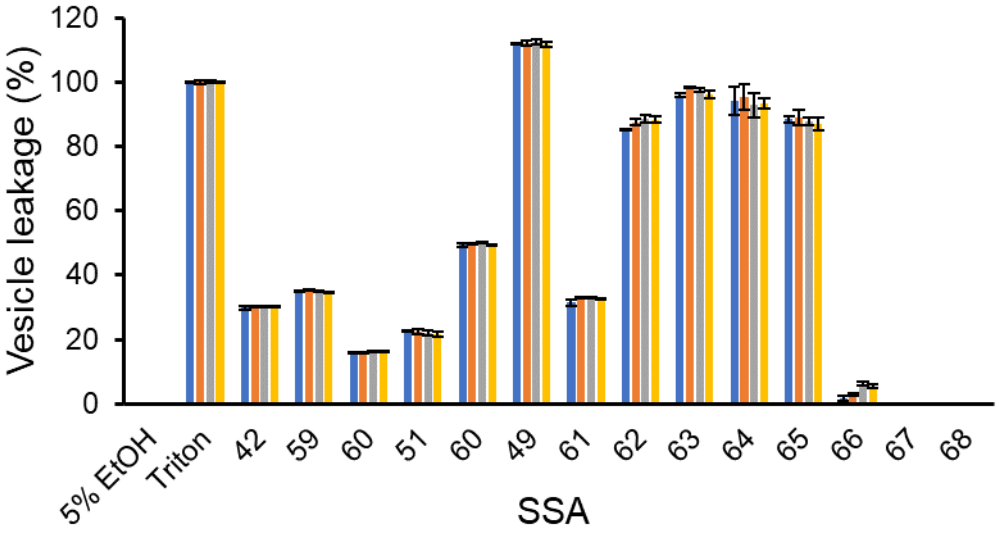

Figure S237 – The percentage lysis of PG lipid membranes (λ_{em} = 515 nm) following the addition of a series of SSAs (1.5 mM). Blue = 30 secs, Orange = 5 mins, Grey = 10 mins and Yellow = 15 mins. Triton X-100 (1 %) was used as a positive control for 100 % cell lysis.

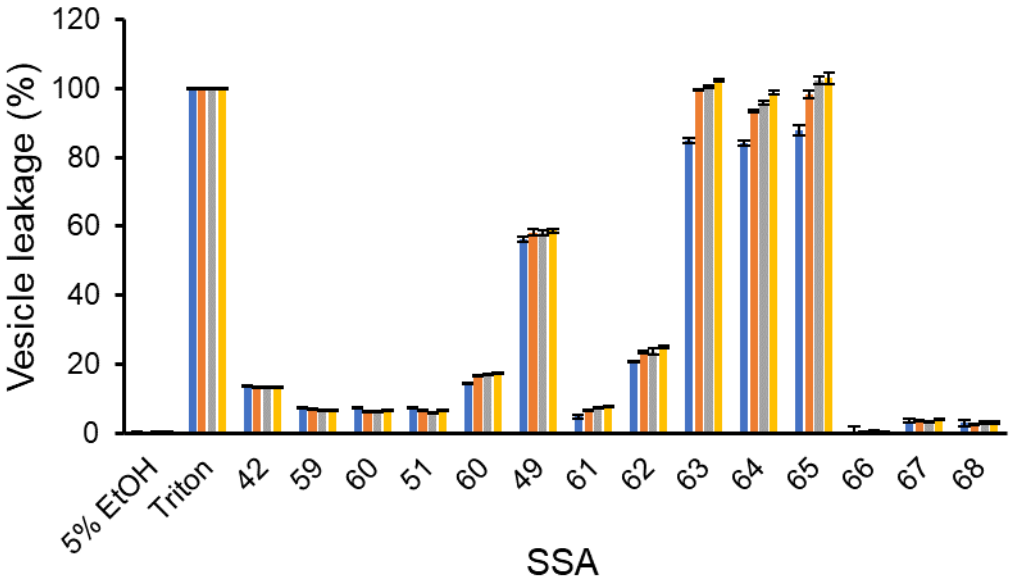

Figure S238 – The percentage lysis of PE-PG mix lipid membranes (λ_{em} = 515 nm) following the addition of a series of SSAs (1.5 mM). Blue = 30 secs, Orange = 5 mins, Grey = 10 mins and Yellow = 15 mins. Triton X-100 (1 %) was used as a positive control for 100 % cell lysis.

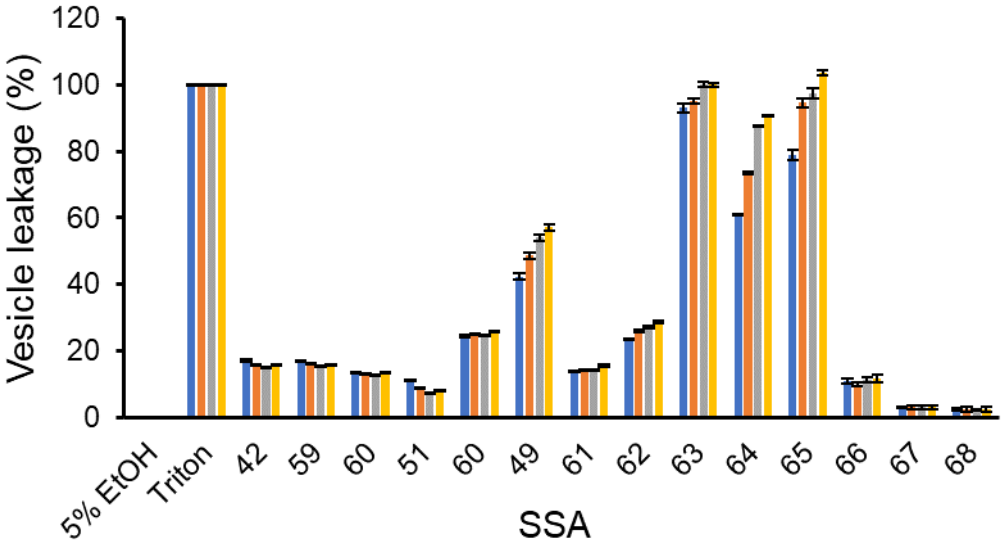

Figure S239 – The percentage lysis of *E. coli* polar lipid membranes (λ_{em} = 515 nm) following the addition of a series of SSAs (1.5 mM). Blue = 30 secs, Orange = 5 mins, Grey = 10 mins and Yellow = 15 mins. Triton X-100 (1 %) was used as a positive control for 100 % cell lysis.

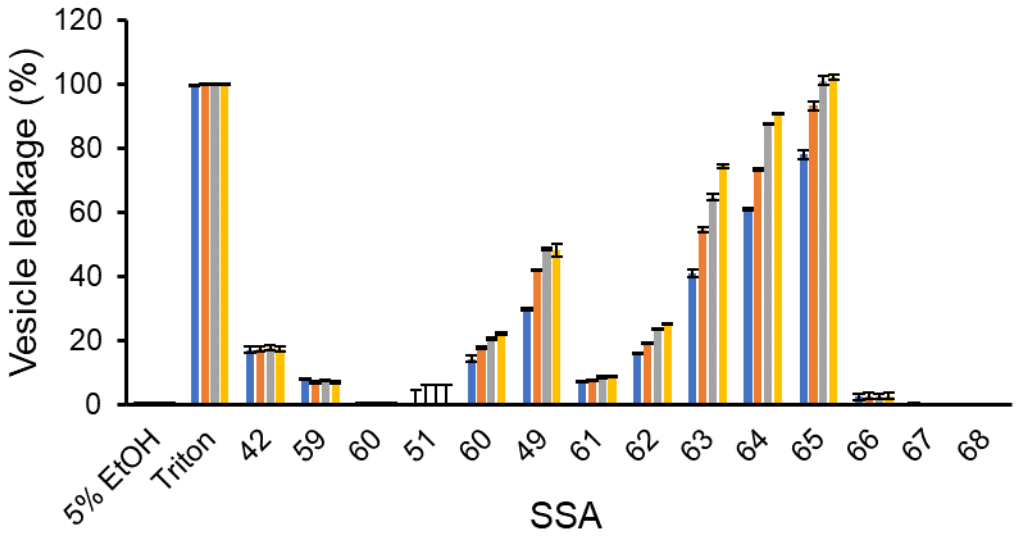

Figure S240 – The percentage lysis of *E. coli* total lipid membranes (λ_{em} = 515 nm) following the addition of a series of SSAs (1.5 mM). Blue = 30 secs, Orange = 5 mins, Grey = 10 mins and Yellow = 15 mins. Triton X-100 (1 %) was used as a positive control for 100 % cell lysis.

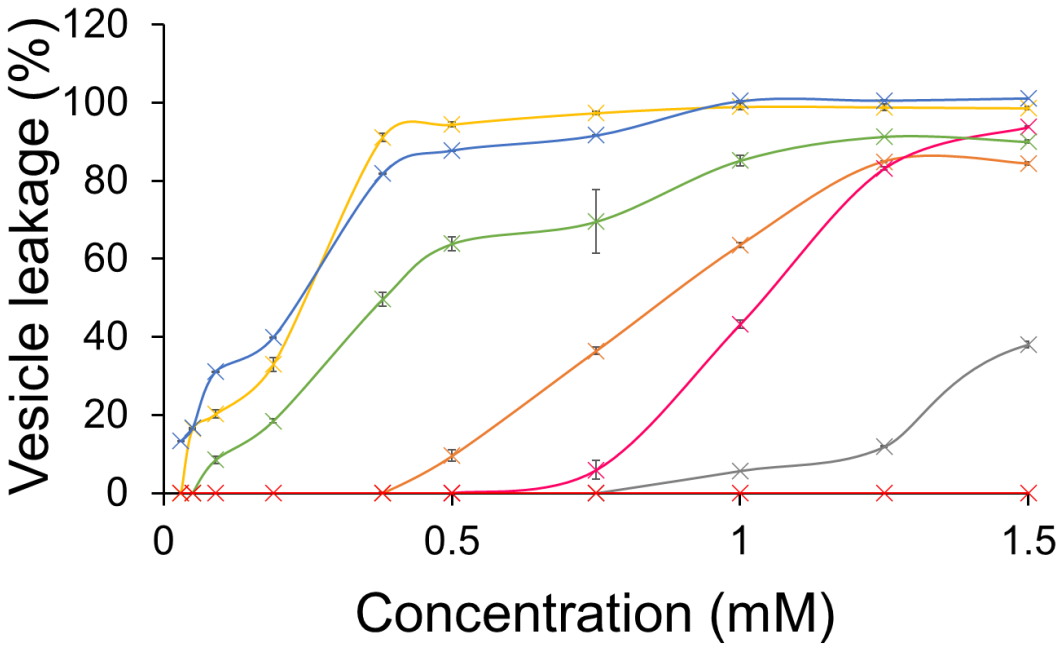

Figure S241 - The percentage lysis of PC lipid membranes (30 µM) following addition of SSA **50** (grey), SSA **49** (orange), SSA **62** (pink), SSA **63** (yellow), SSA **64** (blue), SSA **65** (green) and control solution 5 % EtOH (red) after 15 mins.

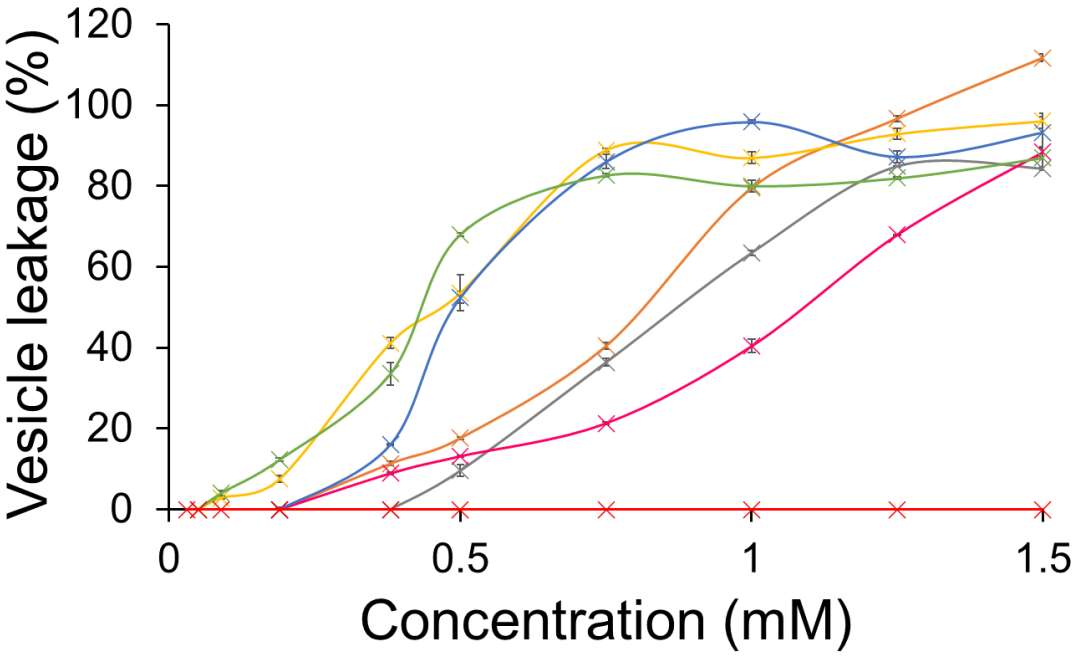

Figure S242 - The percentage lysis of PG lipid membranes (30 μM) following addition of SSA **50** (grey), SSA **49** (orange), SSA **62** (pink), SSA **63** (yellow), SSA **64** (blue), SSA **65** (green) and control solution 5 % EtOH (red) after 15 mins.

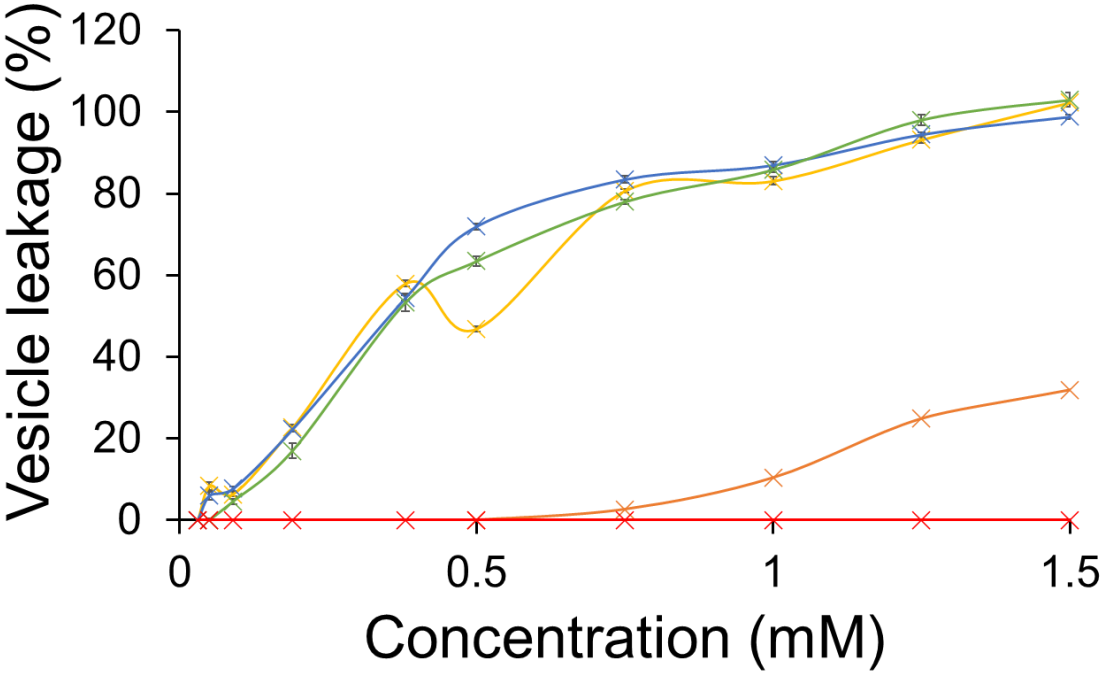

Figure S243 - The percentage lysis of PE-PG mix lipid membranes (30 μM) following addition of SSA **50** (grey), SSA **49** (orange), SSA **62** (pink), SSA **63** (yellow), SSA **64** (blue), SSA **65** (green) and control solution 5 % EtOH (red) after 15 mins.

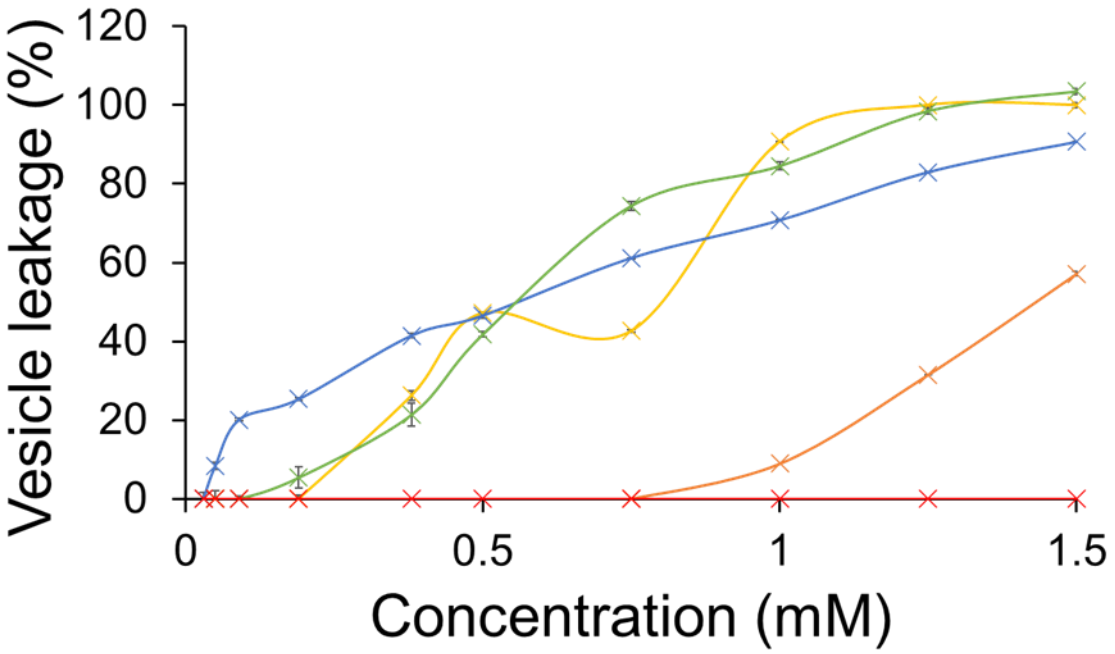

Figure S244 - The percentage lysis of *E. coli* polar mix lipid membranes (30 µM) following addition of SSA **50** (grey), SSA **49** (orange), SSA **62** (pink), SSA **63** (yellow), SSA **64** (blue), SSA **65** (green) and control solution 5 % EtOH (red) after 15 mins.

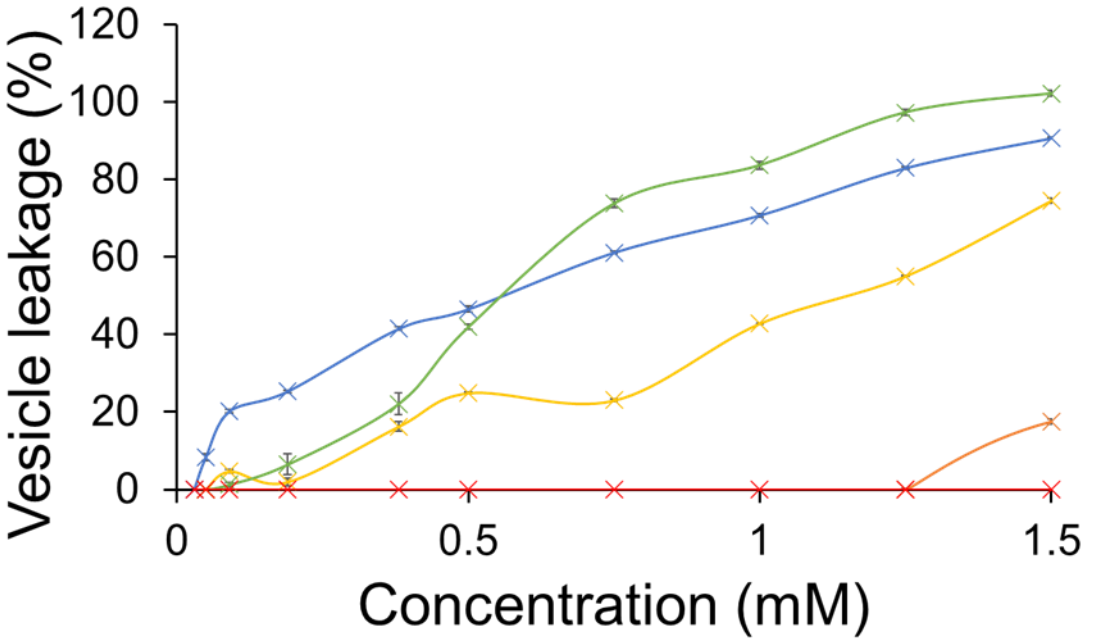

Figure S245 - The percentage lysis of *E. coli* total mix lipid membranes (30 µM) following addition of SSA **50** (grey), SSA **49** (orange), SSA **62** (pink), SSA **63** (yellow), SSA **64** (blue), SSA **65** (green) and control solution 5 % EtOH (red) after 15 mins.

3.5 Membrane Fluidity

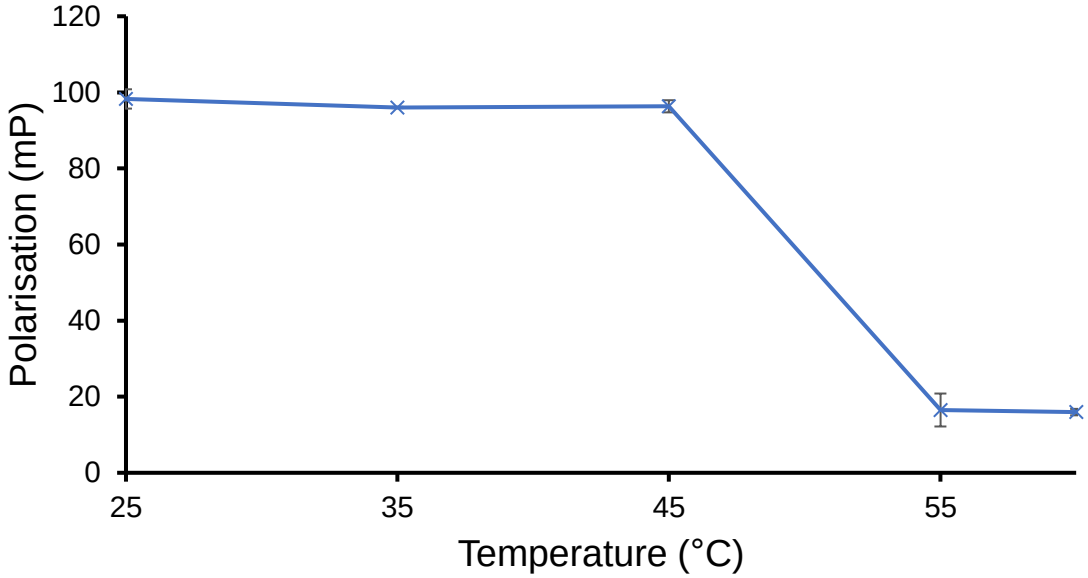

Figure S246 – Effect of temperature on FP measurements in DPH-labelled DSPG vesicles. A target FP value of 100 mP was set to the DPH-labelled vesicles at 25 °C.

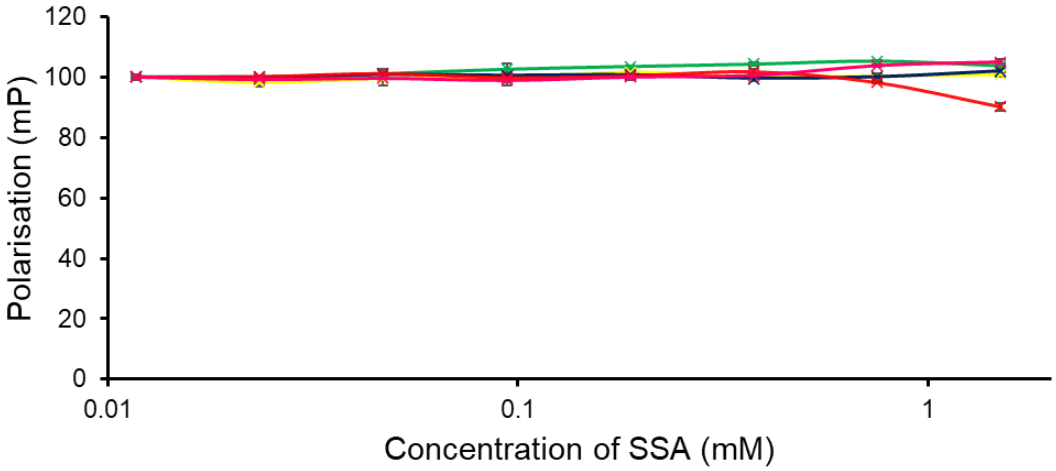

Figure S247 – Effect of SSA on FP measured in DPH-labelled PC vesicles at 25 °C. A target FP value of 100 mP was set to the DPH-labelled vesicles. Green = **42**, Yellow = **59**, Blue = **60,** Red = **51**, Pink = **61**. Error = standard error.

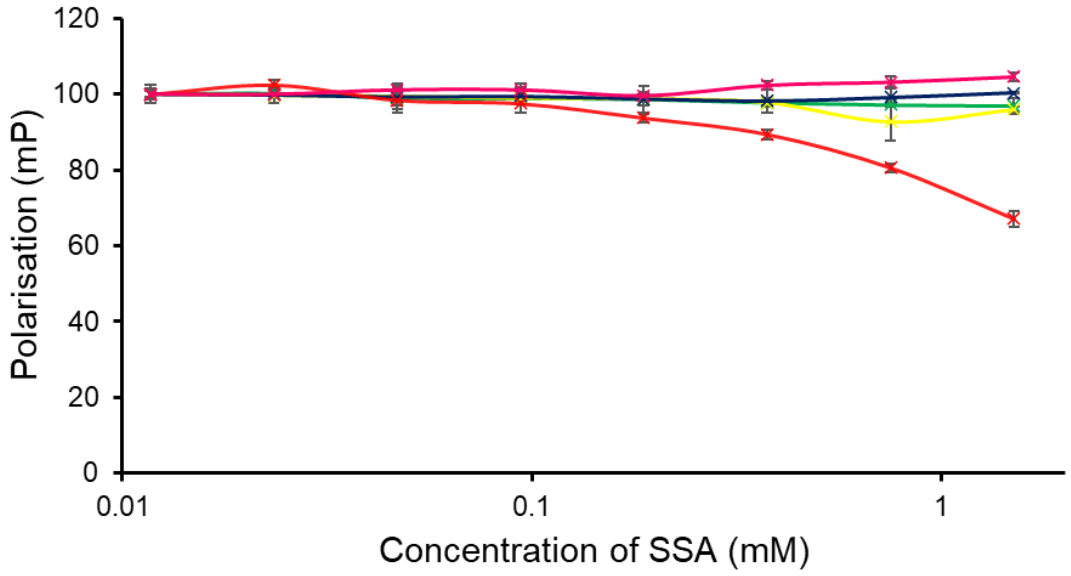

Figure S248 – Effect of SSA on FP measured in DPH-labelled PG vesicles at 25 °C. A target FP value of 100 mP was set to the DPH-labelled vesicles. Green = **42**, Yellow = **59**, Blue = **60,** Red = **51**, Pink = **61**. Error = standard error.

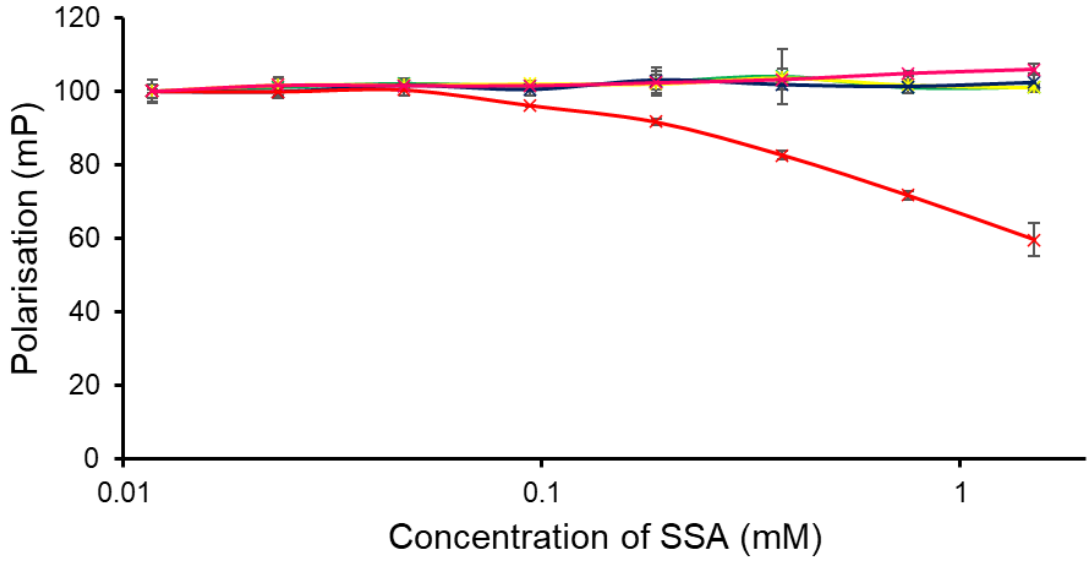

Figure S249 – Effect of SSA on FP measured in DPH-labelled PE:PG 3:1 vesicles at 25 °C. A target FP value of 100 mP was set to the DPH-labelled vesicles. Green = **42**, Yellow = **59**, Blue = **60,** Red = **51**, Pink = **61**. Error = standard error.

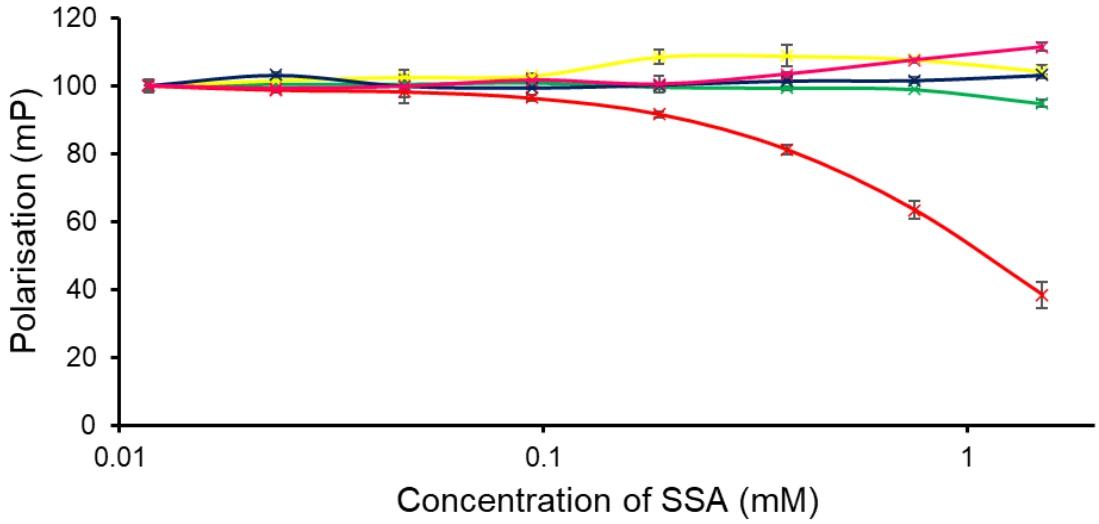

Figure S250 – Effect of SSA on FP measured in DPH-labelled *E. coli* total vesicles at 25 °C. A target FP value of 100 mP was set to the DPH-labelled vesicles. Green = **42**, Yellow = **59**, Blue = **60,** Red = **51**, Pink = **61**. Error = standard error.

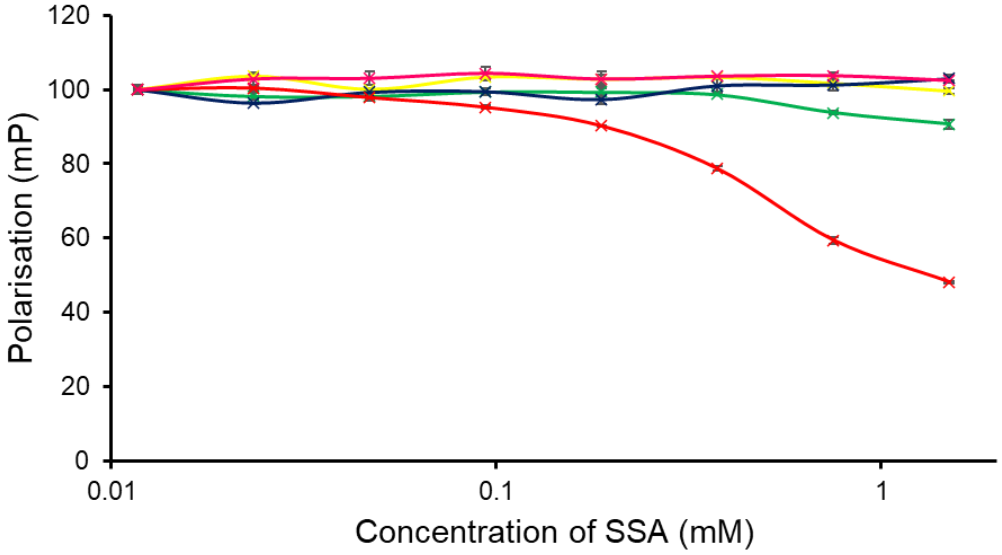

Figure S251 – Effect of SSA on FP measured in DPH-labelled *E. coli* polar vesicles at 25 °C. A target FP value of 100 mP was set to the DPH-labelled vesicles. Green = **42**, Yellow = **59**, Blue = **60,** Red = **51**, Pink = **61**. Error = standard error.

3.6 Fluorescence polarisation

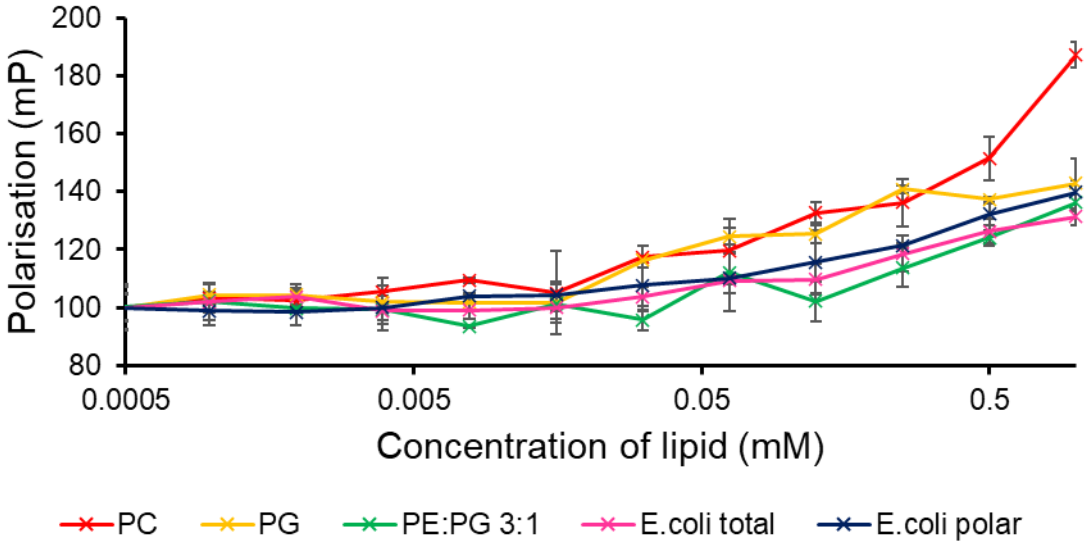

Figure S252 – Effect of fluorescent SSA **50** (0.15 mM) on FP measured in synthetic vesicles at 25 °C. A target FP value of 100 mP was set to fluorescent SSA **50** alone.

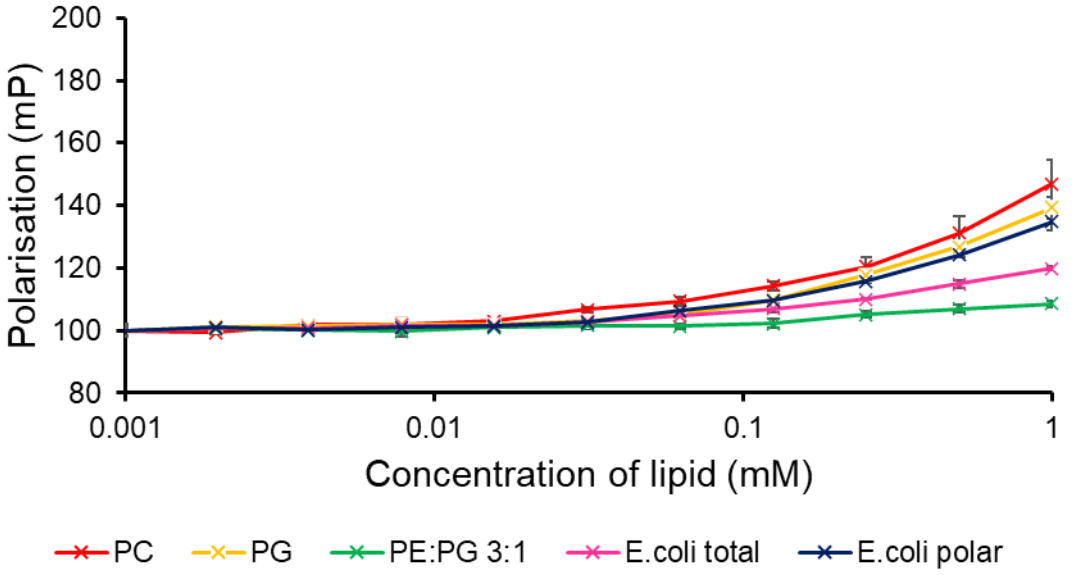

Figure S253 – Effect of fluorescent SSA **49** (0.15 mM) on FP measured in synthetic vesicles at 25 °C. A target FP value of 100 mP was set to fluorescent SSA **49** alone.

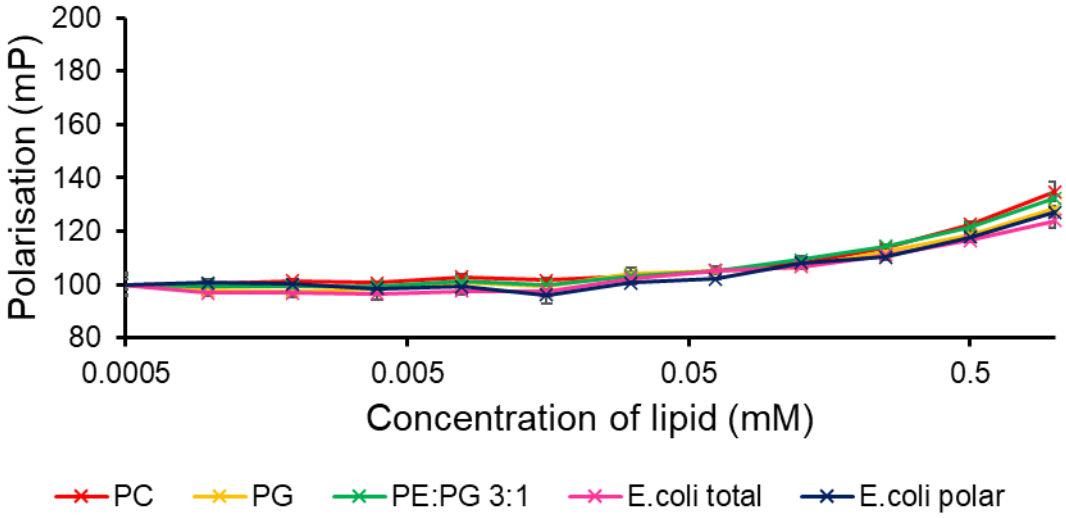

Figure S254 – Effect of fluorescent SSA **62** (0.15 mM) on FP measured in synthetic vesicles at 25 °C. A target FP value of 100 mP was set to fluorescent SSA **62** alone.

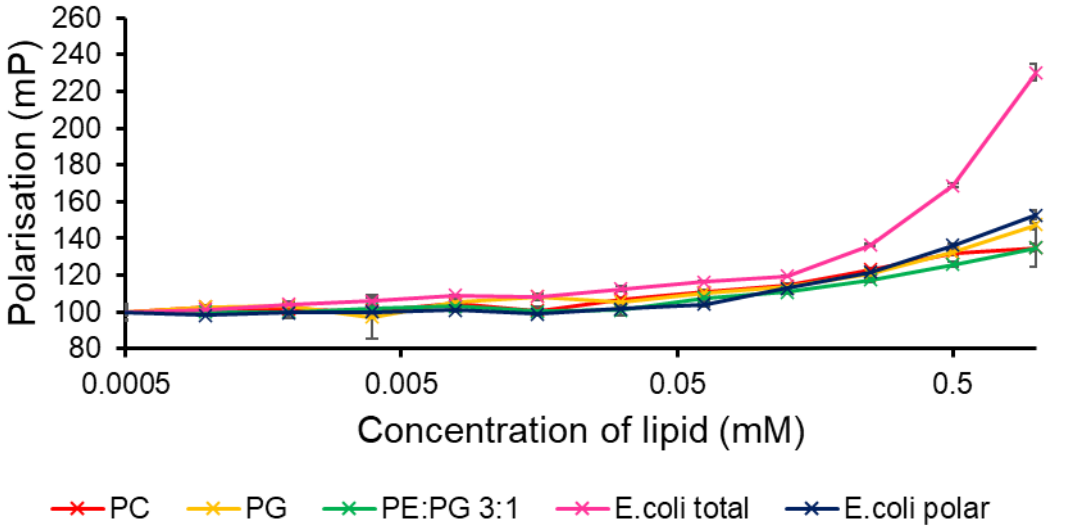

Figure S255 – Effect of fluorescent SSA **63** (0.15 mM) on FP measured in synthetic vesicles at 25 °C. A target FP value of 100 mP was set to fluorescent SSA **63** alone.

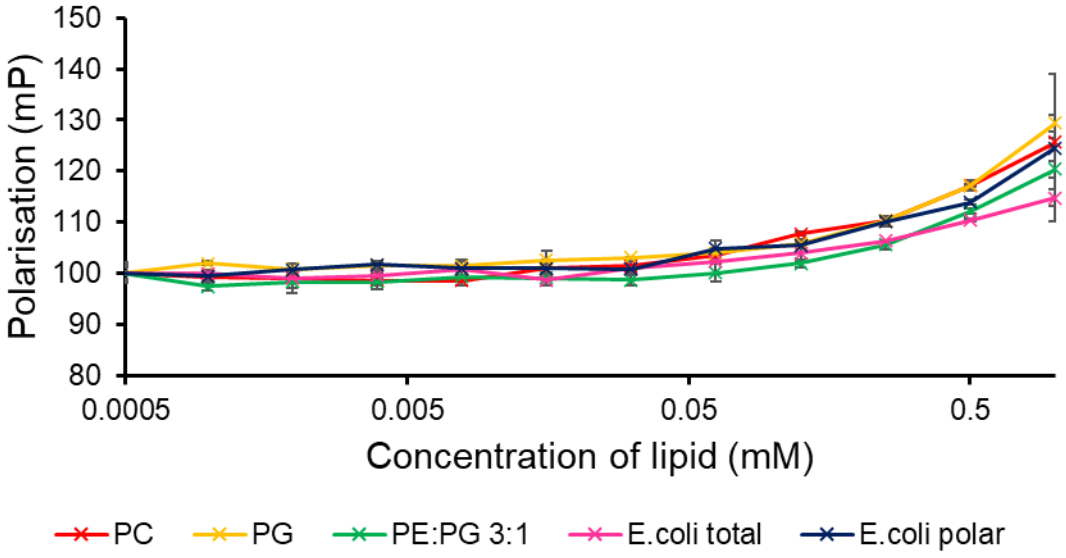

Figure S256 – Effect of fluorescent SSA **64** (0.15 mM) on FP measured in synthetic vesicles at 25 °C. A target FP value of 100 mP was set to fluorescent SSA **64** alone.

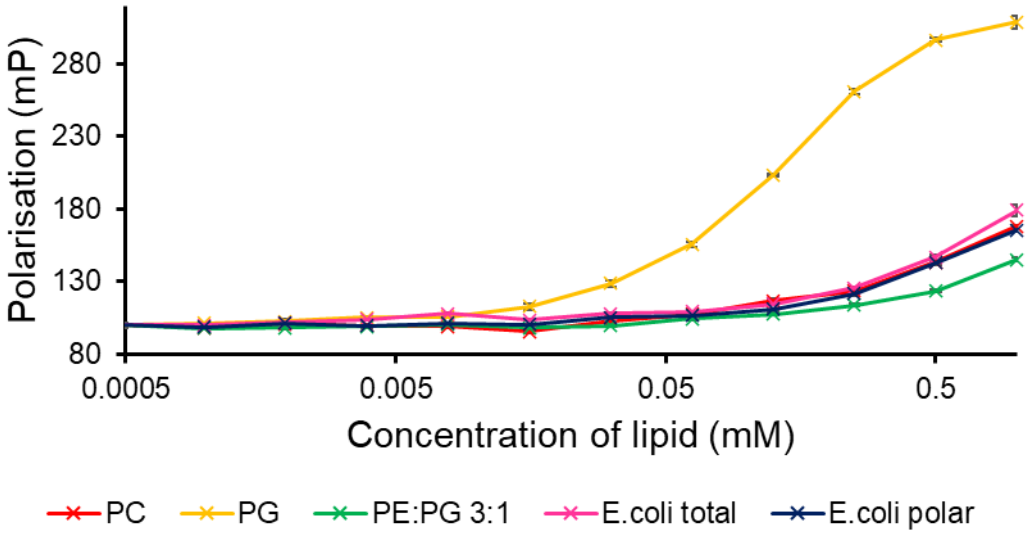

Figure S257 – Effect of fluorescent SSA **65** (0.15 mM) on FP measured in synthetic vesicles at 25 °C. A target FP value of 100 mP was set to fluorescent SSA **65** alone.

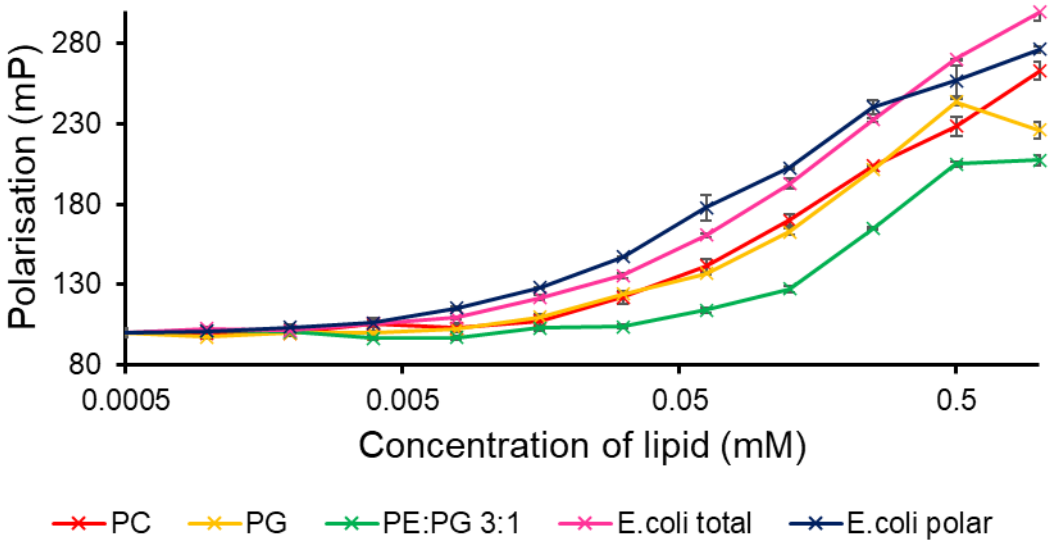

Figure S258 – Effect of fluorescent SSA **66** (0.15 mM) on FP measured in synthetic vesicles at 25 °C. A target FP value of 100 mP was set to fluorescent SSA **66** alone.

3.7 Patch clamp

3.7.1 Controls

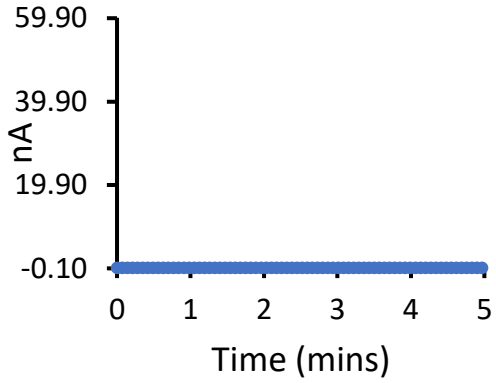

Figure S259 - Experimental recording 1 of a DPhPC bilayer at 100 mV, addition of DMSO control.

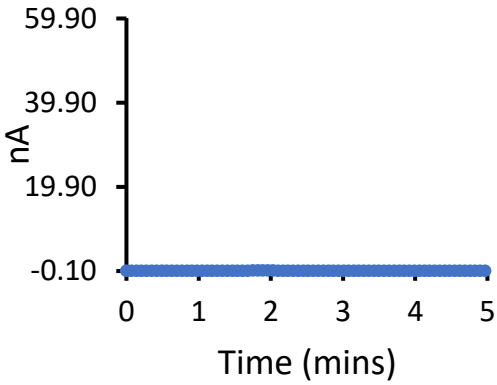

Figure S260 - Experimental recording 2 of a DPhPC bilayer at 100 mV, addition of DMSO control.

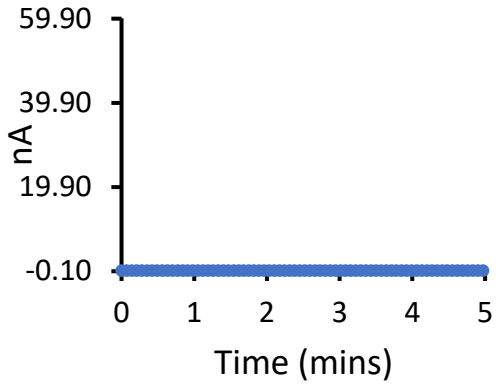

Figure S261 - Experimental recording 3 of a DPhPC bilayer at 100 mV, addition of DMSO control.

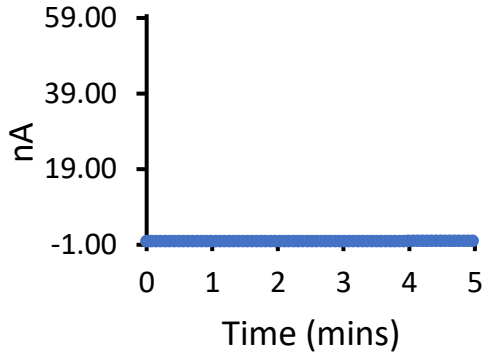

Figure S262 - Experimental recording 1 of a DPhPC bilayer at 100 mV, addition of **anionophore** (0.01 mM).

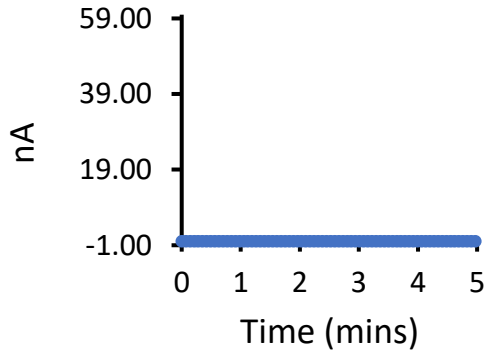

Figure S263 - Experimental recording 2 of a DPhPC bilayer at 100 mV, addition of **anionophore** (0.01 mM).

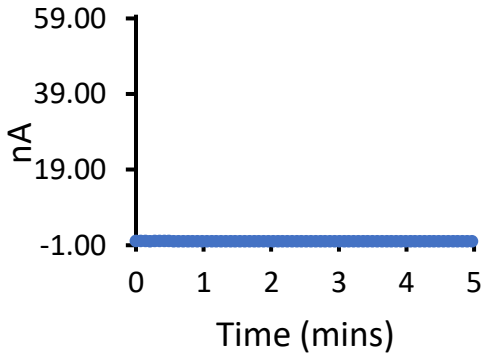

Figure S264 - Experimental recording 3 of a DPhPC bilayer at 100 mV, addition of **anionophore** (0.01 mM).

3.7.2 SSA 50

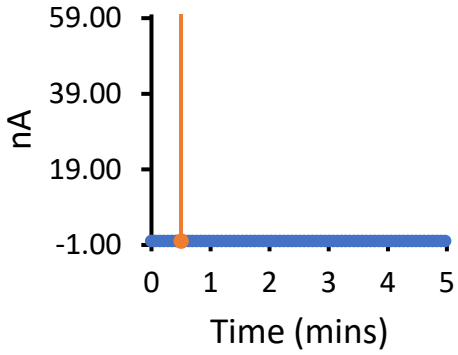

Figure S265 – Experimental recording 1 of a DPhPC bilayer at 100 mV, addition of **50** (0.1 mM) after 30 seconds indicated by the orange line.

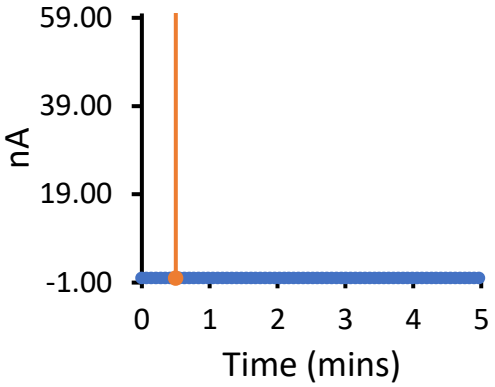

Figure S266 - Experimental recording 2 of a DPhPC bilayer at 100 mV, addition of **50** (0.1 mM) after 30 seconds indicated by the orange line.

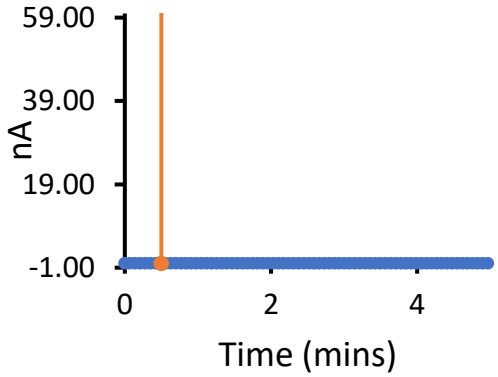

Figure S267 - Experimental recording 3 of a DPhPC bilayer at 100 mV, addition of **50** (0.1 mM) after 30 seconds indicated by the orange line.

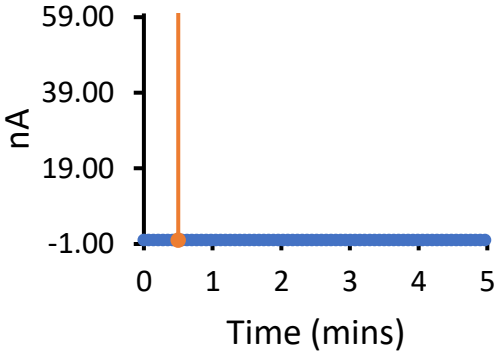

Figure S268 – Experimental recording 1 of a DPhPC bilayer at 100 mV, addition of **anionophore** (0.01 mM) at 0 seconds and **50** (0.1 mM) after 30 seconds indicated by the orange line.

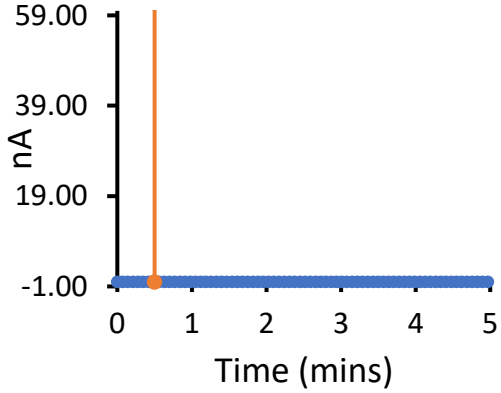

Figure S269 - Experimental recording 2 of a DPhPC bilayer at 100 mV, addition of **anionophore** (0.01 mM) at 0 seconds and **50** (0.1 mM) after 30 seconds indicated by the orange line.

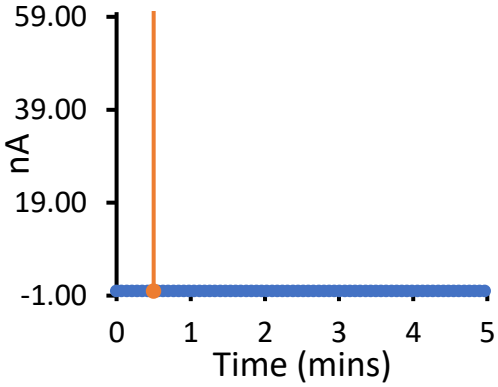

Figure S270 - Experimental recording 3 of a DPhPC bilayer at 100 mV, addition of **anionophore** (0.01 mM) at 0 seconds and **50** (0.1 mM) after 30 seconds indicated by the orange line.

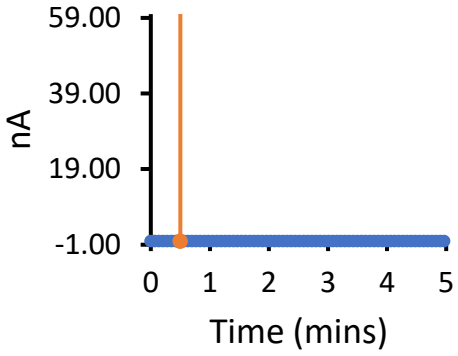

Figure S271 – Experimental recording 1 of a DPhPC bilayer at 100 mV, addition of **50** (0.25 mM) after 30 seconds indicated by the orange line.

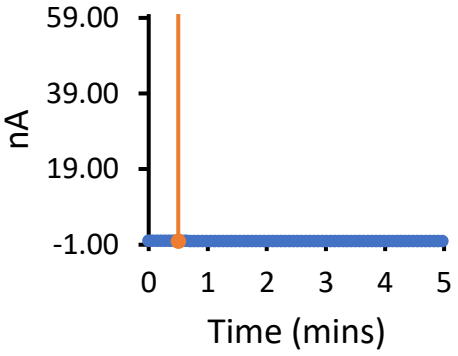

Figure S272 - Experimental recording 2 of a DPhPC bilayer at 100 mV, addition of **50** (0.25 mM) after 30 seconds indicated by the orange line.

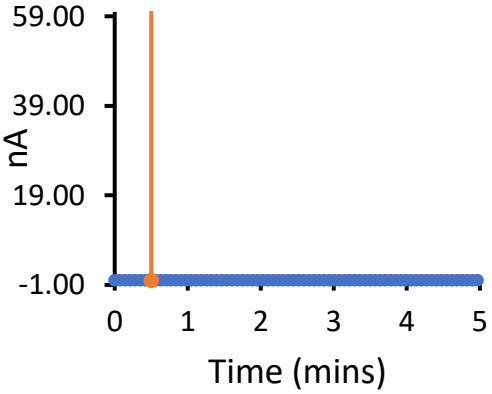

Figure S273 - Experimental recording 3 of a DPhPC bilayer at 100 mV, addition of **50** (0.25 mM) after 30 seconds indicated by the orange line.

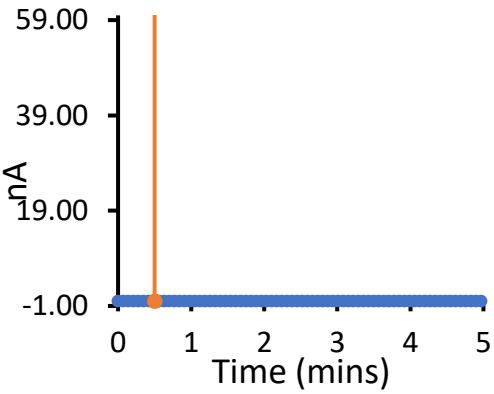

Figure S274 – Experimental recording 1 of a DPhPC bilayer at 100 mV, addition of **anionophore** (0.01 mM) at 0 seconds and **50** (0.25 mM) after 30 seconds indicated by the orange line.

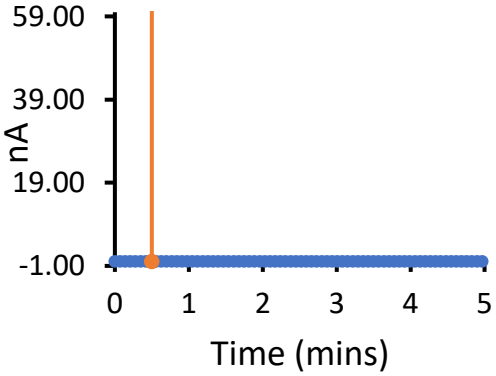

Figure S275 - Experimental recording 2 of a DPhPC bilayer at 100 mV, addition of **anionophore** (0.01 mM) at 0 seconds and **50** (0.25 mM) after 30 seconds indicated by the orange line.

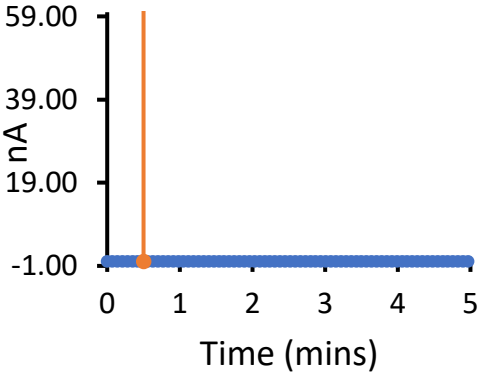

Figure S276 - Experimental recording 3 of a DPhPC bilayer at 100 mV, addition of **anionophore** (0.01 mM) at 0 seconds and **50** (0.25 mM) after 30 seconds indicated by the orange line.

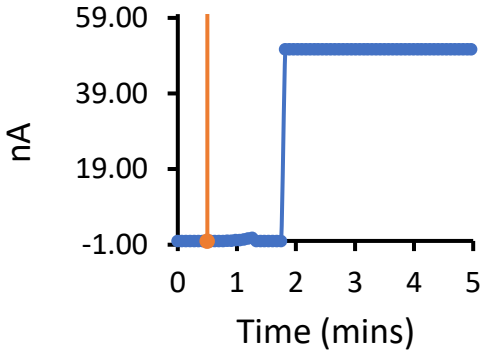

Figure S277 – Experimental recording 1 of a DPhPC bilayer at 100 mV, addition of **50** (0.375 mM) after 30 seconds indicated by the orange line.

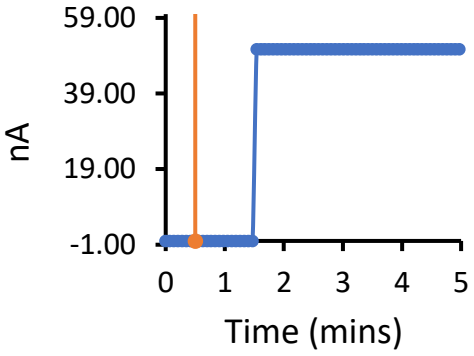

Figure S278 - Experimental recording 2 of a DPhPC bilayer at 100 mV, addition of **50** (0.375 mM) after 30 seconds indicated by the orange line.

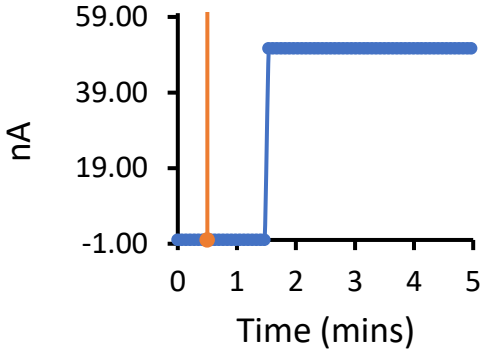

Figure S279 - Experimental recording 3 of a DPhPC bilayer at 100 mV, addition of **50** (0.375 mM) after 30 seconds indicated by the orange line.

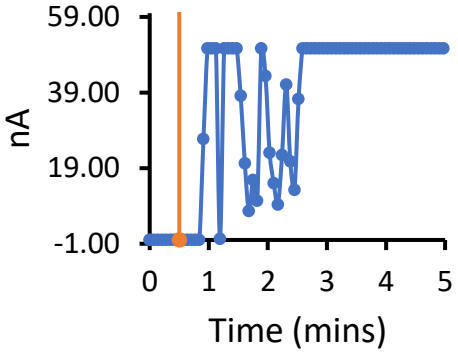

Figure S280 – Experimental recording 1 of a DPhPC bilayer at 100 mV, addition of **anionophore** (0.01 mM) at 0 seconds and **50** (0.375 mM) after 30 seconds indicated by the orange line.

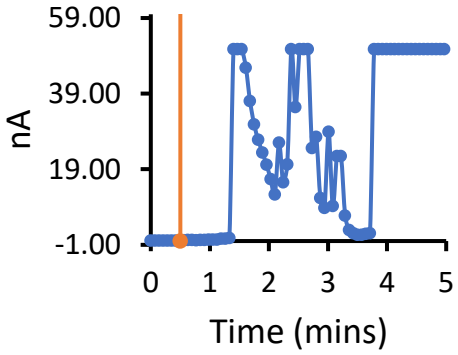

Figure S281 - Experimental recording 2 of a DPhPC bilayer at 100 mV, addition of **anionophore** (0.01 mM) at 0 seconds and **50** (0.375 mM) after 30 seconds indicated by the orange line.

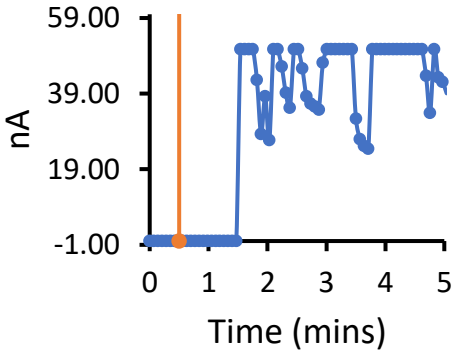

Figure S282 - Experimental recording 3 of a DPhPC bilayer at 100 mV, addition of **anionophore** (0.01 mM) at 0 seconds and **50** (0.375 mM) after 30 seconds indicated by the orange line.

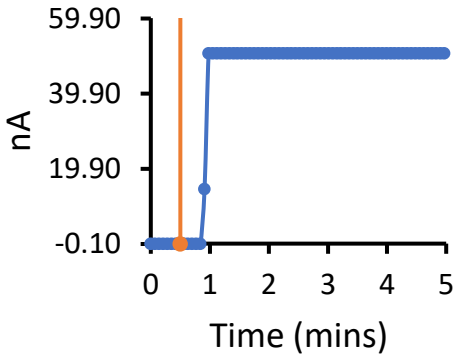

Figure S283 – Experimental recording 1 of a DPhPC bilayer at 100 mV, addition of **50** (0.5 mM) after 30 seconds indicated by the orange line.

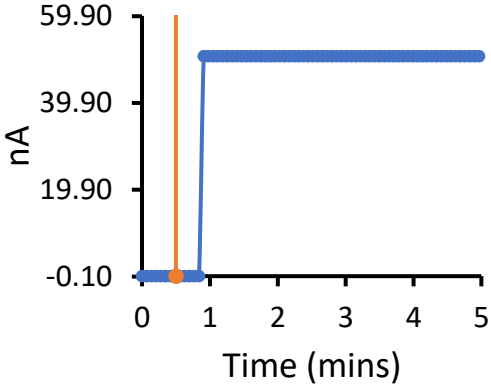

Figure S284 - Experimental recording 2 of a DPhPC bilayer at 100 mV, addition of **50** (0.5 mM) after 30 seconds indicated by the orange line.

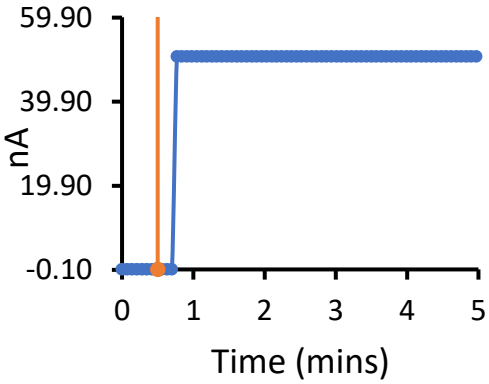

Figure S285 - Experimental recording 3 of a DPhPC bilayer at 100 mV, addition of **50** (0.5 mM) after 30 seconds indicated by the orange line.

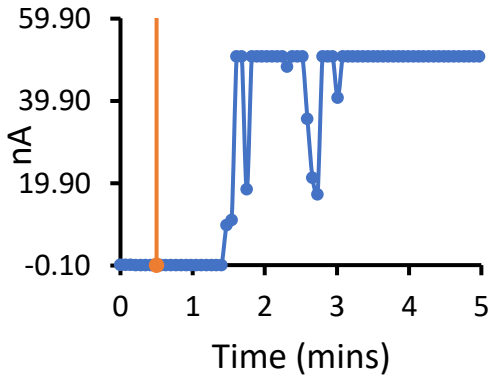

Figure S286 – Experimental recording 1 of a DPhPC bilayer at 100 mV, addition of **anionophore** (0.01 mM) at 0 seconds and **50** (0.5 mM) after 30 seconds indicated by the orange line.

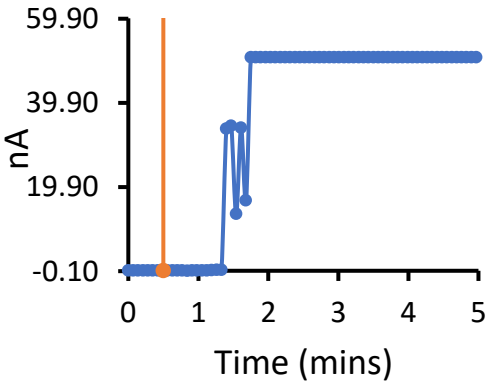

Figure S287 - Experimental recording 2 of a DPhPC bilayer at 100 mV, addition of **anionophore** (0.01 mM) at 0 seconds and **50** (0.5 mM) after 30 seconds indicated by the orange line.

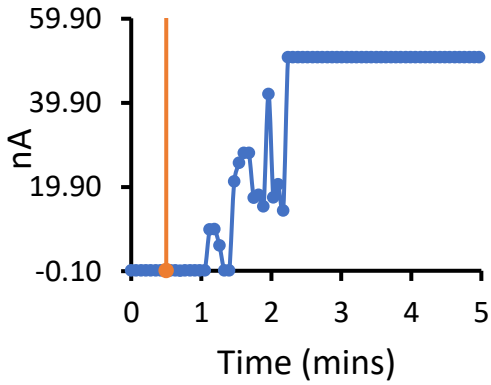

Figure S288 - Experimental recording 3 of a DPhPC bilayer at 100 mV, addition of **anionophore** (0.01 mM) at 0 seconds and **50** (0.5 mM) after 30 seconds indicated by the orange line.

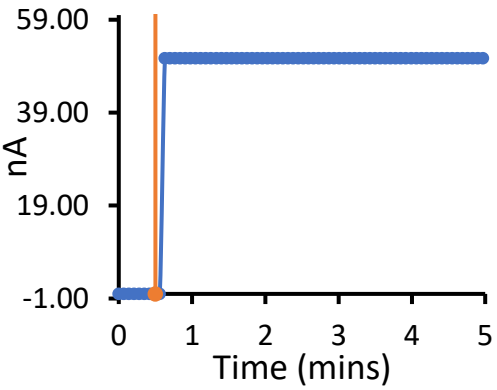

*Fi*gure S289 – Experimental recording 1 of a DPhPC bilayer at 100 mV, addition of **50** (1.00 mM) after 30 seconds indicated by the orange line.

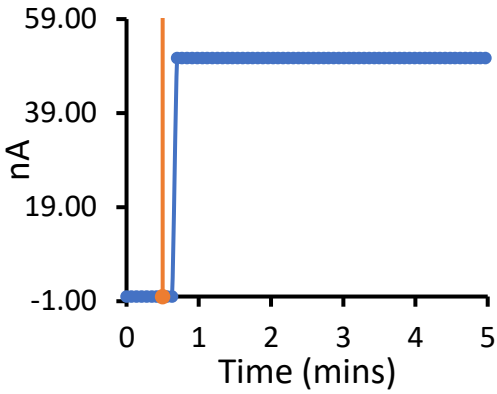

Figure S290 - Experimental recording 2 of a DPhPC bilayer at 100 mV, addition of **50** (1.00 mM) after 30 seconds indicated by the orange line.

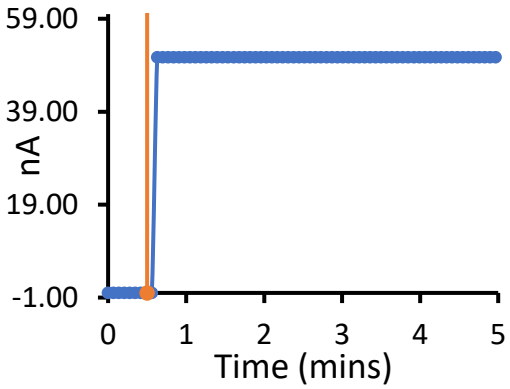

Figure S291 - Experimental recording 3 of a DPhPC bilayer at 100 mV, addition of **50** (1.00 mM) after 30 seconds indicated by the orange line.

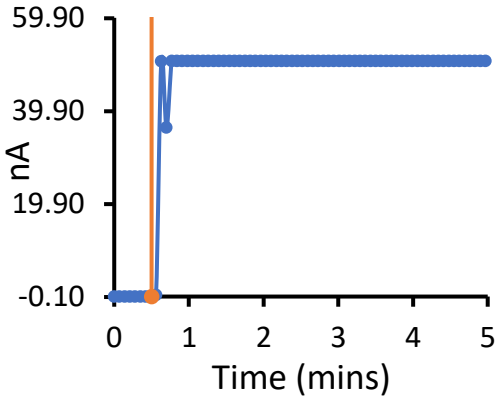

Figure S292 – Experimental recording 1 of a DPhPC bilayer at 100 mV, addition of **anionophore** (0.01 mM) at 0 seconds and **50** (1.00 mM) after 30 seconds indicated by the orange line.

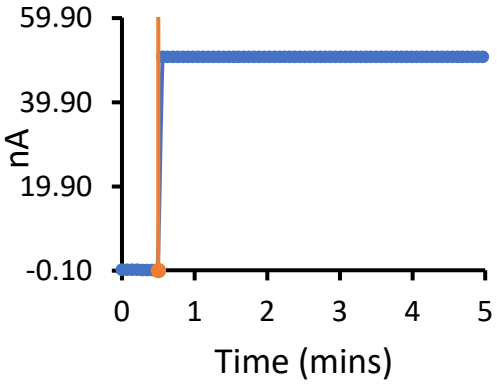

Figure S293 - Experimental recording 2 of a DPhPC bilayer at 100 mV, addition of **anionophore** (0.01 mM) at 0 seconds and **50** (1.00 mM) after 30 seconds indicated by the orange line.

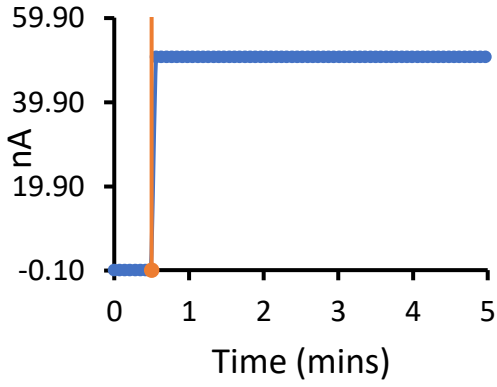

Figure S294 – Experimental recording 3 of a DPhPC bilayer at 100 mV, addition of **anionophore** (0.01 mM) at 0 seconds and **50** (1.00 mM) after 30 seconds indicated by the orange line.

3.7.3 SSA 49

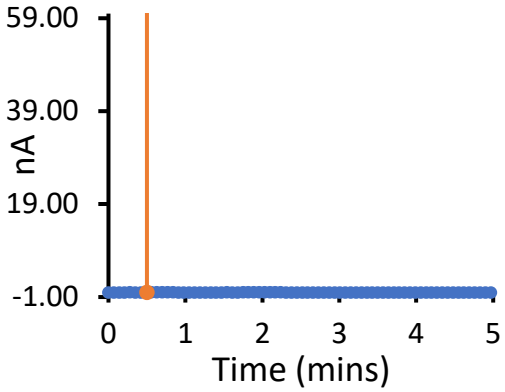

Figure S295 – Experimental recording 1 of a DPhPC bilayer at 100 mV, addition of **49** (0.1 mM) after 30 seconds indicated by the orange line.

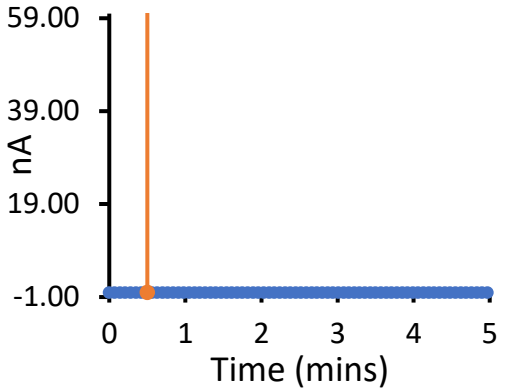

Figure S296 - Experimental recording 2 of a DPhPC bilayer at 100 mV, addition of **49** (0.1 mM) after 30 seconds indicated by the orange line.

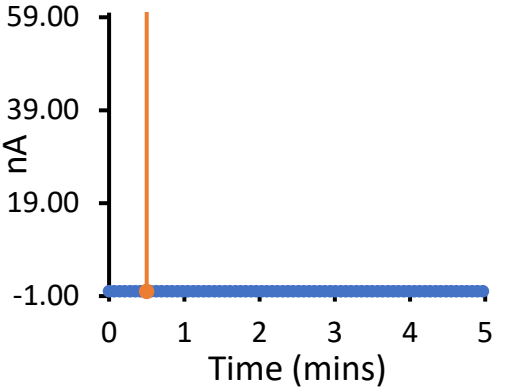

Figure S297 - Experimental recording 3 of a DPhPC bilayer at 100 mV, addition of **49** (0.1 mM) after 30 seconds indicated by the orange line.

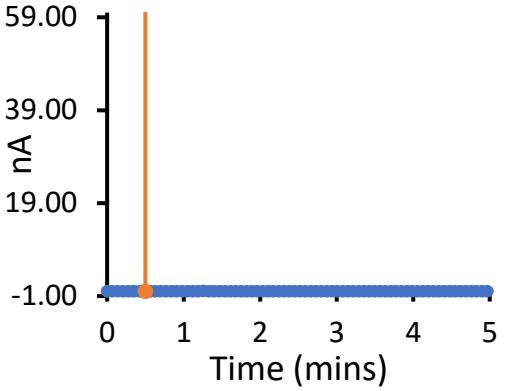

Figure S298 – Experimental recording 1 of a DPhPC bilayer at 100 mV, addition of **anionophore** (0.01 mM) at 0 seconds and **49** (0.1 mM) after 30 seconds indicated by the orange line.

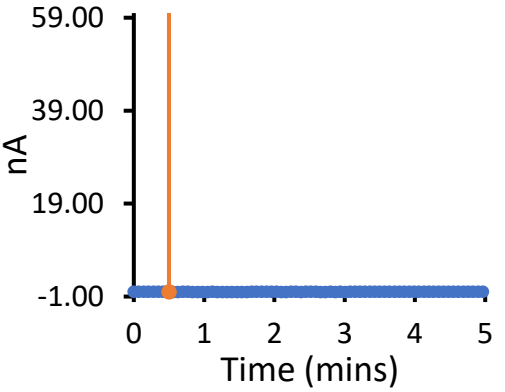

Figure S299 - Experimental recording 2 of a DPhPC bilayer at 100 mV, addition of **anionophore** (0.01 mM) at 0 seconds and **49** (0.1 mM) after 30 seconds indicated by the orange line.

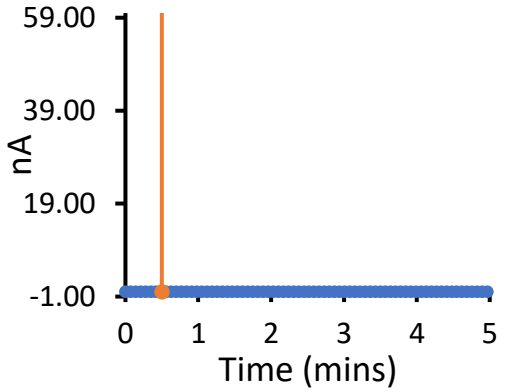

Figure S300 – Experimental recording 3 of a DPhPC bilayer at 100 mV, addition of **anionophore** (0.01 mM) at 0 seconds and **49** (0.1 mM) after 30 seconds indicated by the orange line.

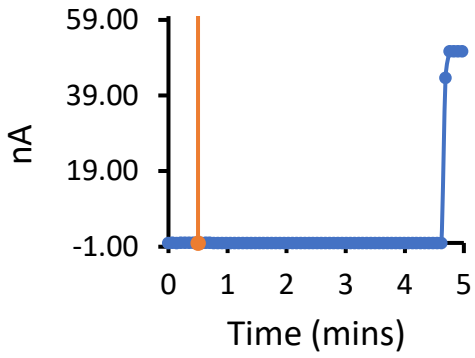

Figure S301 – Experimental recording 1 of a DPhPC bilayer at 100 mV, addition of **49** (0.25 mM) after 30 seconds indicated by the orange line.

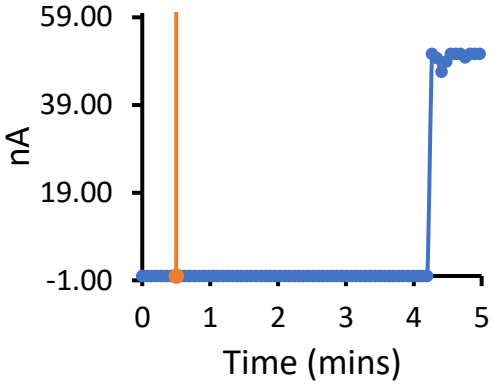

Figure S302 - Experimental recording 2 of a DPhPC bilayer at 100 mV, addition of **49** (0.25 mM) after 30 seconds indicated by the orange line.

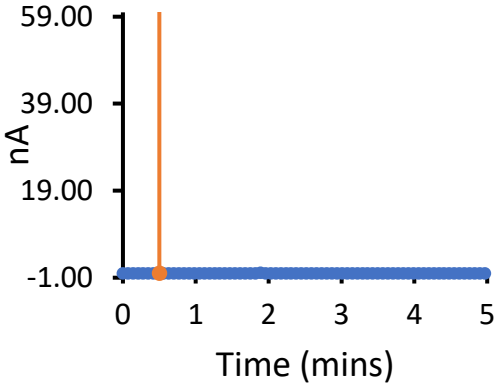

Figure S303 - Experimental recording 3 of a DPhPC bilayer at 100 mV, addition of **49** (0.25 mM) after 30 seconds indicated by the orange line.

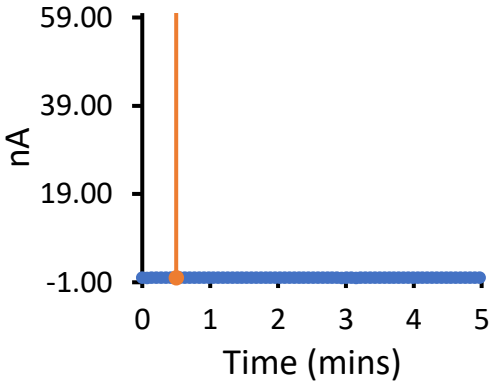

Figure S304 – Experimental recording 1 of a DPhPC bilayer at 100 mV, addition of **anionophore** (0.01 mM) at 0 seconds and **49** (0.25 mM) after 30 seconds indicated by the orange line.

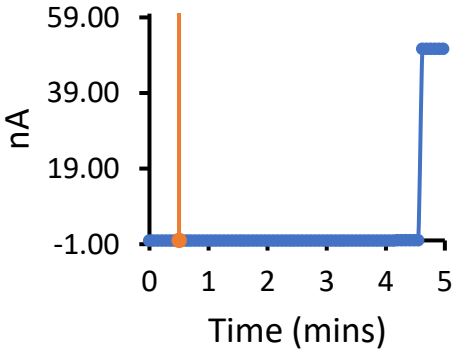

Figure S305 - Experimental recording 2 of a DPhPC bilayer at 100 mV, addition of **anionophore** (0.01 mM) at 0 seconds and **49** (0.25 mM) after 30 seconds indicated by the orange line.

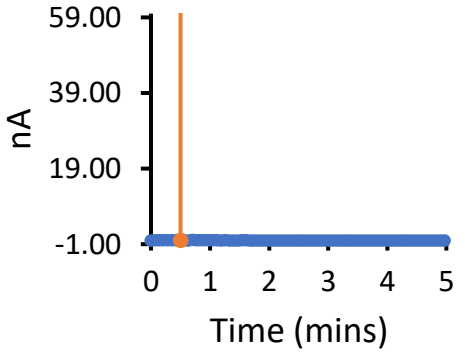

Figure S306 - Experimental recording 3 of a DPhPC bilayer at 100 mV, addition of **anionophore** (0.01 mM) at 0 seconds and **49** (0.25 mM) after 30 seconds indicated by the orange line.

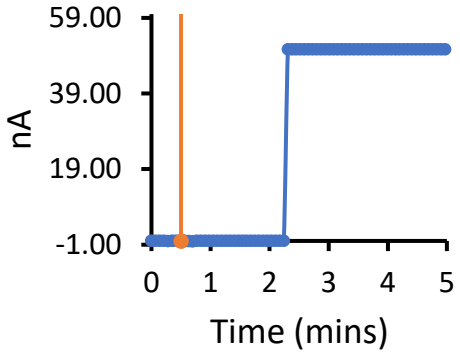

Figure S307 – Experimental recording 1 of a DPhPC bilayer at 100 mV, addition of **49** (0.375 mM) after 30 seconds indicated by the orange line.

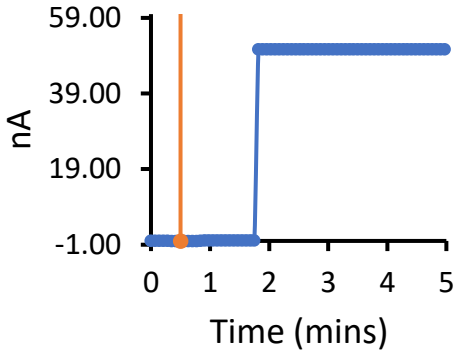

Figure S308 -– Experimental recording 2 of a DPhPC bilayer at 100 mV, addition of **49** (0.375 mM) after 30 seconds indicated by the orange line.

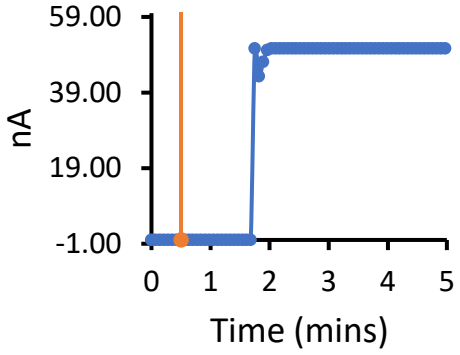

Figure S309 – Experimental recording 3 of a DPhPC bilayer at 100 mV, addition of **49** (0.375 mM) after 30 seconds indicated by the orange line.

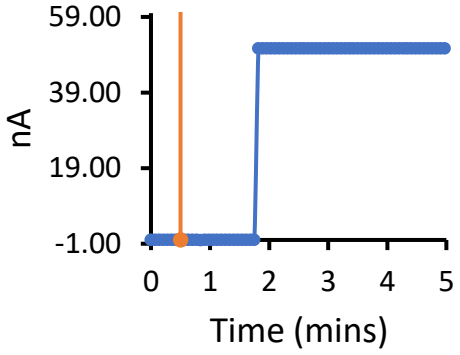

Figure S310 – Experimental recording 1 of a DPhPC bilayer at 100 mV, addition of **anionophore** (0.01 mM) at 0 seconds and **49** (0.375 mM) after 30 seconds indicated by the orange line.

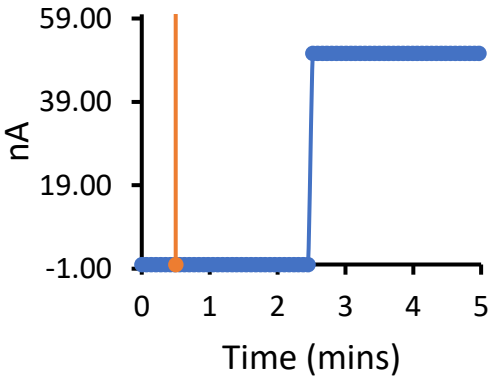

Figure S311 - Experimental recording 2 of a DPhPC bilayer at 100 mV, addition of **anionophore** (0.01 mM) at 0 seconds and **49** (0.375 mM) after 30 seconds indicated by the orange line.

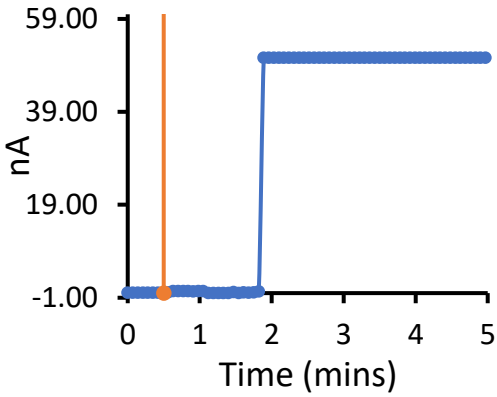

Figure S312 - Experimental recording 3 of a DPhPC bilayer at 100 mV, addition of **anionophore** (0.01 mM) at 0 seconds and **49** (0.375 mM) after 30 seconds indicated by the orange line.

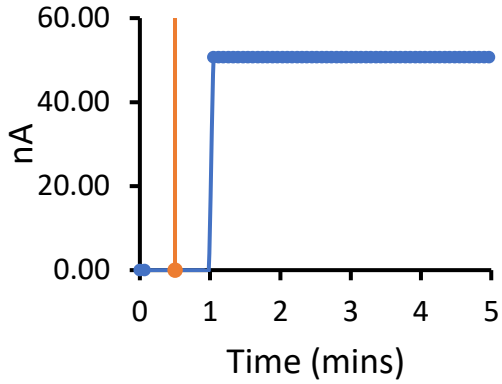

.

Figure S313 – Experimental recording 1 of a DPhPC bilayer at 100 mV, addition of **49** (0.5 mM) after 30 seconds indicated by the orange line.

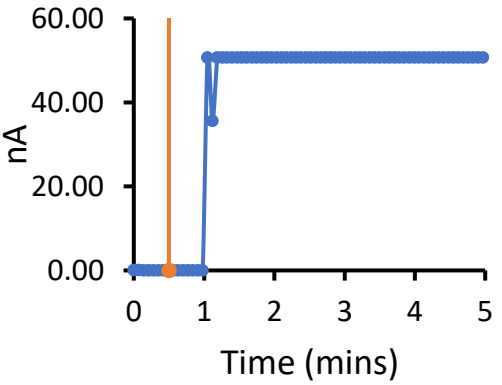

Figure S314 - Experimental recording 3 of a DPhPC bilayer at 100 mV, addition of **49** (0.5 mM) after 30 seconds indicated by the orange line.

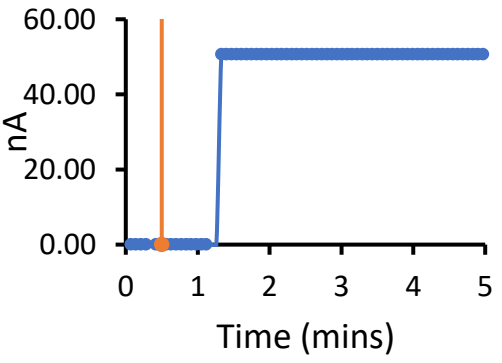

Figure S317 - Experimental recording 2 of a DPhPC bilayer at 100 mV, addition of **anionophore** (0.01 mM) at 0 seconds and **49** (0.5 mM) after 30 seconds indicated by the orange line.

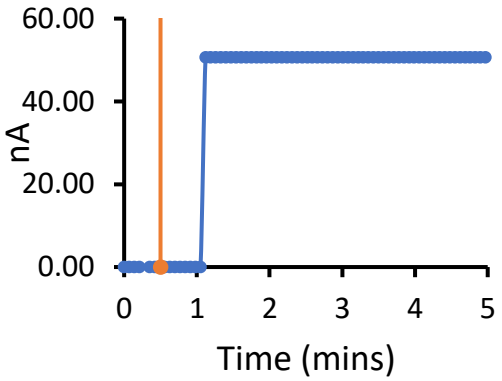

Figure S315 - Experimental recording 2 of a DPhPC bilayer at 100 mV, addition of **49** (0.5 mM) after 30 seconds indicated by the orange line.

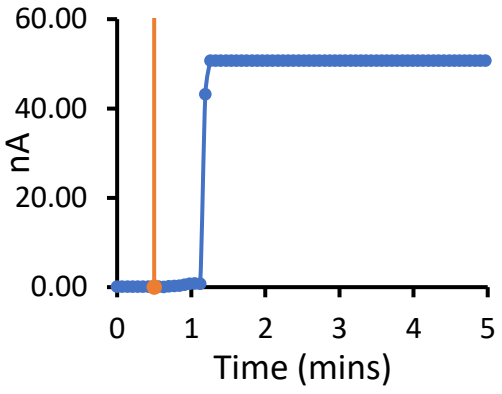

Figure S316 – Experimental recording 1 of a DPhPC bilayer at 100 mV, addition of **anionophore** (0.01 mM) at 0 seconds and **49** (0.5 mM) after 30 seconds indicated by the orange line.

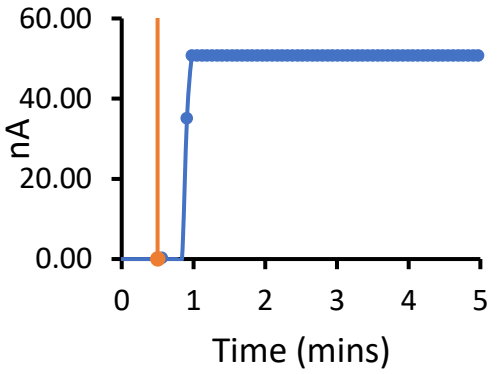

Figure S318 - Experimental recording 3 of a DPhPC bilayer at 100 mV, addition of **anionophore** (0.01 mM) at 0 seconds and **49** (0.5 mM) after 30 seconds indicated by the orange line.

3.7.4 SSA 61

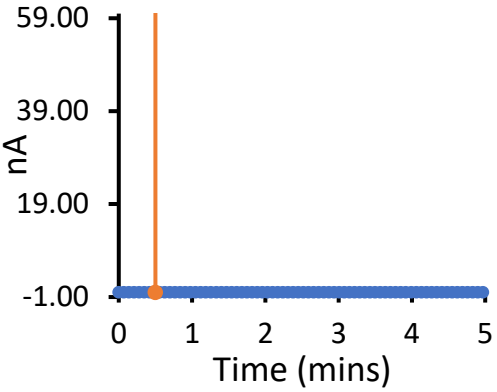

Figure S319 – Experimental recording 1 of a DPhPC bilayer at 100 mV, addition of **61** (0.1 mM) after 30 seconds indicated by the orange line.

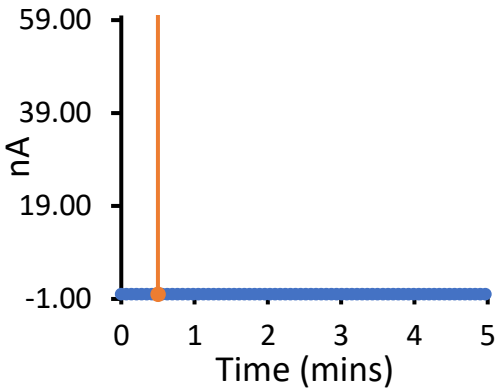

Figure S320 - Experimental recording 2 of a DPhPC bilayer at100 mV, addition of **61** (0.1 mM) after 30 seconds indicated by the orange line.

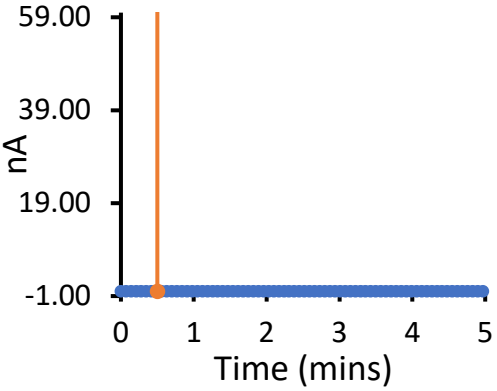

Figure S321 - Experimental recording 3 of a DPhPC bilayer at 100 mV, addition of **61** (0.1 mM) after 30 seconds indicated by the orange line.

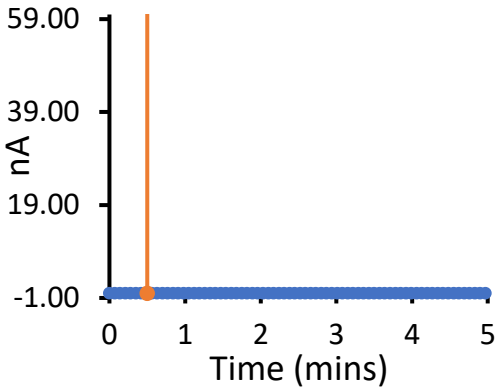

Figure S322 – Experimental recording 1 of a DPhPC bilayer at 100 mV, addition of **anionophore** (0.01 mM) at 0 seconds and **61** (0.1 mM) after 30 seconds indicated by the orange line.

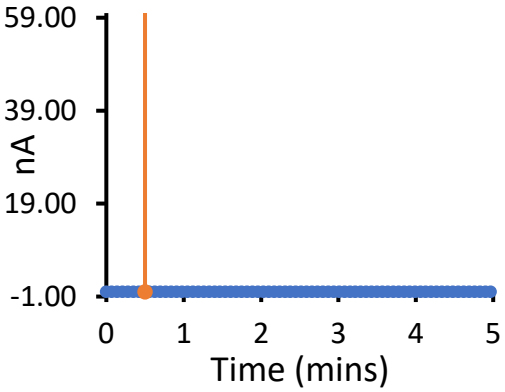

Figure S323 - Experimental recording 2 of a DPhPC bilayer at 100 mV, addition of **anionophore** (0.01 mM) at 0 seconds and **61** (0.1 mM) after 30 seconds indicated by the orange line.

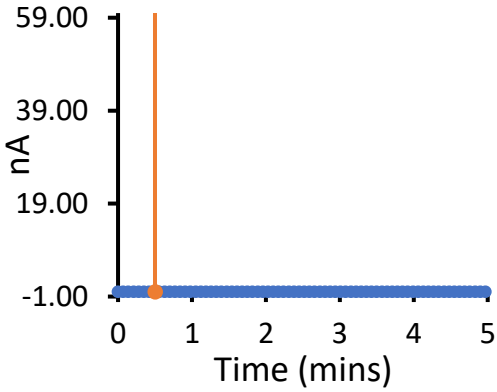

Figure S324 – Experimental recording 3 of a DPhPC bilayer at 100 mV, addition of **anionophore** (0.01 mM) at 0 seconds and **61** (0.1 mM) after 30 seconds indicated by the orange line.

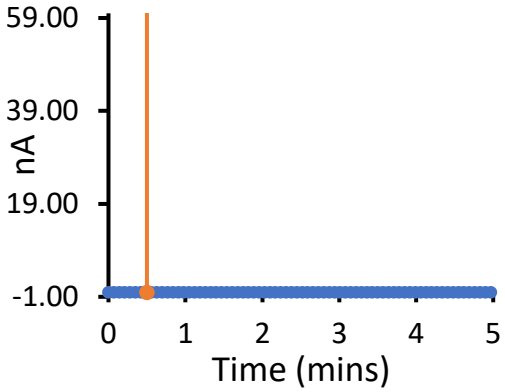

Figure S325 – Experimental recording 1 of a DPhPC bilayer at 100 mV, addition of **61** (0.25 mM) after 30 seconds indicated by the orange line.

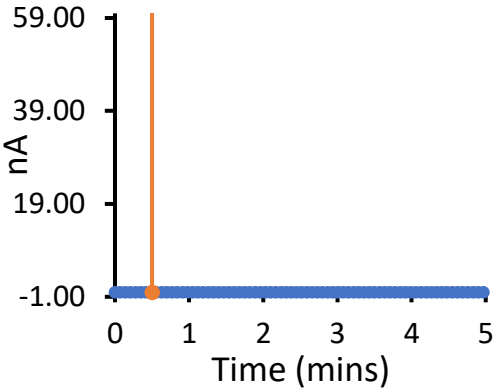

Figure S326 - Experimental recording 2 of a DPhPC bilayer at 100 mV, addition of **61** (0.25 mM) after 30 seconds indicated by the orange line.

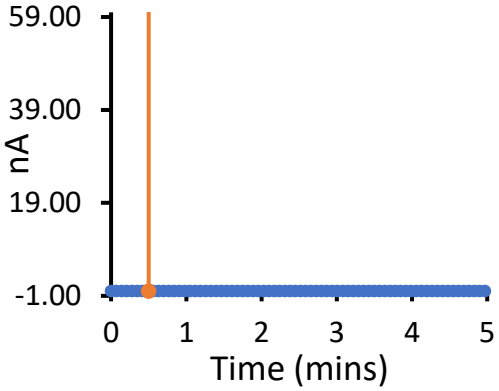

Figure S327 - Experimental recording 3 of a DPhPC bilayer at 100 mV, addition of **61** (0.25 mM) after 30 seconds indicated by the orange line.

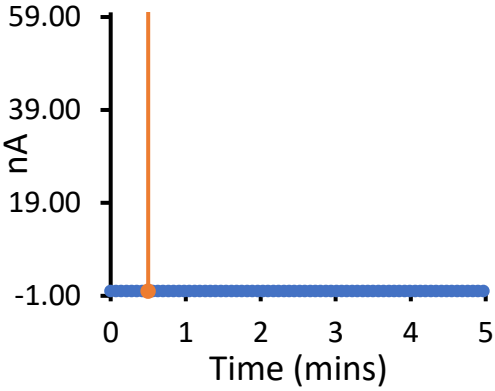

Figure S328 – Experimental recording 1 of a DPhPC bilayer at 100 mV, addition of **anionophore** (0.01 mM) at 0 seconds and **61** (0.25 mM) after 30 seconds indicated by the orange line.

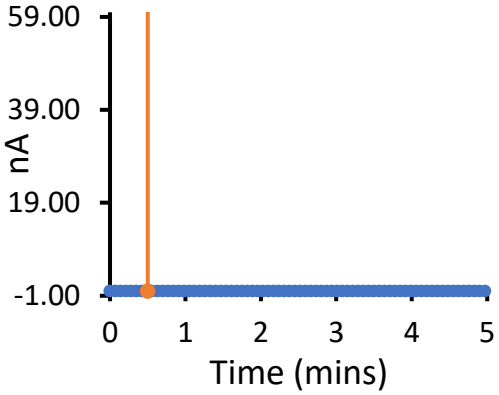

Figure S329 - Experimental recording 2 of a DPhPC bilayer at 100 mV, addition of **anionophore** (0.01 mM) at 0 seconds and **61** (0.25 mM) after 30 seconds indicated by the orange line.

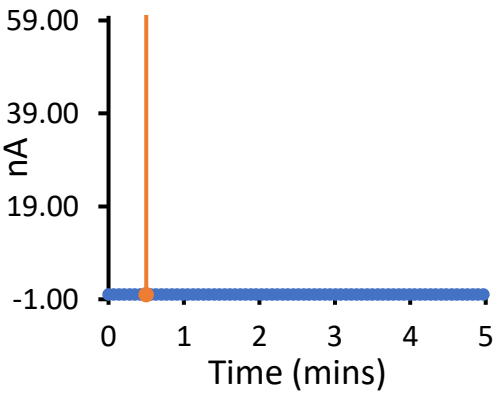

Figure S330 - Experimental recording 3 of a DPhPC bilayer at 100 mV, addition of **anionophore** (0.01 mM) at 0 seconds and **61** (0.25 mM) after 30 seconds indicated by the orange line.

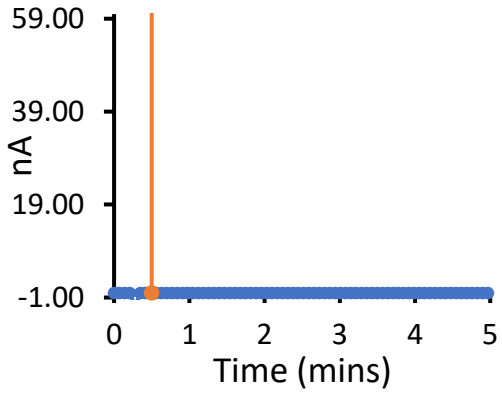

Figure S331 – Experimental recording 1 of a DPhPC bilayer at 100 mV, addition of **61** (0.375 mM) after 30 seconds indicated by the orange line.

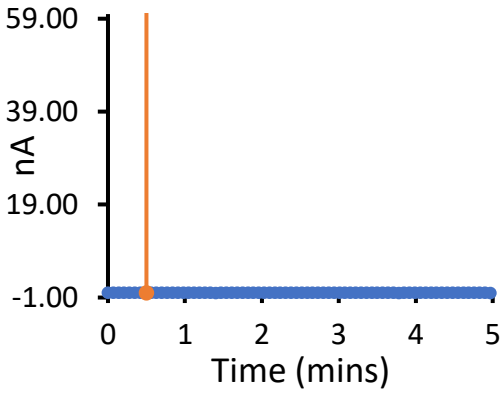

Figure S332 - Experimental recording 2 of a DPhPC bilayer atm100 mV, addition of **61** (0.375 mM) after 30 seconds indicated by the orange line.

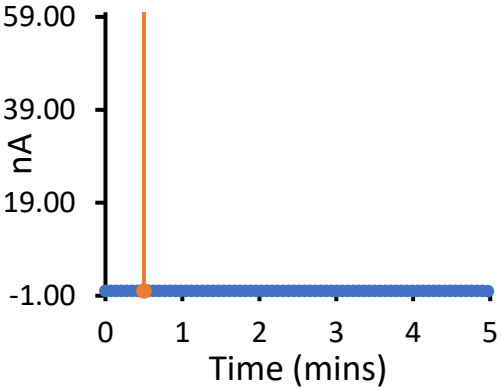

Figure S333 - Experimental recording 3 of a DPhPC bilayer at 100 mV, addition of **61** (0.375 mM) after 30 seconds indicated by the orange line.

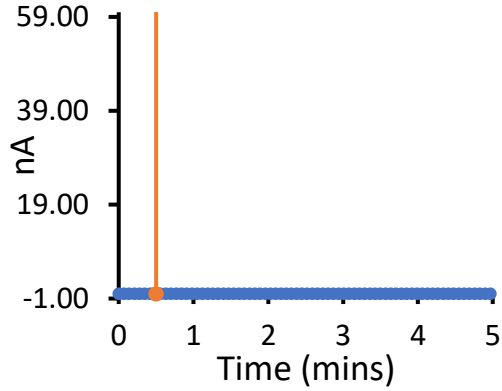

Figure S334 – Experimental recording 1 of a DPhPC bilayer at 100 mV, addition of **anionophore** (0.01 mM) at 0 seconds and **61** (0.375 mM) after 30 seconds indicated by the orange line.

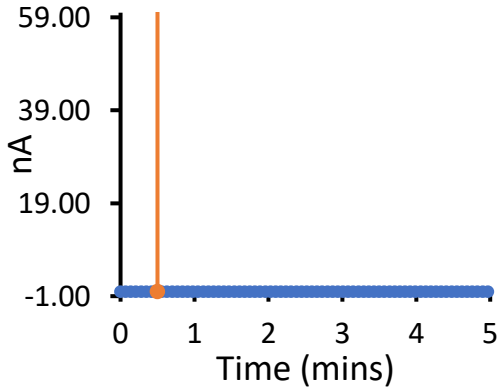

Figure S335 - Experimental recording 2 of a DPhPC bilayer at 100 mV, addition of **anionophore** (0.01 mM) at 0 seconds and **61** (0.375 mM) after 30 seconds indicated by the orange line.

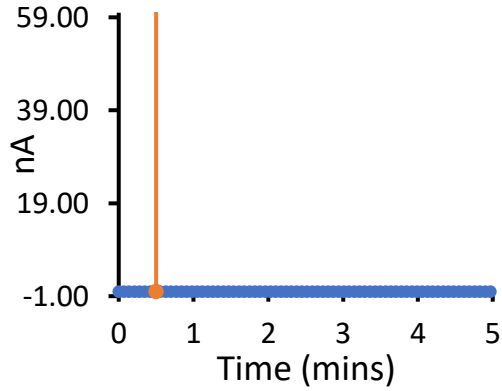

Figure S336 - Experimental recording 3 of a DPhPC bilayer at 100 mV, addition of **anionophore 4** (0.01 mM) at 0 seconds and **61** (0.375 mM) after 30 seconds indicated by the orange line.

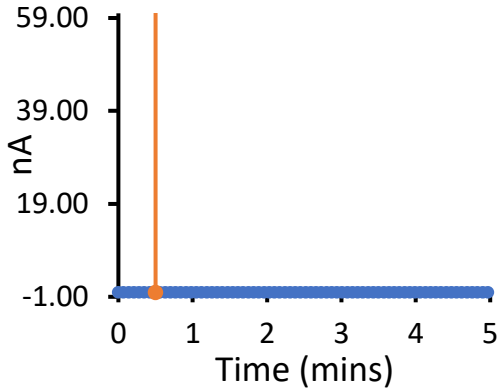

Figure S337 – Experimental recording 1 of a DPhPC bilayer at 100 mV, addition of **61** (0.5 mM) after 30 seconds indicated by the orange line.

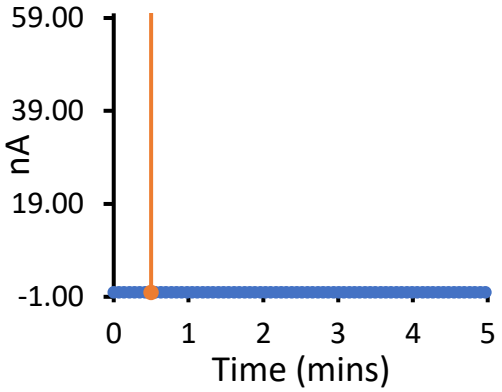

Figure S338 - Experimental recording 2 of a DPhPC bilayer at 100 mV, addition of **61** (0.5 mM) after 30 seconds indicated by the orange line.

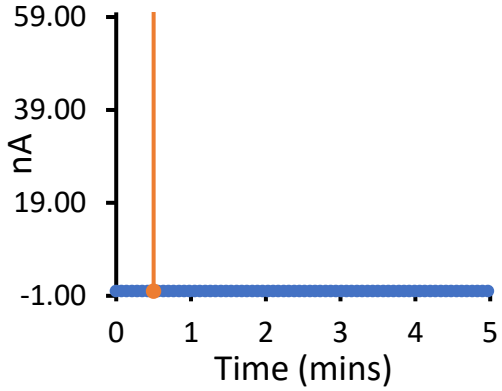

Figure S339 - Experimental recording 3 of a DPhPC bilayer at 100 mV, addition of **61** (0.5 mM) after 30 seconds indicated by the orange line.

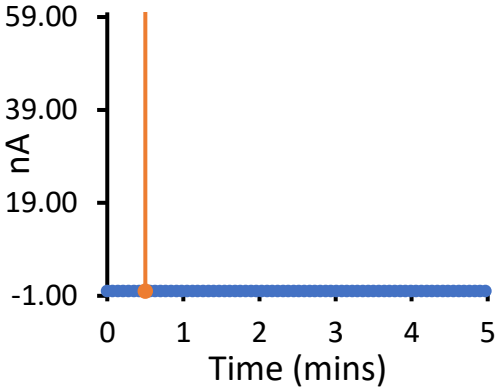

Figure S340 – Experimental recording 1 of a DPhPC bilayer at 100 mV, addition of **anionophore** (0.01 mM) at 0 seconds and **61** (0.5 mM) after 30 seconds indicated by the orange line.

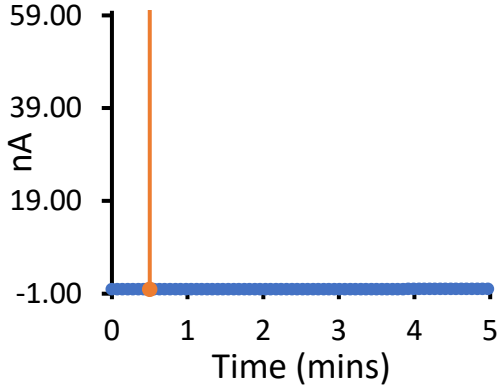

Figure S341 - Experimental recording 2 of a DPhPC bilayer at 100 mV, addition of **anionophore** (0.01 mM) at 0 seconds and **61** (0.5 mM) after 30 seconds indicated by the orange line.

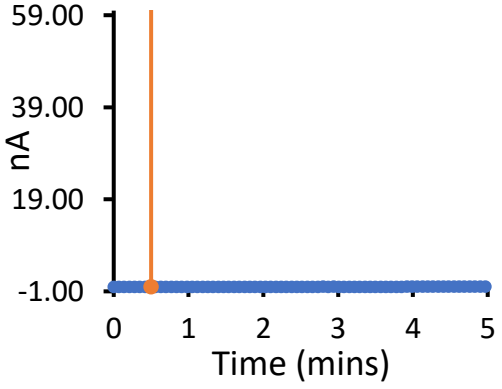

Figure S342 – Experimental recording 3 of a DPhPC bilayer at 100 mV, addition of **anionophore** (0.01 mM) at 0 seconds and **61** (0.5 mM) after 30 seconds indicated by the orange line.

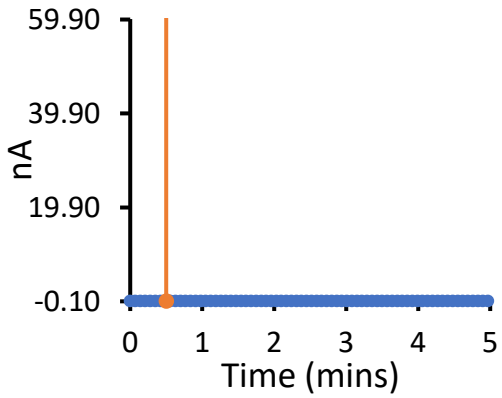

Figure S343 – Experimental recording 1 of a DPhPC bilayer at 100 mV, addition of **61** (1.0 mM) after 30 seconds indicated by the orange line.

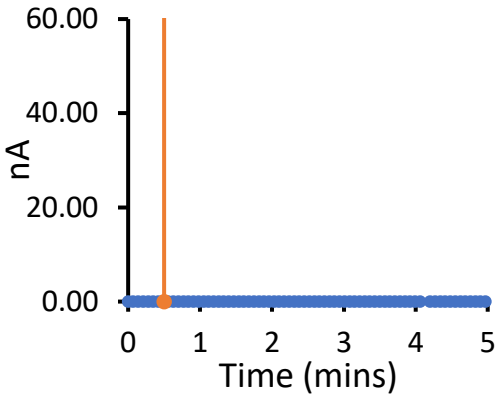

Figure S344 - Experimental recording 2 of a DPhPC bilayer at 100 mV, addition of **61** (1.0 mM) after 30 seconds indicated by the orange line.

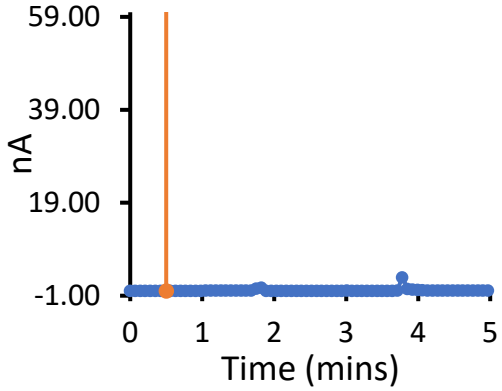

Figure S345 - Experimental recording 3 of a DPhPC bilayer at 100 mV, addition of **61** (1.0 mM) after 30 seconds indicated by the orange line.

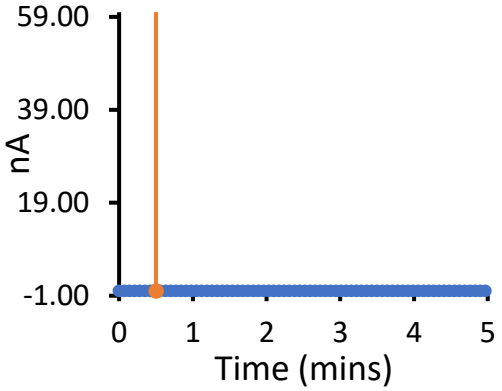

Figure S346 – Experimental recording 1 of a DPhPC bilayer at 100 mV, addition of **anionophore** (0.01 mM) at 0 seconds and **61** (1.0 mM) after 30 seconds indicated by the orange line.

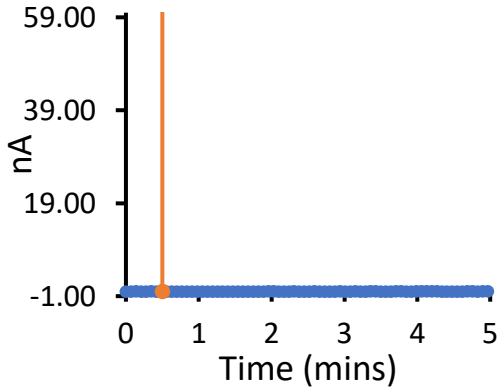

Figure S347 - Experimental recording 2 of a DPhPC bilayer at 100 mV, addition of **anionophore** (0.01 mM) at 0 seconds and **61** (1.0 mM) after 30 seconds indicated by the orange line.

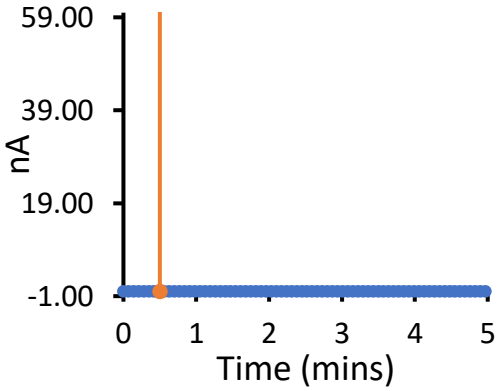

Figure S348 - Experimental recording 3 of a DPhPC bilayer at 100 mV, addition of **anionophore** (0.01 mM) at 0 seconds and **61** (1.0 mM) after 30 seconds indicated by the orange line.